UNIVERSITY OF SOUTHAMPTON

Faculty of Social, Human and Mathematical Sciences

- Mathematical Sciences -

COSMIC CONDENSATES – VORTEX, FLUXTUBE AND NEUTRON STAR DYNAMICS

by

Vanessa Graber

Thesis for the degree of Doctor of Philosophy

August 2016

UNIVERSITY OF SOUTHAMPTON

ABSTRACT

Faculty of Social, Human and Mathematical Sciences

- Mathematical Sciences -

Doctor of Philosophy

COSMIC CONDENSATES – VORTEX, FLUXTUBE AND NEUTRON STAR DYNAMICS

by Vanessa Graber

This thesis studies the implications of cosmic condensates, specifically the dynamics of superfluid vortices and superconducting fluxtubes, on astrophysical observables. Firstly, several mutual friction forces, arising from the interactions of vortices and their surroundings, are examined. We separately address mesoscopic mechanisms acting in the neutron star core and crust and analyse the strength of the resulting macroscopic mutual friction for realistic equations of state. It is obtained that the coupling strengths vary significantly within both layers and the dissipation changes drastically across the crust-core boundary. In analogy with helium experiments, the interface should therefore have important implications for the stars' rotational properties.

This is followed by an analysis of mechanisms affecting the superconducting fluxtubes. Their motion governs the dynamics of the interior magnetic field and characteristic evolution timescales are presented for a realistic equation of state. While these results are only preliminary and a more detailed analysis of additional processes is needed, they point towards deficiencies in earlier work on this subject. Subsequently, one of the fluxtube mechanisms is investigated in more detail and the analogy with normal magnetohydrodynamics is employed to derive a superconducting induction equation. While this equation differs significantly from the normal resistive equivalent, several key notions of standard magnetohydrodynamics are retained. From the field evolution equation we further deduce that the canonical fluxtube dissipation is not strong enough to explain field evolution timescales invoked from observations. To reconcile these, entirely different fluxtube coupling mechanisms are required.

Finally, the possibility of using laboratory condensates to study aspects of neutron star physics, only poorly understood, is examined. Specifically helium, ultra-cold gases and superconductors are prime candidates to mimic the behaviour of neutron stars on smaller scales. By looking at typical characteristics such as the two-fluid nature, superfluid turbulence and pinning, we find that terrestrial quantum states could provide a promising new angle to fill the missing pieces of neutron star astrophysics.

Contents

List of Figures

List of Tables

Declaration of Authorship

I, Vanessa Graber, declare that this thesis entitled *Cosmic Condensates – Vortex, Flux-tube and Neutron Star Dynamics* and the work presented within are both my own, and have been generated by me as the result of my own original research. I confirm that:

- this work was done wholly or mainly while in candidature for a research degree at the University of Southampton;
- where any part of this thesis has previously been submitted for a degree or any other qualification at the University of Southampton or any other institution, this has been clearly stated;
- where I have consulted the published work of others, this is clearly attributed;
- where I have quoted from the work of others, the source is always given. With the exception of such quotations, this thesis is entirely my own work;
- I have acknowledged all main sources of help;
- where this thesis is based on work done by myself jointly with others, I have made clear exactly what was done by others and what I have contributed myself;
- parts of this work have been published as
  - V. Graber, N. Andersson, K. Glampedakis, and S. K. Lander, "Magnetic field evolution in superconducting neutron stars," *Monthly Notices of the Royal Astronomical Society*, vol. 453, pp. 671-681, Oct 2015.
  - V. Graber, N. Andersson, and M. Hogg, "Neutron Stars in the Laboratory," *International Journal of Modern Physics D*, in preparation, 2016

Signed:.....

Date:.....

Acknowledgements

With a unique mixture of joy and despair, two extremes that sometimes lie very close to each other, the doctorate degree poses an extraordinary challenge; its dimensions often only grasped by those who have pursued a similar path. Trying to push the boundaries of what we know that little bit further, many dedicated scientists have been responsible for improving our understanding of the world around us. Following in the footsteps of some of the greatest physicists, I have spent the past four years trying to understand a small fraction of their discoveries in order to contribute a, though seemingly insignificant, piece to the bigger picture of scientific achievements. This experience, funded by the Evangelisches Studienwerk Villigst e.V. and the University of Southampton, has been extremely gratifying and many individuals have played a crucial role along the way. While I will not attempt to thank everyone who has supported me during my PhD, I want to mention a few people whose influence has been particularly important.

First of all, I want to thank my supervisor, Nils Andersson, for his guidance and help during the last four years. I appreciated your open and honest, sometimes brutally honest but always enlightening, style of teaching. I am grateful for having been given the opportunity to complete my PhD and I would like to thank you for not only sharing your knowledge of neutron stars with me but also teaching me a lot about the academic profession itself. I am sure that I will benefit from this insight in the years to come.

I am similarly grateful to the gravity group at the University of Southampton, in particular the members working on neutron stars. The friendly atmosphere, discussions, seminars and meetings have taught me a lot and always fuelled my curiosity and interest in science. I would especially like to thank Kiki Dionysopoulou, Sam Lander and Wynn Ho for their help and encouragement. I would also like to mention Kostas Glampedakis, who introduced me to the topic of superfluid neutron stars, while I was completing my physics Diplom at the Eberhard Karls University Tübingen, and suggested Southampton as a great place to do a PhD. I would further like to thank my examiners, James Vickers and Jim Sauls, who took their time to read this thesis and raised comments and questions that helped me to improve this work.

To the many other people who have made Southampton feel like home, I would like to say: it was absolutely amazing meeting you. All these trips, walks, squash battles (thank you Christian, Sandra, Stephanos and Stuart), the board game evenings (thank you Alice and Will), dinners (thank you Emma, Liana and Vallia) and conversations about life in general helped me to escape the PhD madness and kept me sane. I would

particularly like to highlight three *partners in crime*: Having started our PhD journey together and lived through the same ups and downs, they have been truly irreplaceable in the last four years. Thank you Greg, for being my always-in-the-office-neutron-star-tea-break buddy; thank you Marta, for introducing me to the best Italian comfort food (I don't think I could ever live without gnocchi, gorgonzola and walnuts again), and thank you Yafet, for asking all those philosophical questions that have been so difficult to answer but taught us a lot more than science.

Moving to a new country and leaving a large fraction of your old life behind can be a challenging adventure, but it also helps to appreciate the true friends back home. Those people that keep in contact no matter how far you live away, that you can only meet once a year but will always feel like family. While I am fortunate enough to have a few of these friends in my life, one of them deserves special mentioning. Thank you Anne for being my connection to the outside world, your numerous visits, the endless Skype conversations and all those laughs. I don't know what I would have done without that. Additionally, I would like to thank Gerrit, Johanna, Maren, Nadine and Sonja for their support during these last years and all the great times we have had together.

Finally, I would like to thank the person that has made the last four years so much better than I could have ever imagined. Thank you John for proofreading all these pages, for making the right comments that helped me write a better thesis (including our little arguments about English grammar) and for cheering me up whenever I thought I have had enough of neutron stars. I am incredibly grateful. You have helped me find my balance and become such an important part of my life; I am looking forward to all the adventures ahead.

Last but not least, I would like to thank my family, without whom I would have never gotten this far; especially my brother, Sebastian, who always encouraged me to follow my dreams understanding at the same time how difficult the academic life can be, and my parents, Ulrike and Reinhard, who a long time ago, by giving me endless difficult games, puzzles and books, have laid the foundation for my interest in solving problems and science. Thank you for always believing in me all these years and teaching me that if I work hard enough, everything is possible.

Chapter 1

Preface

While the existence of compact stars mainly composed of neutrons was originally proposed by Baade and Zwicky in 1934 [1], it took more than thirty years after their prediction until the first neutron star signal was detected by Bell and Hewish in 1967 [2]. Since then, a lot of scientific effort has been invested into understanding these compact objects. Over the last few decades, observations have shown that the properties of neutron stars are remarkably diverse [3] and complex theoretical modelling is necessary to explain the observed phenomena. This complexity arises because many different areas of physics have to be considered in order to form a comprehensive picture of the neutron star dynamics. Describing the compact objects in their entirety, hence, poses a serious challenge to theorists.

However, neutron stars offer the unique possibility to study matter under conditions that cannot be recreated on Earth. Each of these objects is expected to contain a mass comparable to the Sun's within a radius of only about twelve kilometres [4]. They exhibit extreme densities and pressures, have very high magnetic fields and short rotation periods and, thus, serve as cosmic laboratories allowing one to test new theories and discover unknown physics. Additionally, future observations will provide researchers with the ability to probe the interior of a neutron star. Asteroseismology based on gravitational and electromagnetic signals appears to be particularly promising. Telescopes such as LOFAR [5] and SKA [6] should deliver high-precision radio observations, while the gravitational wave band will be accessible with the Advanced LIGO and VIRGO detectors and possibly the third generation detector ET [7]. Moreover, X-ray timing could become attainable with the proposed ESA space mission LOFT [8]. Improving the observational methods in these different channels raises the need for more realistic theoretical models in order to decode the collected data and deduce information about the neutron stars' interior.

The research presented in this thesis aims at complementing the current theoretical framework used to describe the properties and dynamics of these compact objects. The succeeding discussion will in particular focus on the implications of cosmic neutron

star condensates [9] on observable parameters and specifically address the impact of superfluid vortices and superconducting fluxtubes [10]. As discussed in detail in the following, an advanced framework would allow the study of dynamical phenomena associated with the stars' rotational and magnetic field evolution, respectively, and help to answer some of the open questions concerning neutron star astrophysics.

The outline of this thesis is as follows: Chapter 2 will present a summary of the current understanding of neutron star physics, including the canonical picture of their structure and observational aspects. This is followed by an introduction to the classical treatment of quantum condensates based on terrestrial superfluids and superconductors (see Chapter 3). The mathematical framework building the foundation for the work on superfluid and superconducting neutron stars, i.e. magnetohydrodynamics in the presence of vortices and fluxtubes, is derived in Chapter 4. Subsequently, various mutual friction mechanisms coupling the neutron superfluids and the charged components in the star's interior and implications for the rotational evolution are addressed in Chapter 5. Whereas Chapter 6 will discuss several aspects of the stars' magnetism, in particular, the processes affecting superconducting fluxtubes, Chapter 7 introduces a new induction equation for the macroscopic magnetic field in superconducting neutron stars. This will be succeeded by a detailed investigation of the possibility to design laboratory neutron star analogues using well-known terrestrial condensates (see Chapter 8). Finally, this work on *cosmic condensates* is concluded in Chapter 9.

Chapter 2

Neutron Star Physics

Before addressing in more detail the inclusion of new physics related to the presence of macroscopic quantum condensates into theoretical neutron star models, this chapter gives a short summary of the current understanding of their formation and structure. It also briefly introduces important aspects of neutron star observations and the gravitational physics that will be referred to at multiple instances later in this thesis.

2.1 Formation Scenarios

White dwarfs, neutron stars and black holes constitute the astronomical class of compact objects. These objects are created during the final stages of stellar evolution, with the type of remnant being determined by the mass, M_*, of the progenitor. Whereas the lighter ones will generate white dwarfs, neutron star and black hole formation requires an initial mass larger than eight solar masses, i.e. $M_* > 8\,M_\odot$ [4], where $M_\odot$ denotes the mass of the Sun. Neutron stars, in particular, are thought to form in two different environments. These formation mechanisms are crucial for understanding their extreme physical characteristics.

2.1.1 Core-collapse supernovae

The first scenario is the stellar explosion of a single massive star that has undergone all possible burning stages; it has run out of fuel and is composed of a shell-like structure with a heavy iron core in the centre. Up to this point, the main sequence star has spent most of its life in hydrostatic equilibrium, because the thermal energy, released during the burning, stabilised the star against its self-gravity. As iron has the lowest binding energy per nucleon, the production of heavier elements would require energy and cannot take place. Therefore, the mass of the iron core increases until the Chandrasekhar mass limit of $\sim 1.44\,M_\odot$ is reached [11]. For higher masses, the electron degeneracy pressure, a result of Pauli's exclusion principle for fermions, can no longer support the

star against the gravitational attraction and it undergoes a sudden collapse [4]. The contracted outer layers fall onto the compact iron core and bounce off, producing an outward propagating shock wave. The gravitational energy is transferred to the ejected matter and powers a supernova explosion. These events release about 10^{53} erg [12] and belong to the most energetic phenomena in our visible Universe.

The exact supernova mechanism is not fully understood and detailed numerical simulations are computationally expensive. However, it is known that neutrinos, formed at high pressures in the iron core, are playing a key role in keeping the shock wave alive. Together with a large number of neutrons, they are generated by electron capture, i.e. inverse beta decay, described by the following balance equation

$$p + e^- \rightarrow n + \nu_e. \tag{2.1}$$

Due to their weakly interacting nature, neutrinos can escape the star and intensify the explosion [13]. The neutrons, on the other hand, are compressed in the centre creating neutron-rich, highly degenerate matter. Like the electrons, they are fermions that have to obey the Pauli principle. It is this neutron degeneracy pressure that stabilises the compact remnant against further collapse and allows it to cool down and reach a new equilibrium state. The ejected matter is often observed as a large gas halo such as the Crab nebula or Cassiopeia A. Young neutron stars have been found at the centre of both structures [14, 15].

Finally, if the amount of material ejected in the supernova process is not sufficient, more mass is accreted onto the central core. It will reach the Tolman-Oppenheimer-Volkoff (TOV) limit [16, 17] and the degeneracy pressure of the neutrons can no longer support a stable configuration; the neutron star collapses to a black hole. The TOV limit is therefore equivalent to the Chandrasekhar limit of an electron gas. However, it is not uniquely defined, as it depends on the unknown equation of state of the nuclear matter inside neutron stars (see Subsection 2.2.1).

2.1.2 Binary systems

The second scenario assumes that neutron stars are created in binary systems. The formation and evolution of these systems are rather complicated and not fully understood, but the idea is as follows: Initially, a binary system of two main sequence stars with different masses is considered. The more massive one starts to evolve first and, ultimately, enters a red-giant phase, causing an enormous increase in its radius. If this *donor* star is able to fill its entire Roche lobe (the region around the star inside which gas is bound by its gravitational attraction), then matter is transferred to the companion star labelled the *acceptor*. This describes the so-called *Roche-lobe overflow* [18]. If the material cannot be accreted wholly onto the acceptor's surface, its Roche lobe is filled as well, creating a situation where both stars are situated in a common envelope

[19]. The motion of the two stars in this stage is highly dissipative and causes the loss of angular momentum, i.e. the orbital distance of the binary decreases, resulting in the ejection of the envelope. If the initial donor mass is high enough, the star then collapses and explodes. This asymmetric supernova creates a neutron star or a black hole [18] and results in the formation of a low-mass X-ray binary (LMXB), i.e. a close binary system containing a compact object and a main sequence star. Neutron stars in such systems are strongly influenced by the presence of the companion and are commonly observed as millisecond pulsars (see Subsection 2.3.2).

The remaining main sequence star, the original acceptor, subsequently evolves into a second compact object. These compact binaries are strongly affected by general relativity and serve as an important testing tool for the strong gravity regime. In 1993, Hulse and Taylor were awarded the Nobel Prize in Physics for the discovery of the first binary pulsar, PSR B1913+16, and the first indirect detection of gravitational waves [20, 21]. Double neutron stars are further considered one of the most promising sources for the direct detection of continuous gravitational waves [22] (see Subsection 2.3.4).

2.2 Neutron Star Structure

Since direct access to the neutron star interior through gravitational observations is not yet available, information has to be deduced from electromagnetic data and theoretical modelling. As this only allows an indirect approach to studying the behaviour of matter and underlying processes, a lot of questions are still unanswered. Nonetheless, calculations of nuclear properties and certain observations indicate that the density varies over several orders of magnitude from the outermost region to the neutron stars' centre with the matter being highly stratified [23] (see Figure 2.1). The exact positions of the interfaces, however, are model-dependent and not known.

The following subsections describe a neutron star that has reached its thermal equilibrium and has cooled down to 10^6 to 10^8 K [24], well below its Fermi temperature, $T_\mathrm{F} \approx 10^{12}$ K [4]. This temperature is related to the Fermi energy, $E_\mathrm{F} = k_\mathrm{B}\, T_\mathrm{F}$, where k_B is the Boltzmann constant, that represents the quantum mechanical ground state of a Fermi gas at zero temperature.

2.2.1 Equation of state

The global structure of a neutron star is obtained by solving Einstein's equations [25]. Treating the star as a non-rotating, spherical, ideal fluid fixes the space-time to be spherically symmetric. With these specific constraints, one obtains the relativistic Tolman-Oppenheimer-Volkoff equation of hydrostatic equilibrium [16, 17],

$$\frac{\mathrm{d}P(r)}{\mathrm{d}r} = -\frac{G}{r^2}\left[\rho(r) + \frac{P(r)}{c^2}\right]\left[M(r) + 4\pi r^3 \frac{P(r)}{c^2}\right]\left[1 - \frac{2GM(r)}{c^2 r}\right]^{-1}, \qquad (2.2)$$

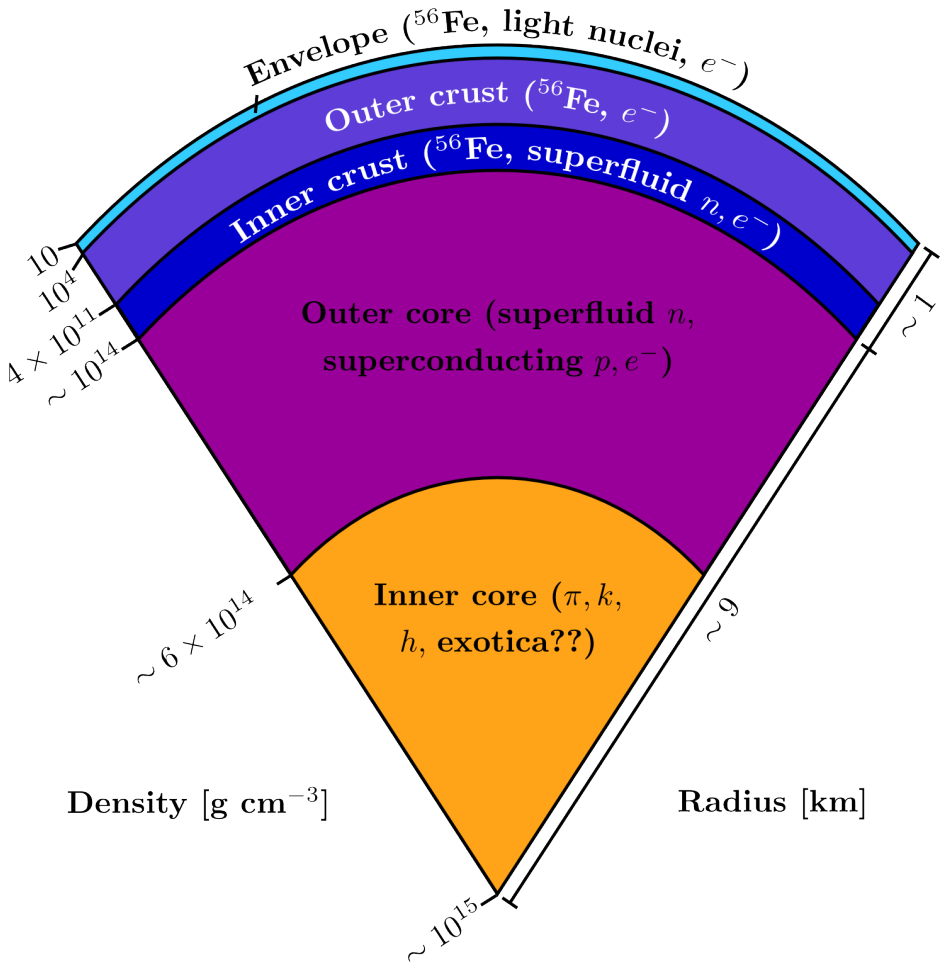

Figure 2.1: Illustration of the cross-section of a neutron star. The outermost layer is the envelope containing iron atoms, light nuclei and relativistic electrons. It is followed by the outer core that is composed of an iron lattice and a relativistic electron gas. For higher densities the neutrons start to drip out of the nuclei creating a superfluid neutron gas. At the transition to the core, all lattice structures have vanished and pure nuclear matter, consisting of superfluid neutrons, superconducting protons and relativistic electrons, is expected. At very high densities, in the centre of the neutron star, the state of matter is not known but pions π, kaons k, hyperons h or other exotic phases could be present.

where $P(r)$ and $\rho(r)$ are the pressure and density, respectively, and $M(r)$ is the mass within the radius r. G and c denote the universal gravitational constant and the speed of light, respectively. In order to solve Equation (2.2) and, ultimately, determine the structure of a neutron star, an equation of state (EoS) relating the pressure and density, i.e. $P(\rho)$, is needed. This relation is one of the key unknowns in modelling neutron stars, as it requires detailed knowledge of the microphysical interactions between single particles. Instead of being given in analytical form, EoSs are usually presented in tabulated form. For a recent review see Lattimer and Prakash [26].

Equations of state differ mainly at high densities and low temperatures. In those regions, various assumptions can be made about the forces between individual nucleons. EoSs predict different radii, R, and maximum masses, $M_{\max}$, and are usually separated

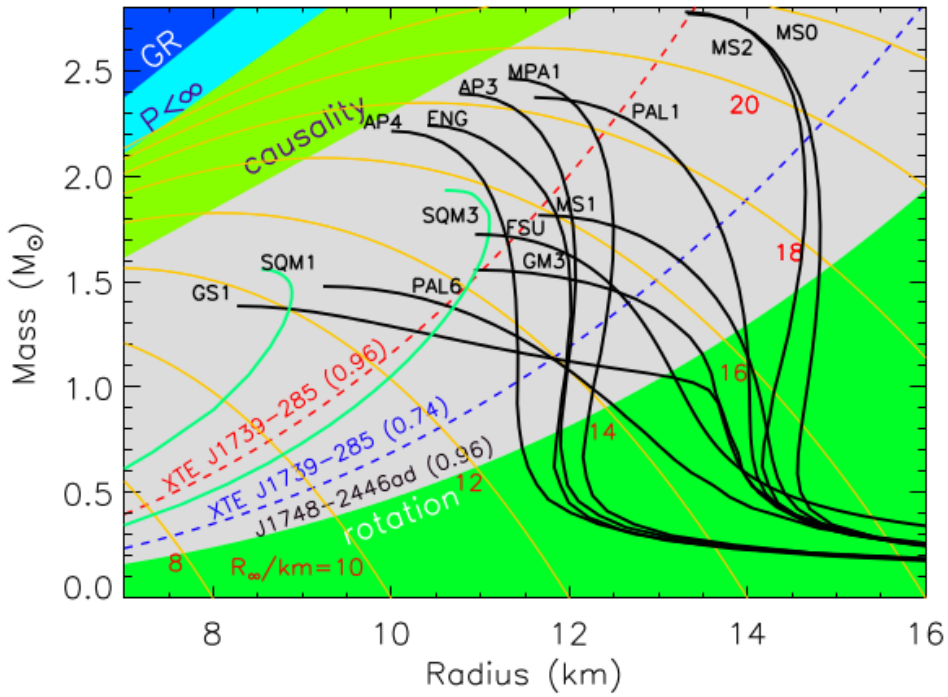

Figure 2.2: Mass-radius relations for different EoSs. Causality excludes the upper green region, whereas the lower green one is a restriction from the period measurement of PSR J1748-2446ad [27]. The figure is reproduced from Lattimer and Prakash [26] (p. 117).

into two classes, so-called *soft* and *stiff* equations of state. The former describe matter that is compressible to some extent and are characterised by larger central densities, smaller radii and maximum masses. Stiff equations of state, on the other hand, are used for relatively incompressible matter and produce smaller central densities, larger radii and masses. Mass-radius trajectories for different equations of state are shown in Figure 2.2. The majority of them predict maximum masses in the range of 2 to 2.5 $M_\odot$. The existence of $M_{\max}$ is a purely relativistic effect that results from the denominator of the Tolman-Oppenheimer-Volkoff equation (2.2) and cannot be found in Newtonian gravity. Therefore, precise measurements of the neutron star masses, radii and rotation periods can put very stringent limits on the relativistic equations of state or even rule out certain models [28]. For example, the most massive neutron star known to date is the pulsar PSR J0348+0432, located in a binary system with a white dwarf. It has a mass of $2.01 \pm 0.04\, M_\odot$ [29], a value close to the maximum mass prediction of several EoSs. Moreover, the pulsar PSR J1748-244ad, with a rotation frequency of 716 Hz [27] it is the fastest-spinning pulsar known, constrains the maximum radius of a neutron star and excludes the green region at the bottom of $M(R)$-diagram. Additionally, equations of state should not violate causality, implying that the speed of sound, c_{s}, in the stars' interior cannot exceed the speed of light, i.e. $c_{\mathrm{s}}^2 = \mathrm{d}P/\mathrm{d}\rho \leq c^2$. Therefore, the light green region in the upper left corner of Figure 2.2 forms another boundary for theoretical models.

A typical choice for the mass and the radius for a neutron star is $M \approx 1.4\,M_\odot$ and $R \approx 10\,\mathrm{km}$, respectively. These canonical parameters will also be adopted in the remainder of this thesis, when numerical values are calculated.

2.2.2 Envelope

The outermost layer of a neutron star is only a few decimetres thick and has a density in the range of 10 to $10^4\,\mathrm{g\,cm^{-3}}$ [30]. This envelope consists of iron atoms and lighter nuclei which are permeated by relativistic electrons. Despite its thinness, the plasma in this region is responsible for a neutron star's thermal radiation, one of the fundamental observables used to infer the neutron star surface temperature. Moreover, the structure of these outer layers and their transport properties, hence the emitted spectrum, are strongly influenced by the presence of magnetic fields [31, 32] and disruptive changes in the interior [33]. Therefore, observations of oscillations or other spectral features can give insight into the properties of the neutron star.

2.2.3 Crust

The crust of a neutron star is approximately 1 km thick; a sketch of its structure is given in Figure 2.3. For a comprehensive summary on the physics of neutron star crusts see Chamel and Haensel [30]; the values for the densities in the remainder of this section are taken from their paper. In thermodynamic equilibrium, the strong Coulomb forces in the outer crust result in the formation of a ^{56}Fe lattice [4]. At about $10^4\,\mathrm{g\,cm^{-3}}$ the atoms are fully ionised, creating a free relativistic electron gas. The lattice energy in this density regime can be calculated in the Wigner-Seitz approximation [34], where crustal nuclei are separated into independent spheres centred around individual lattice sites. Each of these spheres is electrically neutral and it is found that a body-centred cubic (bcc) configuration minimises the energy of the lattice.

For increasing densities, the nuclei become more and more neutron rich and the distance between individual lattice sites decreases. At $\rho_\mathrm{D} \sim 4\times10^{11}\,\mathrm{g\,cm^{-3}}$, the neutron drip density, it is energetically favourable for the neutrons to drip out of the nuclei and form a free neutron gas. This state of matter has been studied intensively through theoretical approaches such as modified liquid-drop models [35]. Quantum calculations have additionally shown that the number of protons per nuclei is almost constant with $Z = 32, 40, 50$ [36]. As the free neutron gas has similar properties to the conducting electrons in metals, nuclear band theory [37] has also proven very useful in studying the characteristics of the inner crust. Chamel has, for example, shown that the free neutrons are less mobile due to *entrainment* [38], an effect that refers to the coupling of the neutron gas to the nuclear lattice. Their *effective mass* could be considerably higher than their *bare mass*, which would have important implications for the dynamics of the star [39] (see also Subsection 2.3.3). Additionally, the crustal dynamics are influenced by

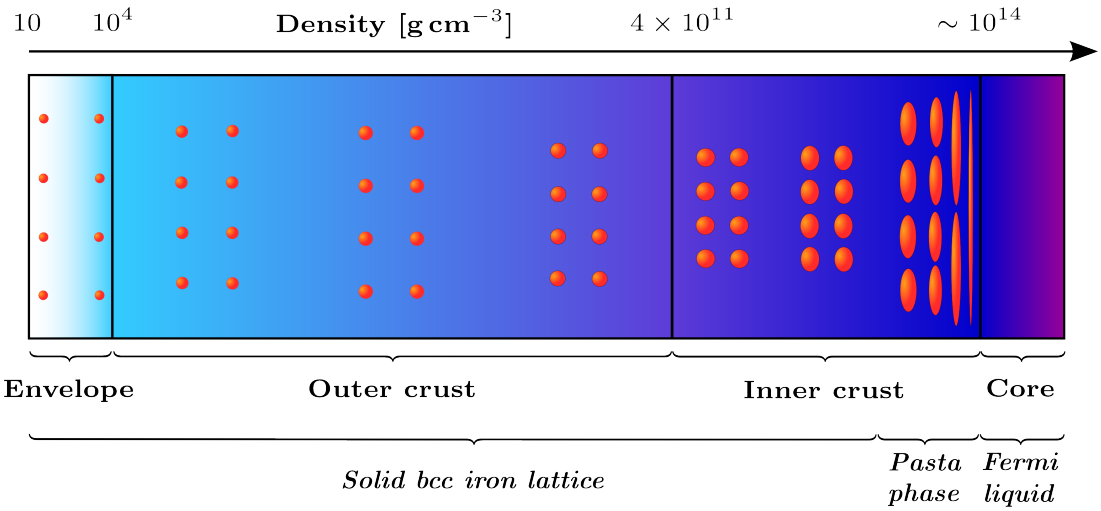

Figure 2.3: Sketch of the neutron star crust for increasing density. The focus lies on the change in the structure of the crustal lattice. The envelope is only a few decimetres thick and has a density in the range of 10 to $10^4\,\mathrm{g\,cm^{-3}}$. It contains iron atoms and lighter nuclei permeated by relativistic electrons. Strong Coulomb forces in the crust result in the formation of a body-centred cubic ^{56}Fe lattice. For increasing densities, the nuclei become more and more neutron rich and the distance between individual lattice sites decreases. At $\rho_\mathrm{D} \sim 4 \times 10^{11}\,\mathrm{g\,cm^{-3}}$, the neutron drip density, it is energetically favourable for the neutrons to drip out of the nuclei and form a free, superfluid neutron gas. At approximately $10^{14}\,\mathrm{g\,cm^{-3}}$, the particles start to form exotic shapes, giving this part of the neutron star crust the name *pasta phase*, indicated by the change in shape of the lattice nuclei in the inner crust. The spherical nuclei turn into cylinders and slabs. The crustal structures have completely vanished at densities above $\rho_0/3 \sim 10^{14}\,\mathrm{g\,cm^{-3}}$.

macroscopic quantum effects. As a result of an attractive contribution to the nucleon-nucleon interaction, neutrons can form Cooper pairs, giving rise to superfluidity [40]. It is expected that the crustal superfluid pairs in a spin-singlet, s-wave ($^1S_0$) state, having properties similar to isotropic helium II (see also Sections 3.1 and 8.1).

As the density increases further, the number of bound neutrons in the nuclei decreases and the lattice sites move closer to each other. The transition to the core state, where the lattice structure vanishes completely and pure nuclear matter dominates, is not sharp but rather smooth. At approximately $10^{14}\,\mathrm{g\,cm^{-3}}$, the particles start to form exotic shapes, giving this part of the neutron star crust the name *pasta phase* [41, 42]. The spherical nuclei first turn into cylinders (spaghetti) and slabs (lasagne). Further inside the star, the situation is inverted and the free neutrons form tubes and bubbles enclosed by nuclear matter. The pasta has the properties of solids and liquids and its behaviour may be described by the theory of liquid crystals [43]. This layer, although very thin, comprises most of the crust's mass and could therefore influence the stars' rotational properties. Pons et al. [44] suggested that the observed lack of isolated long-period X-ray pulsars could be explained by a layer of high electrical resistivity such as the nuclear pasta phase, causing effective dissipation of magnetic energy subsequently resulting in the saturation of the electromagnetic spin-down behaviour.

2.2.4 Core

The core contains about 90% of the neutron star's mass and has a radius of approximately 9 km. The crustal structures have completely vanished at densities above $\rho_0/3 \sim 10^{14}\,\mathrm{g\,cm^{-3}}$, where $\rho_0 \sim 2.8 \times 10^{14}\,\mathrm{g\,cm^{-3}}$ is the nuclear saturation density. For larger values, information about the state of the nuclear matter has not been experimentally tested on Earth. Usually, existing theories of bulk matter are extrapolated to the outer core of a neutron star. Up to densities of $2\rho_0$, it is thought to consist of neutrons and a small fraction of protons and relativistic electrons [4]. The neutrons in the interior are described by a spin-triplet, p-wave ($^3P_2$) order parameter [40], a quantum state comparable to the anisotropic helium-3 superfluid created in laboratory experiments, whereas protons are pairing in a $^1S_0$ superconducting state and most likely exhibit properties of a type-II superconductor [45]; more general information on classical superfluidity and superconductivity is given in Chapters 3 and 8.

In the inner core for densities above $2\rho_0$, the structure of neutron stars is completely unknown. The main problem for theoretical calculations at these densities is the appearance of new degrees of freedom [46]. Particles such as kaons, pions, hyperons or other exotic species could be generated and change the properties of nuclear matter. At extremely high densities in the centre, $\rho \sim 10^{15}\,\mathrm{g\,cm^{-3}}$, quantum-chromodynamical calculations even predict transitions to a deconfined quark plasma, creating exotic states such as colour superconductors [47, 48]. However, it is not known, if neutron stars are compact enough to create such high densities and detailed observations are required to determine which equation of state adequately captures the properties of the interior of a neutron star.

2.3 Observing Neutron Stars

The electromagnetic radiation observed from neutron stars is generated in their magnetospheres and thin atmospheres. This does not allow direct access to the inner layers of the star and information about the internal structure and physics has to be deduced indirectly. Therefore, in order to test and validate new theoretical models of the neutron star interior, high-precision electromagnetic observations are required. In turn, astronomical discoveries can spark the development of new hypotheses and raise the need for more accurate models. This inevitable symbiosis between observers and theoreticians is well illustrated in the first prediction of neutron star existence in 1934 and their first detection almost 30 years later. As neutron stars were expected to be rather dim and emit no observable radiation, only little attention had been paid to Baade's and Zwicky's proposition [1]. However, in 1967 Bell and Hewish detected a very regular radio source [2] that was named *pulsar* due to its steady radio pulsation. The object was later identified as an isolated, rotating neutron star and the findings earned Hewish along with Ryle the 1974 Nobel Prize in Physics.

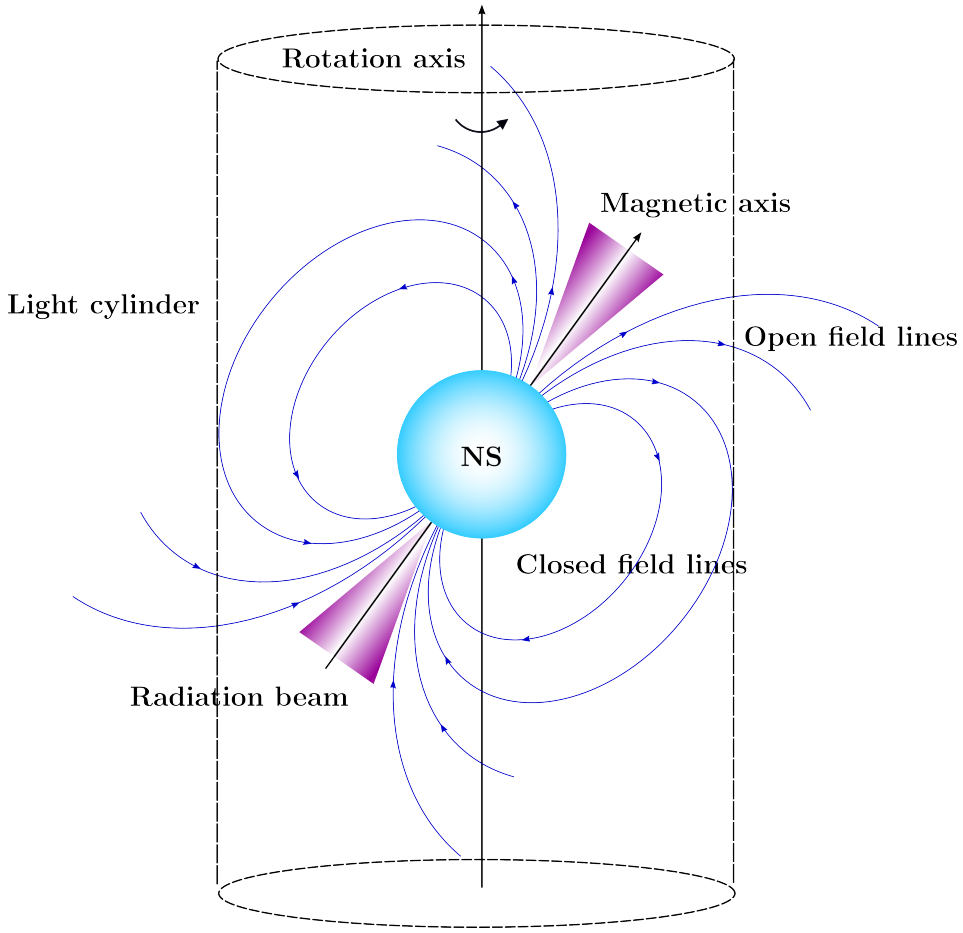

Figure 2.4: A sketch of the magnetic field of a neutron star. The magnetic field lines are given in blue. Within the light cylinder (black, dashed lines) the magnetic field lines are closed and form an almost dipolar field. Outside this region, the field lines are not closed and become radial, allowing particles to escape. The light cylinder marks the boundary of the domain, where the radial velocity of a corotating particle is smaller than the speed of light. In this plot, the magnetic and the rotation axes are misaligned, causing the radiation beam to create the lighthouse effect that can be detected as a radio pulse by a distant observer on Earth.

Since the discovery of the first radio pulsar almost 50 years ago, many more neutron stars have been detected; the current number of objects in the ATNF catalogue is 2536 [49] (see also `http://www.atnf.csiro.au/people/pulsar/psrcat/` and Figure 2.5). Neutron stars can emit radiation in the radio, infrared, optical, ultraviolet, X-ray or gamma-ray band. In general, the mechanisms and thus the observational data depend on whether the star is isolated or has a companion. In the latter case for example, the compact object accretes matter onto its surface, which triggers thermonuclear flashes that can be observed as X-ray bursts [50]. On the other hand, the bright radio emission of pulsars is thought to be powered by strong magnetic fields (see Subsection 2.3.1). Hence, neutron stars exhibit a huge variety of physical properties as observed spin frequencies and measured spectral data show a diverse distribution of rotational periods and magnetic field strengths, surface temperatures, transient or persistent behaviour

and environmental conditions. These distinct characteristics are used to classify the compact objects and different categories are introduced in Subsection 2.3.2.

One tool that has proven particularly useful in the study of neutron stars and forms the basis for most of the dynamics discussed in the remainder of this thesis is the so-called *pulsar timing*. As explained in the next subsection, pulsars emit very regular radio pulses that mirror the rotation period of the compact source. Any changes in the stars' interior and on their surface produce irregularities in the observed radio signal. The rotation periods of several pulsars are known to very high precision, some of them even challenge the precision of atomic clocks on Earth [51], and, therefore, allow one to trace any deviations from the theoretically expected pulsation back to the neutron star itself. Phenomena that can be observed this way are for example *glitches*, sudden jumps in the rotation period of the neutron star discussed in more detail in Subsection 2.3.3, *precession* caused by the misalignment of principal and rotation axes, or *timing noise*, a widespread feature in pulsar timing observations [52] that, despite its name, is not necessarily random but has not yet been attributed to a specific mechanism [53].

2.3.1 Spin period and magnetic fields

The progenitors of neutron stars are rotating objects and penetrated by magnetic fields. Assuming that the initial angular momentum and magnetic flux are conserved during the collapse, the compact remnants will end up with very short spin periods and extremely high magnetic fields [54]. Due to their observational advantages, the main focus will be put on pulsars and the associated physics in the remainder of this section.

A model that captures various features of the pulsed radio emission is the magnetic dipole model based on work by Goldreich and Julian in 1969 [55]. A sketch of the neutron star and its exterior magnetosphere are shown in Figure 2.4. Within the so-called *light cylinder* the magnetic field lines are closed and form an almost dipolar field. The light cylinder marks the boundary of the domain, where the radial velocity of a particle corotating with the star is smaller than the speed of light. Outside of this region, particles cannot follow the stars' motion any more; the field lines are no longer closed and become radial. Although the exact emission mechanism is not understood, it is believed that the strong magnetic fields could create electron-positron pairs in the magnetosphere [56]. These are then accelerated along the open field lines, generating radiation in direction of the magnetic axis. If the magnetic and the rotation axis are misaligned as in Figure 2.4, the radiation beam rotates about the rotation axis creating a *lighthouse effect* that leads to the observation of radio pulses on the Earth.

Pulsars are measured to have rotation frequencies in the range of 0.085 Hz for PSR J1841-0456 [57] to 716 Hz for PSR J1748-244ad [27]. In the absence of a companion, the loss of energy due to the lighthouse effect, i.e. an electromagnetic braking torque created by the misalignment of the rotation axis and the magnetic axis, causes the

neutron star to continuously slow down. This spin-down is generally described by a torque balance equation,

$$I\,\dot{\Omega} = \alpha\,\Omega^n, \tag{2.3}$$

where I is the star's moment of inertia, $\dot{\Omega}$ the measured spin-down rate, α a proportionality constant, Ω the observed angular velocity and n the so-called *braking index*. Depending on the spin-down mechanism, n varies: for the pure electromagnetic dipole torque described above $n = 3$, whereas the slow-down due to the loss of gravitational energy gives $n = 5$. Differentiating Equation (2.3) with respect to time, one is able to express the braking index in terms of the observables Ω and its time derivatives,

$$n = \frac{\Omega\,\ddot{\Omega}}{\dot{\Omega}^2}. \tag{2.4}$$

For several young objects the rotation frequencies and time derivatives have been measured and the braking indices calculated. This allows a comparison between the theoretical predictions of spin-down models and the actual mechanism present. As for the Crab pulsar with $n \approx 2.515 \pm 0.005$ [58], almost all values lie below the one expected for the classical, pure dipole model [59]. Note, however, that one object has recently been observed to show $n > 3$ [60]. The general tendency for $n < 3$ might be an indication for new physics in the neutron stars' interior. One possible explanation for the discrepancy is to allow for a variable moment of inertia, which could be caused by changes in the fraction of the core superfluid component [61]. Alternatively, deviations from pure dipole spin-down could also be induced by variations in the external spin-down torque generated by the emergence of a magnetic field buried in the stars' interior [62, 63].

Under the assumption that the rotation period of the newly born neutron star is a lot shorter than the one currently observed, Equation (2.3) can be integrated in time to obtain a measure for a star's age. The so-called *characteristic age* is defined as

$$\tau_\mathrm{c} = -\frac{1}{n-1}\,\frac{\Omega}{\dot{\Omega}} = \frac{1}{n-1}\,\frac{P}{\dot{P}}, \tag{2.5}$$

where P is the rotation period related to the angular rotation frequency via $P = 2\pi/\Omega$. The Crab pulsar for example, created during a supernova observed in 1054 by several astronomers on Earth, has a rotation period of $P \approx 33.1\,\mathrm{ms}$ and a period derivative of $\dot{P} \approx 4.2 \times 10^{-13}\,\mathrm{s/s}$ [58]. For pure magnetic dipole spin-down, these values correspond to a characteristic age of $\tau_\mathrm{c} \approx 1.2 \times 10^3\,\mathrm{yr}$, very close to its actual age.

Neutron stars are sourcing the strongest magnetic fields in our Universe. Whereas a typical pulsar has a magnetic field strength of $\sim 10^{12}\,\mathrm{G}$, some neutron stars may have fields up to $10^{15}\,\mathrm{G}$. This is many orders of magnitude larger than the typical surface magnetic field strength of the Earth ($0.5\,\mathrm{G}$ [64]) or the strongest, pulsed field of $10^6\,\mathrm{G}$ [65] generated non-destructively in a laboratory. In order to estimate the field strengths of isolated pulsars, one can take advantage of Equation (2.4). In the case of a magnetic

dipole torque acting on the star, the proportionality constant α in cgs units is given by

$$\alpha = \frac{2}{3}\,\frac{B^2 R^6 \sin^2\gamma}{c^3}, \tag{2.6}$$

where B is the dipole surface magnetic field at the pole, R the radius of the pulsar and γ the angle between the magnetic and the rotation axes. Substituting this back into the torque balance equation gives an estimate for the magnetic dipole field strength,

$$B = \left(\frac{3Ic^3}{2R^6\sin^2\gamma}\,\frac{|\dot{\Omega}|}{\Omega^3}\right)^{1/2} = \left(\frac{3Ic^3}{8\pi^2 R^6\sin^2\gamma}\,P\dot{P}\right)^{1/2}. \tag{2.7}$$

Considering a star of radius $R = 10\,\mathrm{km}$, a moment of inertia $I = 10^{45}\,\mathrm{g\,cm^2}$, $\sin\gamma = 1$ and the rotation period P given in seconds, Equation (2.7) leads to

$$B \approx 3.2 \times 10^{19}\,\left(P\dot{P}\right)^{1/2}\ \mathrm{G}. \tag{2.8}$$

For the Crab pulsar, the measured spin period and its time derivative yield an estimated magnetic dipole field strength of $B \approx 3.8 \times 10^{12}\,\mathrm{G}$. Alternatively, the magnetic field strength in a pulsar's atmosphere can be obtained from the analysis of cyclotron absorption features in the X-ray spectrum leading to results that are in agreement with the estimate given above [66].

2.3.2 Neutron star classification

One way to illustrate the variety of pulsar properties is by using a so-called $P\dot{P}$*-diagram*. All objects with a measured rotation period and period derivative in the ATNF Pulsar catalogue (`http://www.atnf.csiro.au/people/pulsar/psrcat/`, [49]) are plotted in Figure 2.5. Additionally, lines of characteristic age for electromagnetic spin-down and lines of constant magnetic field, determined by Equations (2.5) and (2.8), are shown. This allows the comparison of individual neutron stars and the tracking of their evolution. With more than two thousand data points available, it has become possible to identify specific groups that are characterised by similar physical properties.

A major challenge in previous decades has been the idea of establishing evolutionary links between these neutron star classes and combining them into a coherent framework [3, 67]. Viganò et al. [68] recently considered the close relationship between spin and magnetic field evolution in combination with different initial masses, magnetic fields and atmospheric conditions in order to reproduce the observed phenomenological diversity. With the sample size constantly increasing, more and more features will be unveiled, ultimately paving the way to a unified theory of neutron star formation and evolution. The following subsections will briefly discuss standard rotation powered pulsars, magnetars, X-ray dim isolated neutron stars, millisecond and Fermi pulsars and the current understanding of the different stages of neutron star *metamorphosis*.

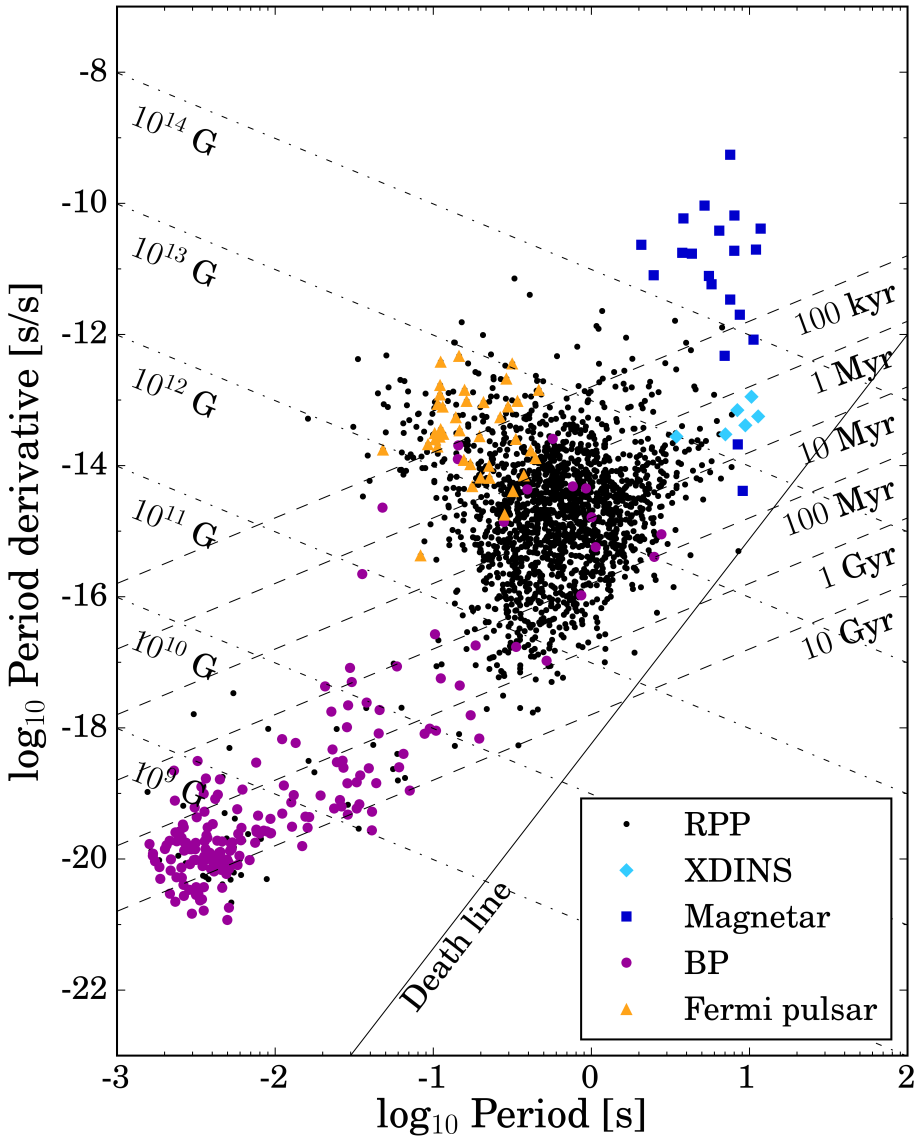

Figure 2.5: $P\dot{P}$-diagram illustrating the variety of pulsar properties and the standard classification for neutron stars. The data is taken from the ATNF Pulsar catalogue (`http://www.atnf.csiro.au/people/pulsar/psrcat/`). Black dots mark rotation powered pulsars (RRPs), cyan diamonds the X-ray dim, isolated neutron stars (XDINSs), blue squares the high magnetic field magnetars and purple circles the objects orbiting a binary companion (BP). Yellow triangles represent radio-quiet γ-ray pulsars detected by the Large Area Telescope (LAT) on the Fermi satellite [69]. Millisecond pulsars (MSPs) are located in the lower left with $P \lesssim 20$ ms. Additionally, lines of constant magnetic field (dot-dashed) and characteristic age (dashed) and the death line (solid) are given.

Rotation powered pulsars

Normal rotation powered pulsars (RRPs), given as black dots in Figure 2.5, have rotation periods in the range of 20 ms to 8 s. Magnetic field strengths inferred from Equation (2.8) typically range between 10^{10} to 10^{13} G. Young pulsars such as the Crab pulsar and the Vela pulsar belong to this class of isolated neutron stars. RRPs loose energy due

to an electromagnetic braking torque acting on the crust. The emission, predominantly seen as radio pulsations, is powered by this rotational energy loss. Additionally, for several RRPs thermal components have been observed. These are particularly valuable for fitting theoretical cooling curves and constraining the nuclear equation of state [70].

As pulsars age and slow down, they move from left to right on the $P\dot{P}$-diagram. The braking index defined in Equation (2.4) is the parameter describing this motion; for $n = 3$, neutron stars should follow a line of slope -1. However, as mentioned previously, most young pulsars exhibit $n < 3$, thus moving along lines of different slope. At some point during their evolution, pulsars are expected to cross the *death line* into a region of large P and low $\dot{P}$, commonly named the pulsar *graveyard*. Below this line, the radio emission mechanism is thought to switch off and pulsars are no longer visible.

Magnetars

Objects with rather long spin periods (2 to 10 s) and very high inferred magnetic field strengths (10^{14} to 10^{15} G) are called magnetars (blue squares in Figure 2.5). Since these enormous fields are causing the stars to spin down rapidly, they are located in the upper right corner of the $P\dot{P}$-diagram. The idea of a highly magnetised neutron star was first proposed by Duncan and Thompson in 1992 [71] to explain the observations of Soft Gamma Repeaters (SGRs). They suggested that the decay of the magnetic field could power their characteristic, high-energetic X-ray or soft gamma-ray emission and giant flares. Magnetars have also been considered as a model for Anomalous X-ray Pulsars (AXPs). These objects have measured X-ray luminosities that are many times greater than the ones expected from standard, magnetic dipole spin-down. Observations, however, could be explained by taking an extremely large reservoir of magnetic energy into account. AXPs do not show the burst characteristics typical for SGRs, but have recently been found to exhibit transient behaviour [72]. This suggests the existence of an unseen population of high magnetic field stars, considerably increasing the number of the about two dozen magnetars known to date. Quiescent objects could also be an explanation for the overlap between the magnetar and the rotation powered pulsar population. There are several high-B RRPs that show no burst activity and have spectra comparable to low-B RRPs. If one of these was observed to switch into an active flaring state, this would provide a clear evolutionary link between the two types.

X-ray dim isolated neutron stars

Another type of neutron star, located in-between the rotation powered pulsars and the magnetars, is the so-called X-ray dim, isolated neutron star (XDINS). These are given as cyan diamonds in Figure 2.5. The seven objects observed to date are sometimes informally referred to as the *Magnificent Seven* ($P\dot{P}$-measurements are only available for six of them). They are characterised by their proximity as they are located at a distance

of only 200 to 500 pc from the Solar system. Their inferred fields are slightly higher than 10^{12} G with rather large periods of 3 to 12 s. In contrast to high-B RRPs, XDINSs are generally radio-quiet and show quasi-thermal X-ray emission with a relatively low X-ray luminosity, hence the name. In addition to conventional cooling, another heating source has to be considered to explain the spectra. As for magnetars, the additional heating could be caused by the decay of the magnetic field.

Millisecond pulsars

Millisecond pulsars (MSPs) form a fourth group of neutron stars. They have rotation periods below 20 ms and are thus located in the lower left of the $P\dot{P}$-diagram. Similar to RRPs, they are powered by rotational energy, but evolve in a very different environment [73]. As can be seen in Figure 2.5, the majority of MSPs are observed as binary pulsars (BPs), especially LMXBs, and are thought to accrete matter from their companions. This process would transfer angular momentum to the compact object and spin it up to very high frequencies. The accretion mechanism is also utilised as an explanation for the bright X-ray burst emission as it could trigger thermonuclear explosions on the stars' surface [50]. Moreover, mass transfer from the companion could be responsible for the rather weak magnetic fields of MSPs. Old, recycled pulsars typically have $B < 10^{10}$ G, which could be explained by the accreted matter burying the magnetic flux.

Fermi pulsars

Another subclass of rotation powered emitters are the so-called γ-ray pulsars. They are emitting pulsed gamma radiation, thought to be generated by synchrotron curvature processes in the stars' magnetospheres [74]. The number of neutron stars, which have been observed as γ-ray pulsars, has significantly increased in recent years due to data acquired by the Large Area Telescope (LAT) on the Fermi satellite [69]. While many of these objects are also visible as RRPs or MSPs and had already been detected by other surveys, blind searches of Fermi-LAT data revealed about 40 unknown radio-quiet γ-ray sources. We refer to these as Fermi pulsars. The young and energetic objects, given as yellow triangles in Figure 2.5, are found in the upper left of the $P\dot{P}$-diagram. They have periods of 50 to 500 ms and moderate magnetic field strengths of 10^{11} to 10^{13} G.

2.3.3 Glitches

Rotating isolated neutron stars loose energy by emitting electromagnetic and gravitational radiation, which causes the rotational frequency to slowly decrease over time. However, pulsar timing data has revealed that the smooth time-averaged spin-down can occasionally be punctuated by glitches. These jumps in the rotation frequency were first observed in the Vela and the Crab pulsar in 1969 [75, 76, 77, 78], two archetypal glitching pulsars analysed in great detail. Since then, several hundred events have

been detected in over 150 objects (see Glitch Catalogue `http://www.jb.man.ac.uk/pulsar/glitches.html`), which include standard RRPs and magnetars. For a recent review on glitch statistics see Espinoza et al. [79].

Phenomenology

Analysing observational glitch data reveals several distinct features. Firstly, note that glitch rising times have not been resolved yet. To date, the best upper limit is obtained from the 2000 Vela glitch indicating that the spin-up takes place within 30 s [80]. However, the discrete jumps can be characterised by the fractional change in spin frequency, $\Delta\nu/\nu$, which ranges between $\Delta\nu/\nu \sim 10^{-11}$ and $\Delta\nu/\nu \sim 10^{-4}$. As can be seen from Figure 2.6, glitch sizes also exhibit a bimodal distribution with the two peaks located at $\Delta\nu/\nu \sim 10^{-9}$ and $\Delta\nu/\nu \sim 10^{-6}$. Whereas glitches of the Crab pulsar can be associated with the first peak, most of Vela's glitches belong to the second group. This distribution is generally explained by invoking two different trigger mechanisms (see below). Secondly, the data suggests a correlation between a neutron star's characteristic age and its glitch activity. While middle-aged pulsars are observed to glitch most frequently, older pulsars rarely undergo sudden spin-ups [81]. This is naturally explained if the glitch activity is driven by the electromagnetic spin-down, as older objects would spin down slower and, thus, experience fewer glitches. Moreover, the post-glitch behaviour of neutron stars is characterised by a change in the spin-down rate. This change can be separated into a perpetual increase and a series of decaying exponentials describing a long-term recovery on the order of months to years. In case of the 2000 Vela glitch, for example, four relaxation timescales are needed to explain the post-glitch characteristics [82]. Finally, we mention the potential observation of an *anti-glitch* in a magnetar [83]. If indeed being a robust feature and not the result of incomplete data, the sudden spin-down of the star's rotation frequency challenges the understanding of the glitch mechanism, as a spin-down is not explained within the standard theoretical glitch models.

Mechanisms

The bimodal distribution of glitch sizes may be related to different physical processes. Due to the lack of correlation between changes in the radiative profiles and glitch observations, internal mechanisms are mainly held responsible for the observed frequency jumps. Haskell and Melatos [84] presented a comprehensive summary of relevant pulsar glitch models. Historically, two main mechanisms have been discussed in the literature. The first one envisages glitches as star-quakes and was originally developed by Ruderman in 1969 [85] and Baym and Pines in 1971 [86]. The star-quake model is based on rearrangements of the crust and could be a possible explanation for the smaller glitches. As a neutron star slows down, it would evolve from an oblate shape towards a more spherical shape. Whereas a pure fluid star would be able to instantly adjust to this

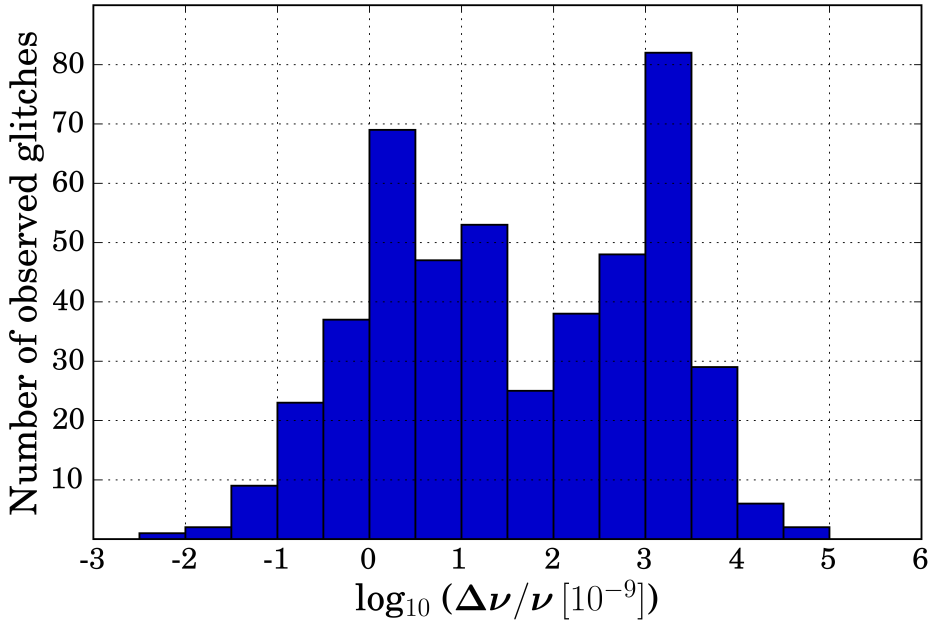

Figure 2.6: Fractional step size of 472 glitches detected in 165 pulsars. The histogram shows a bimodal distribution with peaks located at $\Delta\nu/\nu \simeq 10^{-9}$ and $\Delta\nu/\nu \simeq 10^{-6}$. The data is taken from `http://www.jb.man.ac.uk/pulsar/glitches.html`.

change, the nuclei in the crust form a solid lattice and resist the centrifugal forces acting to decrease the star's oblateness. Stresses build up in the solid until a critical value is reached, which causes the crust to crack and releases elastic energy. The removal of residual oblateness is realised by rearrangements in the crust that also reduce the moment of inertia. Hence, the star is spun up due to the conservation of angular momentum and the rotation frequency is observed to increase abruptly. After the glitch, the neutron star continues to spin down until the critical strain is approached again, producing another quake, which allows one to estimate the typical time between two glitches. While observations of Crab glitches could be explained within the star-quake model [84], it cannot account for the higher activity of Vela, where large glitches are observed approximately every two years [87, 80].

Originally considered by Baym et al. in 1969 [45] and further improved by Anderson and Itoh in 1975 [88], glitches could also be related to the presence of a superfluid in the stars' interior. This model can not only describe the smaller Crab-like jumps but also the giant Vela glitches. It has proven particularly successful due to modifications in the form of the *vortex-creep* [89, 90] and the *snowplough* model [91, 92]. The basic idea is as follows: As will be discussed in Subsection 3.2.3, the superfluid rotates by forming quantised vortices. Its spin-down would, thus, imply the expulsion of vortices from the interior of the star. However, vortices could be pinned to the lattice nuclei close to the crust-core boundary impeding a normal slow-down of the interior superfluid. The crust, on the other hand, spins down electromagnetically generating a frequency lag. As soon as a critical lag is reached, the pinning force is overcome by the increasing Magnus

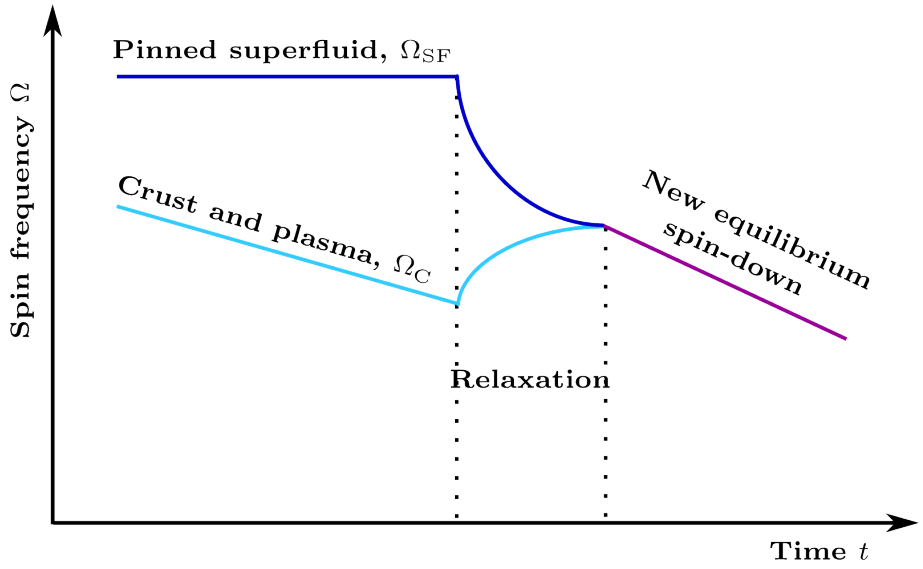

Figure 2.7: Illustration of the two-component model. The spin frequencies of the superfluid and the normal constituent, representing the crust and everything tightly coupled to it, are shown during an idealised glitch. While the crust is spinning down electromagnetically, the superfluid spin-down is impeded. At some critical lag, a large number of vortices are expelled, both components are recoupled and relax to a new equilibrium configuration.

force, exerted on each vortex by the surrounding neutron fluid (see Subsection 4.3.3). A large number of vortices are simultaneously unpinned and expelled, suddenly releasing angular momentum. A recent analysis of the Crab pulsar glitches by Espinoza et al. [93] suggests the existence of a minimum glitch size above the detectability limit. In terms of the superfluid model, this implies that a minimum of several billion vortices has to be involved in a single glitch. The spin-down of the superfluid is then compensated by the speed-up of the crust, observed as a glitch by a distant observer. As illustrated in Figure 2.7, this behaviour can be phenomenologically described by a simple two-component model, representing a normal constituent and the weakly coupled inviscid fluid [94]. While originally the crustal superfluid was considered to be responsible for the observed glitches, recent calculations taking entrainment in the crust into account [38] have shown that the crustal superfluid might not carry enough angular momentum to account for large glitches. As discussed by Andersson et al. [39], the core superfluid could serve as an additional angular momentum reservoir.

Finally note that the distribution of glitch sizes can also be described by power-law statistics with the exponent changing from pulsar to pulsar. This is consistent with the behaviour of self-organised critical processes as can be observed in scale invariant phenomena such as earthquakes or vortex avalanches. Warszawski and Melatos [95, 96] took advantage of the close analogy between the crustal superfluid and a Bose-Einstein condensate (see also Sections 3.1 and 8.2) to model the neutron stars' dynamics. It was found that the collective motion of vortices in the condensate could indeed trigger different glitch sizes reflecting the power-law distribution of observed jumps in pulsars.

2.3.4 Gravitational radiation

Neutron stars are very compact objects, with large gravitational forces acting on comparatively small lengthscales. This causes highly non-classical behaviour and Einstein's theory of general relativity (GR) is required to accurately capture the physics. Therefore, neutron stars are prime candidates for the emission of gravitational waves serving as a perfect testing tool for the strong-field regime of GR.

Gravitational waves, generated by the coherent motion of bulk matter at very high velocities, can be divided into two categories: continuous and transient signals. While transient waves are expected to be much stronger than continuous ones, they occur in a more unpredictable manner, are difficult to model theoretically and computationally expensive to detect.

The most promising candidates in this category are core-collapse supernovae [97] and coalescing binaries [22]. In the latter case, due the binaries' fast rotation and their small separation, every deviation from axisymmetry is radiated away in milliseconds, generating a characteristic *chirp* signal in the final stages of the merger. For stellar black holes and neutron stars, this chirp has a frequency in the range of 10 to 10^3 Hz [98], detectable with gravitational wave interferometers on Earth. For comparison, merging supermassive black holes and extreme mass ratio inspirals would radiate between 10^{-5} and 10^{-2} Hz and could potentially be observed with space interferometers such as eLISA [99]. The first direct detection of gravitational waves, announced by the LIGO collaboration earlier this year [100], was indeed associated with the coalescence of an intermediate-mass binary black hole system. Signal analysis showed that the two objects had initial masses of $36\,M_\odot$ and $29\,M_\odot$ and collapsed to a black hole of $62\,M_\odot$, leaving $3.0\,M_\odot\,c^2$ radiated in gravitational waves. The signal of a binary neutron star merger would similarly provide information about the two constituents. While the direct detection of such an event poses a new challenge for modern detectors due to the complexity of the compact objects, the coalescence of two neutron stars prominently led to the first indirect detection of gravitational waves. In 1975, Hulse and Taylor showed that the orbital period decrease in the binary pulsar PSR B1913+16 was in excellent agreement with the gravitational wave emission rate predicted by GR [101]. For their discovery, the two scientists were awarded the Nobel Prize in Physics in 1993.

The first gravitational wave detection has not only confirmed Einstein's predictions [102] but also opened a new window to study astrophysical phenomena. Despite being a task for the coming decades, gravitational wave astronomy could help to significantly improve our understanding of the neutron star interior. This is in particular related to the second class of continuous gravitational waves, generally of smaller amplitudes than transient ones but periodic and persistent. The large amount of information stored in the data would allow researchers to observe continuous waves for a long time and, thus, to increase the sensitivity by coherently integrating the signal. Neutron stars are strong candidates for this (for a recent summary see Lasky [103]), because any ob-

ject, not perfectly axisymmetric or rotating about an axis misaligned with the principal axes, has a time-varying quadrupole moment and, thus, emits gravitational waves. This is most likely true for pulsars, where asymmetries can arise from an elliptic, solid crust or dynamical changes in the interior fluid. A crustal ellipticity large enough to create a detectable gravitational wave signal could be supported by magnetic stresses, elastic strains or accretion from a companion [104, 105, 106]. Gravitational wave observations with ground-based detectors, in turn, would set limits on these mechanisms and provide information about the physics of the star. Alternatively, the fluid motion in the interior of a neutron star could source gravitational waves, if oscillations cause large changes in the mass distribution. Two modes that are particularly interesting for this scenario are the r- and f-modes. The former are inertial modes present in rotating stars where the Coriolis force acts as the restoring force [107], while the latter are fundamental pressure modes [108]. These fluid modes are susceptible to the Chandrasekhar-Friedman-Schutz instability [109, 110], arising from rotational dragging, i.e. the change of oscillations from counterrotating in the laboratory frame to corotating in the frame of the rotating star. For r- and f-modes, the emission of gravitational waves does not damp their amplitudes but instead increases them exponentially until they saturate. Depending on the value of the saturation amplitudes, the gravitational wave strain of these perturbations might be large enough to be detected by Advanced LIGO [111, 112].

Calculating mode frequencies and detectability limits is generally complicated by the existence of superfluid and superconducting neutron star components as hydrodynamics are considerably modified by entrainment, mutual friction and vortex/fluxtube pinning. Understanding the influence of these effects is hence crucial for gravitational wave asteroseismology and several aspects are addressed in the remainder of this thesis.

Chapter 3

Macroscopic Quantum States

As mentioned in Section 2.2, superfluid and superconducting components are expected to be present in a neutron star's interior. The former characterises matter behaving like a fluid with zero viscosity, while the latter describes a state of vanishing electrical resistance accompanied by the expulsion of magnetic flux. Similarities between these two phases are evident, since both are capable of maintaining particle currents at constant velocities without any forces being applied. These currents involve large numbers of particles that are condensed into the same quantum state. Therefore, superfluidity and superconductivity are characterised as macroscopic quantum phenomena, closely related to the concept of Bose-Einstein condensation. Understanding their formation and properties is crucial for developing a more realistic neutron star model.

Before discussing new aspects of superfluid and superconducting dynamics in neutron stars, an introduction to the classical treatment of macroscopic quantum states is presented in this chapter. It will start off with a historical overview of the research in *low-temperature condensed matter physics*, followed by two sections addressing the main properties of superfluids and superconductors and the theoretical approaches used to describe them, more precisely the two-fluid model and the Ginzburg-Landau theory of second-order phase transitions. These sections are mainly based on the books *Superfluidity and Superconductivity* by Tilley and Tilley [113], *Introduction to Superconductivity* by Tinkham [114] and *Quantized Vortices in Helium II* by Donnelly [115].

3.1 Historical Overview

Superconductivity was discovered by Heike Kamerlingh Onnes in Leiden in 1911 [116], only three years after he had succeeded in liquefying helium. Cooling several metals such as mercury to small temperatures, Onnes observed that their electrical resistance disappeared completely. For his ground-breaking work on low-temperature physics and condensed matter, he was awarded the Nobel Prize in Physics in 1913. Two decades later in 1933, Walther Meissner and Robert Ochsenfeld showed that superconductivity was a

unique new thermodynamical state and not just a manifestation of infinite conductivity. Cooling lead samples in the presence of a magnetic field below their superconducting transition temperature, they expelled the magnetic field and exhibited perfect diamagnetism [117]. Using a phenomenological approach, this mechanism known today as the *Meissner-Ochsenfeld effect* was first described by the two London brothers in 1935 [118] (see Subsection 3.3.1). Fritz London himself developed a semi-classical explanation for the London equations several years later [119] and was the first one to point out that the quantum nature of particles could play an important role in the superconducting phase transition.

Developed in the 1920s, quantum mechanics has significantly influenced the way scientists interpret the world. This is most apparent in the definition of an abstract wave function that allows a probabilistic interpretation of physical quantities such as the momentum and the position of a particle. This wave function is a complex quantity and it was the success of microscopic theories to relate its properties to the quantum mechanical condensate; the amplitude of the wave function is directly related to the density of the superconducting particles and the phase is proportional to the superconducting current. The first microscopic description of superconductivity was developed by John Bardeen, Leon Cooper and John Robert Schrieffer in 1957 [120]. Their BCS theory is based on the concept of pairing that results from an attractive potential. Below a critical temperature, the weak interactions between electrons and the lattice in an ordinary metal are strong enough to overcome the repulsive Coulomb force. This causes the electrons to form Cooper pairs that obey Bose-Einstein statistics and can condense into a quantum mechanical ground state. BCS theory explained, for example, the existence of a temperature-dependent energy gap, half the energy necessary to break a Cooper pair, and, hence, the presence of critical quantities above which superconductivity is destroyed. For their theory, Bardeen, Cooper and Schrieffer obtained the Nobel Prize in 1972. BCS theory has also shown to be useful in describing anisotropic superfluids such as helium-3 (see below).

A second approach to superconductivity that has proven particularly successful to describe the properties of the condensate close to the transition and will be mainly considered in the remainder of this thesis is the Ginzburg-Landau theory (see Subsection 3.3.4). Formulated in 1950 by Vitaly Ginzburg and Lev Landau [121], it phenomenologically describes a second-order phase transition by means of an order parameter. In the case of superconductivity, this quantity can be identified with the microscopic electron Cooper pair density. The phase transition itself is then interpreted as a symmetry breaking, because the density of superconducting pairs changes drastically at the transition point. Ginzburg and Landau postulated that close to the critical temperature the free energy of the system could be written as an expansion of the order parameter. Minimising the energy with respect to the order parameter and the vector potential, one arrives at the Ginzburg-Landau equations. These introduce two lengthscales char-

acteristic for superconductivity; the penetration depth, λ, and the coherence length, ξ. The ratio of these two is commonly referred to as the *Ginzburg-Landau parameter*, $\kappa_{\mathrm{GL}} = \lambda/\xi$. Although the approach of the Russian physicists was purely phenomenological and not based on an analysis of the microscopic features of a superconductor, Lev Gor'kov showed in 1959 that close to the critical temperature it is possible to derive the Ginzburg-Landau theory from the microscopic BCS theory [122]. In 1957, Alexei Abrikosov further investigated the order-parameter approach and predicted the existence of two classes of superconductors [123]. He found that matter characterised by $\kappa_{\mathrm{GL}} > 1/\sqrt{2}$ would be penetrated by magnetic fluxtubes, if an applied field would exceed a critical field strength. These fluxtubes contain normal matter that is screened by circular currents from the surrounding superconducting material. Up to that point, this state had been considered unphysical, since only $\kappa_{\mathrm{GL}} < 1/\sqrt{2}$ superconductors were known. Abrikosov gave this new phase the name type-II superconductor and calculated that the fluxtubes would arrange themselves in a regular lattice structure (see Subsection 3.3.4 for more details). Abrikosov and Landau were two of the three physicists who obtained the Nobel Prize in Physics in 2003 for their contributions to the modelling of superconductors.

In the last four decades, superconductors have found increasing commercial success ranging from sensitive magnetometers based on the Josephson effect [124], the quantum mechanical tunnelling of Cooper pairs across a normal barrier between two superconducting wires, to high-field electromagnets. Especially, the discovery of high-temperature superconductivity in ceramics at around 100 K has fuelled new research efforts [125]. For their findings in 1986, Georg Bednorz and Alexander Müller were given the Nobel Prize in Physics one year later. This type of superconductivity is still not fully understood and an ongoing research area that has led to revolutionary ideas. One example is the theory of holographic superconductors based on the duality between gravity and a quantum field theory (AdS/CFT correspondence) that might give new insight into the behaviour of experimental condensed matter [126].

Superfluidity was first observed in liquid helium-4 by Pyotr Kapitsa in Russia [127] and John Allen and Don Misener in the United Kingdom in 1937 [128]. The Soviet physicist was awarded the Nobel Prize in Physics in 1978 for his experimental findings. Helium forms two stable isotopes, helium-4 and helium-3, that have a relative abundance of 10^6:1 in the Earth's atmosphere and boiling points at 4.21 K and 3.19 K, respectively. Right below these, both isotopes behave like ordinary liquids with small viscosities. However, instead of solidifying, at 2.171 K helium-4 undergoes a transition into a new fluid phase, first detected by Kapitsa, Allen and Misener as a characteristic change in the specific heat capacity. The observed behaviour resembled the Greek letter Lambda and the transition temperature was, therefore, called the *Lambda point* (see Figure 3.1). Above 2.171 K, helium-4 is named helium I, whereas the superfluid phase is usually referred to as helium II. As predicted by Lev Pitaevskii [129], helium-3 also

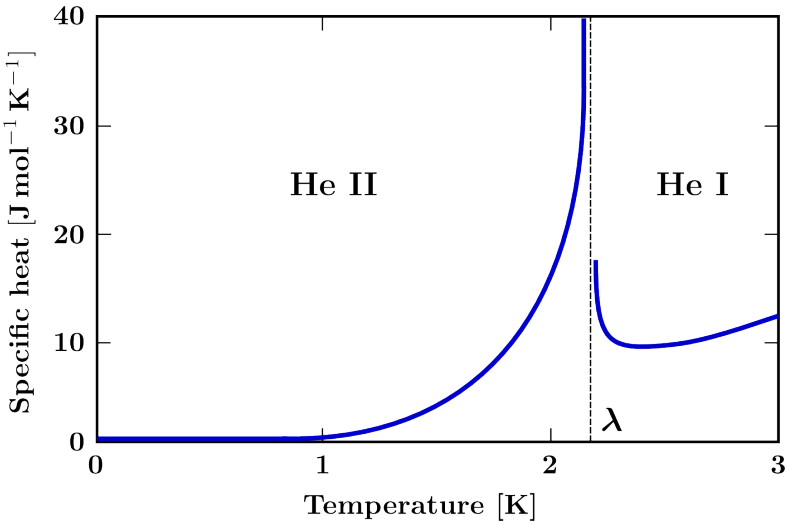

Figure 3.1: Sketch of the specific heat capacity of helium-4 as a function of temperature. At 2.171 K, the specific heat changes drastically, marking the superfluid phase transition. Above the Lambda point, helium-4 is usually referred to as helium I, whereas the superfluid phase is called helium II.

undergoes a superfluid transition in the mK-regime. To reach such low temperatures, the cooling techniques available in the first half of the twentieth century were not sufficient and new methods had to be developed. In 1971, more than thirty years after the discovery of helium II, Douglas Osheroff, Robert Coleman Richardson and David Lee detected two superfluid phases of helium-3 [130, 131].

The discovery of superfluid helium-4 stimulated the development of many new experiments and resulted in a lot of theoretical work analysing the new phase. The first model that was able to explain several observed phenomena was developed by László Tisza in 1938 [132]. Experiments measuring the viscous drag on a body moving in the superfluid had shown non-viscous behaviour [133], while rotation viscometers had revealed viscous characteristics [134]. Tisza solved this seemingly inconsistent nature by introducing a two-fluid interpretation. He assumed that helium II is a mixture of two physically inseparable fluids, one exhibiting frictionless flow and the other having an ordinary viscosity (see Subsection 3.2.2). This phenomenological approach provided, for example, an interpretation for the *fountain effect* first observed by Allen Jones in 1938 [135] and predicted the existence of *second sound*, which describes heat transfer in a wave-like process [136]. For more information on theoretical predictions for helium II and their experimental verifications see *An Introduction to the Theory of Superfluidity* by Isaac Khalatnikov [137].

The two-fluid model was further improved by Lev Landau in the 1940s [138]. He put the phenomenological idea on more solid grounds by providing a semi-microphysical explanation that earned him the Nobel Prize in Physics in 1962. He proposed that a fluid at absolute zero would be in a perfect, frictionless state. Increasing the temperature would then result in the local excitation of phonons, quantised collisionless sound waves,

and quasi-particles of higher momentum and energy that Landau called rotons. These excitations should behave like an ordinary gas, responsible for the transport of heat, and form the viscous fluid component, hence, providing a basis for the two-fluid model of superfluidity. His ideas also led Landau to suggest the classic experiment, performed by Elepter Andronikashvili in 1946, that measured the superfluid fraction of rotating helium II as a function of temperature. It was shown that below 1 K almost the entire sample is in a superfluid state [139].

Whereas Landau had thought that vorticity entered helium II in sheet-like structures, Lars Onsager and, later independently, Richard Feynman showed that vorticity enters rotating superfluids in the form of quantised vortex lines [140, 141]. Their ideas are summarised in the Onsager-Feynman *quantisation conditions* that will play an important role in the derivation of multi-fluid hydrodynamics presented in Chapter 4. The problem of rotating superfluid helium discussed by Onsager and Feynman is equivalent to that of type-II superconductivity in a strong magnetic field considered by Alexei Abrikosov two years later [123]. The first measurement of quantised vortices in rotating helium II was performed by Henry Hall and William Vinen in 1956 [142].

As implied in Landau's interpretation of the two-fluid model, at absolute zero helium II is completely superfluid and carries no entropy, marking the ground state of the system. Fritz London was the first one to suggest that bosonic helium-4 atoms could become superfluid by Bose-Einstein condensation [143]. This concept had been introduced by Satyendra Bose and Albert Einstein in 1924 and 1925 [144]. Governed by Bose-Einstein statistics, identical particles with integer spin such as photons or helium-4 atoms are allowed to share the same quantum state with each other. At very low temperatures, they tend to occupy the lowest accessible quantum state, resulting in a new phase that is referred to as a Bose-Einstein condensate (BEC). In the case of superfluid helium II, the Lambda point would then reflect the onset of this condensation. The original idea of Bose and Einstein was improved by Eugene Gross [145] and Lev Pitaevskii [146] by including interactions of the ground-state bosons. Their work led to the Gross-Pitaevskii equation that determines the wave function of the condensate and is similar in form to one of the Ginzburg-Landau equations. London's original proposition gained significant support in 1995, when Carl Wieman and Eric Cornell created the first atomic Bose-Einstein condensate by cooling a dilute gas of Rubidium-87 atoms to 170 nK [147]. Together with Wolfgang Ketterle, whose group created a BEC only a few months later [148], Cornell and Wieman won the Nobel Prize in Physics in 2001. In 1999, the first superfluid transition and the formation of vortices was observed in a Rubidium-87 boson gas [149, 150], opening the possibility to study vortex dynamics in such systems (see also Chapter 8).

For helium-3 however, the story is somewhat different, as it is a fermionic particle which is subject to the Pauli exclusion principle. Pairing into Cooper pairs is required before any condensation can take place; a mechanism that is similar to the electron

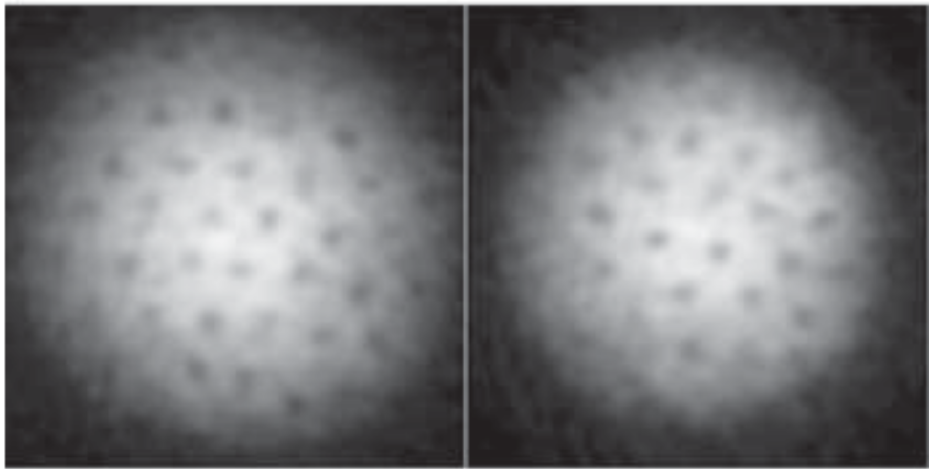

Figure 3.2: Vortex array in a strongly interacting fermionic condensate at two different magnetic field strengths; 792 G (left) and 833 G (right). Each image has a field of view of 880 µm × 880 µm. The figure is adapted from Zwierlein et al. [151] (p. 1048).

pairing in the BCS theory. This explains why fermionic condensates generally appear at lower temperatures than bosonic ones. In contrast to ordinary superconductivity, the Cooper pairs in helium-3 form in states of non-zero angular momentum, so-called p-wave pairing opposed to s-wave pairing in zero angular momentum states. This gives the helium-3 superfluid an intrinsic anisotropy and results in the formation of three different superfluid phases, which are stable under specific external conditions (see also Section 8.1). The first Fermi gas analogue of rotating superfluid helium-3 was observed in 2005 by Zwierlein and collaborators [151]. A snapshot of two regular vortex arrays formed at different external magnetic field strengths in a strongly interacting fermionic condensate is shown in Figure 3.2.

3.2 Modelling Superfluid Flow

Much of the discussion of superfluid dynamics is based on Landau's original explanation of the behaviour of superfluid helium [138]. In his seminal work, Landau assumed that in order to spontaneously excite sound-waves such as phonons or rotons, helium-4 required a flow velocity above a critical value. Landau then showed that these quasi-particles could move separately from the ground-state particles, which motivated him to combine the excitations to form the *normal*, viscous fluid. Its density vanishes at $T = 0$ and increases with temperature, ultimately leading to the destruction of superfluidity; at the Lambda point, the normal fluid density equals the total density and helium is no longer superfluid. In deriving the two-fluid equations for superfluid helium, the first step is to consider a quantum mechanical condensate at absolute zero with no viscous counterpart present. Thereafter, its description is extended to account for the second component and other effects such as vortex formation, mutual friction and turbulence. Finally, the close connection between superfluid helium and ultra-cold gases is discussed.

3.2.1 Wave function and potential flow

In order to understand the behaviour of the inviscid ground-state component, one can draw on the well-known formalism of quantum mechanics. The condensate at $T = 0$ is completely characterised by a single macroscopic wave function. Instead of representing a specific particle, this wave function is a coherent superposition of all individual superfluid states. The most general case is time- and space-dependent with

$$\Psi(\mathbf{r}, t) = \Psi_0(\mathbf{r}, t) \exp\left[i\varphi(\mathbf{r}, t)\right], \tag{3.1}$$

where $\Psi_0(\mathbf{r}, t)$ and $\varphi(\mathbf{r}, t)$ denote the real amplitude and phase, respectively, and bold symbols represent three dimensional vectors. The complex wave function, $\Psi(\mathbf{r}, t)$, is the solution to a Schrödinger equation of the form,

$$i\hbar \frac{\partial \Psi(\mathbf{r}, t)}{\partial t} + \frac{\hbar^2}{2m_\mathrm{c}} \nabla^2 \Psi(\mathbf{r}, t) - \mu \Psi(\mathbf{r}, t) = 0, \tag{3.2}$$

with the reduced Planck constant $\hbar$, the fluid's chemical potential μ and the mass m_c of one bosonic particle that has condensed into the quantum state. For helium II, m_c represents the mass of a helium atom, while it equals the mass of a Cooper pair in the case of a fermionic condensate. The absolute value of the wave function is defined by $|\Psi|^2 \equiv \Psi\Psi^*$, with $(*)$ denoting the complex conjugate. While for a single particle wave function, $|\Psi|^2$ denotes the probability of finding this particle at a point $\mathbf{r}$ at time t, the amplitude of the condensate wave function is related to the number density of the bosons constituting the quantum state, i.e. $|\Psi(\mathbf{r}, t)|^2 = |\Psi_0(\mathbf{r}, t)|^2 = n_\mathrm{c}(\mathbf{r}, t)$. Integrating over the volume of the entire condensate, one can thus obtain the total number of indistinguishable particles present in the superfluid ground state at a specific time t.

A connection between the quantum mechanical description and a hydrodynamical formalism can be derived by substituting the definition of the wave function (3.1) into the Schrödinger equation (3.2) and separating the resulting equation into its real and imaginary parts. This *Madelung transformation* [152] results in two coupled equations of motion for the amplitude, Ψ_0, and phase, φ,

$$\hbar \frac{\partial \varphi}{\partial t} + \frac{\hbar^2}{2m_\mathrm{c}} (\nabla\varphi)^2 + \mu - \frac{\hbar^2}{2m_\mathrm{c}\Psi_0} \nabla^2 \Psi_0 = 0, \tag{3.3}$$

$$\frac{\partial \Psi_0}{\partial t} + \frac{\hbar}{2m_\mathrm{c}} \left(2\nabla\Psi_0 \cdot \nabla\varphi + \Psi_0 \nabla^2 \varphi\right) = 0. \tag{3.4}$$

Multiplying the second equation with Ψ_0 and using the chain rule, we arrive at

$$\frac{\partial |\Psi_0|^2}{\partial t} + \frac{\hbar}{m_\mathrm{c}} \nabla \cdot \left(|\Psi_0|^2 \nabla\varphi\right) = 0. \tag{3.5}$$

This is equivalent to the continuity equation of fluid mechanics, i.e.

$$\frac{\partial \rho_{\rm s}}{\partial t} + \nabla \cdot \mathbf{j}_{\rm s} = 0, \tag{3.6}$$

if one substitutes the superfluid mass density, $\rho_{\rm s} \equiv m_{\rm c} n_{\rm c}$, and takes advantage of the standard definition of the quantum mechanical momentum density,

$$\mathbf{j}_{\rm s} = \frac{i\hbar}{2}\left[\Psi \nabla \Psi^* - \Psi^* \nabla \Psi\right] = \hbar |\Psi_0|^2 \nabla \varphi, \tag{3.7}$$

where Equation (3.1) has been used to obtain the last equality. We can further identify the momentum density with the product of the superfluid mass density and a superfluid velocity, i.e. $\mathbf{j}_{\rm s} \equiv \rho_{\rm s} \mathbf{v}_{\rm s}$ [137], which allows one to define the latter in the following way:

$$\mathbf{v}_{\rm s} \equiv \frac{\hbar}{m_{\rm c}} \nabla \varphi. \tag{3.8}$$

It is important to note that this superfluid velocity is generally not a direct observable in laboratory experiments and not necessarily a *real* kinematic quantity. Describing the interior of neutron stars, we will therefore choose the conceptually different, yet mathematically equivalent, variational approach developed by Carter, Prix and collaborators [153, 154, 155]. This formalism introduced in Chapter 4 clearly distinguishes between fluid momenta and velocities allowing a better understanding of the physics of a strongly coupled multi-fluid system. For the remainder of this chapter, however, the classical approach identifying superfluid velocities with momenta is employed.

Taking the curl of Equation (3.8), one finds

$$\nabla \times \mathbf{v}_{\rm s} = 0. \tag{3.9}$$

Hence, the condensate is characterised by irrotational, potential flow with the phase of the wave function playing the role of a scalar velocity potential. As we will see later on, this fundamental property is responsible for the formation of quantised vortex lines in a rotating superfluid sample.

Furthermore, by taking the gradient of Equation (3.3), substituting the superfluid velocity, $\mathbf{v}_{\rm s}$, and number density, $n_{\rm c}$, and accounting for the irrotationality, we have

$$\frac{D\mathbf{v}_{\rm s}}{Dt} \equiv \frac{\partial \mathbf{v}_{\rm s}}{\partial t} + \left(\mathbf{v}_{\rm s} \cdot \nabla\right) \mathbf{v}_{\rm s} = -\nabla \tilde{\mu} + \nabla\left(\frac{\hbar^2}{2 m_{\rm c}^2 \sqrt{n_{\rm c}}} \nabla^2 \sqrt{n_{\rm c}}\right) \simeq -\nabla \tilde{\mu}, \tag{3.10}$$

where D/Dt denotes the material derivative and $\tilde{\mu} \equiv \mu / m_{\rm c}$ the specific chemical potential. This equation of motion for the quantum condensate at $T = 0$ resembles the Euler equation of an ideal fluid; the only difference being the second term on the right-hand side. This contribution reflects the quantum nature of the system and is often referred to as the *quantum pressure* term. As it captures forces that depend on the curvature of the amplitude of the wave function, the term is negligible if the spatial variations of Ψ_0 occur on large scales, specifically those larger than the coherence length, ξ [115, 156]. One is then left with the standard momentum equation for a perfect fluid.

3.2.2 Two-fluid equations

For temperatures above zero, the condensate coexists with excitations constituting the viscous component. Following Landau's model, it is convenient to continue labelling the hydrodynamical properties of the superfluid component with 'S', while the index 'N' refers to the normal part. Any quantities without labels describe parameters of the entire fluid. Assigning a local velocity and density to each of the constituents of the two-fluid system, the total mass density and mass current density are given by

$$\rho = \rho_{\mathrm{N}} + \rho_{\mathrm{S}}, \tag{3.11}$$

$$\mathbf{j} = \rho_{\mathrm{N}}\mathbf{v}_{\mathrm{N}} + \rho_{\mathrm{S}}\mathbf{v}_{\mathrm{S}}. \tag{3.12}$$

Using these two relations, the simplest form of the hydrodynamical equations is derived from conservation laws and the main assumption that the fluid velocities are sufficiently small. This ensures that the dissipation introduced by the viscosity, η, of the normal fluid and the formation of vortices in the superfluid counterpart are negligible. Implicitly excluding turbulence makes it possible to treat the fluids individually and to neglect any coupling between them. Then, first of all, the total mass of the sample is conserved, leading to the following continuity equation,

$$\frac{\partial \rho}{\partial t} + \nabla \cdot \mathbf{j} = 0. \tag{3.13}$$

Additionally assuming that dissipation mechanisms are weak, every process in the two-fluid system is reversible. This implies that the entropy per unit mass, s, is conserved and results in a second continuity equation. Since entropy and heat are transported by the normal fluid, one finds

$$\frac{\partial(\rho s)}{\partial t} + \nabla \cdot (\rho s \mathbf{v}_{\mathrm{N}}) = 0, \tag{3.14}$$

where ρs is the entropy density and $\rho s \mathbf{v}_{\mathrm{N}}$ represents the entropy current density.

For incompressible fluid flow, $\nabla \cdot \mathbf{v}_{\mathrm{S}} = \nabla \cdot \mathbf{v}_{\mathrm{N}} = 0$, the conservation of momentum in the entire system provides a two-fluid Navier-Stokes equation. It can be separated into momentum conservation equations for each individual component by taking advantage of the Euler equation (3.10). If changes in the pressure, p, and the temperature, T, are responsible for variations in the superfluid chemical potential (therefore inducing motion in the fluid), one is left with the following expressions,

$$\rho_{\mathrm{S}} \frac{D\mathbf{v}_{\mathrm{S}}}{Dt} + \frac{\rho_{\mathrm{S}}}{\rho}\nabla p - \rho_{\mathrm{S}} s \nabla T = 0, \tag{3.15}$$

$$\rho_{\mathrm{N}} \frac{D\mathbf{v}_{\mathrm{N}}}{Dt} + \frac{\rho_{\mathrm{N}}}{\rho}\nabla p + \rho_{\mathrm{S}} s \nabla T - \eta \nabla^2 \mathbf{v}_{\mathrm{N}} = 0. \tag{3.16}$$

The former is an Euler equation describing the atoms condensed into the ground state.

At low temperatures, due to the existence of discrete quantum levels, particles cannot exchange energy with the environment and are responsible for the inviscid, frictionless behaviour of the fluid. For $\rho = \rho_S$ at absolute zero, Equation (3.15) reduces to Equation (3.10). Finally, Equation (3.16) is the equation of motion for the normal component, which is composed of all elementary excitations and has properties similar to that of a classical Navier-Stokes fluid with viscosity η.

Before discussing a rotating condensate, where the dynamics are more complicated since the velocities are no longer small, it is important to clarify that the two-fluid model is a mathematical simplification. In reality, the two components are physically inseparable and atoms cannot be designated as belonging to either one of them.

3.2.3 Characteristics of a rotating superfluid

Considering a normal fluid inside a rotating vessel, the fluid motion is characterised by rigid-body behaviour, where the velocity, $\mathbf{v}$, in the inertial frame is given by

$$\mathbf{v} = \boldsymbol{\Omega} \times \mathbf{r}. \tag{3.17}$$

Here, $\boldsymbol{\Omega}$ denotes the container's angular velocity vector and $\mathbf{r}$ the position vector. As a consequence of shearing, vorticity is created when the fluid is flowing past container walls. The vorticity is defined by

$$\boldsymbol{\omega} \equiv \nabla \times \mathbf{v} = 2\boldsymbol{\Omega}, \tag{3.18}$$

where the second identity is satisfied in the case of rigid-body rotation. Taking the curl of the Navier-Stokes equation and neglecting external forces, it is thus possible to show that vorticity transport is described by a diffusion-type equation.

Although the concept of vorticity had been familiar from viscous hydrodynamics, condensed matter physicists were initially unsure whether it would be possible to spin up the frictionless component inside a superfluid or not; the main problem being the property of potential flow as given in Equation (3.9). For a smooth, irrotational velocity field, $\mathbf{v}_S$, the circulation around an arbitrary contour $\mathcal{L}$ vanishes, i.e.

$$\Gamma = \oint_{\mathcal{L}} \mathbf{v}_S \cdot \mathrm{d}\mathbf{l} = \int_{\mathcal{A}} (\nabla \times \mathbf{v}_S) \cdot \mathrm{d}\mathbf{S} = 0, \tag{3.19}$$

because Stokes' theorem can be used to rewrite the expression as an integral over the surface $\mathcal{A}$ enclosed by the contour $\mathcal{L}$. This makes it impossible for an inviscid superfluid to develop circulation in a *classical manner*. The state, where no superfluid rotation is present, is generally referred to as the *Landau state* [157].

However contrary to this discussion, several experiments in the 1960s showed that both components in rotating helium II move at the same angular velocity, implying that

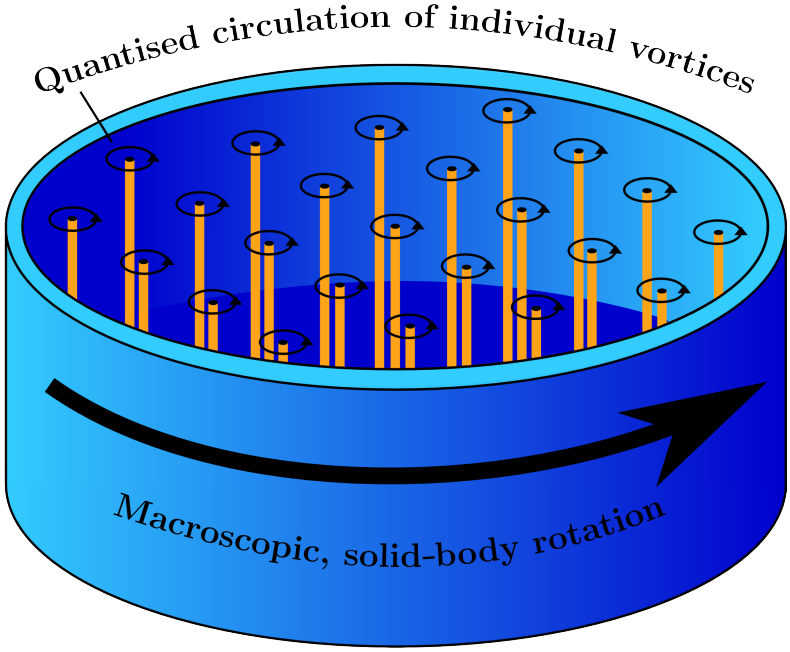

Figure 3.3: Illustration of a rotating superfluid. In contrast to a viscous fluid, a superfluid has to form vortices given in yellow that are aligned with the axis of rotation and form a triangular lattice. Each vortex carries a quantum of circulation that add up to mimic solid-body rotation on macroscopic lengthscales.

the superfluid component also exhibits rigid-body rotation (see for example Osborne [158]). The contradiction between theory and observations is resolved by recollecting that the quantum mechanical wave function, Ψ, is invariant under changes in the phase, φ, that are multiples of 2π. Taking this and Equation (3.8) into account, the circulation is given by

$$\Gamma = \oint_{\mathcal{L}} \mathbf{v}_{\mathrm{S}} \cdot \mathrm{d}\mathbf{l} = \frac{\hbar}{m_{\mathrm{c}}} \oint_{\mathcal{L}} \nabla\varphi \cdot \mathrm{d}\mathbf{l} = \frac{h}{m_{\mathrm{c}}}\, n \equiv \kappa n, \qquad n \in \mathbb{Z}. \tag{3.20}$$

The discrete set of phase values introduces a quantisation to the problem and results in the formation of vortices, singular points at which the circulation is non-zero. $h = 2\pi\hbar$ denotes the Planck constant and the quantity κ is defined as the *quantum of circulation* carried by a single vortex. Each individual one has a rotational velocity profile that is inversely proportional to the distance, r, from its center and additionally a core that is normal and not superfluid. Using cylindrical coordinates $\{r, \theta, z\}$, one obtains for the superfluid velocity

$$\mathbf{v}_{\mathrm{S}}(r) = \frac{\Gamma}{2\pi r}\, \hat{\boldsymbol{\theta}}, \tag{3.21}$$

where $\hat{\boldsymbol{\theta}}$ is the unit vector in θ-direction. The idea of quantisation goes back to the work of Onsager [140] and Feynman [141]. The latter was the first one to suggest that vortices could form a regular array, in which the circulation of all vortices mimics the rotation on macroscopic lengthscales as illustrated in Figure 3.3. Hence, via the formation of

vortices, the superfluid minimises its energy and appears to be moving as a rigid body on macroscopic scales, having a classical moment of inertia. In this picture, any change in angular momentum implies the creation (spin-up) and the destruction (spin-down) of vortices. Thus, the vortex area density, $\mathcal{N}_{\rm v}$, is directly proportional to the total circulation within a unit area, which corresponds to the definition of an averaged vorticity,

$$\boldsymbol{\omega} \equiv \mathcal{N}_{\rm v}\boldsymbol{\kappa}, \tag{3.22}$$

where $\boldsymbol{\kappa} \equiv \kappa\,\hat{\boldsymbol{\kappa}}$ with the unit vector $\hat{\boldsymbol{\kappa}}$ pointing along the direction of the vortices. In the case of straight lines, this direction coincides with the rotation axis of the cylindrical container, $\hat{\boldsymbol{\Omega}} = \hat{\boldsymbol{\kappa}}$. With Equations (3.18) and (3.22), the vortex line density equates to

$$\mathcal{N}_{\rm v} = \frac{2\Omega}{\kappa}. \tag{3.23}$$

For example, a helium II sample rotating at $1\,\mathrm{rad\,s^{-1}}$ contains an average vortex density of $\mathcal{N}_{\rm v} \approx 10^4\,\mathrm{cm^{-2}}$. The exact shape of the vortex array that minimises the energy of the condensate was first calculated by Abrikosov [123] (see Subsection 3.3.4). He considered the case of a strong type-II superconductor, a problem equivalent to that of a rotating superfluid, and found that the vortices would form a triangular lattice. Using Equation (3.23), one can determine an average distance, $d_{\rm v}$, between individual vortices,

$$d_{\rm v} \simeq \mathcal{N}_{\rm v}^{-1/2} = \left(\frac{\hbar\pi}{\Omega m_{\rm c}}\right)^{1/2}. \tag{3.24}$$

For the rotating helium II sample discussed above, one obtains an intervortex spacing of $d_{\rm v} \approx 0.1\,\mathrm{mm}$. The quantisation of circulation in the form of vortices will also serve as the basis for the description of the multi-fluid system in the interior of the neutron star introduced in Chapter 4.

3.2.4 Mutual friction and HVBK equations

The derivation of the two fluid equations presented in Subsection 3.2.2 relied on the fact that the respective velocities, $\mathbf{v}_{\rm N}$ and $\mathbf{v}_{\rm S}$, are small and dissipation can be neglected. If this is however no longer satisfied, additional terms have to be included into the equations of motion. This is especially necessary if the relative velocity of the individual fluids, $\mathbf{w}_{\rm NS} \equiv \mathbf{v}_{\rm N} - \mathbf{v}_{\rm S}$, is large or the superfluid is rotating and vortices are present, as additional forces couple the two components. Based on the improved understanding of the underlying physical processes, several extensions to the original two-fluid model have been suggested. Specifically the Hall-Vinen-Bekarevich-Khalatnikov (HVBK) equations [142, 159], which are based on the use of an averaged vorticity, provide a more complete model of superfluid hydrodynamics.

Large velocity differences, $\mathbf{w}_{\rm NS}$, modify the chemical potential of the frictionless fluid and, therefore, alter the momentum equations. Incorporating these changes into

the Equations (3.15) and (3.16) gives two coupled partial differential equations,

$$\rho_{\mathrm{S}} \frac{D\mathbf{v}_{\mathrm{S}}}{Dt} + \frac{\rho_{\mathrm{S}}}{\rho} \nabla p - \rho_{\mathrm{S}} s \nabla T - \frac{\rho_{\mathrm{S}} \rho_{\mathrm{N}}}{2\rho} \nabla \mathbf{w}_{\mathrm{NS}}^2 = 0, \tag{3.25}$$

$$\rho_{\mathrm{N}} \frac{D\mathbf{v}_{\mathrm{N}}}{Dt} + \frac{\rho_{\mathrm{N}}}{\rho} \nabla p + \rho_{\mathrm{S}} s \nabla T + \frac{\rho_{\mathrm{S}} \rho_{\mathrm{N}}}{2\rho} \nabla \mathbf{w}_{\mathrm{NS}}^2 - \eta \nabla^2 \mathbf{v}_{\mathrm{N}} = 0. \tag{3.26}$$

These relations can be further improved to capture the dynamics of a rotating superfluid. The presence of vortices has an effect on the hydrodynamical equations, because they interact with the normal fluid component and cause dissipation. This coupling mechanism is generally referred to as *mutual friction*. It is, for example, responsible for spinning up the superfluid as it communicates the changes in the normal component (coupled viscously to the rotating container) to the frictionless counterpart. Major advances in understanding the mutual friction force in helium II are based on research performed by Hall and Vinen in the 1960s. They realised that the main mechanism for the dissipative interaction is the collision of rotons with the normal cores of the vortex lines. For a helium II sample rotating at constant angular velocity, $\mathbf{\Omega} = \Omega \hat{\mathbf{\Omega}}$, Hall and Vinen suggested the following form of the mutual friction force [142]

$$\mathbf{F}_{\mathrm{mf}} = \mathcal{B}_{\mathrm{He}} \frac{\rho_{\mathrm{S}} \rho_{\mathrm{N}}}{\rho} \hat{\mathbf{\Omega}} \times [\mathbf{\Omega} \times (\mathbf{v}_{\mathrm{S}} - \mathbf{v}_{\mathrm{N}})] + \mathcal{B}'_{\mathrm{He}} \frac{\rho_{\mathrm{S}} \rho_{\mathrm{N}}}{\rho} \mathbf{\Omega} \times (\mathbf{v}_{\mathrm{S}} - \mathbf{v}_{\mathrm{N}}) \,. \tag{3.27}$$

The two parameters $\mathcal{B}_{\mathrm{He}}$ and $\mathcal{B}'_{\mathrm{He}}$ reflect the strength of the mutual friction coupling and can be experimentally determined (see Subsection 8.1.3 for details). Additionally, the fluid velocities $\mathbf{v}_{\mathrm{N}}$ and $\mathbf{v}_{\mathrm{S}}$ are no longer mesoscopic quantities but instead obtained by averaging over regions that contain a large number of vortices. Therefore, this form of the mutual friction between individual vortices and the viscous fluid implicitly relies on an averaging procedure. This way, the discrete behaviour of the vorticity is smoothed out and the dynamics on small lengthscales are neglected. This process is often called *coarse-graining*. So when taking account of the presence of vortices, other quantities in the hydrodynamical equations also have to be replaced with their averaged equivalents.

In addition to roton collisions, there is another force acting on the helium vortices that is particularly important for the study of highly dissipative or turbulent behaviour in superfluids. The original mutual friction force given in Equation (3.27) assumes that vortices are straight, forming a regular array. This condition however is not necessarily satisfied, as vortices could be bent or even form tangled structures [160], making it important to include the vortex tension, $\mathbf{T}$. Postulated as an explanation for experimental results in superfluid helium-4, the mutual friction in the case of curved vortices, which are sufficiently far apart so that no reconnections can take place, has the form [161]

$$\mathbf{F}_{\mathrm{mf}} = -\mathcal{B}_{\mathrm{He}} \frac{\rho_{\mathrm{S}} \rho_{\mathrm{N}}}{2\rho} \hat{\boldsymbol{\omega}} \times \left(\boldsymbol{\omega} \times \mathbf{w}_{\mathrm{NS}} + \frac{\mathbf{T}}{\rho_{\mathrm{S}}} \right) - \mathcal{B}'_{\mathrm{He}} \frac{\rho_{\mathrm{S}} \rho_{\mathrm{N}}}{2\rho} \left(\boldsymbol{\omega} \times \mathbf{w}_{\mathrm{NS}} + \frac{\mathbf{T}}{\rho_{\mathrm{S}}} \right), \tag{3.28}$$

where Equation (3.18) is used to substitute the averaged vorticity $\boldsymbol{\omega} \equiv \omega \hat{\boldsymbol{\omega}}$ with $\hat{\boldsymbol{\omega}} = \hat{\mathbf{\Omega}}$.

Due to its large self-energy, comparable to the tension of a guitar string, a vortex resists bending, which generates a restoring force that attempts to bring the vortex back into its equilibrium position. Although this process is non-dissipative, it is possible to assign an effective viscosity, ν_{S}, to the superfluid. It depends on the curvature of the vortices and is given by [113]

$$\nu_{\mathrm{S}} = \frac{\kappa}{4\pi} \ln\left(\frac{d_{\mathrm{v}}}{a}\right), \tag{3.29}$$

where d_{v} denotes the intervortex spacing and a the vortex core radius, which is typically of the order of the coherence length, ξ. The tension force is then determined by

$$\mathbf{T} = -\rho_{\mathrm{S}}\nu_{\mathrm{S}}\,\boldsymbol{\omega} \times (\nabla \times \hat{\boldsymbol{\omega}}) = \rho_{\mathrm{S}}\nu_{\mathrm{S}}\,(\boldsymbol{\omega} \cdot \nabla)\,\hat{\boldsymbol{\omega}}. \tag{3.30}$$

Combining the momentum conservation equations (3.25) and (3.26), the extended version of the mutual friction (3.28) and the tension force (3.30), one finally arrives at the HVBK equations describing the hydrodynamics of a rotating two-component superfluid in the presence of averaged vorticity [142, 159, 161],

$$\rho_{\mathrm{S}}\frac{D\mathbf{v}_{\mathrm{S}}}{Dt} + \frac{\rho_{\mathrm{S}}}{\rho}\nabla p - \rho_{\mathrm{S}} s \nabla T - \frac{\rho_{\mathrm{S}}\rho_{\mathrm{N}}}{2\rho}\nabla\left(\mathbf{v}_{\mathrm{N}} - \mathbf{v}_{\mathrm{S}}\right)^2 = \mathbf{T} + \mathbf{F}_{\mathrm{mf}}, \tag{3.31}$$

$$\rho_{\mathrm{N}}\frac{D\mathbf{v}_{\mathrm{N}}}{Dt} + \frac{\rho_{\mathrm{N}}}{\rho}\nabla p + \rho_{\mathrm{S}} s \nabla T + \frac{\rho_{\mathrm{S}}\rho_{\mathrm{N}}}{2\rho}\nabla\left(\mathbf{v}_{\mathrm{N}} - \mathbf{v}_{\mathrm{S}}\right)^2 - \eta\nabla^2\mathbf{v}_{\mathrm{N}} = -\mathbf{F}_{\mathrm{mf}}. \tag{3.32}$$

In Chapter 4, it will be shown how to rigorously derive similar phenomenological expressions for a neutron star by using a multi-fluid perspective that accounts for the presence of vortices and fluxtubes. The mutual friction mechanisms in the stars' interior will be further addressed in Chapters 5 and 6.

3.2.5 Vortex dynamics and turbulence

While the hydrodynamical model provides information about the averaged dynamics of superfluids on macroscopic scales, several phenomena cannot easily be studied within this framework. Specifically when vortices are no longer straight and very close to each other, the standard averaging procedure introduced in Subsection 3.2.3 can no longer be performed, because vortices start to interact and reconnect, which leads to a turbulent state. The analysis of this new regime of fluid dynamics has significantly advanced in recent decades due to increasing computational resources. In the following, the mathematical foundation for the study of *superfluid turbulence* is briefly reviewed, whereas a more detailed discussion (including experimental aspects) is presented in Chapter 8.

The modern models of the chaotic flow in superfluids are based on the concept of following individual vortices on mesoscopic scales. In these *filament approaches*, which were pioneered by Schwarz [162], the vortices are reduced to infinitesimally thin three-dimensional curves $\mathbf{s}(\xi, t)$ (parametrised by the length ξ along the line and the time t)

of circulation κ. A description of the corresponding dynamics is then obtained by first assuming that the vortices are only slightly bent and no reconnections take place. Due to this curvature, the mesoscopic velocity field generated at a specific point on a line also influences the rest of the vortex. Hence, each point on a vortex moves according to the total superfluid velocity induced at this point plus any additionally forces present. More precisely, the induced velocity of the superfluid component is given by [163]

$$\mathbf{v}_{\mathrm{S}}(\mathbf{r},t) = \frac{\kappa}{4\pi}\int_{\mathcal{L}} \frac{(\mathbf{s}-\mathbf{r})\times \mathrm{d}\mathbf{s}}{|\mathbf{s}-\mathbf{r}|^3}, \tag{3.33}$$

with the integral being evaluated over the full vortex length $\mathcal{L}$. Note that this is of the same form as the *Biot-Savart law* known from standard electromagnetism which is used to calculate the magnetic field induced by a steady current. Equation (3.33) is further singular at any point $\mathbf{s}$ on the vortex line and only well-defined outside the vortex. This can be avoided by introducing a cut-off to regularise the integral. Ignoring the detailed core structure, a suitable choice would be to cut off the integral at the distance $a \simeq \xi$. The self-induced contribution to the superfluid flow, caused by the vortex curvature, is also responsible for the modification of the mutual friction as given in Equation (3.28). By introducing an additional cut-off at large distances from the vortex (a reasonable estimate is the intervortex spacing d_{v}), Equation (3.33) can be evaluated and directly related to the tension, $\mathbf{T}$, that enters the vortex-averaged force, $\mathbf{F}_{\mathrm{mf}}$.

On mesoscopic scales, the motion of a single vortex filament is obtained by balancing the individual forces acting on it. While a more detailed discussion of the respective forces is postponed to Subsections 4.3.3 and 8.1.3, the balance of the *Magnus force* and a *dissipative drag* leads to the following equation for the mesoscopic vortex velocity $\mathbf{u}_{\mathrm{v}}$,

$$\mathbf{u}_{\mathrm{v}} = \mathbf{v}_{\mathrm{S}} + \alpha_{\mathrm{He}}\,\hat{\mathbf{s}}'\times(\mathbf{v}_{\mathrm{N}}-\mathbf{v}_{\mathrm{S}}) - \alpha'_{\mathrm{He}}\,\hat{\mathbf{s}}'\times\left[\hat{\mathbf{s}}'\times(\mathbf{v}_{\mathrm{N}}-\mathbf{v}_{\mathrm{S}})\right], \tag{3.34}$$

where $\mathbf{v}_{\mathrm{S}}$ is given by Equation (3.33) and the prime denotes a partial derivative with respect to the arc length ξ, implying that $\hat{\mathbf{s}}'$ is the unit tangent of the vortex line. Moreover, α_{He} and α'_{He} form a second set of mutual friction coefficients, whose connection to the parameters $\mathcal{B}_{\mathrm{He}}$ and $\mathcal{B}'_{\mathrm{He}}$ will also be addressed in Subsection 8.1.3. While Equation (3.34) allows an analysis of the dynamics of curved vortices, the filament model does not automatically account for vortex interactions and reconnections, which eventually drive the superfluid towards a turbulent state. This non-equilibrium behaviour can however be incorporated by introducing an additional algorithmic procedure that ensures the immediate separation and subsequent reconnection of vortex lines if they get to close to each other or the surface of the sample. More details of this reconnecting vortex-filament model, which has been successfully applied to capture various features of quantum turbulence (see Hänninen and Baggaley [163] for a review), can be found in Schwarz [162].

The mesoscopic approach is for example providing new insight into the so-called *counterflow behaviour*. The first studies of quantum turbulence focused on this chaotic

flow regime and were pioneered by Vinen in the 1950s [164, 165, 166, 167]. By applying a thermal gradient to non-rotating superfluid helium (only affecting the viscous fluid and hence causing a velocity difference between the normal and the superfluid component), Vinen showed that the energy was dissipated as a result of the interactions between a turbulent vortex tangle and the excitations. In such a turbulent state the mutual friction force (3.28) is no longer suitable to describe the dissipation and an alternative expression needs to be used. The main challenge remains the calculation of an appropriate average as one cannot simply count the vortices per unit area in the tangle. To circumvent this problem, Vinen used a phenomenological approach to determine the form of the mutual friction. More precisely, he postulated that for the case of isotropic turbulence, where vortices do not exhibit a preferred direction, the force per unit volume is [166]

$$\mathbf{F}_{\mathrm{mf}} = \frac{2}{3} L \rho_{\mathrm{S}} \kappa \alpha_{\mathrm{He}} \left(\mathbf{v}_{\mathrm{S}} - \mathbf{v}_{\mathrm{N}} \right). \tag{3.35}$$

Here, L is the total length of vortices per unit volume. In order to obtain an estimate for this quantity, one can balance the effects that increase and suppress turbulence and, therefore, alter the parameter L. Whereas its growth can be attributed to the Magnus effect, the decay of quantum turbulence on large scales satisfies the same Kolmogorov scaling [168] as observed in classical fluids [169]. If both mechanisms are in equilibrium, the following steady-state solution for L is found [166],

$$L = \left(\frac{2\pi}{\kappa} \right)^2 \left(\frac{\chi_1}{\chi_2} \right)^2 \alpha_{\mathrm{He}}^2 \left(v_{\mathrm{S}} - v_{\mathrm{N}} \right)^2, \tag{3.36}$$

where χ_1 and χ_2 are dimensionless parameters of order unity. For an isotropic vortex tangle, the mutual friction force is thus proportional to the cube of the relative velocity as had previously been suggested by Gorter and Mellik [170]. Note that by averaging the filament model of Schwarz [162] over all vortex segments inside a sample, a qualitatively similar result can be obtained for the macroscopic mutual friction force [171].

The mesoscopic framework can further help to improve our understanding of the stability of superfluid vortices [172]. Whereas Vinen's early experiments were performed with non-rotating helium, subsequent studies also examined the counterflow behaviour in rotating samples which similarly exhibited turbulent characteristics [173]. It has been suggested by Glaberson et al. [174] that this could be the result of a hydrodynamical vortex array instability. As soon as the counterflow, applied along the vortex tangent, exceeds a critical velocity, the vortex lines become unstable towards the excitation of *Kelvin waves*. These helical displacements are named after their discoverer Lord Kelvin [175] and will play an important role at several instances in the remainder of this thesis. Using a simple plane-wave analysis, the dispersion relation associated with the excitation of a Kelvin mode of wave number k reads as [174] (see also Sidery et al. [176])

$$\omega(k) = 2\Omega + \nu_{\mathrm{S}} k^2, \tag{3.37}$$

where Ω denotes the macroscopic angular velocity and ν_{S} the effective superfluid viscosity defined in Equation (3.29). Equation (3.37) displays the typical critical behaviour, which can be quantified by minimising $\omega(k)/k$. This leads to the critical wave number, $k_{\mathrm{c}} \equiv \sqrt{2\Omega/\nu_{\mathrm{S}}}$, at which the vortex line instability (often named the *Donnelly-Glaberson instability*) is triggered. The corresponding critical counterflow velocity is then given

$$w_{\mathrm{NS,c}} = \frac{\omega(k_{\mathrm{c}})}{k_{\mathrm{c}}} = 2\sqrt{2\Omega\nu}. \tag{3.38}$$

By exceeding this value, an initially regular vortex array can hence be destabilised and transformed into a turbulent tangle of vortices, which drastically changes the rotational dynamics. We will return to the problem of superfluid turbulence in Chapter 8, where the characteristics of laboratory systems and neutron stars are compared in more detail.

3.2.6 Ultra-cold gases

The close analogy between superfluid helium and a bosonic gas at low temperatures is illustrated by the presence of a quantum mechanical condensate that exhibits macroscopic properties. Since all particles in the BEC occupy the same minimum energy state, a mean-field description can be employed to obtain the macroscopic wave function as the symmetrised product of the single-particle wave functions. This does, however, not account for the interactions between individual bosons. In the limit $T \to 0$, the scattering length in a BEC is typically of the order of a few nm, whereas the particle separation is about 100 nm [156], implying that ultra-cold gases are dilute and two-body scattering is the dominant interaction mechanism. While such processes are strong, they only play a role when two atoms come very close to each other. This can be easily captured by including an effective interaction (an additional source term proportional to $|\Psi|^2\Psi$) into Equation (3.2). The resulting non-linear Schrödinger equation, referred to as the *time-dependent Gross-Pitaevskii (GP) equation* [145, 146], usually applied to model the properties of a Bose-Einstein condensate in the low temperature limit, then reads as

$$i\hbar \frac{\partial \Psi(\mathbf{r},t)}{\partial t} + \frac{\hbar^2}{2m_{\mathrm{c}}}\nabla^2\Psi(\mathbf{r},t) + V(\mathbf{r})\Psi(\mathbf{r},t) + U_0|\Psi(\mathbf{r},t)|^2\Psi(\mathbf{r},t) = 0. \tag{3.39}$$

As before, $\Psi(\mathbf{r},t)$ denotes the complex macroscopic wave function and m_{c} the bosonic mass. Furthermore, $V(\mathbf{r},t)$ represents the external potential confining the BEC and the effective interaction parameter, U_0, is related to the scattering length, a, via

$$U_0 = \frac{4\pi\hbar^2 a}{m_{\mathrm{c}}}. \tag{3.40}$$

The time-independent version of Equation (3.39) is of similar form as the first Ginzburg-Landau equation, which will be given in Subsection 3.3.4.

The time-dependent GP equation is particularly useful for studying the dynamics

of a BEC, the reason being the close connection between the quantum mechanical and the hydrodynamical picture. As illustrated for helium II, the Madelung transformation can be applied to express the non-linear Schroedinger equation in terms of the two new degrees of freedom, i.e. the amplitude Ψ_0 and phase φ of the wave function. By substituting the condensate density, n_c, and the gradient of the phase, which is proportional to the condensate velocity, $\mathbf{v}_\mathrm{S}$, as defined in Equation (3.8), the behaviour of the wave function can be mapped to the equations of motion for a fluid. Because the non-linear interaction term in Equation (3.39) is real and does not contribute to the imaginary part, the Madelung transformation results in the same continuity equation as the linear Schrödinger equation (see Equation (3.6)). On the other hand, the second equation of motion has to be adjusted by replacing the chemical potential $\mu \to V(\mathbf{r}) + U_0|\Psi(\mathbf{r},t)|^2$. This leads to the following momentum equation

$$\frac{D\mathbf{v}_\mathrm{S}}{Dt} + \frac{1}{m_\mathrm{c}} \nabla \left(V + U_0 n_\mathrm{c} - \frac{\hbar^2}{2m_\mathrm{c}\sqrt{n_\mathrm{c}}} \nabla^2 \sqrt{n_\mathrm{c}} \right) = 0. \tag{3.41}$$

The quantum pressure term is again negligible if the typical lengthscale for variations of the macroscopic wave function is much larger than the coherence length, ξ [156], so that one is left with

$$\frac{D\mathbf{v}_\mathrm{S}}{Dt} + \frac{1}{m_\mathrm{c}} \nabla \left(V + U_0 n_\mathrm{c} \right) = 0. \tag{3.42}$$

This is equivalent to the Euler equation of hydrodynamics in the presence of an external potential and a modified chemical potential. In the context of neutron star modelling, the former could be identified with the gravitational potential, while the quantity $U_0 n_\mathrm{c}$ has taken the place of the chemical potential. As this term originates from the addition of an effective interaction in the Schrödinger equation, we see that two-body scattering processes in the BEC produce a pressure-like term in the momentum equation similar to what one would expected from normal fluid dynamics. Note that for a boson gas of uniform density, $U_0 n_\mathrm{c}$ is indeed equal to the chemical potential [156]. This analogy will again form the basis of the discussion in Section 8.2.

3.3 Modelling Superconductors

Following Onnes' discovery [116], the first three decades were dominated by experimental studies aimed at determining the basic properties of the superconducting phase. In addition to the disappearance of the electrical resistivity below a critical temperature, the complete expulsion of magnetic flux in the presence of an external field was found to be the main characteristic of a superconducting sample. The Meissner effect, the theoretical work of the London brothers and a quantum mechanical description that forms the justification for their phenomenological approach are presented in the following subsections. This will be succeeded by a discussion of the differences between type-I and type-II superconductors and the quantisation of magnetic flux. Finally, the section on

superconductivity will conclude with an introduction to the Ginzburg-Landau theory. It provides the possibility to calculate the critical quantities of the phase transitions in a superconductor and lays the foundation for several analyses of a neutron star's fluid interior. Gaussian units will be employed throughout the remainder of this thesis.

3.3.1 Meissner effect and London equations

In order to determine the behaviour of matter condensing into a superconducting state below a critical temperature, T_c, one can study its response to external magnetic fields. The simplest reaction would be the generation of surface currents that flow in a small sheet of order λ (see below) provoking the expulsion of the interior magnetic field. For the purpose of a theoretical description, a distinction between an external current density, $\mathbf{j}_\mathrm{ext}$, that generates a macroscopic, averaged field, $\mathbf{H}$, and so-called *magnetisation currents* affecting only the mesoscopic magnetic induction, $\bar{\mathbf{B}}$, is beneficial. The electronic supercurrent density, $\mathbf{j}_\mathrm{S}$, present inside a superconductor is of mesoscopic origin and therefore attributed to the second class. Hence, the exterior field, $\mathbf{H}$, is unaffected by the presence of the superconductor. Moreover, a macroscopic average of the magnetic induction is defined by $\mathbf{B}$. For a superconducting sample, this quantity could vary smoothly over macroscopic lengthscales, while in the case of vacuum or a normal metal, where no magnetisation currents are present, one finds $\mathbf{H} = \bar{\mathbf{B}} = \mathbf{B}$.

Based on experimental observations, Fritz and Heinz London suggested that the mesoscopic electric field, $\bar{\mathbf{E}}$, and the mesoscopic magnetic induction, $\bar{\mathbf{B}}$, inside a superconductor are governed by the following two equations [118],

$$\bar{\mathbf{E}} = \frac{m_\mathrm{c}}{n_\mathrm{c} q^2} \frac{\partial \mathbf{j}_\mathrm{S}}{\partial t}, \qquad \bar{\mathbf{B}} = -\frac{m_\mathrm{c} c}{n_\mathrm{c} q^2} \nabla \times \mathbf{j}_\mathrm{S}, \tag{3.43}$$

where m_c and q are the mass and charge, respectively, and n_c is the number density of the charged particles responsible for the superconducting behaviour. The first London equation captures the perfect conductivity feature, whereas the second one describes the Meissner effect. This can be seen by combining the second Equation of (3.43) with Ampère's law, which locally reads as

$$\nabla \times \bar{\mathbf{B}} = \frac{4\pi}{c} \mathbf{j}_\mathrm{S}. \tag{3.44}$$

In this relation displacement currents have been neglected. This is possible because in an equilibrium or steady-state superconductor, the supercurrent density is no longer time-dependent [113]. Hence, the electric field vanishes in those cases (see first Equation (3.43)), allowing one to neglect the displacement current that is proportional to $\partial \bar{\mathbf{E}}/\partial t$. Moreover, no magnetic monopoles are present and, therefore, the Maxwell equation

$$\nabla \cdot \bar{\mathbf{B}} = 0 \tag{3.45}$$

is satisfied. One then arrives at an equation for the mesoscopic magnetic induction,

$$\lambda^2 \nabla^2 \bar{\mathbf{B}} = \bar{\mathbf{B}}, \tag{3.46}$$

where we define the penetration depth as

$$\lambda \equiv \left(\frac{m_\mathrm{c} c^2}{4\pi n_\mathrm{c} q^2} \right)^{1/2}. \tag{3.47}$$

Considering a flat boundary between a superconducting surface and free space that lies in the z-direction and a constant external field, $\mathbf{H} = \mathbf{B} = B_0 \hat{\boldsymbol{z}}$, applied parallel to the boundary, the solution for the magnetic field inside the superconductor is

$$\bar{\mathbf{B}}(x) = B_0 \, \exp(-x/\lambda) \, \hat{\boldsymbol{z}}. \tag{3.48}$$

The x-direction is perpendicular to the boundary and Equation (3.48), thus, implies that the magnetic field decays exponentially inside the superconductor. The London penetration depth, λ, describes how far the field reaches into the sample and determines the thickness of the surface sheet in which the superconducting currents are generated.

The origin of the phenomenological London equation (3.46) is enlightened by considering a quantum mechanical picture, in which the wave function represents the superposition of all superconducting states in the condensate. As first pointed out by Fritz London himself [119], this relies on the usage of a vector potential, $\mathbf{A}$, defined by

$$\bar{\mathbf{B}} \equiv \nabla \times \mathbf{A}. \tag{3.49}$$

With an approach similar to the one presented in Subsection 3.2.1 for a superfluid, a quantum mechanical current density can be derived for the charged superconducting condensate. Using the standard formula for minimal coupling, one replaces

$$\nabla \to \nabla - \frac{iq}{\hbar c} \mathbf{A}, \tag{3.50}$$

in order to obtain

$$\mathbf{j}_\mathrm{s} = \frac{iq\hbar}{2m_\mathrm{c}} \left[\Psi \left(\nabla + \frac{iq}{\hbar c} \mathbf{A} \right) \Psi^* - \Psi^* \left(\nabla - \frac{iq}{\hbar c} \mathbf{A} \right) \Psi \right]. \tag{3.51}$$

In this picture, $m_\mathrm{c} \equiv 2m_\mathrm{e}$ and $q \equiv -2e$, where m_e denotes the mass of an electron and $e \equiv |e|$ the elementary charge. Substituting the macroscopic wave function, Ψ, given in Equation (3.1) leads to an expression for the charge current density in a superconductor,

$$\mathbf{j}_\mathrm{s} = \frac{q\hbar}{m_\mathrm{c}} \, n_\mathrm{c} \, \nabla\varphi - \frac{q^2}{m_\mathrm{c} c} \, n_\mathrm{c} \, \mathbf{A}, \tag{3.52}$$

where $n_\mathrm{c} = |\Psi|^2$ represents the number density of electron Cooper pairs in the super-

conductor. The first term in Equation (3.52) is equivalent to the result of the superfluid case, while the second term reflects the charge property of the condensate. Defining the supercurrent density as $\mathbf{j}_\mathrm{S} \equiv q n_\mathrm{c} \mathbf{v}_\mathrm{S}$, one finds a relation for the velocity of the superconducting particles,

$$\mathbf{v}_\mathrm{S} = \frac{\hbar}{m_\mathrm{c}} \nabla\varphi - \frac{q}{m_\mathrm{c} c} \mathbf{A}. \tag{3.53}$$

Moreover, the quantum mechanical wave function is invariant under specific changes in the phase. As it can be set to zero in an appropriate gauge, it is possible to eliminate the term proportional to $\nabla\varphi$ in Equation (3.52). Hence, the supercurrent density, $\mathbf{j}_\mathrm{S}$, is proportional to the vector potential, $\mathbf{A}$,

$$\mathbf{j}_\mathrm{S} = -\frac{q^2}{m_\mathrm{c} c} n_\mathrm{c} \mathbf{A}. \tag{3.54}$$

Taking the curl of this relation and eliminating the current with the help of Ampère's law (3.44), one finds the following equation valid inside the superconductor,

$$\lambda^2 \nabla^2 \bar{\mathbf{B}} = \bar{\mathbf{B}}. \tag{3.55}$$

This is exactly the phenomenological London result given in Equation (3.55), describing the Meissner effect as the exponential decay of the mesoscopic magnetic induction, $\bar{\mathbf{B}}$.

3.3.2 London field in rotating superconductors

In contrast to a superfluid, a superconducting sample is able to rotate without quantising its circulation, i.e. forming vortices. The fluxtubes themselves are not related to the macroscopic rotation, as these dynamics induce an additional characteristic magnetic field inside the superconductor, whose axis is parallel to the rotation axis. This *London field*, $\mathbf{b}_\mathrm{L}$, is a fundamental property of the superconducting state and can be calculated by combining the definition of the superconducting velocity (3.53) and the condition for solid-body rotation given in Equation (3.17). For vanishing phase gradients, $\nabla\varphi = 0$, the energy of a rigidly rotating superconductor is minimised by a vector potential of the form,

$$\mathbf{A}_\mathrm{L} = -\frac{m_\mathrm{c} c}{q} \boldsymbol{\Omega} \times \mathbf{r}, \tag{3.56}$$

which according to Equation (3.54) is supported by surface currents. For a cylindrical geometry and rotation about the z-axis, i.e. $\boldsymbol{\Omega} = \Omega \hat{\boldsymbol{z}}$, this potential corresponds to the following magnetic field,

$$\mathbf{b}_\mathrm{L} = \frac{2 m_\mathrm{c} c}{q} \boldsymbol{\Omega}. \tag{3.57}$$

As discussed in more detail in Section 4.2, the London field is also present in the neutron star interior. Although small in magnitude, i.e. $b_\mathrm{L} \approx 0.1\,\mathrm{G}$ (see Equation (4.53)), it has important consequences for the electrodynamical properties of a rotating star.

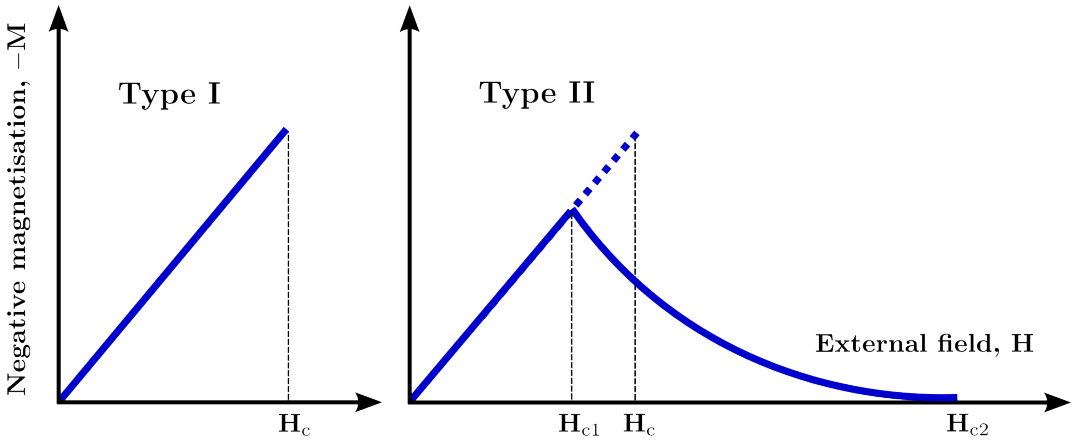

Figure 3.4: Magnetisation curves for a type-I (left) and type-II (right) superconductor with the same thermodynamical critical field, H_c. The areas below the curves are equal in both cases and given by the condensation energy, E_{cond}.

3.3.3 Two types of superconductors and flux quantisation

The first experiments analysing superconductivity did not provide access to the mesoscopic magnetic induction, $\bar{\mathbf{B}}$, because they measured the total magnetic flux present in a sample. Hence, one rather obtained information about the spatially averaged magnetic induction, $\mathbf{B}$. This macroscopic induction is connected to the external field, $\mathbf{H}$, and the average magnetisation, $\mathbf{M}$, via

$$\mathbf{B} = \mathbf{H} + 4\pi\mathbf{M}. \tag{3.58}$$

The magnetisation, $\mathbf{M}$, is a function of $\mathbf{H}$ and its behaviour strongly dependent on the properties of the medium. In vacuum or a normal conducting metal, i.e. in a superconductor above the transition temperature, T_c, the average induction and the external field are equivalent, so the average magnetisation has to vanish. Measurements of $\mathbf{M}$ in superconductors have revealed features that allow a separation into two distinct classes, *type-I* and *type-II* media. Typical magnetisation curves are shown in Figure 3.4.

For type-I systems, the magnetisation increases linearly with the external field. In this Meissner state, no magnetic flux is present in the interior of the superconductor, i.e. $\mathbf{B} = 0$, and the magnetisation generated by the supercurrents in the surface layer balances the external field. As soon as $H \equiv |\mathbf{H}|$ reaches the critical value, H_c, the magnetisation drops to zero. The superconducting quantum state is destroyed and the material turns normal in a first-order phase transition. The critical magnetic field, H_c, is thermodynamically related to the condensation energy, E_{cond}. This is the temperature-dependent difference in the free energy densities of the normal and the superconducting state in the absence of external fields, f_{N0} and f_{S0}, respectively. It is given by

$$E_{cond}(T) = f_{N0}(T) - f_{S0}(T) = \frac{H_c(T)^2}{8\pi}. \tag{3.59}$$

Depending on the geometry of a type-I superconductor, characterised by the so-called

demagnetisation factor, it is possible to create an intermediate state for external fields close to H_c. Considering, for example, a superconducting sphere, its averaged surface field, $B \equiv |\mathbf{B}|$, is not constant. It exceeds the applied field, H, in the equatorial plane and is smaller than H close to the poles [114]. Therefore, certain regions could have $B > H_\mathrm{c}$, while others could not, creating a state where superconducting and normal regions coexist. The size of the corresponding domains depends crucially on the *surface energy*, δ, of the interfaces, which will be studied in the next subsection.

For a type-II superconductor, the Meissner state does not break down abruptly. Instead, above a critical field, $H_{\mathrm{c}1}$, it is energetically favourable for the medium to let magnetic flux continuously enter in the form of fluxtubes. The quantity responsible for this behaviour is again the surface energy. It also dictates that the resulting magnetic structures are ordered in a triangular array. This was first investigated by Abrikosov [123], whose work will be further discussed below. Inside the fluxtubes, the material is in a normal state, which is screened from the superconducting region by additional, circulating supercurrents. As discussed in Subsection 3.2.3 for the quantised circulation of a rotating superfluid, the quantum mechanical wave function, Ψ, is invariant under changes in the phase, φ, that are multiples of 2π. Taking account of this invariance, one can integrate Equation (3.53) for the superconducting velocity around a closed contour $\mathcal{L}$ located inside the sample to obtain

$$\frac{c\hbar}{q} \oint_{\mathcal{L}} \nabla\varphi = \frac{c}{q} \oint_{\mathcal{L}} \left(m_\mathrm{c}\mathbf{v}_\mathrm{S} + \frac{q}{c}\,\mathbf{A} \right) \cdot \mathrm{d}\mathbf{l} = \frac{ch}{2e}\, n, \qquad n \in \mathbb{Z}. \tag{3.60}$$

In contrast to the superfluid vortex, the velocity profile of a superconducting fluxtube does not have a $1/r$-dependence but decays exponentially for large distances, r, from the core, i.e. $|\mathbf{v}_\mathrm{S}| \sim \exp(-r/\lambda)$. Choosing a contour sufficiently far away from the centres of individual fluxtubes, the integral over $\mathbf{v}_\mathrm{S}$ vanishes. Moreover, Stokes' theorem can be applied to rewrite the contour integral into a surface integral over the surface, $\mathcal{A}$, enclosed by $\mathcal{L}$. By using the definition of the vector potential given in Equation (3.49), a quantisation condition for the total magnetic flux, ϕ, inside a superconductor is found,

$$\phi = \oint_{\mathcal{L}} \mathbf{A} \cdot \mathrm{d}\mathbf{l} = \int_{\mathcal{A}} (\nabla \times \mathbf{A}) \cdot \mathrm{d}\mathbf{S} = \int_{\mathcal{A}} \bar{\mathbf{B}} \cdot \mathrm{d}\mathbf{S} = \frac{ch}{2e}\, n \equiv \phi_0 n, \tag{3.61}$$

where ϕ_0 is the magnetic flux quantum. The flux quanta of all individual fluxtubes have to add up to the total flux inside the superconductor. Hence, one can define the magnitude of the averaged magnetic induction inside a superconducting sample by

$$B \equiv \mathcal{N}_\mathrm{ft}\phi_0, \tag{3.62}$$

with the fluxtube surface density $\mathcal{N}_\mathrm{ft}$. As in the case of helium II, where the vortex density could be determined from the angular velocity of the solid-body equivalent, it is possible to determine the number of fluxtubes per unit area in a superconductor for a

specific magnetic induction. This provides again the possibility to estimate an average distance, $d_{\rm ft}$, between individual fluxtubes,

$$d_{\rm ft} \simeq \mathcal{N}_{\rm ft}^{-1/2} = \left(\frac{\phi_0}{B}\right)^{1/2}. \tag{3.63}$$

At the upper critical field, $H_{\rm c2}$, the fluxtubes become so densely packed that their cores start to touch. This destroys the superconducting properties and the entire sample is turned into a normal conductor in a second-order phase transition. $H_{\rm c2}$ can be much greater than the thermodynamical critical field, $H_{\rm c}$, a fact exploited in high-field superconducting magnets. If a type-I and a type-II superconductor have the same $H_{\rm c}$, then the magnetisation depends on the external field as shown in Figure 3.4. However, the area under both curves is the same, as it equals the condensation energy, $E_{\rm cond}$.

3.3.4 Ginzburg-Landau theory in a nutshell

One approach to superconductivity that allows the reproduction of many observed phenomena is based on the theory of phase transitions. It represents a generalisation of the theory developed by the London brothers and was pioneered by Ginzburg and Landau in 1950 [121]. The basic idea developed by the Russian physicists is that a second-order phase transition can be characterised by a change in an order parameter. In the case of a superconductor, this role is taken over by the macroscopic wave function, $|\Psi|^2$, i.e. the Cooper pair density. The temperature is the quantity governing the transition. Above the superconducting transition temperature, $T_{\rm c}$, no Cooper pairs are present, whereas the number of paired states increases drastically below $T_{\rm c}$. Hence, the phase transition can be interpreted as a symmetry breaking in $|\Psi|^2$. Some of the major successes of the phenomenological Ginzburg-Landau theory are the derivation of the critical fields of a type-II superconductor and the inclusion of interaction effects depending non-linearly on the order parameter. Although not obtained from microscopic principles but rather from physical intuition, the theory is particularly useful for the description of phenomena that are observable on macroscopic scales. Thus, it can also be valuable in determining the characteristics of the superconducting neutron star interior [177, 178].

Free energy densities and Ginzburg-Landau equations

Close to $T_{\rm c}$, Ginzburg and Landau assumed that the order parameter would be small and vary only slowly in the spatial coordinate, $\mathbf{r}$. This led to the postulate that close to the transition the Helmholtz free energy of a system could be written as an expansion in the order parameter. For matter turning superconducting in a second-order phase transition, the free energy density, $f_{\rm s0}$, in the absence of an external field is given by

$$f_{\rm s0}(\mathbf{r}) = f_{\rm n0}(\mathbf{r}) + \alpha\,|\Psi(\mathbf{r})|^2 + \frac{\beta}{2}\,|\Psi(\mathbf{r})|^4 + \frac{\hbar^2}{2m_{\rm c}}\left|\left(\nabla - \frac{iq}{\hbar c}\,\mathbf{A}(\mathbf{r})\right)\Psi(\mathbf{r})\right|^2 + \frac{\left|\bar{\mathbf{B}}(\mathbf{r})\right|^2}{8\pi}, \tag{3.64}$$

where the phenomenological parameters α and β depend on the temperature and f_{N0} is the free energy density of the normal phase in the absence of fields. All other parameters have been defined in the previous subsections. The total free energy, F_{S0}, is found by integrating f_{S0} over the volume considered. For a vanishing order parameter, i.e. the normal state above T_{c}, the free energy density reduces to the expected value $f_{\mathrm{N0}}+\bar{B}^2/8\pi$ with $\bar{B}^2 \equiv |\bar{\mathbf{B}}|^2$. Note that the free energy density is not only related to the order parameter, $|\Psi|^2$, but also to the vector potential, $\mathbf{A}$. This dependence was also found in BCS theory, where the supercurrent is proportional to the potential (see Equation (3.54)), illustrating the similarities between the two models, i.e. the fact that the Ginzburg-Landau theory can be deduced from the microscopic framework for $T \to T_{\mathrm{c}}$ [122].

In the presence of an external field $\mathbf{H}$, f_{S0} has to be modified, because the energy density of the normal phase contains an additional contribution. It is given by $H^2/8\pi$ and generated by the external currents. Hence, to calculate the free superconducting energy density, this term has to be subtracted and one obtains

$$f_{\mathrm{S}} = f_{\mathrm{N}} + \alpha\,|\Psi|^2 + \frac{\beta}{2}\,|\Psi|^4 + \frac{\hbar^2}{2m_{\mathrm{c}}}\left|\left(\nabla - \frac{iq}{\hbar c}\,\mathbf{A}\right)\Psi\right|^2 + \frac{\bar{B}^2}{8\pi} - \frac{H^2}{8\pi}, \tag{3.65}$$

where f_{S} and f_{N} represent the free energy densities of the superconducting and normal phase in the presence of an external field H, respectively. The spatial dependences have been omitted for clarity. The need for paying attention to the energy density generated by the external currents becomes superfluous when another thermodynamical potential is considered. In situations where the external field, H, is held constant and controlling the system, it is more convenient to consider Gibbs free energy densities, $g_{\mathrm{S,N}}$, related to the Helmholtz free energy densities, $f_{\mathrm{S,N}}$, via a Legendre transformation, i.e.

$$g_{\mathrm{S,N}} = f_{\mathrm{S,N}} - \frac{\bar{B}H}{4\pi}. \tag{3.66}$$

The difference between these potentials is illustrated by taking into account the definition of the thermodynamical critical field, H_{c}, given in Equation (3.59). Applying the external field, $H = H_{\mathrm{c}}$, one obtains for the difference in the Helmholtz energy densities of the normal and the superconducting state,

$$f_{\mathrm{N}} - f_{\mathrm{S}} = f_{\mathrm{N0}} + \frac{H_{\mathrm{c}}^2}{8\pi} - f_{\mathrm{S0}} = \frac{H_{\mathrm{c}}^2}{4\pi}. \tag{3.67}$$

The difference in the Gibbs energy densities, on the other hand, reduces to

$$g_{\mathrm{N}} - g_{\mathrm{S}} = f_{\mathrm{N0}} + \frac{H_{\mathrm{c}}^2}{8\pi} - \frac{H_{\mathrm{c}}^2}{4\pi} - f_{\mathrm{S0}} = 0. \tag{3.68}$$

In contrast to the Helmholtz energy, the Gibbs energy density remains constant during the phase change of a superconducting medium. The latter is therefore examined later on in order to calculate the critical fields of superconductivity.

Using the standard Euler-Lagrange equations, it is further possible to minimise g_S with respect to the complex conjugate wave function, Ψ^*, and the vector potential, $\mathbf{A}$, to arrive at the two Ginzburg-Landau equations [114],

$$\frac{\partial g_\mathrm{S}}{\partial \Psi^*} - \sum_{j=1}^{3} \frac{\partial}{\partial x_j} \frac{\partial g_\mathrm{S}}{\partial \left(\nabla_j \Psi^*\right)} = \alpha\, \Psi + \beta\, |\Psi|^2\, \Psi - \frac{\hbar^2}{2m_\mathrm{c}} \left(\nabla - \frac{iq}{\hbar c}\mathbf{A}\right)^2 \Psi = 0, \tag{3.69}$$

$$\frac{\partial g_\mathrm{S}}{\partial A_i} - \sum_{j=1}^{3} \frac{\partial}{\partial x_j} \frac{\partial g_\mathrm{S}}{\partial \left(\nabla_j A_i\right)} = \frac{iq\hbar}{2m_\mathrm{c}} \left(\Psi \nabla \Psi^* - \Psi^* \nabla \Psi\right) - \frac{q^2}{m_\mathrm{c} c} |\Psi|^2\, \mathbf{A} - \frac{c}{4\pi} \nabla \times (\nabla \times \mathbf{A}) = 0. \tag{3.70}$$

Here, x_j and A_j represent the three components of $\mathbf{r}$ and $\mathbf{A}$, respectively. The first equality is a modified Schrödinger equation for the quantum mechanical wave function, Ψ. Employing the definition of the vector potential (3.49) and Ampère's law (3.44), the second one defines the quantum mechanical current density as in Equation (3.51).

Characteristic lengthscales

The Ginzburg-Landau equations (3.69) and (3.70) introduce two characteristic lengthscales to the problem of superconductivity; the penetration depth, λ, and the coherence length, ξ. They are defined as

$$\lambda \equiv \left(\frac{m_\mathrm{c} c^2}{4\pi n_\mathrm{c} q^2}\right)^{1/2}, \tag{3.71}$$

and

$$\xi \equiv \left(\frac{\hbar^2}{2m_\mathrm{c}|\alpha|}\right)^{1/2}. \tag{3.72}$$

The former quantity is equal to the London penetration depth derived with the phenomenological London theory (see Equation (3.47)). It describes the lengthscale on which the Meissner effect suppresses the magnetic induction in the interior of the superconductor. Since the density of superconducting particles vanishes at the transition temperature, the penetration depth diverges as $T \to T_\mathrm{c}$. The second quantity represents the typical distance over which the order parameter, $|\Psi|^2$, varies in space. It is also temperature-dependent and diverges close to the transition temperature. For comparison, in BCS theory, the coherence length is identified with the dimension of a single Cooper pair. It is defined in terms of the temperature-dependent energy gap, Δ, and the Fermi velocity, v_F, related to the Fermi wave number, k_F, via $v_\mathrm{F} = \hbar k_\mathrm{F}/m_\mathrm{c}^*$. One therefore has

$$\xi_\mathrm{BCS} \equiv \frac{\hbar v_\mathrm{F}}{\pi \Delta} = \frac{\hbar^2 k_\mathrm{F}}{m_\mathrm{c}^* \pi \Delta}. \tag{3.73}$$

The effective mass m_c^*, also referred to as the *Landau effective mass*, characterises the static quantum mechanical ground state. Note that, as discussed in the next chapter, it

differs from the dynamical effective masses used in the context of neutron stars [179].

The ratio of the two lengthscales defined in Equations (3.71) and (3.72) is referred to as the Ginzburg-Landau parameter, κ_{GL}. There exists a critical value, $\kappa_{\mathrm{crit}} \equiv 1/\sqrt{2}$, that classifies the type of superconductivity. More precisely

$$\text{type-I:} \qquad \kappa_{\mathrm{GL}} \equiv \frac{\lambda}{\xi} < \kappa_{\mathrm{crit}}, \tag{3.74}$$

$$\text{type-II:} \qquad \kappa_{\mathrm{GL}} \equiv \frac{\lambda}{\xi} > \kappa_{\mathrm{crit}}. \tag{3.75}$$

The first case is characterised by $\lambda \lesssim \xi$ and a positive surface energy for the superconducting region. In the second case, $\lambda \gtrsim \xi$, the surface energy is negative and the material is in an unstable state. It becomes energetically favourable for the superconductor to divide into regions of order ξ and form a fluxtube array, each fluxtube carrying the flux quantum, ϕ_0. The existence of κ_{crit} is thus related to the surface energy (see below).

Critical fields I

The Ginzburg-Landau formalism also provides the means to calculate the critical fields of superconductivity. Firstly, the thermodynamical field, H_{c}, is related to the two free parameters, α and β. An expression is found by equating the Gibbs free energy densities of the normal and the superconducting state at equilibrium, i.e. $H = H_{\mathrm{c}}$. For the bulk of a superconducting medium, the free energy density is minimised by a constant order parameter and a zero vector potential, $\mathbf{A} = 0$, which implies that the induction vanishes, $\bar{\mathbf{B}} = 0$. The exact value obtained from Equation (3.69) is given by

$$|\Psi_\infty|^2 \equiv -\frac{\alpha}{\beta} = \frac{|\alpha|}{\beta}, \tag{3.76}$$

where $\alpha < 0$ and $\beta \approx$ constant for a superconductor [114]. In the normal phase, on the other hand, the minimum of the energy density is related to a vanishing order parameter, $|\Psi|^2 = 0$, and $\bar{\mathbf{B}} = \mathbf{B} = \mathbf{H}$. Hence, the Gibbs free energy densities that have to be equal at the phase transition are

$$g_{\mathrm{S}} = f_{\mathrm{S}} = f_{\mathrm{N}} - \frac{|\alpha|^2}{2\beta} - \frac{H^2}{8\pi}, \qquad g_{\mathrm{N}} = f_{\mathrm{N}} - \frac{H^2}{4\pi}. \tag{3.77}$$

Using $H = H_{\mathrm{c}}$ leads to the following identity for the critical thermodynamical field,

$$H_{\mathrm{c}} = \left(4\pi|\alpha|^2\beta^{-1}\right)^{1/2}. \tag{3.78}$$

Additionally, the lower critical field, H_{c1}, can be determined. It marks the value at which flux first enters the superconductor. Hence, the Gibbs energy, G_{S}, of the sample without fluxtubes must be equal to the case where exactly one fluxtube is present, i.e.

$$G_{\mathrm{S}}\big|_{\text{no flux}} = G_{\mathrm{S}}\big|_{\text{one fluxtube}}. \tag{3.79}$$

The total Gibbs energy, G_{S}, is then obtained by integrating the Gibbs energy density, g_{S}, over the superconductor's volume, $\mathcal{V}$,

$$G_{\mathrm{S}} = \int_{\mathcal{V}} g_{\mathrm{S}}\,\mathrm{d}V = F_{\mathrm{S}} - \frac{H}{4\pi}\int_{\mathcal{V}} \bar{B}\,\mathrm{d}V. \tag{3.80}$$

In the Meissner state, where fluxtubes are absent and $\bar{B} = 0$, the Gibbs energy equals the Helmholtz energy, $G_{\mathrm{S}}\big|_{\text{no flux}} = F_{\mathrm{S}}$. For the single fluxtube case, one has instead

$$G_{\mathrm{S}}\big|_{\text{one fluxtube}} = F_{\mathrm{S}} + \mathcal{E}_{\mathrm{ft}} L - \frac{H_{\mathrm{c1}}\phi_0 L}{4\pi}. \tag{3.81}$$

Here, $\mathcal{E}_{\mathrm{ft}}$ denotes the increase in the free energy per unit length (see Subsection 4.3.3) due to the presence of a fluxtube of length L. Hence, the lower critical field is given by

$$H_{\mathrm{c1}} = \frac{4\pi\mathcal{E}_{\mathrm{ft}}}{\phi_0}, \qquad \text{with} \qquad \mathcal{E}_{\mathrm{ft}} = \left(\frac{\phi_0}{4\pi\lambda}\right)^2 \ln\kappa_{\mathrm{GL}}. \tag{3.82}$$

Surface energy

A similar energy statement can be used to calculate the surface energy, δ, which determines how magnetic flux is distributed inside a superconducting sample to minimise the total energy. More precisely, δ is obtained by comparing the Gibbs free energies of the pure, flux-free type-I phase and the coexisting state, in which magnetic flux is able to penetrate the superconductor, at the thermodynamical critical field, $H = H_{\mathrm{c}}$. The physical behaviour of type-I and type-II superconductors is fundamentally different at this point and the surface energy is thus given by

$$\delta = G_{\mathrm{S}}\big|_{H=H_{\mathrm{c}},\ \text{coexisting}} - G_{\mathrm{S}}\big|_{H=H_{\mathrm{c}},\ \text{no flux}}. \tag{3.83}$$

To simplify the problem, a one-dimensional set-up along the x-axis is considered. The total Gibbs energies are obtained by integrating the corresponding densities along this coordinate. At $H = H_{\mathrm{c}}$, the energy density of the flux-free Meissner state is equal to the Gibbs energy density of the normal state (see Equation (3.77)), which gives

$$\delta = \int_{-\infty}^{\infty} \left(g_{\mathrm{S}} - g_{\mathrm{S}}\big|_{\text{no flux}}\right)\mathrm{d}x = \int_{-\infty}^{\infty} \left(f_{\mathrm{S}} - \frac{\bar{B}(x)H_{\mathrm{c}}}{4\pi} - f_{\mathrm{N}} + \frac{H_{\mathrm{c}}^2}{4\pi}\right)\mathrm{d}x, \tag{3.84}$$

where the definition of g_{S} given in Equation (3.66) has also been used. In the coexisting phase, the magnetic induction is no longer zero but instead a function of x. Substituting the Ginzburg-Landau free energy density (3.65) for f_{S}, we obtain

$$\delta = \int_{-\infty}^{\infty} \left(\alpha\,|\Psi|^2 + \frac{\beta}{2}\,|\Psi|^4 + \frac{\hbar^2}{2m}\left|\left(\nabla - \frac{iq}{\hbar c}\,\mathbf{A}\right)\Psi\right|^2 + \frac{\bar{B}^2}{8\pi} + \frac{H_{\mathrm{c}}^2}{8\pi} - \frac{\bar{B}H_{\mathrm{c}}}{4\pi}\right)\mathrm{d}x. \tag{3.85}$$

This can be further simplified by taking advantage of the first Ginzburg-Landau equation. Multiplying Equation (3.69) with Ψ^*, integrating over the x-direction and performing an integration by parts gives the following

$$\int_{-\infty}^{\infty} \left(\alpha \left|\Psi\right|^2 + \beta \left|\Psi\right|^4 + \frac{\hbar^2}{2m} \left| \left(\nabla - \frac{iq}{\hbar c} \mathbf{A} \right) \Psi \right|^2 \right) \mathrm{d}x = 0. \tag{3.86}$$

Substituting this back into Equation (3.85), the surface energy reduces to

$$\delta = \int_{-\infty}^{\infty} \left(-\frac{\beta}{2} \left|\Psi(x)\right|^4 + \frac{\left[\bar{B}(x) - H_\mathrm{c}\right]^2}{8\pi} \right) \mathrm{d}x. \tag{3.87}$$

In general, this expression has to be integrated numerically while simultaneously solving the Ginzburg-Landau equations to provide expressions for the order parameter and the vector potential. However, Equation (3.87) can be rewritten in terms of dimensionless quantities, which allow for a more intuitive interpretation. Using Equations (3.76) and (3.78), one obtains

$$\delta = \int_{-\infty}^{\infty} \frac{H_\mathrm{c}^2}{4\pi} \left(-\frac{|\tilde{\Psi}(x)|}{2} + \left[\tilde{B}(x) - \frac{1}{\sqrt{2}} \right]^2 \right) \mathrm{d}x, \tag{3.88}$$

where

$$\tilde{\Psi}(x) \equiv \frac{\Psi(x)}{\Psi_\infty}, \qquad \tilde{B}(x) \equiv \frac{\bar{B}(x)}{\sqrt{2} H_\mathrm{c}}. \tag{3.89}$$

Deep inside the normal and superconducting regions, the integrand of Equation (3.88) is constant and of small magnitude. Thus, δ is localised around the interface, justifying the name surface energy. The relation also explains the different behaviour of the two types of superconductors. For $\kappa_\mathrm{GL} \gg 1$, the field reaches far into the superconducting sample, which results in $\bar{B} \approx H_\mathrm{c}$ and $\tilde{B} \approx 1/\sqrt{2}$. δ is thus negative and it becomes energetically favourable for the superconductor to increase the surface of superconducting-normal domain walls. Hence, it divides into microscopic structures of order ξ, which exactly describes the formation of the fluxtube array. For $\kappa_\mathrm{GL} \ll 1$, however, the field in the superconducting region vanishes, i.e. $\bar{B} = 0$. Since, the normalised order parameter is always smaller than one, i.e. $\tilde{\Psi} \leq 1$, the surface energy, δ, of the interface is positive and regions of macroscopic flux represents the lowest energy state. The type-I sample, therefore, forms an intermediate state and does not split into individual fluxtubes.

Critical fields II

The Ginzburg-Landau theory also allows one to determine the upper critical field, H_{c2}. For a decreasing external field, H_{c2} represents the maximum value at which a sample can still become superconducting in a second-order phase transition. At this point, the order parameter stays small and the non-linear term in the Ginzburg-Landau equation (3.69) is negligible. Moreover, screening effects caused by supercurrents remain small, implying

that the averaged and the mesoscopic magnetic induction inside the superconductor are close to the external field, $\mathbf{H}$. This allows the identification $\mathbf{A} = \mathbf{A}_{\text{ext}}$ and results in the decoupling of the two Ginzburg-Landau equations, where $\mathbf{A}_{\text{ext}}$ is the vector potential describing the external field, $\mathbf{H}$. Linearising Equation (3.69) leads to

$$-\left(\nabla - \frac{iq}{\hbar c}\mathbf{A}\right)^2 \Psi = \frac{\Psi}{\xi^2}. \tag{3.90}$$

Using Cartesian coordinates $\{x, y, z\}$ and assuming $\mathbf{H} = H_0\hat{\boldsymbol{z}}$, a possible choice for the potential would be $\mathbf{A} = xH_0\hat{\boldsymbol{y}}$. In this case, the effective potential will only depend on the spatial coordinate x, suggesting that the solution of Equation (3.90) is of the form $\Psi(x, y, z) = f(x)\,\mathrm{e}^{ik_y y}\,\mathrm{e}^{ik_z z}$, with the wave numbers k_y and k_z in y- and z-direction, respectively. For an infinite medium, one then obtains an equation equivalent to a modified Schrödinger equation for a particle in a harmonic oscillator potential,

$$\frac{\hbar^2}{2m_{\text{c}}}\left[-\partial_x^2 + \left(\frac{2\pi H_0}{\phi_0}\right)^2\left(x - \frac{k_y\phi_0}{2\pi H_0}\right)^2\right] f(x) = \frac{\hbar^2}{2m_{\text{c}}}\left(\frac{1}{\xi^2} - k_z^2\right) f(x). \tag{3.91}$$

Its solutions correspond to discrete Landau levels (see for example Landau and Lifshitz [180] for details) that are highly degenerate and characterised by the energy eigenvalues

$$E_n = \hbar\omega_c\left(\frac{1}{2} + n\right) = \frac{\hbar q H_0}{m_{\text{c}}c}\left(\frac{1}{2} + n\right), \tag{3.92}$$

where ω_c is the cyclotron frequency related to the magnitude of the average induction. These quantised energies have to be identical to the right-hand side of Equation (3.91), providing a relation for the parameter H_0. Its maximum value then corresponds to the upper critical field, H_{c2}, which is obtained for $n = 0$ and $k_z = 0$ and given by

$$H_{\text{c2}} = \frac{\phi_0}{2\pi\xi^2}. \tag{3.93}$$

For higher external fields, the medium no longer condenses into a superconducting state but stays normal. For a more detailed derivation see Tinkham [114]. The eigenfunctions related to the minimum energy state at H_{c2} are

$$\Psi(x, y) = \exp\left[-\frac{1}{2\xi^2}\left(x - \frac{k_y\phi_0}{2\pi H_0}\right)^2\right] \exp\left[ik_y y\right]. \tag{3.94}$$

These linearised solutions play a crucial role in deriving the fluxtube array structure.

Fluxtube array formation

Studies of the fluxtube arrangement in type-II superconductors were pioneered by Abrikosov [123] and his work is briefly summarised in the following. The original calculation

is based on the same concepts as employed in the derivation of the upper critical field. However, for external fields below H_{c2}, the non-linear term in the Ginzburg-Landau equation (3.69) can no longer be neglected. Using the linearised, decoupled Ginzburg-Landau equations is thus not sufficient any more. Instead, for $H \lesssim H_{c2}$, the effects of the non-linear term can be included by applying perturbation theory. In this case, the averaged and the mesoscopic magnetic induction in the bulk are no longer equal to the applied field but rather the sum of the external field and a small correction produced by the circulating supercurrents, $\mathbf{j}_s$. Hence, the vector potential, $\mathbf{A}$, satisfies

$$\bar{\mathbf{B}} = \mathbf{H} + \bar{\mathbf{B}}_s = \nabla \times \mathbf{A}, \tag{3.95}$$

where

$$\nabla \times \bar{\mathbf{B}}_s = \frac{4\pi}{c}\mathbf{j}_s. \tag{3.96}$$

At this point, it is beneficial to separate the potential into two contributions, i.e. $\mathbf{A} \equiv \mathbf{A}_{c2} + \mathbf{A}_1$. The former part is the potential generating the upper critical field and the latter perturbative contribution contains all information about the additional magnetic fields. Combining these relations, one finds

$$\nabla \times \mathbf{A}_1 = \mathbf{H} - \mathbf{H}_{c2} + \bar{\mathbf{B}}_s. \tag{3.97}$$

Taking as before an external field parallel to the z-axis allows the choice $\mathbf{A}_{c2} = xH_{c2}\hat{\boldsymbol{y}}$. Right below H_{c2}, one would further expect the solution for Ψ to be close to the solution of the linearised equations calculated previously. Hence, $\Psi \equiv \Psi_0 + \Psi_1$, where the two functions are orthogonal and satisfy the condition

$$\int \Psi_0^* \Psi_1 \, \mathrm{d}V = 0. \tag{3.98}$$

This implies that the lowest energy eigenfunctions, Ψ_0, and the perturbative contributions, Ψ_1, are linear independent. Having calculated the eigenfunctions of the linearised system (see Equation (3.94)), the k_y-dependence of the resulting order parameter shows that there are infinitely many flux configurations able to generate the energy state H_{c2}. Below H_{c2}, the non-linearity breaks this degeneracy and favours a particular fluxtube arrangement. As any regular array has a lower energy than a random flux distribution, the wavefunction is expected to be periodic. This behaviour can be ensured by choosing the ansatz $k_y = nk$ with $n \in \mathbb{N}$. The most general solution of the linearised Ginzburg-Landau equations keeping periodicity in y-direction is, thus, the linear combination

$$\Psi_0(x, y) = \sum_n C_n \exp\left[-\frac{1}{2\xi^2}\left(x - \frac{nk\phi_0}{2\pi H_{c2}}\right)^2\right] \exp\left[inky\right]. \tag{3.99}$$

The periodicity in x-direction can also be recovered if the coefficients satisfy $C_{n+N} = C_n$ for $N \in \mathbb{N}$. A square lattice is then represented by $N = 1$, implying that all coefficients

are equal, whereas $N = 2$ together with $C_1 = iC_0$ characterises a triangular lattice.

Substituting the periodic wave function (3.99) and the external potential $\mathbf{A}_{c2}$ into the left-hand side of the second Ginzburg-Landau equation (3.70), one can determine the quantum mechanical current density associated with the linear solution,

$$\mathbf{j}_s = \frac{q\hbar}{2m_c}\left(-\partial_y|\Psi_0|^2\hat{\boldsymbol{x}} + \partial_x|\Psi_0|^2\hat{\boldsymbol{y}}\right). \tag{3.100}$$

In turn, this current generates an additional magnetic induction inside the superconductor. According to Equation (3.96), it reads as

$$\bar{\mathbf{B}}_s = -\frac{qh}{m_c c}|\Psi_0|^2\hat{\boldsymbol{z}}. \tag{3.101}$$

Using these results, it is possible to calculate a more accurate approximate solution to the first Ginzburg Landau equation. Substituting the decompositions for $\mathbf{A}$ and Ψ into Equation (3.69) and linearising the result gives an equation for the perturbation Ψ_1,

$$\mathcal{H}_0\Psi_1 + \beta|\Psi_0|^2\Psi_0 + \frac{1}{c}\mathbf{A}_1\cdot\left(\frac{iq\hbar}{m_c c}\nabla + \frac{q^2}{m_c c}\mathbf{A}_{c2}\right)\Psi_0 = 0. \tag{3.102}$$

The zeroth-order operator $\mathcal{H}_0$ is defined by

$$\mathcal{H}_0 \equiv \alpha - \frac{\hbar^2}{2m_c}\left(\nabla - \frac{iq}{\hbar c}\mathbf{A}_{c2}\right)^2 \tag{3.103}$$

and by construction satisfies $\mathcal{H}_0\Psi_0 = 0$. Taking advantage of the orthogonality of Ψ_0 and Ψ_1, the normalisation condition (3.98) can then be extended to

$$\int \Psi_0^*\,\mathcal{H}_0\Psi_1\,\mathrm{d}V = 0, \tag{3.104}$$

which can be rewritten using Equation (3.102),

$$\int\left[\beta|\Psi_0|^4 - \frac{1}{c}\mathbf{A}_1\cdot\left(-\frac{iq\hbar}{2m_c c}\,2\Psi_0^*\nabla\Psi_0 - \frac{q^2}{m_c c}\mathbf{A}_{c2}|\Psi_0|^2\right)\right]\mathrm{d}V = 0. \tag{3.105}$$

After integrating the second term by parts and neglecting the surface term contribution, the expression in round brackets is equivalent to the linear quantum mechanical current density, $\mathbf{j}_s$ (see Equation (3.70)). Using Ampère's law (3.96), one can further simplify

$$\int\left(\beta|\Psi_0|^4 - \frac{1}{c}\mathbf{A}_1\cdot\mathbf{j}_s\right)\mathrm{d}V = \int\left[\beta|\Psi_0|^4 - \frac{1}{4\pi}\mathbf{A}_1\cdot\left(\nabla\times\bar{\mathbf{B}}_s\right)\right]\mathrm{d}V = 0. \tag{3.106}$$

Employing a vector identity for the second term and ignoring again the total gradient, which would only contribute at the surface of the sample and not the bulk, one obtains

$$\frac{1}{4\pi}\mathbf{A}_1\cdot\left(\nabla\times\bar{\mathbf{B}}_s\right) = \frac{1}{4\pi}\bar{\mathbf{B}}_s\cdot\left(\nabla\times\mathbf{A}_1\right) = \frac{1}{4\pi}\bar{\mathbf{B}}_s\cdot\left(\mathbf{H} - \mathbf{H}_{c2} + \bar{\mathbf{B}}_s\right), \tag{3.107}$$

where Equation (3.97) has been used to simplify the result. Based on the initial choice for **H**, all magnetic fields are aligned in z-direction, which allows the right-hand side to be simplified. Using Equation (3.101) then leads to

$$\int \left[|\Psi_0|^4 \left(\beta - \frac{\pi q^2 \hbar^2}{m_\mathrm{c}^2 c^2} \right) - \frac{q\hbar}{2 m_\mathrm{c} c} |\Psi_0|^2 \left(H_{\mathrm{c}2} - H \right) \right] \mathrm{d}V = 0. \tag{3.108}$$

As the parameter β is related to the Ginzburg-Landau parameter, κ_GL, via [114]

$$\kappa_\mathrm{GL}^2 = \frac{\beta c^2 m_\mathrm{c}^2}{2\pi \hbar^2 q^2}, \tag{3.109}$$

one can rewrite

$$\int \left[|\Psi_0|^4 \left(2\kappa_\mathrm{GL}^2 - 1 \right) - \frac{m_\mathrm{c} c}{qh} |\Psi_0|^2 \left(H_{\mathrm{c}2} - H \right) \right] \mathrm{d}V = 0. \tag{3.110}$$

This again illustrates the importance of the critical value $\kappa_\mathrm{crit} = 1/\sqrt{2}$. The linear order parameter, Ψ_0, is position-dependent and the exact configuration of the fluxtube array has to be known to evaluate the integral. However, it is possible to deduce more general information about the fluxtube distribution close to the upper critical field by defining a macroscopic average of a function $f(\mathbf{r})$ by,

$$\langle f(\mathbf{r}) \rangle \equiv \int f(\mathbf{r}) \, \mathrm{d}V. \tag{3.111}$$

Equation (3.110) then reduces to

$$\langle |\Psi_0|^4 \rangle \left(2\kappa_\mathrm{GL}^2 - 1 \right) = \frac{m_\mathrm{c} c}{qh} \langle |\Psi_0|^2 \rangle \left(H_{\mathrm{c}2} - H \right). \tag{3.112}$$

Using Equations (3.95), (3.101) and (3.112), the average magnetic induction is this

$$\mathbf{B} = \langle \bar{\mathbf{B}} \rangle = \langle \mathbf{H} \rangle + \langle \bar{\mathbf{B}}_\mathrm{s} \rangle = \mathbf{H} - \frac{\mathbf{H}_{\mathrm{c}2} - \mathbf{H}}{\left(2\kappa_\mathrm{GL}^2 - 1 \right) \beta_A}, \tag{3.113}$$

where we followed Abrikosov's work and defined

$$\beta_A \equiv \frac{\langle |\Psi_0|^4 \rangle}{\left(\langle |\Psi_0|^2 \rangle \right)^2}. \tag{3.114}$$

Note that β_A is independent of the normalisation condition, reduces to unity for order parameters constant in space and becomes larger for more localised wave functions, i.e. $\beta_A \geq 1$. With the help of Equation (3.58), one can finally obtain an expression for the magnetisation of the superconductor, i.e.

$$\mathbf{M} = -\frac{1}{4\pi} \frac{\mathbf{H}_{\mathrm{c}2} - \mathbf{H}}{\left(2\kappa_\mathrm{GL}^2 - 1 \right) \beta_A}, \tag{3.115}$$

which is directly related to the total Gibbs energy via $\partial G/\partial H|_T = -M$. Integrating $M \equiv |\mathbf{M}|$ with respect to the external field, one therefore arrives at

$$G(H) = G(H_{c2}) - \frac{1}{4\pi} \frac{(H_{c2} - H)^2}{\left(2\kappa_{\mathrm{GL}}^2 - 1\right) \beta_A}. \tag{3.116}$$

The smaller the parameter β_A is, the smaller the Gibbs energy of the system for a given external field H compared to the corresponding value at H_{c2}. As Abrikosov first showed in his seminal paper, β_A ultimately determines the structure of the fluxtube array because the free energy is minimised for the smallest β_A value. Comparing a square and a triangular lattice, distinguished by the choice of coefficients C_n (see Equation (3.99)), one finds that in the former case $\beta_A = 1.18$ and in the latter $\beta_A = 1.16$, making the hexagonal configuration the favourable one.

Having presented the main aspects of the classical treatment of macroscopic quantum condensates, the following chapters of this thesis will focus on the implications of vortices and fluxtubes on a neutron star's dynamics. In several instances however, the reader is referred back to the discussion of laboratory superfluids and superconductors.

Chapter 4

Superfluid and Superconducting Magnetohydrodynamics

The purpose of this chapter is to present a derivation of the magnetohydrodynamical (MHD) equations that characterise the neutron star interior and form the basis of the following chapters. The presence of superfluid or superconducting components implies the existence of distinct fluid degrees of freedom and requires a multi-fluid formalism. Its constituents do not necessarily correspond to physically separable fluids as observed for superfluid helium, where the excitations and the ground-state condensate formed the basis of the two-fluid model. However, the simplest representation of the neutron stars' outer core is a mixture of three components, namely relativistic electrons, superconducting protons and superfluid neutrons. These three constituents will be governed by two MHD equations. The hydrodynamical description first introduced in Subsection 3.2.4 characterises the large-scale behaviour of a system. This is fundamentally different to the microscopic dynamics that involve the motion and interactions of individual particles. In the following, a third intermediate picture will be used to incorporate the influence of quantised vorticity and flux. On these mesoscopic lengthscales, one can determine the forces between individual vortices or fluxtubes and the surrounding fluids, which are in turn obtained by averaging the particle flows of individual species. Hence, the macroscopic MHD equations developed here will be valid within fluid elements, in which it is possible to determine a macroscopic average over the vortex (fluxtube) array and obtain a continuum model of the circulation (magnetic flux).

This chapter is structured as follows. Firstly, observational and theoretical evidence for the existence of macroscopic quantum states in neutron stars is presented in Section 4.1. This is succeeded by a discussion of recent work by Glampedakis et al. [181], presenting a general set of macroscopic hydrodynamic equations for a multi-fluid mixture. Using the variational formalism developed by Carter, Prix and collaborators [153, 154, 155], which distinguishes between fluid momenta and velocities, the Euler equations for a Fermi liquid in the absence of vortices and fluxtubes are derived (see

Section 4.2). In Section 4.3, changes arising from the presence of vortices and fluxtubes are incorporated. The quantised structures not only introduce new force terms into the MHD equations but also lead to modified macroscopic Maxwell equations.

4.1 Astrophysical Condensates

As discussed in Section 2.3, neutron stars are characterised by large magnetic fields and fast rotation. A few hundred years after birth, the compact objects are in thermal equilibrium and have temperatures of 10^6 to 10^8 K [24]. These are extremely high compared to typical temperatures in laboratory condensates such as the 2.171 K Lambda point of helium and the situation seems very different upon initial inspection. However, due to the high densities in neutron stars, the Fermi temperature of nuclear matter is $\sim 10^{12}$ K [4], which is several orders of magnitude larger than the equilibrium temperature. Thus, compact objects contain a highly degenerate Fermi liquid of strongly interacting particles and it is sufficient to assume that their interior forms a ground-state condensate in the zero-temperature limit [182, 181], implying that no excitations are present. For a discussion of this approximation and the extension to a finite-temperature mixture see Andersson et al. [183] and references therein. Besides theoretical calculations, observations support the existence of superconductivity and superfluidity in neutron stars and the main arguments are briefly discussed in the next subsection. This section concludes with an examination of several more aspects of superconductivity in neutron stars.

4.1.1 Theoretical and observational evidence

The idea of superfluidity and superconductivity in astrophysical objects was first put forward by Migdal in 1959 [184], several years before the first pulsar signal was observed [2]. Generalising the theory developed for terrestrial macroscopic quantum systems to the neutron star case would imply the presence of a neutron superfluid and a proton superconductor, while the relativistic electrons are in a normal state, as their transition temperature lies well below the typical neutron star temperatures (see Section 2.2). As nucleons are fermions, they have to form Cooper pairs before condensing into a superfluid phase. At densities below $\rho_0/3 \sim 10^{14}\,\mathrm{g\,cm^{-3}}$, i.e. in the stars' crust, the particles are most likely to experience pairing in a spin-singlet, s-wave state with vanishing angular momentum ($^1S_0$). In the core, where densities above ρ_0 are present, the spin-triplet, p-wave pairing channel of non-zero angular momentum ($^3P_2$) is the most attractive one. The crustal phase is, hence, similar to helium II, while at high densities the superfluid neutrons behave like an anisotropic helium-3 superfluid. Moreover, the protons in the core are expected to condense into a $^1S_0$ state and exhibit superconducting properties. The neutron and proton transition temperatures typically range between [185, 186, 24]

$$T_{\mathrm{cn,\,singlet}} \approx 10^9 - 10^{10}\,\mathrm{K}, \tag{4.1}$$

$$T_{\mathrm{cn,\,triplet}} \approx 10^8 - 10^9\,\mathrm{K}, \tag{4.2}$$

$$T_{\mathrm{cp,\,singlet}} \approx 10^9 - 10^{10}\,\mathrm{K}. \tag{4.3}$$

For more information on pairing in neutron stars see Sauls [40] and Gezerlis et al. [187].

The presence of quantum condensates has a crucial influence on the rotational and magnetic properties of the compact object. Firstly, a superfluid interior drastically changes the rotational dynamics in comparison to a normal matter core. As originally observed in helium II, the bulk spin is controlled by the dynamics of vortices quantising the circulation. Secondly, in comparison to a normal conductor, the magnetic field is no longer locked to the charged plasma but instead contained within fluxtubes. The evolution of the magnetic field is, thus, determined by the behaviour of these fluxtubes. The numerical values for the quantum of circulation and magnetic flux are

$$\kappa = \frac{h}{2m_{\mathrm{n}}} \approx 2.0 \times 10^{-3}\,\mathrm{cm^2\,s^{-1}}, \tag{4.4}$$

$$\phi_0 = \frac{ch}{2e} \approx 2.1 \times 10^{-7}\,\mathrm{G\,cm^2}, \tag{4.5}$$

where m_{n} denotes the mass of a neutron and e the charge of a proton. Assuming that the two macroscopic quantum states are indeed present in the interior of a neutron star, Equations (3.23) and (3.62) can be used to estimate typical values for the neutron vortex and proton fluxtube surface densities, $\mathcal{N}_{\mathrm{n}}$ and $\mathcal{N}_{\mathrm{p}}$, respectively (see also Subsection 4.3.1). Normalising the results for a typical rotation period of $P_{10} \equiv P/(10\,\mathrm{ms})$ and an estimated dipole field strength of $B_{12} \equiv B/(10^{12}\,\mathrm{G})$, one finds

$$\mathcal{N}_{\mathrm{n}} = \frac{2\Omega}{\kappa} = \frac{4\pi}{\kappa P} \approx 6.3 \times 10^5 P_{10}^{-1}\,\mathrm{cm^{-2}}, \tag{4.6}$$

$$\mathcal{N}_{\mathrm{p}} = \frac{B}{\phi_0} \approx 4.8 \times 10^{18}\,B_{12}\,\mathrm{cm^{-2}}, \tag{4.7}$$

which correspond to the following intervortex and interfluxtube spacings,

$$d_{\mathrm{n}} \simeq \mathcal{N}_{\mathrm{n}}^{-1/2} \approx 1.3 \times 10^{-3}\,P_{10}^{1/2}\,\mathrm{cm}, \tag{4.8}$$

$$d_{\mathrm{p}} \simeq \mathcal{N}_{\mathrm{p}}^{-1/2} \approx 4.6 \times 10^{-10}\,B_{12}^{-1/2}\,\mathrm{cm}. \tag{4.9}$$

This implies that there are significantly more fluxtubes per unit area than neutron vortices in the interior of a canonical neutron star. In addition to new forces that arise from the coupling of vortices or fluxtubes with their respective fluid components and the charged plasma, the two arrays are also able to interact with each other. In the outer core, fluxtubes and vortices might be strongly interacting, which could have an influence on the magnetic and rotational evolution as they would be no longer independent [188,

189]. Additional source terms in the hydrodynamical equations generated by quantised vorticity and magnetic flux will be discussed in Section 4.3.

Besides calculations of microscopic parameters, there are observations that support the presence of quantum condensates in neutron stars. Traditionally, glitches and post-glitch relaxation timescales on the order of months to years are seen as evidence of superfluidity. As briefly discussed in Subsection 2.3.3, Baym et al. [45] and Anderson and Itoh [88] proposed that the neutron stars' dynamical evolution during and after a glitch could be explained by the presence of a superfluid component weakly coupled to the crust. Moreover, recent spectral analyses of the neutron star in the supernova remnant Cassiopeia A indicate that the surface temperature of this young object decreases faster than one would expect from standard theoretical cooling models [185, 186]. It has been suggested that the rapid cooling could be explained by enhanced neutrino emission, resulting from the onset of neutron superfluidity in the core. Future measurements of the surface temperature will allow more accurate comparison between observations and models and, thus, provide the possibility to confirm the rapid-cooling hypothesis.

4.1.2 Further aspects of superconductivity

Analogous to experiments with laboratory superconductors, one would expect the magnetism of a superconducting neutron star core to be strongly influenced by the Meissner effect. However, as discussed in detail in Section 6.1, Baym et al. [45] argue that due to the high electrical conductivity of normal nuclear matter, the diffusion timescale for magnetic flux expulsion is extremely large. The Meissner effect would, thus, act on the order of a million years, much longer than dynamical timescales of neutron stars. This implies that the macroscopic magnetic induction cannot be expelled from the interior and the flux is frozen into the matter. Therefore, condensation into the superconducting state has to take place at a constant magnetic flux. As mentioned in Subsection 3.3.3, there are two ways to satisfy this constraint, either by creating an intermediate state in a type-I superconductor or a mixed-fluxtube phase in a type-II superconductor. The physical state realised inside a neutron star depends on the characteristic lengthscales involved. Having defined the penetration depth in Equation (3.71) and the coherence length in Equation (3.73), one can calculate typical estimates for both parameters.

Compared to laboratory superconductors however, the critical distances have to be modified because of entrainment. As first discussed by Andreev and Bashkin [190], this effect is a universal characteristic of interacting Fermi liquids. In a neutron star, it results from the strong nuclear forces present at high densities and causes protons and neutrons to be coupled. This will be explicitly incorporated into the multi-fluid hydrodynamics in Section 4.2 and it will be shown that entrainment can be included into the formalism by using the concept of effective masses, m^*. These effective masses characterise the dynamical response of the fluid components to a change in momentum. They are, therefore, different to the static Landau masses entering the coherence length

defined in Equation (3.73). However, as addressed in detail by Chamel and Haensel [179] (see also Prix et al. [191]), deviations between the two types of effective masses are very small for neutron star matter, where $n_\mathrm{p} \ll n_\mathrm{b}$ (see Subsection 5.1.1). Thus, the dynamical effective masses are employed in the following to determine the coherence lengths.

Substituting for the Cooper pair parameters $q = +2e$, $m_\mathrm{c} = 2m_\mathrm{p}$ and $n_\mathrm{c} = n_\mathrm{p}/2$, where m_p and n_p are the proton mass and number density, respectively, one can find for the condensate in the zero-temperature limit (see Equation (4.42) and Mendell [182]),

$$\lambda_* \approx 1.3 \times 10^{-11} \left(\frac{m_\mathrm{p}^*}{m_\mathrm{p}}\right)^{1/2} \rho_{14}^{-1/2} \left(\frac{x_\mathrm{p}}{0.05}\right)^{-1/2} \mathrm{cm}, \tag{4.10}$$

$$\xi_\mathrm{p} \approx 3.9 \times 10^{-12} \left(\frac{m_\mathrm{p}}{m_\mathrm{p}^*}\right) \rho_{14}^{1/3} \left(\frac{x_\mathrm{p}}{0.05}\right)^{1/3} \left(\frac{10^9\,\mathrm{K}}{T_\mathrm{cp}}\right) \mathrm{cm}. \tag{4.11}$$

Here, $\rho_{14} \equiv \rho/10^{14}\,\mathrm{g\,cm^{-3}}$ denotes the total normalised mass density, x_p the proton fraction and m_p^* the effective proton mass; in the outer neutron star core typically

$$\frac{m_\mathrm{p}^*}{m_\mathrm{p}} \approx 0.6 - 0.9, \tag{4.12}$$

according to Chamel [192] (see also Subsection 5.1.1). Equivalently, the neutron condensates in the crust and the core can be assigned coherence lengths that correspond to the dimension of the neutron Cooper pairs, i.e. the size of the superfluid vortex cores. As the following discussion focuses on the outer core, an estimate for the p-wave paired condensate is given [182], i.e.

$$\xi_\mathrm{n} \approx 1.5 \times 10^{-11} \left(1 - x_\mathrm{p}\right)^{1/3} \left(\frac{m_\mathrm{n}}{m_\mathrm{n}^*}\right) \rho_{14}^{1/3} \left(\frac{10^9\,\mathrm{K}}{T_\mathrm{cn}}\right) \mathrm{cm}, \tag{4.13}$$

where the effective mass is $m_\mathrm{n}^* \approx m_\mathrm{n}$ (see Subsection 5.1.1). For comparison, the s-wave paired vortex in the crust is about one order of magnitude smaller (see Subsection 5.2.2).

With Equations (4.10) and (4.11), the Ginzburg-Landau parameter equates to

$$\kappa_\mathrm{NS} = \frac{\lambda_*}{\xi_\mathrm{p}} \approx 3.3 \left(\frac{m_\mathrm{p}^*}{m_\mathrm{p}}\right)^{3/2} \rho_{14}^{-5/6} \left(\frac{x_\mathrm{p}}{0.05}\right)^{-5/6} \left(\frac{T_\mathrm{cp}}{10^9\,\mathrm{K}}\right) \gtrsim \frac{1}{\sqrt{2}}. \tag{4.14}$$

For typical neutron star parameters, Equation (4.14) gives results that are larger than the critical value, κ_crit, obtained from the phenomenological Ginzburg-Landau approach. The behaviour of κ_NS for a typical neutron star equation of state is illustrated in Figure 4.1. In the outer core, the proton fluid is, thus, expected to form a type-II superconductor penetrated by a quantised fluxtube array. Due to the long diffusion timescale of normal matter [193], this state would form even if the magnetic induction right above the transition temperature was lower than H_c1. This is one of the main differences between superconductivity in an astrophysical context and a laboratory con-

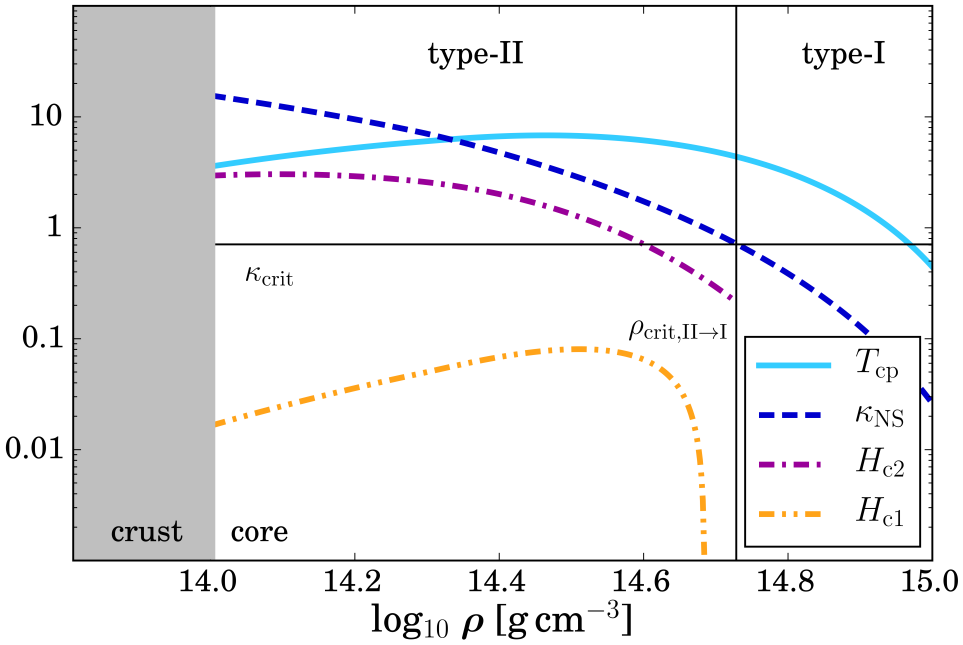

Figure 4.1: Density-dependent parameters of superconductivity. Shown are the transition temperature for proton superconductivity (cyan, solid) (normalised to $10^9\,\mathrm{K}$), the Ginzburg-Landau parameter (blue, dashed) and the two critical fields, $H_{\rm c2}$ (purple, dot-dashed) and $H_{\rm c1}$ (yellow, dot-dot-dashed) (normalised to $10^{16}\,\mathrm{G}$). The horizontal and vertical line mark $\kappa_{\rm crit}$ and $\rho_{\rm crit,II\to I}$, respectively. The cross-section is given for the NRAPR effective equation of state discussed in detail in Chapter 5.

densate, where the mixed-fluxtube state only prevails for $H_{\rm c1} < B < H_{\rm c2}$ and the flux is expelled from the interior as soon as $B < H_{\rm c1}$. Using the estimates given in Equations (4.10) and (4.11), the critical fields defined in Equations (3.82) and (3.93) are

$$H_{\rm c1} \approx 1.9 \times 10^{14} \left(\frac{m_{\rm p}}{m_{\rm p}^*}\right) \rho_{14} \left(\frac{x_{\rm p}}{0.05}\right) \mathrm{G}, \tag{4.15}$$

and

$$H_{\rm c2} \approx 2.1 \times 10^{15} \left(\frac{m_{\rm p}^*}{m_{\rm p}}\right)^2 \rho_{14}^{-2/3} \left(\frac{x_{\rm p}}{0.05}\right)^{-2/3} \left(\frac{T_{\rm cp}}{10^9\,\mathrm{K}}\right)^2 \mathrm{G}. \tag{4.16}$$

The fields' behaviour as a function of density is also included in Figure 4.1. Note that in calculating the estimate (4.15), $\ln\kappa_{\rm NS} \approx 2$ has been used. This simplification, generally considered in the context of laboratory superconductors [114], is also an approximation for the outer neutron star core, where $\kappa_{\rm NS}$ does not change significantly. The full logarithmic dependence, originating from the fluxtube's energy per unit length, is however accounted for in Figure 4.1, since it results in the divergent behaviour of $H_{\rm c1}$ at higher densities. As discussed in more detail in Subsection 4.3.2, this is ultimately related to the local distribution of the fluxtubes' magnetic induction; more precisely the divergence of the Bessel function for small arguments (see Equation (4.43)). Nonetheless, as

just explained, the lower critical field is not of crucial importance in neutron stars and the outer core of pulsars with typical field strengths between 10^{11} to 10^{13} G should be in a metastable type-II state (see also Subsection 6.1.2).

Special caution needs to be applied when modelling magnetars. Magnetic fields in these objects could be high enough to create interfluxtube spacings that are comparable to the fluxtube core radius. This would no longer allow a treatment based on infinitesimally thin, non-interacting fluxtubes. Moreover, magnetar fields might even reach values above H_{c2}. In this case, superconductivity could be completely destroyed, having crucial effects on the magnetars' dynamics [194]. The situation may be further complicated by the fact that there is a critical density in the inner core of the neutron star at which $\kappa_{\rm NS}$ should fall below the critical value, $\kappa_{\rm crit}$. In this case, the dominant state of matter would be an intermediate type-I superconductor, where single proton fluxtubes cannot be present. Using Equation (4.14), the transition density can be derived,

$$\rho_{\rm crit,II\to I} \approx 6.4\times10^{14}\left(\frac{m_{\rm p}^*}{m_{\rm p}}\right)^{9/5}\left(\frac{0.05}{x_{\rm p}}\right)\left(\frac{T_{\rm cp}}{10^9\,{\rm K}}\right)^{6/5}{\rm g\,cm^{-3}}. \tag{4.17}$$

Above this value, fluxtubes might form bundles and create an intermediate state with large but irregularly distributed regions of zero and non-zero magnetic flux [195, 177]. Note however that other phases of matter could be preferred at such densities [48] and an intermediate type-I state might not form after all.

4.2 MHD in the Absence of Vortices/Fluxtubes

Several methods are available to derive the hydrodynamical equations of a multi-fluid system. As presented in Subsection 3.2.4, combining the irrotationality of the superfluid flow with conservation equations can serve as one approach. However, this classical treatment identifies fluid momenta with superfluid velocities (see for example Mendell and Lindblom [196]) that do not necessarily correspond to physical particle flows. Making a clear distinction between these variables is possible by using the Lagrangian formalism developed by Prix [154, 197], which additionally allows for the direct inclusion of the various interactions present in the multi-component system (see Section 4.3). Conveniently, this approach also represents the Newtonian limit of the general-relativistic framework of Carter [198].

4.2.1 Lagrangian derivation

The characteristic variables of the multi-fluid model are the number densities, $n_{\rm x}$, the kinematic velocities, $v_{\rm x}^i$, the masses, $m_{\rm x}$, and the charges, $q_{\rm x}$, where each particle species is denoted by the label x, respectively. Note that for convenience tensor notation will be adopted in this chapter. Using these variables, the mass and charge densities, $\rho_{\rm x}$

and $\sigma_{\rm x}$, and the corresponding particle and charge current densities, $n^i_{\rm x}$ and $j^i_{\rm x}$, are

$$\rho_{\rm x} \equiv m_{\rm x} n_{\rm x}, \qquad n^i_{\rm x} \equiv n_{\rm x} v^i_{\rm x} \qquad \text{and} \qquad \sigma_{\rm x} \equiv q_{\rm x} n_{\rm x}, \qquad j^i_{\rm x} \equiv \sigma_{\rm x} v^i_{\rm x}. \tag{4.18}$$

The total quantities, σ, ρ and j^i, of the full multi-fluid system are given by summing over all individual constituents. Hence, the Lagrangian, $\mathcal{L}$, has to be a function of the number densities, the particle current densities, the gravitational potential, Φ, and the scalar and vector electromagnetic potentials, A^0 and A^i, respectively. More precisely, $\mathcal{L}$ contains a hydrodynamical contribution also including the effects of entrainment, the gravitational potential and additional electromagnetic terms [181],

$$\mathcal{L} = \underbrace{\sum_{\rm x} m_{\rm x} \frac{n^{\rm x}_i n^i_{\rm x}}{2n_{\rm x}} - \mathcal{E}}_{\equiv \mathcal{L}_{\rm H}} - \frac{(\nabla\Phi)^2}{8\pi G} + \frac{E^2 - B^2}{8\pi} + \left(\sigma A_0 + \frac{1}{c} j_i A^i\right) - \rho\Phi, \tag{4.19}$$

where the Einstein summation conventions and Gaussian units are used. $\mathcal{E} = \mathcal{E}(n_{\rm x}, w^2_{\rm xy})$ represents the energy of the system containing all information about the equation of state and $w^i_{\rm xy} \equiv v^i_{\rm x} - v^i_{\rm y}$ is the relative velocity. The electric field, E^i, and the magnetic induction, B^i, are defined by electromagnetic degrees of freedom in the standard way,

$$E^i \equiv \nabla^i A_0 - \frac{1}{c}\,\partial_t A^i, \qquad\qquad B^i \equiv \epsilon^{ijk} \nabla_j A_k, \tag{4.20}$$

with the antisymmetric Levi-Civita tensor ϵ^{ijk}. Using standard vector identities, E^i and B^i produce Faraday's law and the divergence condition for the magnetic induction. The remaining two Maxwell equations, Gauss's law and Ampère's law, are found by varying the Lagrangian (4.19) with respect to the potentials, A^0 and A^i. The latter reads as

$$\epsilon^{ijk} \nabla_j H_k = \frac{4\pi}{c} j^i + \frac{1}{c} \partial_t D^i, \tag{4.21}$$

where the displacement current, D^i, and the magnetic field, H^i, are defined by

$$D^i \equiv 4\pi \frac{\partial \mathcal{L}}{\partial E_i}, \qquad\qquad H^i \equiv -4\pi \frac{\partial \mathcal{L}}{\partial B_i}. \tag{4.22}$$

Maxwell's equations are discussed in more detail below (see Subsection 4.3.4). Variation with respect to the gravitational potential, Φ, provides the standard Poisson equation,

$$\nabla^2 \Phi = 4\pi G \rho. \tag{4.23}$$

Additionally, by minimising the Lagrangian with respect to the fluid variables, $n_{\rm x}$, it is possible to derive continuity equations for the number densities [154], which also translate into continuity equations for the charge densities. These are

$$\partial_t n_{\rm x} + \nabla_i n^i_{\rm x} = 0, \qquad\qquad \partial_t \sigma_{\rm x} + \nabla_i j^i_{\rm x} = 0. \tag{4.24}$$

On the other hand, variation with respect to the current density, $n_{\rm x}^i$, leads to an Euler equation for the momentum of each constituent, which reads as

$$n_{\rm x}\left[\left(\partial_t + v_{\rm x}^j\nabla_j\right)p_{\rm x}^i + m_{\rm x}\sum_{\rm y}\left(\varepsilon_{\rm xy}w_j^{\rm yx}\right)\nabla^i v_{\rm x}^j + \nabla^i\mu_{\rm x}\right] + \rho_{\rm x}\nabla^i\Phi = F_{\rm EMx}^i. \tag{4.25}$$

Here, $p_{\rm x}^i$ are the hydrodynamical momenta related to the hydrodynamical piece of the Lagrangian, $\mathcal{L}_{\rm H}$. These are different to the canonical momenta, $\pi_{\rm x}^i$, which are obtained by differentiating the full Lagrangian, $\mathcal{L}$, i.e.

$$p_{\rm x}^i \equiv \frac{\partial\mathcal{L}_{\rm H}}{\partial n_i^{\rm x}} = m_{\rm x}v_{\rm x}^i + m_{\rm x}\sum_{\rm y}\varepsilon_{\rm xy}w_{\rm yx}^i, \qquad \pi_{\rm x}^i \equiv \frac{\partial\mathcal{L}}{\partial n_i^{\rm x}} = p_{\rm x}^i + \frac{q_{\rm x}}{c}A^i. \tag{4.26}$$

The canonical momenta play a crucial role in determining the effects that the fluxtube and vortex array have on macroscopic lengthscales (see Section 4.3). Moreover, the electromagnetic force density on the right-hand side of Equation (4.25) is of standard form

$$F_{\rm EMx}^i = \sigma_{\rm x}\left(E^i + \frac{1}{c}\epsilon^{ijk}v_j^{\rm x}B_k\right). \tag{4.27}$$

Finally, the entrainment parameters and the chemical potentials are defined as

$$\varepsilon_{\rm xy} \equiv \frac{2}{\rho_{\rm x}}\left(\frac{\partial\mathcal{E}}{\partial w_{\rm xy}^2}\right)_{n_{\rm x}}, \qquad \mu_{\rm x} \equiv \left(\frac{\partial\mathcal{E}}{\partial n_{\rm x}}\right)_{n_{\rm y},w_{\rm xy}^2}. \tag{4.28}$$

Entrainment is a fundamental property of a Fermi liquid. If strong nuclear forces are present, particles of different interpenetrating species do not move independently but are coupled. Hence, a momentum induced in one component implies that parts of the other constituents are dragged along and vice versa. This is exactly reflected in Equation (4.26). Using the definition (4.28), it can be seen that the following condition holds,

$$\varepsilon_{\rm xy}n_{\rm x} = \varepsilon_{\rm yx}n_{\rm y}. \tag{4.29}$$

4.2.2 MHD approximation

As discussed in Section 2.2, a neutron star's outer core contains superfluid neutrons, a small fraction of relativistic electrons and superconducting protons, hence $\mathrm{x} \in \{\mathrm{n},\mathrm{e},\mathrm{p}\}$. The two charged components can be combined into a single constituent by taking the concept of macroscopic charge neutrality into account. Due to the electrons' small mass, they are very mobile and able to quickly equilibrate any electric charge imbalances. On typical hydrodynamical lengthscales, the combined proton-electron conglomerate can be considered as charge neutral, giving $\sigma_{\rm p} + \sigma_{\rm e} = 0$. Due to $q_{\rm p} = -q_{\rm e} = e$ and $q_{\rm n} = 0$, one is left with $n_{\rm p} = n_{\rm e}$. The second continuity equation (4.24), thus, implies that the

total macroscopic electromagnetic current density satisfies $\nabla^i j_i = 0$, where

$$j^i = e n_{\rm p} w^i_{\rm pe}. \tag{4.30}$$

Note at this point that in order to keep the discussion clear, the presence of muons is neglected. However, generalising to the four-constituent case would be straightforward, since electrons and muons are strongly coupled and move as one component on macroscopic lengthscales [182]. In order to determine an equation for the combined charged constituent, the electron and the proton Euler equations have to be added together. This firstly eliminates the electric field, E^i. Moreover, the contribution of the electron fluid to the total mass of the system is small, which allows one to neglect the electron inertial terms in the resulting equation. Additionally, compared to the strong nuclear interactions between the protons and the neutrons, it is reasonable to ignore the electron entrainment. With these simplifications, one finally arrives at two equations for the superfluid neutrons and the charged-particle conglomerate,

$$\rho_{\rm n}\left[(\partial_t + v^j_{\rm n}\nabla_j)(v^i_{\rm n} + \varepsilon_{\rm n} w^i_{\rm pn}) + \nabla^i(\tilde{\mu}_{\rm n} + \Phi) + \varepsilon_{\rm n} w^j_{\rm pn}\nabla^i v^{\rm n}_j\right] = 0, \tag{4.31}$$

$$\rho_{\rm p}\left[(\partial_t + v^j_{\rm p}\nabla_j)(v^i_{\rm p} + \varepsilon_{\rm p} w^i_{\rm np}) + \nabla^i(\tilde{\mu} + \Phi) + \varepsilon_{\rm p} w^j_{\rm np}\nabla^i v^{\rm p}_j\right] = F^i_{\rm L}, \tag{4.32}$$

where we write $\varepsilon_{\rm n} \equiv \varepsilon_{\rm np}$ and $\varepsilon_{\rm p} \equiv \varepsilon_{\rm pn}$ and the specific chemical potentials are

$$\tilde{\mu}_{\rm n} \equiv \frac{\mu_{\rm n}}{m}, \qquad \tilde{\mu} \equiv \frac{\mu_{\rm p} + \mu_{\rm e}}{m}. \tag{4.33}$$

Ignoring the mass difference between the baryons, one has $m \equiv m_{\rm p} = m_{\rm n}$. Furthermore, it is assumed that the fluid motion is slow compared to the speed of light, c. In this case, the displacement current in Equation (4.21) is zero and Ampère's law reduces to

$$\epsilon^{ijk}\nabla_j H_k = \frac{4\pi}{c}\, j^i. \tag{4.34}$$

The Lorentz force density in the second Euler equation (4.61) is then given by

$$F^i_{\rm L} \equiv \frac{1}{c}\,\epsilon^{ijk} j_j B_k = \frac{1}{4\pi} B^j \left(\nabla_j H^i - \nabla^i H_j\right). \tag{4.35}$$

In normal conducting matter, where the magnetic induction, B^i, and the magnetic field, H^i, are identical, this expression simplifies to the standard form, which is composed of a tension and a pressure term, i.e.

$$F^i_{\rm L} = \frac{1}{4\pi}\left[B_j\nabla^j B^i - \frac{1}{2}\nabla^i\left(B_k B^k\right)\right]. \tag{4.36}$$

In the presence of vortices and fluxtubes, additional forces have to be included into the momentum equations (4.31) and (4.32). These are addressed in the following section.

4.3 MHD in the Presence of Vortices/Fluxtubes

4.3.1 Quantisation conditions

As the hydrodynamic model is based on averaged quantities, it reflects the macroscopic behaviour of the fluids. It is on these large scales that a method for consistently dealing with the presence of the quantum condensates is available. By taking advantage of the large numbers of vortices/fluxtubes, one can average over the two arrays and obtain a smooth-averaged picture. Using this formalism, one can determine how the condensates influence the macroscopic dynamics of neutron stars such as rotation and magnetism.

If individual vortices and fluxtubes do not overlap and are distant enough so that interactions within one array can be neglected, then the averaging procedure is obtained from the macroscopic quantisation conditions originally developed by Onsager [140] and Feynman [141] for the description of rotating superfluid helium. Assuming that neutron vortices and proton fluxtubes are locally straight and directed along the unit vectors, $\hat{\kappa}^i_{\rm n}$ and $\hat{\kappa}^i_{\rm p}$, the arrays can be assigned vortex and fluxtube surface densities, $\mathcal{N}_{\rm n}$ and $\mathcal{N}_{\rm p}$, respectively. As the vorticities, $\mathcal{W}^i_{\rm x}$, are related to the circulation of the averaged canonical momenta, $\pi^i_{\rm x}$, the macroscopic quantisation conditions are given by

$$\mathcal{W}^i_{\rm n} = \frac{1}{m}\,\epsilon^{ijk}\nabla_j\pi^{\rm n}_k = \frac{1}{m}\,\epsilon^{ijk}\nabla_j p^{\rm n}_k = \epsilon^{ijk}\nabla_j\left(v^{\rm n}_k + \varepsilon_{\rm n} w^{\rm pn}_k\right) = \mathcal{N}_{\rm n}\kappa^i_{\rm n}, \tag{4.37}$$

and

$$\mathcal{W}^i_{\rm p} = \frac{1}{m}\,\epsilon^{ijk}\nabla_j\pi^{\rm p}_k = \epsilon^{ijk}\nabla_j\left(v^{\rm p}_k + \varepsilon_{\rm p} w^{\rm np}_k\right) + a_{\rm p}B^i = \mathcal{N}_{\rm p}\kappa^i_{\rm p}, \tag{4.38}$$

where $\kappa^i_{\rm x} \equiv \kappa\hat{\kappa}^i_{\rm x}$ points along the local vortex/fluxtube direction and we define

$$a_{\rm p} \equiv \frac{e}{mc} \approx 9.6\times10^3\,{\rm G}^{-1}\,{\rm s}^{-1}. \tag{4.39}$$

4.3.2 Macroscopic magnetic induction

In the averaged framework, the total magnetic induction, B^i, is the sum of three individual components, namely the averaged vortex/fluxtube fields and the London field,

$$B^i = B^i_{\rm n} + B^i_{\rm p} + b^i_{\rm L}. \tag{4.40}$$

The former contributions are obtained by multiplying the surface densities, $\mathcal{N}_{\rm x}$, with the flux carried by a single line of the lattice, $\phi_{\rm x}$. These fluxes can be derived by studying the dynamics on mesoscopic length scales. Considering distances from the vortex/fluxtube core that are larger than the respective coherence lengths, $\xi_{\rm x}$, the structure of the cores can be neglected. Using the corresponding quantisation condition and the mesoscopic Ampère law (see Appendix A1 of Glampedakis et al. [181] for details), it is possible to derive generalised London equations for the mesoscopic magnetic fields, $\bar{B}^i_{\rm x}$,

$$\lambda_*^2 \nabla^2 \bar{B}_{\rm x}^i - \bar{B}_{\rm x}^i = -\phi_{\rm x} \hat{\kappa}_{\rm x}^i \delta(\mathbf{r}), \tag{4.41}$$

where $\delta(\mathbf{r})$ is the two-dimensional delta function located at the centre of each vortex/fluxtube, $\phi_{\rm x}$ is given below and the effective London penetration depth is defined as

$$\lambda_* \equiv \left(\frac{1}{4\pi \rho_{\rm p} a_{\rm p}^2} \, \frac{1 - \varepsilon_{\rm n} - \varepsilon_{\rm p}}{1 - \varepsilon_{\rm n}} \right)^{1/2}. \tag{4.42}$$

In the absence of entrainment, i.e. $\varepsilon_{\rm n} = \varepsilon_{\rm p} = 0$, this expression reduces to the standard result of superconductivity given in Equation (3.71). Taking advantage of the symmetry and using cylindrical coordinates, the inhomogeneous Helmholtz equation (4.41) can be solved by means of a Green's function approach in two dimensions [199]. One finds

$$\bar{B}_{\rm x}^i = \frac{\phi_{\rm x}}{2\pi \lambda_*^2} \, K_0 \left(\frac{r}{\lambda_*} \right) \hat{\kappa}_{\rm x}^i, \tag{4.43}$$

where $K_0(r/\lambda_*)$ is the modified Bessel function of second kind and $r \equiv |\mathbf{r}|$ the radial distance from the vortex or fluxtube core. Note that as a result of $K_0(r/\lambda_*)$, the mesoscopic inductions exhibit characteristic behaviour for large and small r. More precisely, approximating the Bessel function in the respective limits leads to

$$\bar{B}_{\rm x}(r) \to \frac{\phi_{\rm x}}{2\pi \lambda_*^2} \left(\frac{\pi \lambda_*}{2r} \right)^{1/2} {\rm e}^{-r/\lambda_*} \qquad \text{for } r \to \infty, \tag{4.44}$$

and

$$\bar{B}_{\rm x}(r) \approx \frac{\phi_{\rm x}}{2\pi \lambda_*^2} \left[\ln \left(\frac{\lambda_*}{r} \right) + 0.12 \right] \qquad \text{for } \xi_{\rm x} \ll r \ll \lambda_*. \tag{4.45}$$

In the former case, the magnetic inductions fall off exponentially, whereas they diverge for small r. In reality however, the superfluid and superconducting states break down in the vortex and fluxtube core, respectively, and normal fluid matter is present. Thus, $\bar{B}_{\rm x}(r)$ should remain regular at $r = 0$, which is usually achieved by introducing a cut-off at the vortex/fluxtube radius, i.e. $r \sim \xi_{\rm x}$, where the Cooper pair density vanishes and the penetration depth, λ_*, becomes infinite. The same cut-off will also enter the vortex and fluxtube energy per uni length as addressed below.

Integrating the mesoscopic magnetic induction, $\bar{B}_{\rm x}^i$, over a disc of radius $r \gg \lambda_*$ perpendicular to $\hat{\kappa}_{\rm x}^i$ gives for the magnetic flux

$$\int \bar{B}_{\rm x}^i \, {\rm d}S = \phi_{\rm x} \hat{\kappa}_{\rm x}^i. \tag{4.46}$$

For the proton fluxtube, we obtain the expected unit of flux, $\phi_{\rm p} \equiv \phi_0$, calculated in Equation (4.5), whereas the flux of a superfluid vortex is

$$\phi_{\rm n} \equiv -\frac{\varepsilon_{\rm p}}{1 - \varepsilon_{\rm n}} \, \phi_0. \tag{4.47}$$

The minus sign originates from $\hat{\kappa}_{\rm n}^i$ and $\bar{B}_{\rm n}^i$ pointing into opposite directions. One ob-

serves that in the absence of entrainment the neutron flux would be zero. With entrainment, the two fluxes, $\phi_{\rm x}$, are comparable as the entrainment parameters are [200]

$$\varepsilon_{\rm p} = 1 - \frac{m_{\rm p}^*}{m} \approx 0.1 - 0.4, \tag{4.48}$$

where the estimate (4.12) was used, and

$$\varepsilon_{\rm n} = 1 - \frac{m_{\rm n}^*}{m} = \varepsilon_{\rm p} x_{\rm p} \ll 1, \tag{4.49}$$

For $x_{\rm p} \ll 1$, which is a valid approximation in the stars' interior (see Subsection 5.1.1), the neutron entrainment parameter is, thus, negligible. The averaged contributions from the two arrays to the macroscopic induction, B^i, are then given by

$$B_{\rm x}^i = \mathcal{N}_{\rm x} \phi_{\rm x} \hat{\kappa}_{\rm x}^i. \tag{4.50}$$

Despite the fluxes being of similar magnitude, the contribution of fluxtubes dominates as $\mathcal{N}_{\rm p} \gg \mathcal{N}_{\rm n}$ (see Equations (4.6) and (4.7)). This shows that the dynamics of the fluxtube array indeed determine the evolution of the stars' macroscopic magnetic induction.

The final contribution to the induction is the London field, $b_{\rm L}^i$. As discussed in Subsection 3.3.2, it is a fundamental property of a superconductor, which is associated with its rotation. In contrast to $B_{\rm x}^i$, the London field is not of microscopic origin but equivalent to the magnetic field, H^i, and, thus, related to the macroscopic electromagnetic current (see Subsection 4.3.4). Combining the quantisation conditions (4.37) and (4.38) with Equation (4.50), the London field is related to macroscopic variables via

$$b_{\rm L}^i = \frac{1}{a_{\rm p}} \left[\frac{\varepsilon_{\rm p}}{1-\varepsilon_{\rm n}} \epsilon^{ijk} \nabla_j (v_k^{\rm n} + \varepsilon_{\rm n} w_k^{\rm pn}) - \epsilon^{ijk} \nabla_j (v_k^{\rm p} + \varepsilon_{\rm p} w_k^{\rm np}) \right]. \tag{4.51}$$

Assuming that the hydrodynamical lengthscales are sufficiently small to ensure constant entrainment parameters, the previous expression simplifies to

$$b_{\rm L}^i = -\frac{1}{a_{\rm p}} \frac{1-\varepsilon_{\rm n}-\varepsilon_{\rm p}}{1-\varepsilon_{\rm n}} \epsilon^{ijk} \nabla_j v_k^{\rm p} \approx -\frac{1}{a_{\rm p}} (1-\varepsilon_{\rm p}) \epsilon^{ijk} \nabla_j v_k^{\rm p}. \tag{4.52}$$

This illustrates again that the London field is locked to the rotation of the proton fluid. Taking it to be tightly coupled to the neutron star crust through the magnetic field, the protons rotate rigidly at the observed pulsar frequency, i.e. $\epsilon^{ijk} \nabla_j v_k^{\rm p} = 2\Omega^i$. One could then substitute a canonical rotation period to calculate an estimate for the magnitude of the London field. Using the normalised parameter P_{10} leads to

$$b_{\rm L} \approx 0.1 \left(\frac{m_{\rm p}^*}{m} \right) P_{10}^{-1} \, {\rm G}, \tag{4.53}$$

which is several orders of magnitude smaller than the magnetic field strengths usually invoked for neutron star physics (see Subsection 2.3.2). Hence, in addition to ignoring

the vortex magnetic field contribution, it is generally justified to also neglect the London field in Equation (4.40), a simplification that will be used in Chapter 7.

4.3.3 Euler equations and additional forces

Modifying the Lagrangian approach

In order to account for neutron superfluidity and proton superconductivity, the variational approach discussed in Subsection 4.2.1 has to be modified accordingly. This can be achieved by, firstly, including a term, $\mathcal{L}_{\rm v}$, into the Lagrangian, $\mathcal{L}$, given in Equation (4.19). This new piece represents the change in energy due to the presence of the quantised arrays and is obtained by multiplying the energy per unit length, $\mathcal{E}_{\rm x}$, of a single vortex/fluxtube with the respective surface density, $\mathcal{N}_{\rm x}$,

$$\mathcal{L}_{\rm v} \equiv -\sum_{\rm x} \mathcal{N}_{\rm x}\mathcal{E}_{\rm x}. \tag{4.54}$$

This expression explicitly assumes that the interactions of individual vortices and fluxtubes within one array are negligible. Then, the energy per unit length can be derived by considering the properties of an isolated vortex or fluxtube surrounded by a macroscopic fluid flow. As shown by Glampedakis et al. (see Appendix A2 in [181] for details), $\mathcal{E}_{\rm x}$ is dominated by the kinetic contribution and can be approximated by

$$\mathcal{E}_{\rm n} \equiv \left(\frac{\phi_{\rm n}}{4\pi\lambda_*}\right)^2 \frac{1-\varepsilon_{\rm n}-\varepsilon_{\rm p}}{\varepsilon_{\rm n}\varepsilon_{\rm p}} \ln\left(\frac{d_{\rm n}}{\xi_{\rm n}}\right) \approx \frac{\kappa^2\rho_{\rm n}}{4\pi}\left(\frac{m}{m^*_{\rm n}}\right)\ln\left(\frac{d_{\rm n}}{\xi_{\rm n}}\right) \tag{4.55}$$

and

$$\mathcal{E}_{\rm p} \equiv \left(\frac{\phi_0}{4\pi\lambda_*}\right)^2 \ln\left(\frac{\lambda_*}{\xi_{\rm p}}\right) \approx \frac{\kappa^2\rho_{\rm p}}{4\pi}\left(\frac{m}{m^*_{\rm p}}\right)\ln\left(\frac{\lambda_*}{\xi_{\rm p}}\right). \tag{4.56}$$

In both cases, the detailed structure of the core is ignored and the logarithmic function, which diverges at the centre, is cut off at the coherence length, $\xi_{\rm x}$. Additionally, there is a second cut-off reflecting the fact that the assumption of an isolated vortex/fluxtube breaks down at large distances. Due to the different rotational profiles far away from the core, $1/r$ for a superfluid vortex and $\exp(-r/\lambda_*)$ for a superconducting fluxtube, respectively (see Subsections 3.2.3 and 3.3.3), the cut-off distance in the former case is of the order of the intervortex spacing, $d_{\rm n}$, while for the latter the London penetration depth, λ_*, is important. Using the numerical values calculated in Section 4.1, one finds

$$\mathcal{E}_{\rm n} \approx 5.9\times10^8\left(\frac{m}{m^*_{\rm n}}\right)(1-x_{\rm p})\,\rho_{14}\,{\rm g\,cm\,s^{-2}} \tag{4.57}$$

and

$$\mathcal{E}_{\rm p} \approx 3.2\times10^6\left(\frac{m}{m^*_{\rm p}}\right)\rho_{14}\left(\frac{x_{\rm p}}{0.05}\right){\rm g\,cm\,s^{-2}}. \tag{4.58}$$

In addition to including the contribution $\mathcal{L}_{\rm v}$, the magnetic induction, B^i, in the total Lagrangian needs to be corrected. Since the energy per unit length, $\mathcal{E}_{\rm x}$, already accounts for the magnetic energy of a magnetised neutron vortex and proton fluxtube, respectively, the electromagnetic piece in Equation (4.19) has to solely provide information about the third contribution to the magnetic induction, i.e. the London field $b^i_{\rm L}$. The modified Lagrangian is, therefore, given by

$$\mathcal{L} = \sum_{\rm x} \left(m_{\rm x} \frac{n^{\rm x}_i n^i_{\rm x}}{2 n_{\rm x}} - \mathcal{N}_{\rm x} \mathcal{E}_{\rm x} \right) - \mathcal{E} - \frac{(\nabla \Phi)^2}{8\pi G} + \frac{E^2 - b^2_{\rm L}}{8\pi} + \left(\sigma A_0 + \frac{1}{c} j_i A^i \right) - \rho \Phi. \quad (4.59)$$

While the variation of $\mathcal{L}$ leaves the continuity equations (4.24) unchanged, one obtains the following macroscopic Euler equations for the neutron fluid and the proton-electron conglomerate in the presence of vortices and fluxtubes,

$$\rho_{\rm n} \Big[(\partial_t + v^j_{\rm n} \nabla_j)(v^i_{\rm n} + \varepsilon_{\rm n} w^i_{\rm pn}) + \nabla^i (\tilde{\mu}_{\rm n} + \Phi) + \varepsilon_{\rm n} w^j_{\rm pn} \nabla^i v^{\rm n}_j \Big] = F^i_{\rm mf} + F^i_{\rm mag,n}, \quad (4.60)$$

$$\rho_{\rm p} \Big[(\partial_t + v^j_{\rm p} \nabla_j)(v^i_{\rm p} + \varepsilon_{\rm p} w^i_{\rm np}) + \nabla^i (\tilde{\mu} + \Phi) + \varepsilon_{\rm p} w^j_{\rm np} \nabla^i v^{\rm p}_j \Big] = -F^i_{\rm mf} + F^i_{\rm mag,p}. \quad (4.61)$$

Compared to Equations (4.31) and (4.32), the new momentum equations contain forces going beyond the standard electromagnetic Lorentz force density, $F^i_{\rm L}$. The additional terms are the mutual friction and magnetic forces per unit volume, $F^i_{\rm mf}$ and $F^i_{\rm mag,x}$, respectively. The former ones arise from the dissipative coupling of the two arrays with the fluids and are discussed below, while the latter are caused by interactions of the vortex/fluxtube magnetic field with the charged components.

The total magnetic force acting on the charged fluids is the sum of the Lorentz force, where the substitution $H^i = b^i_{\rm L}$ has to be made, and two new contributions. The latter are given by a new potential term arising from the modifications of the chemical potential, i.e. $\tilde{\mu}_{\rm p} \to \tilde{\mu}_{\rm p} + \tilde{\zeta}_{\rm p}$, and an averaged force density due to the fluxtubes. Part of the latter exactly cancels the Lorentz force and one is left with the force density

$$F^i_{\rm mag,p} = -\frac{\mathcal{N}_{\rm p} \phi_0}{4\pi} \epsilon^{ijk} \hat{\kappa}^{\rm p}_j \epsilon_{klm} \nabla^l \left(H_{\rm c1} \hat{\kappa}^m_{\rm p} \right) + \frac{1}{4\pi a_{\rm p} m} \epsilon^{ijk} \epsilon_{jlm} \nabla^l p^m_{\rm p} \epsilon_{kst} \nabla^s b^t_{\rm L} - \rho_{\rm p} \nabla^i \tilde{\zeta}_{\rm p}, \quad (4.62)$$

where the additional potential is

$$\tilde{\zeta}_{\rm p} \equiv \frac{\phi_0}{4\pi} \left[\mathcal{N}_{\rm n} \frac{\partial H_{\rm cn}}{\partial \rho_{\rm p}} + \mathcal{N}_{\rm p} \frac{\partial H_{\rm c1}}{\partial \rho_{\rm p}} + \mathcal{N}_{\rm n} \hat{\kappa}^i_{\rm n} b^{\rm L}_i \frac{\partial}{\partial \rho_{\rm p}} \left(\frac{\varepsilon_{\rm p}}{1 - \varepsilon_{\rm n}} \right) \right]. \quad (4.63)$$

In analogy to the lower critical field of superconductivity given in Equation (3.82), the *critical field* of the superfluid neutron component can be defined by

$$H_{\rm cn} \equiv \frac{4\pi \mathcal{E}_{\rm n}}{\phi_0} \approx 3.5 \times 10^{16} \, (1 - x_{\rm p}) \left(\frac{m}{m^*_{\rm n}} \right) \rho_{14} \, {\rm G}, \quad (4.64)$$

where Equation (4.57) has been used to obtain the numerical estimate. Considering the special case of constant entrainment and a non-rotating neutron star, i.e. $\epsilon^{ijk}\nabla_j v^{\mathrm{x}}_k = 0$, which in turn imply $b_{\mathrm{L}} = \mathcal{N}_{\mathrm{n}} = 0$, $B = \mathcal{N}_{\mathrm{p}}\phi_0$ and $\hat{\kappa}^i_{\mathrm{p}} = \hat{B}^i$, the magnetic force density acting on a type-II superconductor reduces to the well-known form [201, 181, 202]

$$F^i_{\mathrm{mag,p}} = \frac{1}{4\pi}\left[B^j\nabla_j H^i_{\mathrm{c1}} - \nabla^i\left(\rho_{\mathrm{p}} B\,\frac{\partial H_{\mathrm{c1}}}{\partial \rho_{\mathrm{p}}}\right)\right], \tag{4.65}$$

with $H^i_{\mathrm{c1}} \equiv H_{\mathrm{c1}}\hat{B}^i$ pointing along the direction of the averaged induction. This result was first obtained by Easson and Pethick [203] from considerations of the stress tensor of a type-II superconducting medium. Like the standard Lorentz force (4.36), Equation (4.65) contains a tension- and a pressure-like term but scales with B^i and H^i_{c1} instead of B^2, which could increase the magnetic force significantly.

Further note that the neutron fluid also experiences a magnetic force, $F^i_{\mathrm{mag,n}}$, per unit volume, since protons are entrained around each neutron vortex, creating an effective magnetic field (see Equation (4.47)). In the absence of entrainment, the magnetic force on the neutron component vanishes. Similar to the total magnetic force acting on the proton-electron component, the force $F^i_{\mathrm{mag,n}}$ is the sum of a potential term modifying the chemical potential, i.e. $\tilde{\mu}_{\mathrm{n}} \to \tilde{\mu}_{\mathrm{n}} + \tilde{\zeta}_{\mathrm{n}}$, and an averaged force density due to the vortices. This leads to

$$F^i_{\mathrm{mag,n}} = -\frac{\mathcal{N}_{\mathrm{n}}\phi_0}{4\pi}\,\epsilon^{ijk}\hat{\kappa}^{\mathrm{n}}_j\epsilon_{klm}\nabla^l\left(H_{\mathrm{cn}}\hat{\kappa}^m_{\mathrm{n}} + \frac{\varepsilon_{\mathrm{p}}}{1-\varepsilon_{\mathrm{n}}}\,b^m_{\mathrm{L}}\right) - \rho_{\mathrm{n}}\nabla^i\tilde{\zeta}_{\mathrm{n}}, \tag{4.66}$$

with the potential term

$$\tilde{\zeta}_{\mathrm{n}} \equiv \frac{\phi_0}{4\pi}\left[\mathcal{N}_{\mathrm{n}}\frac{\partial H_{\mathrm{cn}}}{\partial \rho_{\mathrm{n}}} + \mathcal{N}_{\mathrm{p}}\frac{\partial H_{\mathrm{c1}}}{\partial \rho_{\mathrm{n}}} + \mathcal{N}_{\mathrm{n}}\hat{\kappa}^i_{\mathrm{n}}b^{\mathrm{L}}_i\frac{\partial}{\partial \rho_{\mathrm{n}}}\left(\frac{\varepsilon_{\mathrm{p}}}{1-\varepsilon_{\mathrm{n}}}\right)\right]. \tag{4.67}$$

Considering the limit of constant entrainment and vanishing rotation, the first contribution in Equation (4.66) is zero and the magnetic force density acting on neutrons is

$$F^i_{\mathrm{mag,n}} = -\frac{\rho_{\mathrm{n}}}{4\pi}\nabla^i\left(B\frac{\partial H_{\mathrm{c1}}}{\partial \rho_{\mathrm{n}}}\right). \tag{4.68}$$

Conservation of vorticity

Despite the fact that the variational formalism allows one to calculate the total effective magnetic forces arising from the presence of quantum condensates, it does not provide sufficient physical insight into how the macroscopic forces are related to the mesoscopic interactions of the arrays. This can, however, be achieved by using a different approach based upon the more intuitive concept of individual vortex or fluxtube dynamics. This method, which ultimately provides the same Euler equations (4.60) and (4.61), was established by Hall and Vinen [142] to describe the behaviour of superfluid helium (see also Subsection 3.2.4). It will also be applied to derive the macroscopic mutual friction.

The formalism relies on the fact that within a fluid element vortices/fluxtubes do not reconnect and, hence, their total numbers are conserved. In the absence of frictional forces, each surface density, then, satisfies a continuity equation of the form

$$\partial_t \mathcal{N}_{\rm x} + \nabla^i \left(\mathcal{N}_{\rm x} u^{\rm x}_i \right) = 0, \tag{4.69}$$

where $u^i_{\rm x}$ denotes the averaged velocity of a large collection of vortices or fluxtubes inside the fluid element. Further, differentiating the macroscopic quantisation conditions (4.37) and (4.38) with respect to time and substituting Equation (4.69), one arrives at

$$\partial_t \mathcal{W}^i_{\rm x} - \mathcal{N}_{\rm x} \partial_t \kappa^i_{\rm x} + \kappa^i_{\rm x} \nabla_j \left(\mathcal{N}_{\rm x} u^j_{\rm x} \right) = 0. \tag{4.70}$$

Taking into account that the vorticities are given by the curl of the canonical momenta and, thus, satisfy $\nabla^i \mathcal{W}^{\rm x}_i = 0$, one can add the zero $u^i_{\rm x} \nabla_j \mathcal{W}^j_{\rm x}$ to Equation (4.70). Using the inverse product rule and rearranging terms leads to

$$\partial_t \mathcal{W}^i_{\rm x} - \nabla_j \left(\mathcal{W}^j_{\rm x} u^i_{\rm x} \right) + \nabla_j \left(\mathcal{W}^i_{\rm x} u^j_{\rm x} \right) - \mathcal{N}_{\rm x} \underbrace{\left(\partial_t \kappa^i_{\rm x} + u^j_{\rm x} \nabla_j \kappa^i_{\rm x} - \kappa^j_{\rm x} \nabla_j u^i_{\rm x} \right)}_{= \partial_t \kappa^i_{\rm x} + \mathcal{L}_{u_{\rm x}} \kappa^i_{\rm x} = 0} = 0. \tag{4.71}$$

The final terms describe how the circulation vector, $\kappa^i_{\rm x}$, of a single vortex or fluxtube is transported with the velocity, $u^i_{\rm x}$. Using the concept of differential geometry, this can be represented by the Lie derivative, defined in the standard way via

$$\mathcal{L}_{u_{\rm x}} \kappa^i_{\rm x} \equiv u^j_{\rm x} \nabla_j \kappa^i_{\rm x} - \kappa^j_{\rm x} \nabla_j u^i_{\rm x}. \tag{4.72}$$

Hence, the last piece in Equation (4.71) vanishes. Rewriting the remaining terms using Levi-Civita tensors, one is left with

$$\partial_t \mathcal{W}^i_{\rm x} - \nabla_j \left(\mathcal{W}^j_{\rm x} u^i_{\rm x} \right) + \nabla_j \left(\mathcal{W}^i_{\rm x} u^j_{\rm x} \right) = \partial_t \mathcal{W}^i_{\rm x} - \epsilon^{ijk} \nabla_j \epsilon_{klm} \left(u^l_{\rm x} \mathcal{W}^m_{\rm x} \right) = 0. \tag{4.73}$$

This relation implies that the vorticity is locally conserved and advected with the flow $u^i_{\rm x}$. For the case of constant entrainment and zero rotation, i.e. $B = \mathcal{N}_{\rm p} \phi_0$ and $\hat{\kappa}^i_{\rm p} = \hat{B}^i$, the conservation equation for the charged-particle component simplifies to

$$\partial_t B^i = \epsilon^{ijk} \nabla_j \epsilon_{klm} \left(u^l_{\rm p} B^m \right), \tag{4.74}$$

characterising the neutron stars' magnetic field evolution in absence of dissipative mutual friction mechanisms. This equation is obtained as a limit of the superconducting induction equation derived in Chapter 7.

Taking advantage of the macroscopic quantisation conditions, Equation (4.73) can be rewritten in terms of the canonical momenta,

$$\partial_t \pi^i_{\rm x} - \epsilon^{ijk} u^{\rm x}_j \epsilon_{klm} \nabla^l \pi^m_{\rm x} + \nabla^i \mathcal{P}_{\rm x} = 0, \tag{4.75}$$

where $\mathcal{P}_{\rm x}$ are unspecified scalar potentials. Adding the term $\epsilon^{ijk}v^{\rm x}_j\epsilon_{klm}\nabla^l\pi^m_{\rm x}$ onto both sides of this equation yields the following result

$$n_{\rm x}\left(\partial_t\pi^i_{\rm x}-\epsilon^{ijk}v^{\rm x}_j\epsilon_{klm}\nabla^l\pi^m_{\rm x}+\nabla^i\mathcal{P}_{\rm x}\right)=\rho_{\rm x}\mathcal{N}_{\rm x}\epsilon^{ijk}\kappa^{\rm x}_j\left(v^{\rm x}_k-u^{\rm x}_k\right)=-F^i_{\rm Mx}. \tag{4.76}$$

Multiplying this with the number density, $n_{\rm x}$, and substituting the canonical momenta given in Equation (4.26), the left-hand side can be manipulated to take the form

$$n_{\rm x}\left[\left(\partial_t+v^j_{\rm x}\nabla_j\right)p^i_{\rm x}+m\,\varepsilon_{\rm x}w^{\rm yx}_j\nabla^iv^j_{\rm x}+\nabla^i\left(q_{\rm x}A_0+\frac{1}{2}mv^2_{\rm x}-v^{\rm x}_jp^i_{\rm x}-\mathcal{P}_{\rm x}\right)\right]-F^i_{\rm EMx}. \tag{4.77}$$

The electromagnetic contribution, $F^i_{\rm EMx}$, was defined in Equation (4.27). Identifying the scalar potentials, $\mathcal{P}_{\rm x}$, accordingly, these equations are equivalent to the Euler equations (4.25) obtained within the Lagrangian framework in the absence of vortices/fluxtubes. Moreover, the right-hand side of Equation (4.76) reflects the force density acting on the fluids due to the presence of quantised arrays. It is proportional to the relative velocity between the vortices/fluxtubes and the bulk fluids and is equal to the negative of the averaged *Magnus force* density, given by $F^i_{\rm Mx}=\mathcal{N}_{\rm x}f^i_{\rm Mx}$. Here, $f^i_{\rm Mx}$ is the Magnus force per unit length, acting as a lift force on a single vortex/fluxtube immersed into a fluid,

$$f^i_{\rm Mx}\equiv\rho_{\rm x}\kappa\,\epsilon^{ijk}\hat{\kappa}^{\rm x}_j(u^{\rm x}_k-v^{\rm x}_k). \tag{4.78}$$

This force governs the motion of free vortices/fluxtubes and causes them to be dragged along with the superfluid/superconducting component. However, in the neutron stars' outer core, additional forces are expected to influence the motion of an individual vortex/fluxtube [181]. By balancing all the contributions, solving the result for the Magnus force and substituting this back into Equation (4.76), one is able to relate the dynamics on mesoscopic lengthscales to the macroscopic behaviour of the hydrodynamical fluids.

Firstly, vortices and fluxtubes have a large self-energy, which causes them to resist bending and leads to a tension force per unit length

$$f^i_{\rm tx}\equiv\mathcal{E}_{\rm x}\hat{\kappa}^j_{\rm x}\nabla_j\hat{\kappa}^i_{\rm x}, \tag{4.79}$$

where the energies per unit length, $\mathcal{E}_{\rm x}$, were given in Equations (4.55) and (4.56). Apart from modifications due to entrainment, the tension on a neutron vortex is equivalent to the force defined for superfluid vortices in helium II (see Equation (3.30)). Moreover, the vortices and fluxtubes are magnetised and, thus, experience a conservative Lorentz-type force due to the electromagnetic coupling with the macroscopic, charged conglomerate. This contribution is given by

$$f^i_{\rm emx}\equiv\frac{en_{\rm p}}{c}\,\phi_{\rm x}\,\epsilon^{ijk}\hat{\kappa}^{\rm x}_jw^{\rm pe}_k=\frac{1}{c}\,\phi_{\rm x}\,\epsilon^{ijk}\hat{\kappa}^{\rm x}_jj_k. \tag{4.80}$$

As suggested by Sauls et al. [204] and Alpar et al. [205], the magnetic fields of individual

vortices/fluxtubes can further interact with the electron fluid, resulting in a dissipative force. This coupling would depend on the relative velocity between the charged particles and the vortex or fluxtube and be characterised by a mesoscopic drag of the form

$$f^i_{\rm dx} \equiv \gamma_{\rm x}\,(v^i_{\rm e} - u^i_{\rm x}) = \rho_{\rm x}\kappa\mathcal{R}_{\rm x}\,(v^i_{\rm e} - u^i_{\rm x}). \tag{4.81}$$

It is fully characterised by the positive drag coefficient, $\gamma_{\rm x}$, or its dimensionless equivalent, $\mathcal{R}_{\rm x}$. The small-scale physics of several different coupling mechanisms discussed in the literature and their strengths are examined in more detail in the following chapters. We already note at this point, however, that the drag coefficients are a function of the total mass density and, therefore, change for different depths inside the star. The mesoscopic drag force, $f^i_{\rm Dp}$, will also play an important role in deriving the superconducting induction equation for the macroscopic magnetic induction in a neutron star's interior (see Chapter 7 for details).

Finally, we note that other frictional mechanisms, such as the coupling of vortices and fluxtubes due to magnetic short-range interactions, could be present. This could give rise to *pinning* between the two arrays and connect the star's rotational and field evolution [188, 189, 206]. However, a detailed microscopic understanding of the pinning interaction is not yet available and is thus ignored here. Neglecting the inertia of the vortex/fluxtube, the force balance per unit length reads as

$$\sum f^i_{\rm x} = f^i_{\rm Mx} + f^i_{\rm tx} + f^i_{\rm emx} + f^i_{\rm dx} = 0. \tag{4.82}$$

Multiplying this result with the surface density, $\mathcal{N}_{\rm x}$, one obtains a macroscopic, averaged equation for the vortex/fluxtube array, i.e.

$$F^i_{\rm Mx} + F^i_{\rm tx} + F^i_{\rm emx} + F^i_{\rm dx} = 0, \tag{4.83}$$

where we identify the force per unit volume with $F^i_{\rm x} \equiv \mathcal{N}_{\rm x} f^i_{\rm x}$ for each mechanisms.

Mutual friction force

Replacing the Magnus force in the Euler equations (4.76) with the force balance (4.83), the mesoscopic vortex/fluxtube velocity, $u^i_{\rm x}$, present in the drag force, is not removed from the equations. However, to describe the multi-fluid system's large-scale behaviour all quantities defined on mesoscopic scales have to be expressed in terms of macroscopic variables. The resulting drag force is referred to as mutual friction, $F^i_{\rm mfx}$ (see Equations (4.60), (4.61) and Andersson et al. [155]). In order to illustrate the mathematical formalism employed to derive $F^i_{\rm mfx}$, it is convenient to neglect the electromagnetic contribution and the tension. Hence, the force balance reduces to the following,

$$\rho_{\rm x}\kappa\,\epsilon^{ijk}\hat{\kappa}^{\rm x}_j(u^{\rm x}_k - v^{\rm x}_k) + \rho_{\rm x}\kappa\mathcal{R}_{\rm x}\,(v^i_{\rm e} - u^i_{\rm x}) = 0. \tag{4.84}$$

This can be solved for the vortex or fluxtube velocity in the second term and one has

$$u_{\mathrm{x}}^{i} = v_{\mathrm{e}}^{i} + \mathcal{R}_{\mathrm{x}}^{-1}\epsilon^{ijk}\hat{\kappa}_{\mathrm{x}}^{j}\Big(u_{\mathrm{x}}^{k} - v_{\mathrm{x}}^{k}\Big). \tag{4.85}$$

Contracting Equation (4.85) with $\epsilon_{ghi}\kappa_{\mathrm{x}}^{h}$ yields

$$\epsilon^{ghi}\hat{\kappa}_{h}^{\mathrm{x}}u_{i}^{\mathrm{x}} = \epsilon^{ghi}\hat{\kappa}_{h}^{\mathrm{x}}v_{i}^{\mathrm{e}} + \frac{1}{\mathcal{R}_{\mathrm{x}}}\,\epsilon^{ghi}\hat{\kappa}_{h}^{\mathrm{x}}\epsilon_{ijk}\hat{\kappa}_{\mathrm{x}}^{j}\left(u_{\mathrm{x}}^{k} - v_{\mathrm{x}}^{k}\right). \tag{4.86}$$

Repeating the same contraction again and simplifying the result, one arrives at

$$\begin{aligned}
\epsilon_{efg}\hat{\kappa}_{\mathrm{x}}^{f}\epsilon^{ghi}\hat{\kappa}_{h}^{\mathrm{x}}u_{i}^{\mathrm{x}} &= \epsilon_{efg}\hat{\kappa}_{\mathrm{x}}^{f}\epsilon^{ghi}\hat{\kappa}_{h}^{\mathrm{x}}v_{i}^{\mathrm{e}} + \frac{1}{\mathcal{R}_{\mathrm{x}}}\,\epsilon_{efg}\hat{\kappa}_{\mathrm{x}}^{f}\epsilon^{ghi}\hat{\kappa}_{h}^{\mathrm{x}}\epsilon_{ijk}\hat{\kappa}_{\mathrm{x}}^{j}\left(u_{\mathrm{x}}^{k} - v_{\mathrm{x}}^{k}\right) \\
&= \epsilon_{efg}\hat{\kappa}_{\mathrm{x}}^{f}\epsilon^{ghi}\hat{\kappa}_{h}^{\mathrm{x}}v_{i}^{\mathrm{e}} + \frac{1}{\mathcal{R}_{\mathrm{x}}}\left[\underbrace{\epsilon_{efg}\hat{\kappa}_{\mathrm{x}}^{f}\hat{\kappa}_{\mathrm{x}}^{g}}_{=0}\,\hat{\kappa}_{h}^{\mathrm{x}}\left(u_{\mathrm{x}}^{h} - v_{\mathrm{x}}^{h}\right) - \epsilon_{efg}\hat{\kappa}_{\mathrm{x}}^{f}\Big(u_{\mathrm{x}}^{g} - v_{\mathrm{x}}^{g}\Big)\right] \\
&= \epsilon_{efg}\hat{\kappa}_{\mathrm{x}}^{f}\epsilon^{ghi}\hat{\kappa}_{h}^{\mathrm{x}}v_{i}^{\mathrm{e}} - \frac{1}{\mathcal{R}_{\mathrm{x}}}\,\epsilon_{efg}\hat{\kappa}_{\mathrm{x}}^{f}\Big(u_{\mathrm{x}}^{g} - v_{\mathrm{x}}^{g}\Big).
\end{aligned} \tag{4.87}$$

This equation can be substituted back into the last term of Equation (4.86) and then solved for the vortex/fluxtube-velocity term,

$$\epsilon_{ghi}\hat{\kappa}_{\mathrm{x}}^{h}u_{\mathrm{x}}^{i}\left(1 + \frac{1}{\mathcal{R}_{\mathrm{x}}^{2}}\right) = \epsilon_{ghi}\hat{\kappa}_{\mathrm{x}}^{h}v_{\mathrm{e}}^{i} + \frac{1}{\mathcal{R}_{\mathrm{x}}}\,\epsilon_{ghi}\hat{\kappa}_{\mathrm{x}}^{h}\epsilon^{ijk}\hat{\kappa}_{j}^{\mathrm{x}}\Big(v_{\mathrm{e}}^{k} - v_{k}^{\mathrm{x}}\Big) + \frac{1}{\mathcal{R}_{\mathrm{x}}^{2}}\,\epsilon_{ghi}\hat{\kappa}_{\mathrm{x}}^{h}v_{\mathrm{x}}^{i}. \tag{4.88}$$

Inserting this back into Equation (4.85) gives a relation between the mesoscopic velocity of a vortex/fluxtube and the macroscopic fluid variables,

$$u_{\mathrm{x}}^{i} = v_{\mathrm{e}}^{i} + \frac{\mathcal{B}_{\mathrm{x}}'}{\mathcal{R}_{\mathrm{x}}}\,\epsilon^{ihg}\hat{\kappa}_{h}^{\mathrm{x}}w_{g}^{\mathrm{ex}} + \frac{\mathcal{B}_{\mathrm{x}}}{\mathcal{R}_{\mathrm{x}}}\,\epsilon^{ihg}\hat{\kappa}_{h}^{\mathrm{x}}\epsilon_{gjk}\hat{\kappa}_{\mathrm{x}}^{j}w_{\mathrm{ex}}^{k}, \tag{4.89}$$

where the following dimensionless mutual friction parameters are defined as

$$\mathcal{B}_{\mathrm{x}} \equiv \frac{\mathcal{R}_{\mathrm{x}}}{1 + \mathcal{R}_{\mathrm{x}}^{2}}, \qquad \mathcal{B}_{\mathrm{x}}' \equiv \mathcal{R}_{\mathrm{x}}\mathcal{B}_{\mathrm{x}} = \frac{\mathcal{R}_{\mathrm{x}}^{2}}{1 + \mathcal{R}_{\mathrm{x}}^{2}}. \tag{4.90}$$

Substituting Equation (4.89) into the averaged drag force finally provides an equation for the macroscopic mutual friction force per unit volume,

$$F_{\mathrm{mfx}}^{i} = \mathcal{N}_{\mathrm{x}}\kappa\rho_{\mathrm{x}}\left(\mathcal{B}_{\mathrm{x}}\epsilon^{ijk}\hat{\kappa}_{j}^{\mathrm{x}}\epsilon_{klm}\hat{\kappa}_{\mathrm{x}}^{l}w_{\mathrm{xe}}^{m} + \mathcal{B}_{\mathrm{x}}'\epsilon^{ijk}\hat{\kappa}_{j}^{\mathrm{x}}w_{k}^{\mathrm{xe}}\right). \tag{4.91}$$

While F_{mfx}^{i} acts on the neutron and proton component, respectively, the electron fluid experiences the opposite forces, $-F_{\mathrm{mfx}}^{i}$. Keeping in mind that the MHD approximation discussed in Subsection 4.2.2 holds, the charged particles move as a single constituent and are described by a combined relation, obtained from adding the individual momentum equations. Hence, the two terms $-F_{\mathrm{mfp}}^{i}$ and F_{mfp}^{i} cancel each other and only the superfluid mutual friction, F_{mfn}^{i}, remains in the Euler equations (4.60) and (4.61). Note,

however, that the coupling between the electrons and the protons will play an important role for the magnetic field evolution discussed in Chapter 7.

When identifying the relative velocity, $w^i_{\rm ne}$, with the velocity difference between the superfluid condensate and the excitations in helium II and slightly modifying the friction coefficients (see also Subsection 8.1.3), the result (4.91) coincides with the expression for the dissipative force given in Equation (3.27). The following chapters will revisit the concepts of mutual friction in neutron stars, discuss several more aspects of the resistive coupling in a multi-fluid mixture and examine astrophysical implications.

4.3.4 Macroscopic Maxwell equations

In order to capture the electromagnetic response of the multi-fluid system correctly, the Euler equations (4.60) and (4.61) together with the quantisation conditions (4.37) and (4.38) have to be supplemented by Maxwell's equations. Taking these to be valid in the multi-fluid mixture, one has to redefine, or rather reinterpret, the various fields, briefly introduced in Subsection 4.2.1, accordingly to make Maxwell's equations suitable for a type-II superconductor.

Following the steps performed in the absence of vortices/fluxtubes (see Equation (4.21)), one can derive a macroscopic Ampère's law in the presence of quantised arrays. In contrast to standard MHD, where the equality $H^i = B^i$ is satisfied, the averaged magnetic induction, B^i, and the macroscopic magnetic field, H^i, are no longer equivalent in a type-II superconducting sample. As discussed by Carter [207] and Glampedakis et al. [181], instead, the London field replaces the macroscopic field, i.e. $H^i = b^i_{\rm L}$, and the modified Ampère's law, accurately capturing the dynamics of a type-II superconductor, reads as

$$\epsilon^{ijk}\nabla_j b^{\rm L}_k = \frac{4\pi}{c}\, j^i = \frac{4\pi e n_{\rm p}}{c}\, w^i_{\rm pe}. \tag{4.92}$$

This shows that the London field, despite being of small magnitude, is closely connected to the macroscopic electromagnetic current density, j^i, and, thus, plays an important role for the electrodynamics.

The deviation from standard MHD can also be understood in terms of the classification generally applied to terrestrial superconductors, which was introduced in Subsection 3.3.1. In laboratory experiments, one distinguishes between macroscopic electromagnetic currents that generate a macroscopic field, H^i, and magnetisation currents *only* affecting the mesoscopic induction, $\bar{B}^i$. The supercurrents, circulating around each vortex/fluxtube and generating $\bar{B}^i_{\rm x}$, are attributed to the second class. They do not contribute to the magnetic field $H^i = b^i_{\rm L}$, which is created by the current density j^i. Hence, the macroscopic magnetic induction, B^i, given in Equation (4.40) differs from the field, H^i. For comparison, in vacuum or normal conductors, no magnetisation currents are present and the identification $H^i = B^i = \bar{B}^i$ can be made, leading to

$$\epsilon^{ijk}\nabla_j H_k = \epsilon^{ijk}\nabla_j B_k = \frac{4\pi}{c} j^i. \tag{4.93}$$

In addition to Ampère's law, the averaged magnetic induction has to be divergence free everywhere in the superconducting fluid, i.e.

$$\nabla_i B^i = 0. \tag{4.94}$$

Finally, the macroscopic Faraday law is given by

$$\partial_t B^i = -c\,\epsilon^{ijk}\nabla_j E_k. \tag{4.95}$$

However, instead of defining the macroscopic electric field as the average over the mesoscopic equivalent, we take advantage of the remaining fluid degree of freedom, namely the electron Euler equation (4.25), to obtain an expression for E^i. Neglecting again the electron inertial terms, one finds

$$E^i = -\frac{1}{c}\epsilon^{ijk} v^{\mathrm{e}}_j B_k - \frac{m_{\mathrm{e}}}{e}\nabla^i\left(\tilde{\mu}_{\mathrm{e}} + \Phi\right) - \frac{F^i_{\mathrm{e}}}{e n_{\mathrm{e}}}. \tag{4.96}$$

Here, F^i_{e} denotes the total dissipative force exerted on the electrons per unit volume due to interactions with the surrounding fluid components, which has been added to the left-hand side of Equation (4.25). Combining Equations (4.95) and (4.96) eventually leads to an evolution equation for the magnetic induction that only depends on macroscopic fluid variables. Chapter 7 discusses in detail the derivation of the superconducting induction equation for the standard drag force presented in Equation (4.81).

Chapter 5

Coupling the Superfluid

The previous chapter introduced the hydrodynamical equations for a multi-component system in the presence of vortices and fluxtubes. As these quantised structures interact with their surroundings, additional force terms have to be included into the momentum equations. In particular, the macroscopic mutual friction force, representing the volume average of the mesoscopic drag acting on individual vortices, is expected to have an impact on the neutron star observables such as the rotation period. The degree to which the mutual friction influences these dynamics is fully characterised by the macroscopic, dimensionless coefficients, $\mathcal{B}$ and $\mathcal{B}'$. As the following analysis is only concerned with the mutual friction arising from the coupling of superfluid vortices with their environment, the index n will be neglected. The discussion of how the charged condensate couples to the other components is resumed in Chapters 6 and 7.

Both mutual friction parameters, $\mathcal{B}$ and $\mathcal{B}'$, are determined by a single mesoscopic drag coefficient, γ, or its dimensionless equivalent $\mathcal{R}$, which depend on the small-scale physics of the mechanisms considered. In the remainder of this chapter, several coupling processes will be addressed, looking at the neutron star core and the crust separately. In discussing the strength of these mechanisms, particular attention will be paid to the fact that the drag coefficients are not constant within both layers but changing for different depths inside the star. This density-dependence of the coupling strength is usually neglected when consequences of mutual friction for neutron stars are examined. However, the varying dissipation could significantly affect a neutron star.

At the crust-core boundary, for example, where the underlying physics of the dominant coupling mechanism should change abruptly, different mutual friction strengths on both sides of the interface might result in the development of unexpected dynamics. Indications for such behaviour, discussed in more detail in Subsection 8.1.4, have been observed in laboratory experiments with two superfluid phases of helium-3 confined to a cylindrical vessel. As the rotational velocity of the container is modified, vortices, which are initially straight and connected across the interface, become distorted due to the dissipation acting on different timescales. This leads to the formation of vortex

tangles [208], notably altering the spin-down and spin-up characteristics. Additionally, interface instabilities causing transfer of angular momentum have been observed [209]. In order to assess, if the conditions for such turbulent features could also be satisfied in neutron stars, the standard assumption of constant mutual friction coefficients is improved in the following chapter. More precisely, the spatial variation of $\mathcal{B}$ and $\mathcal{B}'$ are analysed for *realistic* equations of state in the core and crust, respectively, with the aim of presenting coupling strengths for a neutron star cross-section for the first time.

5.1 Core Mutual Friction

The aim of this section is to determine the strength of mutual friction in the neutron star core as a function of the density. Before addressing the physics of possible coupling mechanisms in more detail, the equilibrium configuration of a specific stellar model is discussed. By applying the two-fluid formalism of Chamel [192], one is able to specify the variations in particle fractions and effective masses, which are needed to calculate the mutual friction coefficients. Besides the composition, the characteristics of the superfluid condensates also change with density. Modifications of the superfluid energy gap, which are directly related to the transition temperatures, will be accounted for by using the parametrisation of Ho et al. [24]. This will be succeeded by a discussion of the coupling mechanisms expected to be present in the core.

Note that the following section will not address the possibility of directly coupling the superfluid neutrons and the superconducting protons via the interaction of vortices and fluxtubes. These dynamics are rather poorly understood and studying the combined magneto-rotational evolution of the two fluids is beyond the scope of this chapter. We will, however, briefly return to the vortex-fluxtube interplay in Chapter 6.

5.1.1 Core composition

The stellar model considered here is the so-called NRAPR parametrisation of Steiner et al. [210]. This effective theory is based on many-body quantum simulations and fitted to the Akmal-Pandharipande-Ravenhall (APR) equation of state [211], which is often used to describe realistic neutron stars. While other stellar models could equivalently be employed to specify the core composition, the typical NRAPR parametrisation allows an illustration of how the equation of state generally affects the mutual friction strength and which density-dependent parameters enter the problem. In order to calculate the relevant quantities in terms of the total mass-energy density, ρ, the equilibrium configuration of nuclear matter has to be determined. Its composition is governed by the rates of processes, converting particles from one species into the others. In the following, a mixture of neutrons, protons, electrons and muons will be studied. Note that the presence of the latter had been ignored in the hydrodynamical model discussed in Chapter 4, since electrons and muons are strongly coupled on macroscopic lengthscales.

Nonetheless, addressing nuclear physics on microscopic scales, muons have to be taken into account because they take part in the transfusion processes. Moreover, note that unlike the nucleons, the leptons behave relativistically on small scales. This, however, does not imply that their averaged motion on macroscopic scales follows the same law.

The equilibrium composition is regulated by four equations [192]. First of all, the total baryon number density, n_b, is conserved. Secondly, the relaxation timescales of electromagnetic processes are much smaller than the typical hydrodynamical timescales, implying that the matter can be treated as electrically neutral. Additionally, neglecting the mass difference between protons and neutrons, the beta equilibrium condition allows one to relate the chemical potentials of the particles involved. The final equation controls the production rate of muons, which are present at densities where the electron kinetic energy exceeds the muon rest-mass energy. More precisely,

$$\text{baryon conservation:} \qquad n_\mathrm{b} = n_\mathrm{p} + n_\mathrm{n}, \tag{5.1}$$

$$\text{charge neutrality:} \qquad n_\mathrm{p} = n_\mathrm{e} + n_\mu, \tag{5.2}$$

$$\text{beta equilibrium:} \qquad \mu_\mathrm{n} = \mu_\mathrm{p} + \mu_\mathrm{e}, \tag{5.3}$$

$$\text{muon production:} \qquad \mu_\mathrm{e} = \mu_\mu. \tag{5.4}$$

Here, n_x with $\mathrm{x} \in \{\mathrm{b,p,n,e},\mu\}$ denotes the baryon, proton, neutron, electron and muon particle number density, respectively, while the chemical potentials, μ_x, of each particle species are defined as

$$\mu_\mathrm{x} \equiv \frac{\partial U_\mathrm{ins}}{\partial n_\mathrm{x}}. \tag{5.5}$$

The internal static energy density, U_ins, is thus crucial in determining the composition of the neutron star interior. It can be decomposed into four terms that depend on the number densities of the particle species involved,

$$U_\mathrm{ins}(n_\mathrm{n}, n_\mathrm{p}, n_\mathrm{e}, n_\mu) = U_\mathrm{C}(n_\mathrm{p}) + U_\mathrm{L}(n_\mathrm{e}) + U_\mathrm{L}(n_\mu) + U_\mathrm{N}(n_\mathrm{n}, n_\mathrm{p}). \tag{5.6}$$

The first contribution is the Coulomb energy due to the presence of the protons, U_C. It is of quantum mechanical nature, since the classical counterpart vanishes due to charge neutrality, and reads as

$$U_\mathrm{C}(n_\mathrm{p}) = -\frac{3}{4}\, e^2 \left(\frac{3}{\pi}\right)^{1/3} n_\mathrm{p}^{4/3}. \tag{5.7}$$

Additionally, there are two lepton contributions, U_L, given by the kinetic energy densities of ideal, relativistic Fermi gases. These will depend on the respective Fermi wave numbers, k_Fx, which are related to the number densities via

$$k_\mathrm{Fx} \equiv (3\pi^2 n_\mathrm{x})^{1/3}. \tag{5.8}$$

For the muons, one has

B_1	B_2	B_3	B_4	B_5	B_6	ν
-1469.69	899.595	85.0067	-55.9836	1338.81	-797.364	0.14416

Table 5.1: Fit parameters for the effective NRAPR Hamiltonian that enter the nucleon contribution to the internal static energy density. The units of energy and length are MeV and fm, respectively. See Steiner et al. [210] or Chamel [192] for details.

$$U_{\mathrm{L}}(n_\mu) = \frac{\hbar c}{8\pi^2\lambda_\mu^4}\left[\lambda_\mu k_{\mathrm{F}\mu}\left(2\lambda_\mu^2 k_{\mathrm{F}\mu}^2+1\right)\sqrt{\lambda_\mu^2 k_{\mathrm{F}\mu}^2+1} - \ln\left(\lambda_\mu k_{\mathrm{F}\mu} + \sqrt{\lambda_\mu^2 k_{\mathrm{F}\mu}^2+1}\right)\right], \tag{5.9}$$

where $\lambda_\mu \equiv \hbar/(m_\mu c)$ is the muon Compton wave length and $m_\mu \simeq 0.113m$ the muon mass with the baryon mass m. Note that since $m, m_\mu \gg m_{\mathrm{e}}$ the electron mass can be set to zero, so that the corresponding kinetic energy density of the electrons reads as

$$U_{\mathrm{L}}(n_{\mathrm{e}}) = \frac{\hbar c k_{\mathrm{Fe}}^4}{4\pi^2}. \tag{5.10}$$

Finally, there is a nucleon contribution, U_{N}, caused by the strong interactions between the neutrons and the protons. It is characterised by an effective Hamiltonian [210] and captures specific details of the equation of state, i.e. it contains information about the NRAPR parametrisation. More precisely,

$$\begin{aligned} U_{\mathrm{N}}(n_{\mathrm{n}}, n_{\mathrm{p}}) = {} & n_{\mathrm{b}} mc^2 + \frac{\hbar^2}{2m}\tau_{\mathrm{b}} + B_1 n_{\mathrm{b}}^2 + B_2(n_{\mathrm{n}}^2 + n_{\mathrm{p}}^2) + B_3 n_{\mathrm{b}}\tau_{\mathrm{b}} \\ & + B_4(n_{\mathrm{n}}\tau_{\mathrm{n}} + n_{\mathrm{p}}\tau_{\mathrm{p}}) + B_5 n_{\mathrm{b}}^{2+\nu} + B_6 n_{\mathrm{b}}^{\nu}(n_{\mathrm{n}}^2 + n_{\mathrm{p}}^2) \end{aligned} \tag{5.11}$$

with $\tau_{\mathrm{x}} \equiv 3k_{\mathrm{Fx}}^2 n_{\mathrm{x}}/5$ denoting the neutron and proton kinetic energy densities in units of $\hbar^2/(2m)$ and we define $\tau_{\mathrm{b}} \equiv \tau_{\mathrm{n}} + \tau_{\mathrm{p}}$. The constants B_i for $i \in \{1, \dots 6\}$ and ν are numbers characteristic for the NRAPR equation of state. They are given in Table 5.1, with MeV and fm being chosen as the units of energy and length, respectively.

Given the different terms of the internal static energy density, the chemical potentials of the four particle species can be calculated. As expected in the zero-temperature limit, the electron and muon chemical potentials are equivalent to the relativistic Fermi energies, i.e. $\mu_{\mathrm{e},\mu} = E_{\mathrm{Fe},\mu}$. These depend on the Fermi momenta, p_{Fx}, which in turn are related to the Fermi wave numbers via $p_{\mathrm{Fx}} = \hbar k_{\mathrm{Fx}}$. One finds

$$\mu_{\mathrm{e}} = E_{\mathrm{Fe}} = c p_{\mathrm{Fe}} = c\hbar\left(3\pi^2 n_{\mathrm{e}}\right)^{1/3}, \tag{5.12}$$

$$\mu_\mu = E_\mu = \left(c^2 p_{\mathrm{F}\mu}^2 + m_\mu^2 c^4\right)^{1/2} = \left[c^2\hbar^2\left(3\pi^2 n_\mu\right)^{2/3} + m_\mu^2 c^4\right]^{1/2}. \tag{5.13}$$

The electron rest-mass term vanishes as the electron mass was assumed to be negligible.

Combining Equations (5.2), (5.4), (5.12) and (5.13), the muon and proton number densities can be expressed in terms of n_{e},

$$n_\mu(n_\mathrm{e}) = \left(n_\mathrm{e}^{2/3} - \frac{m_\mu^2 c^2}{\hbar^2 (3\pi^2)^{2/3}} \right)^{3/2}, \tag{5.14}$$

$$n_\mathrm{p}(n_\mathrm{e}) = n_\mathrm{e} + n_\mu(n_\mathrm{e}). \tag{5.15}$$

In order to proceed, the neutron and proton chemical potentials have to be determined. Note that whereas for the neutrons only the nucleon term, U_N, is needed, the Coulomb energy density, in principle, also contributes to the proton chemical potential. However, this contribution is very small and will be neglected. Using the beta equilibrium condition (5.3), substituting the nucleon chemical potentials and the baryon conservation relation (5.1), one is then left with

$$\begin{aligned} \mu_\mathrm{n} - \mu_\mathrm{p} = 2\,(n_\mathrm{b} - 2n_\mathrm{p})\,(B_2 + B_6 n_\mathrm{b}^\nu) + \frac{8}{5}\,(3\pi^2)^{2/3} B_4 \left[(n_\mathrm{b} - n_\mathrm{p})^{5/3} - n_\mathrm{p}^{5/3} \right] \\ + (3\pi^2)^{2/3} \left[(n_\mathrm{b} - n_\mathrm{p})^{2/3} - n_\mathrm{p}^{2/3} \right] \left[\frac{\hbar^2}{2m} + B_3 n_\mathrm{b} \right] = c\hbar\,(3\pi^2 n_\mathrm{e})^{1/3}. \end{aligned} \tag{5.16}$$

As Equation (5.15) expresses the proton number density as a function of n_e, the last relation connects the electron number density to n_b. Hence, for any given baryon density the electron density can be obtained by numerically solving Equation (5.16). Subsequently the muon, proton and neutron number densities can be evaluated. This allows the particle fractions, which are defined by $x_\mathrm{x} \equiv n_\mathrm{x}/n_\mathrm{b}$, and the Fermi wave numbers, k_Fx, to be computed. The results as a function of the total mass density, ρ, are illustrated in Figures 5.1 and 5.2. Note that the mass-energy density is generally obtained from $\rho = U_\mathrm{ins}/c^2$. However, in the density range of interest, namely $n_\mathrm{b} \lesssim 3n_0$ [192], where $n_0 \sim 0.17\,\mathrm{fm}^{-3}$ is the nuclear saturation density (see also Subsection 2.2.4), one can approximate $\rho \simeq m n_\mathrm{b}$. This is equivalent to the definition of the total mass density used within the hydrodynamical framework of Chapter 4. A closer look at Figure 5.1 shows that protons, electrons and muons constitute several percent of the total mass of a neutron star's outer core, illustrating that neutrons are the dominant particle species. Moreover, close to the crust-core boundary, proton and electron fractions are equal until muons start to appear at a density of $\sim 2 \times 10^{14}\,\mathrm{g\,cm}^{-3}$.

With the particle fractions given, the effective neutron and proton masses, resulting from the strong entrainment between the nucleons, can be deduced. According to Chamel [192], they are defined as

$$\frac{m_\mathrm{p}^*}{m} \equiv \frac{1 + \mathcal{D}\, n_\mathrm{b}(1 - x_\mathrm{p})}{1 + \mathcal{D}\, n_\mathrm{b}}, \qquad \frac{m_\mathrm{n}^*}{m} \equiv \frac{1 + \mathcal{D}\, n_\mathrm{b}\, x_\mathrm{p}}{1 + \mathcal{D}\, n_\mathrm{b}}, \tag{5.17}$$

where $\mathcal{D} \equiv 2B_3 m/\hbar^2$ depends on the equation of state. The results are given in Figure 5.3, showing that the effective neutron mass is close to its bare mass. Protons, on the other hand, are significantly affected by entrainment, their effective mass being reduced to less than 40% of the bare baryon mass at densities above $\sim 8 \times 10^{14}\,\mathrm{g\,cm}^{-3}$.

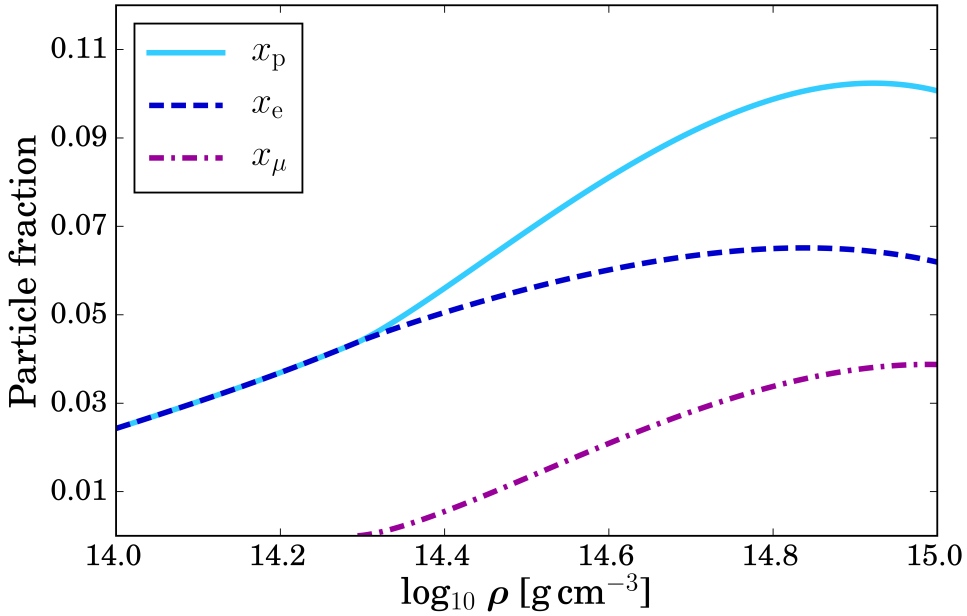

Figure 5.1: Particle fractions of protons (cyan, solid), electrons (blue, dashed) and muons (purple, dot-dashed) as a function of the total mass density in the neutron star core. Note that the neutron fraction is given by $x_\mathrm{n} = 1 - x_\mathrm{p}$. The values are computed for the NRAPR effective equation of state.

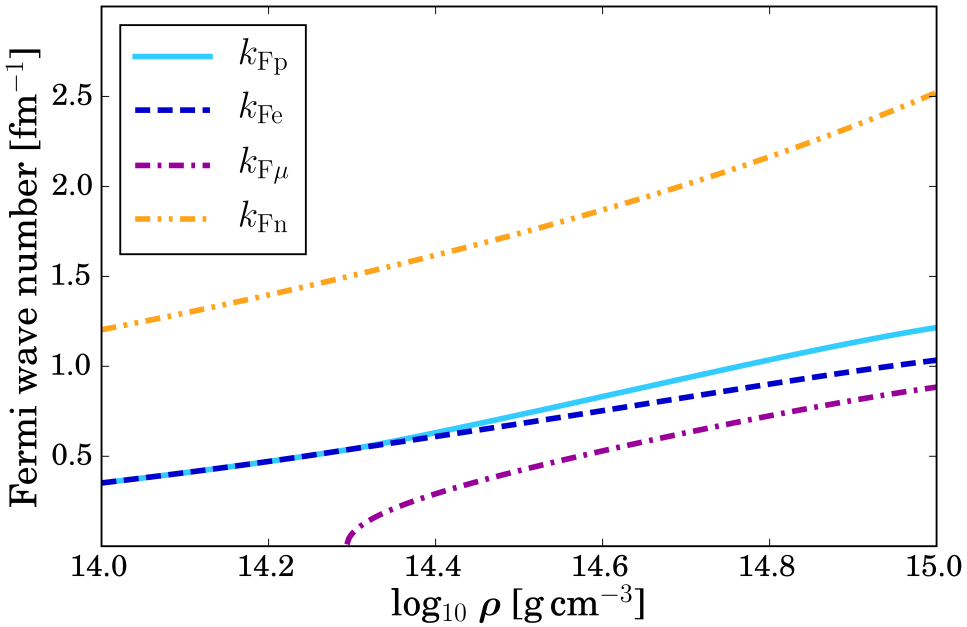

Figure 5.2: Fermi wave numbers of the protons (cyan, solid), electrons (blue, dashed), muons (purple, dot-dashed) and neutrons (yellow, dot-dot-dashed) as a function of the total mass density in the neutron star core. The values are computed for the NRAPR effective equation of state.

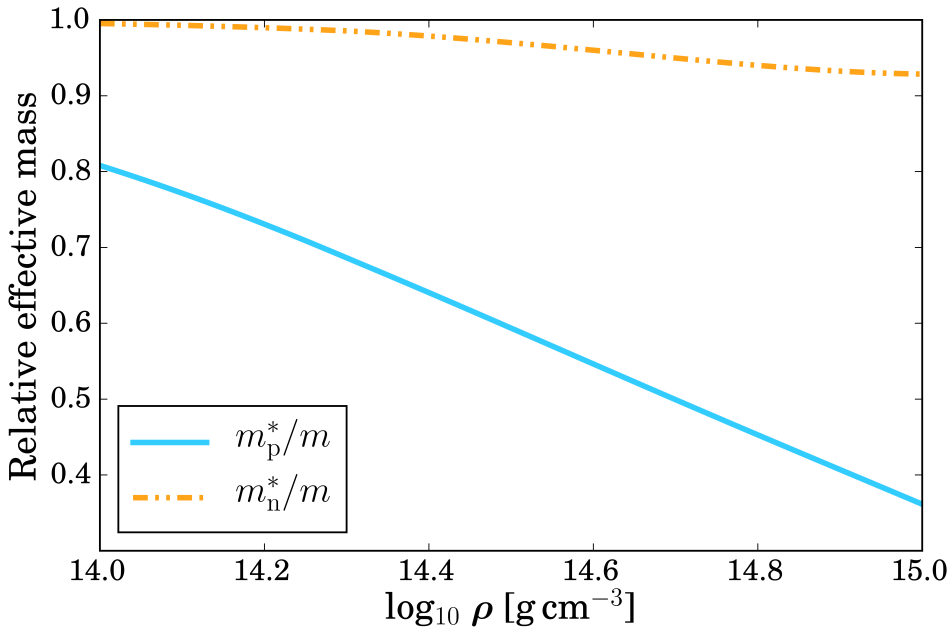

Figure 5.3: Relative effective masses of the protons (cyan, solid) and neutrons (yellow, dot-dot-dashed) as a function of the total mass density in the neutron star core. Deviations from the bare baryon mass are a result of entrainment coupling. The values are computed for the NRAPR effective equation of state.

5.1.2 Parametrised energy gap

As discussed in the next subsection, the coupling between the vortices and the charged particles not only depends on the equilibrium composition but also on the properties of the superfluid condensate, more precisely the size of the vortices. In the standard BCS picture, their dimension is generally associated with the coherence length, ξ, that as given in Equation (3.73) is related to the energy gap, Δ, of the quantum condensate. This introduces an additional density-dependence that can be captured by parametrising the superfluid energy gaps at the Fermi surface as given in Ho et al. [24] (see also Andersson et al. [212] and Kaminker et al. [213]), i.e.

$$\Delta(k_{\mathrm{Fx}}) = \Delta_0 \frac{(k_{\mathrm{Fx}} - g_0)^2}{(k_{\mathrm{Fx}} - g_0)^2 + g_1} \frac{(k_{\mathrm{Fx}} - g_2)^2}{(k_{\mathrm{Fx}} - g_2)^2 + g_3}. \tag{5.18}$$

Here, Δ_0, g_0, g_1, g_2 and g_3 are phenomenological fit parameters for specific gap models, namely a proton singlet [214], neutron singlet [215], shallow (s) [216] and deep (d) [186] neutron triplet model. Numerical values are given in Table 5.2 and the behaviour of $\Delta(k_{\mathrm{Fx}})$ is illustrated in Figure 5.4. As the equilibrium neutron star can be well approximated in the zero-temperature limit, BCS theory also predicts that the energy gaps are proportional to the critical temperatures, T_{c}. The proportionality constant depends on the type of pairing involved and for singlet/triplet states one has [24]

$$\Delta_{\mathrm{singlet}} \approx 1.764\, k_{\mathrm{B}} T_{\mathrm{c}}, \qquad \Delta_{\mathrm{triplet}} \approx 1.188\, k_{\mathrm{B}} T_{\mathrm{c}}. \tag{5.19}$$

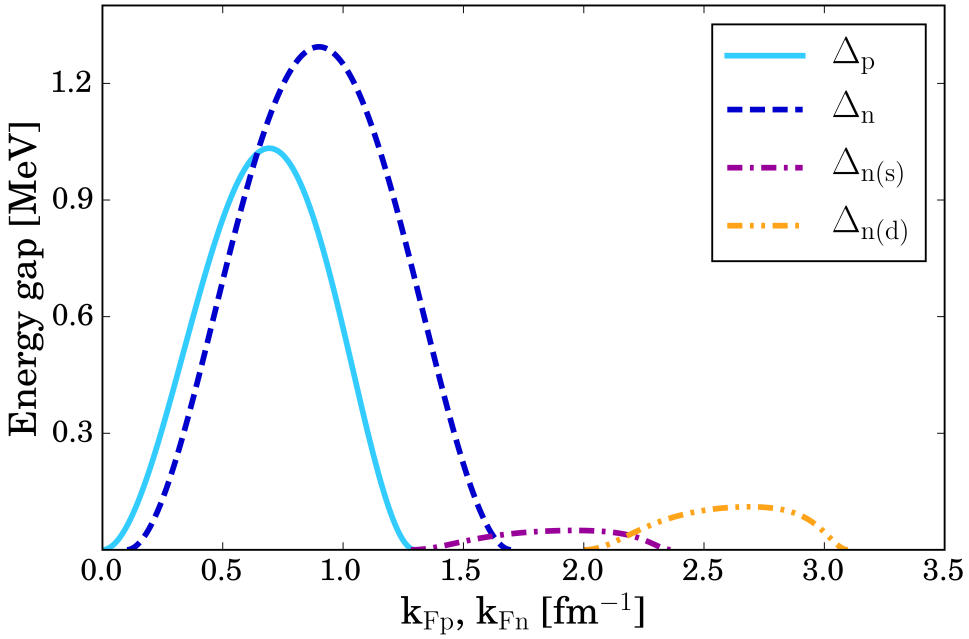

Figure 5.4: Parametrised energy gaps shown as a function of the proton and neutron Fermi wave numbers, k_{Fp} and k_{Fn}, respectively. Singlet-paired gaps for the protons (cyan, solid) and neutrons (blue, dashed) are found on the left. Further on the right, two different neutron triplet gaps are given, i.e. a shallow (purple, dot-dashed) and a deep (yellow, dot-dot-dashed) model.

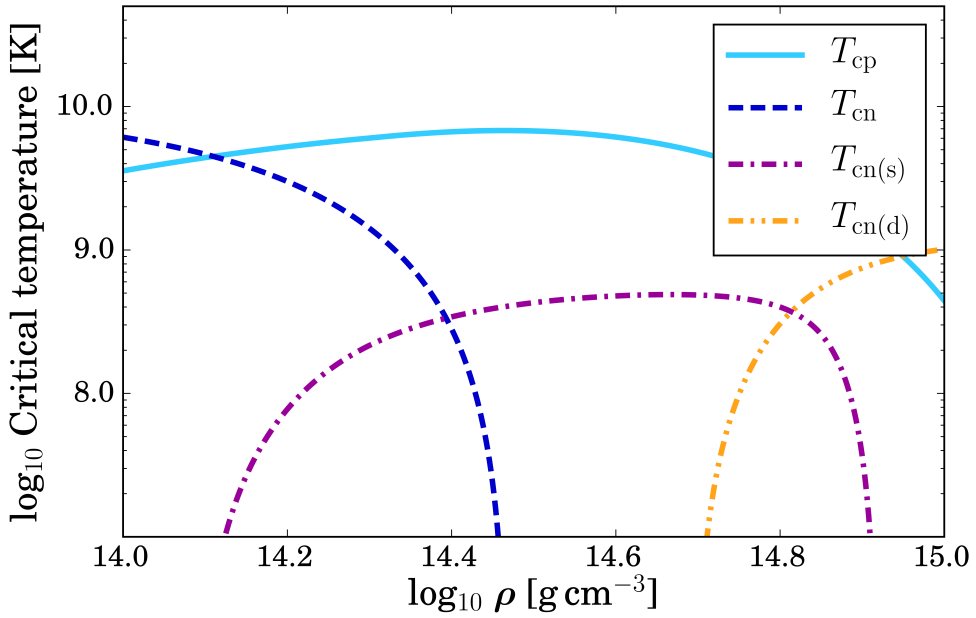

Figure 5.5: Critical temperatures for superconductivity/superfluidity as a function of the total mass density in the neutron star core. Temperatures correspond to the energy gaps given in Figure 5.4, i.e. singlet-paired protons (cyan, solid) and neutrons (blue, dashed) and triplet-paired neutrons with a shallow (purple, dot-dashed) and a deep (yellow, dot-dot-dashed) model. The values are computed for the NRAPR effective equation of state.

	p singlet	n singlet	n triplet (s)	n triplet (d)
Δ_0 [MeV]	120	68	0.068	0.15
g_0 [fm^{-1}]	0	0.1	1.28	2
g_1 [fm^{-2}]	9	4	0.1	0.1
g_2 [fm^{-1}]	1.3	1.7	2.37	3.1
g_3 [fm^{-2}]	1.8	4	0.02	0.02

Table 5.2: Fit parameters for the superconducting proton singlet gap and various superfluid gap models, namely the neutron singlet, the shallow (s) and deep (d) neutron triplet model. Numbers are taken from Ho et al. [24].

Thus, the parametrised energy gaps (5.18) are directly linked to the transition temperatures. The corresponding density-dependence of the different T_c is shown in Figure 5.5, illustrating that as the star is cooling down, the core protons are first to undergo the phase transition, while the neutrons remain normal. As the core temperature decreases further, the neutrons eventually become superfluid. In the following, the interactions of superfluid vortices and charged particles are considered and the focus will be put on the singlet and shallow triplet parametrisation to model the mutual friction strength.

5.1.3 Coupling physics

Various dissipative mechanisms caused by the interaction of neutron vortices with their surroundings have been studied in the literature. The main purpose of these analyses is the comparison of calculated relaxation timescales with those observed in glitching neutron stars, such as the Vela or the Crab pulsar, in order to provide constraints on the interior physics. Feibelman [217], for example, determines the velocity relaxation timescale for the scattering of electrons off quasi-particles thermally excited inside the vortex cores. This mechanism depends exponentially on the temperature and is, thus, strongly suppressed well below the superfluid transition temperature, T_c. However, as Feibelman considers $^1S_0$ vortices, the coupling process predominantly applies to the crustal superfluid and a more detailed discussion is given in Section 5.2. Despite this fact, Sauls et al. [204] have argued that his results also approximate the corresponding relaxation timescale for p-wave paired vortices in the neutron star core. They further compare this dissipative mechanism to the mutual friction arising from the scattering of ultra-relativistic electrons off a constant vortex core magnetisation, which is present in the interior of anisotropic $^3P_2$ vortices. The latter mechanism does not directly depend on the temperature and, therefore, dominates for $T \ll T_\mathrm{c}$, whereas the interaction of electrons with the core quasi-particles should govern the dynamics close to T_c.

Following these studies, Alpar et al. [205] proposed another mutual friction process, which is in essence similar to the electron-magnetic-vortex scattering considered by Sauls et al. [204] but invokes a different magnetic field. Instead of relativistic elec-

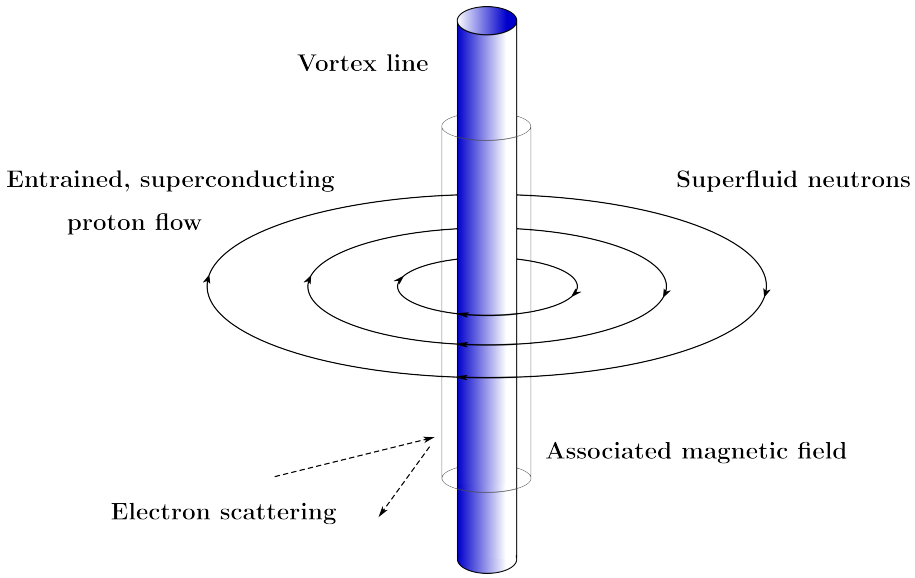

Figure 5.6: Illustration of the dominant dissipative force acting on a neutron vortex. As a result of entrainment, protons are dragged around the neutron vortex generating its magnetisation. On these mesoscopic scales, the electrons are not coupled to the protons and cannot follow their motion. Instead, electrons are dissipatively scattered off the vortex magnetic field, which causes a mesoscopic drag force.

trons scattering off the persistent core magnetisation, they interact with the vortex field generated by the entrained proton flow (see also Subsection 4.3.2). The dissipative process relies on protons and electrons, despite being coupled on large hydrodynamical scales, to move independently on mesoscopic scales. This is ensured by the fact that the protons are superconducting and can be assigned a characteristic lengthscale of the order of 10^{-12} cm (see Equation (4.11)), whereas the electron mean free path is of the order of millimetres and much longer. Hence, the electrons cannot follow the protons' entrained motion on small scales but instead interact with the vortex magnetic field, resulting in the coupling of the neutron component and the charged-particle conglomerate. This dissipative scattering mechanism is illustrated in Figure 5.6. As the entrained magnetic field is several orders of magnitude larger than the persistent magnetisation [205], the former is expected to dominate the dynamics of the outer neutron star core at low temperatures. In order to determine its characteristic coupling timescale, the corresponding drag and mutual friction coefficients, the formalism of Alpar et al. [205] and Sauls et al. [204] is employed. In the following, the theoretical approach is reviewed and modifications due to the density-dependence of various quantities are emphasised.

Velocity relaxation timescale

For a mechanism coupling the superfluid neutrons and the charged conglomerate via electron-vortex interactions, the relaxation timescale of the electrons' velocity distribution characterises the strength of the process. This quantity describes how fast the

particles' velocity relaxes back to equilibrium after a relative velocity, $\mathbf{w}$, between vortices and electrons is applied. Note that vector notation will be used in the remainder of this chapter. More precisely, the electrons' velocity relaxation timescale, $\tau_{\rm v}$, can be defined as the initial rate of decay of the electron mass current density, $\mathbf{g}_{\rm e}$, i.e.

$$\tau_{\rm v}^{-1} \equiv -\left.\frac{\partial \mathbf{g}_{\rm e}(t)}{\partial t}\right|_{t=0} \frac{1}{\mathbf{g}_{\rm e}(t=0)}, \tag{5.20}$$

where the time-dependent mass current density is given by

$$\mathbf{g}_{\rm e}(t) \equiv 2\int \frac{{\rm d}^3 p}{(2\pi\hbar)^3}\, \mathbf{p}\, \delta n_{\mathbf{p},s}(t). \tag{5.21}$$

Here, $\delta n_{\mathbf{p},s}(t)$ is the deviation of the electron distribution function, $n_{\mathbf{p},s}(t)$, from equilibrium, n_0, with $\mathbf{p}$ and s representing momentum and spin of the electrons, respectively. According to Sauls et al. [204], the deviation can be calculated in the so-called *relaxation-time approximation*, giving

$$\delta n_{\mathbf{p},s}(t) \equiv n_{\mathbf{p},s}(t) - n_0 \sim \delta(E_{\mathbf{p}} - E_{\rm Fe})\, \Phi_{\mathbf{p}}(t) = \delta(E_{\mathbf{p}} - E_{\rm Fe})\, \Phi_{\mathbf{p}}(0)\, {\rm e}^{-t/\tau_{\rm e}}, \tag{5.22}$$

where $\delta(x - x_0)$ is the one-dimensional Dirac delta function, $E_{\mathbf{p}}$ the energy associated with electrons of momentum $\mathbf{p}$ and $E_{\rm Fe}$ the relativistic electron Fermi energy. Moreover, the initial electron distribution, $\Phi_{\mathbf{p}}(0)$, is related to the initial velocity, $\mathbf{w}$, (see below) and $\tau_{\rm e}$ represents the relaxation timescale of the electron distribution function itself.

Relativistic quantum mechanics

The timescale, $\tau_{\rm e}$, depends on the specific interaction mechanism at hand and can be determined from the kinetic equation of the electron distribution function. Considering the coupling of ultra-relativistic electrons with a dilute array of N vortices, treated as fixed scattering centres, the change in $n_{\mathbf{p},s}(t)$ is obtained by summing over all possible scattering transitions for each individual vortex,

$$\frac{\partial n_{\mathbf{p},s}}{\partial t} = N \sum_{\mathbf{p}',s'} \frac{2\pi}{\hbar} \delta(E_{\mathbf{p}} - E_{\mathbf{p}'}) |M(\mathbf{p}s \to \mathbf{p}'s')|^2 \left(n_{\mathbf{p},s} - n_{\mathbf{p}',s'}\right). \tag{5.23}$$

While $\mathbf{p}$ and s represent the electron's momentum and spin before the scattering, $\mathbf{p}'$ and s' denote the parameters after the interaction with a superfluid vortex. The small-scale transition characteristics are encoded in the matrix element, M, defined as

$$M(\mathbf{p}s \to \mathbf{p}'s') \equiv \int {\rm d}^3 x\, \Psi^{\dagger}_{\mathbf{p}',s'}(\mathbf{r}) H_{\rm int}(\mathbf{r}) \Psi_{\mathbf{p},s}(\mathbf{r}). \tag{5.24}$$

Here, $\Psi_{\mathbf{p},s}(\mathbf{r})$ is the quantum mechanical wave function of an electron and (†) symbolises the Hermitian conjugate. For the scattering of ultra-relativistic electrons off a localised

time-independent magnetic field, the interaction Hamiltonian can be obtained by generalising the covariant expression of classical electrodynamics, i.e. $H_{\mathrm{int}} \equiv j_\mu A^\mu / c$. The quantum mechanical, relativistic charge current is given by $j_\mu = -ec\Psi^\dagger \gamma_0 \gamma_\mu \Psi$, where $\mu \in \{0, 1, 2, 3\}$ and the γ matrices are

$$\gamma_0 = \begin{pmatrix} \mathbb{1}_2 & 0 \\ 0 & -\mathbb{1}_2 \end{pmatrix}, \qquad \boldsymbol{\gamma} = \begin{pmatrix} 0 & \boldsymbol{\sigma} \\ -\boldsymbol{\sigma} & 0 \end{pmatrix}, \tag{5.25}$$

with $\mathbb{1}_2$ representing the two-by-two unit matrix and $\boldsymbol{\sigma}$ the Pauli spin matrices,

$$\sigma_x = \begin{pmatrix} 0 & 1 \\ 1 & 0 \end{pmatrix}, \qquad \sigma_y = \begin{pmatrix} 0 & -i \\ i & 0 \end{pmatrix}, \qquad \sigma_z = \begin{pmatrix} 1 & 0 \\ 0 & -1 \end{pmatrix}. \tag{5.26}$$

Choosing an electromagnetic four-potential of the form $A^\mu(\mathbf{r}) = \{0, \mathbf{A}(\mathbf{r})\}$, the relativistic interaction Hamiltonian reduces to

$$H_{\mathrm{int}}(\mathbf{r}) = -e \begin{pmatrix} 0 & \boldsymbol{\sigma}\mathbf{A}(\mathbf{r}) \\ \boldsymbol{\sigma}\mathbf{A}(\mathbf{r}) & 0 \end{pmatrix}. \tag{5.27}$$

To determine the matrix element defined in Equation (5.24), the electron wave function has to be specified. Assuming to first order that the electron state is not significantly affected by the scattering event, the Born approximation can be applied [204, 205]. In this case, the electron is described by the plane-wave solution of the free particle Dirac equation, which has positive energy, $E_{\mathbf{p}}$. For a time-independent problem, the spinor is

$$\Psi_{\mathbf{p},s}(\mathbf{r}) = \frac{1}{\sqrt{V}} \frac{\mathrm{e}^{i\mathbf{p}\mathbf{r}/\hbar}}{\sqrt{2E_{\mathbf{p}}(E_{\mathbf{p}} + m_{\mathrm{e}}c^2)}} \begin{pmatrix} (E_{\mathbf{p}} + m_{\mathrm{e}}c^2)\chi_s \\ c\mathbf{p}\boldsymbol{\sigma}\chi_s \end{pmatrix}, \tag{5.28}$$

where an electron occupies the volume $V \equiv \Psi^\dagger \Psi$ and χ_s are the two Pauli spinors,

$$\chi_+ \equiv \begin{pmatrix} 1 \\ 0 \end{pmatrix}, \qquad \chi_- \equiv \begin{pmatrix} 0 \\ 1 \end{pmatrix}. \tag{5.29}$$

Combining the expression for the wave function (5.28) with the interaction Hamiltonian (5.27), the matrix element simplifies to

$$M(\mathbf{p}s \to \mathbf{p}'s') = -\frac{ec}{2E_{\mathbf{p}}V} \int \mathrm{d}^3x\, \mathrm{e}^{i(\mathbf{p}-\mathbf{p}')\mathbf{r}/\hbar} \left[\left(\mathbf{p} + \mathbf{p}'\right) \mathbf{A}(\mathbf{r}) \delta_{ss'} + \hbar\, \bar{\mathbf{B}}(\mathbf{r}) \boldsymbol{\sigma}_{ss'} \right] \tag{5.30}$$

where $\delta_{ss'}$ denotes the Kronecker delta and $\bar{\mathbf{B}}(\mathbf{r}) \equiv \nabla \times \mathbf{A}(\mathbf{r})$ the mesoscopic induction.

Scattering geometry

In order to evaluate the integral (5.30), one can take into account that the persistent core magnetisation [204] and the entrained field (see Equation (4.43)) point along the

vortex direction, suggesting the use of cylindrical coordinates $\{r, \theta, z\}$. Taking the z-axis to be aligned with the vortex, one has $\bar{\mathbf{B}}(\mathbf{r}) = \bar{B}(r)\hat{\boldsymbol{z}}$, where r is the radial distance from its centre. Then, the magnetic vector potential is given by $\mathbf{A}(\mathbf{r}) = A(r)\hat{\boldsymbol{\theta}}$ with

$$A(r) \equiv \frac{1}{r}\int_0^r \mathrm{d}r' r' \bar{B}(r'). \tag{5.31}$$

Additionally, the scattering problem can be simplified by decomposing momentum vectors and the position vector into their z-components and the orthogonal contributions,

$$\mathbf{p} = p_z\hat{\boldsymbol{z}} + \mathbf{p}_\perp, \qquad \mathbf{p}' = p'_z\hat{\boldsymbol{z}} + \mathbf{p}'_\perp, \qquad \mathbf{r} = z\hat{\boldsymbol{z}} + \mathbf{r}_\perp, \tag{5.32}$$

with $\mathbf{r}_\perp = \{r\cos\theta, r\sin\theta, 0\}$ in cylindrical coordinates. Looking closer at the scattering event in the plane perpendicular to the vortex axis, one can construct the two vectors

$$\mathbf{K}_\perp \equiv \mathbf{p}_\perp + \mathbf{p}'_\perp, \qquad \hbar\mathbf{q}_\perp \equiv \mathbf{p}_\perp - \mathbf{p}'_\perp. \tag{5.33}$$

Defining the angle α between $\mathbf{p}_\perp$ and $\mathbf{p}'_\perp$ as shown in Figure 5.7, the following relations can be extracted from the scattering geometry

$$|\mathbf{K}_\perp| \equiv K_\perp = 2p_\perp\cos\alpha/2, \qquad |\mathbf{q}_\perp| \equiv q_\perp = 2\hbar^{-1}p_\perp\sin\alpha/2, \tag{5.34}$$

where one has $p_\perp \equiv |\mathbf{p}'_\perp| = |\mathbf{p}_\perp|$ in the first Born approximation. Executing the volume integration in Equation (5.30) leads to two contributions to the matrix element

$$M_1 = -\frac{e\hbar}{2m_\mathrm{e}c}\frac{m_\mathrm{e}c^2}{E_\mathbf{p}V}2\pi\hbar\,\delta(p_z - p'_z)\,\frac{iK_\perp}{\hbar q_\perp}\,\Pi\left(q_\perp\right)\delta_{ss'} \tag{5.35}$$

and

$$M_2 = -\frac{e\hbar}{2m_\mathrm{e}c}\frac{m_\mathrm{e}c^2}{E_\mathbf{p}V}2\pi\hbar\,\delta(p_z - p'_z)\,\Pi\left(q_\perp\right)\left(\sigma_z\right)_{ss'}. \tag{5.36}$$

To express these results in a compact form, the following quantity was defined

$$\Pi(q) \equiv 2\pi\int_0^\infty \mathrm{d}r\, r\bar{B}(r)J_0(qr) \tag{5.37}$$

and the integral representation of the zeroth-order Bessel function of first kind used,

$$J_0(qr) = \frac{1}{2\pi}\int_0^{2\pi}\mathrm{d}\theta\,\mathrm{e}^{iqr\cos\theta}. \tag{5.38}$$

Combining the kinetic equation for $n_{\mathbf{p},s}$ given in Equation (5.23) with the relaxation-time approximation (5.22) and the matrix element contributions (5.35) and (5.36), the electron distribution relaxation timescale, τ_e, becomes [204]

$$\tau_\mathrm{e}^{-1} = C_\tau\int_0^\pi \mathrm{d}\alpha\,\Pi\left(q_\perp\right)^2, \tag{5.39}$$

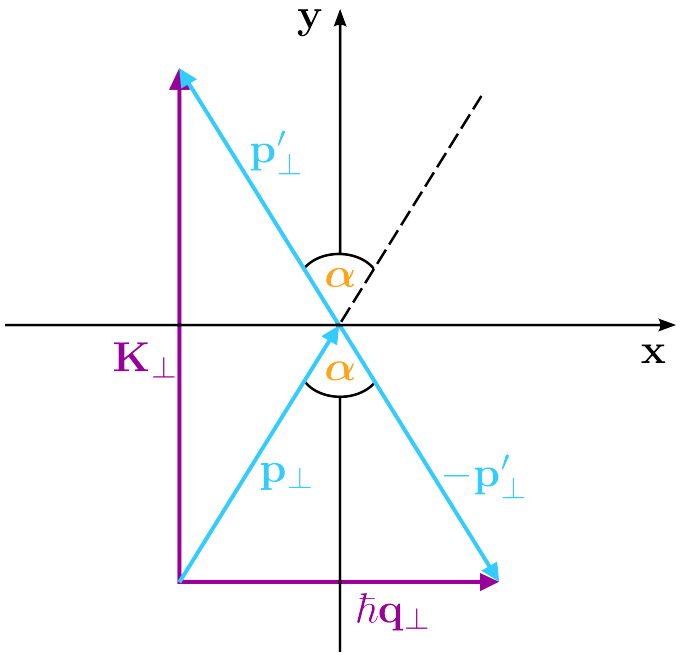

Figure 5.7: Sketch of the scattering geometry in the plane orthogonal to the vortex axis. The direction of the electron momentum changes due to the interaction with the localised magnetic induction. Using the incident momentum, $\mathbf{p}_\perp$, and the scattered momentum, $\mathbf{p}'_\perp$, two new vectors can be constructed. The coordinate axes can be chosen so that $\mathbf{K}_\perp$ and $\mathbf{q}_\perp$ point in the y- and the x-direction, respectively. Magnitudes of the different vectors are connected by trigonometric functions of the angle α.

where the prefactor is given by

$$C_\tau \equiv \mathcal{N}_\mathrm{n} \frac{2\pi}{\hbar} \left(\frac{m_\mathrm{e} c^2}{E_\mathrm{Fe}}\right)^2 \left(\frac{e\hbar}{2m_\mathrm{e} c}\right)^2 \frac{E_\mathrm{Fe}}{(\pi\hbar c)^2} = \frac{e^2}{2\pi\hbar} \frac{\mathcal{N}_\mathrm{n}}{E_\mathrm{Fe}} \tag{5.40}$$

and $\mathcal{N}_\mathrm{n}$ denotes the surface density of the superfluid vortices.

In order to proceed with the calculation of the velocity relaxation timescale, τ_v, the mass current, $\mathbf{g}_\mathrm{e}(t)$, defined in Equation (5.21) has to be determined. This, in turn, requires the initial electron distribution to be specified. According to Sauls et al. [204], $\Phi_\mathbf{p}(0) \equiv \hbar k_\mathrm{Fe}(\hat{\mathbf{p}} \cdot \mathbf{w})$, where the initial relative velocity between the electron and the vortex lies in the plane perpendicular to the vortex axis, i.e. $\mathbf{w} \cdot \hat{\boldsymbol{z}} = 0$. Therefore, the electron mass current can be written as

$$\mathbf{g}_\mathrm{e}(t) = \frac{\hbar k_\mathrm{Fe}}{4\pi^3 c} \int \mathrm{d}^3k\, \mathbf{k}\, \delta(k - k_\mathrm{Fe})\, (\hat{\mathbf{p}} \cdot \mathbf{w})\, \mathrm{e}^{-t/\tau_\mathrm{e}(k)}. \tag{5.41}$$

The electron wave number, k, is the magnitude of the wave vector, $\mathbf{k}$, which is related to the electron momentum via $\mathbf{p} = \hbar\mathbf{k}$. The k-dependence of τ_e can be illustrated by connecting to the scattering geometry orthogonal to the vortex direction. The component of the electron momentum in this plane can be expressed as $p_\perp = \hbar k_\perp = \hbar k \sin\vartheta$, where the angle ϑ is measured from the z-axis. Hence, $q_\perp$ is proportional to the wave number and the electron distribution relaxation timescale also depends on k. Taking

advantage of the constraints on the relative velocity, Equation (5.41) reduces to

$$\mathbf{g}_{\mathrm{e}}(t) = \frac{\hbar k_{\mathrm{Fe}}^4}{4\pi^2 c}\,\mathbf{w}\int_0^\pi \mathrm{d}\vartheta \sin\vartheta^3\,\mathrm{e}^{-t/\tau_{\mathrm{e}}(k_{\mathrm{Fe}})}. \tag{5.42}$$

The electron velocity relaxation timescale defined in Equation (5.20) is thus given by

$$\tau_{\mathrm{v}}^{-1} = \frac{3}{4}\int_0^\pi \mathrm{d}\vartheta\,\frac{\sin\vartheta^3}{\tau_{\mathrm{e}}(k_{\mathrm{Fe}})} = \frac{3}{4}\,C_\tau\int_0^\pi \mathrm{d}\vartheta\sin\vartheta^3\int_0^\pi \mathrm{d}\alpha\,\Pi\left(2k_{\mathrm{Fe}}\sin\vartheta\sin\alpha/2\right)^2. \tag{5.43}$$

Specifying the magnetic induction

Evaluating Equation (5.43) requires detailed knowledge of the spatial distribution of the mesoscopic magnetic induction. At this point, the calculations of Sauls et al. [204] and Alpar et al. [205] deviate from each other as they consider electron scattering off different magnetic fields, leading to different results for the function $\Pi(q)$. In the former case, a thorough analysis of the vortex magnetic field distribution gives

$$\Pi_{\mathrm{persistent}}(q) = 2\pi\,\xi_{\mathrm{n}} q^{-1} J_1(q\xi_{\mathrm{n}})\bar{B}_{\mathrm{persistent}}, \tag{5.44}$$

where ξ_{n} denotes the neutron coherence length and $J_1(x)$ the first-order Bessel function of first kind. Moreover, $\bar{B}_{\mathrm{persistent}}$ represents the magnitude of the persistent core magnetisation, which can be approximated by [204]

$$\bar{B}_{\mathrm{persistent}} \simeq -\frac{e\hbar}{mc}\,\frac{k_{\mathrm{Fn}}^3}{3\pi^2}\left(\frac{\Delta_{\mathrm{n}}}{k_{\mathrm{B}}T_{\mathrm{Fn}}}\right)^2, \tag{5.45}$$

with the triplet-paired neutron energy gap, Δ_{n}, the Fermi wave number and temperature, k_{Fn} and T_{Fn}, respectively. As the neutrons behave non-relativistically, the latter two are related to the Fermi energy, E_{Fn}, via

$$E_{\mathrm{Fn}} = \frac{\hbar^2 k_{\mathrm{Fn}}^2}{2m} = k_{\mathrm{B}}T_{\mathrm{Fn}}. \tag{5.46}$$

Thus, with fiducial values for the stellar interior (see Figures 5.2 and 5.4), one finds

$$\bar{B}_{\mathrm{persistent}} \approx -9.8\times10^8\left(\frac{2\,\mathrm{fm}^{-1}}{k_{\mathrm{Fn}}}\right)\left(\frac{\Delta_{\mathrm{n}}}{0.05\,\mathrm{MeV}}\right)^2\,\mathrm{G}. \tag{5.47}$$

Substituting Equation (5.44) into Equation (5.43) and changing the second integration variable from α to $x \equiv \sin\alpha/2$ then leads to

$$\tau_{\mathrm{v,persistent}}^{-1} = \frac{3}{2}\,C_\tau\left(\frac{\pi\xi_{\mathrm{n}}}{k_{\mathrm{Fe}}}\right)^2\bar{B}_{\mathrm{persistent}}^2\int_0^\pi \mathrm{d}\vartheta\sin\vartheta\int_0^1 \mathrm{d}x\,\frac{J_1(2k_{\mathrm{Fe}}\xi_{\mathrm{n}}\sin\vartheta\,x)^2}{x^2(1-x^2)^{1/2}}. \tag{5.48}$$

In principle, for a given density, the right-hand side of this result has to be integrated numerically. However, an approximate solution can be obtained by taking into account

that for typical neutron star parameters one has $2k_{\mathrm{Fe}}\xi_{\mathrm{n}} \gg 1$ (see also Equation (5.59)). Expanding the second integral in Equation (5.48) to leading order, thus, allows the following approximation for sufficiently large scattering angles ϑ,

$$\tau^{-1}_{\mathrm{v,persistent}} \simeq \frac{3}{2}\, C_\tau \left(\frac{\pi\xi_{\mathrm{n}}}{k_{\mathrm{Fe}}}\right)^2 \bar{B}^2_{\mathrm{persistent}} \int_0^\pi \mathrm{d}\vartheta\, 2k_{\mathrm{Fe}}\xi_{\mathrm{n}}\, \frac{4}{3\pi}\, \sin^2\vartheta. \tag{5.49}$$

Evaluating the integral and substituting C_τ defined in Equation (5.40) finally gives

$$\tau^{-1}_{\mathrm{v,persistent}} = \frac{\pi e^2}{c\hbar^2}\, \frac{\mathcal{N}_{\mathrm{n}}\xi_{\mathrm{n}}^3}{k_{\mathrm{Fe}}^2}\, \bar{B}^2_{\mathrm{persistent}}. \tag{5.50}$$

Using Equation (4.6), which relates the vortex area density to the neutron stars' rotation period, the BCS expression for the coherence length given in Equation (3.73) and Equation (5.47), one can estimate the velocity relaxation timescale

$$\tau_{\mathrm{v,persistent}} \approx 2.8\times 10^7 \left(\frac{m^*_{\mathrm{n}}}{m}\right)^3 P_{10} \left(\frac{k_{\mathrm{Fe}}}{0.75\,\mathrm{fm}^{-1}}\right)^2 \left(\frac{2\,\mathrm{fm}^{-1}}{k_{\mathrm{Fn}}}\right) \left(\frac{0.05\,\mathrm{MeV}}{\Delta_{\mathrm{n}}}\right) \mathrm{s}, \tag{5.51}$$

where $P_{10} \equiv P/(10\,\mathrm{ms})$ was chosen. Hence, the characteristic timescale for the coupling of electrons with the persistent core magnetisation of p-wave vortices is of the order of months to years. The density-dependence is illustrated in Figure 5.8, indicating that this mechanism is strongest around a density of $\sim 3.6\times 10^{14}\,\mathrm{g\,cm^{-3}}$. The relaxation timescale increases significantly towards the crust-core boundary and the inner neutron star core. Figure 5.8 also allows a comparison with the coupling achieved by the interaction of electrons with the entrained vortex magnetic field, which as expected is much stronger.

To examine this second scattering process first discussed by Alpar et al. [205], the field distribution needs to be specified. A generalised form of the magnetic induction presented in Subsection (4.3.2) has to be used. Accounting for the structure of a neutron vortex with a core size of the order of the coherence length, ξ_{n}, and the magnetic flux located within the radius λ_*, the entrained magnetic induction is given by [205, 182]

$$\bar{B}_{\mathrm{entrained}}(r) = \frac{\phi_{\mathrm{n}}}{\pi\xi_{\mathrm{n}}^2} \begin{cases} 1 - \frac{\xi_{\mathrm{n}}}{\lambda_*} K_1\left(\frac{\xi_{\mathrm{n}}}{\lambda_*}\right) I_0\left(\frac{r}{\lambda_*}\right) & \text{for } 0 \le r \le \xi_{\mathrm{n}}, \\ \frac{\xi_{\mathrm{n}}}{\lambda_*} I_1\left(\frac{\xi_{\mathrm{n}}}{\lambda_*}\right) K_0\left(\frac{r}{\lambda_*}\right) & \text{for } r \ge \xi_{\mathrm{n}}. \end{cases} \tag{5.52}$$

The neutron vortex flux, ϕ_{n}, depends on the effective masses and is defined in Equation (4.47), while $I_{0,1}(x)$ and $K_{0,1}(x)$ denote the modified Bessel functions of first and second kind, respectively. Using the interior solution, the magnitude of the magnetisation at the centre of the vortex can be estimated. For $r = 0$, the second term containing Bessel functions is negligibly small. Taking only the prefactor into account, one has

$$\bar{B}_{\mathrm{entrained}} \approx -2.3\times 10^{13} \left(\frac{m^*_{\mathrm{n}}}{m}\right) \left(1 - \frac{m^*_{\mathrm{p}}}{m}\right) \left(\frac{2\,\mathrm{fm}^{-1}}{k_{\mathrm{Fn}}}\right)^2 \left(\frac{\Delta_{\mathrm{n}}}{0.05\,\mathrm{MeV}}\right)^2 \mathrm{G}. \tag{5.53}$$

For these fiducial parameters of the p-wave paired neutron superfluid, the entrained field is approximately four orders of magnitude larger than the persistent core magnetisation given in Equation (5.47), causing the former to dominate the mutual friction coupling.

In the limit $\xi_{\rm n} \to 0$, which is equivalent to ignoring the vortex core, the exterior solution of Equation (5.52) reduces to the approximate result used in the hydrodynamical formalism (see Equation (4.43)), i.e.

$$\bar{B}_{\rm entrained}(r) \simeq \frac{\phi_{\rm n}}{2\pi\lambda_*^2} K_0\left(\frac{r}{\lambda_*}\right). \tag{5.54}$$

With this simplified expression, the function $\Pi(q)$ defined in Equation (5.37) can be easily determined because the integral has an analytic solution. Further assuming that the flux is located within a tube of infinitely small radius, i.e. $\lambda_* \to 0$, one finds that $\Pi(q)$ is constant and simply reduces to the magnetic flux, $\Pi(q) = \phi_{\rm n}$. Thus, the electron distribution relaxation timescale for an infinitely thin vortex equates to

$$\tau_{\rm e0}^{-1} \equiv C_\tau \phi_{\rm n}^2 \pi. \tag{5.55}$$

Using Equation (5.43), the corresponding velocity relaxation timescale can be obtained. Since $\tau_{\rm e0}$ does not depend on the angle ϑ, the two relaxation timescale are equivalent in the zero-radius limit. For typical parameters, one finds (see also Figure 5.8)

$$\tau_{\rm v0} = \tau_{\rm e0} \approx 8.0 \times 10^{-5} \left(\frac{m_{\rm n}^*}{m}\right)^2 \left(1 - \frac{m_{\rm p}^*}{m}\right)^{-2} P_{10}\left(\frac{k_{\rm Fe}}{0.75\,{\rm fm}^{-1}}\right) {\rm s}. \tag{5.56}$$

A more accurate calculation of the relaxation timescale has to take the detailed structure of the vortex, i.e. its finite size, into account. Integrating the full expression (5.52) for the magnetic field distribution leads to

$$\Pi_{\rm entrained}(q) = \frac{2\phi_{\rm n}}{1 + q^2\lambda_*^2} \frac{J_1(q\xi_{\rm n})}{q\xi_{\rm n}}. \tag{5.57}$$

With this result, one obtains an improved estimate for the electron distribution relaxation timescale, subsequently leading to the following velocity relaxation timescale

$$\tau_{\rm v,entrained}^{-1} = \frac{3\tau_{\rm e0}^{-1}}{2\pi\xi_{\rm n}^2 k_{\rm Fe}^2} \int_0^\pi {\rm d}\vartheta \sin\vartheta \int_0^1 {\rm d}x \, \frac{J_1(2k_{\rm Fe}\xi_{\rm n}\sin\vartheta\, x)^2}{x^2(1-x^2)^{1/2}\left(1 + 4k_{\rm Fe}^2\lambda_*^2\sin^2\vartheta\, x^2\right)^2}. \tag{5.58}$$

The zero-radius scattering timescale is therefore significantly altered due to the finite size of the vortex. As with the electron-magnetic-vortex interaction considered by Sauls et al. [204], the right-hand side cannot be integrated analytically. However, comparison with the corresponding relation (5.48) reveals the presence of an additional factor in the second integral that contains the angle ϑ. This complicates the derivation of an approximate solution. To proceed, we define two dimensionless parameters, $\beta_1 \equiv \xi_{\rm n}/\lambda_*$

and $\beta_2 \equiv 2k_{\rm Fe}\xi_{\rm n}$, respectively. For the triplet-paired superfluid, one estimates

$$\beta_1 \approx 4.1 \left[\left(\frac{m}{m_{\rm n}^*}\right)\left(\frac{m_{\rm n}^*}{m} - 1 + \frac{m_{\rm p}^*}{m}\right)^{-1} \rho_{14}\left(\frac{x_{\rm p}}{0.05}\right)\right]^{1/2} \left(\frac{k_{\rm Fn}}{2\,{\rm fm}^{-1}}\right)\left(\frac{0.05\,{\rm MeV}}{\Delta_{\rm n}}\right), \quad (5.59)$$

$$\beta_2 \approx 8.0 \times 10^2 \left(\frac{m}{m_{\rm n}^*}\right)\left(\frac{k_{\rm Fe}}{0.75\,{\rm fm}^{-1}}\right)\left(\frac{k_{\rm Fn}}{2\,{\rm fm}^{-1}}\right)\left(\frac{0.05\,{\rm MeV}}{\Delta_{\rm n}}\right), \quad (5.60)$$

where $\rho_{14} \equiv \rho/10^{14}\,{\rm g\,cm^{-3}}$. Thus, for the velocity relaxation timescale it follows

$$\tau_{\rm v,entrained}^{-1} = 6\,\frac{\tau_{\rm e0}^{-1}\beta_1^4}{\pi\beta_2^3}\int_0^{\pi} {\rm d}\vartheta \sin\vartheta \int_0^{\beta_2} {\rm d}y\, \frac{\beta_2^2}{(1-y^2/\beta_2^2)^{1/2}}\,\frac{J_1(\sin\vartheta\, y)^2}{y^2\left(\beta_1^2 + \sin^2\vartheta\, y^2\right)^2}. \quad (5.61)$$

This equation can be solved numerically for a specific density inside the star. However, the integration is computationally expensive and, instead, two approximations can be used to significantly decrease the computation time, while retaining a high accuracy (the relative error is smaller than 10^{-5}). Taking advantage of the symmetric form of the integrand, the ϑ-integration is well approximated by fixing the angle ϑ to $\pi/2$, where the integrand is maximal, and dividing the final result by 2. Moreover, for typical neutron star parameters $\beta_2 \gg 1$, which allows the square-root term in the second integral to be replaced by a Taylor expansion. To leading order, one obtains[1]

$$\tau_{\rm v,entrained}^{-1} \simeq 3\,\frac{\tau_{\rm e0}^{-1}\beta_1^4}{\beta_2^3}\int_0^{\beta_2} {\rm d}y\, \frac{\beta_2^2 + y^2/2}{\left(\beta_1^2 + y^2\right)^2}\left[\frac{J_1(y)}{y}\right]^2. \quad (5.62)$$

Figure 5.8 shows the various frictional coupling timescales in the outer core as a function of the total density for a fiducial neutron star rotation period of 10 ms. Firstly, one can observe that the timescale for the scattering of electrons off the persistent core magnetisation is several orders of magnitude larger than the timescales associated with the coupling to the entrained magnetic field.[2] The latter mechanism thus dominates the interaction between the neutron vortices and the charged-particle conglomerate. The corresponding velocity relaxation timescale for the shallow triplet gap model is of the order of seconds for a large range of densities but increases towards to the crust-core boundary and the inner core. For comparison, $\tau_{\rm v,entrained}$ has also been calculated for the singlet energy gap model, leading to shorter coupling timescales at lower densities. Both velocity relaxation timescales are several orders of magnitude larger than the zero-radius scattering time, $\tau_{\rm v0}$, given in Equation (5.56), which demonstrates that the finite vortex size increases the relaxation timescale and weakens the mutual friction

[1] Solution (5.62) agrees with Equation (30b) of Alpar et al. [205], apart from the additional factor 1/2 in the first term of the integrand, which however has little influence on the result.

[2] For typical neutron star equilibrium temperatures of 10^6 to 10^8 K, the timescale for the scattering of electrons off the entrained vortex field is also much shorter than the coupling timescale calculated by Feibelman [217] for the scattering of electrons off quasi-particles thermally excited in the vortex cores. For more details see Alpar et al. [205].

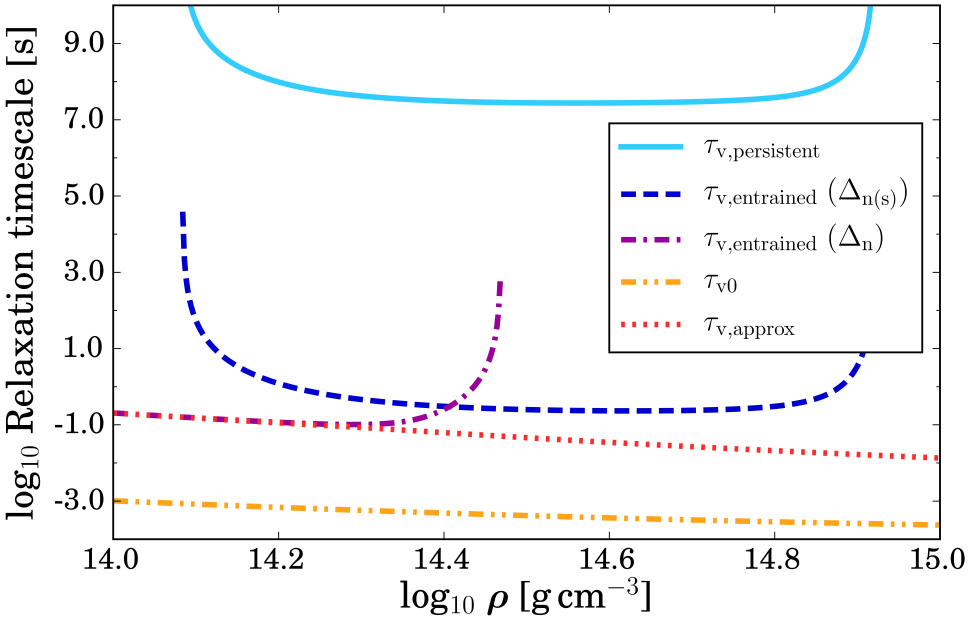

Figure 5.8: Relaxation timescales in the neutron star core as a function of density. Shown are the timescale for electrons interacting with the persistent magnetisation of $^3P_2$ vortices (cyan, solid) defined in Equation (5.50) and four timescales associated with the scattering of electrons off the entrained vortex magnetic field. $\tau_{\rm v,entrained}$ is given for the shallow triplet gap (blue, dashed) and the singlet gap (purple, dot-dashed). For comparison, the zero-radius scattering timescale, $\tau_{\rm v0}$, (yellow, dot-dot-dashed) and the approximate timescale, $\tau_{\rm v,approx}$, (red, dotted) defined in Equation (5.63) are also included. The values are computed for the NRAPR effective EoS and a fiducial rotation period of 10 ms.

coupling. Finally, Figure 5.8 also shows the timescale

$$\tau_{\rm v,approx} \equiv \frac{16}{3\pi}\,\tau_{\rm e0}\,\frac{\beta_2}{\beta_1}. \tag{5.63}$$

This approximation, obtained by expanding the integrand in Equation (5.62) to lowest order in β_2^{-1} and using $\beta_1 \approx 1$ [205], has been considered by Andersson et al. [200] to estimate the strength of mutual friction in the outer neutron star core. Note, however, that the term β_2/β_1 is independent of the neutron coherence length and, hence, does not capture the density-dependence arising from the superfluid energy gap. As shown in Figure 5.8, $\tau_{\rm v,approx}$ is a good approximation to the coupling timescale for the electron-magnetic-vortex interaction of a *s*-wave paired superfluid at low densities. The corresponding timescale for the *p*-wave vortex interaction, on the other hand, is overestimated by at least a factor 5 because $\beta_1 \approx 1$ is no longer satisfied.

Moment of inertia increase

As explained previously, at the heart of the dominant mutual friction mechanism lies the independent motion of electrons and protons on mesoscopic scales. However, both particle species are strongly coupled on hydrodynamical scales, effectively moving as

one component (see Subsection 4.2.2), implying that the macroscopic charge current vanishes. Hence, in order to obtain the characteristic relaxation timescale, $\tau_{\rm ev}$, between the neutron vortices and the charged-particle conglomerate, the electron velocity relaxation timescale has to be corrected to account for the increase in moment of inertia due to the electron-proton coupling. This is achieved by extending $\tau_{\rm v,entrained}$ by

$$\tau_{\rm ev} \equiv \frac{mc^2}{E_{\rm Fe}}\,\tau_{\rm v,entrained} \approx 6.3\left(\frac{0.75\,{\rm fm}^{-1}}{k_{\rm Fe}}\right)\tau_{\rm v,entrained}. \tag{5.64}$$

Thus, the larger moment of inertia increases the frictional timescale by a factor of 10.

Mutual friction coefficients

The relaxation timescale $\tau_{\rm ev}$ dictates how quickly the neutron vortex motion relaxes to the charged fluids, if an initial relative velocity is present. Hence, on hydrodynamic scales, the neutron vortices experience the following frictional force due to the interaction with the electron-proton conglomerate,

$$\mathbf{F}_{\rm d} = \frac{\rho_{\rm p}}{\tau_{\rm ev}}\,(\mathbf{v}_{\rm p} - \mathbf{u}_{\rm n}), \tag{5.65}$$

where $\mathbf{v}_{\rm p}$ and $\mathbf{u}_{\rm n}$ are the averaged velocities of the electron-proton component and the vortices, respectively. This force is equivalent to the macroscopic form of the mesoscopic drag, $\mathbf{f}_{\rm d}$, exerted on a single vortex that was defined in Equation (4.81). The averaging is achieved by multiplying $\mathbf{f}_{\rm d}$ with the vortex surface density, $\mathcal{N}_{\rm n}$. Hence, the dimensionless drag coefficient, $\mathcal{R}$, and the velocity relaxation timescale, $\tau_{\rm ev}$, are related. One has

$$\mathcal{R} = \frac{\rho_{\rm p}}{\rho_{\rm n}}\,\frac{1}{\mathcal{N}_{\rm n}\kappa}\,\frac{1}{\tau_{\rm ev}} \approx 1.3\times10^{-5}\left(\frac{x_{\rm p}}{0.05}\right)P_{10}\left(\frac{10\,{\rm s}}{\tau_{\rm ev}}\right) \ll 1, \tag{5.66}$$

where typical neutron star parameters were used to give the numerical value. Hence, the frictional electron-magnetic-vortex coupling is rather weak. Neglecting the electromagnetic force exerted on a vortex and its tension as explained in detail in Subsection 4.3.3, the drag coefficient $\mathcal{R}$ and the mutual friction coefficients, $\mathcal{B}$ and $\mathcal{B}'$, are related to each other by Equation (4.90). More, precisely in the limit of weak mutual friction,

$$\mathcal{B} = \frac{\mathcal{R}}{1+\mathcal{R}} \simeq \mathcal{R}, \qquad\qquad \mathcal{B}' \simeq \mathcal{R}^2. \tag{5.67}$$

5.1.4 Core cross-section

After combining Equations (5.66) and (5.67) and substituting the definitions of $\tau_{\rm ev}$ and $\tau_{\rm v,entrained}$ respectively, one is left with the following

$$\mathcal{B} \simeq \frac{3\pi}{2}\,\frac{x_{\rm p}}{1-x_{\rm p}}\left(\frac{m}{m_{\rm n}^*}\right)^2\left(1-\frac{m_{\rm p}^*}{m}\right)^2\frac{\beta_1^4}{\beta_2^3}\int_0^{\beta_2}{\rm d}y\,\frac{\beta_2^2+y^2/2}{\left(\beta_1^2+y^2\right)^2}\left[\frac{J_1(y)}{y}\right]^2. \tag{5.68}$$

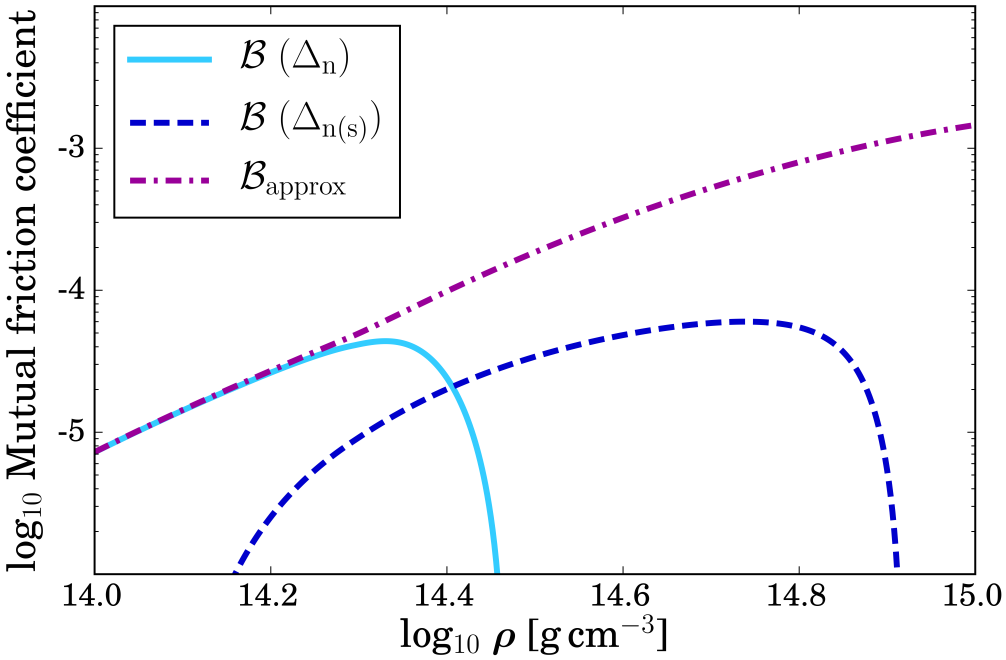

Figure 5.9: Mutual friction strength in the core, generated by the scattering of relativistic electrons off the entrained vortex field. The coupling strength depends on the energy gap parametrisation considered. Shown are results for the neutron singlet (cyan, solid) and the shallow triplet (blue, dashed) model. For comparison, the mutual friction coefficient, $\mathcal{B}_{\rm approx}$ (purple, dot-dashed), obtained from the gap-independent approximation, $\tau_{\rm v,approx}$, is given. The values are computed for the NRAPR effective equation of state.

The strength of the mutual friction clearly depends on the properties of the superfluid condensate. The resulting estimates as a function of the density are shown in Figure 5.9 for the singlet and the shallow triplet gap parametrisation. The differences between both models originate in the different vortex size. Since the ${}^1S_0$ vortices are approximately an order of magnitude smaller than the ${}^3P_2$ vortices close to the crust-core interface, the interaction between relativistic electrons and the entrained magnetic field is stronger in the former case. For densities above $\sim 2.4 \times 10^{14}\,{\rm g\,cm^{-3}}$ however, the case is reversed and the coupling to p-wave paired neutron vortices dominates. For comparison, Figure 5.9 further shows the mutual friction coefficient corresponding to the gap-independent relaxation timescale $\tau_{\rm v,approx}$. Using $m_{\rm n}^* \approx m$ and $x_{\rm p} \approx x_{\rm e} \ll 1$ for simplicity leads to

$$\mathcal{B}_{\rm approx} \approx 3.9 \times 10^{-4} \left(1 - \frac{m_{\rm p}^*}{m}\right)^2 \left(\frac{m}{m_{\rm p}^*}\right)^{1/2} \rho_{14}^{1/6} \left(\frac{x_{\rm p}}{0.05}\right)^{7/6}, \tag{5.69}$$

which agrees with Equation (66) of Andersson et al. [155]. As illustrated in Figure 5.9, Equation (5.69) gives good approximations for the s-wave condensate at low densities because $\beta_1 \approx 1$ holds. However, it deviates significantly at higher densities, where the p-wave superfluid is present. Taking both energy gap models into account, a representative choice for the core mutual friction coefficient would be $\mathcal{B} \approx 10^{-5}$, which further

implies $\mathcal{B}' \approx 10^{-10}$. Note that despite being rather weak, the electron-magnetic-vortex interaction is strong enough to couple the neutron superfluid and the charged conglomerate in the neutron star core on the order of seconds, having important implications for the post-glitch dynamics. As the crust and the electron-proton component are expected to be strongly coupled by the magnetic field [218], the short mutual friction timescales imply that a very large fraction of the core has to follow the crust's motion. Hence, the core neutron superfluid cannot be responsible for the long-term glitch recovery observed to be of the order of months to years. Instead, the component thought to cause these long timescales is the neutron superfluid in the inner crust. The following section will address possible mutual friction mechanisms in this layer of the neutron star.

5.2 Crustal Mutual Friction

While the hydrodynamical framework of Chapter 4 focused on the mixture of neutrons, protons and electrons in the outer neutron star core, a similar multi-fluid formalism should characterise the averaged dynamics of the inner crust. This region corresponds to the density range between the neutron drip, $\rho_{\mathrm{D}} \sim 4 \times 10^{11}\,\mathrm{g\,cm^{-3}}$, and the crust-core interface at $\sim 10^{14}\,\mathrm{g\,cm^{-3}}$ (see also Subsection 2.2.3). There, proton-rich lattice nuclei are permeated by relativistic electrons and a free neutron gas, which is expected to form Cooper pairs due to an attractive long-range contribution to the nucleon-nucleon interaction. Similar to the core superfluid, the crustal condensate exhibits macroscopic rotation by the formation of quantised vortices, which interact with their environment. The core mutual friction mechanisms, however, studied in the previous section, cannot be responsible for the coupling in the crust, as ${}^1S_0$ vortices do not possess a permanent magnetisation [204] or carry an entrained magnetic field, since the protons are normal and locked to the nuclei. Instead different mechanisms have to be considered. In the remainder of this section, three processes that could be present in the inner crust will be addressed and their strengths compared. As before, the characteristic drag and mutual friction coefficients are calculated for a specific equation of state in order to evaluate how the coupling strengths change throughout the star.

5.2.1 Crustal composition

Several theoretical approaches are available to study the equilibrium composition of the inner neutron star crust, ranging from classical liquid-drop models over semi-classical frameworks to those accounting for quantum effects. For a recent summary see Chamel and Haensel [30] and references therein. First to include quantum mechanics into crustal equation of state calculations were Negele and Vautherin [36]. As their work forms the foundation of the succeeding discussion, the underlying concept is briefly reviewed and the resulting equilibrium composition for five regions in the inner crust is presented.

Negele's and Vautherin's *recipe* to obtain the crustal ground state, i.e. its zero-temperature composition, is based on the use of the Wigner-Seitz approximation [34]. This implies that the inner crust is decomposed into identical spheres, which are each centred around one lattice site. The volume of a single Wigner-Seitz sphere is chosen to be equal to $1/n_{\rm N}$, where $n_{\rm N}$ is the density of lattice nuclei. Calculating the crustal structure, thus, reduces to determining the equilibrium configuration of a lattice nucleus and the free neutron gas inside the Wigner-Seitz cell. As discussed in Subsection 5.1.1, the quantity controlling the composition of a nuclear many-body system is the internal energy density. Similar to Equation (5.6), the inner crustal matter can be characterised by a nucleon, Coulomb and electron contribution to the energy density. Negele and Vautherin determine the former via two-body nucleon-nucleon interactions, providing them with the means to self-consistently derive the particle wave functions inside a unit cell for a given radius and number of nucleons; more precisely Z protons locked inside the nucleus and N neutrons, combining the ones inside the lattice structure and the surrounding gas. The resulting wave functions are connected to the number and kinetic energy densities of the protons and neutrons, respectively, which in turn enter the total energy density. The equilibrium composition for a given baryon density is then obtained by minimising the total energy density per nucleon under the constraint that Equations (5.1)-(5.3) are satisfied within a Wigner-Seitz sphere. Note that charge neutrality is ensured by assuming that each cell also contains Z electrons, which are approximated as a uniformly distributed relativistic Fermi gas.

Performing this procedure for various regions in the inner crust, Negele and Vautherin [36] obtain the ground-state composition given in Table 5.3. Besides Z and N, the table contains the number density of the free neutron gas, $n_{\rm G}$, and the approximate ratio of protons to neutrons, $\tilde{x}$, inside a nucleus. These parameters are related to the total mass density, $\rho \simeq m n_{\rm b}$, the total number of baryons inside a nucleus, i.e. $A \equiv Z(1 + 1/\tilde{x})$, and the radius of the Wigner Seitz sphere,

$$R_{\rm WS} \equiv \left(\frac{3}{4\pi} \frac{N+Z}{n_{\rm b}} \right)^{1/3} . \tag{5.70}$$

Since the volume of the unit cell is connected to the density of lattice sites, $n_{\rm N}$ can also be calculated. For a given crystal structure, this further allows the lattice constant, a, to be determined. For the bcc configuration, thought to be present in the inner crust, one has $a \equiv (2/n_{\rm N})^{1/3}$. The data in Table 5.3 given for Wigner-Seitz spheres at five different densities firstly illustrates that every unit cell comprises several hundred to a few thousand nucleons. Furthermore, for an increasing baryon density, the distance between the lattice sites decreases while the total baryon number, A, increases. However, due to the presence of quantum effects, the number of protons is roughly constant taking the values $Z = 32, 40, 50$. At the same time, more and more neutrons are dripping out of the nuclei leading to a density increase for the free neutron gas permeating the nuc-

	I	II	III	IV	V
n_b $[10^{-4}\,\mathrm{fm}^{-3}]$	8.8	57.7	204.0	475.0	789.0
Z	40	50	50	40	32
N	280	1050	1750	1460	950
$\tilde{x}$	0.53	0.45	0.35	0.28	0.16
n_G $[10^{-4}\,\mathrm{fm}^{-3}]$	4.8	47.0	184.0	436.0	737.0
ρ $[10^{12}\,\mathrm{g\,cm}^{-3}]$	1.5	9.6	33.9	78.9	131.0
A	115	161	193	183	232
R_WS [fm]	44.3	35.7	27.6	19.6	14.4
n_N $[10^{-6}\,\mathrm{fm}^{-3}]$	2.7	5.2	11.3	31.7	80.3
a [fm]	90.0	72.5	56.1	39.8	29.2

Table 5.3: Equilibrium composition for five regions in the inner neutron star crust. The values for the baryon density, n_b, the number of protons, Z, and neutrons, N, within a Wigner-Seitz sphere, the ratio of protons to neutrons, $\tilde{x}$, inside a nucleus and the number density of the free neutron gas, n_G, are taken from Negele and Vautherin [36]. Additionally, the total mass density, ρ, the total number of baryons inside a nucleus, A, the Wigner-Seitz radius, R_WS, the density of lattice sites, n_N, and the bcc lattice constant, a, are given.

lear structures. At a density of $\sim 10^{14}\,\mathrm{g\,cm}^{-3}$, the nuclear structures eventually disappear, marking the smooth transition to a uniform density gas.

Before proceeding, we point out that the Wigner-Seitz approximation has several limitations. Firstly, the nucleons are treated as independent particles, implying that the effects arising from pairing, i.e. superfluidity, are neglected. An attractive long-range interaction should, in principle, affect the bound and the free neutrons and could alter the composition of the lattice nuclei [36, 30]. Moreover, the theory does not provide access to the transport properties of the neutrons, as they are artificially restricted to the unit spheres. To account for the motion of particles across the cell boundaries, alternative approaches are needed. One possibility would be nuclear band theory, which has recently been used by Chamel [37] to show that the free neutron gas is influenced by entrainment with the lattice nuclei. While such modifications could have important implications for the macroscopic dynamics of neutron stars, they are neglected here. Finally, the model of Negele and Vautherin [36] does not take the formation of inhomogeneous nuclear structures, such as the nuclear pasta [41, 42], into consideration. This phase is expected to appear at $\sim 10^{14}\,\mathrm{g\,cm}^{-3}$ and should, thus, affect the composition in region (V). Despite these limitations, the results of Negele and Vautherin [36] are still widely used to describe the crustal equilibrium composition. In particular, calculations of the interaction strength between the superfluid component and the lattice [219, 220], needed in the following, are based on the parameters presented in Table 5.3.

5.2.2 Pinning characteristics

The frictional mechanisms discussed in the next subsection are sensitive to the coupling between the vortices and the crustal lattice, being influenced in particular by the size of the vortices, $\xi_{\rm n}$, and the *pinning energy*, $E_{\rm p}$. Note, however, that since comprehensive quantum calculations of the problem are not feasible, the pinning phenomenon is not fully understood and only approximate models are available. In the following, results from Donati and Pizzochero [219], which are summarised in Table 5.4, will be employed.[3] Based on the equilibrium composition of Negele and Vautherin [36], Donati and Pizzochero use a semi-classical model to characterise the vortex-nucleus interaction in the inner crust and obtain the pinning energy per pinning site. This quantity represents the energy gain or loss for positioning a single lattice nucleus inside a vortex and depends crucially on the competition between the internal, kinetic and condensation energy of the superfluid [221, 219]. Due to these competing energies, different pinning configurations are present at different densities. If E_p is positive, energy has to be provided to move a nucleus into the vortex, giving a repulsive vortex-nucleus interaction and weak *interstitial pinning*. Vortices positioning themselves at equal distances from the nuclei is observed in segments (I) and (II) of the inner crust. In regions (III)-(V) on the other hand, the pinning energies are positive, implying an attractive vortex-nucleus interaction and *nuclear pinning*, which makes it energetically favourable for vortices to move towards the lattice structures. Note also that at very high densities close to the crust-core boundary, for (IV) and (V), the coherence length exceeds the radius of a Wigner-Seitz sphere. This suggests that each vortex contains several nuclei, sometimes also referred to as *collective pinning*, which is also of a rather weak nature.

Estimates for the pinning energy per nucleus given in Table 5.4 are generally in agreement with post-glitch relaxation timescales [89, 90]. However, E_p was determined from microscopic considerations, which in principle do not allow one to draw conclusions about the mesoscopic pinning characteristics of a vortex. In order to better understand the macroscopic dynamics of the crustal superfluid, such as its role in the generation of glitches or the strength of the mutual friction, the pinning energy per unit length of a vortex needs to be known (see Subsection 4.3.3). As a mesoscopic vortex is exposed to many different lattice orientations [222, 220], the pinning energy per unit length can be obtained by averaging coherently over the lengthscale, where vortices are straight. Hence, the rigidity of the vortices, i.e. their ability to bend and adapt a pinning configuration, has strong influences on the dynamics [223]. Using a simple argument comparing the energy of an unpinned, straight vortex and a pinned, bent vortex, Seveso et al. [220]

[3] Note that Donati and Pizzochero [219] use a definition of the neutron coherence length that differs by a factor $\sqrt{6}/\pi$ from the one presented in Equation (3.73). Moreover, the set of parameters in Table 5.4 reflects the choice $\beta = 3$, which represents the reduction factor for the neutron pairing gap due to in-medium corrections, i.e. $\Delta_{\rm n} \equiv \Delta_{\rm n0}/\beta$, where $\Delta_{\rm n0}$ characterises the bare interaction. A suppression by $\beta = 3$ corresponds to a weaker pairing interaction giving a maximum for the mean pairing gap of about 1 MeV [220], which is similar to the singlet gap parametrisation discussed in Subsection 5.1.2.

	I	II	III	IV	V
ξ_n [fm]	20.0	13.0	15.4	33.5	116.4
E_p [MeV]	0.21	0.29	−2.74	−0.72	−0.02
c_s [10^8 cm s^{-1}]	4.73	5.57	5.78	5.64	4.68

Table 5.4: Neutron coherence lengths, ξ_n, and microscopic pinning energies, E_p, for five regions in the inner crust. $E_p > 0$ corresponds to interstitial pinning, while $E_p < 0$ marks the nuclear pinning regions. The values are taken from Donati and Pizzochero [219]. The final row gives estimates for the lattice phonon velocity, c_s, defined in Equation (5.73).

estimate this lengthscale to be of the order of $\sim 10^3$ Wigner-Seitz radii (see also Grill and Pizzochero [224]). Averaging the pinning interaction between vortices and randomly orientated nuclear structures over this, somewhat arbitrary, distance leads to a decrease in the mesoscopic pinning energy by up to two orders of magnitude compared to the microscopic pinning energy. This change, despite being poorly constrained, also affects the strength of the coupling mechanisms discussed below [92] and will be accounted for by including the *reduction factor*, δ, which is of the order $\sim 10^{-4}$ [225].

5.2.3 Coupling physics

Three different mechanisms coupling the superfluid neutron component and the crustal lattice in the inner crust of a neutron star are examined in the following. More precisely, mutual friction that results from the interaction between vortices and the nuclear structures leading to the excitation of lattice phonons or the excitations of Kelvin waves along the vortex axis is discussed. Moreover, the scattering of electrons off thermally excited quasi-particles is addressed. As shown below, each mechanism dominates under certain conditions generating drag forces of varying strengths.

Note that these three examples only form a selection of possible dissipative processes in the neutron star crust and additional mechanisms could be present [225, 226]. In particular, interactions between the normal vortex-core neutrons and phonons via higher-order scattering events, lattice defects or impurities could play a role. According to Harding et al. [226], the latter might dominate the coupling even for low impurity rates. However, accurate calculation of the corresponding mutual friction would require more detailed knowledge of the crustal composition than provided in Subsection 5.2.1. We, therefore, restrict ourselves to the three mechanisms mentioned above.

Mechanism I: phonon contribution

The motion of a superfluid vortex past the crustal lattice is expected to cause two types of mutual friction. At low relative velocities, i.e. $|\Delta\mathbf{v}| \equiv |\mathbf{v}_{LN} - \mathbf{u}_n| \leq 10^2\,\mathrm{cm\,s^{-1}}$ [92], where $\mathbf{v}_{LN}$ and $\mathbf{u}_n$ represent the velocity of a lattice nucleus and a vortex, respectively, the dominant effect of the interaction between the two components is the displacement

of the lattice structures, which results in the excitations of sounds waves. Jones [222] (see also Jones [225]) addresses the dissipation generated by this process. Analogous to the mesoscopic drag acting on a core vortex, which was defined in Equation (4.81), Jones postulates that the straight vortex segments present in the inner crust experience a resistive force per unit length of the form

$$\mathbf{f}_{\rm phonon} = \gamma_{\rm phonon}\,(\mathbf{v}_{\rm LN} - \mathbf{u}_{\rm n}) = \rho_{\rm G}\kappa\mathcal{R}_{\rm phonon}\,(\mathbf{v}_{\rm LN} - \mathbf{u}_{\rm n}), \tag{5.71}$$

where $\rho_{\rm G} \equiv m n_{\rm G}$ is the mass density of the free superfluid neutron gas. Using a quantum mechanical approach to characterise the interaction, Jones [222, 225] subsequently calculates the energy transfer, $\mathcal{E}$, between the vortex and the electron-phonon system of the nuclei. The magnitude of the corresponding resistive force per unit length is then approximately given by $|\mathbf{f}_{\rm phonon}| \approx \mathcal{E}/a^2$, where a is the bcc lattice constant. Working in the rest frame of the nuclear lattice, i.e. $\mathbf{v}_{\rm LN} = 0$, $\mathcal{E}$ is proportional to $|\mathbf{u}_{\rm n}|$. This allows a comparison with Equation (5.71) and leads to the following drag coefficient

$$\gamma_{\rm phonon} = \frac{3}{32\pi^{1/2}}\,\frac{a}{\xi_{\rm n}^3}\,\frac{E_{\rm p}^2}{M c_{\rm s}^3}. \tag{5.72}$$

The parameters a, $\xi_{\rm n}$ and $E_{\rm p}$ have been defined above, while $M \equiv mA$ represents the total mass of a single lattice nucleus and $c_{\rm s}$ is the lattice phonon velocity,

$$c_{\rm s} = \frac{\omega_{\rm Z}}{q_{\rm D}} = \left(\frac{4\pi n_{\rm N} Z^2 e^2}{M}\right)^{1/2} \left(6\pi^2 n_{\rm N}\right)^{-1/3}, \tag{5.73}$$

defined as the ratio of the ion plasma frequency, $\omega_{\rm Z}$, and the Debye wave number, $q_{\rm D}$. Numerical estimates for the phonon velocity can be found in Table 5.4.

With the help of Equation (5.71), the drag coefficient, $\gamma_{\rm phonon}$, can be expressed in dimensionless form. For the five regions of the inner crust discussed in Subsection 5.2.1, one obtains $\mathcal{R}_{\rm p} \ll 1$, so that the weak mutual friction limit (5.67) applies. Hence, the mutual friction coefficients associated with the excitation of sound waves read as

$$\mathcal{B}_{\rm phonon} \simeq \mathcal{R}_{\rm phonon} = \frac{\gamma_{\rm phonon}}{\kappa\rho_{\rm G}}, \qquad \mathcal{B}'_{\rm phonon} \simeq \mathcal{B}^2_{\rm phonon}. \tag{5.74}$$

One also has to account for the reduction factor, δ, arising from averaging the pinning interactions over a mesoscopic vortex length. Substituting fiducial parameters, one finds

$$\begin{aligned}\mathcal{B}_{\rm phonon} \approx 1.5\times10^{-8} &\left(\frac{10^{-2}\,{\rm fm}^{-3}}{n_{\rm G}}\right)\left(\frac{a}{60\,{\rm fm}}\right)\left(\frac{15\,{\rm fm}}{\xi_{\rm n}}\right)^3 \\ &\times\left(\frac{|E_{\rm p}|}{1\,{\rm MeV}}\right)^2\left(\frac{180}{A}\right)\left(\frac{5.5\times10^8\,{\rm cm\,s^{-1}}}{c_{\rm s}}\right)^3\left(\frac{\delta}{10^{-4}}\right).\end{aligned} \tag{5.75}$$

Detailed results for the drag and mutual friction coefficients in the crustal layers are shown in Table 5.5. Note that the vortex-lattice coupling via the excitations of phonons

	I	II	III	IV	V
$\gamma_{\rm phonon}$ $[10^5\,{\rm g\,cm^{-1}\,s^{-1}}]$	3.33	8.17	252.64	1.37	0.00
$\mathcal{B}_{\rm phonon}$ $[10^{-5}]$	20.93	5.24	41.44	0.09	0.00
with δ: $\mathcal{B}_{\rm phonon}$ $[10^{-9}]$	20.93	5.24	41.44	0.09	0.00
$\tau_{\rm phonon}$ $[10^5\,{\rm s}]$	0.38	1.52	0.19	83.97	7.62×10^6

Table 5.5: Drag and mutual friction coefficients and the corresponding post-glitch relaxation timescale for the weak vortex-phonon interaction for five regions in the inner crust. The values are calculated for the equilibrium composition obtained by Negele and Vautherin [36] and the superfluid parameters given by Donati and Pizzochero [219]. $\tau_{\rm phonon}$ includes the reduction factor, δ, and is determined for a rotation period of 10 ms.

is strongest in segments (I)-(III) and decreases towards the crust-core boundary. Neglecting region (V), where $\mathcal{B}_{\rm phonon}$ is several orders of magnitude smaller than in the other layers, the mutual friction strength ranges between $10^{-10} \lesssim \mathcal{B}_{\rm phonon} \lesssim 10^{-8}$. Haskell et al. [92] used the same estimate to develop a better hydrodynamical glitch model.

Jones [222] further suggests that this weak coupling mechanism could explain the observations of long post-glitch relaxation timescales. Using a simple two-component framework as illustrated in Figure 2.7, the recoupling of crustal vortices, which are unpinned by some mechanism once a critical lag is reached, and the rest of the star can be modelled. This relaxation process depends on the strength of the mutual friction and is characterised by the timescale

$$\tau_{\rm phonon} = \frac{1}{2\mathcal{B}_{\rm phonon}\Omega} \approx 8.0 \times 10^5 P_{10} \left(\frac{10^{-9}}{\mathcal{B}_{\rm phonon}}\right) {\rm s}, \tag{5.76}$$

where a canonical pulsar rotation period of 10 ms was chosen. Numerical estimates for the five crustal zones are given in Table 5.5. For (I)-(III), $\tau_{\rm phonon}$ is of the order of days, whereas for regions (IV) and (V) the relaxation timescale is of the order of months and years, respectively. Provided the relative velocity between the vortices and the crustal lattice is small, the dissipative force due to the excitation of phonons could thus indeed explain the observed pulsar relaxation timescales.

Mechanism II: kelvon contribution

A second type of mutual friction generated by the vortex motion past the nuclear lattice is expected to be present for $|\Delta\mathbf{v}| \geq 10^2\,{\rm cm\,s^{-1}}$. In contrast to the low-velocity dynamics causing vibrations in the crustal lattice, large relative velocities predominantly affect the vortices. Due to the lattice interactions, a moving vortex starts to oscillate exciting *Kelvin waves* along its axis and destroying its rigidity. Named after the discoverer Lord Kelvin [175], the corresponding quasi-particles are sometimes referred to as *kelvons*. The associated dissipation has been studied by Epstein and Baym [227] and Jones [225]. While the former approach considers the loss of energy due to the excitation of

	I	II	III	IV	V
R_N [fm]	6.0	6.7	7.3	6.7	5.2
E_s [MeV]	4.2	−1.3	−16.4	−10.0	−7.8
E_l [MeV]	0.16	0.94	1.40	1.00	0.49

Table 5.6: Values for the radius of the lattice nuclei, R_N and the short- and long-range contributions to the vortex-nucleus interaction, E_s and E_l, respectively, for five regions in the inner crust. While R_N parameters are taken from Donati and Pizzochero [219], energy estimates can be found in Epstein and Baym [227]. In order to account for uncertainties in the short-range term, the value $E_\mathrm{s,red} \equiv E_\mathrm{s}/10$ is also considered below.

unperturbed Kelvin modes along the vortices, the latter includes mode perturbations arising from the disorder of the pinning interaction. As this mechanism is rather poorly understood and both theoretical treatments involve various approximations, the mutual friction coefficients resulting from both calculations will be given below.

Following earlier work on the pinning interaction between a displaced vortex and a nucleus [228], Epstein and Baym [227] determine the dissipation proportional to a small vortex displacement, effectively caused by the transformation of free energy from the relative motion of the two components into the vortex excitation. Using a first-order perturbative approach, the net number of kelvons, Δn_k, of wave number k, excited in the vortex as it moves past a nucleus, can be calculated. The total energy transferred to a vortex segment of length L during each nucleus encounter is, thus, given by

$$E_\mathrm{kelvon}(b) = \sum_k \hbar\omega_\mathrm{k}\Delta n_\mathrm{k}(b), \tag{5.77}$$

where b is the vortex-nucleus impact parameter and $\omega_\mathrm{k} \equiv \hbar k^2/(2m_\mathrm{k})$ the frequency of a kelvon. Its mass, m_k, can be estimated by considering the dispersion relation [175, 222],

$$\omega_\mathrm{k}(k) = -\frac{\kappa}{4\pi}k^2\ln(k\xi_\mathrm{n}). \tag{5.78}$$

According to Epstein and Baym [227], the logarithm is well approximated by $-\ln(k\xi_\mathrm{n}) \simeq 3$, leading to a kelvon mass of $m_\mathrm{k} \equiv 2m/3$. Considering the continuum limit of infinitely long vortices, $L \to \infty$, the summation in Equation (5.77) is replaced by a k-integral

$$E_\mathrm{kelvon}(b) = \frac{\hbar}{4\pi\kappa\rho_\mathrm{G}m_\mathrm{k}}\int_{-\infty}^{\infty}|\tilde{f}(k,b)|^2\,k^2\,\mathrm{d}k. \tag{5.79}$$

Here, $\tilde{f}(k,b)$ denotes the Fourier transform of the force per unit length that acts on the vortex due to the interaction with the nuclear lattice. According to Epstein and Baym (see Appendix B of [227] for more details), the transform reads as

$$\tilde{f}(k,b) = \int_{-\infty}^{\infty}\frac{\tau+i\tau_b}{\Delta v}\left[\frac{4\sqrt{2}E_\mathrm{s}}{(1+\tau^2+\tau_b^2)^5}+\frac{\sqrt{2}E_\mathrm{l}}{(1+\tau^2+\tau_b^2)^2}\right]\mathrm{e}^{i\frac{R_\mathrm{N}\omega_\mathrm{k}}{\Delta v}\tau}\mathrm{d}\tau, \tag{5.80}$$

with $\Delta v \equiv |\Delta \mathbf{v}|$ representing the magnitude of the relative velocity between a vortex and a nucleus and we define

$$\tau \equiv \frac{t\Delta v}{R_{\rm N}}, \qquad\qquad \tau_b \equiv \frac{b}{R_{\rm N}}, \tag{5.81}$$

where t is the time and $R_{\rm N}$ represents the typical, density-dependent size of the lattice nuclei. Furthermore, the energies $E_{\rm s}$ and $E_{\rm l}$ in Equation (5.80) denote the short-range and long-range contributions to the vortex-nucleus interaction, respectively. Numerical estimates for $R_{\rm N}$, $E_{\rm s}$ and $E_{\rm l}$ are shown in Table 5.6. Note that as estimates for $E_{\rm s}$ are rather uncertain due to the lack of detailed microscopic models [227], the strength of the frictional drag will also be calculated for a reduced value, i.e. $E_{\rm s,red} \equiv E_{\rm s}/10$.

Integration of Equation (5.80) yields[4]

$$\tilde{f}(k,b) = \frac{i\pi}{\sqrt{2}\Delta v}\, \mathrm{e}^{-K^2 T_b} \left[\frac{E_{\rm l}}{T_b^3} \left\{ \tau_b + K^2 T_b \left(T_b + \tau_b \right) \right\} + \frac{E_{\rm s}}{48 T_b^9} \left\{ 15 K^2 T_b \left(T_b + 7\tau_b \right) \right.\right.$$
$$\left.\left. + 15 K^4 T_b^2 \left(T_b + 3\tau_b \right) + 2K^6 T_b^3 \left(3T_b + 5\tau_b \right) + K^8 T_b^4 \left(T_b + \tau_b \right) + 105 \tau_b \right\} \right], \tag{5.82}$$

where the following parameters are defined to write the expression in a compact form

$$K \equiv \sqrt{\frac{k^2 \hbar R_{\rm N}}{2 m_{\rm k} \Delta v}}, \qquad\qquad T_b \equiv \sqrt{1 + \tau_b^2}. \tag{5.83}$$

Having determined the energy transfer per vortex-nucleus interaction, the corresponding power, $p_{\rm kelvon}$, dissipated per unit length of vortex due to the coupling with nuclei of number density, $n_{\rm N}$, can be obtained by integrating $E_{\rm kelvon}$ over the impact parameter. Multiplying the result with $n_{\rm N}$ and Δv gives

$$p_{\rm kelvon} = n_{\rm N} \Delta v \int_{-\infty}^{\infty} E_{\rm kelvon}(b)\, \mathrm{d}b. \tag{5.84}$$

Combining this with Equations (5.79) and (5.82) leads to the simplified expression

$$p_{\rm kelvon} = \kappa \rho_{\rm G} \left(\Delta v \right)^{1/2} v_*^{3/2}, \tag{5.85}$$

where the characteristic velocity of the vortex dynamics is given by[5]

$$v_* \equiv 1.24 \left(0.49 E_{\rm l}^2 + 0.98 E_{\rm l} E_{\rm s} + E_{\rm s}^2 \right)^{2/3} \left(\frac{m_{\rm k}}{\hbar \kappa^4} \frac{n_{\rm N}^2}{R_{\rm N} \rho_{\rm G}^4} \right)^{1/3}. \tag{5.86}$$

[4]Note that the integrated Fourier transform (5.82) does not agree with the relation given in Epstein and Baym [227]. Their result, presented in Equation (B14), misses an overall factor $1/\sqrt{2}$ and the term K^4. The following calculation will be based on Equation (5.82).

[5]Definition (5.86) disagrees with the result quoted by Epstein and Baym in Equation (3.17) [227]. Different coefficients in the interaction energy term give velocities about an order of magnitude larger than the estimate in Equation (5.87). Note that expression (5.86) will be used in the following.

For fiducial parameters, one can estimate

$$v_* \approx 2.1 \times 10^6 \left(\frac{n_\mathrm{N}}{10^{-5}\,\mathrm{fm}^{-3}}\right)^{2/3} \left(\frac{7\,\mathrm{fm}}{R_\mathrm{N}}\right)^{1/3} \left(\frac{10^{-2}\,\mathrm{fm}^{-3}}{n_\mathrm{G}}\right)^{4/3} \mathrm{cm\,s^{-1}}, \tag{5.87}$$

where the two energy contributions are fixed to $E_\mathrm{s} = 1\,\mathrm{MeV}$ and $E_\mathrm{l} = 1\,\mathrm{MeV}$ (see Table 5.6). Specific values of v_* for the five regions in the inner crust are shown in Table 5.7.

Moreover, the power defined in Equation (5.85) has to be equivalent to the product of the mesoscopic drag, f_kelvon, and the relative velocity, i.e. $p_\mathrm{kelvon} = f_\mathrm{kelvon}\Delta v$. Using a similar ansatz for the resistive force per unit length as given in Equation (5.71), one can determine the drag coefficient resulting from the excitation of Kelvin waves,

$$\gamma_\mathrm{kelvon} = \frac{p_\mathrm{kelvon}}{\Delta v^2} = \kappa\rho_\mathrm{G} \left(\frac{v_*}{\Delta v}\right)^{3/2}. \tag{5.88}$$

Writing this in dimensionless form gives

$$\mathcal{R}_\mathrm{kelvon} = \left(\frac{v_*}{\Delta v}\right)^{3/2}. \tag{5.89}$$

This clearly illustrates that the strength of the frictional coupling crucially depends on the relative velocity between the lattice nuclei and the vortices. While the magnitude of this velocity difference is theoretically not well constrained, the body-averaged glitch model provides the means to obtain an estimate. The two-component framework, illustrated in Figure 2.7, is based on the assumption that vortices are pinned to the nuclei, therefore, impeding the spin-down of the crustal superfluid. Once a critical lag between the superfluid and the lattice is reached, the Magnus force generated by the neutron flow past the vortices overcomes the pinning force and causes the unpinning of a large number of vortices. In the absence of strong drag forces, the Magnus force further couples the free vortices and the neutrons, bringing the two components into corotation [222]. Hence, the vortex-nucleus velocity difference can be approximated by the velocity lag, Δv_SN, between the superfluid and the crust. By considering the averaged glitch dynamics, a lower bound can be calculated from $\Delta v \simeq \Delta v_\mathrm{SN} \gtrsim |\dot{\Omega}| t_\mathrm{glitch} R$ [229], with $|\dot{\Omega}|$ denoting the pulsar spin-down rate, t_glitch the waiting time between two glitches and R the neutron star radius. Using a canonical neutron star radius of 10 km and, in particular, observational data from the Vela pulsar, where sudden spin-ups are observed at an interval $t_\mathrm{glitch} \approx 2\,\mathrm{yr}$ [87, 80] and $|\dot{\Omega}| \approx 10^{-10}\,\mathrm{s^{-2}}$ [82], one obtains

$$\Delta v \approx 6.3 \times 10^4\,\mathrm{cm\,s^{-1}}. \tag{5.90}$$

Lacking better understanding, this estimate will be used to determine the characteristic coupling coefficients. Note that as $v_* \gg \Delta v$, we in principle have $\mathcal{R}_\mathrm{kelvon} \gg 1$, which implies that the weak mutual friction limit no longer applies (see Table 5.7). However, as explained previously, the pinning interaction on macroscopic scales is significantly

$E_{\rm s}$	I	II	III	IV	V
v_* $[10^7\,{\rm cm\,s^{-1}}]$	20.58	0.20	2.18	0.72	0.53
$\gamma_{\rm kelvon}$ $[10^{13}\,{\rm g\,cm^{-1}\,s^{-1}}]$	29.68	0.28	39.12	17.65	18.97
$\mathcal{R}_{\rm kelvon}$ $[10^4]$	18.67	0.02	0.64	0.12	0.08
$\mathcal{B}_{\rm kelvon}$ $[10^{-4}]$	0.05	56.43	1.56	8.18	12.87
$\mathcal{B}'_{\rm kelvon}$	1.00	1.00	1.00	1.00	1.00
with δ: $\mathcal{B}_{\rm kelvon}$ $[10^{-2}]$	5.34	1.77	45.46	12.04	7.72
with δ: $\mathcal{B}'_{\rm kelvon}$ $[10^{-2}]$	99.71	0.03	29.17	1.47	0.60
$E_{\rm s,red}$	I	II	III	IV	V
v_* $[10^6\,{\rm cm\,s^{-1}}]$	11.91	1.00	0.69	0.23	0.18
$\gamma_{\rm kelvon}$ $[10^{11}\,{\rm g\,cm^{-1}\,s^{-1}}]$	41.34	9.90	22.06	9.89	11.63
$\mathcal{R}_{\rm kelvon}$ $[10^2]$	26.00	0.64	0.36	0.07	0.05
$\mathcal{B}_{\rm kelvon}$ $[10^{-2}]$	0.04	1.57	2.76	14.30	20.11
$\mathcal{B}'_{\rm kelvon}$	1.00	1.00	1.00	0.98	0.96
with δ: $\mathcal{B}_{\rm kelvon}$ $[10^{-2}]$	24.35	0.64	0.36	0.07	0.05
with δ: $\mathcal{B}'_{\rm kelvon}$ $[10^{-3}]$	63.31	0.04	0.01	0.00	0.00

Table 5.7: Parameters of the vortex-lattice coupling caused by the excitation of Kelvin waves as calculated by Epstein and Baym [227] for five crustal regions. Estimates for the velocity, v_*, the drag coefficients, $\gamma_{\rm kelvon}$ and $\mathcal{R}_{\rm kelvon}$, and the mutual friction coefficients, $\mathcal{B}_{\rm kelvon}$ and $\mathcal{B}'_{\rm kelvon}$, are given. The top and bottom half of the table use $E_{\rm s}$ and $E_{\rm s,red}$, respectively, to account for uncertainties in the short-range term. For comparison, the mutual friction coefficients are calculated with and without the reduction factor, $\delta = 10^{-4}$.

reduced when an average over randomly orientated pinning sites is considered. While this reduction is not included in the discussion of Epstein and Baym [227], it will be accounted for in the following. Multiplying $\mathcal{R}_{\rm kelvon}$ with the factor δ, the dimensionless mutual friction coefficients associated with the excitations of vortex Kelvin waves are

$$\mathcal{B}_{\rm kelvon} = \frac{\delta(v_*\Delta v)^{3/2}}{(\Delta v)^3 + \delta^2 v_*^3}, \qquad \mathcal{B}'_{\rm kelvon} = \frac{\delta^2 v_*^3}{(\Delta v)^3 + \delta^2 v_*^3}. \tag{5.91}$$

Estimates calculated with $\delta = 10^{-4}$ and without it are presented in Table 5.7. Neglecting the reduction, we can observe that for both choices of the short-range energy, $E_{\rm s}$ and $E_{\rm s,red}$, the mutual friction coefficients satisfy $\mathcal{B}_{\rm kelvon} \ll 1$ and $\mathcal{B}'_{\rm kelvon} \approx 1$, respectively, which is generally attributed to the strong coupling limit. Accounting for the reduction factor, the following cases can be distinguished: Using $E_{\rm s}$, the coefficients range between $10^{-2} \lesssim \mathcal{B}_{\rm kelvon} \lesssim 1$ and $10^{-4} \lesssim \mathcal{B}'_{\rm kelvon} \lesssim 1$, whereas the reduced energy $E_{\rm s,red}$ reproduces the weak coupling limit with $10^{-4} \lesssim \mathcal{B}_{\rm kelvon} \lesssim 10^{-1}$ and $\mathcal{B}'_{\rm kelvon} \simeq \mathcal{B}^2_{\rm kelvon}$.

The second approach to study inner crustal dissipation due to the excitation of Kelvin waves along a vortex was developed by Jones [225], using a similar approach as discussed above for the vortex-phonon mutual friction. While for large relative vortex-nucleus velocities the lattice phonon excitations are suppressed, the net production of

	I	II	III	IV	V
$\gamma_{\rm kelvon}$ $[10^{12}\,{\rm g\,cm^{-1}\,s^{-1}}]$	0.81	0.57	11.07	0.07	0.00
$\mathcal{R}_{\rm kelvon}$ [10]	50.84	3.68	18.16	0.05	0.00
$\mathcal{B}_{\rm kelvon}$ $[10^{-2}]$	0.20	2.71	0.55	37.46	0.00
$\mathcal{B}'_{\rm kelvon}$	1.00	1.00	1.00	0.17	0.00
with δ: $\mathcal{B}_{\rm kelvon}$ $[10^{-3}]$	50.71	3.68	18.15	0.05	0.00
with δ: $\mathcal{B}'_{\rm kelvon}$ $[10^{-4}]$	25.78	0.14	3.30	0.00	0.00
$\tau_{\rm kelvon}$ [s]	0.02	0.22	0.04	17.66	1.08×10^6

Table 5.8: Drag, mutual friction coefficients and corresponding coupling timescales for the strong drag caused by the excitations of Kelvin waves for five regions in the crust. The values are calculated according to Jones [225] for the equilibrium composition of Negele and Vautherin [36] and the superfluid parameters of Donati and Pizzochero [219]. $\tau_{\rm kelvon}$ includes the reduction factor, $\delta = 10^{-4}$, and is determined for a rotation period of 10 ms.

kelvons strongly contributes to the dissipation of energy. Calculating the energy transfer and the corresponding resistive force, Jones again considers a mesoscopic drag of the form (5.71) to deduce the drag coefficient for the lattice-kelvon coupling, i.e.

$$\gamma_{\rm kelvon} = \frac{E_{\rm p}^2}{2\kappa\rho_{\rm G} a \xi_{\rm n}^2}\left[\frac{1}{2\pi\xi_{\rm n} c_{\rm k} (\Delta v)^3}\right]^{1/2}. \tag{5.92}$$

Estimates for the lattice constant, a, the coherence length, $\xi_{\rm n}$, and the pinning energy, $E_{\rm p}$, were given in Tables 5.3 and 5.4, respectively. The parameter $c_{\rm k}$ is related to the kelvon frequency, $\omega_{\rm k}$, via

$$c_{\rm k} = \frac{\omega_{\rm k}}{k^2} = \frac{3\kappa}{4\pi} \approx 4.8 \times 10^{-4}\,{\rm cm^2\,s^{-1}}. \tag{5.93}$$

The dimensionless drag coefficient is, thus, given by

$$\mathcal{R}_{\rm kelvon} = \frac{E_{\rm p}^2}{2\kappa^2\rho_{\rm G}^2 a \xi_{\rm n}^2}\left[\frac{1}{2\pi\xi_{\rm n} c_{\rm k} (\Delta v)^3}\right]^{1/2}. \tag{5.94}$$

Numerical estimates for the inner crust are shown in Table 5.8. Without the reduction δ, one obtains $\mathcal{R}_{\rm kelvon} \gg 1$ in the outer regions (I)-(III), thus, displaying strong mutual friction with $\mathcal{B}_{\rm kelvon} \ll 1$ and $\mathcal{B}'_{\rm kelvon} \approx 1$. At higher densities in the segments (IV) and (V), the vortex-lattice coupling is much weaker with $\mathcal{B}_{\rm kelvon}, \mathcal{B}'_{\rm kelvon} \ll 1$. Accounting for the disorder in the pinning interaction, the weak frictional limit, i.e. $\mathcal{B}_{\rm kelvon} \simeq \mathcal{R}_{\rm kelvon}$, applies everywhere in the inner crust. Canonical parameters lead to

$$\mathcal{B}_{\rm kelvon} \approx 8.2 \times 10^{-3}\left(\frac{|E_{\rm p}|}{1\,{\rm MeV}}\right)^2\left(\frac{10^{-2}\,{\rm fm^{-3}}}{n_{\rm G}}\right)^2\left(\frac{60\,{\rm fm}}{a}\right)\left(\frac{15\,{\rm fm}}{\xi_{\rm n}}\right)^{5/2}\left(\frac{\delta}{10^{-4}}\right). \tag{5.95}$$

Ignoring the innermost crustal region, where the coupling parameters are much smaller

than in the outer layers, the frictional coefficient $\mathcal{B}_{\rm kelvon}$ ranges between 10^{-5} and 10^{-1}, whereas $\mathcal{B}'_{\rm kelvon} \simeq \mathcal{B}^2_{\rm kelvon}$. These estimates, similar to the ones calculated with Equation (5.91) for the reduced short-range interaction $E_{\rm s,red}$, are several orders of magnitude larger than the coupling strength resulting from the excitation of lattice phonons given in Equation (5.75). The corresponding relaxation timescale is thus much shorter with

$$\tau_{\rm kelvon} = \frac{1}{2\mathcal{B}_{\rm kelvon}\Omega} \approx 0.1 P_{10} \left(\frac{10^{-2}}{\mathcal{B}_{\rm kelvon}}\right) \text{s}. \tag{5.96}$$

The estimates for the equilibrium configuration of Negele and Vautherin [36] are given in Table 5.8. For the outermost layers (I)-(III) of the inner crust, the coupling timescale is of the order of milliseconds, increasing to seconds for segment (IV) finally reaching the order of days close to the crust-core boundary in (V). Due to these short coupling timescales between the superfluid and the lattice, the excitation of Kelvin waves cannot be responsible for the long post-glitch relaxation. However, this mechanism has been invoked as an explanation for the abrupt spin-up timescales of the neutrons star crust during glitches [227, 225, 92] observed to be shorter than 120 s [230].

Mechanism III: electron contribution

Finally, we address dissipation caused by the interaction between relativistic electrons and the *s*-wave paired superfluid in the crust. This mechanism, originally studied by Feibelman [217], is strongly dependent on the temperature and the superfluid parameters. Its contribution to the vortex drag is, therefore, suppressed well below the superfluid transition temperature, $T_{\rm c}$, but could contribute in the very early stages of neutron star evolution, where $T \simeq T_{\rm c}$. According to Feibelman, the dominant coupling mechanism, requiring the least amount of thermal energy, is the scattering of electrons off quasi-particles thermally excited in the neutron vortex cores. The corresponding relaxation timescale for an initial relative velocity between the electrons and a dilute vortex array can be determined by using a method similar to the one discussed in Subsection 5.1.3 for the electron-magnetic-vortex scattering [217]. Treating the vortices as isolated, the total relaxation rate is obtained by summing over all individual scattering events, captured in the kinetic Boltzmann equation (see also Equation (5.23)). This further involves the matrix transition element, M, dependent on the interaction Hamiltonian, which in the case of electron-quasi-particle scattering represents the magnetic-dipole coupling between the two components. Specifying the Hamiltonian and the particle wave functions, Feibelman subsequently solves the linearised kinetic equation and obtains the following approximation for the velocity relaxation timescale [217]

$$\tau_{\rm v} = \frac{16 g_1 g_2}{3\pi^3 g_{\rm n}^2} \frac{{\rm e}^{1/\sqrt{4\pi}}}{K_0(1/\sqrt{4\pi})} \frac{\hbar^2 c^2}{e^4} \frac{1}{\mathcal{N}_{\rm n}\xi_{\rm n}^2} \frac{E_{\rm FG}}{\Delta_{\rm n}} \left(\frac{E_{\rm Fe}}{E_{\rm FG}}\right)^2 \left(\frac{E_{\rm FG}}{2mc^2}\right)^{1/2} \frac{\hbar}{k_{\rm B}T} \exp\left[\frac{\pi g_2 \Delta_{\rm n}^2}{4k_{\rm B}T E_{\rm FG}}\right], \tag{5.97}$$

	I	II	III	IV	V
n_e $[10^{-4}\,\mathrm{fm}^{-3}]$	1.10	2.62	5.67	12.67	25.71
Δ_n [MeV]	0.21	0.68	0.91	0.55	0.19
$\log_{10}\tau_\mathrm{v}$ [s] at $T = 10^9\,\mathrm{K}$	1.87	1.83	1.50	0.96	0.42
$\log_{10}\tau_\mathrm{v}$ [s] at $T = 10^8\,\mathrm{K}$	4.11	5.77	4.59	2.40	1.46
$\log_{10}\tau_\mathrm{v}$ [s] at $T = 10^7\,\mathrm{K}$	17.52	36.14	26.52	7.82	2.83

Table 5.9: Electron density, superfluid energy gap and relaxation timescales caused by electron-quasi-particle scattering for five regions in the crust. The equilibrium composition of Negele and Vautherin [36] and the superfluid parameters of Donati and Pizzochero [219] are used. The coupling timescales are determined for a rotation period of 10 ms and three crustal temperatures, 10^9, 10^8 and 10^7 K, respectively.

where g_1 and g_2 are constants of order one, $g_\mathrm{n} \approx -3.826$ is the neutron g-factor, T the temperature of the crust and Δ_n the energy gap of the neutron superfluid. Moreover, $\mathcal{N}_\mathrm{n}$ represents the vortex surface density (see Equation (4.6)), ξ_n the neutron coherence length, E_Fe and E_FG the Fermi energies of the relativistic electron component and the non-relativistic free neutron gas, respectively. Substituting Equations (5.12) and (5.46) for the energies and using $g_1, g_2 = 1$, the relaxation timescale can be reduced to

$$\tau_\mathrm{v} \approx 6.3 \times 10^2 \, \frac{1}{\mathcal{N}_\mathrm{n}\xi_\mathrm{n}^2} \, \frac{\hbar c\, n_\mathrm{e}^{2/3}}{\Delta_\mathrm{n} n_\mathrm{G}^{1/3}} \, \frac{\hbar}{k_\mathrm{B}T} \exp\left[\frac{1}{2(9\pi)^{1/3}} \, \frac{m}{\hbar^2 n_\mathrm{G}^{2/3}} \, \frac{\Delta_\mathrm{n}^2}{k_\mathrm{B}T}\right]. \tag{5.98}$$

Considering the ground-state composition of Negele and Vautherin [36], each Wigner-Seitz cell is charge neutral and contains Z electrons, which are uniformly distributed. This implies that $n_\mathrm{e} = 3Z/(4\pi R_\mathrm{WS}^3)$ (see Table 5.9). Furthermore, the energy gap of the crustal superfluid can be obtained from the coherence length, ξ_n. The corresponding estimates, using the equations given by Donati and Pizzochero [219] to keep consistency, are shown in Table 5.9. These are slightly lower compared to the parametrised singlet gap model discussed in Subsection 5.1.2. For canonical values, we then find

$$\begin{aligned}\tau_\mathrm{v} \approx 6.7\, P_{10} &\left(\frac{15\,\mathrm{fm}}{\xi_\mathrm{n}}\right)^2 \left(\frac{n_\mathrm{e}}{10^{-4}\,\mathrm{fm}^{-3}}\right)^{2/3} \left(\frac{10^{-2}\,\mathrm{fm}^{-3}}{n_\mathrm{G}}\right)^{1/3} \left(\frac{1\,\mathrm{MeV}}{\Delta_\mathrm{n}}\right) \\ &\times \left(\frac{10^9\,\mathrm{K}}{T}\right) \exp\left[\left(\frac{\Delta_\mathrm{n}}{1\,\mathrm{MeV}}\right)^2 \left(\frac{10^9\,\mathrm{K}}{T}\right) \left(\frac{10^{-2}\,\mathrm{fm}^{-3}}{n_\mathrm{G}}\right)^{2/3}\right] \mathrm{s}. \end{aligned} \tag{5.99}$$

Due to the presence of the exponential factor, the resulting timescale is strongly dependent on the temperature and the neutron gap. Note that for our choice of parameters, the exponent is approximately one, giving $\tau_\mathrm{v} \approx 18\,\mathrm{s}$. Results for a range of temperatures are illustrated in Table 5.9 for the five segments of the inner crust. The minimum relaxation timescale, observed in region (V), changes from the order of seconds at 10^9 K close to the superfluid transition temperature to the order of minutes at 10^8 K reaching hours at 10^7 K. At the same time, τ_v increases significantly towards lower densities with

$T = 10^9\,\mathrm{K}$	I	II	III	IV	V
$\log_{10}\gamma_{\mathrm{electron}}\ [\mathrm{g\,cm^{-1}\,s^{-1}}]$	3.59	4.00	4.68	5.57	6.41
$\log_{10}\mathcal{R}_{\mathrm{electron}}, \mathcal{B}_{\mathrm{electron}}$	−5.61	−6.19	−6.11	−5.59	−4.98
$T = 10^8\,\mathrm{K}$	I	II	III	IV	V
$\log_{10}\gamma_{\mathrm{electron}}\ [\mathrm{g\,cm^{-1}\,s^{-1}}]$	1.35	0.07	1.59	4.12	5.37
$\log_{10}\mathcal{R}_{\mathrm{electron}}, \mathcal{B}_{\mathrm{electron}}$	−7.85	−10.12	−9.20	−7.04	−6.02
$T = 10^7\,\mathrm{K}$	I	II	III	IV	V
$\log_{10}\gamma_{\mathrm{electron}}\ [\mathrm{g\,cm^{-1}\,s^{-1}}]$	−12.06	−30.30	−20.34	−1.30	4.00
$\log_{10}\mathcal{R}_{\mathrm{electron}}, \mathcal{B}_{\mathrm{electron}}$	−21.26	−40.50	−31.13	−12.46	−7.38

Table 5.10: Drag and mutual friction coefficients resulting from the scattering of electrons off thermally excited neutron quasi-particles for five regions in the crust. The values are calculated according to Feibelman [217] for the equilibrium composition of Negele and Vautherin [36], the superfluid parameters of Donati and Pizzochero [219] and a rotation period of 10 ms. Estimates are given for three temperatures, 10^9, 10^8 and 10^7 K, respectively. Moreover, $\mathcal{B}_{\mathrm{electron}} \simeq \mathcal{R}_{\mathrm{electron}}$ due to the weak mutual friction limit.

maximum coupling timescales of the order of minutes, hours and 10^{28} yr for 10^9, 10^8 and 10^7 K, respectively, in region (II). These estimates indicate that in early stages of neutron star evolution, the scattering of electrons of thermally excited quasi-particles could contribute to the drag acting on vortices and possibly be invoked as an explanation for the long post-glitch relaxation timescales of very young pulsars. However, far below the critical transition temperature, this mechanism will be strongly suppressed and, therefore, unimportant for the coupling of the superfluid and the crustal lattice.

Following an initial relative velocity, the timescale τ_{v} dictates how quickly the neutron vortex motion relaxes to the electron fluid, which is ultimately coupled to the neutron star crust via electromagnetic processes. However, different to the discussion of the core mutual friction (see Subsection 5.1.3), the charged particles in the crust are not moving as a single component on large scales, as the protons are locked inside the lattice nuclei. This is equivalent to the statement that the charge current in the crust is non-zero, generally playing an important role for the magnetic field evolution of the star [231, 232, 233]. Hence, we do not have to account for any increase in the moment of inertia. On hydrodynamic scales, vortices experience a frictional force of the form

$$\mathbf{F}_{\mathrm{d}} = \frac{\rho_{\mathrm{e}}}{\tau_{\mathrm{v}}}\,(\mathbf{v}_{\mathrm{e}} - \mathbf{u}_{\mathrm{n}}), \tag{5.100}$$

where $\mathbf{v}_{\mathrm{e}}$ and $\mathbf{u}_{\mathrm{n}}$ are the averaged velocity of the electron component and the vortices, respectively. As discussed before, this force is equivalent to the macroscopic drag obtained by averaging the resistive force, $\mathbf{f}_{\mathrm{d}}$, exerted on a single vortex, which gives for the drag coefficient and its dimensionless equivalent

$$\gamma_{\mathrm{electron}} = \frac{\rho_{\mathrm{e}}}{\mathcal{N}_{\mathrm{n}}\tau_{\mathrm{v}}}, \qquad \mathcal{R}_{\mathrm{electron}} = \frac{\rho_{\mathrm{e}}}{\rho_{\mathrm{G}}}\,\frac{1}{\mathcal{N}_{\mathrm{n}}\kappa}\,\frac{1}{\tau_{\mathrm{v}}}. \tag{5.101}$$

Estimates for the two quantities can be found in Table 5.10 for three different values of T. For all temperatures and crustal segments, one finds $\mathcal{R}_{\text{electron}} \ll 1$, which implies that the weak mutual friction limit applies, so that $\mathcal{B}_{\text{electron}} \simeq \mathcal{R}_{\text{electron}}$ and $\mathcal{B}'_{\text{electron}} \simeq \mathcal{B}^2_{\text{electron}}$. Substituting canonical parameters leads to the following estimate

$$\mathcal{B}_{\text{electron}} \approx 6.4 \times 10^{-10} \left(\frac{\xi_{\text{n}}}{15\,\text{fm}}\right)^2 \left(\frac{n_{\text{e}}}{10^{-4}\,\text{fm}^{-3}}\right)^{1/3} \left(\frac{10^{-2}\,\text{fm}^{-3}}{n_{\text{G}}}\right)^{2/3} \left(\frac{\Delta_{\text{n}}}{1\,\text{MeV}}\right) \times \left(\frac{T}{10^9\,\text{K}}\right) \exp\left[-\left(\frac{\Delta_{\text{n}}}{1\,\text{MeV}}\right)^2 \left(\frac{10^9\,\text{K}}{T}\right) \left(\frac{10^{-2}\,\text{fm}^{-3}}{n_{\text{G}}}\right)^{2/3}\right]. \tag{5.102}$$

This is much weaker than the phonon and kelvon mutual friction mechanisms discussed previously as soon as the neutron star temperature falls below $T \leq 10^7\,\text{K}$.

5.2.4 Crustal cross-section

In the preceding subsections, three mutual friction mechanisms coupling the superfluid and the normal component in the neutron star crust have been addressed. Interpolating the results given in Tables 5.5, 5.7, 5.8 and 5.10 for the five ground-state segments, a profile for the frictional coefficients within the inner crust can be obtained. This is shown in Figure 5.10, where the reduction factor δ arising from the randomly orientated vortex-nucleus interaction is accounted for in the phonon and kelvon parameters. We keep in mind that each process dominates under specific conditions: whereas electron-quasi-particle scattering could contribute significantly to the resistive vortex drag in superfluid neutron stars close to the transition temperature, the other two mechanisms are temperature-independent. If the relative velocity between the vortices and the lattice nuclei is low, i.e. $\Delta v \leq 10^2\,\text{cm}\,\text{s}^{-1}$ [92], than the excitation of lattice phonons governs the coupling physics, while for higher velocities the excitation of vortex kelvin waves becomes important.

Figure 5.10 illustrates in detail that these mechanisms span a wide range of coupling strengths, in particular at higher densities close to the crust-core interface. Additionally, several parameters such as the pinning energy, the reduction factor or the relative vortex-lattice velocity that enter the various calculations are poorly constrained. These uncertainties and the wide parameter range make it difficult to assign a typical mutual friction coefficient to the crustal superfluid. In order to obtain the coupling strength entering the macroscopic momentum equations, one would in principle have to average the resistive drag over the length of a vortex. However, as this would require detailed knowledge of the crustal vortex distribution not available to date, a suitable averaging procedure is not possible at this point. Following instead a more naive approach, a reasonable choice would be $\mathcal{B}_{\text{strong}} \approx 10^{-2}$ for the stronger kelvon drag and $\mathcal{B}_{\text{weak}} \approx 10^{-8}$ for the two weaker dissipation processes, respectively, keeping in mind the various uncertainties associated with these mechanisms.

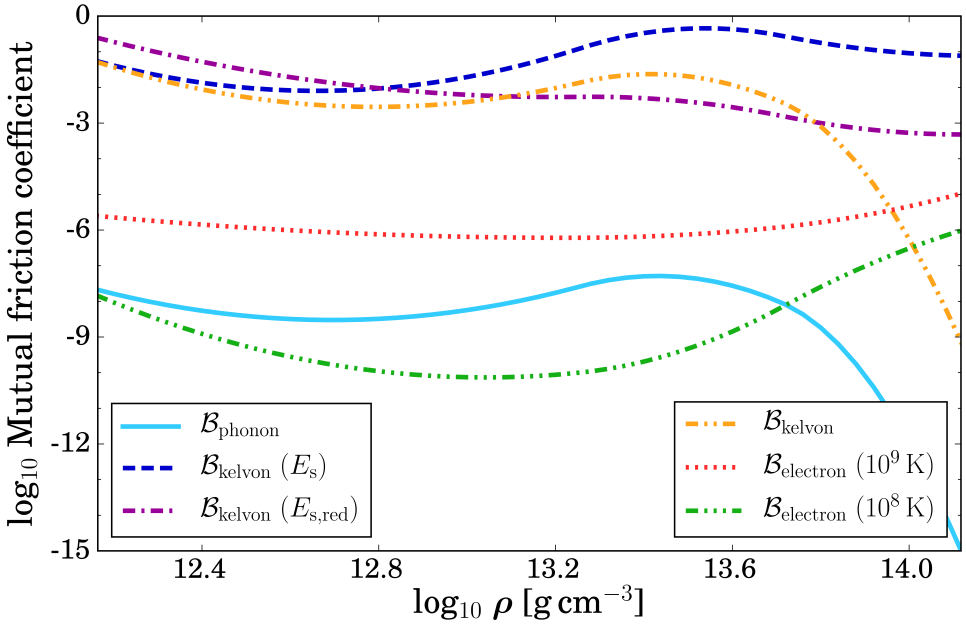

Figure 5.10: Mutual friction strength in the crust caused by three mechanisms. Shown are phonon coupling (cyan, solid) and kelvon contribution determined by Epstein and Baym [227] for two different short range interactions, i.e. E_{s} (blue, dashed) and $E_{\mathrm{s,red}}$ (purple, dot-dashed), and the kelvon drag given in Jones [225] (yellow, dot-dot-dashed). Moreover, the electron-quasi-particle scattering coupling for two temperatures, i.e. $T = 10^9\,\mathrm{K}$ (red, dotted) and $T = 10^8\,\mathrm{K}$ (green, dot-dot-dot-dashed), is included. The results are obtained by using a second-degree interpolating spline for the values presented in Tables 5.5, 5.7, 5.8 and 5.10, respectively. In calculating the fits, it is assumed that all quantities vary continuously in the inner crust and no jumps are present. The estimates are based on the crustal equation of state of Negele and Vautherin [36], the superfluid parameters of Donati and Pizzochero [219], a reduction factor of $\delta = 10^{-4}$ and a relative vortex-lattice velocity of $\Delta v = 6.3 \times 10^4\,\mathrm{cm\,s^{-1}}$.

5.3 Summary

The purpose of this chapter was to present new studies of macroscopic mutual friction mechanisms for the neutron star cross-section. These dissipative terms emerge in the hydrodynamical equations as a result of the interactions between quantised vortices, characteristic for a rotating condensate, and their surroundings. The coupling strengths are determined by the parameters $\mathcal{B}$ and $\mathcal{B}'$ that are dependent on the small-scale physics of the vortex interactions. Since these are different for the neutron star core and crust, mutual friction in the two layers was studied separately. For the core, scattering of electrons off the permanent vortex core magnetisation and the entrained magnetic field were compared and the latter was found to be more important. For the crust, dissipation caused by phonon and kelvon excitation and electron-quasi-particle scattering were addressed, with each mechanism dominating under certain conditions. Additionally, realistic equations of state and parameters of the superfluid condensates were used to illustrate that $\mathcal{B}$ and $\mathcal{B}'$ are not constant but vary significantly with density, making it

difficult to determine the frictional strength ultimately entering the averaged momentum equations that govern the macroscopic neutron star dynamics.

Nonetheless, several implications of the interaction between the superfluid neutrons and the remaining components can be identified for the rotational evolution of a neutron star. Firstly, core coupling strengths of order $\mathcal{B} \approx 10^{-5}$ suggest that the neutrons and the charged-particle conglomerate are coupled on the order of seconds. As the latter is thought to be electromagnetically coupled to the crust, the core superfluid follows the crustal rigid-body rotation and cannot be responsible for observed post-glitch relaxation timescale on the order of months to years. This leads to the conclusion that the crustal quantum condensate governs the post-glitch dynamics. Whereas the strong drag, i.e. $\mathcal{B}_{\rm strong} \approx 10^{-2}$, associated with vortex kelvin waves could provide the initial coupling mechanism between the superfluid and the crust and explain the very short glitch rising timescales, a mutual friction strength of the order of $\mathcal{B}_{\rm weak} \approx 10^{-9}$, possible for phonon and electron dissipation, could govern the long post-glitch relaxation. Note, however, that recent work by Andersson et al. [39] accounting for entrainment between the crustal superfluid and the lattice, which was neglected in the calculation above, has shown that the crustal superfluid might not carry enough angular momentum to account for large glitches. This could be resolved by assuming that the core superfluid is involved in the glitch mechanism after all, implying that the core coupling physics presented above are incomplete. One aspect that could play an important role is the vortex-fluxtube interaction. As the neutron star is spinning down, vortices have to move radially outwards and encounter fluxtubes of the type-II proton superconductor, expected to be present in the outer core. Cutting the magnetised vortices through fluxtubes is associated with an energy cost leading to dissipation that could result in even shorter coupling timescales between the neutron and the proton fluid [188, 234]. If the energy cost is however too large, vortices could become *pinned* to the fluxtubes due to their magnetic short-range interaction. This would completely impede their motion and effectively decouple the core superfluid from the crust [188, 206]. Vortex-fluxtube pinning will be addressed in more detail in Subsection 6.2.4.

Finally, we return to the comparison with laboratory experiments to assess if the mutual friction within the two distinct superfluids in the neutron star crust and the core could trigger the development of turbulent dynamics. Continuous superfluid interfaces have been examined by confining two phases of helium-3, namely the A-phase and the B-phase, to cylindrical vessels. As discussed in Subsection 8.1.4, the vortices in these two states have different properties resulting in very different mutual friction strengths. At $T = 0.2\,T_{\rm c}$, for example, one has $\alpha_{\rm 3B} \approx 4.3 \times 10^{-3}$ and $\alpha'_{\rm 3B} \approx 0$ for the B-phase and $\alpha_{\rm 3A} \approx 2$ and $\alpha'_{\rm 3A} \approx 0.8$ for the A-phase [208], respectively, which implies that the latter evolves much faster. Using nuclear magnetic resonance measurements and vortex-line simulations, it is possible to address the influence of the change in the mutual friction across the interface on the rotational properties of the two phases. In particular, the

vortex response after a modification of the container's angular velocity can be analysed. Due to the distinct dissipation strengths, the vortices, which are initially straight and connected across the AB-interface, evolve on different timescales. Among other effects, this leads to the formation of a vortex tangle in the B-phase, accompanied by increasing dissipation, and generates differential rotation, since vortices are accumulated close to the container walls. Furthermore, it has been demonstrated that the AB-interface itself can be driven unstable [209]. More precisely, it is the Kelvin-Helmholtz instability that causes wave-like distortions of the interface, which result in the injection of vortex tangles from the A-phase to the B-phase [235], effectively transferring angular momentum between the two layers.

In order to obtain insight to whether similar turbulent features are present in neutron stars, one could as a first step compare the mutual friction coefficients in both systems. As explained in detail in Subsection 8.1.3, the two parameters $\mathcal{B}$ and $\mathcal{B}'$ introduced in the hydrodynamical two-component model directly correspond to α and α' of superfluid helium. Comparing the coupling strength in helium-3, which jumps by approximately three orders of magnitude across the interface, to the estimates calculated for the various mechanisms in the core and the crust, one finds that the relative difference in mutual friction between the two neutron star layers is of similar magnitude, i.e. 10^{-5} to 10^{-2} and 10^{-9}, respectively. However, due to the large uncertainties in the crustal dissipation, it is not possible to identify one of the layers with the A-phase or the B-phase, respectively, and deduce which part of the star would be predominantly affected by the presence of the interface. The simple comparison between $\mathcal{B}$ and α would, however, suggest that unexpected vortex dynamics are likely to be present in neutron stars and could significantly alter their rotational evolution. For additional information on the characteristics of helium experiments, which could serve as an analogue for neutron star physics, we refer the reader to Section 8.1.

Chapter 6

Coupling the Superconductor

Having addressed mutual friction, which arises due to a neutron star's superfluid properties and affects its rotational evolution, this chapter will focus on the physics of the superconducting component and implications for the stars' magnetic field. As numerous phenomena have been proposed to be of importance, the purpose of this chapter is to review several of these mechanisms to form a more comprehensive picture, provide links to features previously discussed and raise questions that remain to be addressed.

Firstly, Section 6.1 concerns the two seminal papers of Baym, Pethick and Pines published in 1969 [45, 193], which are generally quoted in the context of neutron star superconductivity and still represent the central reference point for studies of the interior magnetic field evolution. Understanding these papers is therefore essential. The main implication of the work by Baym et al. is the presence of type-II superconducting protons in the outer neutron star core. This suggests that magnetic flux is constrained to fluxtubes, whose motion governs the magnetic field evolution. An analysis of various mesoscopic forces, thought to alter the macroscopic properties of the star, is presented in Section 6.2. However, in contrast to the previous chapter relating mesoscopic physics of superfluid vortices to the large-scale mutual friction, the following discussion will not only address standard dissipation characterised by macroscopic, dimensionless coefficients $\mathcal{B}$ and $\mathcal{B}'$ (note that the index p is dropped since this chapter is only concerned with the charged quantum condensate). We also examine additional mechanisms that could influence the fluxtubes' motion but are not intrinsically dissipative and can hence not simply be represented by a set of dimensionless friction parameters. Instead, these processes will affect the fluxtube distribution in the neutron star interior, potentially driving them towards the crust, where magnetic field evolution timescales [231] are of the order of the decay timescales deduced from observations [236, 237, 238, 239]. To analyse these additional mechanisms, a more mesoscopic point of view is adapted in the following. The more rigorous framework relating the small-scale dynamics to the evolution of the averaged magnetic induction will be given in Chapter 7. This chapter concludes with a discussion and a brief comment on open problems (see Section 6.3).

6.1 Classical Argument for Type-II Superconductivity

6.1.1 Normal matter resistivity

The argument presented by Baym et al. [45] centres around the induction equation of normal resistive MHD, discussed in detail in Subsection 7.1.1. Neglecting superfluidity and superconductivity and thus effectively describing young neutron stars before the phase transitions, i.e. $T > T_{\mathrm{cn,p}}$, Baym et al. study the properties of matter consisting of neutrons, normal conducting but degenerate protons and ultra-relativistic electrons. As the latter particle species is the most mobile one, the dynamics of the system are governed by the interactions of electrons with the other two components; the dominant process being the scattering off protons. The coupling to neutrons does not contribute significantly, since the electrons only weakly interact with the small magnetic dipole moment of the uncharged particles. According to Baym et al. [193], the characteristic velocity relaxation timescale for electron-proton scattering is given by

$$\tau_{\mathrm{v}}^{-1} = \frac{k_{\mathrm{Fe}}^2}{48\pi c}\left(\frac{T}{T_{\mathrm{Fp}}}\right)^2 \int_0^{2k_{\mathrm{Fe}}} \mathrm{d}k\, \hbar^2 k^2 |M(k)|^2, \tag{6.1}$$

where corrections due to strong interactions in the Fermi liquids have been neglected. As before, k_{Fe} denotes the electron Fermi wave number, which is equivalent to the proton Fermi wave number, k_{Fp}, as the charge neutrality condition is satisfied. Moreover, T_{Fp} is the proton Fermi temperature, related to the non-relativistic Fermi energy, E_{Fp}, via

$$T_{\mathrm{Fp}} = \frac{E_{\mathrm{Fp}}}{k_{\mathrm{B}}} = \frac{\hbar^2 k_{\mathrm{Fe}}^2}{2m k_{\mathrm{B}}} \approx 1.4 \times 10^{11} \left(\frac{k_{\mathrm{Fe}}}{0.75\,\mathrm{fm}^{-1}}\right)^2 \mathrm{K}. \tag{6.2}$$

For typical neutron star core parameters the temperature term in Equation (6.1), arising due to the proton degeneracy, is thus of the order of $(T/T_{\mathrm{Fp}})^2 \simeq 10^{-6}$. Finally, the momentum transfer for a single electron-proton collision is represented by $\hbar k$, while $|M(k)|$ is the scattering matrix element as given in Equation (5.24) for the superfluid coupling.

Despite being highly relativistic, the electron Fermi energy is about one order of magnitude smaller than the rest-mass energy of the protons. In this case, the matrix element can be approximated by the Mott formula [240] obtained from solving the relativistic Dirac equation for the interaction of an electron beam with a proton's Coulomb potential. Additionally, the Mott formula has to be corrected to account for a reduction of the Coulomb coupling due to the surrounding charge carriers. As the electrons are ultra-relativistic, this *screening effect* is mainly caused by the protons [193]. It can be included by introducing the *Thomas-Fermi wave number*, k_{TF}, which is defined by

$$k_{\mathrm{TF}}^2 \equiv 4\pi e \frac{\partial n_{\mathrm{p}}}{\partial E_{\mathrm{Fp}}} = \frac{6e^2\pi n_{\mathrm{e}}}{E_{\mathrm{Fp}}} = \frac{4e^2 m}{\pi\hbar^2}\, k_{\mathrm{Fe}}, \tag{6.3}$$

where the Equations (5.8) and (6.2) have been used to relate the density to the Fermi

energy and evaluate the partial derivative. Canonical neutron star parameters lead to

$$k_{\mathrm{TF}} \approx 0.2 \left(\frac{k_{\mathrm{Fe}}}{0.75\,\mathrm{fm}^{-1}} \right)^{1/2} \mathrm{fm}^{-1}. \tag{6.4}$$

This is approximately a factor 4 smaller than the electron and proton Fermi wave numbers, respectively. The matrix element for the electron-proton scattering is then [193]

$$|M(k)|^2 = \left[\frac{4\pi e^2}{\hbar^2 (k^2 + k_{\mathrm{TF}}^2)} \right]^2 \left(1 - \frac{k^2}{4k_{\mathrm{Fe}}^2} \right). \tag{6.5}$$

Substituting this back into Equation (6.1), the integral can be easily evaluated to give

$$\tau_{\mathrm{v}}^{-1} = \frac{\pi}{24} \frac{e^4}{c\hbar^2} \left(\frac{T}{T_{\mathrm{Fp}}} \right)^2 \frac{k_{\mathrm{Fe}}^2}{k_{\mathrm{TF}}} \frac{-6z + (3 + 4z^2) \arctan(2z)}{z^2}, \tag{6.6}$$

where $z \equiv k_{\mathrm{Fe}}/k_{\mathrm{TF}}$. Taking advantage of Equation (6.4), the z-dependent term can be approximated by the leading order contribution, which results in the following velocity relaxation timescale also found by Baym et al. [193],

$$\tau_{\mathrm{v}} = \frac{12}{\pi^2} \frac{c\hbar^2}{e^4} \left(\frac{T_{\mathrm{Fp}}}{T} \right)^2 \frac{k_{\mathrm{TF}}}{k_{\mathrm{Fe}}^2} \approx 4.6 \times 10^{-14}\, T_8^{-2} \left(\frac{k_{\mathrm{Fe}}}{0.75\,\mathrm{fm}^{-1}} \right)^{5/2} \mathrm{s} \tag{6.7}$$

with the normalised interior temperature $T_8 \equiv T/(10^8\,\mathrm{K})$. A very similar result for the relaxation timescale of electron-proton scattering has also been obtained by Kelly [241], the only difference being a numerical prefactor of $16/\pi^2$ instead of $12/\pi^2$.

A dissipative coupling mechanism between the protons and relativistic electrons, characterised by the relaxation timescale τ_{v}, damps the relative motion between the components and tries to bring them into comotion. Hence, τ_{v} determines the electrical conductivity, $\tilde{\sigma}_{\mathrm{e}}$, of the system. For normal, degenerate matter in the neutron star core, $\tilde{\sigma}_{\mathrm{e}}$ is approximated by (see also Equation (7.3))

$$\tilde{\sigma}_{\mathrm{e}} = \frac{n_{\mathrm{e}} e^2 c \tau_{\mathrm{v}}}{\hbar k_{\mathrm{Fe}}} \approx 5.5 \times 10^{28}\, T_8^{-2}\, \rho_{14}^{3/2} \left(\frac{x_{\mathrm{p}}}{0.05} \right)^{3/2} \mathrm{s}^{-1}, \tag{6.8}$$

where $\rho_{14} \equiv \rho/(10^{14}\,\mathrm{g\,cm}^{-3})$ represents the normalised total mass density. This large electrical conductivity is a direct result of the proton degeneracy [193], which suppresses a significant fraction of the interactions between the two charged particle species. We further observe that as the star cools down, the conductivity becomes even larger.

6.1.2 Relation to the Meissner effect

Based upon the estimate given in Equation (6.8), Baym et al. [45] determine the corresponding Ohmic diffusion timescale, associated with the decay of the core magnetic field. For typical estimates (see Subsection 7.1.2 for details), one finds

$$\tau_{\rm Ohm} = \frac{4\pi\tilde{\sigma}_{\rm e}L^2}{c^2} \approx 2.5\times10^{13}\,T_8^{-2}\,L_6^2\,\rho_{14}^{3/2}\left(\frac{x_{\rm p}}{0.05}\right)^{3/2}\,{\rm yr}, \tag{6.9}$$

where the characteristic magnetic field lengthscale is normalised to the neutron star's radius, i.e. $L_6 \equiv L/(10^6\,{\rm cm})$. The variation of the Ohmic timescale for different densities in the core is illustrated in Figure 7.1 for the effective NRAPR equation of state, which leads to $\tau_{\rm Ohm} \approx 10^{13} - 10^{15}\,{\rm yr}$. These estimates not only exceed typical pulsar evolution timescales but are also much longer than the age of the Universe, which is of the order of $10^{10}\,{\rm yr}$. This suggests that above the transition temperature, $T_{\rm c}$, magnetic flux cannot be expelled from the interior of normal conducting neutron stars.

Owing to this circumstance, Baym et al. [45] conclude that, as the star is cooling down and eventually reaches $T_{\rm c}$, where it becomes energetically favourable for the outer core to turn superconducting, the transition into the macroscopic quantum state has to occur at constant flux. More precisely, they invoke the timescale $\tau_{\rm nucl} \sim \tau_{\rm Ohm}B^2/H_{\rm c}^2$ for the nucleation of superconductivity, i.e. the confinement of magnetic flux (continuously distributed in the normal state) into mesoscopic regions. While quoting $\tau_{\rm nucl} \sim 10^7\,{\rm yr}$, suggesting that flux expulsion cannot accompany the nucleation of superconductivity, the origin of this timescale is somewhat elusive since Baym et al. provide no derivation. However, based on the conclusion of constant flux, the Ginzburg-Landau parameter is determined to establish whether the neutron star interior is in a type-II superconducting state penetrated by a regular fluxtube array or in an intermediate type-I state, where macroscopic flux-free regions alternate with normal conducting ones. For typical equation of state parameters, the outer core is characterised by $\kappa_{\rm GL} > 1/\sqrt{2}$, implying the presence of a type-II state and a phase transition into a metastable state as illustrated in Figure 6.1. This result forms the foundation of many studies concerning the dynamics of neutron star cores, such as the discussions presented in previous chapters.

While the derivation of $\tau_{\rm nucl}$ is not apparent, we can easily assess how the Ohmic dissipation mechanism acting in normal nuclear matter affects a type-II superconducting star. In this case, the electron-proton scattering is restricted to the normal fluxtube cores, which only occupy a small fraction of the neutron star's volume, thus entailing an even larger conductivity and Ohmic decay timescale. As the increase should be inversely proportional to the fraction occupied by the fluxtube cores, which have a combined volume of $\mathcal{V}_{\rm fluxtubes} = A_{\rm fluxtubes}L$, one can estimate (see also Harrison [242])

$$\frac{\mathcal{V}_{\rm fluxtubes}}{\mathcal{V}} \simeq \frac{A_{\rm fluxtubes}L}{AL} = \frac{N\pi\xi_{\rm p}^2}{A} = \mathcal{N}_{\rm p}\,\frac{\phi_0}{2H_{\rm c2}} = \frac{B}{2H_{\rm c2}} \simeq \frac{B}{H_{\rm c2}}, \tag{6.10}$$

where we have approximated the total volume of the type-II superconductor as $\mathcal{V} \simeq AL$ and used Equations (3.93) and (3.62) to rewrite the result. As before, the cross-sectional area of a single fluxtube is $\pi\xi_{\rm p}$, whereas $\mathcal{N}_{\rm p} \equiv N/A$ denotes the fluxtube surface density and $H_{\rm c2}$ the upper critical field. The same fractional change in dissipation between the superconducting and the normal state has been experimentally observed and theoretically modelled in laboratory systems. The resistivity of this so-called *flux-flow* state

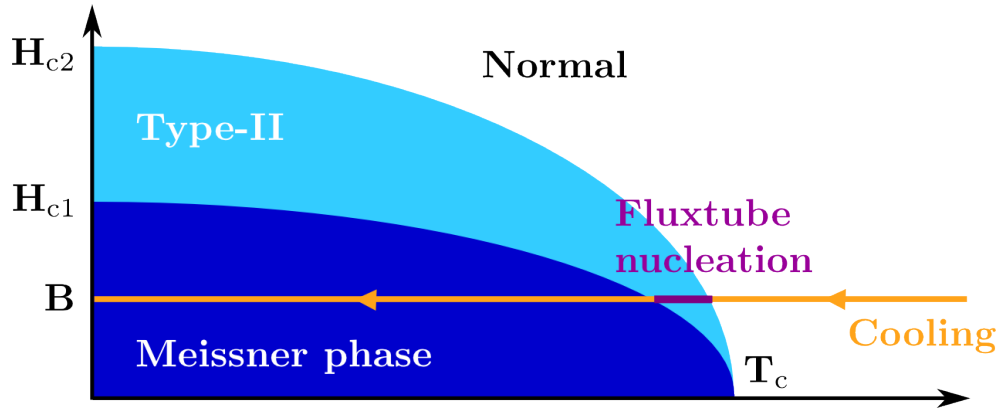

Figure 6.1: $H(T)$-diagram of a type-II superconductor illustrating the phase transition. As the medium permeated by the induction $B < H_{c1}$ is cooled down, it follows the yellow line from right to left. Below the transition temperature, T_c, magnetic flux (continuously distributed in the normal state) is first nucleated into fluxtubes. These are subsequently expelled if the matter is cooled further and a flux-free Meissner state is formed.

is discussed in more detail in Subsection 8.3.2. In the outer neutron star core, H_{c2} is typically of the order of 10^{16} G (see Equation (4.16)). For a canonical magnetic induction of the order of 10^{12} G, the volume fraction occupied by the fluxtubes is then $\sim 10^{-4}$. Therefore, the Ohmic decay timescale associated with the coupling of the electrons and normal conducting protons in a type-II system is four orders of magnitude larger than the estimate given in Equation (6.9), i.e. of the order of 10^{17} yr. Classical Ohmic diffusion is hence not affecting the core magnetic field of type-II superconducting stars.

The lack of flux expulsion led Baym et al. to deduce that superconducting neutron stars would not be affected by the Meissner effect [45], although typically $B \lesssim H_{c1}$ since the lower critical field, H_{c1}, is of the order 10^{15} G (see Equation (4.15)). While this statement is commonly repeated in the literature, there seems to be general misconception over its interpretation. The Meissner effect, observed in laboratory systems as the complete or incomplete expulsion of magnetic flux in type-I and type-II media, respectively, is the characteristic feature of the thermodynamical phase. However, apart from a few exceptions (for more information see Subsection 8.3.2), terrestrial experiments are predominantly concerned with the equilibrium state of superconductors and not interested in the formation of the macroscopic quantum state. In neutron stars the situation is different. The Meissner effect solely dictates that the equilibrium field should be exponentially screened from the interior but it is not known how the superconducting phase transition proceeds. In this context, the Ohmic dissipation mechanism of Baym et al. [193] does not give an explanation for the Meissner effect dynamics or the corresponding timescale. Statements like "The Meissner effect acts on very large timescales due to the enormous conductivity of normal nuclear matter," can hence be misleading. In order to understand the detailed processes of flux expulsion and deduce the small-scale physics, new studies of the phase transition are needed. Only this would allow the exact nature of the superconducting interior and its evolution to be determined.

6.2 Forces Acting on the Fluxtubes

As explained in detail in Section 6.1, standard Ohmic dissipation, limited to the normal conducting fluxtube cores, cannot generate magnetic field evolution of superconducting neutron stars. Hence, in order to explain field changes on the order of 10^7 [236, 237] and 10^4 yr [238, 239] as invoked from the observations of rotation-powered pulsars and magnetars, respectively, other mechanisms have to be considered. The purpose of this section is to examine processes that have been suggested to affect fluxtubes and should, therefore, also influence a star's interior magnetic field. Since the framework for obtaining the macroscopic field evolution, i.e. deriving a superconducting induction equation, is presented in the next chapter, the following discussion is primarily concerned with the fluxtube physics on mesoscopic lengthscales.

6.2.1 Resistive drag

The first mechanism we address is the dissipative coupling of fluxtubes and the electron component. This represents the counterpart of the electron-magnetic-vortex scattering analysed in Subsection 5.1.3 for the neutron stars' core superfluid. The superconducting case, i.e. the strength of the electron-fluxtube coupling, can be equivalently studied by means of the Alpar et al. formalism [205] by simply repeating the calculation with a modified induction, $\bar{B}_{\rm p}$, and a surface density, $\mathcal{N}_{\rm p}$. The necessary modifications of the relevant equations will be presented in the following. Vector notation will be employed.

Velocity relaxation timescale

As before, the quantity that is governing the strength of the interaction is the velocity relaxation timescale of the relativistic electrons, specifying how fast an initial relative velocity between the particles and the fluxtubes is damped. It is (see Equation (5.43))

$$\tau_{\rm vp}^{-1} = \frac{3}{4}\,\frac{e^2}{2\pi\hbar}\,\frac{\mathcal{N}_{\rm p}}{E_{\rm Fe}}\int_0^\pi {\rm d}\vartheta \sin\vartheta^3 \int_0^\pi {\rm d}\alpha\, \Pi_{\rm p}\left(2k_{\rm Fe}\sin\vartheta\sin\alpha/2\right)^2, \tag{6.11}$$

where the function $\Pi_{\rm p}(q)$, related to the fluxtube's induction $\bar{B}_{\rm p}$, is defined by

$$\Pi_{\rm p}(q) = 2\pi\int_0^\infty {\rm d}r\, r\bar{B}_{\rm p}(r)J_0(qr). \tag{6.12}$$

Accounting for the detailed structure of a proton fluxtube with a core size, $\xi_{\rm p}$, and the magnetic flux located within the radius λ_*, one obtains the following induction, which is a function of r (the distance from the fluxtube centre), [205, 182]

$$\bar{B}_{\rm p}(r) = \frac{\phi_0}{\pi\xi_{\rm p}^2}\begin{cases} 1-\frac{\xi_{\rm p}}{\lambda_*}K_1\left(\frac{\xi_{\rm p}}{\lambda_*}\right)I_0\left(\frac{r}{\lambda_*}\right) & \text{for } 0\le r\le\xi_{\rm p},\\ \frac{\xi_{\rm p}}{\lambda_*}I_1\left(\frac{\xi_{\rm p}}{\lambda_*}\right)K_0\left(\frac{r}{\lambda_*}\right) & \text{for } r\ge\xi_{\rm p}. \end{cases} \tag{6.13}$$

We can again estimate the strength of the induction at $r = 0$, where the Bessel functions of the interior solution are negligible. Substituting typical estimates for the proton wave number and the s-wave energy gap (see Figures 5.2 and 5.4) into the prefactor leads to

$$\bar{B}_{\rm p} \approx -6.6 \times 10^{16} \left(\frac{m_{\rm p}^*}{m}\right)^2 \left(\frac{0.75\,{\rm fm}^{-1}}{k_{\rm Fp}}\right)^2 \left(\frac{\Delta_{\rm p}}{1\,{\rm MeV}}\right)^2 {\rm G}. \tag{6.14}$$

In the limit of an infinitely thin fluxtube, i.e. applying $\xi_{\rm p} \to 0$ and $\lambda_* \to 0$, $\bar{B}_{\rm p}(r)$ can be significantly simplified and the function $\Pi_{\rm p}(q)$ is found to be constant and equal to the magnetic flux, i.e. $\Pi_{\rm p}(q) = \phi_0$. Substituting this into Equation (6.11), the velocity relaxation timescale for a point-like fluxtube reduces to (see also Figure 6.2)

$$\tau_{\rm vp,0} = \frac{2\pi\hbar}{e^2} \frac{E_{\rm Fe}}{\mathcal{N}_{\rm p}} \frac{1}{\phi_0^2 \pi} = 1.0 \times 10^{-17} B_{12}^{-1} \left(\frac{k_{\rm Fe}}{0.75\,{\rm fm}^{-1}}\right) {\rm s}, \tag{6.15}$$

where a canonical magnetic field of $10^{12}\,{\rm G}$ has been chosen, i.e. $B_{12} \equiv B/(10^{12}\,{\rm G})$. This relaxation timescale is many orders of magnitude smaller than the one obtained for infinitely thin neutron vortices in Equation (5.56). This arises due to the different surface densities, $\mathcal{N}_{\rm p} \gg \mathcal{N}_{\rm n}$ (see Equation (4.9)), and implies that interactions between the electrons and the fluxtubes are much more frequent.

In order to account for the finite size of the fluxtube, the full mesoscopic magnetic induction defined in Equation (6.13) has to be considered. In this case, one obtains

$$\Pi_{\rm p}(q) = \frac{2\phi_0}{1 + q^2\lambda_*^2} \frac{J_1(q\xi_{\rm p})}{q\xi_{\rm p}}. \tag{6.16}$$

Replacing the function $\Pi_{\rm p}(q)$ in Equation (6.11) accordingly, an improved estimate for the electron velocity relaxation timescale can be determined,

$$\tau_{\rm vp}^{-1} = \frac{3\tau_{\rm vp,0}^{-1}}{2\pi\xi_{\rm p}^2 k_{\rm Fe}^2} \int_0^\pi {\rm d}\vartheta \sin\vartheta \int_0^1 {\rm d}x \, \frac{J_1(2k_{\rm Fe}\xi_{\rm p}\sin\vartheta\, x)^2}{x^2(1-x^2)^{1/2}\left(1 + 4k_{\rm Fe}^2\lambda_*^2\sin^2\vartheta\, x^2\right)^2}. \tag{6.17}$$

Again, the zero-radius scattering timescale is significantly altered due to the fluxtube's finite size. Since Equation (6.17) cannot be integrated analytically, we first define two dimensionless parameters to rewrite the expression for $\tau_{\rm vp}^{-1}$ in more compact form, i.e. $\alpha_1 \equiv \xi_{\rm p}/\lambda_*$ and $\alpha_2 \equiv 2k_{\rm Fe}\xi_{\rm p}$. The former quantity corresponds to the inverse Ginzburg-Landau parameter, $\kappa_{\rm NS}$, given in Equation (4.14). For typical parameters in the outer neutron star core, one can estimate

$$\begin{aligned}\alpha_1 \approx 7.6 \times 10^{-2} &\left(\frac{m}{m_{\rm p}^*}\right)\left(\frac{m_{\rm n}^*}{m}\right)^{1/2}\left(\frac{m_{\rm n}^*}{m} - 1 + \frac{m_{\rm p}^*}{m}\right)^{-1/2} \\ &\times \rho_{14}^{1/2}\left(\frac{x_{\rm p}}{0.05}\right)^{1/2}\left(\frac{k_{\rm Fp}}{0.75\,{\rm fm}^{-1}}\right)\left(\frac{1\,{\rm MeV}}{\Delta_{\rm p}}\right),\end{aligned} \tag{6.18}$$

and

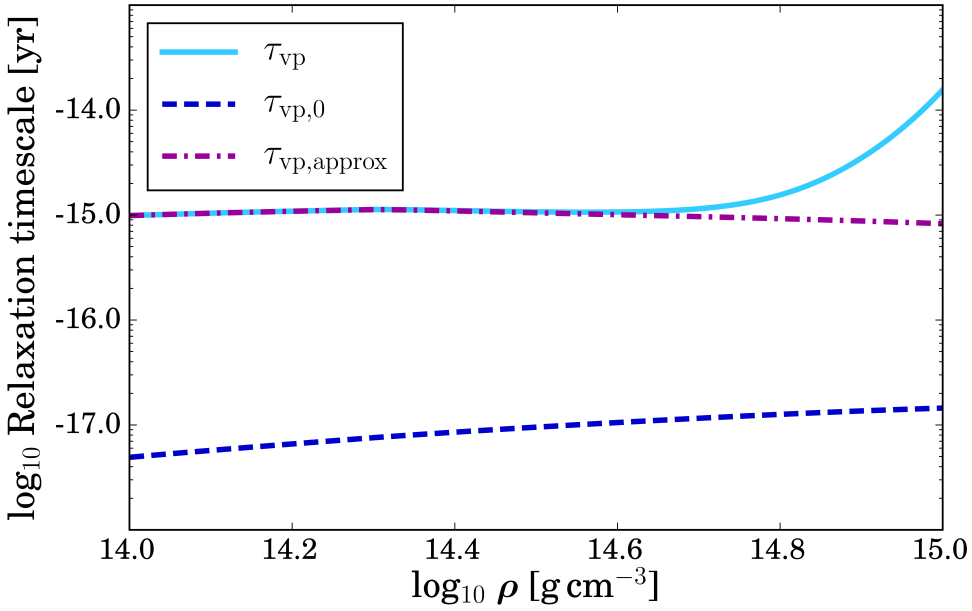

Figure 6.2: Relaxation timescales for electron-magnetic-fluxtube coupling in the neutron star core as a function of the mass density. Shown are the estimates for electrons scattering off a finite-sized fluxtube, $\tau_{\rm vp}$, (cyan, solid), the coupling to point-like fluxtubes, i.e. $\tau_{\rm vp,0}$ (blue, dashed), and the approximate timescale, $\tau_{\rm vp,approx}$, (purple, dot-dashed) defined in Equation (6.21). The values are computed for the NRAPR effective EoS and $B = 10^{12}$ G.

$$\alpha_2 \approx 15.0 \left(\frac{m}{m_{\rm p}^*}\right) \left(\frac{k_{\rm Fe}}{0.75\,{\rm fm}^{-1}}\right) \left(\frac{k_{\rm Fp}}{0.75\,{\rm fm}^{-1}}\right) \left(\frac{1\,{\rm MeV}}{\Delta_{\rm p}}\right). \tag{6.19}$$

Substituting α_1 and α_2 into Equation (6.17) and applying the same simplifications as explained in deriving Equation (5.62) for the electron-vortex coupling in order to save computation time, one finally arrives at

$$\tau_{\rm vp}^{-1} \simeq 3\,\frac{\tau_{\rm vp,0}^{-1}\,\alpha_1^4}{\alpha_2^3} \int_0^{\alpha_2} {\rm d}y\, \frac{\alpha_2^2 + y^2/2}{\left(\alpha_1^2 + y^2\right)^2} \left[\frac{J_1(y)}{y}\right]^2. \tag{6.20}$$

Expanding the integrand to lowest order in $\alpha_2^{-1} \ll 1$ and further approximating $\alpha_1 \simeq 1$, the following timescale, which is independent of the proton energy gap, can be found

$$\tau_{\rm vp,approx} \equiv \frac{16}{3\pi}\,\tau_{\rm vp,0}\,\frac{\alpha_2}{\alpha_1}. \tag{6.21}$$

The density-dependent frictional coupling timescales are shown in Figure 6.2 for a fiducial magnetic induction of 10^{12} G. We can observe that the scattering timescales accounting for the finite fluxtube size are approximately two orders of magnitude larger than the zero-radius scattering timescale, $\tau_{\rm vp,0}$. Including the structure of the fluxtube, thus, weakens the mutual friction coupling as already discussed for the electron-vortex interaction. Furthermore, it can be seen that the simple timescale, $\tau_{\rm vp,approx}$, provides a very good approximation to the full result. Therefore, for a wide range, the density-

dependence of the proton energy gap does not significantly affect the coupling strength between the electrons and the fluxtubes and the gap-independent result can be used.

Mutual friction cross-section

Before relating the relaxation timescale to the macroscopic drag, one again has to correct $\tau_{\rm vp}$ to account for the strong coupling of electrons and protons on hydrodynamical scales. As shown in Equation (5.64), the increase in the moment of inertia results in an increase of the frictional timescale by one order of magnitude. Hence, on macroscopic scales, the proton fluxtubes experience the following resistive force as a result of being magnetically coupled to the charged-particle conglomerate,

$$\mathbf{F}_{\rm d} = \frac{\rho_{\rm p}}{\tau_{\rm vp}} \frac{E_{\rm Fe}}{mc^2} (\mathbf{v}_{\rm p} - \mathbf{u}_{\rm p}), \tag{6.22}$$

where $\mathbf{v}_{\rm p}$ and $\mathbf{u}_{\rm p}$ denote the averaged velocities of the electron-proton component and fluxtubes, respectively. This force coincides with the macroscopic version of the mesoscopic drag, $\mathbf{f}_{\rm d}$, exerted on a single fluxtube (see also Equation (4.81)). The averaging is performed by multiplying $\mathbf{f}_{\rm d}$ with the fluxtube density, $\mathcal{N}_{\rm p}$. Hence, the dimensionless drag coefficient, $\mathcal{R}$, and the velocity relaxation timescale, $\tau_{\rm vp}$, are related via

$$\mathcal{R} = \frac{1}{\mathcal{N}_{\rm p}\kappa} \frac{E_{\rm Fe}}{mc^2} \frac{1}{\tau_{\rm vp}}. \tag{6.23}$$

For typical neutron star parameters, we obtain

$$\mathcal{R} \approx 1.6 \times 10^{-2} B_{12}^{-1} \left(\frac{k_{\rm Fe}}{0.75\,{\rm fm}^{-1}} \right) \left(\frac{10^{-15}\,{\rm s}}{\tau_{\rm vp}} \right) \ll 1, \tag{6.24}$$

which is much smaller than one and implies that the weak mutual friction limit given in Equation (5.67) applies. Replacing the velocity relaxation timescale in Equation (6.23) with the full expression (6.20), we find for the dimensionless mutual friction coefficient

$$\mathcal{B} \simeq \frac{3\pi}{2} \frac{\alpha_1^4}{\alpha_2^3} \int_0^{\alpha_2} {\rm d}y \, \frac{\alpha_2^2 + y^2/2}{\left(\alpha_1^2 + y^2\right)^2} \left[\frac{J_1(y)}{y} \right]^2. \tag{6.25}$$

Note that $\mathcal{B}'$ is equal to $\mathcal{B}^2$ in the weak mutual friction limit. Alternatively, the coefficient can also be estimated using the approximate timescale, $\tau_{\rm vp,approx}$, defined in Equation (6.21). Using for simplicity $m_{\rm p}^* \approx m$ and $x_{\rm p} \approx x_{\rm e}$, the following result can be found

$$\mathcal{B}_{\rm approx} \equiv \frac{3\pi^2}{64} \frac{1}{\lambda_* k_{\rm Fe}}, \tag{6.26}$$

which for typical neutron star parameters can be estimated to

$$\mathcal{B}_{\rm approx} \approx 7.9 \times 10^{-3} \left(\frac{m}{m_{\rm p}^*} \right)^{1/2} \rho_{14}^{1/6} \left(\frac{x_{\rm p}}{0.05} \right)^{1/6}. \tag{6.27}$$

The resulting estimates calculated for different neutron star depths are shown in Figure 5.9. Note that the two curves are almost identical up to a density of $\sim 3 \times 10^{14}\,\mathrm{gcm}^{-3}$. Hence, the approximate result accurately captures the physics of the electron-magnetic-fluxtube interaction in the outer neutron star core. Only for very high densities does $\mathcal{B}_{\mathrm{approx}}$ deviate significantly from the exact solution given in Equation (6.25). Since in the inner core, type-II superconductivity is expected to break down anyway, Equation (6.27) is used in the following chapter to study the implications of this coupling process on the macroscopic magnetic field evolution in the interior of superconducting stars.

Before continuing with a discussion of additional force terms, we point out that the approximate mutual friction coefficient defined in Equation (6.26) correctly reproduces the resistivity, γ, often used in the literature to capture the dissipative interaction between individual fluxtubes and the electron fluid. As first discussed by Harvey et al. [243] and Jones [244] (see also Ruderman et al. [188] and Jahan-Miri [189], one has

$$\gamma = \frac{3\pi}{64}\,\frac{n_{\mathrm{e}} e^2 \phi_0^2}{\lambda_* E_{\mathrm{Fe}} c} \approx 7.9 \times 10^7 \left(\frac{m}{m_{\mathrm{p}}^*}\right)^{1/2} \rho_{14}^{7/6} \left(\frac{x_{\mathrm{p}}}{0.05}\right)^{7/6} \mathrm{g\,cm^{-1}\,s^{-1}}, \tag{6.28}$$

approximating $x_{\mathrm{e}} \approx x_{\mathrm{p}}$ and $m_{\mathrm{n}}^* \approx m$. Since this is related to the dimensionless drag via $\gamma = \rho_{\mathrm{p}} \kappa \mathcal{R}$ (see Equation (4.81)), the same result $\mathcal{B}_{\mathrm{approx}}$ is obtained as given above.

Finally note that Jones [244, 245, 246] has argued that the mesoscopic coupling between the electron fluid and the fluxtubes might not affect the dynamics on macroscopic scales after all, since the derivation of Equation (6.25) implicitly assumes that individual fluxtubes move independently. Within a rigid lattice, however, fluxtubes are expected to move in large numbers. By coherently summing over the electron scattering events in these *bundles*, Jones finds that the macroscopic relative velocity between the charged particles and the fluxtubes is very small. This would imply that the resulting drag is much weaker than the estimate (6.27) obtained using a non-coherent average.

6.2.2 Repulsive force

Magnetic field evolution in a type-II superconducting star resulting from the repulsive interaction between individual fluxtubes has been discussed by Kocharovsky et al. [247] and Istomin and Semerikov [248] in a simplified cylindrical geometry. Both calculations rely on the interaction between two quantised structures, which will be studied in detail below. When generalising the interaction between two fluxtubes to the entire array, the net force on a single line is obtained by summing up all individual contributions. This implies that in a perfectly triangular lattice, the net force vanishes because the repulsive forces of opposite fluxtubes exactly cancel each other (see Figure 6.4). In the equilibrium state of the fluxtube array, the averaged magnetic induction does not change and hence no magnetic field evolution takes place. If, however, the fluxtubes were inhomogeneously distributed, the net force would be non-zero and could potentially drive the fluxtubes

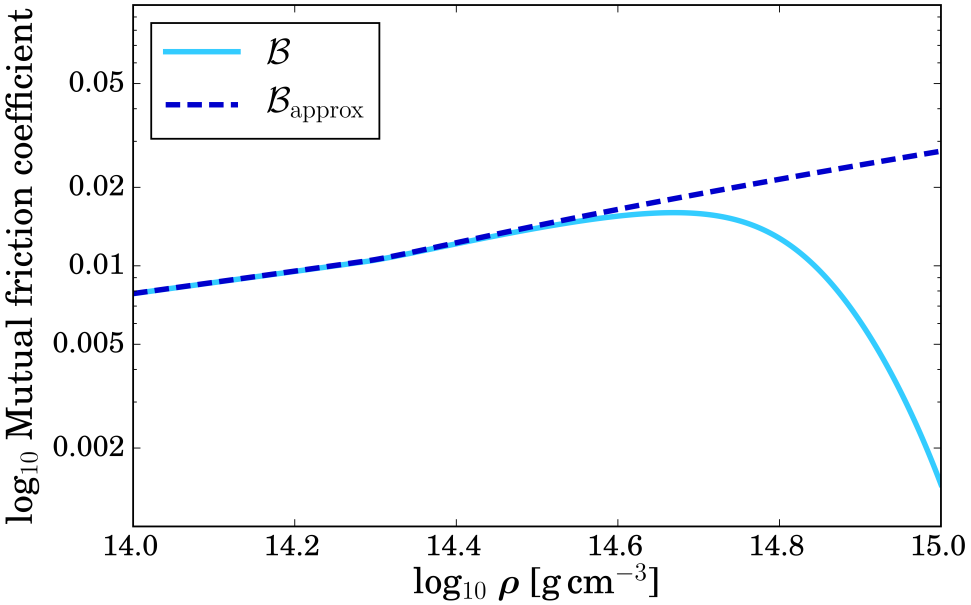

Figure 6.3: Mutual friction strength in the core, generated by the scattering of relativistic electrons off the fluxtube magnetic field. Shown are results for the full coefficient accounting for the density-dependent proton energy gap (cyan, solid) and the approximate, gap-independent coefficient $\mathcal{B}_{\rm approx}$ (blue, dashed). The values are computed for the NRAPR EoS.

towards the crust-core interface. This would effectively decrease the averaged magnetic field in a star's interior, since standard Ohmic decay timescales are much shorter in the crust [231]. Such a gradient in the fluxtubes' area density could, for example, be induced by additional forces. Whereas it should be difficult to move single fluxtubes away from their equilibrium positions due to the elastic properties of the array, strong interactions could displace a large number of fluxtubes. As observed in laboratory experiments with type-II superconductors (see Subsection 8.3.2), the lattice would then locally retain its hexagonal structure but loose its long-range order, resulting in the non-uniform distribution of fluxtubes on large scales. Alternatively, the inhomogeneity could arise if some region in the neutron star's outer core was normal-conducting. Istomin and Semerikov [248], for example, consider the destruction of superconductivity in a small region close to the magnetic axis, supposedly caused by an increase in the local magnetic field due to accretion. As a result of this fluxtube gradient, the quantised structures migrate into the normal-conducting zone, predicted to drive magnetic field decay on the order of 10^3 yr [248] for a standard field of about 10^{12} G. As this is much shorter than the timescales associated with Ohmic dissipation and electron-magnetic-fluxtube scattering, the repulsive interaction between the fluxtubes in the outer neutron star core is analysed here.

In order to determine the repulsion between two fluxtubes located at $\mathbf{r}_1$ and $\mathbf{r}_2$, directed along the z-axis, we take advantage of $\xi_{\rm p} \lesssim \lambda_*$ (see Equation (4.14)) to neglect their interior structure and take them to be point-like. In this case, the mesoscopic magnetic induction of each single fluxtube is given by Equation (4.43). Employing vector

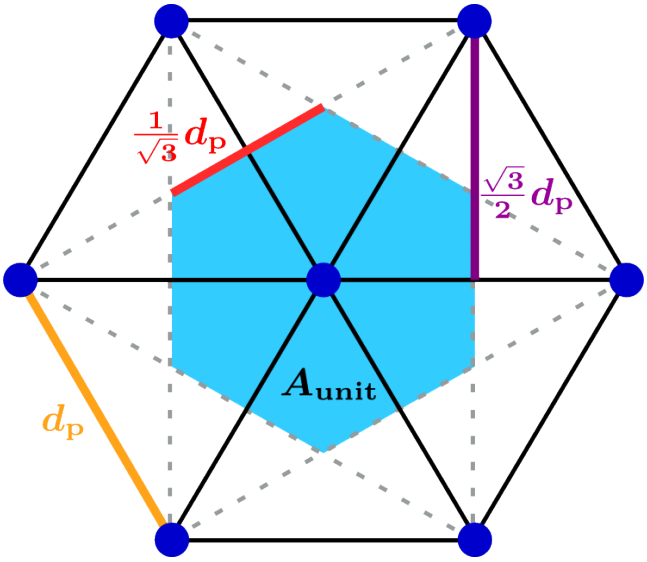

Figure 6.4: Geometry of the triangular array. The fluxtube positions in this equilibrium configuration are marked as blue circles. The distance between two neighbouring points is given by the yellow line, d_p. Two more distances are shown for clarity. The cyan hexagon marks the unit cell of the triangular lattice. Containing exactly one fluxtube, its area A_unit can be used calculate the fluxtube surface density, $\mathcal{N}_\mathrm{p}$.

notation, the total induction at a point, $\mathbf{r}$, is then determined by superposition, i.e.

$$\bar{\mathbf{B}}(\mathbf{r}) \equiv \bar{\mathbf{B}}_1(\mathbf{r}) + \bar{\mathbf{B}}_2(\mathbf{r}) = \left[\bar{B}(|\mathbf{r}-\mathbf{r}_1|) + \bar{B}(|\mathbf{r}-\mathbf{r}_2|)\right]\hat{\boldsymbol{z}}. \tag{6.29}$$

Ignoring the detailed structure of the fluxtube cores by introducing a cut-off at ξ_p, the total magnetic energy for two interacting fluxtubes is obtained from [114]

$$\mathcal{E} = \frac{\lambda_*^2}{8\pi}\oint\left[\bar{\mathbf{B}}\times\left(\nabla\times\bar{\mathbf{B}}\right)\right]\cdot\mathrm{d}\mathbf{s}. \tag{6.30}$$

While the line integral, in principle, has to be evaluated at the inner and outer perimeter of the integration area, the contribution at infinity vanishes since $\bar{\mathbf{B}}$ falls off exponentially far away from the fluxtubes as seen from Equation (4.44). Substituting Equation (6.29) into Equation (6.30) and employing the symmetry of the problem, we find

$$\mathcal{E} = 2\mathcal{E}_\mathrm{p} + \mathcal{E}_\mathrm{int}, \tag{6.31}$$

where $\mathcal{E}_\mathrm{p}$ is the energy per unit length of a single fluxtube previously defined in Equation (4.56). Moreover, $\mathcal{E}_\mathrm{int}$ represents the total interaction energy given by

$$\mathcal{E}_\mathrm{int} = \frac{\lambda_*^2}{4\pi}\oint\left[\bar{\mathbf{B}}_1\times\left(\nabla\times\bar{\mathbf{B}}_2\right)\right]\cdot\mathrm{d}\mathbf{s_2}. \tag{6.32}$$

Here, the line integral encloses the fluxtube at $\mathbf{r}_2$. Alternatively, we could exchange the inductions $\bar{\mathbf{B}}_1$ and $\bar{\mathbf{B}}_2$ and integrate around the fluxtube 1. Using cylindrical coordinates

$\{r, \theta, z\}$ and Equation (4.45) to approximate the induction at small distances from the core and evaluate the curl of $\bar{\mathbf{B}}_2$, the interaction energy simplifies to

$$\mathcal{E}_{\rm int} = \frac{\phi_0}{4\pi}\,\bar{B}(|\mathbf{r}_2 - \mathbf{r}_1|) = \frac{\phi_0^2}{8\pi\lambda_*^2}\,K_0\left(\frac{r_{21}}{\lambda_*}\right). \tag{6.33}$$

The distance between the two fluxtubes is represented by $r_{21} \equiv |\mathbf{r}_2 - \mathbf{r}_1|$. As a result of the asymptotic behaviour of the Bessel function, $\mathcal{E}_{\rm int}$ becomes exponentially small for large separations. Furthermore, the interaction is repulsive if the two fluxtube magnetic fields are aligned, which is the case expected in the outer neutron star core.

The interaction energy can be further associated with a repulsive force. Assuming the penetration depth to be constant over lengthscales of order r_{21}, the force acting on the fluxtube at $\mathbf{r}_1$ due to the presence of the second fluxtube at $\mathbf{r}_2$ is given by

$$\mathbf{F}_{12} = -\nabla_{\mathbf{r}_1}\mathcal{E}_{\rm int} = -\frac{\phi_0^2}{8\pi^2\lambda_*^3}\,K_1\left(\frac{r_{21}}{\lambda_*}\right)\hat{\mathbf{r}}_{21}, \tag{6.34}$$

where $\hat{\mathbf{r}}_{21}$ is the unit vector pointing from fluxtube 1 to fluxtube 2. With regard to the succeeding discussion, it is convenient to approximate Equation (6.34) in the two limits where $r_{21} \gg \lambda_*$ and $r_{21} \ll \lambda_*$. Expanding the Bessel function accordingly, we find

$$\mathbf{F}_{12} \simeq -\frac{\phi_0^2}{8\sqrt{2}\pi^{3/2}\lambda_*^{5/2}}\,\frac{\mathrm{e}^{-r_{21}/\lambda_*}}{\sqrt{r_{21}}}\,\hat{\mathbf{r}}_{21} \qquad \text{for} \qquad r_{21} \gg \lambda_*, \tag{6.35}$$

$$\mathbf{F}_{12} \simeq -\frac{\phi_0^2}{8\pi^2\lambda_*^2}\,\frac{1}{r_{21}}\,\hat{\mathbf{r}}_{21} \qquad \text{for} \qquad r_{21} \ll \lambda_*. \tag{6.36}$$

The difficulty when generalising this repulsive interaction to the full array is the transition from a discrete mesoscopic picture, studying individual fluxtubes, to an averaged, continuous description valid on large scales. For a perfectly ordered lattice, this step is straightforward since the interfluxtube separation, $d_{\rm p}$, is constant and directly related to the fluxtube surface density, $\mathcal{N}_{\rm p}$. Considering the area of the unit cell, $A_{\rm unit}$, which contains exactly one fluxtube as illustrated in Figure 6.4, we find

$$A_{\rm unit} = \frac{1}{\mathcal{N}_{\rm p}} = \frac{3\sqrt{3}}{2}\left(\frac{d_{\rm p}}{\sqrt{3}}\right)^2 = \frac{\sqrt{3}}{2}\,d_{\rm p}^2. \tag{6.37}$$

Solving for the distance between nearest neighbours gives

$$d_{\rm p} = 3^{-1/4}\sqrt{2}\,\mathcal{N}_{\rm p}^{-1/2}. \tag{6.38}$$

In this configuration, however, the net repulsion vanishes. For an inhomogeneous lattice, on the other hand, the fluxtube separation and density are functions of $\mathbf{r}$, so that the individual contributions to the repulsive force do not necessarily cancel each other. Within the averaged framework, it seems reasonable to postulate that the total repul-

sive force is of the form $-g(\mathcal{N}_\mathrm{p})\nabla\mathcal{N}_\mathrm{p}$. To proceed with the calculation of the function $g(\mathcal{N}_\mathrm{p})$, we assume that despite its inhomogeneity the fluxtube lattice stays triangular on small scales and is locally characterised by a constant d_p. Following the approach of Kocharovsky et al. [247], two limiting cases can then be easily investigated: (I) $d_\mathrm{p} \gg \lambda_*$ and (II) $d_\mathrm{p} \ll \lambda_*$. In the former case, the fluxtube density is rather low and Equation (6.35) approximates the interaction between individual fluxtubes. As the repulsive force decays exponentially, it is sufficient to only account for the six nearest neighbours when deriving the function $g(\mathcal{N}_\mathrm{p})$. The second case represents the high fluxtube density limit, where Equation (6.36) captures the dynamics and the repulsive force is stronger. Since $\mathcal{N}_\mathrm{p}$ changes only little over lengthscales of order λ_*, many more neighbouring fluxtubes have to be included to obtain the total repulsive force and the summation can be substituted by an integral. For typical neutron star magnetic field strengths of the order of $10^{12}\,\mathrm{G}$, the interfluxtube spacing is $\sim 10^{-10}\,\mathrm{cm}$ as given in Equation (4.9). The comparison with canonical estimates of the penetration depth, $\lambda_* \sim 10^{-11}\,\mathrm{cm}$ according to Equation (4.10), shows that the case (I) provides a good approximation for the fluxtube dynamics in a neutron star's outer core. Even for stronger magnetar fields, $B \sim 10^{15}\,\mathrm{G}$, the interfluxtube distance is only of the same order as the penetration depth and not significantly exceeded. This would suggest that the case (II) is not relevant for studying the neutron star magnetic field evolution.[1] We, thus, restrict our attention to case (I).

The geometry in the plane perpendicular to the fluxtube axes, used to determine the average resistive force in the limit $d_\mathrm{p} \gg \lambda_*$, is illustrated in Figure 6.5. Consider the fluxtube 1, located at the origin, to be surrounded by six fluxtubes (2-7). Whereas the points 2 to 5 are located at a distance d_p, fluxtubes 6 and 7 are separated a distance d'_p. The corresponding Cartesian coordinates of the inhomogeneously distributed fluxtubes are given in Figure 6.5. Since the repulsive forces caused by fluxtubes 2 and 5 cancel each other, one only has to consider contributions from fluxtubes 3, 4, 6 and 7, located at the vertices of two equilateral triangles. Adding the forces arising to the left of fluxtube 1 leads to the following

$$\mathbf{F}_{13} + \mathbf{F}_{14} = -\frac{\phi_0^2}{8\sqrt{2}\pi^{3/2}\lambda_*^{5/2}} \frac{\mathrm{e}^{-d_\mathrm{p}/\lambda_*}}{\sqrt{d_\mathrm{p}}} \left(\hat{\mathbf{r}}_{31} + \hat{\mathbf{r}}_{41}\right) = \frac{\sqrt{3}\phi_0^2}{8\sqrt{2}\pi^{3/2}\lambda_*^{5/2}} \frac{\mathrm{e}^{-d_\mathrm{p}/\lambda_*}}{\sqrt{d_\mathrm{p}}}\, \hat{\boldsymbol{x}}, \tag{6.39}$$

while the contribution from the right-hand side is

$$\mathbf{F}_{16} + \mathbf{F}_{17} = -\frac{\phi_0^2}{8\sqrt{2}\pi^{3/2}\lambda_*^{5/2}} \frac{\mathrm{e}^{-d'_\mathrm{p}/\lambda_*}}{\sqrt{d'_\mathrm{p}}} \left(\hat{\mathbf{r}}_{61} + \hat{\mathbf{r}}_{71}\right) = -\frac{\sqrt{3}\phi_0^2}{8\sqrt{2}\pi^{3/2}\lambda_*^{5/2}} \frac{\mathrm{e}^{-d'_\mathrm{p}/\lambda_*}}{\sqrt{d'_\mathrm{p}}}\, \hat{\boldsymbol{x}}. \tag{6.40}$$

The sum of these two terms is non-zero as a result of the different interfluxtube spacings.

[1] Note that Istomin and Semerikov [248] use Equation (6.36) for the repulsive force inside accreting neutron stars. As explained above, for fields of the order of $10^{12}\,\mathrm{G}$, the limit $d_\mathrm{p} \ll \lambda_*$ does not correctly describe the dynamics of the fluxtube lattice because it overestimates the strength of the repulsive interaction. This casts some doubt on the correctness of their results and suggests that magnetic field decay in accreting pulsars should proceed on timescales longer than $10^3\,\mathrm{yr}$.

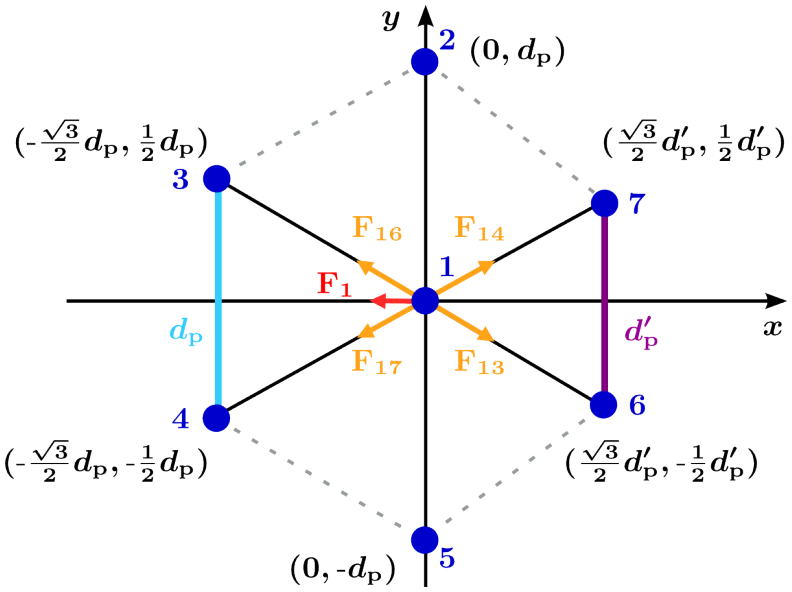

Figure 6.5: Geometry of an inhomogeneous fluxtube lattice used to describe interactions in the limit $d_\mathrm{p} \gg \lambda_*$. As the repulsive forces fall off exponentially, only the six nearest neighbours of fluxtube 1 have to be taken into account. Their locations are given in Cartesian coordinates. Note that two of the fluxtubes are located at a distance d'_p instead of d_p, which results in a non-zero repulsive force, $\mathbf{F}_1$ (red arrow).

More precisely, one obtains for the net repulsive force acting on fluxtube 1

$$\mathbf{F}_1 = \frac{\sqrt{3}\phi_0^2}{8\sqrt{2}\pi^{3/2}\lambda_*^{5/2}} \left(\frac{\mathrm{e}^{-d_\mathrm{p}/\lambda_*}}{\sqrt{d_\mathrm{p}}} - \frac{\mathrm{e}^{-d'_\mathrm{p}/\lambda_*}}{\sqrt{d'_\mathrm{p}}} \right) \hat{\boldsymbol{x}}. \tag{6.41}$$

This result can be further simplified by assuming that the difference between the lattice constants is small, i.e. $\delta_\mathrm{p} \equiv d_\mathrm{p} - d'_\mathrm{p} \ll 1$. This leads to the following approximation

$$\mathbf{F}_1 \simeq -\frac{\sqrt{3}\phi_0^2}{8\sqrt{2}\pi^{3/2}\lambda_*^{7/2}} \frac{\mathrm{e}^{-d_\mathrm{p}/\lambda_*}}{\sqrt{d_\mathrm{p}}} \delta_\mathrm{p}\, \hat{\boldsymbol{x}}. \tag{6.42}$$

In order to relate δ_p, representing the lattice inhomogeneity on mesoscopic lengthscales, to a change in the macroscopic fluxtube density, $\nabla\mathcal{N}_\mathrm{p}$, we use Equation (6.38) to find

$$\nabla\mathcal{N}_\mathrm{p} = \nabla\mathcal{N}_\mathrm{p}(d_\mathrm{p}) = -\frac{4}{\sqrt{3}} \frac{\nabla d_\mathrm{p}}{d_\mathrm{p}^3} \simeq \frac{4}{\sqrt{3}} \frac{\delta_\mathrm{p}}{d_\mathrm{p}^4}\, \hat{\boldsymbol{x}}, \tag{6.43}$$

where the last simplification is based on the geometry shown in Figure 6.5. By solving this relation for δ_p, substituting the result into Equation (6.42) and replacing the inter-fluxtube spacing with the surface density, an expression for the averaged repulsive force per unit length of fluxtube can be deduced. One has

$$\mathbf{F}_\mathrm{rep} \equiv -g(\mathcal{N}_\mathrm{p})\nabla\mathcal{N}_\mathrm{p} \simeq -\frac{3\phi_0^2}{32\sqrt{2}\pi^{3/2}} \left(\frac{\sqrt{2}\,\mathcal{N}_\mathrm{p}^{-1/2}}{3^{1/4}\lambda_*} \right)^{7/2} \exp\left[-\frac{\sqrt{2}\,\mathcal{N}_\mathrm{p}^{-1/2}}{3^{1/4}\lambda_*} \right] \nabla\mathcal{N}_\mathrm{p}. \tag{6.44}$$

The corresponding function $g(\mathcal{N}_\mathrm{p})$ agrees with Equation (2) of Kocharovsky et al. [247] apart from an additional factor $2/\sqrt{3} \approx 1.2$ and an inverse power in the (d_p/λ_*)-term, i.e. $-7/2$. We assume the latter difference to be a typo.

In the outer neutron star core, the repulsive force, $\mathbf{F}_\mathrm{rep}$, is expected to be balanced by various additional forces acting on the fluxtubes. As discussed in detail in Subsection 4.3.3, this should include Magnus force, tension, electromagnetic force and resistive drag due to electron-magnetic-fluxtube scattering. In order to develop an elementary model of the fluxtubes' dynamics and address the influence of the interfluxtube repulsion, we restrict our attention to the resistive force and neglect the former three contributions. The timescales obtained below should hence be taken with a grain of salt, as they could be modified by additional forces. Ignoring the small fluxtube inertia, the averaged force balance reads as

$$\sum \mathbf{F} = -g(\mathcal{N}_\mathrm{p}) \nabla \mathcal{N}_\mathrm{p} - \rho_\mathrm{p} \kappa \mathcal{R} \mathbf{u}_\mathrm{p} = 0, \tag{6.45}$$

where $\mathbf{u}_\mathrm{p}$ denotes the average velocity of a collection of fluxtubes within a fluid element and the rest-frame of the electron-proton conglomerate was chosen as the frame of reference. Since the charged component is coupled to the neutron's crust via the magnetic field, its rest-frame coincides with the rotating frame of the star. As seen in Subsection 6.2.1, the dimensionless drag coefficient $\mathcal{R}$ is altered for different neutron star depths, but it does not directly depend on the fluxtube density. Solving Equation (6.45) for the average velocity, one obtains

$$\mathbf{u}_\mathrm{p} = -\frac{g(\mathcal{N}_\mathrm{p})}{\rho_\mathrm{p} \kappa \mathcal{R}} \nabla \mathcal{N}_\mathrm{p}. \tag{6.46}$$

This relation can be combined with the continuity equation for the surface density, $\mathcal{N}_\mathrm{p}$ (see Equation (4.69)). Under the assumption that fluxtubes cannot be destroyed or created inside a fluid element, we arrive at a non-linear diffusion equation of the form

$$\partial_t \mathcal{N}_\mathrm{p} + \nabla \left(\mathcal{N}_\mathrm{p} \mathbf{u}_\mathrm{p} \right) = \partial_t \mathcal{N}_\mathrm{p} - \nabla \left(\frac{\mathcal{N}_\mathrm{p}\, g(\mathcal{N}_\mathrm{p})}{\rho_\mathrm{p} \kappa \mathcal{R}} \nabla \mathcal{N}_\mathrm{p} \right) = 0. \tag{6.47}$$

Together with suitable boundary and initial conditions, this partial differential equation in principle determines the fluxtube surface density as a function of time and position, i.e. $\mathcal{N}_\mathrm{p} = \mathcal{N}_\mathrm{p}(t, \mathbf{r})$, in the outer neutron star core. However, due to the complicated $\mathcal{N}_\mathrm{p}$-dependence of $g(\mathcal{N}_\mathrm{p})$ and the non-constant drag coefficient, proton density and London penetration depth, finding the solution of Equation (6.47) is far from trivial. Instead of attempting to solve this diffusion problem, we only extract the characteristic timescale for fluxtube motion over a lengthscale L from Equation (6.47) and find

$$\tau_\mathrm{rep} = \frac{L^2 \rho_\mathrm{p} \kappa \mathcal{R}}{\mathcal{N}_\mathrm{p}\, g(\mathcal{N}_\mathrm{p})}. \tag{6.48}$$

In order to obtain a simple estimate for the repulsion timescale, the position-dependence and time-dependence of the fluxtube density can be neglected, which implies that $\mathcal{N}_\mathrm{p}$

B [G]	10^{12}	10^{13}	10^{14}
$\mathcal{N}_{\rm p}$ [cm^{-2}]	5.0×10^{18}	5.0×10^{19}	5.0×10^{20}
$\tau_{\rm rep}$ [yr]	1.2×10^{24}	3.6×10^{10}	6.2×10^{6}

Table 6.1: Characteristic timescales resulting from the interfluxtube repulsion in the outer neutron star core. Estimates are given for three magnetic inductions B, which correspond to different fluxtube surface densities. For higher values of $\mathcal{N}_{\rm p}$, the corresponding distance between individual fluxtubes decreases, which subsequently leads to shorter timescales $\tau_{\rm rep}$. The remaining parameters have been fixed to $L = 10^6\,{\rm cm}$, $\rho = 10^{14}\,{\rm g\,cm^{-3}}$, $x_{\rm p} = 0.05$, $\lambda_* = 10^{-11}\,{\rm cm}$ and $\mathcal{R} = 10^{-2}$, respectively.

is approximately constant and given by Equation (4.7). By choosing the characteristic lengthscale to be equal to the neutron star radius, i.e. $L_6 \equiv L/(10^6\,{\rm cm})$, we calculate

$$\tau_{\rm rep} \approx 5.1 \times 10^{10}\, L_6^2\, \rho_{14} \left(\frac{x_{\rm p}}{0.05}\right) \left(\frac{\mathcal{N}_{\rm p}}{5 \times 10^{18}\,{\rm cm^{-2}}}\right)^{3/4} \left(\frac{\lambda_*}{10^{-11}\,{\rm cm}}\right)^{7/2} \times \left(\frac{\mathcal{R}}{10^{-2}}\right) \exp\left[48.1 \left(\frac{5 \times 10^{18}\,{\rm cm^{-2}}}{\mathcal{N}_{\rm p}}\right)^{1/2} \left(\frac{10^{-11}\,{\rm cm}}{\lambda_*}\right)\right] {\rm s}. \tag{6.49}$$

Typical values for the proton density, penetration depth, dimensionless drag coefficient and fluxtube density have been substituted. The repulsion timescales corresponding to three different averaged magnetic inductions, i.e. $B = 10^{12}, 10^{13}$ and $10^{14}\,{\rm G}$, are quoted in Table 6.1. We note that the estimate for $10^{14}\,{\rm G}$ is several orders of magnitude smaller than the result found in Kocharovsky et al. [247]. While this could, in principle, arise from the inverse power of the $(d_{\rm p}/\lambda_*)$-term in Equation (6.44), the three $\tau_{\rm rep}$-estimates provided by Kocharovsky et al. in the limit $d_{\rm p} \gg \lambda_*$ cannot be reproduced with the equations and parameters given in their paper.

With Equation (6.49) we find the following: For the lowest magnetic field strength, the timescale $\tau_{\rm rep}$ is of the order of $10^{24}\,{\rm yr}$, which greatly exceeds the age of the Universe, so that mutual fluxtube repulsion should not influence the interior dynamics of standard rotation-powered pulsars. However, the timescale drops significantly at higher fields due to the strong $\mathcal{N}_{\rm p}$-dependence in Equation (6.48). For 10^{13} and $10^{14}\,{\rm G}$, the characteristic timescale for fluxtube motion reaches 10^{10} and $10^{6}\,{\rm yr}$, respectively. These estimates are still larger than the field evolution timescales deduced from observations [236, 237, 238, 239], suggesting that the repulsive force in the outer neutron star core should not affect the dynamics. This conclusion is supported by accounting for the density-dependence of the various parameters entering Equation (6.48). Employing, for example, the effective NRAPR equation of state introduced in Subsection 5.1.1, one can include the variation of the parameters $x_{\rm p}$, λ_* and $\mathcal{R}$ and determine the repulsion timescale as a function of the star's total mass density, ρ. As illustrated in Figure 6.6, $\tau_{\rm rep}$ is shortest close to the crust-core interface and strongly increases towards the centre of the star, as it becomes increasingly difficult to distort the fluxtube lattice at higher densities.

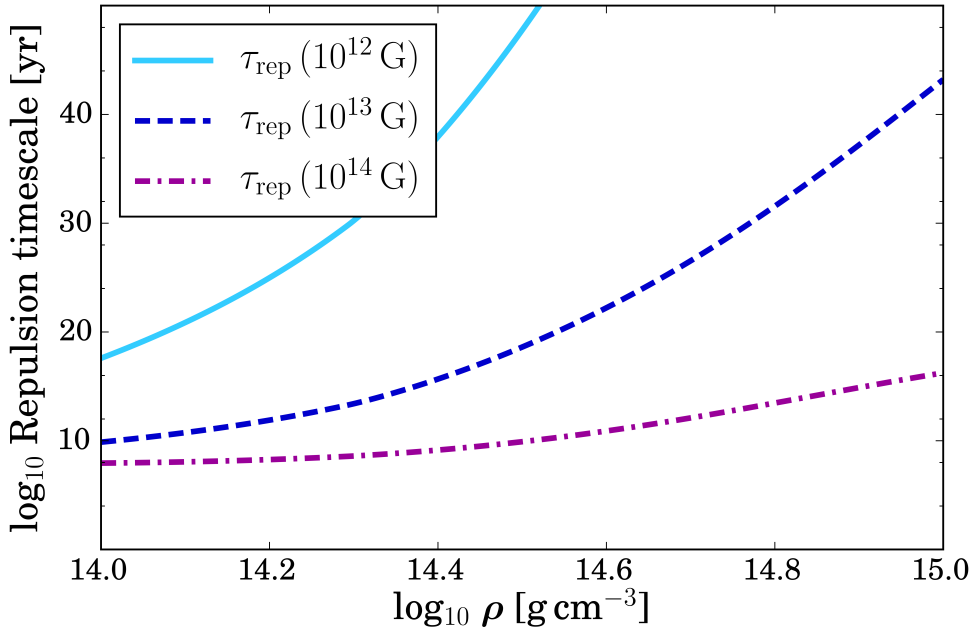

Figure 6.6: Characteristic timescales for fluxtube motion, resulting from balancing inter-fluxtube repulsion and resistive drag, as a function of the total mass density in the neutron star core. The curves represent three magnetic inductions $B = 10^{12}, 10^{13}$ and $10^{14}\,{\rm G}$ and are computed for the NRAPR effective EoS and a characteristic lengthscale of $L = 10^6\,{\rm cm}$.

Nonetheless, the timescale for fluxtube repulsion could be shortened if the resistive drag would be weaker than estimated in Subsection 6.2.1. This has, for example, been suggested by Jones [244]. A decrease in $\mathcal{R}$ by two orders of magnitude would reduce the repulsive timescales at fields $B \gtrsim 10^{13}\,{\rm G}$ to values that would become relevant for neutron star astrophysics. Shorter repulsion timescales could also be obtained by considering different characteristic lengthscales, L. If, for example, magnetic fluxtubes were to be expelled from the 1 km thick layer right below the crust-core boundary, $\tau_{\rm rep}$ would similarly decrease by two orders of magnitude and lead to timescales comparable to the observed ones [236, 237, 238, 239]. Moreover note that for fields $B \gtrsim 10^{14}$, the fluxtube density $\mathcal{N}_{\rm p}$ increases to the point where the initial assumption, $d_{\rm p} \gg \lambda_*$, is no longer valid. In this case, the exponentially decaying force given in Equation (6.44) would have to be replaced by the expression corresponding to $d_{\rm p} \simeq \lambda_*$. This resulting force should, in principle, be stronger and subsequently give shorter timescales. However, this scenario has not been studied yet and needs to be addressed in the future.

Finally we note that the timescale $\tau_{\rm rep}$ does not necessarily describe flux expulsion from a neutron star's core. As the repulsive force acts in the direction opposite to the fluxtube density gradient, suitable magnetic field distributions could drive the fluxtubes towards higher densities or in azimuthal direction. The diffusive rearrangement of flux due to the repulsive interaction of individual fluxtubes does thus not necessarily provide a microscopic explanation for the Meissner effect as stated by Kocharovsky et al. [247].

6.2.3 Buoyancy

The influence of buoyancy on superconducting fluxtubes in the neutron star interior was first studied by Muslimov and Tsygan [249] and Harvey et al. [243]. They noted that the hydrostatic pressure difference between the quantised structures and the surrounding fluids, originating from the magnetic pressure inside the fluxtubes, would locally reduce the plasma density. This in turn creates a radially acting lift force, $f_{\rm b}$, attempting to drive the fluxtubes out of the star's core. The radial motion will further cause the fluxtubes to bend, since their ends are expected to be anchored in the normal-conducting crust [249]. In order to derive an expression for $f_{\rm b}$, two approaches can be used.

On mesoscopic scales, a single fluxtube can be approximated as a normal-conducting cylinder threaded by an average magnetic induction, $\bar{B}_{\rm ft} \simeq \phi_0/(\pi\lambda_*^2)$ [243], because the flux is confined to a circle of radius λ_* around a fluxtube's centre. One can therefore estimate the magnitude of the buoyancy force per unit length of fluxtube as

$$f_{\rm b} = g\pi\lambda_*^2(\rho_{\rm ft} - \rho_{\rm fluid}) \simeq g\pi\lambda_*^2 \frac{{\rm d}\rho}{{\rm d}p}\,\Delta p = \frac{g}{c_{\rm s}^2}\,\pi\lambda_*^2\,\frac{\bar{B}_{\rm ft}^2}{8\pi}, \tag{6.50}$$

where g and $c_{\rm s}^2 \equiv {\rm d}p/{\rm d}\rho$ denote the local gravitational acceleration and speed of sound, respectively. Moreover, the difference in hydrostatic pressure, Δp, is equal to the magnetic pressure inside a fluxtube. In the case of normal matter, one has $P_{\rm mag} = \bar{B}_{\rm ft}^2/8\pi$, which leads to the result given in Equation (12) of Harvey et al. [243]. Further approximating $g/c_{\rm s}^2 \simeq 1/R$, where R is the neutron star radius, Equation (6.50) reduces to

$$f_{\rm b} \simeq \frac{\phi_0^2}{8\pi^2\lambda_*^2 R}. \tag{6.51}$$

Using a macroscopic perspective, the buoyancy force per unit volume can alternatively be calculated from the gradient of the superconducting magnetic pressure, $P_{\rm mag,sc}$ (see for example Jones [246]), which corresponds to the isotropic contribution to the stress tensor of type-II superconducting matter. As first derived by Easson and Pethick [203] in the limit $B \ll H_{\rm c1}$, which also approximates the neutron stars' core (see Subsection 4.1.2), the magnetic pressure is given by $P_{\rm mag,sc} = H_{\rm c1}B/4\pi$ (see also Equation (7.46)). Choosing a lengthscale of the order of the star's radius, R, the magnitude of the buoyancy force per unit volume is found to be

$$F_{\rm b} = |-\nabla P_{\rm mag,sc}| \simeq \frac{H_{\rm c1}B}{4\pi R}. \tag{6.52}$$

The corresponding force per unit length of fluxtube then reads as

$$f_{\rm b} = \frac{F_{\rm b}}{\mathcal{N}_{\rm p}} \simeq \frac{H_{\rm c1}\phi_0}{4\pi R}, \tag{6.53}$$

where $B \simeq \mathcal{N}_{\rm p}\phi_0$ is used. Substituting the lower critical field with Equation (3.82) and

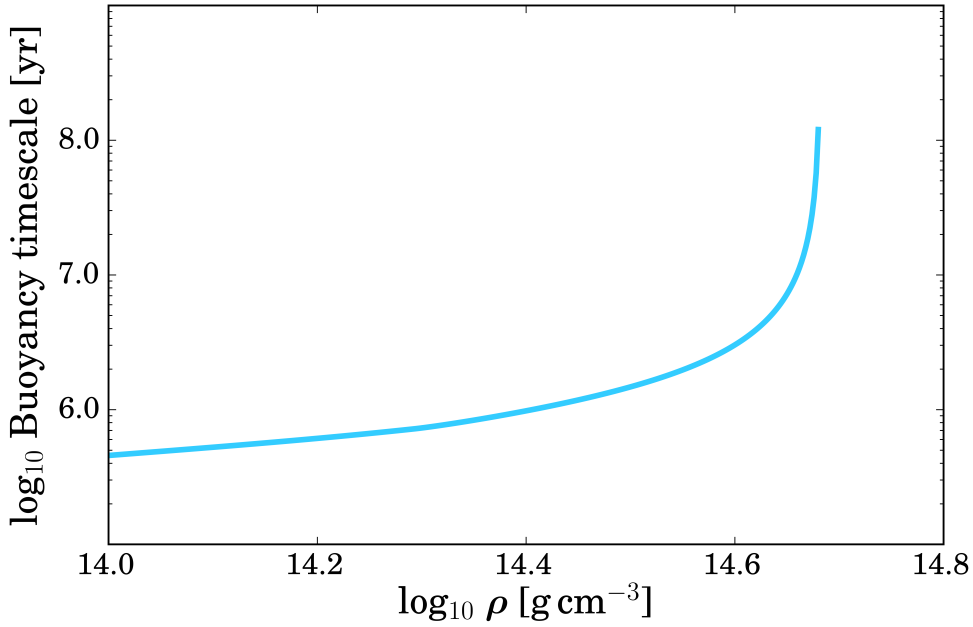

Figure 6.7: Characteristic timescale for fluxtube motion, resulting from a force balance between buoyancy and resistive drag, as a function of the total mass density in the neutron star core. The values are computed for the NRAPR effective EoS and a neutron star radius of $R = 10^6$ cm. Note that the cut-off corresponds to $\lambda_* = \xi_\mathrm{p}$, where τ_b estimates become unphysical due to the presence of a factor $\ln^{-1}(\lambda_*/\xi_\mathrm{p})$ in Equation (6.56).

replacing the fluxtube energy per unit length, $\mathcal{E}_\mathrm{p}$, with Equation (4.56), one is left with

$$f_\mathrm{b} \simeq \frac{\mathcal{E}_\mathrm{p}}{R} = \frac{\phi_0^2}{16\pi^2\lambda_*^2 R} \ln\left(\frac{\lambda_*}{\xi_\mathrm{p}}\right). \tag{6.54}$$

An equivalent relation for the buoyancy force was originally quoted by Muslimov and Tsygan [249]. It illustrates that f_b is of similar order as the macroscopic average of the tension force given in Equation (4.79), if the fluxtubes' curvature radius is of the order of R. Employing again the approximation $\ln(\lambda_*/\xi_\mathrm{p}) \approx 2$ [113], Equation (6.54) reduces to the result (6.51) obtained from mesoscopic considerations.

In order to quantify the influence of the buoyancy force on the fluxtube dynamics, we use the same approach as in the last subsection and balance the lift force by the resistive drag arising from electron-magnetic-fluxtube scattering but neglect any additional mechanisms. In this steady-state scenario, where buoyancy tries to push fluxtubes out of the neutron star core and the drag slows down the expulsion, the magnitude of the fluxtube velocity is given by

$$u_\mathrm{p} = \frac{\mathcal{E}_\mathrm{p}}{R\rho_\mathrm{p}\kappa\mathcal{R}}. \tag{6.55}$$

Note that we again work in the rest-frame of the electron-proton component. Together with the continuity equation (4.69) for the fluxtube surface density, $\mathcal{N}_\mathrm{p}$, Equation (6.55) similarly defines a diffusion problem. Extracting the corresponding timescale gives

$$\tau_{\rm b} = R^2 \rho_{\rm p} \kappa \mathcal{R} \, \frac{16\pi^2 \lambda_*^2}{\phi_0^2 \ln(\lambda_*/\xi_{\rm p})}. \tag{6.56}$$

Substituting Equation (4.42) for the penetration depth and approximating $\ln(\lambda_*/\xi_{\rm p}) \approx 2$ and $m_{\rm n}^* \approx m$, one obtains the following estimate for typical neutron star parameters,

$$\tau_{\rm b} \approx 3.1 \times 10^{13} \left(\frac{m_{\rm p}^*}{m}\right) R_6^2 \left(\frac{\mathcal{R}}{10^{-2}}\right) \, {\rm s}, \tag{6.57}$$

where $R_6 \equiv R/(10^6\,{\rm cm})$. A comparable result should have, in principle, been obtained by Harvey et al. [243], who apply the same force balance as described above. However, they quote a timescale of $10^9\,{\rm yr}$, caused by a computational error. Moreover, Muslimov and Tsygan [249] give a fluxtube drift timescale that is two orders of magnitude smaller than our estimate (6.57) due to an erroneous, temperature-dependent drag in the force balance. The full density-dependent behaviour is shown in Figure 6.7, illustrating that the buoyancy timescale increases from about $10^6\,{\rm yr}$ close to the crust-core interface to $10^8\,{\rm yr}$ at $\rho \sim 4.8 \times 10^{14}\,{\rm g\,cm^{-3}}$, where $\tau_{\rm b}$ has been cut off. Above this density, the proton coherence length exceeds the modified penetration depth, which gives complex and unphysical timescales due to the factor $\ln^{-1}(\lambda_*/\xi_{\rm p})$ in Equation (6.56).

Whereas values of the order of 10^6 to $10^8\,{\rm yr}$ are close to the magnetic field evolution timescales invoked for rotation-powered pulsars [236, 237], self-consistent magneto-thermal simulations of superconducting neutron star cores by Elfritz et al. [250] have recently shown that buoyancy is too weak to account for magnetic flux expulsion from the stars' interior. Finally note that Harrison [242] has argued that the estimate (6.57) should be further lengthened since fluxtubes cannot be considered as individual buoyant structures. Treating the entire array, similar to the argument by Jones for the resistive drag [244], the drift velocity caused by buoyancy is negligible due to the lattice rigidity.

6.2.4 Pinning

Finally, the short-range interaction between fluxtubes and vortices is briefly addressed. While approximate descriptions of this *pinning* process have been studied by numerous authors [251, 188, 206, 252], a microscopic formulation is not available yet. Hence, in the following, the implications of this coupling mechanism are examined from a phenomenological point of view. A more detailed analysis of possible effects on the neutron star magnetic field will be left for future work. Note that the rotational evolution should be similarly influenced by core pinning, which has been neglected in Section 5.1.

Pinning force

To study the pinning mechanism in more detail, an expression for the interaction energy needs to be derived. This can be achieved by generalising the formalism for isolated vortices and fluxtubes discussed in Appendix A of Glampedakis et al. [181], which has

previously been employed in Subsections 4.3.2 and 4.3.3, to the case of two interacting structures. If the vortex and the fluxtube are positioned at $\mathbf{r}_\mathrm{v}$ and $\mathbf{r}_\mathrm{ft}$, respectively, and the mesoscopic quantisation conditions and Ampère's law are modified accordingly, the generalised London equation for the combined mesoscopic induction, $\bar{\mathbf{B}}_\mathrm{c}$, reads as

$$\lambda_*^2 \nabla^2 \bar{\mathbf{B}}_\mathrm{c} - \bar{\mathbf{B}}_\mathrm{c} = -\phi_0 \hat{\boldsymbol{z}} \left[\delta(\mathbf{r} - \mathbf{r}_\mathrm{ft}) - \frac{\varepsilon_\mathrm{p}}{1-\varepsilon_\mathrm{n}} \delta(\mathbf{r} - \mathbf{r}_\mathrm{v}) \right]. \tag{6.58}$$

Note that it has been assumed that the vortex and the fluxtube are orientated along the z-direction. In the simplest case, both structures should be superimposed and aligned with the z-axis, i.e. $\mathbf{r}_\mathrm{v} = \mathbf{r}_\mathrm{ft} = 0$. A comparison with Equation (4.41) and the individual mesoscopic inductions presented in Equation (4.43) leads to the following solution

$$\bar{\mathbf{B}}_\mathrm{c}(r) = \frac{\phi_0}{2\pi\lambda_*^2} \frac{1-\varepsilon_\mathrm{n}-\varepsilon_\mathrm{p}}{1-\varepsilon_\mathrm{n}} K_0\left(\frac{r}{\lambda_*}\right) \hat{\boldsymbol{z}}. \tag{6.59}$$

One can subsequently obtain the energy per unit length, $\mathcal{E}_\mathrm{c}$, of the superimposed vortex-fluxtube configuration by following the procedure given in Glampedakis et al. [181]. The interaction energy is then found by subtracting the energy per unit length of an isolated vortex and fluxtube, $\mathcal{E}_\mathrm{n}$ and $\mathcal{E}_\mathrm{p}$, respectively. We note that the kinetic contributions to $\mathcal{E}_\mathrm{c}$ are exactly cancelled by the kinetic energies of an isolated vortex and fluxtube, which were approximated in Equations (4.55) and (4.56). Therefore, pinning arises primarily from the magnetic interaction of the quantised structures. Integrating the respective magnetic energy densities over a surface perpendicular to the z-axis, we find

$$\mathcal{E}_\mathrm{pin} \simeq \frac{1}{8\pi} \int \left(\bar{\mathbf{B}}_\mathrm{c}^2 - \bar{\mathbf{B}}_\mathrm{n}^2 - \bar{\mathbf{B}}_\mathrm{p}^2\right) \mathrm{d}S = -\frac{\phi_0^2}{16\pi^3\lambda_*^4} \frac{\varepsilon_\mathrm{p}}{1-\varepsilon_\mathrm{n}} \int K_0^2\left(\frac{r}{\lambda_*}\right) \mathrm{d}S. \tag{6.60}$$

Ignoring the detailed structure of the vortex and the fluxtube core by introducing the standard cut-off at the coherence length, $\xi \equiv \xi_\mathrm{p} \simeq \xi_\mathrm{n}$, the surface integral can be easily evaluated. Choosing an upper limit $r \gg \lambda_*$, the Bessel functions decay exponentially and the corresponding contributions far away from the vortex/fluxtube can be ignored. One is therefore left with

$$\mathcal{E}_\mathrm{pin} \simeq \frac{\phi_0^2}{8\pi^2\lambda_*^4} \frac{\varepsilon_\mathrm{p}}{1-\varepsilon_\mathrm{n}} \frac{\xi^2}{2} \left[K_0^2\left(\frac{\xi}{\lambda_*}\right) - K_1^2\left(\frac{\xi}{\lambda_*}\right) \right]. \tag{6.61}$$

Since $\xi \lesssim \lambda_*$ (see Subsection 4.1.2 for typical estimates), we obtain the following pinning energy per unit length to leading order in ξ/λ_*,

$$\mathcal{E}_\mathrm{pin} \simeq -\frac{\phi_0^2}{16\pi^2\lambda_*^4} \frac{\varepsilon_\mathrm{p}}{1-\varepsilon_\mathrm{n}} \lambda_*^2 \simeq \frac{\bar{B}_\mathrm{ft}\bar{B}_\mathrm{v}\lambda_*^2}{16}, \tag{6.62}$$

with $\bar{B}_\mathrm{ft} \simeq \phi_0/(\pi\lambda_*^2)$, $\bar{B}_\mathrm{v} \simeq \phi_\mathrm{n}/(\pi\lambda_*^2)$ being the typical mesoscopic fluxtube and vortex induction, respectively. We note that the pinning energy obtained in Equation (6.62) differs from the standard result of Ruderman et al. [188] or Ding et al. [251] by a factor

$2\pi \ln(\lambda_*/\xi) \approx 4\pi$, where the logarithm is approximated in the standard way [113]. The origin of this discrepancy is not clear because the three mesoscopic magnetic inductions used in the derivation above are equivalent to the expressions found in Appendix A of Ruderman et al [188]. In particular the $\ln(\lambda_*/\xi)$-proportionality seems surprising, since the vortex and the fluxtube field exhibit the same logarithmic dependence for small r (see Equation (4.45)). Thus, one would expect a contribution from both magnetic fields, ultimately resulting in a term $\ln^2(\lambda_*/\xi)$. In the following, we will use Equation (6.62).

In order to connect the pinning energy per unit length, $\mathcal{E}_{\rm pin}$, with the total pinning energy, $E_{\rm pin}$, per vortex-fluxtube intersection, $\mathcal{E}_{\rm pin}$ has to be multiplied with the overlap length, l. A closer look at the corresponding pinning geometry illustrated in Figure 6.8 shows that $l = 2\lambda_*/\sin\beta$, where β is the angle between the local vortex and fluxtube direction. Neglecting for simplicity the possibility of tangled states in the neutron star core condensates, the respective arrays are straight, implying that β corresponds to the misalignment angle between the star's rotation and its magnetic axes on large scales. This illustrates that the pinning mechanism is strongest if the vortices and fluxtubes are parallel, while the interaction is weakest for $\beta = \pi/2$. To avoid additional complications, we will restrict the following discussion to the latter case. Hence, a minimum estimate for the pinning energy per vortex-fluxtube intersection is given by

$$E_{\rm pin} = \mathcal{E}_{\rm pin} l \simeq \frac{\bar{B}_{\rm ft}\bar{B}_{\rm v}\lambda_*^3}{8}. \tag{6.63}$$

For typical neutron star parameters, this can be estimated to

$$E_{\rm pin} \approx 25.9 \left(1 - \frac{m_{\rm p}^*}{m}\right) \left(\frac{m}{m_{\rm p}^*}\right)^{1/2} \rho_{14}^{1/2} \left(\frac{x_{\rm p}}{0.05}\right)^{1/2} \text{MeV}, \tag{6.64}$$

where $m_{\rm n}^* \approx m$ has been used. We can additionally compare this estimate to the pinning interaction arising from perturbations of the proton density in the centre of a fluxtube. According to Sauls [40], the corresponding pinning energy per intersection is

$$E_{\rm pin,\,Sauls} \simeq n_{\rm n} \frac{\Delta_{\rm p}^2}{E_{\rm Fp}^2} \frac{\Delta_{\rm n}^2}{E_{\rm Fn}} \xi_{\rm n}^2 \xi_{\rm p} = n_{\rm n} \frac{8}{\pi^3} \left(\frac{m}{m_{\rm n}^*}\right)^2 \left(\frac{m}{m_{\rm p}^*}\right) \frac{\Delta_{\rm p}}{k_{\rm Fp}^3}. \tag{6.65}$$

Here, $n_{\rm n}$ represents the neutron number density and $\Delta_{\rm x}$ and $E_{\rm Fx}$ denote the energy gap and Fermi energy of the neutrons and protons, respectively. Using canonical estimates (see Subsections 5.1.1 and 5.1.2) together with $m_{\rm n}^* \approx m$ and $x_{\rm n} \approx 1$ subsequently gives

$$E_{\rm pin,\,Sauls} \approx 3.7 \times 10^{-2} \left(\frac{m}{m_{\rm p}^*}\right) \rho_{14} \left(\frac{\Delta_{\rm p}}{1\,\text{MeV}}\right) \left(\frac{0.75\,\text{fm}^{-1}}{k_{\rm Fp}}\right)^3 \text{MeV}. \tag{6.66}$$

This demonstrates that the magnetic interaction is several orders of magnitude larger, thus dominating the coupling between the neutron vortices and the proton fluxtubes.

Based on Equation (6.63), the pinning force per intersection, $\mathcal{F}_{\rm pin}$, can be calcula-

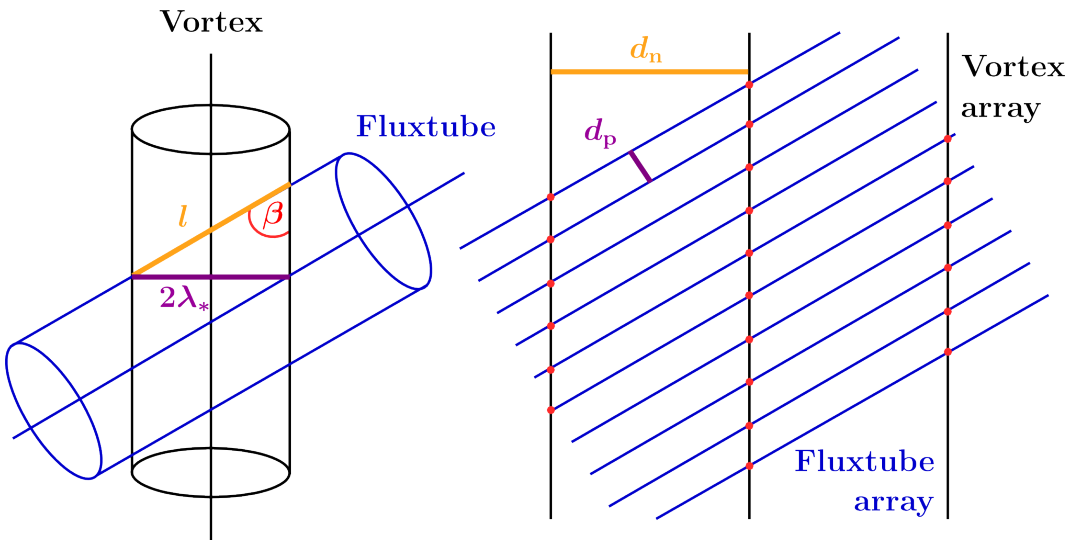

Figure 6.8: Sketch of the pinning geometry. On the left, a single vortex-fluxtube intersection is shown. Both quantised structures are represented as cylinders of radius λ_*. The overlap length l is thus fixed if the angle β between the vortex and the fluxtube is known. The right figure illustrates the macroscopic geometry of two interpenetrating arrays. Since $\mathcal{N}_p \gg \mathcal{N}_n$, the intervortex spacing d_n is much larger than the interfluxtube separation d_p. For $\beta = \pi/2$, the distance between two neighbouring vortex-tube intersections, given as red dots, is equal to d_p, which can be used to estimate the vortex pinning force.

ted. Since the mesoscopic magnetic inductions of both quantised structures are shielded over lengthscales of the order of the penetration depth, the pinning interaction is only *active* when the vortex-fluxtube separation is less than λ_*. The associated force is hence

$$\mathcal{F}_{\rm pin} \simeq \frac{E_{\rm pin}}{\lambda_*} = \frac{\bar{B}_{\rm ft}\bar{B}_{\rm v}\lambda_*^2}{8}, \tag{6.67}$$

which can be approximated as

$$\mathcal{F}_{\rm pin} \approx 0.2\left(1-\frac{m_{\rm p}^*}{m}\right)\left(\frac{m}{m_{\rm p}^*}\right)\rho_{14}\left(\frac{x_{\rm p}}{0.05}\right)\ {\rm MeV\,fm^{-1}}. \tag{6.68}$$

In order to study how the pinning interaction affects the interior magnetic field, the physics of a single vortex-fluxtube junction has to be generalised to the full lattice structures by using appropriate averages. Following Link [206], one can take advantage of $\mathcal{N}_p \gg \mathcal{N}_n$ as given in Equations (4.6) and (4.7) to easily determine the macroscopic pinning force on the neutron vortex array. Since the intervortex spacing d_n is much larger than the interfluxtube spacing d_p, we limit our attention to an individual vortex immersed into a large number of fluxtubes. The distance between two neighbouring intersections is then equivalent to d_p for $\beta = \pi/2$ as shown in Figure 6.8, allowing one to approximate the pinning force per unit length of neutron vortex as

$$f_{\rm pin,n} = \frac{\mathcal{F}_{\rm pin}}{d_p} \simeq \mathcal{N}_p^{1/2}\mathcal{F}_{\rm pin} = \mathcal{N}_p^{1/2}\,\frac{\bar{B}_{\rm ft}\bar{B}_{\rm v}\lambda_*^2}{8}. \tag{6.69}$$

The pinning force density for the full vortex lattice is found in the standard way, i.e.

$$F_{\rm pin,n} = \mathcal{N}_{\rm n} f_{\rm pin,n} = \mathcal{N}_{\rm n} \mathcal{N}_{\rm p}^{1/2} \, \frac{\bar{B}_{\rm ft} \bar{B}_{\rm v} \lambda_*^2}{8}. \tag{6.70}$$

The equivalent averaging procedure cannot be translated to a single fluxtube immersed into the vortex array. Instead, we have to invoke the macroscopic dynamics of the two interacting arrays. More precisely, Newton's third law dictates that the fluxtube lattice experiences the force $F_{\rm pin,p} = -F_{\rm pin,n}$. The corresponding pinning force per unit length of a fluxtube is, hence, given by

$$f_{\rm pin,p} = \frac{F_{\rm pin,p}}{\mathcal{N}_{\rm p}} = -\frac{\mathcal{N}_{\rm n}}{\mathcal{N}_{\rm p}} f_{\rm pin,n} = \frac{\mathcal{N}_{\rm n}}{\mathcal{N}_{\rm p}^{1/2}} \, \frac{\bar{B}_{\rm ft} \bar{B}_{\rm v} \lambda_*^2}{8}. \tag{6.71}$$

Note that $f_{\rm pin,p}$ is many orders of magnitude smaller than $f_{\rm pin,n}$ as a result of the huge fluxtube surface density, $\mathcal{N}_{\rm p}$ (see also Glampedakis et al. [181]). We also point out that (apart from the factor 4π) Equation (6.71) is equivalent to the force density $F_{\rm pin,p}$ given in Appendix A of Ruderman et al. [188] if the lengthscales satisfy $\lambda_* \simeq d_{\rm p}$. As shown in Section 4.1, this is generally true in the outer neutron star core.

Implications

As a result of the short-range vortex-fluxtube interaction, the neutron stars' rotational and magnetic field evolution are strongly correlated, since in the presence of pinning the quantised structures move at the same velocity. It is reasonable to further assume that the fluxtubes, carrying the core magnetic field, follow the proton fluid's motion, leading to $\mathbf{u}_{\rm n} = \mathbf{u}_{\rm p} \simeq \mathbf{v}_{\rm p}$, where $\mathbf{u}_{\rm n}$ and $\mathbf{u}_{\rm p}$ denote the averaged vortex and fluxtube velocities, respectively, and $\mathbf{v}_{\rm p}$ represents the macroscopic flow of the proton component. For an isolated neutron star, which spins down electromagnetically, the rotational velocity of the crust and the charged plasma in the interior decreases continuously, which implies in turn that the vortex and fluxtube velocity will also be altered. However, this change is not communicated to the interior neutron fluid, subsequently exhibiting a different flow velocity, $\mathbf{v}_{\rm n}$. This naturally results in a Magnus force of the form (4.78) acting on the neutron vortices, which tends to move them out of the core. Assuming that vortices and fluxtubes are uniformly distributed throughout the star and approximately straight, one can balance this lift force with the pinning force given in Equation (6.69) and estimate the minimum velocity lag $w_{\rm c}$ between the neutron and proton components below which the pinning interaction is *active*,

$$w_{\rm c} \simeq \frac{f_{\rm pin,n}}{\rho_{\rm n} \kappa} = \mathcal{N}_{\rm p}^{1/2} \, \frac{\bar{B}_{\rm ft} \bar{B}_{\rm v} \lambda_*^2}{8 \rho_{\rm n} \kappa}. \tag{6.72}$$

For typical neutron star parameters, we can approximate this as

$$w_{\rm c} \approx 3.5 \times 10^4 \left(1 - \frac{m_{\rm p}^*}{m}\right) \left(\frac{m}{m_{\rm p}^*}\right) \left(\frac{x_{\rm p}}{0.05}\right) B_{12}^{1/2} \, {\rm cm \, s^{-1}}. \tag{6.73}$$

Below this value, which is not directly dependent on the neutron star mass density, the Magnus force is not strong enough to exceed the pinning force and vortices and fluxtubes remain pinned. Therefore, the two arrays move together and their evolution is strongly coupled. As the stars' spin-down is also associated with a decrease in the vortex density, implying that they move radially outwards, the fluxtubes will be dragged along. Several studies analysing the dynamics of this interpinning regime and the implications for the magnetic field of neutron stars can be found in the literature [251, 215, 188, 189]. The general conclusion is that the pinning interaction is strong enough to allow the vortices to drag fluxtubes towards the crust-core interface, where the field decay is subsequently governed by the crustal physics. The inverse process has further been invoked as an explanation for the weak magnetic fields ($B < 10^{10}\,\mathrm{G}$) of millisecond pulsars [215]. As these objects are thought to be spun up by accretion from their binary companion, an increase in the rotation frequency would result in vortex motion towards the rotation axis, dragging fluxtubes along and effectively burying the magnetic flux in the interior.

If, however, the critical lag is exceeded, the Magnus force would be stronger than the short-range magnetic force and pinning would no longer take place. Instead, vortices would cut through the fluxtubes; a dissipation mechanisms thought to be very effective. Similar to the neutron star crust (see Subsection 5.2.3), where vortex motion past the crustal lattice nuclei was observed to dissipate energy through the excitation of vortex waves, the cutting process in the outer neutron star core could result in the excitation of Kelvin waves propagating along the vortices. The associated energy release per vortex-fluxtube cutting event was first calculated by Link [206] by generalising the formalism of Epstein and Baym [227], discussed previously. Link showed that the vortex-fluxtube cutting is highly dissipative, which implies that any relative motion between the vortices and the fluxtubes is strongly damped and the pinned configuration is likely to represent the equilibrium state. Whereas it has been proposed that this mechanism should have important implications for the rotational characteristics as it would, for example, forbid neutron star precession with periods of the order of years [206] and affect the amplitude of Coriolis driven r-mode oscillations [252], it is not clear how vortex-fluxtube cutting would affect the stars' magnetic field. To determine, if this mechanism could for instance result in magnetic field decay on observable timescales, further studies are needed.

6.3 Discussion

This chapter aimed at providing an overview of several mechanisms affecting the superconducting proton component in a neutron star's interior and implications for its magnetic field. A discussion of the two seminal papers by Baym et al. [45, 193] illustrated that standard Ohmic dissipation, restricted to the normal-conducting fluxtube cores, could not result in observable field evolution. Subsequently, additional fluxtube coupling processes were discussed. As many different suggestions can be found in the literature,

we restricted our attention to four specific examples, namely standard resistivity arising from electron-magnetic-fluxtube scattering, mutual fluxtube repulsion, buoyancy and pinning to the neutron vortices. Since the former mechanism could be represented as a drag of the form (4.81) on mesoscopic lengthscales, it was possible to determine the corresponding macroscopic mutual friction coefficients using the framework introduced in Subsection 5.1.3. Note that the interaction was found to be weak and its effects on the stars' magnetic field are studied in detail in the next chapter. The repulsive and the buoyancy force, on the other hand, do not resemble a standard drag force and are therefore not intrinsically dissipative. Instead, these forces act to redistribute the fluxtubes in the outer core, potentially driving them towards the neutron star crust, where standard Ohmic decay timescales are much shorter and the field could thus evolve on observable timescales [231]. In order to assess the importance of these two mechanisms, steady-state situations between the respective forces and the resistive drag were analysed. In both cases a non-trivial diffusion equation was derived, allowing one to extract the characteristic timescales, which have been estimated for the neutron star core using a typical equation of state. We obtain that the timescales associated with interfluxtube repulsion and buoyancy are shortest at low densities, close to the crust-core interface, reaching a minimum of the order of 10^7 yr and 10^5 yr, respectively, increasing by many orders of magnitude towards the inner core. These estimates suggest that the two mechanisms could, in principle, be strong enough to drive fluxtubes out of a star's core. However, large uncertainties in the parameters entering the respective timescales make it difficult to judge whether the repulsive and the buoyancy force would indeed play a role in the neutron star magnetic field evolution and more detailed calculations accounting for all the fluxtube processes would be needed. Finally, pinning caused by the magnetic short-range interaction between vortices and fluxtubes was briefly addressed. We have derived the corresponding pinning force and discussed several implications on the stars' magnetic field, but did not study the effects in detail. Thus, future calculations will be needed to provide conclusive information on the influence of the pinning interaction on the macroscopic magnetic induction.

We also point out that other mechanisms have been proposed to affect the neutron star magnetic field evolution. One scenario that could be important is *ambipolar diffusion*. This process, first considered by Goldreich and Reisenegger [231], describes the motion of the charged conglomerate and the magnetic field relative to the neutron component. While generally considered unimportant for standard rotation-powered pulsars, this diffusion mechanism could be able to push the fluxtubes out of the cores of magnetars, potentially explaining the high activity of these objects as invoked by Thompson and Duncan [238]. However, recent work by Glampedakis et al. [253] suggests that the timescale for ambipolar diffusion could be significantly lengthened when the quantum nature of the neutrons and the protons is taken into account.

Further note that the analysis performed in this chapter relied on the presence of

a type-II superconducting proton fluid, whose existence was postulated by Baym et al. [45] as a result of the high electrical conductivity of normal-conducting nuclear matter. However as explained previously, associating this process with the Meissner effect is misleading, since the latter only describes the exponential shielding of an equilibrium magnetic field but does not provide a microscopic explanation for the formation of the superconducting phase. One could for example imagine that, as the neutron star cools down and it becomes energetically favourable for a spherical shell in the outer core to turn superconducting, flux cannot be pushed into the inner core as a result of the high conductivity but instead has to be moved towards the crust-core interface. This would effectively leave a flux-free core behind. Alternatively, we could invoke the analogy with terrestrial superconductors, where very rich, irregular flux distributions with alternating normal-conducting, type-I or type-II regions have been observed (see for example Babaev et al. [254] and Subsection 8.3.2 for more information). There have indeed been arguments from observational [206, 232, 68] and theoretical [255, 256, 177] studies that raise doubts on the scenario of purely type-II superconducting outer neutron star cores in favour of mixed type-II/type-I phases. The dynamics and frictional mechanisms in this state have been studied by Sedrakian [257] and Jones [258], arriving, however, at rather different dissipation strengths. These uncertainties make clear that in order to improve our understanding of the neutron star phase transition, the exact nature of the superconductor in the core and the associated frictional mechanisms, additional calculations are needed.

Nonetheless, detailed knowledge of the core dynamics does not necessarily provide conclusive information about the evolution of the neutron star magnetic field. As will be explained in the next chapter, the boundary of the proton superconductor is not well defined, the main reason for this being the poorly understood physics of the crust-core interface and the inner core transition, which significantly complicates an analysis of the combined field evolution for the neutron stars' crust and core. A current sheet at the crust-core transition could, for example, be shielding the entire core dynamics from the outer layer, effectively reducing magnetic field evolution to a process governed by the crustal physics only. These aspects clearly highlight numerous problems with consistently modelling a star's magnetic properties. While one possible path to improving neutron star models, more precisely the rigorous derivation of an induction equation for type-II superconducting matter, will be presented in the next chapter, several other crucial pieces of physics are still missing from our current understanding of the neutron star magnetism and remain to be addressed in the future.

Chapter 7

Magnetic Field Evolution in Superconducting Neutron Stars

Having addressed several mechanisms affecting the neutron stars' fluxtubes, the evolution of the large-scale magnetic field is studied in this chapter. Measured field strengths, generally inferred from the stars' dipole spin-down, by far exceed the strengths of terrestrial magnets. As discussed in Subsection 2.3.2, magnetic fields range from 10^8 G for millisecond pulsars up to 10^{15} G for magnetars. Unsurprisingly, such enormous strengths suggest that magnetic fields are crucial for the neutron stars' dynamics. As first pointed out by Thompson and Duncan [238, 239], the rotational energy of magnetars is not sufficient to explain the observed emission; instead magnetic field decay on a timescale of $\sim 10^4$ yr could power the high activity in these objects. There are further observations indicating that the magnetic dipole fields of standard pulsars evolve on a timescale of the order of 10^7 yr [236, 237]. Thus, understanding the long-term evolution of the stars' magnetic fields might be key to establishing connections between the different species and forming a unified picture of the neutron star *zoo* [3, 67, 68].

The problem of magnetic field evolution in isolated neutron stars has been discussed by a number of authors. Goldreich and Reisenegger [231] determined several mechanisms that are present in an ionised plasma consisting of neutrons, protons and electrons. *Ohmic diffusion* due to the interactions of relativistic electrons and lattice nuclei causes magnetic field dissipation in the crust. This mechanism is most effective on small scales and, thus, not expected to affect the large-scale evolution of the crustal field. However, Ohmic decay could be enhanced by *Hall drift*, which is in itself conservative but may redistribute magnetic energy from large to gradually smaller lengthscales. The combined effect, sometimes referred to as the Hall cascade, could cause field evolution on a timescale of the order of 10^7 yr [231]. However, recent neutron star crust simulations show no strong cascading behaviour but suggest the existence of a quasi-equilibrium established on timescales shorter than the Ohmic timescale [259, 233, 260]. In the core, standard Ohmic decay is negligible because the interior is expected to form

a type-II superconductor [45]. As was discussed in detail in Section 6.1, electron-proton scattering, already acting on very long timescales in a star's interior [193], is restricted to the normal conducting cores of fluxtubes, which only contribute a very small fraction to the stars' total cross-section. Hence, the coupling timescale is increased further, making this dissipation mechanism irrelevant. Additionally, *ambipolar diffusion*, describing the motion of charged particles and magnetic field lines relative to the neutrons, could cause field decay and drive the flux from the core to the crust [231]. This mechanism was considered by Thompson and Duncan [238] to explain the high activity of magnetars. However, more recent results seem to indicate that the timescale for ambipolar diffusion considerably increases when the superfluid nature of the neutrons or proton superconductivity is taken into account [253].

In addition to poorly understanding the mechanisms that could cause the magnetic field to change on the order of the stars' spin-down timescales, there is no definitive answer to the question of which part of the neutron star dominates the magnetic field evolution. Most theoretical studies and numerical simulations focus on the crust as the source of the field decay and neglect the core contribution [232, 68, 233]. Nevertheless, one could argue that the core, which carries the majority of the star's inertia and magnetic energy, should also play a role. Recent simulations for the combined evolution of both neutron star layers by Elfritz et al. [250] indeed indicate that the core slows down the crustal evolution, effectively bringing the magnetic field decay to a halt. Lacking a clear answer, the problem of neutron star magnetic field evolution is revisited here.

The following chapter is based on recent work by Graber et al. [261]. We focus on the outer core and consider a magnetic field generated in this region of the star. Using the multi-fluid formalism of Glampedakis et al. [181], presented in detail in Chapter 4, magnetic field evolution in a superconducting neutron star is studied. The presence of fluxtubes influences the star's magnetic properties since the flux is no longer locked to the charged plasma but mainly confined inside the fluxtubes. As standard coupling mechanisms, like Ohmic dissipation, are suppressed as a result of pairing, interactions of fluxtubes with their surroundings determine the magnetic field evolution on macroscopic scales. The most prominent of these effective coupling processes is the scattering of electrons off the fluxtube magnetic field [205, 182, 200]. Considering this mutual friction mechanism and using the standard resistive magnetohydrodynamics (MHD) framework, briefly summarised in Section 7.1, an evolution equation for the neutron star magnetic field is derived in Section 7.2. This is followed by a discussion in Section 7.3.

7.1 Field Evolution in Standard MHD

Before addressing the more complicated problem of magnetic field evolution in a superfluid and superconducting mixture, the approach taken in normal resistive matter is reviewed. By considering a charged, two-component plasma consisting of highly relati-

vistic electrons and non-relativistic protons, key notions of magnetohydrodynamics are introduced. This will allow us to compare a well-studied model with the new results of the next section. Note that tensor notation is again employed in this chapter.

7.1.1 MHD induction equation

In the charged plasma, the only relative flow present is the motion between the electrons and the protons. It is then straightforward to assume that a frictional mechanism would damp these dynamics and try to bring the two components into comotion. Hence, resistive coupling between the ultra-relativistic electrons and non-relativistic protons, acting on a timescale $\tau_{\rm v}$, leads to a dissipative electron force density,

$$F^i_{\rm e} = \frac{n_{\rm e} E_{\rm Fe}}{c^2 \tau_{\rm v}} w^i_{\rm ep} = -\frac{\hbar k_{\rm Fe}}{ce\tau_{\rm v}} j^i, \tag{7.1}$$

where $E_{\rm Fe}$ and $k_{\rm Fe}$ are the electron Fermi energy (see also Equation (5.12)) and Fermi wave number, respectively, and the electron rest-mass term has been neglected because $m_{\rm e} \ll m$. As before, m is the baryon mass. Moreover, the relative velocity $w^i_{\rm ep}$ is related to the electromagnetic current density j^i via Equation (4.30) and charge neutrality, i.e. $n_{\rm p} = n_{\rm e}$, has been used. Substituting $F^i_{\rm e}$ into the electron Euler equation (4.96) provides an expression for the macroscopic electric field, i.e. a generalised Ohm's law of the form

$$E^i = -\frac{1}{c}\,\epsilon^{ijk}\left(v^{\rm p}_j - \frac{j_j}{e n_{\rm p}}\right) B_k - \frac{m_{\rm e}}{e}\nabla^i \tilde{\Phi}_{\rm e} + \frac{j^i}{\tilde{\sigma}_{\rm e}}, \tag{7.2}$$

where $\tilde{\Phi}_{\rm e} \equiv \tilde{\mu}_{\rm e} + \Phi$ is the combined specific chemical and gravitational potential and the standard conductivity for the relativistic electron fluid is defined by

$$\tilde{\sigma}_{\rm e} \equiv \frac{n_{\rm e} e^2 c \tau_{\rm v}}{\hbar k_{\rm Fe}}. \tag{7.3}$$

Equation (7.2) similarly holds for the non-relativistic case, if the electrical conductivity is modified accordingly [262]. Additionally, Ohm's law can be combined with Faraday's law (4.95) to give an evolution equation for the magnetic induction, B^i. Using Ampère's law for normal matter (4.93) to eliminate the current density j^i, one has

$$\partial_t B^i = \epsilon^{ijk}\nabla_j\,\epsilon_{klm}\left[v^l_{\rm p} B^m - \frac{c^2}{4\pi\tilde{\sigma}_{\rm e}}\nabla^l B^m - \frac{mc}{4\pi e\rho_{\rm p}}\,\epsilon^{lsp}\left(\nabla_s B_p\right) B^m\right]. \tag{7.4}$$

The second and the third terms on the right-hand side of the induction equation represent the Ohmic decay and the Hall evolution, which can be associated with the following well-known timescales,

$$\tau_{\rm Ohm} = \frac{4\pi\tilde{\sigma}_{\rm e} L^2}{c^2}, \qquad \tau_{\rm Hall} = \frac{4\pi e\rho_{\rm p} L^2}{mcB}. \tag{7.5}$$

Here, L represents the characteristic lengthscale over which the magnetic field changes.

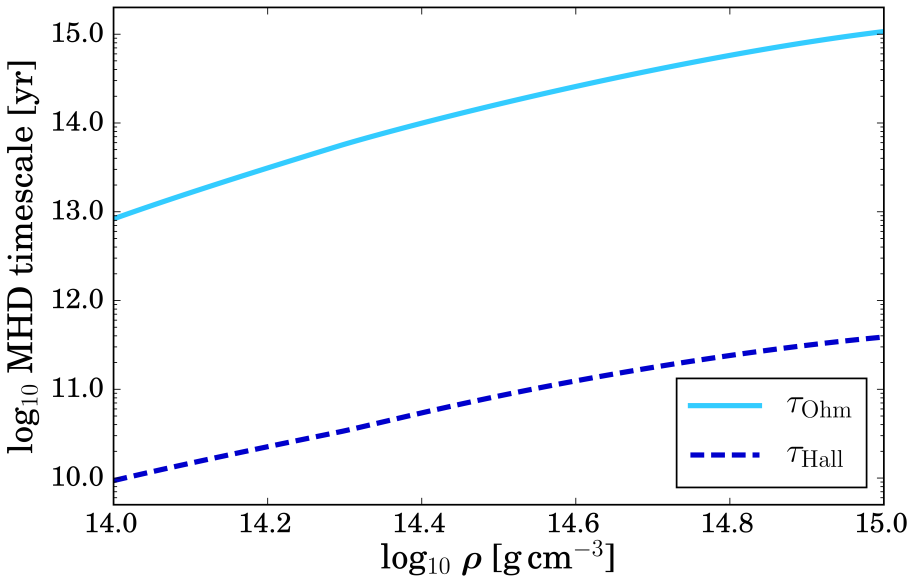

Figure 7.1: Estimates for the characteristic Ohmic (cyan, solid) and Hall (blue, dashed) evolution timescales of standard resistive MHD as a function of the total mass density in the neutron star core. Values are based on $T = 10^8\,\mathrm{K}$, $L = 10^6\,\mathrm{cm}$, $B = 10^{12}\,\mathrm{G}$ and the composition obtained with the NRAPR effective EoS discussed in Subsection 5.1.1.

7.1.2 Flux freezing and magnetic energy

These two characteristic timescales can be estimated for a neutron star core. According to Baym et al. [193], the dominant coupling mechanism in normal neutron star matter is associated with the interactions of highly relativistic electrons and normal, degenerate protons. Having derived the corresponding τ_v in Subsection 6.1.1, the conductivity is

$$\tilde{\sigma}_\mathrm{e} \approx 5.5 \times 10^{28}\, T_8^{-2}\, \rho_{14}^{3/2} \left(\frac{x_\mathrm{p}}{0.05}\right)^{3/2} \mathrm{s}^{-1}, \tag{7.6}$$

where $T_8 \equiv T/(10^8\,\mathrm{K})$ is the star's normalised temperature, $\rho_{14} \equiv \rho/(10^{14}\,\mathrm{g\,cm^{-3}})$ the normalised total density and x_p the proton fraction. Approximating the characteristic lengthscale, L, by the radius of the neutron star, the Ohmic diffusion timescale is

$$\tau_\mathrm{Ohm} \approx 2.5 \times 10^{13}\, T_8^{-2}\, L_6^2\, \rho_{14}^{3/2} \left(\frac{x_\mathrm{p}}{0.05}\right)^{3/2} \mathrm{yr}, \tag{7.7}$$

with $L_6 \equiv L/(10^6\,\mathrm{cm})$. For the Hall timescale, we obtain with $B_{12} \equiv B/(10^{12}\,\mathrm{G})$

$$\tau_\mathrm{Hall} \approx 1.9 \times 10^{10}\, B_{12}^{-1}\, L_6^2\, \rho_{14} \left(\frac{x_\mathrm{p}}{0.05}\right) \mathrm{yr}. \tag{7.8}$$

Both estimates are many orders of magnitude larger than the typical spin-down ages of radio pulsars discussed in Section 2.3. Density-dependent results for a realistic equation of state are illustrated in Figure 7.1. It is, thus, expected that the Ohmic decay and Hall term are negligible for the evolution of the magnetic field. In this idealised case, which is commonly used to approximate astrophysical and laboratory plasmas, the induction

equation (7.4) reduces to

$$\partial_t B^i = \epsilon^{ijk} \nabla_j \epsilon_{klm} \left(v_{\rm p}^l B^m \right). \tag{7.9}$$

Using the fact that the magnetic induction is a solenoidal field satisfying $\nabla_i B^i = 0$, the last equation can be rewritten and then simplified with the Lie derivative (4.72),

$$\partial_t B^i + v_{\rm p}^j \nabla_j B^i - B^j \nabla_j v_{\rm p}^i = \partial_t B^i + \mathcal{L}_{v_{\rm p}} B^i = -B^i \nabla_j v_{\rm p}^j. \tag{7.10}$$

The left-hand side describes how the magnetic field vector, B^i, is transported with the fluid flow, $v_{\rm p}^i$. Taking into account that the mass of the proton plasma is conserved, the continuity equation (4.24) can be employed to give

$$\partial_t \left(\frac{B^i}{\rho_{\rm p}} \right) + \mathcal{L}_{v_{\rm p}} \left(\frac{B^i}{\rho_{\rm p}} \right) = 0. \tag{7.11}$$

This implies that the magnetic field is moving with the fluid, i.e. the fluxlines are frozen to the proton plasma. As soon as Ohmic and Hall term play a role for the dynamics, this frozen-in condition is destroyed and field lines are no longer forced to follow the protons. In particular, if Ohmic decay characterised by the conductivity, $\tilde{\sigma}_{\rm e}$, is included, the induction equation resembles a diffusion equation. It encodes how the magnetic field lines diffuse through the fluid and reconnect, leading to the decay of magnetic energy as discussed below. If, on the other hand, the Hall term is present but Ohmic decay is negligible, the induction equation reduces to

$$\partial_t B^i = \epsilon^{ijk} \nabla_j \epsilon_{klm} \left(v_{\rm e}^l B^m \right). \tag{7.12}$$

In contrast to Equation (7.9), the electron velocity enters the magnetic evolution law. This suggests that the relative motion between electrons and protons becomes important and the magnetic field is frozen into the electron fluid.

The conservative and dissipative nature of the different pieces in Equation (7.4) is illustrated by considering the evolution of the magnetic energy. In order to compare the standard MHD plasma with the superfluid/superconducting mixture later on, we calculate the magnetic energy associated with the work done by the Lorentz force, given in Equation (4.36). The work is obtained by determining the product of the force density $F_{\rm L}^i$ with the position vector, r^i, and integrating over the volume, V,

$$W_{\rm L} = \int r_i F_{\rm L}^i \, {\rm d}V. \tag{7.13}$$

Using the product rule and Equation (4.94), one arrives at

$$W_{\rm L} = \frac{1}{4\pi} \int \left[\nabla^i \left(r_j B^j B_i - \frac{1}{2} B^2 r_i \right) - \left(B^i B_j \nabla^j r_i - \frac{1}{2} B^2 \nabla^i r_i \right) \right] {\rm d}V. \tag{7.14}$$

The total gradient term can be rewritten as a surface integral using Gauss' theorem. As no discontinuities are present at the boundary of a normal plasma region, the integration radius can be pushed to infinity. Provided that the magnetic induction vanishes at infinity, the surface contribution is zero.

The second piece in Equation (7.14) can be further simplified to the well-known magnetic energy density, which is also equivalent to the magnetic pressure in standard magnetohydrodynamics,

$$W_{\mathrm{L}} = -\frac{1}{4\pi}\int \left(B^i B_j \underbrace{\nabla^j r_i}_{=\delta_i^j} - \frac{1}{2} B^2 \underbrace{\nabla^i r_i}_{=3} \right) \mathrm{d}V = \int \frac{B^2}{8\pi}\,\mathrm{d}V \equiv \int \mathcal{E}_{\mathrm{mag}}\,\mathrm{d}V. \tag{7.15}$$

Changes in the magnetic energy are, thus, determined by

$$\partial_t \mathcal{E}_{\mathrm{mag}} = \partial_t \left(\frac{B^2}{8\pi} \right) = \frac{B_i}{4\pi} \partial_t B^i. \tag{7.16}$$

Calculating the product of the induction equation (7.4) with B_i and using the following vector identity for two arbitrary vectors a^i and b^i,

$$b_i\, \epsilon^{ijk} \nabla_j a_k = a^i\, \epsilon_{ijk} \nabla^j b^k - \nabla^i\, \epsilon_{ijk} \left(b^j a^k \right), \tag{7.17}$$

to rewrite the result, one finds

$$\partial_t \mathcal{E}_{\mathrm{mag}} = \frac{1}{4\pi}\, \epsilon^{isp} (\nabla_s B_p)\, \epsilon_{ijk} \left[v_{\mathrm{p}}^j B^k - \frac{c^2}{4\pi\tilde{\sigma}_{\mathrm{e}}} \nabla^j B^k - \frac{mc}{4\pi e \rho_{\mathrm{p}}}\, \epsilon^{jlm} (\nabla_l B_m) B^k \right] - \nabla^i \Sigma_i. \tag{7.18}$$

The last term contains all the contributions that can be written as a divergence. After integrating over the volume, it is possible to convert this part into a surface integral using Gauss' theorem. Additionally, the third term has to be zero due to the properties of the Levi-Civita tensor. This shows that the Hall term in Equation (7.4) is conservative and does not contribute to the change in the magnetic energy density. It may, however, act to redistribute the magnetic energy from large scales to smaller ones, where it can decay Ohmically. Many studies of the induction equation's non-linear behaviour are based on results from hydrodynamic turbulence [168], as it has several similarities with the vorticity equation of a viscous fluid [231]. However, recent numerical simulations in the context of neutron stars have shown no evidence of strong cascading behaviour. Instead, the Hall cascade appears to be saturated at long lengthscales [259, 233, 260].

Using Ampère's law (4.93) and the generalised Ohm's law (7.2), the remaining terms in Equation (7.18) are simplified to

$$\partial_t \mathcal{E}_{\mathrm{mag}} = \frac{1}{c}\, j^i \epsilon_{ijk}\, v_{\mathrm{p}}^j B^k - \frac{j^2}{\tilde{\sigma}_{\mathrm{e}}} - \nabla^i \left[\frac{c}{4\pi} S_i - \frac{m_{\mathrm{e}}}{e} \tilde{\Phi}_{\mathrm{e}} j_i \right], \tag{7.19}$$

where $S^i \equiv \epsilon^{ijk} E_j B_k$ is the Poynting vector. Equation (7.19) clearly shows that any resistive plasma is subject to the decay of magnetic energy due to Ohmic diffusion and the energy loss is proportional to j^2. The inertial term vanishes if the protons are not able to move, which is, for example, the case in a standard metal, or when the macroscopic current density and the proton velocity are aligned.

7.2 Field Evolution in Neutron Stars

7.2.1 Standard resistive coupling

We now return to the question of magnetic field evolution in the superconducting outer neutron star core. In order to apply a formalism similar to the resistive MHD discussion, the forces, $F^i_{\rm e}$, exerted on the electron component by the various fluid constituents and the vortices/fluxtubes, need to be determined. However, due to the multi-fluid nature of the superfluid/superconducting mixture, there are not simply two components coupled by a single resistive force and identifying the dominant coupling is not straightforward. A variety of ways could be imagined for the components to interact with each other; ranging from electron scattering [204, 205, 200] and vortex-fluxtube interactions [188, 189, 206] to shear or bulk viscosity [212, 263, 264]. Choosing a more pedagogical approach to the problem, we address one specific mechanism, determine how it affects the electrons on mesoscopic scales and translate this into a macroscopic picture. While this will not provide a complete picture of the magnetic field evolution in the core, the method provides more insight into how different mechanisms could play a role.

As stated previously, the magnetic flux is locked to the superconducting fluxtubes and their motion determines the evolution of the magnetic field. We, therefore, consider the scattering of electrons off the vortex/fluxtube fields as the main source of friction (see Subsections 5.1.3 and 6.2.1 for details). This *standard* resistive coupling in a superfluid/superconducting mixture, first discussed by Alpar et al. [205], results in two forces acting on the electrons,

$$F^i_{\rm e} = F^i_{\rm pe} + F^i_{\rm ne} \approx F^i_{\rm pe}. \tag{7.20}$$

The contribution from electrons scattering off the neutron vortices is neglected since the fluxtube surface density is many orders of magnitude larger than the vortex density, i.e. $\mathcal{N}_{\rm p} \gg \mathcal{N}_{\rm n}$ (see Subsection 4.1.1). This implies that electron-fluxtube interactions are much more common and, thus, dominate the coupling. The macroscopic force density, $F^i_{\rm e}$, is obtained by multiplying the drag force, $f^i_{\rm d}$, exerted on a single fluxtube, by $\mathcal{N}_{\rm p}$,

$$F^i_{\rm e} = \mathcal{N}_{\rm p} f^i_{\rm d} = \mathcal{N}_{\rm p} \rho_{\rm p} \kappa \mathcal{R} \left(v^i_{\rm e} - u^i_{\rm p} \right). \tag{7.21}$$

The dimensionless drag coefficient, $\mathcal{R}$, contains all the information about the coupling on mesoscopic scales and $u^i_{\rm p}$ is the velocity of a single fluxtube.

In order to determine an evolution equation for the macroscopic magnetic field in superconducting matter, one has to eliminate any quantities from Equation (7.21) that are defined on mesoscopic lengthscales. Hence, the next step is to rewrite the fluxtube velocity, $u_{\rm p}^i$, in terms of macroscopic fluid variables, which can be achieved by using the force balance for an individual fluxtube. This approach introduced by Hall and Vinen [142] (see also Subsection 4.3.3 and note that we drop the index p since only fluxtube dynamics are considered) gives per unit length of the fluxtube

$$\sum f^i = f_{\rm M}^i + f_{\rm t}^i + f_{\rm em}^i + f_{\rm d}^i = 0, \tag{7.22}$$

where the fluxtube inertia is neglected. The force balance equation includes the electron drag force given above, the Magnus force, $f_{\rm M}^i$, the tension force, $f_{\rm t}^i$, and the electromagnetic Lorentz force, $f_{\rm em}^i$. As discussed in Subsection 4.3.3, the different forces have been determined by Glampedakis et al. [181]. More specifically, for a proton fluxtube

$$f_{\rm M}^i = \rho_{\rm p}\kappa\,\epsilon^{ijk}\hat{\kappa}_j^{\rm p}\left(u_k^{\rm p} - v_k^{\rm p}\right), \tag{7.23}$$

$$f_{\rm t}^i = \frac{H_{\rm c1}\kappa}{4\pi a_{\rm p}}\,\hat{\kappa}_{\rm p}^j\nabla_j\hat{\kappa}_{\rm p}^i, \tag{7.24}$$

where $\hat{\kappa}_{\rm p}^i$ points along the local direction of the fluxtube, $H_{\rm c1}$ is the lower critical field for superconductivity and the constant $a_{\rm p}$ is defined in Equation (4.39). Additionally

$$f_{\rm em}^i = \rho_{\rm p}\kappa\,\epsilon^{ijk}\hat{\kappa}_j^{\rm p}w_k^{\rm pe}. \tag{7.25}$$

Note that we are interested in the linear analysis of one specific resistive mechanism. For this reason, the force balance (7.22) does not include a *pinning* force, resulting from the magnetic short-range interaction between the two arrays [188, 189, 206, 265].

Solving for the fluxtube velocity, $u_{\rm p}^i$, present in the drag force term gives

$$u_{\rm p}^i = v_{\rm e}^i + \frac{1}{\rho_{\rm p}\kappa\mathcal{R}}\left[f_{\rm t}^i + f_{\rm em}^i - \rho_{\rm p}\kappa\,\epsilon^{ijk}\hat{\kappa}_j^{\rm p}\left(v_k^{\rm p} - u_k^{\rm p}\right)\right]. \tag{7.26}$$

Calculating repeated cross products of this expression with $\hat{\kappa}_{\rm p}^i$, similar to the procedure in Subsection 4.3.3, it is possible to express the mesoscopic fluxtube velocity in terms of the averaged fluid velocities, i.e.

$$u_{\rm p}^i = v_{\rm e}^i + \frac{1}{1+\mathcal{R}^2}\left(\mathcal{R}f_\star^i + \epsilon^{ijk}\hat{\kappa}_j^{\rm p}f_k^\star\right), \tag{7.27}$$

where

$$f_\star^i = \epsilon^{ijk}\hat{\kappa}_j^{\rm p}w_k^{\rm ep} + \frac{1}{\rho_{\rm p}\kappa}\left(f_{\rm t}^i + f_{\rm em}^i\right). \tag{7.28}$$

Combining the previous relations, one observes that the first term in Equation (7.28) and the electromagnetic force, $f_{\rm em}^i$, exactly cancel each other. Then, the effective force,

$f^i_\star$, is equivalent to the fluxtube tension,

$$f^i_\star = \frac{1}{\rho_\mathrm{p}\kappa}\, f^i_\mathrm{t} = \frac{H_\mathrm{c1}}{4\pi a_\mathrm{p}\rho_\mathrm{p}} \hat{\kappa}^j_\mathrm{p} \nabla_j \hat{\kappa}^i_\mathrm{p}. \tag{7.29}$$

Substituting Equations (7.27) and (7.29) back into Equation (7.21) finally gives for the macroscopic drag force acting on a unit volume of the electron fluid,

$$F^i_\mathrm{e} = -\frac{H_\mathrm{c1}\phi_0\mathcal{N}_\mathrm{p}}{4\pi}\, \frac{\mathcal{R}}{1+\mathcal{R}^2} \left(\mathcal{R}\, \hat{\kappa}^j_\mathrm{p} \nabla_j \hat{\kappa}^i_\mathrm{p} + \epsilon^{ijk} \hat{\kappa}^\mathrm{p}_j \hat{\kappa}^l_\mathrm{p} \nabla_l \hat{\kappa}^\mathrm{p}_k \right). \tag{7.30}$$

While one term is proportional to the fluxtube tension, f^i_t, the other is orthogonal to it. For a straight array, the tension force is zero and the electron coupling thus vanishes.

7.2.2 Superconducting induction equation

Having determined the force, F^i_e, exerted on the electron component due to scattering off the fluxtube magnetic fields, we can use again the modified electron Euler equation (4.96) for the macroscopic electric field. The resulting generalised Ohm's law is valid in the superfluid/superconducting mixture and reads as

$$E^i = -\frac{1}{c}\epsilon^{ijk} v^\mathrm{e}_j B_k - \frac{m_\mathrm{e}}{e}\nabla^i \tilde{\Phi}_\mathrm{e} + \frac{H_\mathrm{c1}\phi_0\mathcal{N}_\mathrm{p}}{4\pi c a_\mathrm{p}\rho_\mathrm{p}}\, \frac{\mathcal{R}}{1+\mathcal{R}^2} \left(\mathcal{R}\, \hat{\kappa}^j_\mathrm{p} \nabla_j \hat{\kappa}^i_\mathrm{p} + \epsilon^{ijk} \hat{\kappa}^\mathrm{p}_j \hat{\kappa}^l_\mathrm{p} \nabla_l \hat{\kappa}^\mathrm{p}_k \right). \tag{7.31}$$

With Faraday's law (4.95), the superconducting induction equation describing the evolution of the macroscopic magnetic field in the outer neutron star core can be derived,

$$\partial_t B^i = \epsilon^{ijk}\nabla_j \left[\epsilon_{klm} v^l_\mathrm{e} B^m - \frac{H_\mathrm{c1}\phi_0\mathcal{N}_\mathrm{p}}{4\pi a_\mathrm{p}\rho_\mathrm{p}}\, \frac{\mathcal{R}}{1+\mathcal{R}^2} \left(\mathcal{R}\, \hat{\kappa}^l_\mathrm{p} \nabla_l \hat{\kappa}^\mathrm{p}_k + \epsilon_{klm} \hat{\kappa}^l_\mathrm{p} \hat{\kappa}^s_\mathrm{p} \nabla_s \hat{\kappa}^m_\mathrm{p} \right) \right]. \tag{7.32}$$

Let us specify the lower critical field, H_c1, to simplify this expression further. According to Equation (3.82), the field is related to the energy of the fluxtube, $\mathcal{E}_\mathrm{p}$, via

$$H_\mathrm{c1} = \frac{4\pi\mathcal{E}_\mathrm{p}}{\phi_0}. \tag{7.33}$$

The fluxtube energy, on the other hand, is determined by the characteristic lengthscales of the superconducting phase, namely the effective London penetration depth, λ_*, and the proton coherence length, ξ_p, and was calculated in Equation (4.56). Using again the estimate $\ln(\lambda_*/\xi_\mathrm{p}) \approx 2$, one finds

$$\mathcal{E}_\mathrm{p} \approx \frac{\kappa^2\rho_\mathrm{p}}{2\pi}\frac{m}{m^*_\mathrm{p}}. \tag{7.34}$$

Combining the previous equations, we obtain the new result

$$\partial_t B^i = \epsilon^{ijk}\nabla_j \left[\epsilon_{klm} v^l_\mathrm{e} B^m - \frac{\kappa\phi_0\mathcal{N}_\mathrm{p}}{2\pi}\frac{m}{m^*_\mathrm{p}}\, \frac{\mathcal{R}}{1+\mathcal{R}^2} \left(\mathcal{R}\, \hat{\kappa}^l_\mathrm{p} \nabla_l \hat{\kappa}^\mathrm{p}_k + \epsilon_{klm} \hat{\kappa}^l_\mathrm{p} \hat{\kappa}^s_\mathrm{p} \nabla_s \hat{\kappa}^m_\mathrm{p} \right) \right]. \tag{7.35}$$

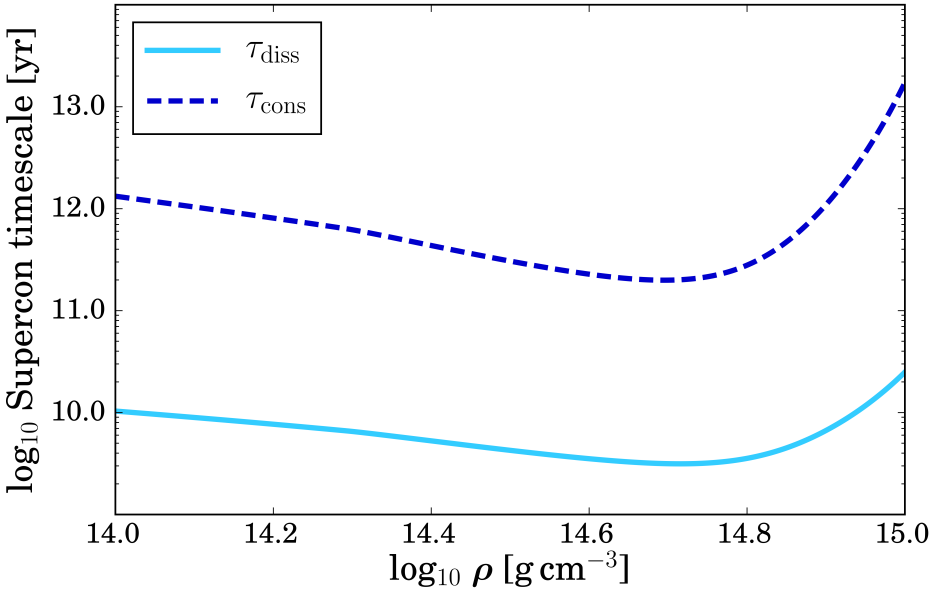

Figure 7.2: Estimates for the dissipative (cyan, solid) and the conservative (blue, dashed) evolution timescale of the superconducting induction equation as a function of the total mass density in the neutron star core. The values are calculated for the NRAPR effective EoS discussed in Subsection 5.1.1 and a characteristic lengthscale of $L = 10^6$ cm.

7.2.3 Simplified set of equations

At this point, it seems natural to make several assumptions about the actual physics of the multi-fluid mixture in order to simplify Equation (7.35). As discussed previously, the main contribution to the macroscopic magnetic induction is given by the fluxtubes. In this case, the weak London field can be neglected and the superconducting Ampère law (4.92) dictates that the protons and electrons are comoving on large scales, i.e. $v^i_{\rm p} \approx v^i_{\rm e}$, and the macroscopic current vanishes. This also implies that the local direction of the fluxtube array is aligned with the direction of the magnetic induction because

$$B^i = B\hat{B}^i \approx \mathcal{N}_{\rm p}\phi_0\hat{\kappa}^i_{\rm p} \qquad \text{gives} \qquad \hat{B}^i \approx \hat{\kappa}^i_{\rm p}. \tag{7.36}$$

Using these simplifications to rewrite the force density on the electron fluid, one obtains

$$F^i_{\rm e} \approx -\frac{H_{\rm c1}B}{4\pi}\,\frac{\mathcal{R}}{1+\mathcal{R}^2}\left(\mathcal{R}\hat{B}^j\nabla_j\hat{B}^i + \epsilon^{ijk}\hat{B}_j\hat{B}^l\nabla_l\hat{B}_k\right). \tag{7.37}$$

The induction equation, on the other hand, reduces to

$$\partial_t B^i \approx \epsilon^{ijk}\nabla_j\left[\epsilon_{klm}v^l_{\rm p}B^m - \frac{\kappa B}{2\pi}\,\frac{m}{m^*_{\rm p}}\,\frac{\mathcal{R}}{1+\mathcal{R}^2}\left(\mathcal{R}\hat{B}^l\nabla_l\hat{B}_k + \epsilon_{klm}\hat{B}^l\hat{B}^s\nabla_s\hat{B}^m\right)\right]. \tag{7.38}$$

This form of the superconducting induction equation can be compared with the standard MHD result given in Equation (7.4). As in the resistive MHD case, two timescales are extracted,

$$\tau_{\rm diss} = \frac{2\pi L^2}{\kappa}\,\frac{1+\mathcal{R}^2}{\mathcal{R}}\,\frac{m_{\rm p}^*}{m} \tag{7.39}$$

and

$$\tau_{\rm cons} = \frac{\tau_1}{\mathcal{R}} = \frac{2\pi L^2}{\kappa}\,\frac{1+\mathcal{R}^2}{\mathcal{R}^2}\,\frac{m_{\rm p}^*}{m}, \tag{7.40}$$

where L is again the characteristic lengthscale over which the magnetic field changes. The naming convention of the two timescales might seem arbitrary at this point but the choice will become clear later on.

One can estimate $\tau_{\rm diss}$ and $\tau_{\rm cons}$ provided the mutual friction strength is known. As previously discussed, a method to determine the dimensionless drag parameter, $\mathcal{R}$, of the *resistive* coupling has been provided by Sauls et al. [204] and Alpar et al. [205]. The approach, analysed in detail in Subsections 5.1.3 and 6.2.1, is based on modifying the velocity relaxation timescale for the scattering of electrons off infinitely thin fluxtubes to account for their finite size and the increase in moment of inertia due to the coupling of electrons and protons on much shorter timescales. The resulting relaxation timescale is in turn related to the dimensionless drag coefficient, $\mathcal{R}$ (see Equation (6.23) for details), which leads to the following numerical estimate (see Equation (6.27))

$$\mathcal{R} \approx 7.9\times10^{-3}\left(\frac{m}{m_{\rm p}^*}\right)^{1/2}\rho_{14}^{1/6}\left(\frac{x_{\rm p}}{0.05}\right)^{1/6}. \tag{7.41}$$

This gives $\mathcal{R} \ll 1$ and implies that the standard friction mechanism is rather weak. Note that according to Jones [246], magnetic scattering off individual fluxtubes is suppressed for large fluxtube densities. Instead, electron scattering by clusters of fluxtubes would dominate the coupling and result in an even smaller drag coefficient, $\mathcal{R}$. Adopting the limit (7.41), one can approximate for the neutron star core,

$$\tau_{\rm diss} \approx 7.4\times10^{9} L_6^2\,\rho_{14}^{-1/6}\left(\frac{x_{\rm p}}{0.05}\right)^{-1/6}\ {\rm yr} \tag{7.42}$$

and

$$\tau_{\rm cons} \approx 7.8\times10^{11} L_6^2\,\rho_{14}^{-1/3}\left(\frac{x_{\rm p}}{0.05}\right)^{-1/3}\ {\rm yr}. \tag{7.43}$$

For simplicity, the effective proton mass was fixed to $m_{\rm p}^* = 0.7m$ (see Equation (4.12)). The detailed density-dependence of the two timescales is shown in Figure 7.2 for the NRAPR effective equation of state introduced in Subsection 5.1.1.

7.2.4 Flux freezing and magnetic energy

For conventional electron-fluxtube coupling, the timescales for the magnetic field evolution are rather long and the dynamics of the macroscopic induction are dominated by the inertial term in the induction equation. In the weak mutual friction limit, we are therefore left with an equation that is equivalent to the one discussed in Subsection

7.1.2. The magnetic field in the superconducting sample is frozen to the proton fluid, which implies that the superconducting fluxtubes are locked to the proton plasma, i.e. $v_{\rm p}^i \approx u_{\rm p}^i$. This result was already obtained in Subsection 4.3.3 using a conservation of vorticity argument (see Equation (4.74)). Hence, electrons, protons and fluxtubes are comoving on large scales, which is different from the weakly resistive case of standard MHD, where the relative motion between the charged particles was important.

In order to determine whether the additional terms in Equation (7.38) are conservative or dissipative and which timescale dominates, the evolution of the superconducting magnetic energy is discussed. As before, the energy associated with the work done by the magnetic force is evaluated. However, in a superfluid/superconducting mixture, the standard Lorentz force (4.36) has to be changed accordingly. The effective magnetic force in the limit of constant entrainment and vanishing rotation was given in Equation (4.65). The work associated with this force density is

$$\begin{aligned} W_{\rm mag} = \frac{1}{4\pi} \int \nabla^i \left(r_j H_{\rm c1}^j B_i - \rho_{\rm p} B \frac{\partial H_{\rm c1}}{\partial \rho_{\rm p}} r_i \right) {\rm d}V \\ - \frac{1}{4\pi} \int \left(H_{\rm c1}^i B_j \nabla^j r_i - \rho_{\rm p} B \frac{\partial H_{\rm c1}}{\partial \rho_{\rm p}} \nabla^i r_i \right) {\rm d}V, \end{aligned} \tag{7.44}$$

where the product rule and Equation (4.94) have been used. Similar to the standard MHD case, the first term can be rewritten using Gauss' theorem. However, in the superconducting outer core, this contribution does not simply vanish because discontinuities are likely to be present at the fluid boundaries. The dynamics that might arise due the presence of a current sheet at the crust-core interface [266, 267] or the type-II to type-I transition region in the neutron stars' inner core [177] are only poorly understood and significantly complicate the problem. Incorporating these interfaces would require a much more detailed understanding of the microphysics involved. In the following, we therefore omit a discussion of the surface terms and focus on the much simpler problem of magnetic field evolution in the bulk fluid.

Since the lower critical field is a function linear in $\rho_{\rm p}$ (see Equation (7.33)), one finds $\partial H_{\rm c1}/\partial \rho_{\rm p} = H_{\rm c1}/\rho_{\rm p}$. Then, the second integral in Equation (7.44) reduces to

$$W_{\rm mag,bulk} = -\frac{1}{4\pi} \int \left(H_{\rm c1}^i B_j \, \delta_i^j - 3 B H_{\rm c1} \right) {\rm d}V = \int \frac{H_{\rm c1} B}{2\pi} \, {\rm d}V \equiv \int \mathcal{E}_{\rm mag,sc} \, {\rm d}V. \tag{7.45}$$

More insight into the magnetic energy density, $\mathcal{E}_{\rm mag,sc}$, can be gained by considering the stress tensor for type-II superconducting matter, σ^{ij}, derived by Easson and Pethick [203]. For the interior of a neutron star, one typically has $B \ll H \approx H_{\rm c1}$ (see also Subsection 4.1.2) in which case the stress tensor is given by

$$\sigma^{ij} = -P_{\rm mag,sc} \, \delta^{ij} + \frac{H_{\rm c1}^i B^j}{4\pi} = -\frac{H_{\rm c1} B}{4\pi} \, \delta^{ij} + \frac{H_{\rm c1}^i B^j}{4\pi}. \tag{7.46}$$

The magnetic energy density is equivalent to the negative trace of this tensor, i.e. $-\sigma^{ii}$, reproducing the result of Equation (7.45). The stress tensor (7.46) also shows that, in contrast to normal MHD, $\mathcal{E}_{\rm mag,sc}$ no longer coincides with the magnetic pressure, $P_{\rm mag,sc}$. The magnetic energy density of a type-II superconductor is also a factor of 2 larger than the total tension associated with the fluxtube array. The latter is given by

$$\mathcal{N}_{\rm p}\mathcal{E}_{\rm p} = \frac{B}{\phi_0}\,\frac{H_{\rm c1}\phi_0}{4\pi} = \frac{H_{\rm c1}B}{4\pi}, \tag{7.47}$$

where Equations (7.33) and (7.36) have been used.

Taking the time derivative of the magnetic energy density gives two contributions,

$$\partial_t\mathcal{E}_{\rm mag,sc} = \frac{B}{2\pi}\partial_t H_{\rm c1} + \frac{H_{\rm c1}}{2\pi}\hat{B}_i\partial_t B^i. \tag{7.48}$$

Comparison with the corresponding expression of standard MHD given in Equation (7.16) shows that the superconducting nature of the mixture gives rise to a new contribution for the change in energy density. In contrast to resistive MHD, the evolution of matter and the magnetic induction are no longer decoupled in the condensate. Equation (7.48) demonstrates that modifying the properties of the superconductor, such as the lower critical field, $H_{\rm c1}$, alters the magnetic energy. This implies that an evolving matter configuration can be closely linked to a changing magnetic field.

The second term in Equation (7.48) is similar to the result for normal conducting matter. Calculating the product of the induction equation (7.38) with $\hat{B}_i$ and using the vector identity (7.17) to simplify the result leads to

$$\begin{aligned}\hat{B}_i\partial_t B^i = \epsilon^{isp}(\nabla_s\hat{B}_p)\Bigg[&\epsilon_{ijk}v_{\rm p}^j B^k - \frac{\kappa B}{2\pi}\,\frac{m}{m_{\rm p}^*}\,\frac{\mathcal{R}^2}{1+\mathcal{R}^2}\,\hat{B}^l\nabla_l\hat{B}_i \\ &- \frac{\kappa B}{2\pi}\,\frac{m}{m_{\rm p}^*}\,\frac{\mathcal{R}}{1+\mathcal{R}^2}\,\epsilon_{ijk}\hat{B}^j\hat{B}^l\nabla_l\hat{B}^k\Bigg] - \nabla^i\Sigma_i.\end{aligned} \tag{7.49}$$

As before, Σ^i denotes the divergence terms. This equation bears some resemblance with the result (7.18) found in standard MHD and one would equivalently expect to obtain a conservative and a dissipative contribution. In order to determine which of the terms are non-zero or zero, the tension is rewritten using the following identity,

$$\hat{B}^l\nabla_l\hat{B}_i = \epsilon_{ijk}\,\epsilon^{jlm}(\nabla_l\hat{B}_m)\hat{B}^k. \tag{7.50}$$

The second term in Equation (7.49) is, thus, proportional to

$$\epsilon^{isp}(\nabla_s\hat{B}_p)\hat{B}^l\nabla_l\hat{B}_i = \epsilon^{isp}(\nabla_s\hat{B}_p)\,\epsilon_{ijk}\,\epsilon^{jlm}(\nabla_l\hat{B}_m)\hat{B}^k. \tag{7.51}$$

Analogous to the Hall term of standard resistive MHD, this vanishes due to the properties of the antisymmetric Levi-Civita tensor. Thus, the second term in the supercon-

ducting induction equation (7.38) is conservative and does not affect the total magnetic energy of the superconducting mixture. The last term in Equation (7.49), on the other hand, is proportional to

$$\epsilon^{isp}(\nabla_s \hat{B}_p)\,\epsilon_{ijk}\hat{B}^j\hat{B}^l\nabla_l\hat{B}^k = \mathcal{J}^i\epsilon_{ijk}\hat{B}^j\epsilon^{klm}\mathcal{J}_l\hat{B}_m, \tag{7.52}$$

where the new vector, $\mathcal{J}^i$, is defined by

$$\mathcal{J}^i \equiv \epsilon^{ijk}\nabla_j\hat{B}_k. \tag{7.53}$$

Rewriting the remaining two Levi-Civita tensors in Equation (7.52) in terms of Kronecker deltas, δ^i_j, gives the following projection

$$\mathcal{J}^i\,\epsilon_{ijk}\hat{B}^j\epsilon^{klm}\mathcal{J}_l\hat{B}_m = \mathcal{J}_i\mathcal{J}^i - \left(\mathcal{J}^i\hat{B}_i\right)\left(\mathcal{J}^j\hat{B}_j\right). \tag{7.54}$$

Decomposing the vector $\mathcal{J}^i$ into a component parallel to $\hat{B}_i$ and one perpendicular to the magnetic field direction, i.e. $\mathcal{J}^i \equiv \mathcal{J}_\parallel\hat{B}_i + \mathcal{J}^i_\perp$, one sees that Equation (7.54) only depends on the component of $\mathcal{J}^i$ that is perpendicular to $\hat{B}_i$,

$$\mathcal{J}_i\mathcal{J}^i - \left(\mathcal{J}^i\hat{B}_i\right)\left(\mathcal{J}^j\hat{B}_j\right) = \mathcal{J}^2_\perp. \tag{7.55}$$

Similar to the Ohmic term in standard resistive MHD, a dissipative contribution to the total magnetic energy is retained in the case of superconducting MHD. One obtains

$$\partial_t\mathcal{E}_{\rm mag,sc} = \frac{B}{2\pi}\partial_t H_{\rm c1} + \frac{H_{\rm c1}}{2\pi}\left(\mathcal{J}^i_\perp\epsilon_{ijk}v^j_{\rm p}B^k - \frac{\kappa B}{2\pi}\,\frac{m}{m^*_{\rm p}}\,\frac{\mathcal{R}}{1+\mathcal{R}^2}\,\mathcal{J}^2_\perp - \nabla^i\Sigma_i\right). \tag{7.56}$$

Having calculated the change in the magnetic energy density, one can associate the timescale $\tau_{\rm diss}$, given in Equation (7.42), with a dissipative mechanism. Comparing the numerical estimate to the Ohmic decay timescale (7.7), we observe that the resistive coupling in a superfluid and superconducting mixture acts on a timescale, which is four orders of magnitude smaller than the standard MHD diffusion,

$$\frac{\tau_{\rm diss}}{\tau_{\rm Ohm}} \approx 3.0\times10^{-4}\,T_8^2\,\rho_{14}^{-5/3}\left(\frac{x_{\rm p}}{0.05}\right)^{-5/3}. \tag{7.57}$$

On the other hand, the timescale (7.8) for the Hall evolution in a normal conducting plasma can be compared to $\tau_{\rm cons}$ in Equation (7.43). In contrast to the standard MHD case, the conservative timescale emerging from the superconducting induction equation is approximately one order of magnitude larger than the Hall timescale,

$$\frac{\tau_{\rm cons}}{\tau_{\rm Hall}} \approx 40.6\,B_{12}\,\rho_{14}^{-4/3}\left(\frac{x_{\rm p}}{0.05}\right)^{-4/3}. \tag{7.58}$$

One can also note that due to the dependence on the dimensionless drag coefficient, $\mathcal{R}$,

the dissipative term in the superconducting induction equation governs the field evolution, whereas in standard MHD the conservative Hall term acts on shorter timescales. In the second case, the order of the two timescales is necessary for any cascading behaviour to take place; the Hall term drives the magnetic field to shorter lengthscales, where it could decay Ohmically. However, if diffusion is dominating the evolution, the redistribution of magnetic energy will happen on much longer timescale not causing a cascade. Hence, despite the close similarities between the conservative terms in Equation (7.38) and standard MHD, we conjecture that the analysis of the Hall cascade by Goldreich and Reisenegger [231] is not transferable to the superconducting case.

7.3 Discussion

Strong magnetic fields are a key ingredient for many phenomena observed in neutron stars. Understanding the fields' long-term evolution might give insight into the *metamorphosis* between the different neutron star classes, the changing fields of standard radio pulsars or the high activity of magnetars. As the mechanisms causing field changes are only poorly understood, the question of magnetic field evolution was revisited and, in particular, the influence of a superconducting component discussed. The aim was to rethink key notions of MHD and develop a better intuition for the magnetic field evolution in a superconductor.

Using the multi-fluid formalism introduced in Chapter 4, the presence of mesoscopic vortices/fluxtubes is translated into the large-scale dynamics of the fluid. As an application of this framework, we analysed the conventional dissipative mechanism, i.e. the scattering of electrons off the fluxtube magnetic field. Based on the approach of standard resistive MHD, a generalised Ohm's law was combined with Faraday's law to derive a superconducting induction equation. Considering the London field as a negligible contribution led to a simplified equation, which should be applicable to most astrophysical scenarios. Caution is required when discussing highly magnetised objects. For field strengths above the critical field, $B > H_{c2} \sim 10^{16}\,\mathrm{G}$ (see Subsection 4.1.2), the superconducting state breaks down and the averaged formalism no longer applies. According to Goldreich and Reisenegger [231], ambipolar diffusion could potentially become important in this regime and drive field decay of the order of magnetar ages.

To compare the new results for magnetic field evolution with the standard MHD case, the magnetic energies associated with the total magnetic forces were calculated. The analysis was significantly simplified by omitting a detailed discussion of the surface terms. This implies that effects originating at the crust-core interface or the type-II to type-I transition in the inner core, which could potentially drive the magnetic field evolution, are not taken into account. Instead, the focus was put on the evolution of the averaged magnetic field in the bulk. We found that for standard electron-fluxtube scattering, which satisfies the condition of weak mutual friction, the inertial term dom-

inates the field evolution. The fluxtubes move with the proton fluid and the flux is, as in the standard MHD case, frozen to the charged particles. It was also shown that the new induction equation contains a dissipative and a conservative contribution, similar to the Ohmic and the Hall term in normal conducting matter. However, the evolution timescales extracted from the superconducting induction equation for weak mutual friction, 10^{10} and 10^{12} yr respectively, are notably longer than the typical spin-down ages of neutron stars. We conclude that the conventional mutual friction mechanism cannot serve as an explanation for the field changes in pulsars or the activity of magnetars, which would require timescales on the order of 10^7 and 10^4 yr, respectively. However, other frictional mechanisms of the form (7.21), which could support electron-fluxtube coupling significantly stronger than the standard mutual friction, cannot provide a solution to this problem either. Instead, in the strong drag limit, $\mathcal{R} \gg 1$, the dissipation timescale is proportional to $\mathcal{R}$ and becomes comparable to the age of the Universe. A closer look at the $\mathcal{R}$-dependence of Equation (7.39) further reveals the presence of a minimum dissipation timescale for the intermediate-drag regime. More precisely,

$$\tau_{\rm min} \equiv \frac{4\pi L^2}{\kappa}\,\frac{m_{\rm p}^*}{m} \approx 1.4\times 10^8 L_6^2\,{\rm yr}, \tag{7.59}$$

for $\mathcal{R} \approx 1$. Note that all numerical estimates crucially depend on the lengthscale L. It can be identified with the curvature radius of the magnetic field and the neutron star radius, R, was chosen to normalise the previous results. Recent work on field equilibria in superconducting neutron star cores [202] suggests that the field configuration actually supports structures on a shorter lengthscale of $L \approx 10^5$ cm. Adopting such an estimate would reduce the characteristic timescales by two orders of magnitude. In particular, the minimum dissipation timescale, $\tau_{\rm min}$, would be shortened to a million years, which is closer to the timescales of astrophysical interest.

Based upon the initial assumption that the currents generating the magnetic field are located in the outer core, the present results additionally suggest that the highly conducting neutron star core might affect the crustal field and slow down its evolution. Making a precise statement at this point is, however, not possible due to the poorly known physics at the crust-core boundary. This transition is crucial in understanding how the changes of the core magnetic field are communicated to the crust. The analysis presented in this chapter does, therefore, not reconcile the discrepancy between short crustal decay timescales [268] and the much longer core evolution. However, one could envisage the following solutions to this problem. Firstly, the magnetic field could be distributed non-uniformly throughout the entire star and anchored mainly in its outer layer. In this alternative configuration, only little magnetic flux would be present in the core and the crust would dominate the magnetic field evolution, resulting in decay timescales which are comparable to the pulsar spin-down ages [269, 232, 68]. Secondly, if the assumption of a core-dominated magnetic field is maintained, the discrepancy could be resolved by either invoking magnetic field configurations varying on lengthscales smaller

than 10^5 cm or considering different frictional mechanisms that significantly reduce the core dissipation timescales. Several other forces acting on fluxtubes were discussed in the previous chapter, including the standard candidate for strong coupling: vortex-fluxtube *pinning* due to short-range magnetic interactions between the two arrays. While pinning was not addressed specifically in this chapter, discussing the vortex-fluxtube interaction would be the natural continuation as the prescription presented here can deal with any coupling mechanism. Based on a mesoscopic description of the pinning process, one would have to determine how the coupling affects the electron fluid and substitute the respective force, $F_{\rm e}^i$, into the generalised Ohm's law. This would allow one to determine the superconducting induction equation corresponding to the pinning interaction.

Chapter 8

Laboratory Neutron Star Analogues

Having discussed several implications resulting from the presence of macroscopic condensates in neutron stars, the importance of studying how quantum states influence a star has hopefully become evident. However, despite having been in the focus of research for almost 50 years, our current understanding is far from complete and a lot remains to be learnt. As the neutron star interior is not directly accessible, the analysis of future high-precision electromagnetic observations and the detection of continuous gravitational waves will play a crucial role in filling in the missing pieces. In addition to these *classical* approaches, information from a rather different direction might also provide insight into various aspects of neutron star physics. Although generally given little attention by astrophysicists, well-known terrestrial superfluids and superconductors could serve as versatile analogues of neutron stars. Whereas in the previous chapters of this thesis, the close connection between these quantum systems became mainly apparent from the underlying mathematical descriptions, this final chapter concentrates on experimental aspects. It examines the possibility of designing new experiments with laboratory condensates that could mimic the behaviour of neutron stars on significantly smaller lengthscales. Since replicating the extreme conditions present in a star is out of reach, the aim of laboratory analogues would instead be to create systems that are easily manipulable and allow one to recreate some of the characteristic features of neutron stars. Among others, the succeeding discussion will address the two-fluid nature, pinning of vortices and fluxtubes, dynamics of interfaces and instabilities.

As briefly introduced in Chapter 3, superfluid helium, ultra-cold gases and superconductors are prime candidates to test such behaviour. Their respective advantages and several limitations in modelling neutron stars will be reviewed. Section 8.1 focuses on the two stable isotopes of liquid helium, helium-4 and helium-3 respectively, whereas Section 8.2 is devoted to ultra-cold condensates. Finally, superconducting analogues are examined in Section 8.3. While some of the aspects presented here, specifically simila-

rities between two-stream instabilities in neutron stars and their laboratory analogues, have already been studied by Hogg [270], the succeeding analysis expands upon those considerations. In particular, the properties of helium-3, mutual friction, vortex dynamics and superconducting analogies are discussed in more detail. Finally, note that the material presented in this chapter contributes a significant fraction to the review paper *Neutron Stars in the Laboratory* by Graber et al. [271] currently in preparation.

8.1 Helium

8.1.1 Two stable isotopes: helium-4 and helium-3

Helium-4 is one of the two naturally occurring, stable isotopes of helium and with a relative abundance of $10^6 : 1$ in the Earth's atmosphere the more common one. Below its boiling point of 4.21 K, helium-4 exhibits characteristics of a standard low viscosity fluid. However, due to the weak interatomic forces in helium, decreasing the temperature further does not lead to a solid state. At the 2.171 K Lambda point (see Figure 3.1), helium-4 instead undergoes a phase transition into a superfluid state, which was first observed by Kapitsa, Allen and Misener in 1937 [127, 128]. This discovery marked the beginning of the era of low temperature experiments.

As explained in detail in Sections 3.1 and 3.2, many features of superfluid helium-4, also referred to as helium II, can be explained by invoking the presence of two co-existing components. The two-fluid model, which was developed by Tisza and Landau [132, 138], assumes that helium II is formed of a normal, viscous constituent, representing the excitations in the fluid, and an inviscid part exhibiting frictionless flow. This two-fluid interpretation offers the possibility to draw a parallel to neutron star cores by identifying the superfluid neutrons with the inviscid ground-state component and the combined electron-proton conglomerate with the excitations. Since the concentration of normal to inviscid fluid in helium II is temperature-dependent, as first observed by Andronikashvili in 1946 [139], one would be particularly interested in the temperature range that gives mass ratios similar to the proton fraction, x_{p}. In the neutron star core, this parameter is typically of the order of a few percent as discussed in Subsection 5.1.1. Further note that while this laboratory analogue does not allow us to specifically study the influence of superconducting fluxtubes and, thus, address the magnetic field evolution of a neutron star, it certainly provides a model for the stars' rotational dynamics. On one hand, the normal helium II component is observed to follow rigid-body rotation (see for example Osborne [158]), a state which also characterises the angular velocity profile of the charged component in the neutron star core, coupled to the crust by the strong magnetic field [218]. On the other hand, the superfluids in both systems rotate by forming quantised vortices. Spin-down experiments as the ones discussed below in Subsection 8.1.2 could therefore help us understand the superfluid's role in generating pulsar glitches.

Recent experiments further provide the possibility of directly imaging the flow behaviour of helium II [272]. By inserting small particles such as liquid neon atoms [273] or hydrogen molecules [274] into the superfluid and tracing their motion, vortices have been visualised. This tool has proven particularly useful in studying superfluid turbulence [275, 276] (see also Subsection 8.1.4) and could further improve our understanding of the fluid motion in neutron stars.

The second stable, naturally occurring helium isotope is helium-3. The book *The Superfluid Phases Of Helium 3* by Vollhardt and Wölfle [277] presents an extensive summary on the topic. The isotope only constitutes a very small fraction of the noble gas in the atmosphere and irradiation of lithium-6 with neutrons is necessary to synthesise larger quantities. Due to these obstacles, experiments with helium-3 did not commence until the 1960s, several decades after the first helium-4 experiments had been performed.

Below the 3.19 K boiling point, helium-3 behaves like a fluid with low viscosity. Similar to helium-4, it does not solidify at normal pressures and lower temperatures. It instead shows superfluid behaviour below 3 mK, as first reported by Osheroff et al. in 1972 [130, 131]. Though, the origin of these phase transitions is very different to that of helium II. Whereas spin-0 helium-4 atoms are described by Bose-Einstein statistics and turn superfluid by condensing into the quantum mechanical ground state [143], helium-3 atoms are fermions of spin 1/2 that are subject to Fermi-Dirac statistics and obey Pauli's exclusion principle. As governed by BCS theory [120], they have to form Cooper pairs before any condensation can take place, which results in the much lower transition temperatures. However, in contrast to standard superconductivity, where the attractive interaction between two electrons is mediated by the underlying lattice, no such crystal network is present in the case of helium-3. Hence, superfluidity has to be an intrinsic property of the atoms. More precisely, helium-3 atoms pair in the spin-triplet, p-wave state characterised by a total spin of $S = 1$ and an orbital angular momentum of $L = 1$. Hence, unlike for singlet, s-wave pairing with $S = 0$ and $L = 0$, the helium-3 Cooper pairs have an internal structure resulting in the formation of different superfluid phases. A total of three distinct phases have been observed, commonly referred to as A, B and A_1 [278]. They populate different parts of the phase diagram depending on the temperature, pressure and magnetic field as illustrated in Figure 8.1. If no magnetic field is applied, only the helium-A and helium-B phases are stable. While the former occupies a small range of temperatures above a critical pressure of ~ 22 bar, the latter dominates the phase diagram and is stable down to the lowest temperatures observed. In the presence of an external field, however, the A-phase is stable even for zero pressure and replaces the B-phase for sufficiently high magnetic field strengths. Additionally, the A_1-phase develops in a very narrow region between the normal and superfluid zones.

In the remainder of this section, we will focus on the importance of helium-A and helium-B in designing new laboratory neutron star analogues. First of all, despite the fundamental differences in the formation of the superfluid phases and the underlying

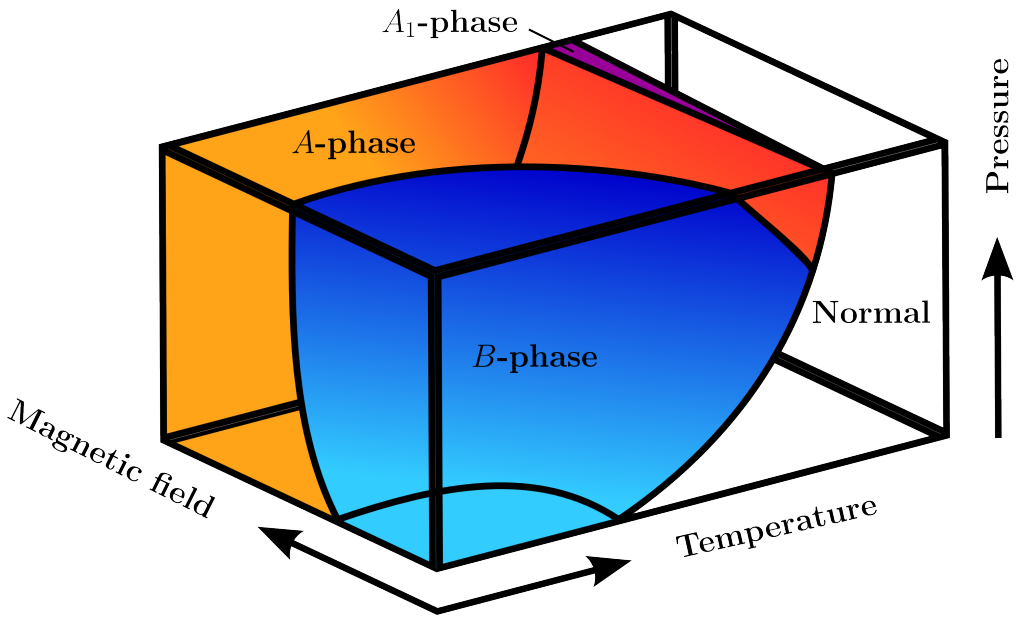

Figure 8.1: Phase diagram of helium-3 illustrating the presence of three different phases depending on the temperature, pressure and magnetic field. In the absence of a magnetic field, only the helium-A (red) and helium-B (blue) phases are stable. While the former occupies a small temperature range above a critical pressure, the latter dominates the phase diagram and is stable down to the lowest temperatures observed. In the presence of an external field, the A-phase is stable even for zero pressure and replaces the B-phase for sufficiently high field strengths. Additionally, the A_1-phase (purple) develops in a very narrow region between the normal and the superfluid zones.

microscopic theories of helium-4 and helium-3, the two-fluid model is also applicable to describe the macroscopic characteristics of the latter. This is related to the close connection between the symmetries of the Fermi system and its hydrodynamical variables. It suggests the presence of an inviscid component responsible for the frictionless behaviour and a normal component representing the quasi-particle excitations, allowing the modelling of the neutron stars' two-fluid behaviour. Experiments in the 1980s confirmed the existence of persistent currents and the onset of dissipation above a critical velocity in both helium-A and helium-B (see for example Gammel et al. [279, 280]). As in helium II, the ratio of superfluid to normal fluid is a function of temperature in the B-phase, whereas in the A-phase the ratio also depends on the applied field. This provides an additional possibility to tune the latter condensate into a state of interest for neutron star experiments and obtain proton fractions as given in Figure 5.1.

Moreover, as discussed in Subsection 3.2.1, the superfluid component of helium II is fully described by a macroscopic wave function, Ψ, which is the product of an amplitude and a phase factor as given in Equation (3.1). According to Equation (3.8), the velocity of the frictionless component is then related to the gradient of the order parameter's phase, showing that the superfluid is characterised by potential flow. This implies that helium II is only able to rotate by quantising its circulation and forming vortices. Helium-B exhibits very similar behaviour. Despite the intrinsic anisotropy of

the helium-3 superfluid, the B-phase has an isotropic energy gap and is represented by an order parameter that is a real quantity times a phase factor, which causes the resemblance with classical superfluids and superconductors. The anisotropic A-phase, on the other hand, has a complex order parameter that not only contains a phase factor but also an orientation as a consequence of the Cooper pairs' internal structure. Thus, the superfluid velocity additionally depends on the preferred direction of the paired atoms and is no longer curl-free. The standard quantisation condition (3.20) does therefore not apply to helium-A, resulting in a richer vortex architecture generally visualised using the concept of textures, i.e. the topology of the complex order parameter [277]. These include planar defects such as domain walls [281] or coreless vortex structures of double integer quantisation [282], generally detected employing modern nuclear magnetic resonance (NMR) spectra. This technique is non-invasive and allows accurate mapping of topological defects in the order parameter.

In principle, one would similarly expect the p-wave paired superfluid in a neutron star's outer core to exhibit diverse features [204, 283]. Discussed in detail in Subsection 5.1.3, the persistent core magnetisation of $^3P_2$ vortices is a direct result of the complicated structure of the order parameter, providing the means to couple the electrons and the superfluid in the stars' interior. However, it is generally not well understood if there are other ways for the vortex anisotropy to manifest itself on hydrodynamical scales. As helium-A is one of the few terrestrial anisotropic superfluids available, it provides the unique opportunity to study the neutron superfluid in the neutron stars' core. Despite this advantage, we note that the rich spectrum of observed phenomena also significantly complicates a comparison between the two systems and raises the question of how far the analogy can be extended. Drawing direct conclusions from experiments with laboratory condensates for neutron star dynamics should thus always be done with caution.

8.1.2 Spin-up experiments

Early efforts of studying the spin-up and spin-down behaviour of superfluid helium-4 contained in closed vessels were undertaken in the late 1950s (see for example Hall [284] and Walmsley and Lane [285]). These experiments measured the torques necessary to accelerate and decelerate containers filled with helium II and additionally monitored the fluid's response by immersing closely spaced discs into the fluid. The studies discovered that acceleration and retardation are asymmetric processes. While the fluid responded with a delay to setting the vessel, initially at rest, into motion, it instantly reacted when the container rotation was stopped. These effects were interpreted as the manifestation of the quantised vortex array. Because the asymmetry of spin-up and spin-down was also influenced by the surface roughness of the container walls and discs, it was further suggested that the pinning and nucleation of vortices could play an important role for the dynamics.

Following these initial endeavours, a systematic analysis of rotating helium II was

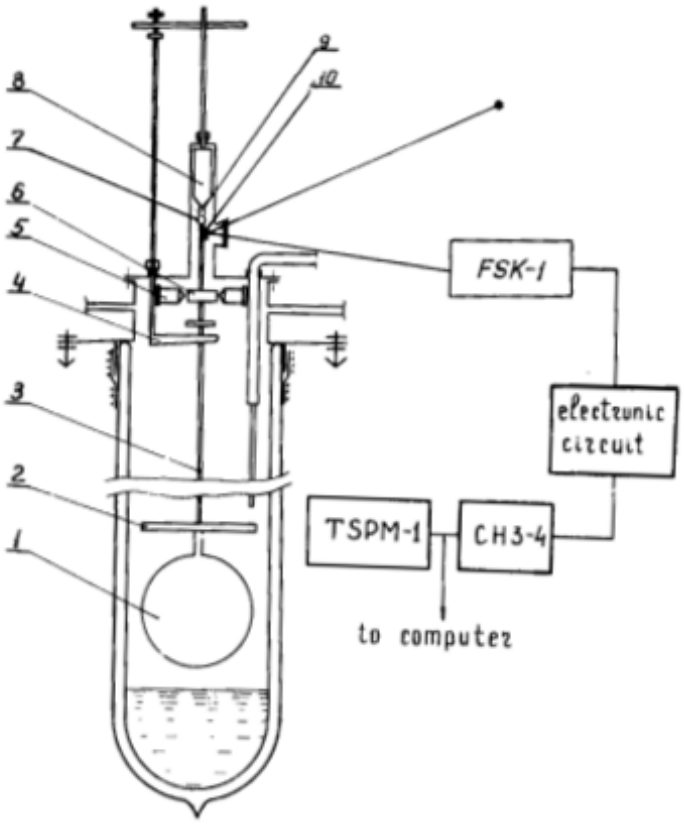

Figure 8.2: Schematic setup of the helium II spin-up experiments performed by Tsakadze and Tsakadze. The test neutron star is represented by a hollow glass sphere (1), which together with a brass disk (2) is rigidly connected to a thin steel rod (3) and magnetically suspended (7-9). The support device (4) is used to lower the sphere into a bath of helium. The freely suspended components (1-3) are then suddenly accelerated using the electric motor (5-6), while the rotation period is measured by a focused light beam reflected off a mirror (10). The figure is reproduced from Tsakadze and Tsakadze [289] (p. 656).

carried out by the Georgian physicists Tsakadze and Tsakadze in the 1970s [286, 287, 288, 289]. These spin-up experiments were performed shortly after the first observations of glitches in the Vela and Crab pulsars [75, 76, 77, 78] and represent the first attempts of modelling neutron star physics with laboratory analogues. However, instead of understanding the underlying mechanism for glitches, the series of experiments was rather aimed at validating the assumption of a superfluid component inside the star. Following an initial increase in the vessel's angular rotation frequency, Tsakadze and Tsakadze determined the relaxation timescales and compared them to the ones obtained from pulsar glitch observations. They found general agreement [287], which supported the idea of astrophysical quantum condensates.

Despite the fact that these experiments were performed more than 30 years ago, they still mark the highlight of research on laboratory neutron star analogues and have remained the only ones specifically focusing on the idea of reproducing the neutron stars' rotational evolution. We will therefore discuss a few more aspects in detail. The schematic setup of the experiments is shown in Figure 8.2. The test neutron star is

represented by a hollow glass sphere (1) with a radius of $3.4 \pm 0.05\,\mathrm{cm}$.[1] Together with a small brass disk (2), which is attached to increase the moment of inertia of the system, the sphere is rigidly connected to a thin steel rod (3) and magnetically suspended (7-9) in order to reduce friction. The support device (4) is used to lower the sphere into a bath of helium, filling it with the fluid before each experiment. The freely suspended components (1-3) are then suddenly accelerated to a desired angular frequency using an electric motor (5-6). Once the motor is switched off, the system is allowed to evolve freely under the frictional forces present. Its rotation period is measured by a focused light beam reflected off a mirror (10), fixed to the rod (3). Because the helium fluid is also spun-up as a result of the coupling to the rotating container walls, the configuration first reacts abruptly to the initiated spin-down. However, eventually the angular velocity is observed to follow exponential decay characterised by a small damping parameter.

This experiment was performed for various temperatures, vessel configurations, initial angular velocities and velocity jumps, primarily showing that below the Lambda point the relaxation time significantly increases. Adopting the two-fluid model, this can be interpreted as a result of the larger fraction of superfluid component present at lower temperatures. Tsakadze and Tsakadze also modified the experimental setup to investigate different coupling strengths and pinning. By introducing impurities in the form of crushed Plexiglas crystals into the fluid, the friction between the normal component and the container walls is increased, resulting in shorter relaxation timescales. Glueing the crystals to the inside of the sphere, effectively providing more nucleation and pinning sites, a larger number of vortices were generated and, thus, the dissipation increased. This also caused shorter relaxation times compared to the experiments with smooth walls. Such a degree of control over the pinning strength and the possibility to study its effect on the macroscopic rotational evolution of the fluid components could be particularly useful for improving the understanding of superfluid pinning in the inner neutron star crust. As discussed in Subsection 5.2.2, large uncertainties prevail for the strength of the vortex-lattice interaction, which is crucial for determining the crustal mutual friction mechanisms, and helium II experiments could provide more insight into the interplay between the mesoscopic coupling and the large-scale dissipation. The Georgian physicists further repeated their experiment with a mixture of helium-4 and helium-3 [291]. Since the temperature was set below the Lambda point but above the transition temperature for helium-3 superfluidity, the normal helium-3 atoms act as an additional viscous fluid, increasing the dissipation. Due to the stronger frictional forces, the relaxation timescales were shorter the more helium-3 was dissolved into helium II.

Furthermore, Tsakadze and Tsakadze detected spontaneous acceleration during periods of observation, which lasted for over an hour. Using a cylindrical Plexiglas vessel with a diameter of 1.5 cm, an external pulse was applied to spin up the container, which

[1] Information about the size of the container is somewhat contradicting. In Tsakadze and Tsakadze [289], $3.4 \pm 0.05\,\mathrm{cm}$ is given as both the radius and the diameter of the sphere. According to Reisenegger [290], the smaller size should be adopted to match the measured relaxation timescales.

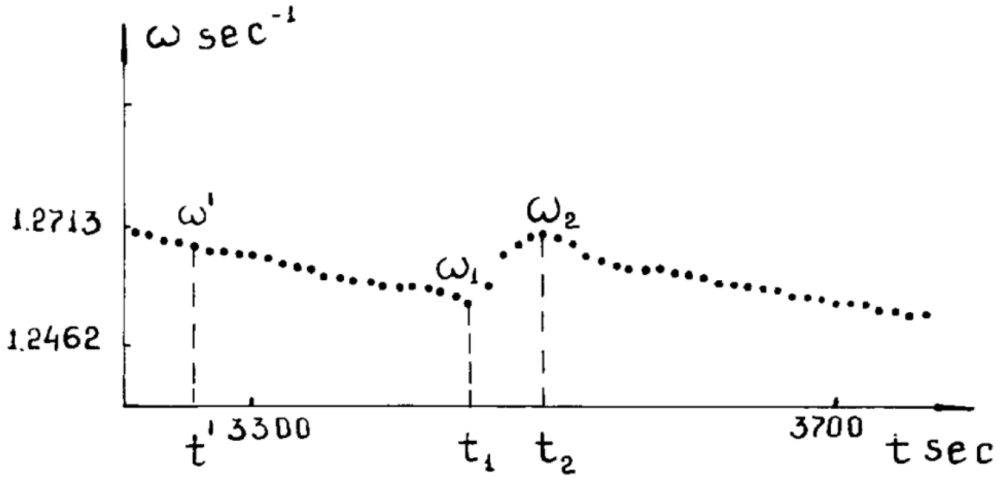

Figure 8.3: Original measurements of the rotational velocity of a rotating cylinder filled with helium II. After an initial acceleration at $t = 0$, the vessel is spinning down and observed to accelerate between the times t_1 and t_2. The figure is reproduced from Tsakadze and Tsakadze [289] (p. 674).

was then let to evolve freely. While the spin-down was initially observed to be linear, it was suddenly impeded by a jump in the rotation frequency as shown in Figure 8.3. This phenomenon was explained in terms of the dynamics of the vortex array. As for the pulsar glitch mechanism discussed in Subsection 2.3.3, the superfluid does not follow the spin-down of the container and forms a metastable state with a non-equilibrium number of vortices. When the superfluid component and the container are recoupled, a large number of vortices decays, leading to the acceleration of the container due to the conservation of angular momentum. While the star-quake model [85, 86] had primarily been in the focus of the astrophysics community up to this point, the new experimental results were pointing towards a purely superfluid-related glitch mechanism, since quake-like disruptions had not been generated in the glitching helium II samples.

Despite the numerous improvements of laboratory techniques in the last 40 years, the research performed by Tsakadze and Tsakadze has not been repeated or improved. While little interest for modern helium II spin-up experiments seems to be present in the low-temperature-physics community, the benefits of studying this terrestrial neutron star analogue have been pointed out by several astrophysicists. Reisenegger [290], for example, examined the laminar spin-up of helium II by analytically solving the fluid equations of motion in the presence of vortices for a simplified geometry. While the analysis agreed quantitatively with the smooth container experiments, detailed comparison was not possible. More recently, van Eysden et al. [292, 293] modelled the dynamics of the superfluid by including the back-reaction torque exerted by the container. They derived a self-consistent, analytical solution of the HVBK equations (see also Subsection 3.2.4) and found good agreement with the Tsakadze and Tsakadze data. However, more detailed experiments would be needed in order to deduce reliable information about the physics of neutron stars.

8.1.3 Mutual friction

In a rotating superfluid, the normal and the inviscid components are coupled by forces that result from interactions of vortices with the viscous fluid. This type of dissipative coupling, called mutual friction, was first investigated by Hall and Vinen in the 1960s [142] in the context of uniformly rotating helium II, which is permeated by an ordered array of straight vortices. They developed a mathematical formalism allowing one to include the dissipation by introducing a macroscopic, averaged mutual friction force that results from coarse-graining over regions containing large numbers of vortices. As given in Equation (3.27), the force for a straight vortex array is

$$\mathbf{F}_{\mathrm{mf}} = \mathcal{B}_{\mathrm{II}} \frac{\rho_{\mathrm{S}} \rho_{\mathrm{N}}}{2\rho} \, \omega \, \hat{\boldsymbol{\omega}} \times [\hat{\boldsymbol{\omega}} \times (\mathbf{v}_{\mathrm{S}} - \mathbf{v}_{\mathrm{N}})] + \mathcal{B}'_{\mathrm{II}} \frac{\rho_{\mathrm{S}} \rho_{\mathrm{N}}}{2\rho} \, \omega \, \hat{\boldsymbol{\omega}} \times (\mathbf{v}_{\mathrm{S}} - \mathbf{v}_{\mathrm{N}}) \, . \tag{8.1}$$

Here ρ_{S}, ρ_{N} and ρ are the superfluid, normal fluid and total mass density, respectively, and $\boldsymbol{\omega} \equiv \omega \hat{\boldsymbol{\omega}}$ denotes the averaged vorticity, while $\mathbf{v}_{\mathrm{S}}$ and $\mathbf{v}_{\mathrm{N}}$ represent the averaged velocities of the inviscid and viscous component. As mutual friction modifies the propagation of second sound in helium II, the dimensionless coefficients $\mathcal{B}_{\mathrm{II}}$ and $\mathcal{B}'_{\mathrm{II}}$ can be directly determined in rotating container experiments. More precisely, $\mathcal{B}_{\mathrm{II}}$ is related to the excess attenuation of second sound caused by the presence of quantised vortices, whereas $\mathcal{B}'_{\mathrm{II}}$ is responsible for the coupling of modes that would be degenerate in the absence of rotation. This type of experiment has been performed in the range of 1.3 to 2.171 K. The results of various studies are discussed in Barenghi et al. [294]. The parameters for superfluid helium-4 are given in Table 8.1 as a function of the temperature, T. This table also contains the reduced temperature, T/T_{c}, the viscous fluid fraction given by $x_{\mathrm{N}} \equiv \rho_{\mathrm{N}}/\rho$ and the modified mutual friction coefficients, usually denoted by α_{II} and α'_{II} in the literature [115, 295, 296]. The coefficients are defined as

$$\alpha_{\mathrm{II}} \equiv \mathcal{B}_{\mathrm{II}} \frac{\rho_{\mathrm{N}}}{2\rho}, \qquad\qquad \alpha'_{\mathrm{II}} \equiv \mathcal{B}'_{\mathrm{II}} \frac{\rho_{\mathrm{N}}}{2\rho}, \tag{8.2}$$

which corresponds to the following mutual friction force,

$$\mathbf{F}_{\mathrm{mf}} = \alpha_{\mathrm{II}} \rho_{\mathrm{S}} \, \omega \, \hat{\boldsymbol{\omega}} \times [\hat{\boldsymbol{\omega}} \times (\mathbf{v}_{\mathrm{S}} - \mathbf{v}_{\mathrm{N}})] + \alpha'_{\mathrm{II}} \rho_{\mathrm{S}} \, \omega \, \hat{\boldsymbol{\omega}} \times (\mathbf{v}_{\mathrm{S}} - \mathbf{v}_{\mathrm{N}}) \, . \tag{8.3}$$

In the absence of dissipation, vortices are free and their motion is simply governed by the Magnus force (see Subsection 4.3.3), which causes them to move with the superfluid. In the presence of a viscous drag however, the vortex motion is modified and balancing the two forces allows one to express the averaged vortex velocity in terms of the macroscopic fluid variables. Generalising Equation (3.34) to the case of straight vortices, one has

$$\mathbf{u}_{\mathrm{v}} = \mathbf{v}_{\mathrm{S}} - \frac{1}{\rho_{\mathrm{S}} \, \omega} \, \hat{\boldsymbol{\omega}} \times \mathbf{F}_{\mathrm{mf}} = \mathbf{v}_{\mathrm{S}} + \alpha_{\mathrm{II}} \, \hat{\boldsymbol{\omega}} \times (\mathbf{v}_{\mathrm{N}} - \mathbf{v}_{\mathrm{S}}) + \alpha'_{\mathrm{II}} \, (\mathbf{v}_{\mathrm{N}} - \mathbf{v}_{\mathrm{S}}) \, . \tag{8.4}$$

As shown in Table 8.1, the experimental values for α_{II} and α'_{II} are of the same order,

T [K]	T/T_c	ρ [g cm^{-3}]	ρ_S [g cm^{-3}]	$\mathcal{B}_{II}$	$\mathcal{B}'_{II}$	x_N	α_{II}	α'_{II}
1.300	0.599	0.1451	0.1383	1.52	0.61	0.047	0.036	0.014
1.350	0.622	0.1451	0.1364	1.46	0.53	0.060	0.044	0.016
1.400	0.645	0.1451	0.1343	1.40	0.45	0.074	0.052	0.017
1.450	0.668	0.1451	0.1317	1.35	0.38	0.092	0.062	0.018
1.500	0.691	0.1452	0.1287	1.29	0.31	0.114	0.073	0.018
1.550	0.714	0.1452	0.1253	1.24	0.25	0.137	0.085	0.017
1.600	0.737	0.1452	0.1213	1.19	0.19	0.165	0.098	0.016
1.650	0.760	0.1452	0.1168	1.14	0.15	0.196	0.111	0.015
1.700	0.783	0.1453	0.1117	1.10	0.10	0.231	0.127	0.012
1.750	0.806	0.1453	0.1059	1.06	0.07	0.271	0.144	0.009
1.800	0.829	0.1453	0.0994	1.02	0.05	0.316	0.161	0.008
1.850	0.852	0.1454	0.0919	0.99	0.04	0.368	0.182	0.007
1.900	0.875	0.1455	0.0836	0.98	0.04	0.425	0.208	0.009
1.950	0.898	0.1455	0.0741	0.98	0.05	0.491	0.240	0.012
2.000	0.921	0.1456	0.0636	1.01	0.04	0.563	0.284	0.011
2.010	0.925	0.1456	0.0613	1.02	0.04	0.579	0.295	0.012
2.020	0.930	0.1456	0.0589	1.04	0.04	0.595	0.310	0.012
2.030	0.935	0.1457	0.0565	1.05	0.03	0.612	0.321	0.009
2.040	0.939	0.1457	0.0540	1.07	0.02	0.629	0.337	0.006
2.050	0.944	0.1457	0.0514	1.10	0.01	0.647	0.356	0.003
2.060	0.948	0.1457	0.0487	1.13	0.00	0.666	0.376	0.000
2.070	0.953	0.1457	0.0459	1.16	-0.01	0.685	0.397	-0.003
2.080	0.958	0.1458	0.0430	1.21	-0.03	0.705	0.427	-0.011
2.090	0.962	0.1458	0.0400	1.26	-0.05	0.726	0.457	-0.018
2.100	0.967	0.1458	0.0368	1.33	-0.08	0.748	0.497	-0.030
2.110	0.971	0.1458	0.0334	1.42	-0.12	0.771	0.547	-0.046
2.120	0.976	0.1459	0.0297	1.53	-0.17	0.796	0.609	-0.068
2.130	0.981	0.1459	0.0258	1.69	-0.24	0.823	0.696	-0.099
2.140	0.985	0.1459	0.0215	1.90	-0.36	0.853	0.810	-0.153
2.150	0.990	0.1460	0.0167	2.21	-0.54	0.886	0.979	-0.239
2.160	0.994	0.1460	0.0111	2.67	-0.83	0.924	1.234	-0.383
2.161	0.995	0.1460	0.0105	2.73	-0.94	0.928	1.267	-0.436
2.162	0.995	0.1460	0.0098	2.80	-1.00	0.933	1.306	-0.466
2.163	0.996	0.1460	0.0092	2.88	-1.07	0.937	1.349	-0.501
2.164	0.996	0.1460	0.0085	2.99	-1.15	0.942	1.408	-0.542
2.165	0.997	0.1460	0.0077	3.12	-1.25	0.947	1.478	-0.592
2.166	0.997	0.1460	0.0070	3.28	-1.37	0.952	1.561	-0.652
2.167	0.998	0.1460	0.0062	3.49	-1.51	0.958	1.671	-0.723
2.168	0.998	0.1461	0.0050	3.75	-1.71	0.966	1.811	-0.826
2.169	0.999	0.1461	0.0044	4.13	-1.98	0.970	2.003	-0.960
2.170	0.999	0.1461	0.0033	4.72	-2.40	0.977	2.307	-1.173
2.171	1.000	0.1461	0.0021	5.93	-3.28	0.986	2.922	-1.616

Table 8.1: Experimental values for helium II as a function of temperature, T. The second column contains the reduced temperature, T/T_c, where $T_c = 2.171\,\mathrm{K}$ is the superfluid transition temperature. The third and fourth column give the total and the superfluid mass density, ρ and ρ_S, respectively, while the fifth and sixth column contain the dimensionless mutual friction coefficients, $\mathcal{B}_{II}$ and $\mathcal{B}'_{II}$, obtained from measurements of the second sound velocity in rotating helium experiments. Values in the last three columns are the viscous fluid fraction, x_N, and the modified mutual friction coefficients, α_{II} and α'_{II}. The data is taken from Barenghi et al. [294].

implying that the mutual friction force induces changes of similar degree in the vortex velocity components parallel and perpendicular to the superfluid velocity.

To allow for a comparison of coupling strengths in helium II and neutron stars, Equation (8.1) or (8.3) has to be compared to the mutual friction derived in Subsection 4.3.3. In vector notation, Equation (4.91) for the neutron superfluid reads as

$$\mathbf{F}_{\rm mf} = \mathcal{B}\rho_{\rm n}\mathcal{N}_{\rm n}\kappa\hat{\boldsymbol{\kappa}} \times [\hat{\boldsymbol{\kappa}} \times (\mathbf{v}_{\rm n} - \mathbf{v}_{\rm e})] + \mathcal{B}'\rho_{\rm n}\mathcal{N}_{\rm n}\kappa\hat{\boldsymbol{\kappa}} \times (\mathbf{v}_{\rm n} - \mathbf{v}_{\rm e})\,, \tag{8.5}$$

where $\mathcal{N}_{\rm n}\kappa\hat{\boldsymbol{\kappa}}$ corresponds to the averaged vorticity. Identifying the neutrons with the inviscid component in helium II and the charged-particle conglomerate with its excitations, $\rho_{\rm S}$ and $x_{\rm N}$ are equal to $\rho_{\rm n}$ and $x_{\rm p}$, respectively. This gives the following relations between the mutual friction coefficients in neutron stars and laboratory systems,

$$\mathcal{B} = \mathcal{B}_{\rm II}\frac{x_{\rm N}}{2} = \alpha_{\rm II}, \qquad\qquad \mathcal{B}' = \mathcal{B}'_{\rm II}\frac{x_{\rm N}}{2} = \alpha'_{\rm II}. \tag{8.6}$$

Hence, the numerical values calculated in Chapter 5 for the dissipation strengths in the neutron star superfluids have to be compared to the modified helium II mutual friction parameters $\alpha_{\rm II}$ and $\alpha'_{\rm II}$, if the analogy between the two systems is to be exploited.

One instantly notices that the experimental values for helium II show little agreement with the ones invoked for neutron stars. While the standard coupling mechanisms in neutron stars are generally attributed to the weak mutual friction limit, with positive parameters $\mathcal{B}$ and $\mathcal{B}'$, the coupling in superfluid helium is much stronger. This implies that the dynamics in neutron star cores are well approximated by the free vortex limit and vortices are dragged along with the superfluid component, whereas in helium II the two components do not move together. Close to the Lambda point, $\alpha_{\rm II}$ and $\alpha'_{\rm II}$ are of order unity with both coefficients expected to diverge as $(T_{\rm c} - T)^{-1/3}$ for $T \to T_{\rm c}$ [297]. Moreover, $\alpha'_{\rm II}$ turns negative for temperatures above 2.07 K, which would suggest rather different physical behaviour. Also note that the fraction of normal fluid in helium II is significantly larger than the proton fraction in neutron star cores (see Figure 5.1). Only for very low temperatures does $x_{\rm N}$ take values between 2 and 10%, the range one would want to examine. Experimental data below 1.3 K would therefore be important in order to develop laboratory neutron star models with helium II. However, the standard rotating helium experiments measuring the speed of second sound are no longer applicable at such low temperatures, because the viscous fluid concentration is too low to provide reliable results. Instead, experiments that measure the drag on vortex rings, which are attached to individual ions, have been designed. While these studies would in principle allow access to the parameters $\mathcal{B}_{\rm II}$ and $\mathcal{B}'_{\rm II}$, no conclusive data is available and the values in Table 8.1 have been restricted to the data from second sound experiments.

When analysing vortex-averaged dissipation, the phenomenological parameters $\mathcal{B}_{\rm II}$ and $\mathcal{B}'_{\rm II}$ provide little information about the underlying mesoscopic or microscopic mechanisms in helium II. However, as first suggested by Landau [138], dissipation in

helium II could result from the interactions of thermally excited quasi-particles with individual vortices. It is hence possible to relate the large-scale dynamics to the small-scale physics by considering a mesoscopic coupling force of the form [294]

$$\mathbf{f}_\mathrm{d} = \rho_\mathrm{S}\kappa\mathcal{R}_\mathrm{II}\left(\mathbf{v}_\mathrm{q} - \mathbf{u}_\mathrm{v}\right) + \rho_\mathrm{S}\kappa\mathcal{R}'_\mathrm{II}\hat{\boldsymbol{\omega}} \times \left(\mathbf{v}_\mathrm{q} - \mathbf{u}_\mathrm{v}\right). \tag{8.7}$$

Here, $\mathbf{v}_\mathrm{q}$ denotes the corresponding quasi-particle velocity and $\mathbf{u}_\mathrm{v}$ the vortex velocity. The force is proportional to the relative velocity and characterised by two mesoscopic friction coefficients, $\mathcal{R}_\mathrm{II}$ and $\mathcal{R}'_\mathrm{II}$. Different theories are available to calculate these parameters, since the coupling mechanism depends on two crucial lengthscales, i.e. the size of the region responsible for mutual friction and the quasi-particles' mean free path [298]. For low temperatures, the former lengthscale is smaller and the scattering of rotons and phonons off rectilinear vortices causes dissipation. Using the scattering theory for non-interacting quasi-particles, the mesoscopic coefficients can be obtained. They typically satisfy $|\mathcal{R}'_\mathrm{II}| \gg \mathcal{R}_\mathrm{II}$ [294]. For temperatures close to the Lambda point, the vortex core size increases considerably and becomes larger than the mean free path, which raises the need for phenomenological approaches such as the time-dependent Ginzburg-Landau theory [298]. Utilising a force balance equation to eliminate the vortex velocity in Equation (8.7), the macroscopic and mesoscopic coefficients can be related to each other. Therefore, $\mathcal{R}_\mathrm{II}$ and $\mathcal{R}'_\mathrm{II}$ are controlled by $\mathcal{B}_\mathrm{II}$ and $\mathcal{B}'_\mathrm{II}$ and vice versa, providing a possibility to constrain mesoscopic theoretical models with experimental data. Studying mutual friction in helium II could therefore provide useful information about the coupling mechanisms in neutron star. There, direct observations are not feasible and microscopic interactions can only be studied from a theoretical point of view as illustrated in detail in Chapter 5. In particular, one could learn how to determine a suitable average over mesoscopic lengthscales in order to match the measured macroscopic dissipation strengths. Such studies might even help to deduce information about the vortex arrangement and deviations from the canonical straight vortex array.

Though, one difference between the two formalisms is immediately evident. Direct comparison between the helium II drag in Equation (8.7) and the ansatz for the force in neutron stars given in Equation (4.81) shows that an additional term proportional to $\mathcal{R}'_\mathrm{II}$ is included in the former system. It acts in the direction orthogonal to the relative velocity and the local orientation of the vortex. This transverse drag component, which is generally not included in the neutron star case, is needed in order to explain the experimental data, in particular the negative values of α'_II close to the Lambda point. As can be seen from Table 8.1, the simple relationship between the neutron star mutual friction coefficients given in Equation (5.67), i.e. $\mathcal{B}' \approx \mathcal{R}\mathcal{B}$, does not hold in superfluid helium-4. By introducing a second parameter $\mathcal{R}'_\mathrm{II}$, this behaviour can be captured. This also illustrates that the problem in neutron stars might be oversimplified and a second mesoscopic drag term $\mathcal{R}'$ should be accounted for.

Although helium II is the best studied system regarding mutual friction, several

attempts have been undertaken at measuring the drag parameters in helium-3. These were not only complicated by the presence of distinct phases but also by the fact that the viscosity of the normal component is four orders of magnitude larger than that of helium II [296]. The latter problem causes second sound to become highly damped, eliminating such studies as a tool to investigate mutual friction in helium-3 and raising the need for new techniques. Whereas earlier efforts [299, 300] had only provided limited information, Bevan et al. [301, 302] designed an experiment allowing one to determine the coefficients of the B-phase and the A-phase. Taking advantage of the normal fluid's large viscosity, the following idea was exploited: Separating two regions of helium-3, a vibrating Kapton film was used to set the superfluid component into motion, while the normal fraction remained stationary due to its viscous properties. As the film's vibrational modes are influenced by the vortex array, the strength of the mutual friction can be deduced by analysing the mode frequencies. This way, experimental estimates of the modified coefficients α_3 and α_3' were obtained for various temperatures and pressures.

The original B-phase results at 1.6 bars and 29.3 bars are shown in Figures 8.4 to 8.6 as a function of the reduced temperature, T/T_c. The critical temperature for the superfluid transition is pressure-dependent and given by $T_\mathrm{c} \sim 1.1\,\mathrm{mK}$ in the former and $T_\mathrm{c} \sim 2.4\,\mathrm{mK}$ in the latter case [303]. Note also that for pressures above $\sim 22\,\mathrm{bar}$, both helium-3 phases are present. For 29.3 bars, the transition temperature T_{AB} is located at around 2 mK [303], which implies that the B-phase only exists up to $T/T_\mathrm{c} \sim 0.8$ as can be seen in Figure 8.6. The data shows that both mutual friction coefficients vanish in the limit $T \to 0$ as expected, while $\alpha_{3\mathrm{B}}$ diverges close to the transition temperature and $\alpha_{3\mathrm{B}}'$ approaches 1. Similar to helium II, the coupling between the normal and the superfluid component in helium-3 is much stronger than predicted for neutron stars. Measurements for the A-phase lead to even stronger dissipation [302]. As before, the macroscopic dissipation parameters can be related to mesoscopic drag coefficients. In contrast to the previous discussion however, it is less clear what kind of interactions between quasi-particles and vortices generate the coupling on small scales. One cannot simply transfer the theoretical predictions for helium II to helium-3 due to the fundamental differences in vortex formation [298]. Instead, dynamical features seem to be well explained using the theories available for superconductors [304] (see also Subsection 8.3.2), which are also characterised by Fermi-Dirac statistics and exhibit quantum properties by forming Cooper pairs. Analysing the dissipative coupling in helium-3 could again help to understand mutual friction in neutron stars, where the dominating coupling mechanisms are not well known. To exploit this analogy further, the ratio of superfluid to normal fluid component should ideally be 2 to 10%. Experimental results for the viscous fluid fraction in helium-3 at various pressure are, for example, discussed by Alvesalo et al. and Archie et al. [305, 306]. As seen from Figure 8.7, the normal fluid fraction in the B-phase and the proton fraction in neutron stars are comparable for temperatures below $\sim 0.4T_\mathrm{c}$. This region is accessible with modern experiments [208], which presents a clear advantage of helium-3 over helium-4.

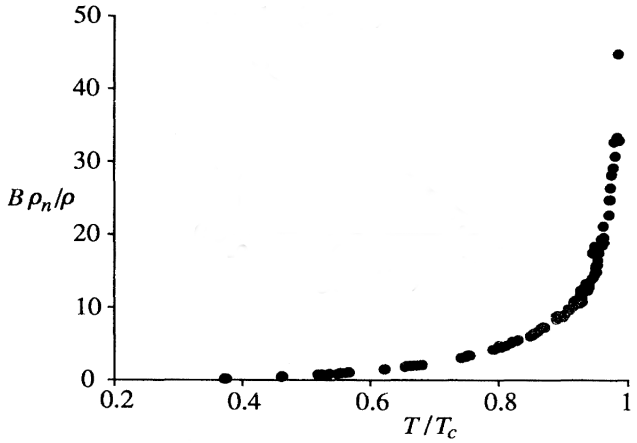

Figure 8.4: Behaviour of the mutual friction parameter ($B_{3B}x_N = 2\alpha_{3B}$) in the B-phase as a function of the reduced temperature, T/T_c. The measurements are taken at a pressure of 1.6 bar. In this case, the critical temperature for the superfluid transition is $T_c \sim 1.1$ mK. The figure is adapted from Bevan et al. [301] (p. 751).

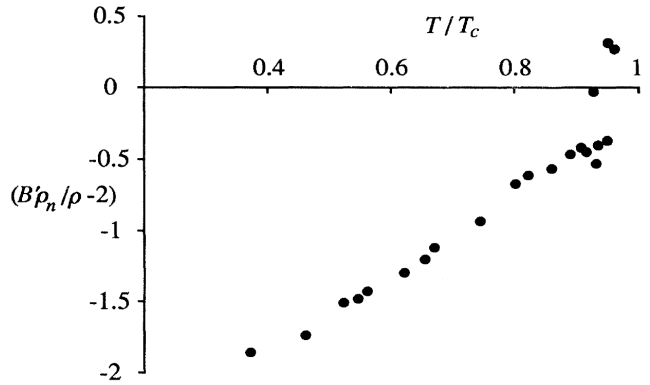

Figure 8.5: Behaviour of the mutual friction parameter ($B'_{3B}x_N - 2 = 2(\alpha'_{3B} - 1)$) in the B-phase as a function of the reduced temperature, T/T_c. The measurements are taken at a pressure of 1.6 bar. In this case, the critical temperature for the superfluid transition is $T_c \sim 1.1$ mK. The figure is adapted from Bevan et al. [301] (p. 751).

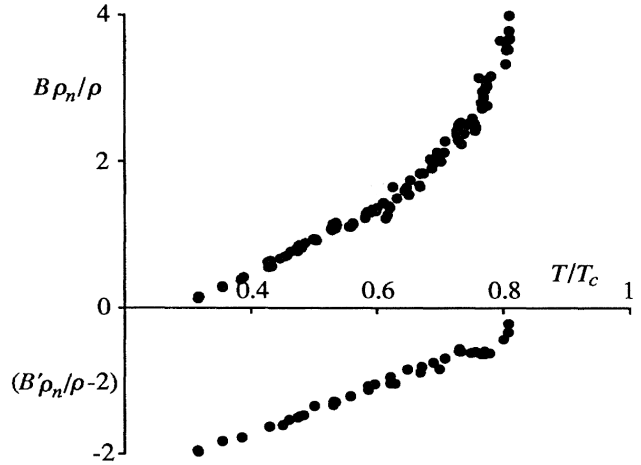

Figure 8.6: Behaviour of both B-phase mutual friction parameters as a function of the reduced temperature, T/T_c. The measurements are taken at a pressure of 29.3 bar, implying that the critical temperature for the superfluid transition is $T_c \sim 2.4$ mK. Above $T \sim 0.8T_c$ the A-phase dominates. The figure is adapted from Bevan et al. [301] (p. 752).

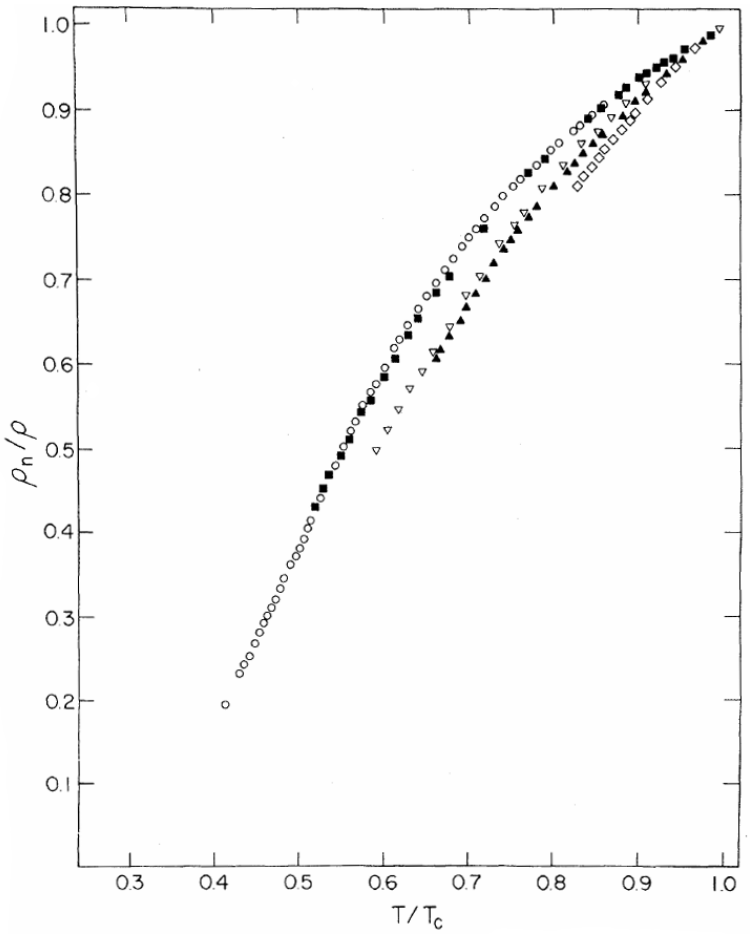

Figure 8.7: Temperature-dependence of the normal-fluid fraction in the helium-3 B-phase measured at different pressures: circles (29 bars), closed squares (20 bars), inverted open triangles (10 bars), closed triangles (5 bars), and diamonds (2 bars). The figure is reproduced from Archie et al. [306] (p. 140).

The experimental drag parameters discussed in this subsection are strongly dependent on the properties of the superfluid. While the values given in Table 8.1 and Figures 8.4 to 8.6 are determined for straight vortices able to move freely through the container, the mutual friction coefficients could be very different when pinning [307] or turbulence [295] are present. External forces that keep vortices at rest could be particularly important at higher temperatures close to the Lambda point. Dissipation in the superfluid is also expected to significantly increase if a turbulent state is formed [166]. There, mutual friction is no longer described by Equation (8.1) but it instead depends on the cube of the relative velocities (see Subsection 3.2.5 for details). While measurements of transport coefficients under these conditions are very difficult and detailed experimental data is not available, superfluid turbulence in helium might provide more insight into how such a chaotic state could influence the neutron star dynamics and is, therefore, discussed in more detail in the next subsection.

Before addressing the behaviour of vortices, we raise one critical issue with helium as a laboratory neutron star analogue. As explained in Chapter 4, in addition to

mutual friction, neutron star dynamics are strongly influenced by entrainment. Number densities in the outer core are expected to reach $10^{38}\,\mathrm{cm}^{-3}$, which corresponds to inter-particle spacings of $10^{-13}\,\mathrm{cm}$. At such short distances, strong nuclear forces are present, which couple the neutron and proton fluids. However, this process is non-dissipative and cannot simply be reproduced in weakly-coupled single-component condensates such as helium II, where the particle density is typically of order $10^{22}\,\mathrm{cm}^{-3}$ resulting in a distance of $10^{-8}\,\mathrm{cm}$. Interpenetrating liquids are necessary to recreate any phenomena resulting from entrainment, which could for example be achieved by studying mixtures of superfluid helium-3 and superfluid helium-4. Note that this situation was originally considered when entrainment was discovered by Andreev and Bashkin [190]. However, due to the strong interactions between the two isotopes, helium mixtures only contain a small fraction of helium-3, which has so far prohibited the realisation of simultaneous superfluidity in both species [308].

8.1.4 Vortex dynamics

Whereas the macroscopic formalism, providing vortex-averaged information about the dynamics of vortices located within large fluid elements, allows one to discuss the superfluids' influence in a rather classical manner and correctly predicts several observed phenomena, some aspects are difficult to study. The subjects of interface physics, turbulence and instabilities are especially challenging [235, 169]. In these areas however, the experimental and theoretical methods for analysing individual vortices have been greatly improved in the last decade. For a recent review on vortex studies in superfluid helium and BECs see Tsubota et al. [309]. One theoretical tool that has been very valuable in modelling the behaviour of superfluids are *vortex-line simulations* [162, 163]. This mesoscopic approach determines the local velocity of a vortex exposed to various forces and follows its evolution using the Biot-Savart-type law in Equation (3.33). Snapshots of such a simulation, modelling the spin-up of the helium-3 B-phase confined to a tilted container, are shown in Figure 8.8. While vortex-line simulations are useful to self-consistently model laboratory condensates, containing only several thousand vortices, large computational costs make it difficult to apply this technique to neutron stars, where significantly more vortices and fluxtubes are present. However, the study of vortex dynamics in laboratory condensates could provide crucial information for the development of better neutron star models, a fact which has generally been ignored. Terrestrial experiments could be particularly valuable in understanding how non-classical phenomena such as instabilities and turbulence influence the behaviour of neutron stars and several ideas will be briefly outlined in the following.

Several aspects of vortex dynamics are similar in superfluid helium-4 and helium-3. Differences arise, however, due to the mutual friction properties and the variations in vortex size, as vortices are generally bigger in the helium-3 phases. While for helium II, the core dimension is of the order of the coherence length and given by $\sim 0.1\,\mathrm{nm}$, the

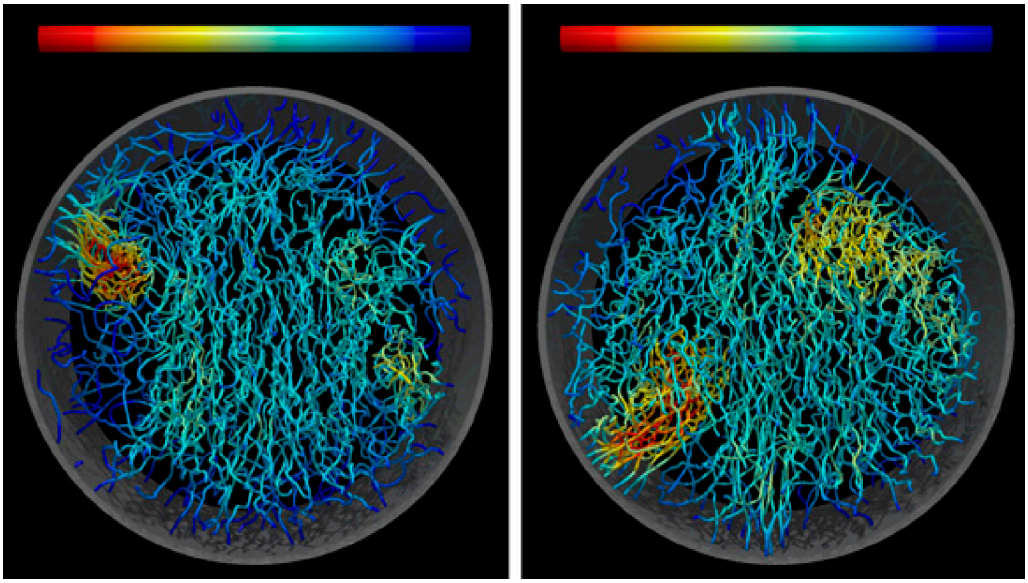

Figure 8.8: Top view of a vortex-line simulation for the spin-up of the B-phase superfluid in a tilted, rotating cylinder. Initially, only one single vortex is present. The two snapshots show the vortex configurations at $t = 1,100\,\mathrm{s}$ (left) and $t = 1,1400\,\mathrm{s}$ (right). The colour code mirrors the relative amplitude of the averaged vorticity. In both configurations coherent structures appear in the form of vortex bundles (orange and red areas). The figure is adapted from Hänninen and Baggaley [163] (p. 4671).

coherence length in the isotropic B-phase is $\sim 10\,\mathrm{nm}$ [235]. In the anisotropic A-phase, the vortex cores are three orders of magnitude larger than in the B-phase [310], because the characteristic lengthscale is no longer the coherence length but the so-called *healing length* of the spin-orbital coupling. With a radius of about $10\,\mu\mathrm{m}$, A-phase vortices are not localised but instead stretching over macroscopic regions. The increase in helium-3 core sizes creates several experimental advantages over helium-4. Not only are the critical velocities for the onset of vortex formation lower in the former superfluid but also the interactions of vortices with the container walls are very different. The latter makes pinning generally negligible [235] and allows better control over the vortices' motion, which is of great importance for laboratory neutron stars. Note at this point that the vortex dimensions in all three helium condensates are several orders of magnitude larger than those in neutron stars (see Equation (4.13)) and one has to be careful with directly inferring information about the stars' physics from terrestrial experiments. Instead, the observed features should be interpreted as an indication for similar phenomena in the astrophysical context that subsequently need to be studied in more detail.

Interface behaviour

The canonical picture of neutron star structure introduced in Section 2.2 invokes the presence of distinct interfaces. In particular, the crust-core boundary connecting the ${}^1S_0$ and the ${}^3P_2$ neutron superfluid phases and the possible type-II to type-I transition of the superconducting protons at high densities are expected to have a crucial influence

on the stars' dynamics. However, as mentioned in Chapters 5, 6 and 7, the physics of these interfaces are only poorly understood and, hence, laboratory experiments could provide valuable insight. Superfluid helium-3 plays a unique role in this endeavour, as two-phase samples provide the possibility of studying vortex behaviour at a stable first-order interface. The advantage is that the order parameter's phase remains continuous across the interface, allowing the vortices to cross the boundary. This is different to the case of two phase-separated superfluid layers, where vortices terminate at the boundary and exhibit little interaction. As addressed previously, the vortices in the A-phase have very different properties as they are much bigger than those in the B-phase and could carry double the quantisation. This raises the question of how the vortices stretch across the interface and how they influence each other during the rotational evolution.

As already briefly mentioned in Chapter 5, Walmsley et al. [208] discuss experimental NMR measurements and vortex-line simulations of a rotating two-phase sample that shows very unusual vortex behaviour. These features could have important implications for neutron star dynamics and will therefore be reviewed in more detail. The two helium-3 superfluids are contained in a cylindrical, smooth-walled quartz container that can be set into motion by rotating the surrounding cryostat. The cylinder has a length of 110 mm, a diameter of 6 mm and a small superconducting solenoid is attached around its middle, which generates an axial magnetic field that stabilises the A-phase. The presence of the anisotropic superfluid thus splits the sample into two identical B-phase regions creating two AB-interfaces. The time evolution and distribution of vortices in the B-phases are monitored with two NMR detectors secured to the bottom and the top of the cylinder. The experiments are performed at $T = 0.2\,T_\mathrm{c}$, where unexpected vortex characteristics are most dominant. At this temperature, the mutual friction coefficients are given by $\alpha_{3\mathrm{B}} \approx 4.3 \times 10^{-3}$ and $\alpha'_{3\mathrm{B}} \approx 0$ for the B-phase and $\alpha_{3\mathrm{A}} \approx 2$ and $\alpha'_{3\mathrm{A}} \approx 0.8$ for the A-phase, respectively [208]. Using this set-up, the vortex response to a change in the container's angular rotation period is studied. The authors note that the jump in the rotational velocity is sufficiently small to ensure that the interface remains stable – as will be explained below, the superfluid Kelvin-Helmholtz instability would become active if a critical velocity is exceeded. The distinct vortex features, discussed in the following, have been simultaneously confirmed by vortex-line simulations and non-invasive NMR measurements.

Spin-down behaviour is investigated by bringing the container from an equilibrium configuration abruptly to rest. Initially both phases are corotating with straight vortices stretching across the interfaces; despite carrying different units of quantisation the vortices of both helium-3 phases interconnect across the boundaries [235]. After applying the external change, both layers are able to evolve freely. However, due to the different strengths in mutual friction, the superfluids do not react to the container's spin-down on the same timescale. Because strong coupling prevails in the A-phase, it responds very quickly to the external change. The B-phase, on the other hand, reacts

much slower. Thus, the A-phase region contains significantly less vortices than the B-phase one, as can be seen from Figure 8.9. Moreover, the interface region between the two states crucially influences the dynamics as it introduces new boundary conditions at the surface. Three main observations can be made.

First of all, the A-phase vortices spiral outwards in a laminar manner to annihilate at the container walls, creating an additional pull on the ends of the B-phase vortices. At the interface, this causes the formation of a vortex sheet since the vortex ends bend parallel to the boundary and terminate at the container walls. Away from the interface, the additional force causes the B-phase vortices to develop a helically twisted tangle. This turbulent state promotes more reconnections in the superfluid bulk, effectively increasing the dissipation. Consequently, the spin-down of the B-phase is faster in the presence of the interface compared to a laminar spin-down in absence of the A-phase.

Secondly, the extra force on the B-phase vortices depletes the region closest to the rotation axis faster than the rest of the container, implying that the superfluid is at rest in the middle of the container. Whereas the centre is almost vortex free, a large number of vortices forming the vortex tangle can be found in a cylindrical shell closer to the container walls (see the cross-section in Figure 8.9). The averaged circulation of this shell exceeds the initial solid-body rotation value, which suggests that the superfluid fraction in the B-phase no longer rotates as a solid body. Instead, it exhibits a differential rotation profile along the radial direction of the cylinder.

Finally, comparison with spin-up experiments from rest shows that spin-down and spin-up are not symmetric phenomena. As the critical velocity for vortex formation is about one order of magnitude lower in the A-phase [235], vortices are first generated in the anisotropic superfluid and a vortex sheet develops on this side of the two-phase sample. The B-phase response to the external perturbation crucially depends on the number of remnant vortices. If several lines are present, the spin-up of the isotropic phase is laminar. If, however, the B-phase is initially vortex-free, the superfluid is spun-up via a sudden burst of vortex formation leading to significantly faster spin-up. This kind of behaviour is not observed in the spin-down experiments.

Assessing to which extent this behaviour can be mapped to the rotational dynamics of neutron stars is rather difficult but one would expect the strength of mutual friction to play an important role in this analogy. As explained before, the interactions between the normal and the superfluid components in helium-3 are much stronger than in neutron stars and, hence, the characteristic timescales are shorter in the laboratory system. However, the main reason the two-phase helium-3 sample exhibits remarkable vortex dynamics during the spin-down and spin-up is the relative difference of the coupling strengths across the interface. Mutual friction is about three orders of magnitude stronger in the A-phase than in the B-phase. As calculated in Chapter 5, the coupling strength is likely to jump several orders of magnitude across the neutron star crust-core boundary, depending on which mechanisms dominate the dynamics. Based upon this

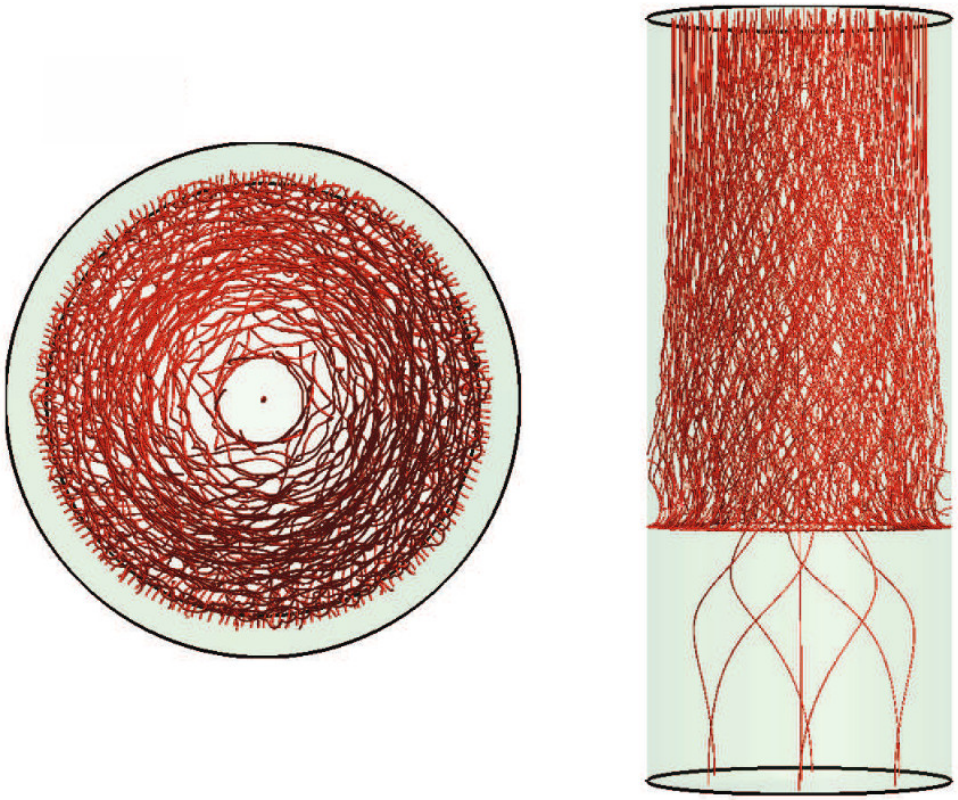

Figure 8.9: Vortex-line simulation for the spin-down behaviour of a two-phase helium-3 sample. Starting from an equilibrium configuration with straight vortices stretching across the interface, both phases evolve freely. Due to differences in mutual friction the A-phase (bottom) responds quickly to the external change, while the B-phase (top) responds slower. The left figure shows a radial cross-section of the B-phase layer with an almost vortex-free centre. The right one illustrates the formation of a turbulent vortex tangle increasing the dissipation. The figure is reproduced from Walmsley et al. [208] (p. 184532-3).

simple criterion, complicated vortex characteristics should also be present in neutron stars. Thus, the general assumption of a straight, regular vortex array, which enables an averaging procedure using a constant vortex surface density, no longer holds. As observed in the helium-3 experiments, the presence of an interface breaks the cylindrical symmetry and spin-up or spin-down of the superfluids can no longer be treated as a two-dimensional problem. The break-down of solid-body rotation further suggests that the superfluid neutrons could be differentially rotating. This would change the neutron stars' macroscopic rotational properties and could, for example, provide a possibility to store supplementary angular momentum. Such an additional reservoir would impact on observational features and could for example be related to recent observations of an anti-glitch in a magnetar [83] or the evolution of pulsar braking indices [61]. Finally, a twisted vortex tangle located in a spherical shell would also increase the dissipation and result in a faster spin-down of the superfluid component. As discussed further in the following subsection, the presence of a turbulent state would thus have significant influence on the observable parameters of neutron star.

Turbulence and instabilities

Turbulence, representing the chaotic regime of fluid flow, has long been studied in classical fluids and is one of the most complex problems of classical physics. A comprehensive discussion of this field of research is given by Lesieur [311]. Since the 1950s, turbulence and instabilities have also been analysed in superfluid helium-4 and, in the last two decades, additional experiments studying the non-classical dynamics of helium-3 and quantum gases have been developed. The ingredient that classical and superfluid systems have in common is that a single hydrodynamical equation is no longer sufficient to accurately capture the non-linear dynamics. Instead, multiple models characterising the behaviour on different lengthscales are needed. However, turbulence in superfluids is strongly influenced by the quantum nature creating features unobservable in classical fluids. Hence, the chaotic flow in superfluids is generally referred to as *quantum turbulence*. For a recent introduction to the subject see Barenghi et al. [169]. Compared to classical turbulence, the main differences in quantum turbulence arise due to the two-fluid nature. While the viscous component experiences standard turbulence reflected as quasi-classical behaviour on large scales, the vortices of the inviscid component generate new features on small scales.

Early studies of quantum turbulence performed with non-rotating helium II samples focused on the *thermal counterflow* behaviour. As first suggested by Feynman [141], the injection of a heat current, acting on the normal component of helium II but not the superfluid fraction and thus generating a velocity difference between the two, leads to turbulence without a classical analogue. In 1957, it was observed that above a critical, temperature-dependent velocity superflow indeed became dissipative [164]. Vinen [165, 166, 167] suggested this to be the result of interactions between a turbulent vortex tangle and the viscous fluid component and derived a mutual friction force similar to the one previously postulated by Gorter and Mellik [170]. For the mathematical description we refer the reader to Subsection 3.2.5. Subsequently, counterflow turbulence was also studied in rotating superfluids. Motivated by experiments showing that a small axial counterflow changes the vortex array properties [312], Glaberson et al. [174] suggested that dissipation could be related to a hydrodynamical instability of the vortex array, referred to as the *Donnelly-Glaberson instability*. It is triggered once the thermal counterflow along the vortex axes exceeds a critical velocity [313]. Experiments by Swanson et al. [173] confirmed the existence of the critical velocity and further showed that rotation stabilises the superfluid, implying that the turbulence onset in absence of rotation is governed by lower critical velocities than in the rotating case.

In addition to the new type of turbulence, an analogue to classical turbulence has been observed [295]. Helium II experiments in the late 1990s [314] found no counterflow turbulence but local pressure fluctuations, which followed the classical, statistical Kolmogorov spectrum [168]. In this regime, an extensive range of coupling strengths has been investigated by dragging a grid through the superfluid (see for example Stalp et

al. [315]), a method usually employed for studying turbulence in classical fluids. These experiments showed that the two-component fluid behaves like a single fluid on macroscopic scales exhibiting quasi-classical flow properties [316]. It has been suggested that this is caused by vortices forming bundles mimicking the behaviour of classical *eddies* [317], which results in a homogeneous and isotropic turbulent state that exhibits classical Kolmogorov decay. However, as soon as the characteristic lengthscale of these eddies decreases to distances comparable to the intervortex spacing, quantum effects become important again. Analyses of hydrogen tracer particles have revealed that the velocity field on these microscopic scales shows a power-law behaviour, which differs from the Gaussian velocity distribution of classical turbulence [318]. Kelvin waves excited by the reconnections of vortices play a crucial role for this, as they are expected to distribute the energy in a cascading manner to lengthscales smaller than the intervortex spacing [319]. These helical displacements propagating along the vortex lines, which were also discussed in Subsection 5.2.3 as a dissipation mechanism for the neutron stars' crustal superfluid, have only recently been observed on reconnecting helium II vortices [320].

Another type of instability that has been discovered in the context of helium II is the *Rayleigh-Taylor instability*. This phenomenon, which generally acts at an interface between two fluids of different densities and initiates the mixing of the two, is known to play a crucial role for many astrophysical mechanisms such as supernova explosions or accretion processes [4]. In laboratory helium-4 experiments, the instability has been observed in the form of crystallisation waves at the superfluid-solid interface during the pressure-controlled growth of a helium crystal immersed in the superfluid phase [321]. The Rayleigh-Taylor instability could thus also be of importance at the neutron stars' crust-core interface, where crustal lattice nuclei are in contact with the neutron superfluids (see Section 2.2).

Besides the standard turbulence experiments performed with helium-4, non-linear dynamics have also been investigated in the B-phase of helium-3 [322, 323, 160]. Note that for the anisotropic A-phase the dissipation is so large that one would not expect superfluid turbulence to play any role in the temperature ranges currently accessible [296]. Most noticeably, superfluid helium-3 contained in a cylindrical container exhibits two regimes of vortex behaviour. While helium II had only been observed to display turbulent characteristics below the Lambda point, the B-phase showed laminar spin-down behaviour above a temperature of about $0.6\,T_\mathrm{c}$ and turbulent behaviour below [324]. There are three main properties [296] helping to stabilise the dynamics of the fermionic superfluid down to low temperatures: the viscosity of its normal fluid exceeds that of helium II by about four orders of magnitude; due to the large vortex core size pinning is negligible and its mutual friction coupling is stronger than in helium II. The last difference is of particular importance since it has been proven experimentally and theoretically (see for example Finne et al. [296] and Eltsov et al. [325]) that the spin-down behaviour is determined by a dimensionless parameter, Re, which only depends

on the modified mutual friction coefficients,

$$\mathrm{Re} \equiv \frac{1-\alpha'}{\alpha}. \tag{8.8}$$

The two regimes are separated by $\mathrm{Re}_{\mathrm{crit}} \sim 1$. For $\mathrm{Re} \gg 1$ turbulence dominates as the inertial terms drive the dynamics, whereas mutual friction stabilises the superfluid for $\mathrm{Re} \lesssim 1$ and laminar behaviour is observed. In analogy with classical fluid dynamics, the parameter Re is sometimes referred to as the *superfluid Reynolds number*. For the B-phase, $\mathrm{Re}_{\mathrm{crit}}$ appears right in the experimental temperature regime (corresponding to $T \sim 0.6\,T_{\mathrm{c}}$), while for helium II the transition lies very close to the Lambda point making the laminar regime almost inaccessible. This highlights one of the main advantages of helium-3 over helium-4 for the studies of non-linear fluid dynamics, as it allows one to perform detailed studies of the onset of turbulence and vortex instabilities [326].

One instability that has been analysed in great detail is the *Kelvin-Helmholtz instability*. Using a magnetically stabilised two-phase sample of helium-3 similar to the set-up discussed for the study of interfaces, Blaauwgeers et al. [209] examined the shear flow between two superfluids. Spinning up the sample from rest, vortices are first formed in the anisotropic A-phase as a result of the stronger mutual friction and organised as a vortex sheet at the interface, while the B-phase remains vortex-free. The average circulation in both layers is different, creating a discontinuity in the tangential superfluid velocities. This state of two superfluids moving relative to each other is stable and non-dissipative up to high relative velocities and, thus, provides the perfect environment for investigating the Kelvin-Helmholtz instability [327]. Compared to studies using classical fluids, the superfluid set-up has the advantage that viscosity does not obscure the instability. However, the classical criterion for the instability onset between two ideal, inviscid fluids no longer applies but has to be modified by taking the two-fluid nature of the quantum condensates into account. The instability threshold is thus not solely related to the relative velocity of the two superfluid components but instead depends on the velocity difference of the normal and inviscid constituents on both sides of the interface [328]. In the case of neutron star cores, where multiple quantum states are present, a combination of the different superfluid and superconducting velocities should enter the instability criterion [329]. Every time the threshold is reached, the Kelvin-Helmholtz instability results in a wave-like distortion of the AB-interface, suggested to cause the *injection* of vortex tangles into the B-phase (see for example Finne et al. [235]). For temperatures above $\sim 0.6\,T_{\mathrm{c}}$, each vortex loop quickly turns into a straight line connecting across the interface to the A-phase defects, with a similar number of vortices being created each time the instability is triggered [209]. Below $\sim 0.6T_{\mathrm{c}}$ however, the instability acts in a very non-linear way, explosively injecting a large number of vortices into the isotropic phase. A detailed, temperature-dependent analysis of the Kelvin-Helmholtz instability thus confirms the laminar and turbulent spin-down regimes separated by the different strengths of mutual friction.

Insight from helium experiments could provide important information for neutron stars, where vortex dynamics are generally assumed to be laminar and little is known about how turbulence and superfluid instabilities manifest themselves. As a first step, one could try to classify the neutron star spin-down behaviour by simply calculating the superfluid Reynolds number associated with the mutual friction mechanisms studied in detail in Chapter 5. Since the coupling is expected to be rather weak with $\mathcal{B}' \approx B^2 \ll 1$, Equation (8.8) would lead to $\mathrm{Re} \gg 1$, which implies that the neutron star interior should be strongly influenced by turbulence. Despite the fact that this criterion neglects effects such as the stars' rapid rotation that could suppress the development of non-linear dynamics [330], turbulence could significantly alter the vortex motion. Peralta et al. [331, 332], for example, study the onset of the Donnelly-Glaberson instability in the neutron star core, which excites unstable Kelvin waves that result in a distortion of the initially straight neutron vortices. As briefly mentioned in Subsection 3.2.5, the frictional coupling in a vortex tangle is very different from the standard force considered above in Equation (8.5). Instead of being proportional to the velocities, the mutual friction force depends on the cube of the relative velocities [170, 165, 166, 167]. Andersson et al. [171] have however recently argued that such a turbulent state might only exist locally and not globally, because a fully developed vortex tangle is isotropic and the averaged vorticity of a macroscopic fluid element would vanish. Hence, for neutron stars, where the superfluid has to form vortices in order to support the observed bulk rotation, a disordered vortex tangle would have to retain rigid-body characteristics to some extent. This could for example be achieved in form of a *polarised turbulent state* [171], where each fluid element contains tangled and straight vortices; the latter being responsible for the macroscopic rotation. The corresponding mutual friction force would then be a superposition of the two underlying structures, which is in agreement with observations made in counterflow studies of rotating helium-II samples [173, 313].

Despite the fact that detailed knowledge of the turbulent state in neutron star interiors is not available, implications for macroscopic observables could be significant. A modified frictional coupling due to the presence of turbulent vortex tangles would generally lead to dissipation timescales that differ from the ones discussed in Chapter 5. This would affect various hydrodynamical phenomena such as the post-glitch relaxation or the damping of neutron star free precession [333] and oscillations modes [334, 112]. Moreover, it has been suggested that timing noise could result from an instability of the vortex array being imperfectly pinned to the proton fluxtubes due to thermal activation [335] or a variation of the crustal rotation phase caused by the turbulent core superfluid exerting a fluctuating torque on the crust [336]. Additionally, the presence of superfluid instabilities are relevant, since they could explain the origin of pulsar glitches. Several mechanisms have been studied in the literature. As discussed by Mastrano and Melatos [329], the Kelvin-Helmholtz instability could act at the neutron star crust-core interface and rapidly transfer circulation between the ${}^1S_0$ and ${}^3P_2$ superfluids, similar to what is observed in helium-3 experiments [209]. This would result in the spin-up of the rigidly

rotating neutron star component, which would manifest itself as a discrete jump in the angular rotation frequency of the crust, observed as the glitch by a distant observer.

In essence similar to the Kelvin-Helmholtz instability, *two-stream instabilities* could also serve as a possible trigger mechanism in differentially rotating neutron stars [337]. The main difference for this type is that the interacting fluids are interpenetrating and not separated by an interface. As before however, the non-linear dynamics set in as soon as a critical velocity lag is reached. The instability mechanism itself may be mediated through various oscillations modes. Andersson et al. [338] discuss the simplified case of two rotating fluids enclosed by an infinitesimally thin spherical shell. Here, entrainment is responsible for the coupling of the two components and the instability sets in through inertial r-modes [107, 339]. This process is particularly interesting as it has been shown that these modes are not only dynamically unstable on small scales but also suffer a global instability, which might not be completely damped by shear viscosity [10, 340]. Thus, the r-mode instability could trigger the unpinning of a large number of vortices and lead to observable glitches. Finally note that this instability has not yet been observed in helium experiments and it is unclear whether one can expect to find unstable r-modes at all, as the coupling mechanisms in laboratory systems differ significantly from those in neutron stars [270].

To conclude our discussion of designing terrestrial neutron star models with helium, we highlight another exciting way to exploit the analogy between both systems. By combining helium-3 with *aerogel*, a mixture which has also attracted a lot of attention in the low-temperature physics community [341, 342], one can study the influence of disorder on a three-dimensional quantum liquid. These aerogels are very porous media formed of strand-like structures that are generated from silica clusters in a gelation process. The strands' diameters are typically of the order of a few nanometres, smaller than the coherence length of pure helium. The advantage of this system is that (due to the different lengthscales) helium-3 superfluidity can be controlled through the aerogel's porosity. It was for example shown that for a 98% porous solid, helium-3 exhibits the typical characteristics of a superfluid phase transition [343, 344]. While the B-phase is suppressed and an A-phase like state seems to dominate, the exact nature of the superfluid phases in aerogel is not known and recent analyses [345, 346] revealed a rather complex phase diagram. However, these experiments present the unique possibility to investigate the normal-superfluid interface as it should be possible to grow aerogel with a continuously changing porosity. As this would provide information about the pairing behaviour of quantum systems undergoing such transitions, it could allow insight into the properties of the neutron star protons turning superconducting at the crust-core boundary. It should be further possible to study the behaviour of superfluid vortices in disordered aerogel. This has obvious analogies to the inner neutron star crust, where a superfluid neutron liquid is thought to coexists with the nuclear pasta, and experiments could thus give information about the interactions between the two components.

8.2 Ultra-cold Gases

It was first suggested by Fritz London [143] that the transition of helium-4 atoms into a superfluid state could be the result of condensation into the quantum mechanical ground state. Since bosons obey Bose-Einstein statistics, when confined in an external potential, they enter the lowest energy state available. At low temperatures, this results in the formation of a new macroscopic quantum phase referred to as a Bose-Einstein condensate (BEC). For a general introduction see Chevy and Dalibard [347]. The state of weakly-interacting bosons was first observed in 1995 by Wieman and Cornell [147] and Ketterle [148], who created BECs by cooling dilute gases of Rubidium atoms to nanokelvin temperatures. Despite the fact that this branch of low temperature physics is relatively new, it became evident soon after the initial detection that these macroscopic quantum condensates could serve as a perfect testing tool for various areas of physics, ranging from solid state physics to many-body physics all the way to astrophysics [156].

The main purpose of this section is to examine if laboratory BECs could be used to probe neutron star dynamics. The following discussion will hence focus on characteristics that are expected to play a crucial role in compact stars, such as the multi-fluid nature, vortex motion, superfluid turbulence and interfaces. This section concludes with a brief analysis of ultra-cold Fermi gases.

8.2.1 General properties of BECs

The most important feature when designing laboratory neutron stars is the presence of distinct components. Whereas the condensate itself occupies the ground state of the external potential, it spatially coexists with a second component, formed by the BEC's collective excitations [156]. This is equivalent to the two-fluid model of helium, where two interpenetrating fluids are invoked to explain superfluid behaviour, and hence the characteristics of superfluidity are also expected to exist in BECs. The corresponding transition in a bosonic gas was first observed in 1999 [149, 150] and associated hydrodynamical features such as macroscopic superfluid flow [348] or the propagation of first and second sound have also been experimentally confirmed [349, 350, 351]. Additionally, ultra-cold gases offer another possibility to mimic the neutron stars' multi-component nature, as multiple condensates can be positioned on top of each other. This was realised shortly after the first detection of BECs. In 1997, Myatt et al. [352] generated two overlapping condensates using two Rubidium-87 BECs in different spin states, which could be analysed using absorption imaging. Examination of the interaction properties revealed that the two clouds exhibited mutual repulsion. Following this initial realisation of a binary BEC, which further serves as an analogue of interpenetrating helium-3 and helium-4 superfluids [353], a lot of effort has been put into theoretically and experimentally investigating multi-component BECs formed of different Alkali atoms. It was found that these systems display a rich variety of phenomena [354, 355, 356]. For in-

stance, it has been demonstrated that depending on the atomic interaction, some binary mixtures are miscible [357], whereas others show immiscible behaviour [358, 359]. In order to model neutron stars, where the matter is homogeneously distributed and coupling between different components is expected to take place, BECs with strong mutual repulsion are less relevant since they display an inhomogeneous matter distribution in their ground state. However, the main advantage of these systems is the great amount of control one has over the experiment, as binary condensates can be prepared in almost every desired density profile by varying the mixing of the states.

Moreover, observational features become very diverse when the condensates are no longer stationary but dynamical. One example is the study of shock wave propagation in BECs, where pulsed and tightly focused laser beams are used to generate blast waves. Compared to classical, dissipative shock waves, the equivalent in BECs is highly non-linear and dispersive causing very different wave structures and shock speeds [360]. The dynamics further change significantly when rotation is added to the picture. This becomes especially important if the condensate is in a superfluid state, as vortex formation takes place. The corresponding dynamics are discussed in the next subsection.

Another tool for studying the properties of BECs is a close examination of their excitation modes, which can be understood as coherent fluctuations in the condensate's density. These excitations were observed shortly after the generation of the first BECs and exhibit several parallels with helium II phonons [349, 361]. Hence, understanding the frequencies of excitations and their evolution [362, 363, 364] would give insight into the interactions between individual atoms. It is also possible to directly image the matter distribution and thus study the excitation modes experimentally. Therefore, BECs are important testing systems, because they could provide clues on how asteroseismology (the analysis of neutron star oscillations) could be used to obtain information about compact objects. This would be particularly valuable when analysing how continuous gravitational waves, generated by the fluid modes of rotating neutron stars, could help to constrain the interior physics [112, 108, 103].

At this point, it seems inevitable to return to the problem of entrainment, the non-dissipative coupling of neutrons and protons, which greatly influences the neutron stars' dynamics. While it is certainly possible to derive a mathematical formalism for a binary BEC with entrainment and determine how observables, such as the excitation modes, would be modified [270], it is not obvious if such a strong, non-dissipative coupling could be present in real systems. As the particle densities in laboratory BECs typically reach 10^{12} to $10^{15}\,\mathrm{cm}^{-3}$ [156], which corresponds to an interparticle distance of 10^{-4} to $10^{-5}\,\mathrm{cm}$, the prospect of recreating entrainment in a weakly-coupled BEC is rather poor. However, recent theoretical studies have examined the superfluid drag behaviour between two BECs confined to optical lattices [365, 366]. An optical lattice consists of a spatially periodic potential created by the interference of laser beams that is superimposed on the condensates to trap individual atoms [367]. These lat-

tices are easy to tune and provide the unique possibility to study transport properties of binary condensates, such as the non-dissipative entrainment coupling between two BECs, which originates from the interspecies interaction on short ranges. Regardless of these developments, studies of entrainment in BECs are still in their infancy and actual experiments are needed before any parallels with neutron star physics can be drawn.

Despite the problem of probing entrainment in bosonic condensates, BECs are brilliant laboratory systems that allow a lot of flexibility, which is crucial when designing neutron star experiments. The main reason fine tuning in BECs is very straightforward is due to so-called *Feshbach resonances*. For a recent review see Chin et al. [368]. These resonances, effectively generating bound states between atoms in the condensate, are named after Herman Feshbach, who studied similar many-body resonances in nuclear physics collisions [369]. The existence of these resonances was theoretically predicted in 1993 [370] and experimentally confirmed by various groups in 1998 [371, 372, 373]. In the case of atomic gases, the resonances between the particles allow one to change the scattering length, i.e. the interaction strength of the condensate, by simply changing the external magnetic fields. This creates an extraordinary degree of control, which could be very valuable when analogies between neutron stars and BECs are exploited.

Before moving on to a more detailed discussion of vortex dynamics, we note that a series of experiments has unveiled another phenomenon, which can be related to neutron stars [374, 375]. While it does not concern the properties of an old, equilibrium star, it is somewhat similar to the formation of the star itself and, thus, illustrates the close analogy between BECs and compact stars. In these experiments, the external magnetic field was tuned to obtain negative scattering lengths, corresponding to an attractive self-interaction, which caused the condensate to become unstable. This was most remarkable as the BEC showed characteristics of a collapse: after shrinking slightly, the condensate underwent an *explosion*, expelling a large number of particles and leaving a small, cold and stable remnant behind. Although the energy scales for this process are obviously smaller than the ones associated with neutron star formation, the collapse of a BEC is called a *bosenova* [362] due to the apparent similarities with a core-collapse supernova.

8.2.2 Vortex dynamics

If bosonic condensates are to serve as laboratory neutron star analogues, the presence of quantised vortices is crucial. In the case of helium experiments, the fluid is confined to a container and rotation of the two components is obtained by setting the vessel into motion. However, superfluid BECs are trapped in an external potential and not enclosed in a container and can thus no longer simply be accelerated. Instead, different methods have been employed in order to set condensed clouds into motion. Two approaches are in operation for the generation of rotating BECs. The first one uses optical beams with a suitable inhomogeneous topology to *imprint* a phase onto an existing condensate. At points where the local density vanishes, the condensate is then forced to forms vortices.

Alternatively, optical stirring beams or distortions in the magnetic field can be applied to rotate the cloud, which subsequently leads to the generation of quantised vortices. The imprinting method was adopted by Matthews et al. [149] in 1999 to create vortices in one of the constituents of a two-component BEC. Using an interference technique [358], it was shown that the phase of a single vortex changed by a factor of 2π as given by the standard quantisation condition. These experiments also allowed an analysis of the vortex stability and its decay behaviour. Shortly after the successful phase-imprinting experiments, Madison et al. [150] observed quantised rotation in a single-component Rubidium-87 BEC after stirring the condensate with a focused laser beam. Similar to rotating helium II experiments, it was demonstrated that vortices are formed as soon as the stirring frequency exceeds a critical value. However, the advantage of BECs is that vortices can be easily visualised using absorption imaging, because they correspond to holes in the resulting density distribution.

Further studies of rapidly rotating, ultra-cold BECs have revealed many interesting vortex features (for recent summaries see Cooper [376] and Tsubota et al. [309]). Two general aspects observed are that the process of vortex formation is highly nonlinear and the regular vortex lattice only becomes apparent once the equilibrium steady state has been reached. The resulting defects are also not necessarily singly quantised but other structures such as vortex sheets [355] or alternative, highly distorted but stable patterns [377] have been predicted. In this respect, BECs show several similarities with the anisotropic A-phase in helium-3. In order to draw information about the dynamics of neutron star vortices from BEC experiments, one would have to ensure that vortices are point-like defects, regularly distributed in a hexagonal array as generally invoked for the stars' interior.

In order to assess whether attributes of BEC vortices could be relevant for neutron stars, the first step would be to compare the size of a BEC and the dimensions of its vortices. Typical BEC clouds extend from 10 to 100 μm [169], whereas the vortex core size, determined by the healing length (similar to the anisotropic helium-3 phase), is given by $\sim 0.5\,\mu$m [376] and the number of vortices in bosonic condensates reaches up to several hundred. This is very different to the case of neutron stars, where significantly more vortices and fluxtubes are expected to be present (see Equations (4.6) and (4.7)). Moreover, the dimension of a BEC vortex is of similar order as the intervortex spacing, implying that ultra-cold atoms probe a regime that is in great contrast to the conditions of the neutron stars' interior, where it is assumed that individual vortices and fluxtubes are distant enough to not influence each other (see Equations (4.9) and (4.9)). Hence, deducing information about the macroscopic dynamics of non-interacting vortices might be difficult with BECs. However, these laboratory condensates are excellent testing grounds for probing the mesoscopic dynamics of vortices and how they interact with each other and possible pinning sites. The latter is particularly important for neutron stars, because vortex-fluxtube pinning is thought to play an important role for their

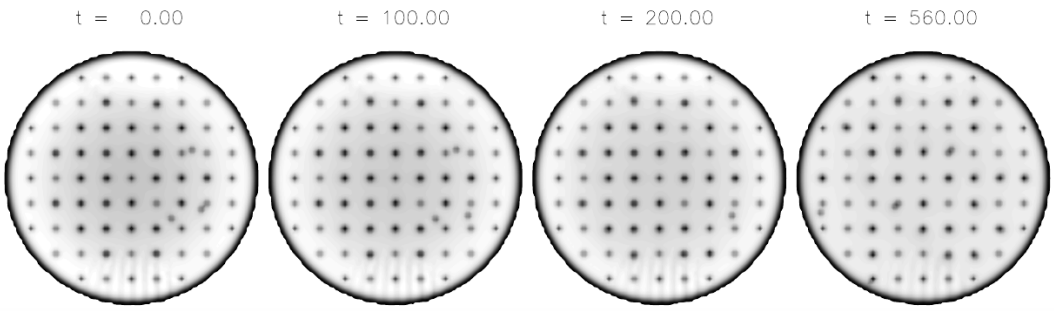

Figure 8.10: Snapshots of the superfluid density during the modelled spin-down of a BEC at different times, $t = 0, 100, 200, 560$ and 810 in arbitrary units. A light grey colour corresponds to a low and dark grey to a high density. The rectangular structures indicate the presence of pinning centres, where dark points mark occupied and light points mark unoccupied sites. Dots that are not part of the array are moving vortices. Note that the vortices initially populate the centre of the cylinder and move outwards as the container is spinning down. The figure is adapted from Warszawski and Melatos [382] (p. 2060).

rotational and magnetic evolution [228]. Regardless of this fact, a detailed mesoscopic theory of pinning is not available yet (see also Chapters 5, 6 and 7) and exploring this phenomenon in more detail would be beneficial. While BECs are not in contact with a surface, which the vortices could pin to, one can take again advantage of optical lattices [378]. Superimposing regular energy barriers could mimic the pinning potential present in the neutron stars' crust or core and would allow one to study the interaction of vortices with these potentials. This type of pinning has been recently observed for a single-component condensate [379] and theoretically extended to a binary BEC [380].

One example, where the analogy between vortex pinning in a neutron star and a BEC has already been exploited, is the theoretical modelling of pulsar glitches. As explained in detail in Subsection 3.2.6, a weakly-interacting BEC is very well described by the Gross-Pitaevskii equation and its time-evolution provides information about the motion of vortices. Despite the fact that many-body forces in neutron stars crusts are not weak as in the bosonic condensate, Warszawski and Melatos [95, 96] suggested that the Gross-Pitaevskii equation could also be used to model the pinned and decelerating crustal superfluid. The authors have shown that collective motion of BEC vortices in the presence of a regular pinning potential can trigger glitch-like events, which have exponentially distributed waiting times and sizes that follow a power-law distribution. These characteristics have also been seen in pulsar glitches and indicate the presence of a self-organised critical process such as observed in earthquakes or BEC vortex avalanches [381]. Typical simulation snapshots of the superfluid density during the spin-down of the condensate are shown in Figure 8.10. However, the BEC simulations only deal with up to several thousand vortices and not the $\sim 10^{16}$ vortices expected in neutron star crusts (see Equation (4.6)). Thus, one has to be careful when generalising the dynamics of small BECs to the much larger system.

Turbulence and instabilities

Being less than a decade old, the analysis of instabilities and superfluid turbulence in BECs is a rather young field. Accordingly, experimental results are not as extensive as for helium. However, several observations have been made, which show relevance for laboratory neutron stars and will be discussed in the following. One benefit of studying non-linear dynamics with BECs is that the turbulent behaviour can be imaged. Because instabilities cause a dephasing of the condensate's wave function, time of flight experiments can be used to directly probe the velocity distribution of the condensate and, thus, provide information about the structure of superfluid turbulence [383].

In order to model non-linear evolution, such as the neutron stars' two-stream instability, which is expected to arise from the differential rotation between the neutrons and the charged conglomerate, with ultra-cold condensates, a similar instability mechanisms is needed. The presence of any superfluid hydrodynamical instability would, first of all, require the existence of a macroscopic, inviscid flow. This was detected in 1999 [348, 384], when experiments showed that a laser beam could be moved through a BEC without generating dissipation. Heat production and the subsequent breakdown of the superfluid state was only observed once a critical stirring velocity was exceeded. This is equivalent to the frictionless flow observed in early helium II counterflow experiments. The advantage of BECs is that ultra-cold atomic clouds are less complex (as surface effects and strong coupling are absent) and therefore easier to analyse. The initial observation of BEC superflow stimulated further experiments studying the macroscopic drag and the onset of dissipation by creating persistent flow patterns [385] and directly probing the flow fields around potential barriers immersed into the fluid [386]. In the latter case, it was shown that the condensate becomes unstable for intermediate flow speeds, developing instabilities in the form of solitons [387].

Fully developed turbulence was recently observed in a single-component BEC by Henn et al. [388], who reported the direct observation of an entangled vortex state (see Figure 8.11), which had previously been identified in numerical simulations [389], and the corresponding change in the hydrodynamic properties of the condensate. In the experiment, the turbulent vortex state was created by applying an oscillatory perturbation to the magnetic trapping potential. This generates excitations, which in turn are thought to lead to vortex formation. Although it is not understood how this proceeds in detail, Henn et al. suggest that the Kelvin-Helmholtz instability could be responsible, since the excited BEC is surrounded by a thermal cloud of atoms [390, 391], creating an interface. The coupling of the superfluid BEC to this thermal cloud has further been predicted to result in the large-scale decay of the turbulent state, which obeys quasi-classical Kolmogorov statistics on large scales [391]. While this power-law behaviour has also emerged in numerical BEC simulations [389, 392], it has not yet been confirmed experimentally. Another feature of superfluid turbulence that has been recreated numerically is the non-classical distribution of the small-scale velocity field, which has

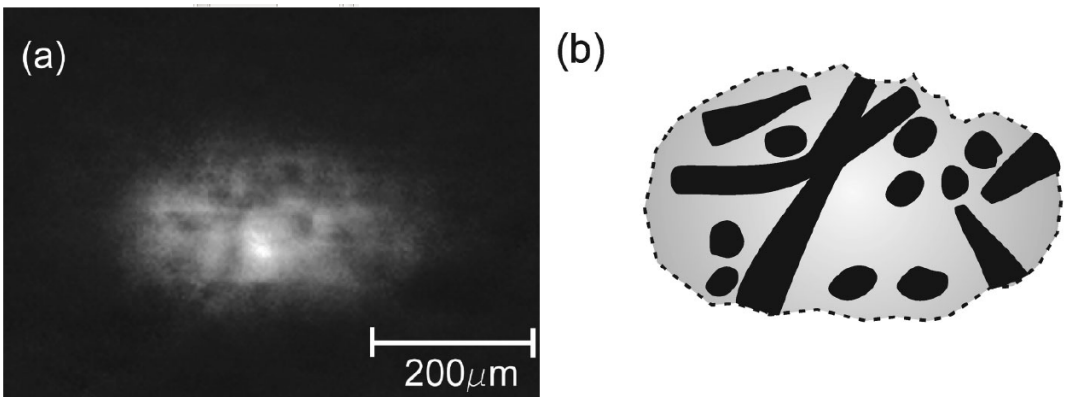

Figure 8.11: (a) Snapshot of the atomic density in a BEC after a 15 ms phase of free expansion. Showing an unordered distribution of vortex structures, this illustrates the first observation of a turbulent tangle. (b) Schematic diagram of the vortex tangle as inferred from the snapshot in (a). The figure is adapted from Henn et al. [388] (p. 045301-2).

already been detected in helium experiments [318]. White et al. [393] study the decay of a vortex tangle for realistic experimental parameters by evolving the Gross-Pitaevskii equation and find that the velocity distribution of the BEC follows a power-law and does not exhibit the classical Gaussian statistics.

Returning to the question if two-stream instabilities could be triggered in laboratory BECs, one again has to consider two interacting condensates. It has been shown theoretically that for the simple case of linear relative flow between two condensates, the binary mixture becomes dynamically unstable once a critical velocity is reached [394, 395]. This is exactly what one would expect for linear relative motion between the neutrons and the protons in the neutron star core [338]. Instabilities between two counter-moving BECs have been modelled numerically (see for example Takeuchi et al. [396]) and observed in experiments, where the superfluids are confined inside a narrow channel [397, 398]. In order to develop an idea whether an analogue of the superfluid r-mode instability could be observable in BECs, the concept of relative flow has to be extended to rotating BECs. In this case, the dynamics get much more complicated and no experimental data is available. However, numerical investigations have predicted the presence of different types of instabilities [399]. Some of these could be relevant for neutron stars as they hint at turbulence and vortex nucleation in the form of ripples or catastrophic events, which also show some resemblance to the instability phenomena previously discussed for helium. For example, it has been determined that similar to vortex formation in a single-component BEC, the Kelvin-Helmholtz and Rayleigh-Taylor instabilities could generate vortices in immiscible binary BECs [400]. It has further been suggested that binary BECs consisting of Rubidium-85 and Rubidium-87 could be used to study the onset and the dynamics of these interface instabilities by tuning the interaction strength of the two condensates through Feshbach resonances [401]. This would allow more flexibility than currently available in helium experiments. Overall, it seems promising that future studies of non-linear evolution in bosonic condensates will pro-

vide more insight into instability formation and how this affects superfluid turbulence, which could contribute to the development of more accurate neutron star models.

Interface behaviour

One advantage of using helium for the modelling of neutron stars is the presence of stable, phase-coherent interfaces. By creating two-phase samples of helium-3, it is possible to study vortex behaviour across such interfaces. If BECs are to be used as laboratory neutron star analogues, it would be beneficial to realise similar conditions in ultra-cold condensates. The interfaces between two BECs mentioned above are generally phase-separated and not suitable for this purpose, as vortices are simply terminated and not connected across the interfaces. However, it may be possible to mimic phase-coherent neutron star interfaces by employing topological defects of spinor BECs. Here, different to standard bosonic condensates, the spin is a manipulable degree of freedom and not fixed by the external magnetic field. This can be achieved by confining the atoms in optical instead of magnetic traps. Spinor BECs, first observed in 1998 [402], exhibit the standard turbulent characteristics of superfluids [403, 404] but can additionally be deformed to more complex structures. Particularly promising seems the behaviour of vortices at the interface of two spin-1 condensates distinguished by their magnetic phases. It has been suggested that coherent interfaces could be constructed by phase-imprinting vortices on each side that would cross in a continuous manner [405, 406].

8.2.3 Fermi gases

Before concluding this section, we briefly mention that due to recent advances in experimental methods not only bosonic but also fermionic condensates are available to study the properties of superfluids. An introduction to Fermi gases, first observed in 2003 [408, 409, 410], is given in Giorgini et al. [411]. Two years after the initial detection, the superfluid state was discovered by observing the presence of quantised vortices [151]. The corresponding superfluid transition at a critical temperature (accompanied by the characteristic Lambda-shaped change in the thermodynamical quantities such as the specific heat) has only recently been recorded by Ku et al. [412]. Hence, fermionic condensates exhibit similar features to bosonic gases [413] and the benefit of studying these systems is analogous to the aspects discussed before. One similarity is for example the observations of first [414] and second sound [407] velocities. As for superfluid helium, the latter phenomenon characterises the wave-like transport of heat and is closely related to the two-fluid nature of the system. Measurements of the second sound velocity thus allow the extraction of the superfluid density fraction in an ultra-cold Fermi gas. Results for the uniform case are illustrated in Figure 8.12.

The main difference to bosonic gases is that fermions obey the Pauli exclusion principle and cannot condense into the minimum energy state. Instead, fermions have to

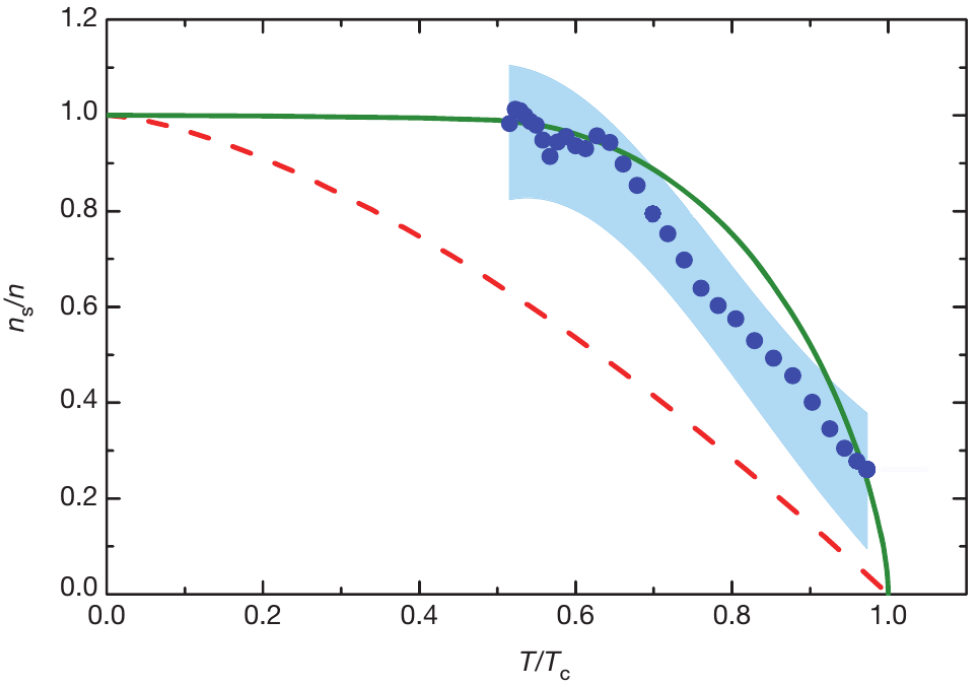

Figure 8.12: Superfluid density fractions for various macroscopic quantum systems. The blue data points and the shaded uncertainty region represent the superfluid fraction of a uniform, resonantly interacting Fermi gas as a function of the reduced temperature, T/T_c. For comparison the superfluid fraction of helium II (green solid line) and the theoretical expression, $1-(T/T_c)^{3/2}$, for the condensed fraction of an ideal Bose gas (dashed red line) are given. The figure is reproduced from Sidorenkov et al. [407] (p. 80).

form Cooper pairs as governed by BCS theory. This causes the superfluid behaviour of Fermi gases to become visible at much lower temperatures than BEC superfluidity. The same characteristic was encountered when discussing the formation of the anisotropic helium-3 phase. Due to the presence of pairing, interactions play an important role in superfluid Fermi gases. In contrast to bosonic condensates, fermionic ones are strongly coupled and, therefore, inherently closer to the nuclear matter present in neutron stars. Hence, fermionic gases could be the perfect candidate for designing laboratory neutron stars. A recent comparison between cold Fermi atoms and low-density neutron matter in the stars' crust [415, 187] has pointed out that both systems have superfluid transition temperatures comparable to the Fermi temperatures and should thus display similar physics. One instance, clearly illustrating the benefit of this analogy, is the numerical simulation of vortex pinning. Solving the Gross-Pitaevskii equation for a unitary Fermi gas, where the scattering length is much larger than the interatomic distance, provides a way to determine the detailed mesoscopic vortex motion initiated by interactions with a pinning site (see for example Bulgac et al. [416]). This could help to considerably improve the understanding of pinning in neutron stars, where detailed models are not available. Moreover, recent work has shown that the unitary Fermi gas also offers unique possibilities to study quantum turbulence [417]. In this system, microscopic vortex dynamics such as reconnections and crossings can not only be modelled theoretically

but new techniques could allow the direct imaging of these phenomena [418].

Finally, we point out that mixtures of Bose and Fermi superfluids have recently been realised by cooling a bosonic and a fermionic lithium isotope below both transition temperatures [419]. It was possible to measure the energy exchange between the two fluids and determine their coupling strength, which was observed to be rather weak. In essence similar to a mixture of helium-3 and helium-4 but significantly easier to control, a lot of attention is currently given to investigate such double superfluid systems [420], which could also prove beneficial for modelling neutron star physics. One example is the recent observation of a superfluid two-stream instability by Delehaye et al. [421], which as mentioned previously is also thought to affect the dynamics of neutron stars [340]. At very low temperatures, two interpenetrating lithium clouds of different spin were kept in a magneto-optical trap and set into motion by displacing their centres of mass. This excited dipole modes of different frequency in the Bose and Fermi component, causing relative motion between the two condensates. Delehaye et al. observed undamped mode behaviour for slow relative motion, whereas for higher relative velocities the oscillations were damped. The existence of a critical velocity for the onset of dissipative dynamics is typical for the presence of an instability. For the case that dissipation is caused by the creation of quasi-particles, the critical velocity has been calculated to be equal to the sum of the sound speeds of both components [422]. While not contradicting this result, the experimental data could not provide conclusive evidence and more work is needed to understand the small-scale physics of this instability in a Bose-Fermi mixture.

Despite these promising results, the study of ultra-cold Fermi gases is still a very new field of research that mainly focuses on investigating the fundamental properties. Building neutron star analogues with these condensates is, therefore, more likely to be a task for the coming decades.

8.3 Superconductors

Superconductors were the first systems to be observed to exhibit macroscopic quantum behaviour and the discovery of superconductivity by Onnes in 1911 [116] sparked a new era of theoretical and experimental research that is still ongoing today. The theoretical advances most notably involve BCS theory [120] and the phenomenological Ginzburg-Landau theory [121], which are still widely applied. The former has proven particularly useful in describing the microphysics of superconductors, whereas the latter is used to study the macroscopic physics close to the transition temperature. Since the first discovery, many different materials have been found to undergo a phase transition into the superconducting state and large numbers of experiments have been conducted to study their behaviour. Superconductors are generally classified as *conventional* if BCS theory can explain their properties and *unconventional* if this is not the case. So-called heavy-fermion superconductors [423] and cuprate superconductors (compounds of copper and

oxygen) [125] are part of the second category. The latter exhibit very high transition temperatures not described within BCS theory and are attributed to the class of high-T_c superconductors, which have attracted a lot of interest due to their potential use in industrial applications. For a review of the wide range of superconducting substances see Hirsch [424].

On one hand, the vast variety of superconductors and experimental data available opens up many possibilities for designing neutron star analogues. On the other hand, it is difficult to filter out which features could provide helpful information in the first place. The following discussion can thus only be viewed as a small tasting sample of possible analogies between laboratory superconductors and neutron stars. In particular, the analysis will focus on fluxtube dynamics in type-II superconductors, the state expected to dominate the outer neutron star core. We address pinning, resistive phenomena, instabilities, interfaces and how such studies could be transferred to the case of neutron stars to improve our understanding of their dynamics. This section concludes with a review of aspects related to the Meissner effect and the formation of the superconducting phase.

8.3.1 General properties

Theoretical models of neutron stars heavily rely on the use of fluid dynamics and, as illustrated multiple times in this thesis, in particular the presence of distinct, interacting fluid components. Hence, superconducting analogues of neutron stars should be able to reflect such behaviour. The first phenomenological theory of superconductivity by Fritz and Heinz London [118], introduced in Subsection 3.3.1, indeed relied on a two-fluid description. Based upon experimental observations, the London brothers postulated relations between the mesoscopic electromagnetic fields, the density and the velocity of a component responsible for the superconducting properties. This bears some obvious resemblance to Landau's two-fluid model [138], usually invoked to explain observations of superfluid helium. It further illustrates how (analogous to the superflow in helium II) a small electric current can flow through the superconducting sample without creating a voltage. Whereas Landau's two-fluid interpretation was based on semi-microphysical considerations, the London equations did not provide any insight into the microphysics of superconductors. As noted in Section 3.1, the development of quantum mechanics played a crucial role in improving the understanding of the small-scale processes and ultimately led to a full microscopic theory of conventional superconductivity. An equivalent formalism for the microphysics of superfluid systems has not yet been developed.

The first person to suggest that the quantum nature of particles could play an important role in the superconducting phase transition was Fritz London himself [119]. His idea found support from Pippard [425] in 1953, who demonstrated by adding impurities to a superconductor that the penetration depth is not constant but dependent on the material parameters. Accounting for this change by introducing a non-local modification to the London equations on the order of a second scale (which he called coher-

ence length), Pippard was the first to illustrate the significance of the wave function's macroscopic properties. Encouraged by these results, Bardeen, Cooper and Schrieffer published their microscopic description of superconductivity in 1957 [120]. The central idea of BCS theory is the presence of an attractive force, which causes two fermions to form a Cooper pair. In standard metals these fermions are electrons, which are coupled to the lattice and can thus bind by exchanging virtual phonons. These electron Cooper pairs can then condense into the ground state and subsequently form a superconducting state, if the attractive interaction is stronger than the repulsive Coulomb force. This phase transition is then observed at a critical temperature, $T_{\rm c}$. It had been previously pointed out that the existence of a critical temperature could also be explained by invoking an energy gap, Δ, at the Fermi level [426]. This implies that a finite energy, more precisely 2Δ, is required to break a Cooper pair and excite electrons out of the ground state. The energy gap is temperature-dependent as it takes its maximum at $T = 0$ and vanishes at $T_{\rm c}$, where the proton coherence length diverges (see Equation (3.73)) and the superconducting state thus breaks down. In these two limits, BCS theory predicts the following behaviour for conventional s-wave pairing [114]

$$\Delta(T = 0) \approx 1.764\, k_{\rm B} T_{\rm c}, \qquad \Delta(T \to T_{\rm c}) \approx 3.06\, k_{\rm B} T_{\rm c} \left(1 - \frac{T}{T_{\rm c}}\right)^{1/2}. \tag{8.9}$$

The first expression has been used in Subsection 5.1.2 to determine the critical temperature of the singlet-paired neutron star condensates and the proton coherence length in Equation (4.11), while a similar relation was employed for the triplet-paired models. Moreover, for $T \to T_{\rm c}$, the energy gap is proportional to the order parameter of the Ginzburg-Landau theory, illustrating the close connection between the two formalisms near the transition temperature, $T_{\rm c}$.

With the microscopic picture in mind, it is possible to re-evaluate the idea of a two-fluid picture for superconductors. Similar to the case of helium II, at zero temperature the system occupies the ground state, whereas a gas of quasi-particle excitations is present above $T = 0$. This, in principle, provides the microphysical justification for a macroscopic two-component model. Bardeen himself examined in 1958 [427] if Landau's model of superfluidity could be applied to fermionic superconductors and pointed out that the analogy is limited due to the presence of the metallic lattice. Whereas superfluid dynamics simply depend on the two components' relative velocity, this can only be an approximation for the superconducting case, where the flow of normal electrons is constantly disrupted by scattering off the lattice and other defects. Hence, the two-fluid description of superconductors is limited to small relative velocities, where the free-electron approximation holds, and phenomena such as second sound that are related to the system's two-fluid nature are most likely not observable [113]. Despite these constraints, the two-fluid model has for example proven useful in calculating the microwave surface impedance, shown to depend on the ratio of normal to superconduct-

ing electrons [428], and the transport properties of granular superconductors[2] [429]. In both cases, good agreement with experimental data has been obtained. The two-fluid model has also been able to account for the excitations of collective modes [430, 431], which have been observed as propagating phase fluctuations in thin superconducting aluminium films [432]. As the normal electrons are effectively immobilised by scattering with the lattice and impurities, these oscillations are very similar to the fourth sound in helium II, where the normal fluid motion is impeded by its large viscosity and the behaviour of the two components is characterised by a phonon-like mode.

The preceding discussion clearly illustrates that the two-fluid model is seldomly applicable to laboratory superconductors. This makes it difficult to address the characteristics of the multi-component neutron star interior. While there could be some parallels to the crustal superfluid, which coexists with the iron lattice and is expected to strongly interact with the lattice nuclei (resulting in various mutual friction mechanisms as discussed in Section 5.2), the terrestrial superconductors are less suitable to perform detailed investigations of a neutron star's multi-fluid dynamics. In particular, creating mixtures of two macroscopic condensates seems out of reach as a result of the solid character of the superconducting samples. Due to these disadvantages, experiments with helium and ultra-cold gases have considerably more potential to improve our understanding of interacting, interpenetrating superfluids.

8.3.2 Fluxtube dynamics

While laboratory superconductors appear less relevant to study phenomena related to the neutron stars' multi-fluid nature, another aspect can be analysed in great detail: the physics of fluxtubes. Most conventional, heavy-fermion and high-T_c superconductors are of type-II [304] and permeated by quantised fluxtubes if an external magnetic field $H > H_{c1}$ is applied. Their magnetic properties are especially important for the industrial design of superconducting wires and magnets, which has resulted in extensive research on the properties of type-II materials. All these studies are based on Abrikosov's seminal work from 1957 [123], which demonstrated for the first time the existence of a class of superconductors, not completely expelling magnetic flux from their interior but instead forming a regular mixed state. The calculation has been discussed in detail in Subsection 3.3.4. The experience, gained from studying the fluxtube lattice in laboratory system over decades (for a review see Brandt [433]), could greatly benefit the development of analogues for neutron stars, where the fluxtubes' motion is expected to govern the magnetic field evolution but only little is known about the mechanisms affecting them.

One advantage of terrestrial superconductors is the possibility to image the magnetic flux structures. It has been possible since the mid 1960s to obtain direct evidence

[2] Granular superconductors are composed of microscopic superconducting grains, separated by normal regions. Quantum mechanical Josephson tunnelling between these weakly-coupled grains generates the macroscopic superconducting state. Many high-T_c superconductors are of this granular structure.

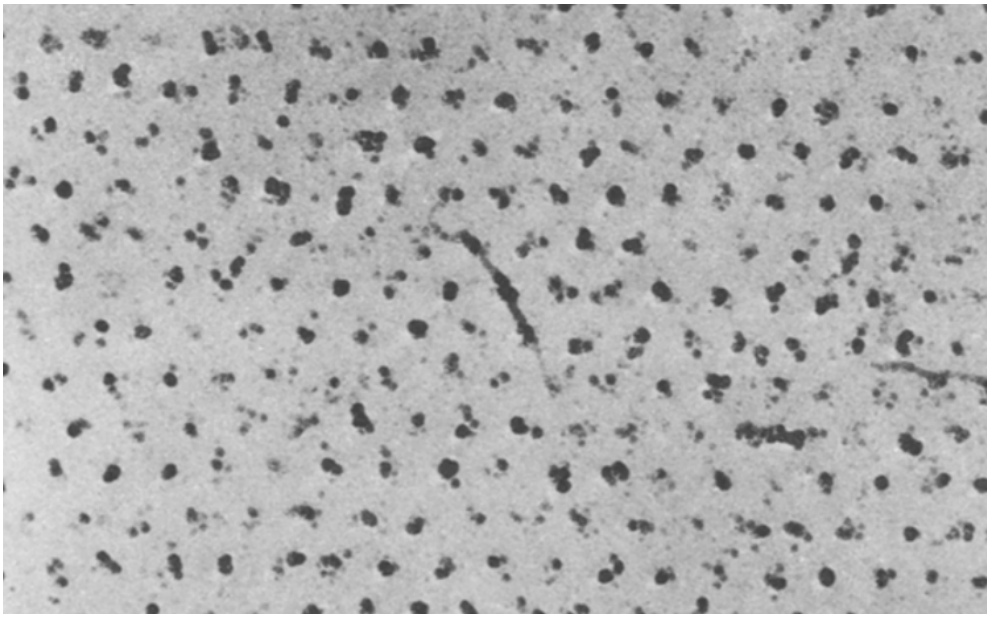

Figure 8.13: Electron micrograph showing the fluxtube lattice of a type-II superconductor at 1.1 K. The dark points are small cobalt particles distributed with the decoration method. The figure is adapted from Essmann und Träuble [434] (p. 526).

of the fluxtube lattice by using the *decoration method* (see for example Essmann und Träuble [434]), which is based on evaporating a metal wire. The resulting magnetised smoke falls onto the surface of a superconductor and settles on the points of highest magnetic field, which coincide with the ends of fluxtubes. The resulting pattern is then observed with an electron microscope as shown in Figure 8.13. Still applied today, this visualisation technique not only provides information about the flux distribution on the surface but also allows the extraction of bulk properties [435]. It has also proven useful in studying high-T_c superconductors [436]. Today, many more methods are available to analyse the interior of type-II superconductors ranging from neutron scattering and magnetic force microscopy to scanning tunnelling spectroscopy [437, 433, 438]. Using these approaches, it has for example been possible to detect the motion and pinning of a single fluxtube, visualise the pinning defects [439] and obtain time-resolved images of fluxtube dynamics [440] and high-resolution pictures of individual fluxtube cores [441].

The typical size of superconducting fluxtubes is given by the coherence length, which is of the order of 10 nm [113]. Comparison with vortices in the superfluid helium condensates shows that the fluxtubes are two orders of magnitude larger than helium II vortices but of similar dimension as the ones in the helium-3 B-phase, where BCS theory is also invoked to explain the macroscopic quantum behaviour (see Subsection 8.1.1). As previously discussed, these dimensions are many orders of magnitude larger than the typical proton and neutron coherence lengths in neutron star cores (see Equations (4.11) and (4.13)). This could cause several problems for superconducting laboratory neutron star analogues. However, because little conclusive evidence has been acquired in

the five decades since the presence of quantised magnetic structures was first suggested [45], understanding the dynamics of vortices and fluxtubes is one of the most important problems of modern neutron star astrophysics. Hence, any system that could provide more information about these mechanisms is worth a more detailed investigation. In the following, various aspects of fluxtube physics in terrestrial media will be explored.

Before proceeding with an analysis of the individual features, we raise two notes of caution. Firstly, almost all experiments are performed in two dimensions. Using thin films, which are also easy to manufacture, simplifies the studies as it ensures that fluxtube bending can be neglected. Moreover, laboratory systems are mainly dominated by two-dimensional phenomena as a result of the underlying crystal structure [442]. In particular, the physics of high-temperature superconductors can be described by considering weakly-coupled layers [443]. While such a two-dimensional geometry is suitable to describe the local dynamics of the proton fluxtubes in the neutron star core, it is certainly insufficient to account for the macroscopic magnetic field characteristics. Thus, experiments with three-dimensional samples would be desirable. However, such superconductors have only recently started to attract attention and only limited studies are available, for example addressing the magnetic properties of superconducting spheres [444, 445, 446] or fluxtube motion in layered systems [447, 448, 449]. Additionally, the proton superconductor in neutron stars is rapidly rotating, which is associated with the *London field* (see Subsection 3.3.2). Although this characteristic magnetic field is of small magnitude in neutron stars, it has important implications for the stars' electromagnetism (see Subsections 4.3.2 and 4.3.4). Measurements of the London field in terrestrial superconductors have been performed in metallic [450], high-temperature [451] and heavy-fermion [452] systems, giving good agreement with Equation (3.57). However, apart from a few exceptions [453, 454, 455], most experiments investigating the dynamics of fluxtubes are performed with static films and non-rotating external fields, thus not providing information about the influence of rotation on the superconductor's properties. For these two reasons, the following discussion primarily concerns aspects which could help to improve our knowledge of mesoscopic neutron star physics.

Pinning

The first evidence that pinning affects the motion of fluxtubes in superconductors was obtained by analysis of their electromagnetic properties. It was observed that impurities modify the current-carrying characteristics of type-II media while not significantly altering their transition temperatures [113]. The effect of impurities or defects is particularly apparent when magnetisation curves of *pure* and *dirty* type-II superconductors are compared. Whereas the curves are reversible in the former case, their behaviour is irreversible in the latter case and strong hysteresis is exhibited for a cycle in the applied magnetic field. The first description, successful in modelling the hysteresis behaviour of superconductors with large Ginzburg-Landau parameter exposed to high fields, was de-

veloped by Bean in the early 1960s [456, 457]. Ignoring the mesoscopic fluxtube physics, Bean postulated that a maximum, critical current density is flowing in the surface layer of a superconductor, its penetration depth depending on the strength of the applied field. The field then decays linearly towards the centre of the sample, which is field free. Depending on the magnetisation history, the superconductor thus responds differently and hysteretic behaviour is observed. This simple so-called *critical-state model*, which gives excellent agreement with experiments [458, 457] and is still widely used in the engineering community [459], can also be interpreted as an average over the mesoscopic quantisation in the limit of large numbers of fluxtubes [460]. Applying a magnetic field, fluxtubes are pushed into the superconductor. In pure systems, they move freely and are able to uniformly distribute in the sample, which explains the reversible magnetisation curves. In dirty systems however, structures are present impeding the fluxtubes' motion and preventing them from moving to the centre of the superconductor. Hence, the fluxtube distribution is much denser at the surface generating a metastable state, which results in irreversible magnetisation curves. This characteristic magnetic field penetration of a dirty type-II superconductor following Bean's critical state model has recently been confirmed with diamond-magnetometric measurements [461].

Since the 1960s, pinning has been studied in much more detail and many reviews have been published on the subject (see for example Campbell and Evetts [462], Dew-Hughes [463] and Blatter et al. [464]). The reason for this lies mainly in the importance of pinning for industrial applications, which can be explained in the following way: the interaction between fluxtubes of parallel magnetic field orientation, $\hat{\mathbf{B}}$, is repulsive (see also Subsection 6.2.2) and a single fluxtube in a lattice experiences the Lorentz force

$$\mathbf{f}_{\mathrm{L}} \equiv \mathbf{j}_{\mathrm{S}} \times \frac{\Phi_0}{c}\hat{\mathbf{B}}. \tag{8.10}$$

Here, $\mathbf{j}_{\mathrm{S}}$ denotes the total supercurrent density generated by all other fluxtubes. Hence, an individual fluxtube can only be in equilibrium if the Lorentz force vanishes, implying $\mathbf{j}_{\mathrm{S}} = 0$ at its centre. This is realised in a regular array where the triangular arrangement has the lowest free energy. Equation (8.10) further illustrates that any additional currents, $\mathbf{j}_{\mathrm{ext}}$, flowing through a superconducting medium will disturb the equilibrium configuration, create a net force, $\mathbf{f}_{\mathrm{ext}}$, on the fluxtubes and cause them to move,

$$\mathbf{f}_{\mathrm{ext}} \equiv \mathbf{j}_{\mathrm{ext}} \times \frac{\mathbf{B}}{c}, \tag{8.11}$$

where $\mathbf{B}$ denotes the averaged magnetic induction. As explained in the next subsection, moving fluxtubes dissipate energy and generate heat. This is very problematic for superconducting wires and magnets, where high fields and currents are desired. However, by using impure materials, fluxtubes can pin to inhomogeneities which obstruct their motion. Due to the benefits of decreasing dissipation and preventing heat generation, pinning is an important field of modern superconductivity research.

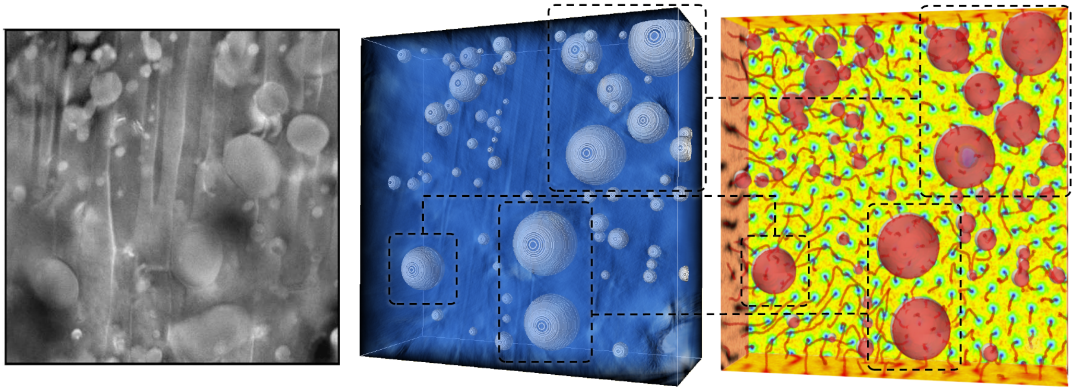

Figure 8.14: Modelled fluxtube motion based upon measurements of the pinning landscape in a high-T_c superconductor. The left figure is the three-dimensional scanning transmission electron microscope (STEM) tomogram of a superconducting sample of dimensions $534 \times 524 \times 129\,\mathrm{nm}^3$. The box contains approximately 71 almost spherical particles with sizes ranging from 12.2 to 100 nm. The middle figure combines the first one with a numerical reconstruction of the model volume. The final figure on the right represents a snapshot of the time-dependent Ginzburg-Landau simulation showing the behaviour of the order parameter. Isosurfaces of the order parameter close to the normal state are marked in red and illustrate the motion of fluxtubes and positions of pinning sites. The colour in the background represents the amplitude of the order parameter with yellow showing superfluid and blue identifying normal regions. The left figure is adapted from Ortalan et al. [471] (p. 2055), the middle and the right one from Sadovskyy et al. [472] (p. 014011-2).

The great benefit of studying pinning physics with laboratory superconductors is the amount of experimental control these systems offer. The different ways to modify the pinning properties seem endless, ranging from standard techniques such as irradiation, doping [113], varying the sample thickness [465] or the introduction of holes [466, 467] to more advanced methods like nanofabrication. Nowadays, the interior of superconductors can be doped with small nanoparticles [468, 469] and the pinning surfaces customized by using electron beams to deposit small particles [470]. The possibility of creating any kind of desired structure with high resolution could prove very important for studying the unknown pinning characteristics of neutron star fluxtubes and vortices.

Above all, the studies of laboratory superconductors demonstrate that pinning is a very common phenomenon since fluxtubes cannot only be locked to defects and impurities but also to dislocations, vacancies, grain boundaries, interstitials, rough surfaces and layered structures. Generally, the pinning centres are most effective if they are of similar dimension as the fluxtubes' normal cores. Among other aspects, understanding the pinning phenomenon theoretically has involved efforts to analyse the depinning of fluxtubes from random pinning potentials [464] and calculate detailed pinning forces from microscopic BCS principles [473, 474] or the phenomenological Ginzburg-Landau theory (see Brandt [433] and references therein). In recent years, it has further become possible to directly image the defects in superconductors and measure the corresponding pinning forces [475, 476]. Besides such small-scale approaches looking at individual fluxtubes, pinning in type-II superconductors has also been examined from a macro-

scopic perspective. The properties of a fluxtube lattice affected by pinning have for example been modelled with a mean-field formalism [477, 459] (leading to a modified, non-linear diffusion-type equation for flux evolution) and by means of a collective theory [478, 479, 480]. The latter is based on the statistical summation of different pinning centres located within a characteristic lengthscale. This scale results from the assumption that weak, randomly distributed pinning sites are able to destroy the long-range order of an elastic lattice but retain its short-range structure. In this picture, (de)pinning events are related to the motion of large numbers of fluxtubes, located within *bundles* associated with the characteristic lengthscale, instead of individual fluxtubes. Theoretical predictions of this collective model agree well with experiments [481, 482, 483]. Similar macroscopic models of the quantum condensates and the associated characteristics could also be applicable to the neutron star interior. The collective motion of vortices is, for example, expected to play an important role in the generation of glitches. Hence, laboratory studies could provide valuable input to model these jumps more accurately and allow one to test macroscopic formalisms against observational data.

Before continuing with the dynamical fluxtube processes, we point out the recent work by Sadovskyy et al. [472], illustrating how experiments and modern theoretical calculations can complement each other in the study of type-II media. Sadovskyy et al. numerically reconstruct the scanning transmission electron microscope (STEM) measurements of pinning defects in a high-T_c superconductor [471] to calculate the motion of fluxtubes in a realistic pinning landscape (see Figure 8.14). By numerically solving the time-dependent Ginzburg-Landau equations [298, 484], they account for features such as pinning defects, fluxtube flexibility, long-range fluxtube repulsion, fluxtube cutting and reconnections. The simulated critical properties are in very good agreement with the experimental results, demonstrating the impact such combined approaches could have. Keeping in mind that laboratory systems further offer the possibility to manufacture arbitrary pinning landscapes, the method provides the unique opportunity to perform detailed studies of the pinning interaction and deduce the fluxtube-averaged properties of the superconducting sample. Such analyses could prove specifically useful to improve our understanding of vortex-fluxtube coupling in neutron star interiors and model the large-scale implications.

Flux creep, flux flow and Hall effect

In the 1960s, Abrikosov's fluxtube interpretation became increasingly popular and several phenomena that had previously been unexplained were interpreted in terms of the fluxtube picture. Two important examples are the *flux-creep* and *flux-flow* behaviour, which represent the non-linear and linear regimes of fluxtube motion in conventional superconductors. The former one was first examined by Kim et al. [458], who found that close to the transition temperature flux could *leak* through a superconductor and create a measurable resistance if the external current, $\mathbf{j}_{\rm ext}$, exceeded a critical value.

More precisely, the experiments revealed that persistent currents decayed proportional to the logarithm of time and the creep behaviour was faster when the transport current was increased [485]. A theoretical model for this phenomenon was provided by Anderson and Kim [486, 487]. They suggested that the creep dynamics are related to the thermal energy of the lattice, which causes the fluxtubes to vibrate. This can result in the unpinning of several fluxtubes, which move as a unit and jump to adjacent pinning sites. The thermal activation of bundles of fluxtubes over the pinning barriers (which decreases exponentially as the temperature goes to zero) is a discrete and stochastic process having the advantage to not require a detailed specification of the nature of the pinning centres. In the absence of an external current, the net jump rate of flux bundles vanishes. If, however, a small transport current is applied, the unpinned fluxtubes move under the influence of the Lorentz force (see Equation (8.10)), which causes the flux distribution to slowly change over time. This dissipates energy, leading to the observed resistance and the characteristic logarithmic decay of the persistent currents. Based on this creep theory for superconductors, Anderson and Itoh [88] proposed that a similar mechanism could be operating on the superfluid vortices in neutron stars, explaining the noisiness of pulsar rotation frequencies. The idea has also been taken up by Alpar et al. [89, 90], who considered vortex creep in the neutron star crust to develop a more realistic model of pulsar glitches. By comparing observational data to the theoretical framework, the creep theory provided estimates of interior characteristics such as the temperature or the pinning energy between the neutron vortices and the crustal nuclei.

Increasing the transport current, $\mathbf{j}_{\rm ext}$, further, the Lorentz force will eventually exceed the pinning force, which enables the fluxtubes to flow through the sample. This is analogous to the scenario invoked for large pulsar glitches (see also Subsection 2.3.3), where neutron vortices are thought to be pinned to the crustal lattice until the pinning force is overcome by the Magnus force and a large number of vortices are released simultaneously. However, in superconductors the Lorentz force is observed to replace the Magnus force as the driving source of fluxtube motion. The two forces can be experimentally distinguished in the following way: As the Lorentz force acts perpendicular to the applied current and the magnetic induction (see Equation (8.11)), the resulting fluxtube velocity is transverse to $\mathbf{j}_{\rm ext}$. This, in turn, induces an electric field, which is parallel to the transport current and generates a longitudinal voltage [113]. If the Magnus force would dominate the dynamics, the fluxtubes would feel no net force and be dragged with the current, similar to the motion of free superfluid vortices. This would induce a transverse voltage, which is characteristic for the conservative *Hall effect* already discussed in Chapter 7. Experiments have shown that for most superconductors the longitudinal voltage is several orders of magnitude larger than the transverse *Hall voltage*, implying that the Lorentz force determines the fluxtube motion [488, 489] and not the Magnus force as would be the case in a superfluid. This difference in superconductors arises because the metallic lattice and impurities complicate the dynamics, acting as scattering centres for the normal electrons and impeding the fluxtube flow.

As noted by multiple authors, only in very pure superconductors in the limit of $T \to 0$, where electron-electron scattering dominates, one would expect the fluxtube motion to be almost free and governed by the Magnus force [490, 491, 492, 298].

Experiments have further demonstrated that at low temperatures the voltage in the dissipative flux-flow regime changes linearly with the applied magnetic field and the *flux-flow resistance* thus obeys the empirical law [493]

$$R_{\rm S} \equiv R_{\rm N} \frac{B}{H_{c2}}. \tag{8.12}$$

Here, $R_{\rm N}$ denotes the normal-state resistance, H_{c2} the upper critical field and B is the magnitude of the magnetic induction. Applying different treatments to the superconducting sample shows that the flux flow is not affected by the surface conditions [494]. Therefore, the fluxtubes' motion is independent of the pinning characteristics and the resistive physics are solely determined by the superconductor's bulk properties. More precisely, the phenomenological relation (8.12) indicates that strong dissipation is directly connected to the fluxtubes, as the factor B/H_{c2} represents the fractional volume their normal cores occupy in the superconductor [493] (see also Equation (6.10)). This illustrates that similar to superfluid helium or the multi-component mixture in neutron stars, the dissipative effects are determined by the drag forces acting on the individual fluxtubes.

The first theoretical calculation of the corresponding microscopic drag coefficient was provided by Tinkham [495]. He pointed out that the order parameter at any specific point would oscillate between zero (normal fluxtube cores) and a constant value (superconducting regions) as the fluxtubes are moving through the sample. Since the equilibrium is not instantaneously restored, Tinkham showed that the ensuing relaxation process would cause dissipation. A process of similar order, Bardeen and Stephen [496] considered the induction of electric fields by the moving fluxtubes, which generate dissipative eddy currents in their normal cores. Based upon electron-lattice scattering, they derived the corresponding drag coefficient. Whereas for Tinkham's mechanism, the dissipation is proportional to the amplitude of the order parameter, the dissipation is related to the supercurrent density and, thus, the phase of the order parameter for the second mechanism. Both processes and the flux-flow resistance (8.12) can be recovered performing a more detailed study of the non-equilibrium physics in type-II superconductors using a time-dependent extension of the Ginzburg-Landau theory [497, 498]. However, Kopnin [304] has pointed out that such models neglect additional dissipation mechanisms due to the relaxation of quasi-particle excitations created by the moving fluxtubes. Other formalisms such as a semi-classical Boltzmann theory [304] or a time-dependent microscopic theory [499] are necessary to correctly capture all microscopic processes, which is particularly important, when the strength of the Hall effect is calculated. The same models have been invoked to explain the strong mutual friction in superfluid helium-3 (see also Subsection 8.1.3), which is conceptually similar to a su-

perconductor despite having a more complicated structure of the order parameter, and could also give useful insight into the dissipation mechanisms affecting a neutron star's interior magnetic field evolution.

Discussing the flux-creep, flux-flow and Hall regimes shows that laboratory superconductors provide the means to directly observe the dissipative fluxtube behaviour. Using the experimental data allows one to investigate the validity of theoretical models, which helps to improve our understanding of the underlying microphysics. The methods applied to terrestrial systems thus proceed analogous to the study of the neutron stars' properties, where macroscopic characteristics are used to constrain the interior physics. However, many questions concerning the magnetic fields of neutron stars are still unanswered. Laboratory superconductors could therefore help to examine the mesoscopic fluxtube dynamics in more detail and, for example, assist in determining the mechanism dominating the neutron stars' magnetic field evolution.

Lattice melting

While conventional superconductors are well described by the flux-creep and flux-flow models, high-temperature systems exhibit more complicated fluxtube physics, predominantly caused by two factors. Firstly, high-T_c superconductors have a strongly layered crystal structure, which results in the formation of weakly-coupled, two-dimensional fluxtubes such as layered pancakes [500, 501]. Amongst other aspects, this highly anisotropic behaviour decreases the strength of the pinning potentials, favouring thermal depinning [433]. Secondly, due to the high transition temperatures, thermal fluctuations play a much more important role than in conventional media. In high-temperature superconductors, these differences can for example lead to the activation of creep over a large temperature range, referred to as *giant flux creep* [114]. As thermal fluctuations destroy the long-range order of an elastic lattice, this is generally described within the collective pinning theory [478, 479, 480]. As discussed previously, this theory is based on the statistical summation over random pinning sites.

The same theory also accounts for the fact that the resistivity of high-T_c superconductors does not decrease exponentially for $T \to 0$ as characterised by the conventional Anderson-Kim model [487], which always predicts a non-zero resistance. Instead, it drops rapidly at low temperatures indicating an abrupt change in the fluxtube dynamics that is usually interpreted as evidence for a second phase transition well below the superconducting one [502]. In analogy with other crystalline structures, this is expected to correspond to a first-order *melting transition*, which is resulting from the destruction of the long-range order and characterises the change from a solid to a liquid fluxtube phase. The discontinuity in the resistance of high-T_c superconductors would thus mark the *freezing* of the fluxtube lattice as $T \to 0$. Clear experimental evidence for such a melting transition was first obtained by measuring the local macroscopic magnetisation of a pure superconductor [503]. Similar to the expansion that accompanies the freezing

of water into ice, the local fluxtube density in a superconductor changes discontinuously at the first-order transition as a function of the applied magnetic field. Since the fluxtube liquid is denser than the solid, the former has a higher averaged induction than the latter and the local induction increases upon melting. The corresponding change was observed experimentally [503]. Additionally, it has been possible to directly record the melting of a two-dimensional lattice using scanning tunnelling microscopy [504], which unambiguously showed the transition into an ordered, isotropic liquid. The first-order nature however is only observed in very pure samples since inhomogeneities and strong pinning introduce additional disorder into the system. As the temperature decreases, the melting transition is thus complicated and thought to be of second order, causing a change from the fluxtube liquid to a *glass-like* phase [505].

Fluxtube lattice melting could also be present in conventional superconductors [506]. Despite predicted to appear very close to the superconducting transition temperature and being difficult to observe [507], several experiments have found indications for a melting transition in conventional type-II systems [508, 509]. This would suggest that a similar mechanism could also be manifested in the proton superconductor of neutron stars if the interior is sufficiently hot. Whereas this scenario is rather unlikely for old, rotation-powered pulsars, the decay of magnetic energy in young high-field magnetars might act as a potential heat source with the ability to locally exceed the critical temperature and initiate the melting transition into a fluxtube liquid. As observed in laboratory systems, this would be accompanied by a local increase in the fluxtube density, i.e. the magnetic induction, that in turn could result in additional dissipation. While highly speculative, this would significantly change the flux-carrying properties of the region compared to the rest of the star and could potentially shorten evolution timescales of the large-scale magnetic field in the neutron star core.

Instabilities

While laboratory superconductors are observed to exhibit non-linear features, this regime is somewhat different to the non-linearity of helium and ultra-cold quantum gases discussed previously. As pointed out in Subsection 8.1.4, the chaotic behaviour of superfluids is mainly influenced by their two-fluid nature, leading to turbulent dynamics such as the counterflow or the two-stream instabilities. Laboratory type-II superconductors, on the other hand, are not exhibiting strong turbulence [477, 169] as a result of several factors. Firstly, due to the presence of the lattice, Landau's two-fluid model is less satisfactory in describing the physics of superconductors and one would therefore not expect the mechanisms for superfluid turbulence to apply to the charged condensates. Moreover, pinning and the strong two-dimensional character of many superconductors stabilise these systems and suppress the development of turbulent behaviour on large scales. Hence, laboratory superconductors are not suitable analogues for the study of the neutron stars' fluid instabilities. However, there are several elements of laboratory

type-II systems, in particular related to the instabilities of individual fluxtubes, which could provide new information on how to determine the local, non-linear behaviour of proton fluxtubes and transfer this to a macroscopic model of the stars' dynamics.

One phenomenon thought to influence type-II superconductors is equivalent to the Donnelly-Glaberson instability of superfluid vortices in helium II [174, 313]. Applying an axial heat current, vortices become unstable to helical displacements and Kelvin waves are excited along the vortex lines. Similarly, Clem [510] has shown that a single, unpinned fluxtube is unstable against helical perturbations if a current applied parallel to the fluxtube's axis exceeds a critical value. The existence of this critical current has been confirmed in experiments [511]. Generalising the mesoscopic to the macroscopic lattice dynamics has, for example, been achieved by modifying the averaged vortex-density model to include the small-scale helical instabilities [477]. Additionally, Brandt [512] has directly shown that the full fluxtube lattice experiences an instability to helical deformations by balancing the driving force with the restoring force resulting from the lattice's elasticity. However, the instability growth is also influenced by the presence of pinning, which stabilises the fluxtube array and thus acts to suppress the instability on large scales. We note that Charbonneau et al. [256] proposed that the same helical instability could be acting on the proton fluxtubes in the neutron star core, destroying the regularity of the lattice, i.e. the type-II state. While not providing any specific details about the phase that would be formed instead, Charbonneau et al. suggest that the intermediate state of a type-I superconductor is one possibility. This would subsequently solve the problem discussed by Link [206], i.e. the incompatibility of type-II superconductivity with observed long-period precession in pulsars [513, 514, 515].

While the helical instability in laboratory systems has not been directly observed yet, experimental evidence for this mechanism has been recovered. Imagine an initially straight fluxtube lattice located inside a cylindrical container that becomes unstable once the critical axial current is exceeded. The distorted fluxtubes would start to spiral outwards in a helical manner [433]. The helices would grow until the fluxtubes hit the sample surface, leading to a measurable change in the magnetic flux density on the container walls [516, 517] or start cutting through each other, resulting in dissipation [518]. Experiments have also made it possible to determine the cutting force between two inclined fluxtubes [519, 520]. This force is independent of the applied magnetic field, i.e. independent of the interfluxtube spacing, only weakly dependent on the temperature and generally found to be rather low (10^{-14} N per intersection in agreement with microscopic calculations [521]). This illustrates that fluxtube cutting could be very important for the dynamics of a superconductor, as it suggests for example that fluxtubes could cut through each other in order to avoid pinning centres. For more information on flux cutting in laboratory superconductors see the recent review by Campbell [522]. Analysing the cutting of fluxtubes could also help to improve our understanding of the short-range magnetic coupling between the two coexisting lattices in the outer neutron

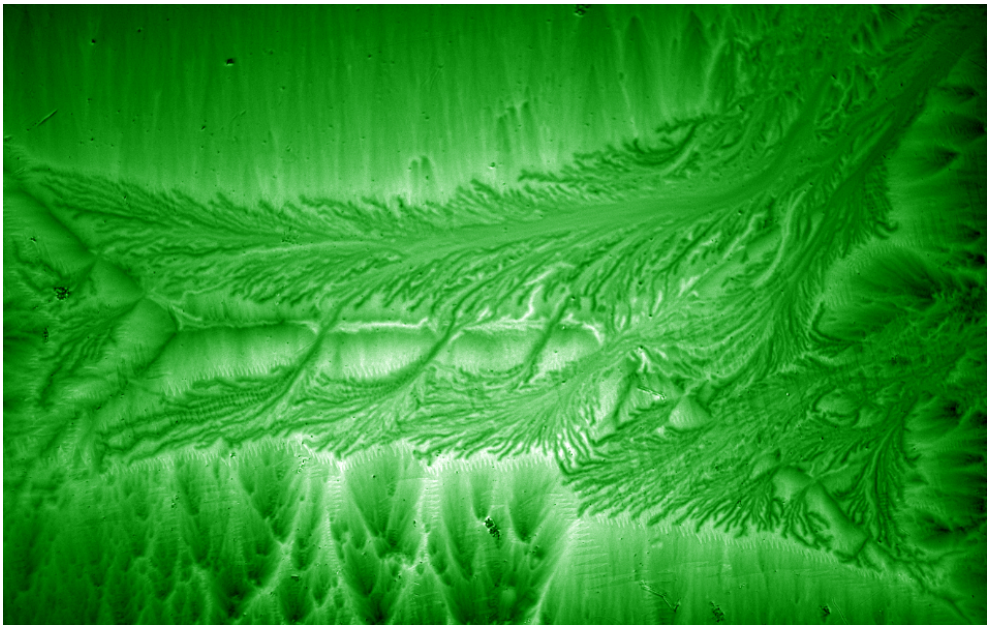

Figure 8.15: Magneto-optical image of the collapsed meta-stable state in a thin superconducting film. Following a thermomagnetic instability, fluxtubes are suddenly redistributed forming avalanche-type patterns. The figure is adapted from Eliasson [523] (p. 53).

star core. While it is not clear how much energy it costs to cut neutron vortices through proton fluxtubes and vice versa, the interaction could lead to strong dissipation in the interior (see also Subsection 6.2.4). If the energy costs for vortex-fluxtube cutting are too large, the quantised arrays could even be locked together. Better models of laboratory fluxtube cutting could hence help to develop improved frameworks of the close connection between the neutron stars' magnetic and rotational evolution [251].

In addition to the helical instability, other dynamical instabilities of the fluxtube lattice in type-II superconductors have been studied. Theoretical models [524, 525, 526] generally neglect the detailed microphysics and instead consider Bean's macroscopic, critical state model, originally introduced to explain the irreversible behaviour of dirty superconductors (see Subsection 8.3.2). The models are based on the assumption that by changing external parameters such as the temperature or the applied magnetic field, the temperature inside the superconductor locally increases, which causes the pinning force and, hence, the critical current density to decrease. Subsequently, the fluxtubes start to move and the metastable state becomes unstable, leading to the uncorrelated propagation of flux through the sample. These sudden bursts of collective motion, also known as *flux jumps*, lead to energy dissipation, creating measurable voltages [527].

As the motion of the fluxtubes in the presence of pinning centres is characterised by a non-linear diffusion equation [433, 459], the catastrophic flux propagation is closely related to the concept of self-organised criticality originally discussed by Bak et al. [381]. Again ignoring the microphysics and simply considering the statistical properties of the non-linear behaviour, the flux jumps can be interpreted as avalanches similar to those

of sand-pile experiments [528] or those discussed previously in the context of BECs and pulsar glitches (see Subsection 8.2.2). These systems have in common that after being driven to the threshold of instability, they organise themselves and exhibit dynamics showing a power law. In case of type-II superconductors, the overall activity and sizes of avalanches follow this power law [529, 527], characteristic for scale-invariant processes.

Laboratory superconductors have the advantage that self-critical behaviour can be easily visualised. In early experiments, heating was applied to a small fraction of the sample surface, triggering a thermomagnetic instability and creating dendritic fluxtube structures, which were recorded with magneto-optical imaging [440]. The distinct lightning-strike pattern has also been found in numerical simulations of several hundred fluxtubes exposed to a strong pinning landscape [526]. Today, the imaging methods have significantly improved [530, 460, 523, 531], providing high-resolution pictures of the fluxtube avalanches as illustrated in Figure 8.15. However, while it has been possible to image different stages of this collective behaviour, time-resolved observations of entire avalanches on nanosecond scales have not been achieved yet [532].

Interfaces and the Meissner effect

One important unknown of neutron stars is the influence of interfaces on their dynamics. Typical neutron star equations of state predict a layered structure with the crust-core transition located at densities of about $\sim 10^{14}\,\mathrm{g\,cm^{-3}}$ (see Subsection 2.2.3). While this change is expected to be smooth and not present as a sharp interface, the charged protons have to undergo a transition from a normal resistive to a type-II superconducting state. The detailed microphysics of this are not understood but could include a highly resistive *pasta layer* [41, 42] and the formation of current sheets [266, 267]. Moreover, at higher densities, protons prefer to be in a type-I state implying the presence of another transition region in the stars' inner core, where an intermediate phase of macroscopic normal and flux-free Meissner regions would exist [195, 177] (see also Subsection 4.1.2). Hence, using superconductors to design laboratory analogues, one could take advantage of experiments in order to shed light onto how such interfaces manifest themselves.

The transition between the two superconducting states in the inner neutron star core is considered first. Laboratory systems exhibiting different types of superconducting behaviour have been observed for decades. Images of the intermediate states in a conventional type-I and type-II superconductor are given in Figure 8.16. For the former, multi-quantum fluxtubes [533] and lamella structures surrounded by flux-free regions are observed. Ge et al. [534] have recently used scanning Hall microscopy to determine the number of flux quanta inside such lamellae and found them to be of integer value. On the other hand, type-II systems characterised by low Ginzburg-Landau parameters show features similar to the intermediate type-I state, the main difference being the presence of a regular fluxtube lattice inside the flux-carrying regions. In both cases however, this alternation of macroscopic flux-free and flux-containing domains is caused by

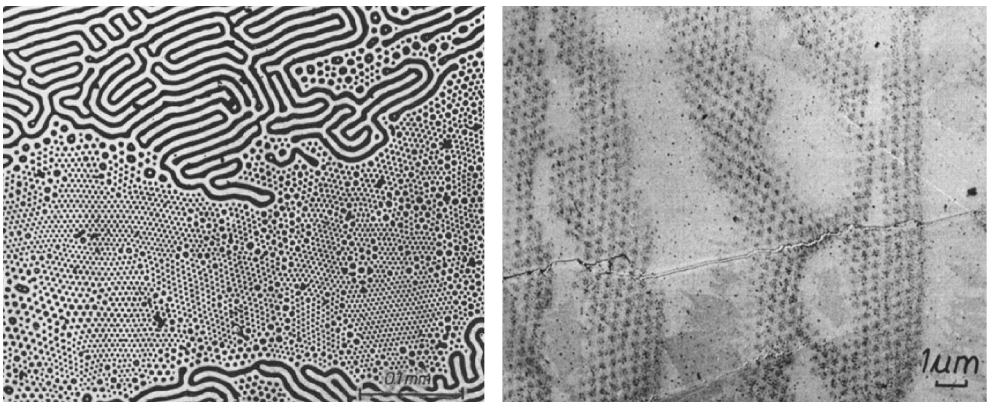

Figure 8.16: Images of the intermediate state of a conventional type-I (left) and a type-II (right) superconductor obtained with the decoration method. The type-I system (Ta) shows regular and irregular multi-quantum flux structures, where the dark domains indicate normal conducting behaviour. The type-II medium (Pb-Tl alloy) has $\kappa_{\mathrm{GL}} \approx 0.73$ and similarly exhibits flux-free regions and normal ones consisting of a regular lattice structure. The two figures are adapted from Brandt [535] (p. 59) and Essmann [540] (p. 85).

the interplay of an attractive interaction on long scales and a repulsive force on short scales. Several mechanisms have been proposed to describe this behaviour theoretically. As pointed out by Brandt [535], demagnetisation effects in combination with the sample geometry could for example serve as one explanation. More recently, Babaev et al. [254, 536] have proposed that alternating domain characteristics could also be obtained by invoking weakly coupled *two-component superconductors*. Such systems would have two energy gaps and coherence lengths and are thus described by two distinct macroscopic wave functions. Experimental evidence for a two-component gap was found in MgB_2 [537], where observed thermodynamical properties were in disagreement with a single isotropic energy gap. Experimental and numerical studies of this alloy have indeed revealed a strong domain-like structure similar to the intermediate state of conventional superconductors [538, 539]. Displaying fluxtube clusters and flux-free voids, MgB_2 has also been referred to as exhibiting a *semi-Meissner* phase or *type-1.5 superconductivity*. Being able to create such systems in laboratory experiments would allow one to model a state possibly present in the high-density neutron star interior and investigate in detail the formation and evolution of the domains and examine their macroscopic properties.

Moreover, recent theoretical work predicts that the transition from type-I to type-II physics could be directly observable in systems with intermediate Ginzburg-Landau parameter, because the interaction between individual fluxtubes undergoes a cross-over from attractive to repulsive as the temperature increases [541]. This thermally induced change from a type-I state (fluxtubes clump together and build the normal conducting clusters) to a type-II state (fluxtubes are separated) illustrates the fact that the Ginzburg-Landau parameter is temperature-dependent [542, 543, 544]. The behaviour of several hundred fluxtubes across a type-I/type-II interface has also been calculated for superconducting bilayers exposed to an external field [545]. As a result of forces competing on

different lengthscales, numerical simulations unearth a very rich palette of mesoscopic patterns in the intermediate state reaching from homogeneous fluxtube distributions to fluxtube chains and flux-free zones surrounded by type-II domains. These arrangements were present in both layers and could be controlled by changing magnetic field, temperature and coupling strength between the two thin films. The latter was regulated by an ultra-thin insulation layer of variable thickness in between the films, as this determines the intensity of Cooper pair tunnelling [546, 547].

While most laboratory studies are concerned with the interfaces of distinct superconducting regions, the transition between the type-II and the type-I state in a neutron star is governed by the density [177], increasing continuously towards the stars' centre. Hence, in order to mimic the behaviour of such an interface with a terrestrial analogue, it would be beneficial to control the type of superconductivity without creating a discontinuity. With this in mind, the work by Aegerter et al. [548], studying the influence of bismuth doping on the properties of a lead superconductor, is briefly mentioned. Whereas pure lead is characterised as a type-I medium, high doping of bismuth creates type-II behaviour. For intermediate doping, on the other hand, both types of superconductivity can be observed depending on the temperature. An intuitive explanation for the effects of doping is the following: An increase in the number of impurities causes a reduction in the electron mean free path and thus the coherence length. This in turn increases the Ginzburg-Landau parameter and eventually leads to type-II characteristics. Therefore, if one could prepare a superconductor with gradually higher degrees of doping, this would provide a promising way to test the physics of the type-II/type-I interface in a neutron star's inner core.

Finally, the normal-superconducting transition in laboratory media is addressed. In recent years, efforts have been concerned with analysing the heat and charge transport properties of this interface [549, 550]. However, these studies are usually performed with mesoscopic *hybrid structures*, as quantum mechanics play a crucial role on small scales leading to new phenomena such as phase-coherent transport of electrons [551]. While these results are less important for the macroscopic dynamics of neutron stars, other aspects of research on the normal-superconducting interface could help to improve our understanding of the stars' magnetism. In particular, laboratory analyses could provide information about the microscopic dynamics of the Meissner effect and the growth of the superconducting phase. As discussed in Chapters 6 and 7, it is poorly understood how the superconducting state in neutron stars is developed in the first place. Baym et al.'s standard argument [45], based on the large conductivity of normal matter, assumes that flux cannot be expelled from the star interior, which therefore has to form a type-II state below the superconducting transition temperature. However, there have been various arguments from observational [206, 232, 68] and theoretical [255, 256, 177] sides, casting doubt on the type-II scenario. Thus, experiments and models linked to the corresponding phenomena in laboratory systems, which could improve our knowledge

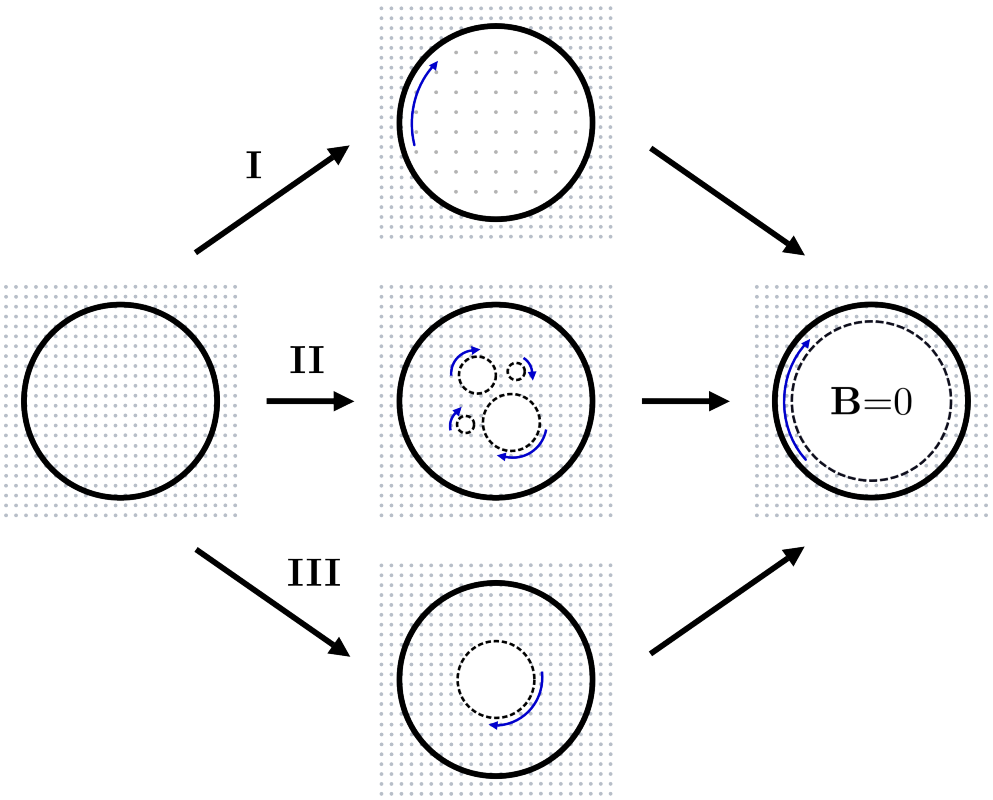

Figure 8.17: Three evolutionary paths for flux expulsion from a cylinder, i.e. the dynamics of the Meissner effect. The grey dots indicate magnetic field lines coming out of the plane, whereas blue arrows mark the presence of surface currents, shielding the flux-free regions.

of neutron star superconductivity, are briefly reviewed in the following.

Before proceeding, we point out that terrestrial experiments generally focus on the equilibrium state of superconductivity and study the system once the macroscopic phase has fully developed. However, it is known that the superconducting transition occurs rather slowly, as it can take up to thirty minutes for the equilibrium to be established (see Liu et al. [552] and references therein). This is usually explained by the fact that the superconducting-normal interface propagation is damped by the formation of eddy currents, an interpretation based on work by Pippard from 1950 [553]. He was the first to study kinematic aspects of the superconducting transition, more precisely the expansion of the normal state into the superconducting phase, when a field larger than the critical field is applied. Pippard showed that the boundary's propagation is governed by electromagnetic processes, as magnetic field changes in the normal region induce dissipative eddy currents slowing down the interface. This further implies that the magnetic field dynamics in the normal phase are well described by a diffusion equation, which can be used to show that the interface propagation is stable [553].

Pippard's idea has recently been resumed by Hirsch [554] to study the microphysics of the inverse problem, i.e. the formation of the superconducting state via Meissner expulsion, in more detail. According to Hirsch, there are three different ways for surface

currents to expel flux from a cylindrical sample and establish a field-free superconducting region. These paths are shown in Figure 8.17: (I) a time-dependent current flows close to the cylinder's surface, gradually decreasing the flux density inside; (II) surface currents shield several *seed regions*, which expand until the interior is field free; (III) a single flux-free region in the centre of the cylinder expands until the characteristic Meissner state is formed. As argued by Hirsch, path (I) is unphysical as it proceeds at non-zero magnetic field, thus not allowing the development of phase-coherence, i.e. the formation of a macroscopic quantum state. On the other hand, path (II) and path (III) are conceptually equivalent relying on the propagation of a superconducting-normal interface. Observational evidence for the latter two was already obtained in the early stages of superconductivity research [555, 556] and Meissner himself noted that the superconducting transition seemed to be initiated in areas of reduced magnetic field or temperature [557]. Using Pippard's formalism, Hirsch discusses the evolution of the superconducting phase into the normal one along paths (II) and (III). He concludes that dissipative currents can damp the interface motion but are not providing a satisfactory explanation for the slow growth of the superconducting phase, since current theories of superconductivity seem to not explain the dissipation microscopically.

Despite this problem, Pippard's linear diffusion model has been repeatedly used to study the growth of the superconducting phase. Using appropriate boundary conditions, it has for example been shown that the planar type-I/normal interface becomes dynamically unstable to long-wavelength perturbations [552, 558]. This behaviour is similar to the instability of the solid-liquid transition [559, 560] and has been confirmed by numerical analyses of the time-dependent Ginzburg-Landau model, which includes non-linear modifications [552, 558]. These simulations have additionally shown that the expansion of the planar type-II/normal interface is stabilised by the absorption of fluxtubes and, as expected, a triangular lattice is left behind. The time-dependent Ginzburg-Landau equations have further proven useful in analysing how a normal-metal coating of tunable resistivity affects the magnetic properties of a two-dimensional, dirty type-II superconductor and how flux enters the sample if a magnetic field is applied [561, 562]. The results are again in accordance with Bean's critical state model.

As a concluding remark, we note that recent work by Martinello et al. [563] gives observational evidence that the method of cooling the superconductor can also significantly affect the equilibrium configuration. They found incomplete Meissner expulsion, i.e. the trapping of flux inside the sample, if the cooling was performed slowly, whereas fast cooling resulted in the complete expulsion of flux. This could have implications for the formation of the superconducting state in neutron stars, since the transition temperature is density-dependent and a spherical shell in the outer core should turn superconducting first [24]. The gradual cooling of the neutron star interior below T_{c} could indicate that several normal conducting domains remain present in the outer core and the type-II state is not fully developed.

8.4 Summary

The purpose of this chapter was to illustrate how laboratory condensates could be employed to improve our understanding of the dynamics of superfluid and superconducting components in neutron stars. While not aimed at building realistic scale models (impossible due to the extreme conditions present in compact objects), terrestrial experiments should be designed to capture characteristic features expected to affect the stars' behaviour. Prime candidates for such studies are superfluid helium, ultra-cold gases and superconductors. We have seen that helium could prove specifically useful in advancing two-fluid hydrodynamics, usually invoked to model a neutron star's rotational evolution and in particular the glitch phenomenon, because spin-up experiments and mutual friction measurements can be performed with this superfluid. Helium also provides the possibility to analyse phase-coherent interfaces and associated phenomena such as the formation of turbulent vortex tangles. This could have important implications for the crust-core interface, one of the elements of neutron star physics very poorly understood. Similarly, the chaotic flow in superfluids can also be investigated with ultra-cold gases. BECs and Fermi gases could generally serve as excellent testing systems for mesoscopic vortex dynamics, i.e. vortex-vortex interactions or pinning, due to the prospect of easily imaging the quantised structures. Furthermore, ultra-cold gases have the advantage that it might be possible to recreate the non-dissipative entrainment behaviour, a key ingredient for the neutron star models which cannot be reproduced in helium or superconductors. The latter primarily provide information about the dynamics of fluxtubes, expected to govern the magnetic field evolution in the neutron stars' core. Superconductors could be particularly valuable for analysing pinning and the different regimes associated with it. Finally, the charged quantum states might allow one to better understand the dynamical processes associated with the formation of the superconducting phase, related to the small-scale structure of the interior field. These examples show that the well-known terrestrial condensates could serve as versatile analogues of neutron stars and mimic their behaviour on smaller lengthscales. By stimulating an exchange between the astrophysics and the low-temperature-physics community, it could thus be possible to answer several of the open questions concerning neutron star astrophysics.

Chapter 9

Conclusions

The aim of this thesis has been to perform detailed studies of the implications of cosmic condensates, specifically the dynamics of superfluid vortices and superconducting fluxtubes, on the neutron star observables. After providing background information on the structure of these extreme objects and the relevant observational aspects in Chapter 2, the treatment of terrestrial quantum condensates, including the two-fluid model and the Ginzburg-Landau theory of second-order phase transitions, was discussed in Chapter 3. This was followed by an introduction to the mathematical framework generally employed to model the multi-component interior of neutron stars (see Chapter 4). The resulting modified magnetohydrodynamical equations formed the basis for the original research concerning the stars' rotational and magnetic properties in Chapters 5 to 8.

Firstly, in Chapter 5, various mutual friction forces, arising from the interactions of vortices and their surroundings, were studied. We separately addressed mesoscopic mechanisms acting in a neutron star's core and crust and analysed the strength of the resulting macroscopic mutual friction for a realistic equation of state. By presenting the corresponding mutual friction coefficients for the cross-section of a neutron star, it was shown that the coupling strengths not only vary significantly within both layers, a fact generally neglected in the literature, but the dissipation also changes drastically across the crust-core boundary. In analogy with laboratory helium experiments, we therefore suggested that the interface could significantly affect the neutron stars' rotation.

The analysis of superfluid coupling was succeeded by an overview of various mechanisms affecting the superconducting fluxtubes in neutron star cores (see Chapter 6). The motion of these quantised structures governs the dynamics of the interior magnetic field and several characteristic evolution timescales were presented for a realistic equation of state. While these results are only preliminary and a more detailed analysis of additional processes is needed to form a comprehensive picture of the mesoscopic fluxtube physics, the discussion allowed us to highlight several problems in earlier research on this subject and point towards key questions that remain to be addressed.

Subsequently, in Chapter 7, the multi-fluid formalism was used to investigate one

of the fluxtube mechanisms in detail. Using a pedagogical approach, the analogy with normal resistive magnetohydrodynamics was employed to derive a new evolution equation for the macroscopic magnetic induction of type-II superconducting neutron star matter. Despite the fact that the resulting induction equation differs significantly from the normal resistive equivalent, it was shown that several key concepts of standard magnetohydrodynamics are retained. Based on the magnetic field evolution equation, it was further deduced that the canonical dissipative mechanism for type-II superconductors is not strong enough to explain the field evolution timescales invoked from observations of rotation-powered pulsars and magnetars. Reconciling these with theoretical predictions of magnetic field evolution models for neutron star cores would require entirely different fluxtube coupling mechanisms or alternatively different magnetic field configurations.

Finally, this thesis studied the possibility of using well-known laboratory condensates to analyse specific aspects of neutron star physics that are only poorly understood. In Chapter 8, we addressed helium, ultra-cold gases and superconductors as these are prime candidates to mimic the behaviour of neutron stars on much smaller lengthscales. By looking at characteristic features such as the two-fluid nature, mutual friction, turbulence and pinning, we found that experiments with terrestrial quantum states provide a promising new angle to fill some of the missing pieces of neutron star astrophysics.

In conclusion, the initial objectives of complementing the theoretical framework used to model neutron stars and improving our current understanding of their rotational and magnetic evolution has been accomplished by incorporating the density-dependence into the discussion of the vortex and fluxtube coupling, deriving a new superconducting induction equation and drawing parallels to laboratory condensates.

However, despite advancing the theoretical neutron star modelling, many questions remain unanswered. While a substantial number of problems wait to be addressed in the future, an exploration of several possible directions would form the logical continuation of the work presented in this thesis. As mentioned before, a key unknown in the neutron star puzzle is the importance of interfaces, specifically the crust-core boundary and the type-II to type-I transition. In the former case, one would like to better understand the pairing properties of nuclear matter and how the quantum transitions proceed in detail as the density increases. In particular, it would be useful to determine to what extent surface currents could be present, since these would have a crucial influence on the stars' magnetic properties. One could further try to analyse the boundary between the two superconducting layers in the inner neutron star core. In the intermediate type-I phase, the spatial flux distribution is unknown and modelling the magnetic field evolution in this state becomes even more challenging. One way to make progress with this problem would be to analyse the instability of the type-II fluxtube array and the subsequent formation of flux clusters by means of an effective Ginzburg-Landau theory. Closely related is the question about the detailed physics of the formation of the superconducting phase and the stars' response to a decreasing temperature. Apply-

ing again the Ginzburg-Landau formalism, one could study the nucleation of superconductivity under such external changes in order to learn more about how nuclear matter becomes superconducting and what kind of equilibrium configuration will eventually be reached. While these open problems are mainly concerned with the stars' macroscopic characteristics, we finally point out that it would also be important to develop a more in-depth model of vortex-fluxtube pinning. Specifically, an improved description of the physics on mesoscopic scales would be needed in order to assess the significance of this interaction mechanism for the neutron stars' dynamics.

Bibliography

[1] W. Baade and F. Zwicky, "On Super-Novae," *Proceedings of the National Academy of Sciences*, vol. 20, pp. 254–259, May 1934.

[2] A. Hewish, S. J. Bell, J. D. H. Pilkington, P. F. Scott, and R. A. Collins, "Observation of a Rapidly Pulsating Radio Source," *Nature*, vol. 217, pp. 709–713, Feb. 1968.

[3] V. M. Kaspi, "Grand unification of neutron stars," *Proceedings of the National Academy of Sciences*, vol. 107, pp. 7147–7152, Apr. 2010.

[4] S. L. Shapiro and S. A. Teukolsky, *Black Holes, White Dwarfs, and Neutron Stars: The Physics of Compact Objects*. Weinheim, Germany: Wiley, 2nd ed., July 2004.

[5] B. W. Stappers, J. W. T. Hessels, A. Alexov, K. Anderson, T. Coenen, T. Hassall, A. Karastergiou, V. I. Kondratiev, M. Kramer, J. van Leeuwen, J. D. Mol, *et al.*, "Observing pulsars and fast transients with LOFAR," *Astronomy & Astrophysics*, vol. 530, p. A80, June 2011.

[6] M. Kramer, "Millisecond Pulsars as Tools of Fundamental Physics," in *Lecture Notes in Physics: Astrophysics, Clocks and Fundamental Constants* (S. G. Karshenboim and E. Peik, eds.), vol. 648, pp. 33–54, Berlin, Heidelberg: Springer Berlin Heidelberg, 2004.

[7] N. Andersson, V. Ferrari, D. I. Jones, K. D. Kokkotas, B. Krishnan, J. S. Read, L. Rezzolla, and B. Zink, "Gravitational waves from neutron stars: promises and challenges," *General Relativity and Gravitation*, vol. 43, pp. 409–436, Aug. 2010.

[8] R. P. Mignani, S. Zane, D. Walton, T. Kennedy, B. Winter, P. Smith, R. H. Cole, D. Kataria, and A. Smith, "LOFT: Large Observatory For X-Ray Timing," *Proceedings of the International Astronomical Union*, vol. 7, pp. 372–375, Sept. 2011.

[9] D. Page, J. M. Lattimer, M. Prakash, and A. W. Steiner, "Stellar Superfluids," in *Novel Superfluids* (K. H. Bennemann and J. B. Ketterson, eds.), vol. 2, ch. 21, pp. 505–579, Oxford: Oxford University Press, Nov. 2014.

[10] K. Glampedakis and N. Andersson, "Hydrodynamical Trigger Mechanism for Pulsar Glitches," *Physical Review Letters*, vol. 102, p. 141101, Apr. 2009.

[11] S. Chandrasekhar, "The highly collapsed configurations of a stellar mass," *Monthly Notices of the Royal Astronomical Society*, vol. 91, pp. 456–466, Mar. 1931.

[12] H.-T. Janka, "Explosion Mechanisms of Core-Collapse Supernovae," *Annual Review of Nuclear and Particle Science*, vol. 62, pp. 407–451, Nov. 2012.

[13] S. A. Colgate and R. H. White, "The Hydrodynamic Behavior of Supernovae Explosions," *The Astrophysical Journal*, vol. 143, pp. 626–681, Mar. 1966.

[14] D. H. Staelin and E. C. I. Reifenstein, "Pulsating Radio Sources near the Crab Nebula," *Science (New York, N.Y.)*, vol. 162, pp. 1481–1483, Dec. 1968.

[15] H. Tananbaum, "Cassiopeia A," *IAU Circulations*, vol. 7246, p. 1, Sept. 1999.

[16] R. C. Tolman, "Static Solutions of Einstein's Field Equations for Spheres of Fluid," *Physical Review*, vol. 55, pp. 364–373, Feb. 1939.

[17] J. R. Oppenheimer and G. M. Volkoff, "On Massive Neutron Cores," *Physical Review*, vol. 55, pp. 374–381, Feb. 1939.

[18] T. M. Tauris and E. van den Heuvel, "Formation and Evolution of Compact Stellar X-ray Sources," *arXiv preprint*, pp. 1–46, Mar. 2003.

[19] N. Ivanova, S. Justham, J. L. Avendano Nandez, and J. C. Lombardi, "Identification of the long-sought common-envelope events.," *Science (New York, N.Y.)*, vol. 339, pp. 433–435, Jan. 2013.

[20] R. A. Hulse, "The discovery of the binary pulsar," *Reviews of Modern Physics*, vol. 66, pp. 699–710, July 1994.

[21] J. H. J. Taylor, "Binary pulsars and relativistic gravity," *Reviews of Modern Physics*, vol. 66, pp. 711–719, July 1994.

[22] S. A. Hughes, "Gravitational Waves from Merging Compact Binaries," *Annual Review of Astronomy and Astrophysics*, vol. 47, pp. 107–157, Sept. 2009.

[23] J. M. Lattimer and M. Prakash, "The physics of neutron stars.," *Science (New York, N.Y.)*, vol. 304, pp. 536–542, Apr. 2004.

[24] W. C. G. Ho, K. Glampedakis, and N. Andersson, "Magnetars: super(ficially) hot and super(fluid) cool," *Monthly Notices of the Royal Astronomical Society*, vol. 422, pp. 2632–2641, May 2012.

[25] A. Einstein, "Zur allgemeinen Relativitätstheorie.," *Sitzungsberichte der Königlich Preußischen Akademie der Wissenschaften (Berlin)*, pp. 778–786, Nov. 1915.

[26] J. M. Lattimer and M. Prakash, "Neutron star observations: Prognosis for equation of state constraints," *Physics Reports*, vol. 442, pp. 109–165, Apr. 2007.

[27] J. W. T. Hessels, S. M. Ransom, I. H. Stairs, P. C. C. Freire, V. M. Kaspi, and F. Camilo, "A Radio Pulsar Spinning at 716 Hz," *Science (New York, N.Y.)*, vol. 311, pp. 1901–1904, Mar. 2006.

[28] H. A. Bethe and G. E. Brown, "Evolution of Binary Compact Objects That Merge," *The Astrophysical Journal*, vol. 506, pp. 780–789, Oct. 1998.

[29] J. Antoniadis, P. C. C. Freire, N. Wex, T. M. Tauris, R. S. Lynch, M. H. van Kerkwijk, M. Kramer, C. Bassa, V. S. Dhillon, *et al.*, "A Massive Pulsar in a Compact Relativistic Binary," *Science*, vol. 340, p. 1233232, Apr. 2013.

[30] N. Chamel and P. Haensel, "Physics of Neutron Star Crusts," *Living Reviews in Relativity*, vol. 11, pp. 1–182, Dec. 2008.

[31] A. Y. Potekhin, "Electron conduction in magnetized neutron star envelopes," *Astronomy & Astrophysics*, vol. 351, pp. 787–797, Aug. 1999.

[32] A. Y. Potekhin, G. Chabrier, and D. G. Yakovlev, "Heat blanketing envelopes and thermal radiation of strongly magnetized neutron stars," *Astrophysics and Space Science*, vol. 308, pp. 353–361, Mar. 2007.

[33] J. S. Heyl, "r-Modes on Rapidly Rotating, Relativistic Stars. I. Do Type I Bursts Excite Modes in the Neutron Star Ocean?," *The Astrophysical Journal*, vol. 600, pp. 939–945, Jan. 2004.

[34] E. Wigner and F. Seitz, "On the Constitution of Metallic Sodium," *Physical Review*, vol. 43, pp. 804–810, May 1933.

[35] F. Douchin and P. Haensel, "A unified equation of state of dense matter and neutron star structure," *Astronomy and Astrophysics*, vol. 380, pp. 151–167, Dec. 2001.

[36] J. W. Negele and D. Vautherin, "Neutron star matter at sub-nuclear densities," *Nuclear Physics A*, vol. 207, pp. 298–320, June 1973.

[37] N. Chamel, "Band structure effects for dripped neutrons in neutron star crust," *Nuclear Physics A*, vol. 747, pp. 109–128, Jan. 2005.

[38] N. Chamel, "Crustal Entrainment and Pulsar Glitches," *Physical Review Letters*, vol. 110, p. 011101, Jan. 2013.

[39] N. Andersson, K. Glampedakis, W. C. G. Ho, and C. M. Espinoza, "Pulsar Glitches: The Crust is not Enough," *Physical Review Letters*, vol. 109, p. 241103, Dec. 2012.

[40] J. A. Sauls, "Superfluidity in the Interiors of Neutron Stars," in *Timing Neutron Stars* (H. Ögelman and E. P. J. van den Heuvel, eds.), vol. 262, pp. 457–490, Dordrecht: Kluwer, 1989.

[41] D. G. Ravenhall, C. J. Pethick, and J. R. Wilson, "Structure of Matter below Nuclear Saturation Density," *Physical Review Letters*, vol. 50, pp. 2066–2069, June 1983.

[42] C. J. Horowitz, D. K. Berry, C. M. Briggs, M. E. Caplan, A. Cumming, and A. S. Schneider, "Disordered Nuclear Pasta, Magnetic Field Decay, and Crust Cooling in Neutron Stars," *Physical Review Letters*, vol. 114, p. 031102, Jan. 2015.

[43] C. J. Pethick and A. Y. Potekhin, "Liquid crystals in the mantles of neutron stars," *Physics Letters B*, vol. 427, pp. 7–12, May 1998.

[44] J. A. Pons, D. Viganò, and N. Rea, "A highly resistive layer within the crust of X-ray pulsars limits their spin periods," *Nature Physics*, vol. 9, pp. 431–434, July 2013.

[45] G. Baym, C. J. Pethick, and D. Pines, "Superfluidity in Neutron Stars," *Nature*, vol. 224, pp. 673–674, Nov. 1969.

[46] F. Weber, R. Negreiros, P. Rosenfield, and M. Stejner, "Pulsars as astrophysical laboratories for nuclear and particle physics," *Progress in Particle and Nuclear Physics*, vol. 59, pp. 94–113, July 2007.

[47] M. G. Alford, A. Schmitt, K. Rajagopal, and T. Schäfer, "Color superconductivity in dense quark matter," *Reviews of Modern Physics*, vol. 80, pp. 1455–1515, Nov. 2008.

[48] M. G. Alford, K. Rajagopal, T. Schäfer, and A. Schmitt, "Color superconductivity in dense quark matter," in *Novel Superfluids* (K.-H. Bennemann and J. B. Ketterson, eds.), vol. 1, ch. 10, pp. 489–569, Oxford: Oxford University Press, Feb. 2013.

[49] R. N. Manchester, G. Hobbs, A. Teoh, and M. Hobbs, "The Australia Telescope National Facility Pulsar Catalogue," *The Astronomical Journal*, vol. 129, pp. 1993–2006, Apr. 2005.

[50] A. L. Watts, "Thermonuclear Burst Oscillations," *Annual Review of Astronomy and Astrophysics*, vol. 50, pp. 609–640, Sept. 2012.

[51] G. Hobbs, W. Coles, R. N. Manchester, M. J. Keith, R. M. Shannon, D. Chen, M. Bailes, N. D. R. Bhat, S. Burke-Spolaor, D. Champion, A. Chaudhary, *et al.*, "Development of a pulsar-based time-scale," *Monthly Notices of the Royal Astronomical Society*, vol. 427, pp. 2780–2787, Dec. 2012.

[52] G. Hobbs, A. G. Lyne, and M. Kramer, "An analysis of the timing irregularities for 366 pulsars," *Monthly Notices of the Royal Astronomical Society*, vol. 402, pp. 1027–1048, Feb. 2010.

[53] J. M. Cordes and G. Greenstein, "Pulsar timing. IV - Physical models for timing noise processes," *The Astrophysical Journal*, vol. 245, pp. 1060–1079, May 1981.

[54] M. Cantiello, J. Fuller, and L. Bildsten, "Asteroseismic signatures of evolving internal stellar magnetic fields," *arXiv preprint*, pp. 1–20, Feb. 2016.

[55] P. Goldreich and W. H. Julian, "Pulsar Electrodynamics," *The Astrophysical Journal*, vol. 157, pp. 869–880, Aug. 1969.

[56] D. B. Melrose, "The models for radio emission from pulsars - The outstanding issues," *Journal of Astrophysics and Astronomy*, vol. 16, pp. 137–164, June 1995.

[57] G. Vasisht and E. V. Gotthelf, "The Discovery of an Anomalous X-Ray Pulsar in the Supernova Remnant Kes 73," *The Astrophysical Journal*, vol. 486, pp. L129–L132, Sept. 1997.

[58] A. G. Lyne, R. S. Pritchard, and F. Graham Smith, "23 years of Crab pulsar rotational history," *Monthly Notices of the Royal Astronomical Society*, vol. 265, pp. 1003–1012, Dec. 1993.

[59] C. M. Espinoza, "The spin evolution of young pulsars," *Proceedings of the International Astronomical Union*, vol. 8, pp. 195–198, Mar. 2013.

[60] R. F. Archibald, E. V. Gotthelf, R. D. Ferdman, V. M. Kaspi, S. Guillot, F. A. Harrison, E. F. Keane, M. J. Pivovaroff, D. Stern, S. P. Tendulkar, and J. A. Tomsick, "A high braking index for a pulsar," *The Astrophysical Journal Letters*, vol. 819, p. L16, Mar. 2016.

[61] W. C. G. Ho and N. Andersson, "Rotational evolution of young pulsars due to superfluid decoupling," *Nature Physics*, vol. 8, pp. 787–789, Sept. 2012.

[62] C. M. Espinoza, A. G. Lyne, M. Kramer, R. N. Manchester, and V. M. Kaspi, "The Braking Index of PSR J1734-3333 and the Magnetar Population," *The Astrophysical Journal Letters*, vol. 741, p. L13, Nov. 2011.

[63] W. C. G. Ho, "Magnetic field growth in young glitching pulsars with a braking index," *Monthly Notices of the Royal Astronomical Society*, vol. 452, pp. 845–851, Sept. 2015.

[64] C. F. Gauss, "Beobachtungen der magnetischen Variation am 1. April 1835, von fuenf Oertern," *Annalen der Physik und Chemie*, vol. 111, pp. 480–481, 1835.

[65] O. Portugall, P. Y. Solane, P. Plochocka, D. K. Maude, and R. J. Nicholas, "Beyond 100 Tesla: Scientific experiments using single-turn coils," *Comptes Rendus Physique*, vol. 14, pp. 115–120, Jan. 2013.

[66] G. F. Bignami, P. A. Caraveo, A. De Luca, and S. Mereghetti, "The magnetic field of an isolated neutron star from X-ray cyclotron absorption lines.," *Nature*, vol. 423, pp. 725–727, June 2003.

[67] A. K. Harding, "The neutron star zoo," *Frontiers of Physics*, vol. 8, pp. 679–692, Feb. 2013.

[68] D. Viganò, N. Rea, J. A. Pons, R. Perna, D. N. Aguilera, and J. A. Miralles, "Unifying the observational diversity of isolated neutron stars via magneto-thermal evolution models," *Monthly Notices of the Royal Astronomical Society*, vol. 434, pp. 123–141, July 2013.

[69] A. A. Abdo, M. Ajello, A. Allafort, L. Baldini, J. Ballet, G. Barbiellini, M. G. Baring, D. Bastieri, A. Belfiore, R. Bellazzini, B. Bhattacharyya, E. Bissaldi, *et al.*, "The Second Fermi Large Area Telescope Catalog of Gamma-Ray Pulsars," *The Astrophysical Journal Supplement Series*, vol. 208, p. 17, Oct. 2013.

[70] D. G. Yakovlev, O. Y. Gnedin, A. D. Kaminker, A. Y. Potekhin, C. Bassa, Z. Wang, A. Cumming, and V. M. Kaspi, "Theory of cooling neutron stars versus observations," *AIP Conference Proceedings*, vol. 983, pp. 379–387, Feb. 2008.

[71] R. C. Duncan and C. Thompson, "Formation of very strongly magnetized neutron stars - Implications for gamma-ray bursts," *The Astrophysical Journal*, vol. 392, pp. L9–L13, June 1992.

[72] A. I. Ibrahim, C. B. Markwardt, J. H. Swank, S. M. Ransom, M. Roberts, V. M. Kaspi, P. M. Woods, S. Safi-Harb, S. Balman, W. C. Parke, C. Kouveliotou, K. Hurley, and T. Cline, "Discovery of a Transient Magnetar: XTE J1810-197," *The Astrophysical Journal*, vol. 609, pp. L21–L24, July 2004.

[73] D. Bhattacharya and E. P. J. van den Heuvel, "Formation and evolution of binary and millisecond radio pulsars," *Physics Reports*, vol. 203, pp. 1–124, May 1991.

[74] D. Viganò and D. F. Torres, "Modelling of the gamma-ray pulsed spectra of Geminga, Crab, and Vela with synchro-curvature radiation," *Monthly Notices of the Royal Astronomical Society*, vol. 449, pp. 3755–3765, Apr. 2015.

[75] V. Radhakrishnan and R. N. Manchester, "Detection of a Change of State in the Pulsar PSR 0833-45," *Nature*, vol. 222, pp. 228–229, Apr. 1969.

[76] P. E. Reichly and G. S. Downs, "Observed Decrease in the Periods of Pulsar PSR 0833-45," *Nature*, vol. 222, pp. 229–230, Apr. 1969.

[77] P. E. Boynton, I. Groth, E. J., R. B. Partridge, and D. T. Wilkinson, "Precision Measurement of the Frequency Decay of the Crab Nebula Pulsar, NP 0532," *The Astrophysical Journal*, vol. 157, pp. L197–L201, Sept. 1969.

[78] D. W. Richards, G. H. Pettengill, I. Counselman, C. C., and J. M. Rankin, "Quasi-Sinusoidal Oscillation in Arrival Times of Pulses from NP 0532," *The Astrophysical Journal*, vol. 160, pp. L1–L6, Apr. 1970.

[79] C. M. Espinoza, A. G. Lyne, B. W. Stappers, and M. Kramer, "A study of 315 glitches in the rotation of 102 pulsars," *Monthly Notices of the Royal Astronomical Society*, vol. 414, pp. 1679–1704, June 2011.

[80] R. G. Dodson, D. R. Lewis, and P. M. McCulloch, "Two decades of pulsar timing of Vela," *Astrophysics and Space Science*, vol. 308, pp. 585–589, Apr. 2007.

[81] S. L. Shemar and A. G. Lyne, "Observations of pulsar glitches," *Monthly Notices of the Royal Astronomical Society*, vol. 282, pp. 677–690, Sept. 1996.

[82] R. G. Dodson, P. M. McCulloch, and D. R. Lewis, "High Time Resolution Observations of the January 2000 Glitch in the Vela Pulsar," *The Astrophysical Journal*, vol. 564, pp. L85–L88, Jan. 2002.

[83] R. F. Archibald, V. M. Kaspi, C. Y. Ng, K. N. Gourgouliatos, D. Tsang, P. Scholz, A. P. Beardmore, N. Gehrels, and J. A. Kennea, "An anti-glitch in a magnetar.," *Nature*, vol. 497, pp. 591–593, May 2013.

[84] B. Haskell and A. Melatos, "Models of pulsar glitches," *International Journal of Modern Physics D*, vol. 24, p. 1530008, Jan. 2015.

[85] M. Ruderman, "Neutron Starquakes and Pulsar Periods," *Nature*, vol. 223, pp. 597–598, Aug. 1969.

[86] G. Baym and D. Pines, "Neutron starquakes and pulsar speedup," *Annals of Physics*, vol. 66, pp. 816–835, Aug. 1971.

[87] B. Link, R. I. Epstein, and J. M. Lattimer, "Pulsar Constraints on Neutron Star Structure and Equation of State," *Physical Review Letters*, vol. 83, pp. 3362–3365, Oct. 1999.

[88] P. W. Anderson and N. Itoh, "Pulsar glitches and restlessness as a hard superfluidity phenomenon," *Nature*, vol. 256, pp. 25–27, July 1975.

[89] M. A. Alpar, D. Pines, P. W. Anderson, and J. Shaham, "Vortex creep and the internal temperature of neutron stars. I - General theory," *The Astrophysical Journal*, vol. 276, pp. 325–334, Jan. 1984.

[90] M. A. Alpar, P. W. Anderson, D. Pines, and J. Shaham, "Vortex creep and the internal temperature of neutron stars. II - VELA pulsar," *The Astrophysical Journal*, vol. 278, pp. 791–805, Mar. 1984.

[91] P. M. Pizzochero, "Angular Momentum Transfer in Vela-like Pulsar Glitches," *The Astrophysical Journal Letters*, vol. 743, p. L20, Dec. 2011.

[92] B. Haskell, P. M. Pizzochero, and T. Sidery, "Modelling pulsar glitches with realistic pinning forces: a hydrodynamical approach," *Monthly Notices of the Royal Astronomical Society*, vol. 420, pp. 658–671, Feb. 2012.

[93] C. M. Espinoza, D. Antonopoulou, B. W. Stappers, A. L. Watts, and A. G. Lyne, "Neutron star glitches have a substantial minimum size," *Monthly Notices of the Royal Astronomical Society*, vol. 440, pp. 2755–2762, Apr. 2014.

[94] T. Sidery, A. Passamonti, and N. Andersson, "The dynamics of pulsar glitches: contrasting phenomenology with numerical evolutions," *Monthly Notices of the Royal Astronomical Society*, vol. 405, pp. 1061–1074, Apr. 2010.

[95] L. Warszawski and A. Melatos, "Gross-Pitaevskii model of pulsar glitches," *Monthly Notices of the Royal Astronomical Society*, vol. 415, pp. 1611–1630, Aug. 2011.

[96] L. Warszawski and A. Melatos, "Knock-on processes in superfluid vortex avalanches and pulsar glitch statistics," *Monthly Notices of the Royal Astronomical Society*, vol. 428, pp. 1911–1926, Jan. 2013.

[97] C. D. Ott, E. P. O'Connor, S. Gossan, E. Abdikamalov, U. C. T. Gamma, and S. Drasco, "Core-Collapse Supernovae, Neutrinos, and Gravitational Waves," *Nuclear Physics B - Proceedings Supplements*, vol. 235-236, pp. 381–387, Feb. 2013.

[98] J. R. Smith, "The path to the enhanced and advanced LIGO gravitational-wave detectors," *Classical and Quantum Gravity*, vol. 26, p. 114013, June 2009.

[99] C. J. Moore, R. H. Cole, and C. P. L. Berry, "Gravitational-wave sensitivity curves," *Classical and Quantum Gravity*, vol. 32, p. 015014, Jan. 2015.

[100] B. P. Abbott, R. Abbott, T. D. Abbott, M. R. Abernathy, F. Acernese, K. Ackley, C. Adams, T. Adams, P. Addesso, R. X. Adhikari, V. B. Adya, C. Affeldt, *et al.*, "Observation of Gravitational Waves from a Binary Black Hole Merger," *Physical Review Letters*, vol. 116, p. 061102, Feb. 2016.

[101] R. A. Hulse and J. H. J. Taylor, "Discovery of a pulsar in a binary system," *The Astrophysical Journal*, vol. 195, pp. L51–L53, Jan. 1975.

[102] A. Einstein, "Näherungsweise Integration der Feldgleichungen der Gravitation.," *Sitzungsberichte der Königlich Preußischen Akademie der Wissenschaften (Berlin)*, pp. 688–696, June 1916.

[103] P. D. Lasky, "Gravitational Waves from Neutron Stars: A Review," *Publications of the Astronomical Society of Australia*, vol. 32, p. e034, Sept. 2015.

[104] A. Melatos and D. J. B. Payne, "Gravitational Radiation from an Accreting Millisecond Pulsar with a Magnetically Confined Mountain," *The Astrophysical Journal*, vol. 623, pp. 1044–1050, Apr. 2005.

[105] B. Owen, "Maximum Elastic Deformations of Compact Stars with Exotic Equations of State," *Physical Review Letters*, vol. 95, p. 211101, Nov. 2005.

[106] K. Wette, M. Vigelius, and A. Melatos, "Sinking of a magnetically confined mountain on an accreting neutron star," *Monthly Notices of the Royal Astronomical Society*, vol. 402, pp. 1099–1110, Feb. 2010.

[107] N. Andersson and K. D. Kokkotas, "The r-mode instability in rotating neutron stars," *International Journal of Modern Physics D*, vol. 10, pp. 381–441, Aug. 2001.

[108] E. Gaertig and K. D. Kokkotas, "Gravitational wave asteroseismology with fast rotating neutron stars," *Physical Review D*, vol. 83, p. 064031, Mar. 2011.

[109] S. Chandrasekhar, "Solutions of Two Problems in the Theory of Gravitational Radiation," *Physical Review Letters*, vol. 24, pp. 611–615, Mar. 1970.

[110] J. L. Friedman and B. F. Schutz, "Secular instability of rotating Newtonian stars," *The Astrophysical Journal*, vol. 222, pp. 281–296, May 1978.

[111] B. Owen, L. Lindblom, C. Cutler, B. F. Schutz, A. Vecchio, and N. Andersson, "Gravitational waves from hot young rapidly rotating neutron stars," *Physical Review D*, vol. 58, p. 084020, Sept. 1998.

[112] N. Andersson, "Gravitational waves from instabilities in relativistic stars," *Classical and Quantum Gravity*, vol. 20, pp. R105–R144, Apr. 2003.

[113] D. R. Tilley and J. Tilley, *Superfluidity and Superconductivity*. Bristol: IoP Publishing, 3rd ed., 1990.

[114] M. Tinkham, *Introduction to Superconductivity*. New York: Dover Press, 2nd ed., 2004.

[115] R. J. Donnelly, *Quantized vortices in helium II*. Cambridge: Cambridge University Press, 1st ed., 1991.

[116] H. K. Onnes, "The resistance of pure mercury at helium temperatures," *Communications from the Physical Laboratory at the University of Leiden*, vol. 120, Apr. 1911.

[117] W. Meissner and R. Ochsenfeld, "Ein neuer Effekt bei Eintritt der Supraleitfaehigkeit," *Die Naturwissenschaften*, vol. 21, pp. 787–788, Nov. 1933.

[118] F. London and H. London, "The Electromagnetic Equations of the Supraconductor," *Proceedings of the Royal Society A*, vol. 149, pp. 71–88, Mar. 1935.

[119] F. London, "On the Problem of the Molecular Theory of Superconductivity," *Physical Review*, vol. 74, pp. 562–573, Sept. 1948.

[120] J. Bardeen, L. N. Cooper, and J. R. Schrieffer, "Theory of Superconductivity," *Physical Review*, vol. 108, pp. 1175–1204, Dec. 1957.

[121] V. L. Ginzburg and L. D. Landau, "On the Theory of Superconductivity," *Zh. Eksp. Teor. Fiz.*, vol. 20, pp. 1064–1082, 1950.

[122] L. P. Gor'kov, "Microscopic Derivation Of The GInzburg-Landau Equations In The Theory Of Superconductivity," *Soviet Physics JETP*, vol. 9, pp. 1364–1368, Dec. 1959.

[123] A. A. Abrikosov, "The magnetic properties of superconducting alloys," *Journal of Physics and Chemistry of Solids*, vol. 2, pp. 199–208, Jan. 1957.

[124] B. D. Josephson, "Possible new effects in superconductive tunnelling," *Physics Letters*, vol. 1, pp. 251–253, July 1962.

[125] J. G. Bednorz and K. A. Mueller, "Possible high Tc superconductivity in the Ba-La-Cu-O system," *Zeitschrift für Physik B Condensed Matter*, vol. 64, pp. 189–193, June 1986.

[126] G. T. Horowitz, "Introduction to holographic superconductors," in *Lecture Notes in Physics: From Gravity to Thermal Gauge Theories: The AdS/CFT Correspondence,* (E. Papantonopoulos, ed.), vol. 828, pp. 313–347, Berlin, Heidelberg: Springer Berlin Heidelberg, Feb. 2011.

[127] P. Kapitza, "Viscosity of Liquid Helium below the Lambda Point," *Nature*, vol. 141, p. 74, Jan. 1938.

[128] J. F. Allen and A. D. Misener, "Flow of Liquid Helium II," *Nature*, vol. 141, p. 75, Jan. 1938.

[129] L. P. Pitaevskii, "On the superfluidity of liquid He-3," *Soviet Physics JETP*, vol. 10, pp. 1267–1275, June 1960.

[130] D. D. Osheroff, R. C. Richardson, and D. M. Lee, "Evidence for a New Phase of Solid He-3," *Physical Review Letters*, vol. 28, pp. 885–888, Apr. 1972.

[131] D. D. Osheroff, W. J. Gully, R. C. Richardson, and D. M. Lee, "New Magnetic Phenomena in Liquid He-3 below 3mK," *Physical Review Letters*, vol. 29, pp. 920–923, Oct. 1972.

[132] L. Tisza, "Transport Phenomena in Helium II," *Nature*, vol. 141, p. 913, May 1938.

[133] J. D. Reppy and D. Depatie, "Persistent Currents in Superfluid Helium," *Physical Review Letters*, vol. 12, pp. 187–189, Feb. 1964.

[134] A. D. B. Woods and A. C. H. Hallett, "The Viscosity of Liquid Helium II Between 0.79K and the Lambda Point," *Canadian Journal of Physics*, vol. 41, pp. 596–609, Apr. 1963.

[135] J. F. Allen and H. Jones, "New Phenomena Connected with Heat Flow in Helium II," *Nature*, vol. 141, pp. 243–244, Feb. 1938.

[136] B. N. Esel'son, M. I. Kaganov, E. Y. Rudavskii, and I. A. Serbin, ""Sound" in superfluid liquids," *Soviet Physics Uspekhi*, vol. 17, pp. 215–238, Feb. 1974.

[137] I. M. Khalatnikov, *An Introduction to the Theory of Superfluidity (Advanced Book Classics)*. Reading, MA: Perseus, revised ed., 2000.

[138] L. D. Landau, "Theory of the Superfluidity of Helium II," *Physical Review*, vol. 60, pp. 356–358, Aug. 1941.

[139] E. L. Andronikashvili *Zh. Eksp. Teor. Fiz.*, vol. 16, p. 780, 1946.

[140] L. Onsager, "Statistical hydrodynamics," *Il Nuovo Cimento*, vol. 6, pp. 279–287, Mar. 1949.

[141] R. P. Feynman, *Application of Quantum Mechanics to Liquid Helium. Progress in Low Temperature Physics*, vol. 1. Amsterdam: North-Holland, 1955.

[142] H. E. Hall and W. F. Vinen, "The Rotation of Liquid Helium II. II. The Theory of Mutual Friction in Uniformly Rotating Helium II," *Proceedings of the Royal Society A*, vol. 238, pp. 215–234, Dec. 1956.

[143] F. London, "The Lambda-Phenomenon of Liquid Helium and the Bose-Einstein Degeneracy," *Nature*, vol. 141, pp. 643–644, Apr. 1938.

[144] W. Ketterle, "Nobel lecture: When atoms behave as waves: Bose-Einstein condensation and the atom laser," *Reviews of Modern Physics*, vol. 74, pp. 1131–1151, Oct. 2002.

[145] E. P. Gross, "Structure of a quantized vortex in boson systems," *Il Nuovo Cimento*, vol. 20, pp. 454–477, May 1961.

[146] L. P. Pitaevskii, "Vortex Lines in an Imperfect Bose Gas," *Soviet Physics JETP*, vol. 13, pp. 451–454, Aug. 1961.

[147] M. H. Anderson, J. R. Ensher, M. R. Matthews, C. E. Wieman, and E. A. Cornell, "Observation of Bose-Einstein condensation in a dilute atomic vapor," *Science*, vol. 269, pp. 198–201, July 1995.

[148] K. Davis, M.-O. Mewes, M. R. Andrews, N. J. van Druten, D. S. Durfee, D. M. Kurn, and W. Ketterle, "Bose-Einstein Condensation in a Gas of Sodium Atoms," *Physical Review Letters*, vol. 75, pp. 3969–3973, Nov. 1995.

[149] M. R. Matthews, B. P. Anderson, P. C. Haljan, D. S. Hall, C. E. Wieman, and E. A. Cornell, "Vortices in a Bose-Einstein Condensate," *Physical Review Letters*, vol. 83, pp. 2498–2501, Sept. 1999.

[150] K. Madison, F. Chevy, W. Wohlleben, and J. Dalibard, "Vortex Formation in a Stirred Bose-Einstein Condensate," *Physical Review Letters*, vol. 84, pp. 806–809, Jan. 2000.

[151] M. W. Zwierlein, J. R. Abo-Shaeer, A. Schirotzek, C. H. Schunck, and W. Ketterle, "Vortices and superfluidity in a strongly interacting Fermi gas," *Nature*, vol. 435, pp. 1047–1051, June 2005.

[152] E. Madelung, "Quantentheorie in hydrodynamischer Form," *Zeitschrift für Physik*, vol. 40, pp. 322–326, Mar. 1927.

[153] B. Carter and D. Langlois, "Equation of state for cool relativistic two-constituent superfluid dynamics," *Physical Review D*, vol. 51, pp. 5855–5864, May 1995.

[154] R. Prix, "Variational description of multifluid hydrodynamics: Uncharged fluids," *Physical Review D*, vol. 69, p. 043001, Feb. 2004.

[155] N. Andersson and G. L. Comer, "A flux-conservative formalism for convective and dissipative multi-fluid systems, with application to Newtonian superfluid neutron stars," *Classical and Quantum Gravity*, vol. 23, pp. 5505–5529, Sept. 2006.

[156] C. J. Pethick and H. Smith, *Bose-Einstein Condensation in Dilute Gases*. Cambridge: Cambridge University Press, 2nd ed., 2008.

[157] H. Kojima, W. Veith, S. Putterman, E. Guyon, and I. Rudnick, "Vortex-Free Landau State in Rotating Superfluid Helium," *Physical Review Letters*, vol. 27, pp. 714–718, Sept. 1971.

[158] D. V. Osborne, "The Rotation of Liquid Helium II," *Proceedings of the Physical Society. Section A*, vol. 63, pp. 909–912, Aug. 1950.

[159] I. L. Bekarevich and I. M. Khalatnikov, "Phenomenological Derivation of the Equations of Vortex Motion in He II," *Soviet Physics JETP*, vol. 13, pp. 643–646, Sept. 1961.

[160] V. Eltsov, R. de Graaf, R. Hänninen, M. Krusius, R. Solntsev, V. L'vov, A. Golov, and P. Walmsley, "Turbulent Dynamics in Rotating Helium Superfluids," in *Progress in Low Temperature Physics: Quantum Turbulence* (M. Tsubota and W. P. Halperin, eds.), vol. 16, ch. 2, pp. 45–146, Elsevier, Mar. 2009.

[161] C. F. Barenghi and C. A. Jones, "The stability of the Couette flow of helium II," *Journal of Fluid Mechanics*, vol. 197, pp. 551–569, Dec. 1988.

[162] K. W. Schwarz, "Three-dimensional vortex dynamics in superfluid 4He: Homogeneous superfluid turbulence," *Physical Review B*, vol. 38, pp. 2398–2417, Aug. 1988.

[163] R. Hänninen and A. W. Baggaley, "Vortex filament method as a tool for computational visualization of quantum turbulence," *Proceedings of the National Academy of Sciences*, vol. 111, pp. 4667–4674, Mar. 2014.

[164] W. F. Vinen, "Mutual Friction in a Heat Current in Liquid Helium II. I. Experiments on Steady Heat Currents," *Proceedings of the Royal Society A: Mathematical, Physical and Engineering Sciences*, vol. 240, pp. 114–127, Apr. 1957.

[165] W. F. Vinen, "Mutual Friction in a Heat Current in Liquid Helium II. II. Experiments on Transient Effects," *Proceedings of the Royal Society A: Mathematical, Physical and Engineering Sciences*, vol. 240, pp. 128–143, Apr. 1957.

[166] W. F. Vinen, "Mutual Friction in a Heat Current in Liquid Helium II. III. Theory of the Mutual Friction," *Proceedings of the Royal Society A: Mathematical, Physical and Engineering Sciences*, vol. 242, pp. 493–515, Nov. 1957.

[167] W. F. Vinen, "Mutual Friction in a Heat Current in Liquid Helium II. IV. Critical Heat Currents in Wide Channels," *Proceedings of the Royal Society A: Mathematical, Physical and Engineering Sciences*, vol. 243, pp. 400–413, Jan. 1958.

[168] A. N. Kolmogorov, "The local structure of turbulence in incompressible viscous fluid for very large Reynolds numberst," *Doklady Akademiia Nauk SSSR*, vol. 30, pp. 301–305, 1941.

[169] C. F. Barenghi, L. Skrbek, and K. R. Sreenivasan, "Introduction to quantum turbulence," *Proceedings of the National Academy of Sciences*, vol. 111, pp. 4647–4652, Mar. 2014.

[170] C. J. Gorter and J. H. Mellink, "On the irreversible processes in liquid helium II," *Physica*, vol. 15, pp. 285–304, May 1949.

[171] N. Andersson, T. Sidery, and G. L. Comer, "Superfluid neutron star turbulence," *Monthly Notices of the Royal Astronomical Society*, vol. 381, pp. 747–756, Oct. 2007.

[172] J. M. Karimäki, R. Hänninen, and E. V. Thuneberg, "Asymptotic motion of a single vortex in a rotating cylinder," *Physical Review B*, vol. 85, p. 224519, June 2012.

[173] C. E. Swanson, C. F. Barenghi, and R. J. Donnelly, "Rotation of a Tangle of Quantized Vortex Lines in He II," *Physical Review Letters*, vol. 50, pp. 190–193, Jan. 1983.

[174] W. I. Glaberson, W. W. Johnson, and R. M. Ostermeier, "Instability of a Vortex Array in He II," *Physical Review Letters*, vol. 33, pp. 1197–1200, Nov. 1974.

[175] S. W. Thomson (Lord Kelvin), "Vibrations of a columnar vortex," *Philosophical Magazine Series 5*, vol. 10, pp. 155–168, Sept. 1880.

[176] T. Sidery, N. Andersson, and G. L. Comer, "Waves and instabilities in dissipative rotating superfluid neutron stars," *Monthly Notices of the Royal Astronomical Society*, vol. 385, pp. 335–348, Feb. 2008.

[177] M. G. Alford and G. Good, "Flux tubes and the type-I/type-II transition in a superconductor coupled to a superfluid," *Physical Review B*, vol. 78, p. 024510, July 2008.

[178] M. Sinha and A. D. Sedrakian, "Magnetar superconductivity versus magnetism: Neutrino cooling processes," *Physical Review C*, vol. 91, p. 035805, Mar. 2015.

[179] N. Chamel and P. Haensel, "Entrainment parameters in a cold superfluid neutron star core," *Physical Review C*, vol. 73, p. 045802, Apr. 2006.

[180] L. D. Landau and E. M. Lifshitz, *Quantum Mechanics: Non-Relativistic Theory.*, vol. 3. Oxford: Butterworth-Heinemann, 3rd ed., 1977.

[181] K. Glampedakis, N. Andersson, and L. Samuelsson, "Magnetohydrodynamics of superfluid and superconducting neutron star cores," *Monthly Notices of the Royal Astronomical Society*, vol. 410, pp. 805–829, Jan. 2011.

[182] G. Mendell, "Superfluid hydrodynamics in rotating neutron stars. I - Nondissipative equations.," *The Astrophysical Journal*, vol. 380, pp. 515–529, Oct. 1991.

[183] N. Andersson, C. Krüger, G. L. Comer, and L. Samuelsson, "A minimal model for finite temperature superfluid dynamics," *Classical and Quantum Gravity*, vol. 30, p. 235025, Dec. 2013.

[184] A. B. Migdal, "Superfluidity and the moments of inertia of nuclei," *Nuclear Physics*, vol. 13, pp. 655–674, Nov. 1959.

[185] D. Page, M. Prakash, J. M. Lattimer, and A. W. Steiner, "Rapid Cooling of the Neutron Star in Cassiopeia A Triggered by Neutron Superfluidity in Dense Matter," *Physical Review Letters*, vol. 106, p. 081101, Feb. 2011.

[186] P. S. Shternin, D. G. Yakovlev, C. O. Heinke, W. C. G. Ho, and D. J. Patnaude, "Cooling neutron star in the Cassiopeia A supernova remnant: evidence for superfluidity in the core," *Monthly Notices of the Royal Astronomical Society: Letters*, vol. 412, pp. L108–L112, Mar. 2011.

[187] A. Gezerlis, C. J. Pethick, and A. Schwenk, "Pairing and superfluidity of nucleons in neutron stars," in *Novel Superfluids* (K. H. Bennemann and J. B. Ketterson, eds.), vol. 2, ch. 22, pp. 580–615, Oxford: Oxford University Press, Nov. 2014.

[188] M. Ruderman, T. Zhu, and K. Chen, "Neutron Star Magnetic Field Evolution, Crust Movement, and Glitches," *The Astrophysical Journal*, vol. 492, pp. 267–280, Jan. 1998.

[189] M. Jahan-Miri, "Flux Expulsion and Field Evolution in Neutron Stars," *The Astrophysical Journal*, vol. 532, pp. 514–529, Mar. 2000.

[190] A. F. Andreev and E. P. Bashkin, "Three-velocity hydrodynamics of superfluid solutions," *Soviet Physics JETP*, vol. 42, pp. 164–167, Sept. 1975.

[191] R. Prix, G. L. Comer, and N. Andersson, "Slowly rotating superfluid Newtonian neutron star model with entrainment," *Astronomy & Astrophysics*, vol. 381, pp. 178–196, Jan. 2002.

[192] N. Chamel, "Two-fluid models of superfluid neutron star cores," *Monthly Notices of the Royal Astronomical Society*, vol. 388, pp. 737–752, Aug. 2008.

[193] G. Baym, C. J. Pethick, and D. Pines, "Electrical Conductivity of Neutron Star Matter," *Nature*, vol. 224, pp. 674–675, Nov. 1969.

[194] A. D. Sedrakian, "Rapid rotational crust-core relaxation in magnetars," *Astronomy & Astrophysics*, vol. 587, p. L2, Mar. 2016.

[195] A. D. Sedrakian and D. M. Sedrakian, "Superfluid Core Rotation in Pulsars. I. Vortex Cluster Dynamics," *The Astrophysical Journal*, vol. 447, pp. 305–323, July 1995.

[196] G. Mendell and L. Lindblom, "The coupling of charged superfluid mixtures to the electromagnetic field," *Annals of Physics*, vol. 205, pp. 110–129, Jan. 1991.

[197] R. Prix, "Variational description of multifluid hydrodynamics: Coupling to gauge fields," *Physical Review D*, vol. 71, p. 083006, Apr. 2005.

[198] B. Carter, *Covariant theory of conductivity in ideal fluid or solid media in Relativistic Fluid Dynamics*, vol. 1385. Heidelberg: Springer, 1989.

[199] A. L. Fetter and P. C. Hohenberg, *Superconductivity*, vol. 2. New York: Dekker, 1969.

[200] N. Andersson, T. Sidery, and G. L. Comer, "Mutual friction in superfluid neutron stars," *Monthly Notices of the Royal Astronomical Society*, vol. 368, pp. 162–170, May 2006.

[201] T. Akgün and I. Wasserman, "Toroidal magnetic fields in type II superconducting neutron stars," *Monthly Notices of the Royal Astronomical Society*, vol. 383, pp. 1551–1580, Jan. 2008.

[202] S. K. Lander, "The contrasting magnetic fields of superconducting pulsars and magnetars," *Monthly Notices of the Royal Astronomical Society*, vol. 437, pp. 424–436, Jan. 2014.

[203] I. Easson and C. J. Pethick, "Stress tensor of cosmic and laboratory type-II superconductors," *Physical Review D*, vol. 16, pp. 275–280, July 1977.

[204] J. A. Sauls, D. L. Stein, and J. W. Serene, "Magnetic vortices in a rotating 3P2 neutron superfluid," *Physical Review D*, vol. 25, pp. 967–975, Feb. 1982.

[205] M. A. Alpar, S. A. Langer, and J. A. Sauls, "Rapid postglitch spin-up of the superfluid core in pulsars," *The Astrophysical Journal*, vol. 282, pp. 533–541, July 1984.

[206] B. Link, "Constraining Hadronic Superfluidity with Neutron Star Precession," *Physical Review Letters*, vol. 91, p. 101101, Sept. 2003.

[207] B. Carter, R. Prix, and D. Langlois, "Energy of magnetic vortices in a rotating superconductor," *Physical Review B*, vol. 62, pp. 9740–9747, Oct. 2000.

[208] P. M. Walmsley, V. B. Eltsov, P. J. Heikkinen, J. J. Hosio, R. Hänninen, and M. Krusius, "Turbulent vortex flow responses at the AB interface in rotating superfluid 3He-B," *Physical Review B*, vol. 84, p. 184532, Nov. 2011.

[209] R. Blaauwgeers, V. B. Eltsov, G. Eska, A. P. Finne, R. P. Haley, M. Krusius, J. J. Ruohio, L. Skrbek, and G. E. Volovik, "Shear Flow and Kelvin-Helmholtz Instability in Superfluids," *Physical Review Letters*, vol. 89, p. 155301, Sept. 2002.

[210] A. W. Steiner, M. Prakash, J. M. Lattimer, and P. J. Ellis, "Isospin asymmetry in nuclei and neutron stars," *Physics reports*, vol. 411, pp. 325–375, June 2005.

[211] A. Akmal, V. R. Pandharipande, and D. G. Ravenhall, "Equation of state of nucleon matter and neutron star structure," *Physical Review C*, vol. 58, pp. 1804–1828, Sept. 1998.

[212] N. Andersson, G. L. Comer, and K. Glampedakis, "How viscous is a superfluid neutron star core?," *Nuclear Physics A*, vol. 763, pp. 212–229, Dec. 2005.

[213] A. D. Kaminker, P. Haensel, and D. G. Yakovlev, "Nucleon superfluidity vs. observations of cooling neutron stars," *Astronomy and Astrophysics*, vol. 373, pp. L17–L20, July 2001.

[214] J. Wambach, T. Ainsworth, and D. Pines, "Quasiparticle interactions in neutron matter for applications in neutron stars," *Nuclear Physics A*, vol. 555, pp. 128–150, Apr. 1993.

[215] J. Chen, J. Clark, R. Davé, and V. Khodel, "Pairing gaps in nucleonic superfluids," *Nuclear Physics A*, vol. 555, pp. 59–89, Apr. 1993.

[216] O. Elgaroy, L. Engvik, M. Hjorth-Jensen, and E. Osnes, "Triplet pairing of neutrons in β-stable neutron star matter," *Nuclear Physics A*, vol. 607, pp. 425–441, Sept. 1996.

[217] P. J. Feibelman, "Relaxation of Electron Velocity in a Rotating Neutron Superfluid: Application to the Relaxation of a Pulsar's Slowdown Rate," *Physical Review D*, vol. 4, pp. 1589–1597, Sept. 1971.

[218] I. Easson, "Postglitch behavior of the plasma inside neutron stars," *The Astrophysical Journal*, vol. 228, pp. 257–267, Feb. 1979.

[219] P. Donati and P. M. Pizzochero, "Realistic energies for vortex pinning in intermediate-density neutron star matter," *Physics Letters B*, vol. 640, pp. 74–81, Sept. 2006.

[220] S. Seveso, P. M. Pizzochero, F. Grill, and B. Haskell, "Mesoscopic pinning forces in neutron star crusts," *Monthly Notices of the Royal Astronomical Society*, vol. 455, pp. 3952–3967, Feb. 2016.

[221] P. Donati and P. M. Pizzochero, "Fully consistent semi-classical treatment of vortex-nucleus interaction in rotating neutron stars," *Nuclear Physics A*, vol. 742, pp. 363–379, Oct. 2004.

[222] P. B. Jones, "Rotation of the neutron-drip superfluid in pulsars: The resistive force," *Monthly Notices of the Royal Astronomical Society*, vol. 243, pp. 257–262, Mar. 1990.

[223] B. Link, "Dynamics of Quantum Vorticity in a Random Potential," *Physical Review Letters*, vol. 102, p. 131101, Apr. 2009.

[224] F. Grill and P. M. Pizzochero, "Vortex-lattice interaction in Pulsar Glitches," *Journal of Physics: Conference Series*, vol. 342, p. 012004, Feb. 2012.

[225] P. B. Jones, "Rotation of the neutron-drip superfluid in pulsars: The Kelvin phonon contribution to dissipation," *Monthly Notices of the Royal Astronomical Society*, vol. 257, pp. 501–506, Aug. 1992.

[226] D. Harding, R. A. Guyer, and G. Greenstein, "Superfluidity in neutron stars. III - Relaxation processes between the superfluid and the crust," *The Astrophysical Journal*, vol. 222, pp. 991–1005, June 1978.

[227] R. I. Epstein and G. Baym, "Vortex drag and the spin-up time scale for pulsar glitches," *The Astrophysical Journal*, vol. 387, pp. 276–287, Mar. 1992.

[228] R. I. Epstein and G. Baym, "Vortex pinning in neutron stars," *The Astrophysical Journal*, vol. 328, pp. 680–690, May 1988.

[229] R. I. Epstein and B. Link, "Starquake-Induced Glitches in Pulsars," in *Stellar Astrophysics: Proceedings of the Pacific Rim Conference held in Hong Kong, 1999* (K. S. Cheng, H. F. Chau, K. L. Chan, and K. C. Leung, eds.), pp. 95–104, Springer Netherlands, 2000.

[230] M. Abney, R. I. Epstein, and A. V. Olinto, "Observational Constraints on the Internal Structure and Dynamics of the Vela Pulsar," *The Astrophysical Journal*, vol. 466, pp. L91–L94, Aug. 1996.

[231] P. Goldreich and A. Reisenegger, "Magnetic field decay in isolated neutron stars," *The Astrophysical Journal*, vol. 395, pp. 250–258, Aug. 1992.

[232] J. A. Pons and U. Geppert, "Magnetic field dissipation in neutron star crusts: from magnetars to isolated neutron stars," *Astronomy & Astrophysics*, vol. 470, pp. 303–315, July 2007.

[233] K. N. Gourgouliatos and A. Cumming, "Hall effect in neutron star crusts: evolution, endpoint and dependence on initial conditions," *Monthly Notices of the Royal Astronomical Society*, vol. 438, pp. 1618–1629, Dec. 2014.

[234] T. Sidery and M. A. Alpar, "The effect of quantized magnetic flux lines on the dynamics of superfluid neutron star cores," *Monthly Notices of the Royal Astronomical Society*, vol. 400, pp. 1859–1867, Dec. 2009.

[235] A. P. Finne, V. B. Eltsov, R. Hänninen, N. B. Kopnin, J. Kopu, M. Krusius, M. Tsubota, and G. E. Volovik, "Dynamics of vortices and interfaces in superfluid 3He," *Reports on Progress in Physics*, vol. 69, pp. 3157–3230, Dec. 2006.

[236] A. G. Lyne, R. N. Manchester, and J. H. J. Taylor, "The galactic population of pulsars," *Monthly Notices of the Royal Astronomical Society*, vol. 213, pp. 613–639, Apr. 1985.

[237] R. Narayan and J. P. Ostriker, "Pulsar populations and their evolution," *The Astrophysical Journal*, vol. 352, pp. 222–246, Mar. 1990.

[238] C. Thompson and R. C. Duncan, "The soft gamma repeaters as very strongly magnetized neutron stars - I. Radiative mechanism for outbursts," *Monthly Notices of the Royal Astronomical Society*, vol. 275, pp. 255–300, July 1995.

[239] R. C. Duncan and C. Thompson, "Magnetars," in *High Velocity Neutron Stars and Gamma-Ray Bursts* (R. E. Rothschild and R. E. Lingenfelter, eds.), vol. 366, (New York), pp. 111–117, AIP Conference Proceedings, 1996.

[240] N. F. Mott, "The Scattering of Fast Electrons by Atomic Nuclei," *Proceedings of the Royal Society A*, vol. 124, pp. 425–442, June 1929.

[241] D. C. Kelly, "Electrical and Thermal Conductivities of a Relativistic Degenerate Plasma," *The Astrophysical Journal*, vol. 179, pp. 599–606, Jan. 1973.

[242] E. Harrison, "The hypothesis that magnetic fields buoyantly convect in neutron stars," *Monthly Notices of the Royal Astronomical Society*, vol. 248, pp. 419–423, Feb. 1991.

[243] J. Harvey, M. Ruderman, and J. Shaham, "Effects of neutron-star superconductivity on magnetic monopoles and core field decay," *Physical Review D*, vol. 33, pp. 2084–2091, Apr. 1986.

[244] P. B. Jones, "Neutron star magnetic field decay: flux expulsion from the superconducting interior," *Monthly Notices of the Royal Astronomical Society*, vol. 228, pp. 513–520, Oct. 1987.

[245] P. B. Jones, "Neutron superfluid spin-down and magnetic field decay in pulsars," *Monthly Notices of the Royal Astronomical Society*, vol. 253, pp. 279–286, Nov. 1991.

[246] P. B. Jones, "Type II superconductivity and magnetic flux transport in neutron stars," *Monthly Notices of the Royal Astronomical Society*, vol. 365, pp. 339–344, Jan. 2006.

[247] V. V. Kocharovsky, V. V. Kocharovsky, and V. A. Kukushkin, "Meissner effect in supercoducting cores of neutron stars," *Radiophysics and Quantum Electronics*, vol. 39, pp. 18–22, Jan. 1996.

[248] Y. N. Istomin and I. A. Semerikov, "Magnetic field evolution of accreting neutron stars," *Monthly Notices of the Royal Astronomical Society*, vol. 455, pp. 1938–1945, Jan. 2016.

[249] A. G. Muslimov and A. I. Tsygan, "Neutron Star Superconductivity and Superfluidity and the Decay of Pulsar Magnetic Fields," *Soviet Astronomy Letters*, vol. 11, pp. 80–83, Mar. 1985.

[250] J. G. Elfritz, J. A. Pons, N. Rea, K. Glampedakis, and D. Viganò, "Simulated magnetic field expulsion in neutron star cores," *Monthly Notices of the Royal Astronomical Society*, vol. 456, pp. 4461–4474, Mar. 2016.

[251] K. Y. Ding, K. S. Cheng, and H. F. Chau, "Magnetic field decay from the core of neutron stars - Effects of interpinning of 3P2 neutron superfluid and 1S0 proton superconducting fluid," *The Astrophysical Journal*, vol. 408, pp. 167–178, May 1993.

[252] B. Haskell, K. Glampedakis, and N. Andersson, "A new mechanism for saturating unstable r-modes in neutron stars," *Monthly Notices of the Royal Astronomical Society*, vol. 441, pp. 1662–1668, May 2014.

[253] K. Glampedakis, D. I. Jones, and L. Samuelsson, "Ambipolar diffusion in superfluid neutron stars," *Monthly Notices of the Royal Astronomical Society*, vol. 413, pp. 2021–2030, May 2011.

[254] E. Babaev and M. Speight, "Semi-Meissner state and neither type-I nor type-II superconductivity in multicomponent superconductors," *Physical Review B*, vol. 72, p. 180502, Nov. 2005.

[255] K. B. W. Buckley, M. A. Metlitski, and A. R. Zhitnitsky, "Neutron Stars as Type-I Superconductors," *Physical Review Letters*, vol. 92, p. 151102, Apr. 2004.

[256] J. Charbonneau and A. R. Zhitnitsky, "Novel mechanism for type I superconductivity in neutron stars," *Physical Review C*, vol. 76, p. 015801, July 2007.

[257] A. Sedrakian, "Type-I superconductivity and neutron star precession," *Physical Review D*, vol. 71, p. 083003, Apr. 2005.

[258] P. B. Jones, "Type I and two-gap superconductivity in neutron star magnetism," *Monthly Notices of the Royal Astronomical Society*, vol. 371, pp. 1327–1333, Sept. 2006.

[259] J. A. Pons and U. Geppert, "Confirmation of the occurrence of the Hall instability in the non-linear regime," *Astronomy & Astrophysics*, vol. 513, p. L12, Apr. 2010.

[260] T. S. Wood and R. Hollerbach, "Three Dimensional Simulation of the Magnetic Stress in a Neutron Star Crust," *Physical Review Letters*, vol. 114, p. 191101, May 2015.

[261] V. Graber, N. Andersson, K. Glampedakis, and S. K. Lander, "Magnetic field evolution in superconducting neutron stars," *Monthly Notices of the Royal Astronomical Society*, vol. 453, pp. 671–681, Oct. 2015.

[262] J. P. H. Goedbloed and S. Poedts, *Principles of Magnetohydrodynamics*. Cambridge: Cambridge University Press, 1st ed., 2004.

[263] P. S. Shternin and D. G. Yakovlev, "Shear viscosity in neutron star cores," *Physical Review D*, vol. 78, p. 063006, Sept. 2008.

[264] C. Manuel, J. Tarrus, and L. Tolos, "Bulk viscosity coefficients due to phonons in superfluid neutron stars," *Journal of Cosmology and Astroparticle Physics*, vol. 1307, pp. 1–24, July 2013.

[265] K. Glampedakis and N. Andersson, "Magneto-rotational neutron star evolution: the role of core vortex pinning," *The Astrophysical Journal*, vol. 740, p. L35, Oct. 2011.

[266] S. Vainshtein, S. Chitre, and A. V. Olinto, "Rapid dissipation of magnetic fields due to the Hall current," *Physical Review E*, vol. 61, pp. 4422–4430, Apr. 2000.

[267] J. Braithwaite, "From pulsar scintillations to coronal heating: discontinuities in magnetohydrodynamics," *Monthly Notices of the Royal Astronomical Society*, vol. 450, pp. 3201–3210, May 2015.

[268] J. A. Pons, J. A. Miralles, and U. Geppert, "Magneto-thermal evolution of neutron stars," *Astronomy & Astrophysics*, vol. 216, pp. 207–216, Mar. 2009.

[269] D. Konenkov and U. Geppert, "The evolution of the core and surface magnetic fields in isolated neutron stars," *Monthly Notices of the Royal Astronomical Society*, vol. 325, pp. 426–434, July 2001.

[270] M. Hogg, *Neutron Stars and their Terrestrial Analogues*. Phd thesis, University of Southampton, Jan. 2014.

[271] V. Graber, N. Andersson, and M. Hogg, "Neutron Stars in the Laboratory," *International Journal of Modern Physics D*, in preparation, 2016.

[272] W. Guo, M. La Mantia, D. P. Lathrop, and S. W. van Sciver, "Visualization of two-fluid flows of superfluid helium-4," *Proceedings of the National Academy of Sciences*, vol. 111, pp. 4653–4658, Mar. 2014.

[273] D. Celik and S. W. van Sciver, "Tracer particle generation in superfluid helium through cryogenic liquid injection for particle image velocimetry (PIV) applications," *Experimental Thermal and Fluid Science*, vol. 26, pp. 971–975, Oct. 2002.

[274] G. P. Bewley, D. P. Lathrop, and K. R. Sreenivasan, "Visualization of quantized vortices," *Nature*, vol. 441, p. 588, June 2006.

[275] D. Kivotides, Y. A. Sergeev, and C. F. Barenghi, "Dynamics of solid particles in a tangle of superfluid vortices at low temperatures," *Physics of Fluids*, vol. 20, p. 055105, May 2008.

[276] W. F. Vinen, "Quantum Turbulence: Aspects of Visualization and Homogeneous Turbulence," *Journal of Low Temperature Physics*, vol. 175, pp. 305–316, Apr. 2014.

[277] D. Vollhardt and P. Woelfle, *The Superfluid Phases Of Helium 3*. London: Taylor & Francis, 1st ed., 1990.

[278] D. Vollhardt, "Pair Correlations in Superfluid Helium 3," in *Pair Correlations in Many-Fermion Systems* (V. Z. Kresin, ed.), pp. 205–220, Boston, MA: Springer US, 1998.

[279] P. L. Gammel, H. E. Hall, and J. D. Reppy, "Persistent Currents in Superfluid 3 He-B," *Physical Review Letters*, vol. 52, pp. 121–124, Jan. 1984.

[280] P. L. Gammel, T.-L. Ho, and J. D. Reppy, "Persistent Currents and Dissipation in the A and B Phases of Liquid 3 Helium," *Physical Review Letters*, vol. 55, pp. 2708–2711, Dec. 1985.

[281] O. V. Lounasmaa and E. V. Thuneberg, "Vortices in rotating superfluid 3He," *Proceedings of the National Academy of Sciences*, vol. 96, pp. 7760–7767, July 1999.

[282] R. Blaauwgeers, V. B. Eltsov, M. Krusius, J. J. Ruohio, R. Schanen, and G. E. Volovik, "Double-quantum vortex in superfluid 3He-A," *Nature*, vol. 404, pp. 471–473, Mar. 2000.

[283] K. Masuda and M. Nitta, "Magnetic properties of quantized vortices in neutron 3P2 superfluids in neutron stars," *Physical Review C*, vol. 93, p. 035804, Mar. 2016.

[284] H. E. Hall, "The Angular Acceleration of Liquid Helium II," *Philosophical Transactions of the Royal Society A: Mathematical, Physical and Engineering Sciences*, vol. 250, pp. 359–385, Dec. 1957.

[285] R. H. Walmsley and C. T. Lane, "Angular Momentum of Liquid Helium," *Physical Review*, vol. 112, pp. 1041–1047, Nov. 1958.

[286] J. S. Tsakadze and S. J. Tsakadze, "Relaxation phenomena at accelaration of rotation of a spherical vessel with helium II and relaxation in pulsars," *Physics Letters A*, vol. 41, pp. 197–199, Sept. 1972.

[287] J. S. Tsakadze and S. J. Tsakadze, "Measurement of the relaxation time on acceleration of vessels with helium II and superfluidity in pulsars," *Soviet Physics JETP*, vol. 37, pp. 918–921, Nov. 1973.

[288] J. S. Tsakadze and S. J. Tsakadze, "On the problem of relaxation time determination in superfluids when their rotation is accelerated," *Physics Letters A*, vol. 47, pp. 477–478, May 1974.

[289] J. S. Tsakadze and S. J. Tsakadze, "Properties of slowly rotating helium II and the superfluidity of pulsars," *Journal of Low Temperature Physics*, vol. 39, pp. 649–688, June 1980.

[290] A. Reisenegger, "The spin-up problem in Helium II," *Journal of Low Temperature Physics*, vol. 92, pp. 77–106, July 1993.

[291] J. S. Tsakadze and Z. S. Nadirashvili, "Investigation of the properties of a rotating He3-He4 solution by the oscillating-disk method," *Soviet Physics JETP*, vol. 45, pp. 96–100, Jan. 1977.

[292] C. A. van Eysden and A. Melatos, "Spin Down of Superfluid-Filled Vessels: Theory Versus Experiment," *Journal of Low Temperature Physics*, vol. 165, pp. 1–14, Oct. 2011.

[293] C. A. van Eysden and A. Melatos, "Spin-up of a two-component superfluid: self-consistent container feedback," *Journal of Fluid Mechanics*, vol. 744, pp. 89–110, Apr. 2014.

[294] C. F. Barenghi, R. J. Donnelly, and W. F. Vinen, "Friction on quantized vortices in helium II. A review," *Journal of Low Temperature Physics*, vol. 52, pp. 189–247, Aug. 1983.

[295] W. F. Vinen and J. J. Niemela, "Quantum Turbulence," *Journal of Low Temperature Physics*, vol. 128, pp. 167–231, Sept. 2002.

[296] A. P. Finne, T. Araki, R. Blaauwgeers, V. B. Eltsov, N. B. Kopnin, M. Krusius, L. Skrbek, M. Tsubota, and G. E. Volovik, "An intrinsic velocity-independent criterion for superfluid turbulence.," *Nature*, vol. 424, pp. 1022–1025, Aug. 2003.

[297] P. Mathieu, A. Serra, and Y. Simon, "Critical-region measurements of the mutual-friction parameters in rotating He II," *Physical Review B*, vol. 14, pp. 3753–3761, Nov. 1976.

[298] E. B. Sonin, "Vortex oscillations and hydrodynamics of rotating superfluids," *Reviews of Modern Physics*, vol. 59, pp. 87–155, Jan. 1987.

[299] H. E. Hall, P. L. Gammel, and J. D. Reppy, "Superfluid Dissipation in Rotating 3He-B," *Physical Review Letters*, vol. 52, pp. 1701–1704, May 1984.

[300] M. Krusius, J. S. Korhonen, Y. Kondo, and E. B. Sonin, "Collective motion of quantized vortex lines in rotating superfluid 3He-B," *Physical Review B*, vol. 47, pp. 15113–15144, June 1993.

[301] T. D. C. Bevan, A. J. Manninen, J. B. Cook, A. J. Armstrong, J. R. Hook, and H. E. Hall, "Vortex Mutual Friction in Rotating Superfluid 3 He-B," *Physical Review Letters*, vol. 74, pp. 750–753, Jan. 1995.

[302] T. D. C. Bevan, A. J. Manninen, J. B. Cook, H. Alles, J. R. Hook, and H. E. Hall, "Vortex Mutual Friction in Superfluid 3He," *Journal of Low Temperature Physics*, vol. 109, pp. 423–459, Nov. 1997.

[303] D. S. Greywall, "3He specific heat and thermometry at millikelvin temperatures," *Physical Review B*, vol. 33, pp. 7520–7538, June 1986.

[304] N. B. Kopnin, "Vortex dynamics and mutual friction in superconductors and Fermi superfluids," *Reports on Progress in Physics*, vol. 65, pp. 1633–1678, Nov. 2002.

[305] T. A. Alvesalo, H. K. Collan, M. T. Loponen, O. V. Lounasmaa, and M. C. Veuro, "The viscosity and some related properties of liquid 3He at the melting curve between 1 and 100 mK," *Journal of Low Temperature Physics*, vol. 19, pp. 1–37, Apr. 1975.

[306] C. N. Archie, T. A. Alvesalo, J. D. Reppy, and R. C. Richardson, "Normal Fluid Density of Liquid 3He-B," *Physical Review Letters*, vol. 43, pp. 139–143, July 1979.

[307] E. B. Sonin, "Mutual friction force in rotating helium II at low temperatures and near the Lambda point," *Journal of Low Temperature Physics*, vol. 42, pp. 417–432, Mar. 1981.

[308] J. Rysti, J. T. Tuoriniemi, and A. J. Salmela, "Effective 3He interactions in dilute 3He-4He mixtures," *Physical Review B*, vol. 85, p. 134529, Apr. 2012.

[309] M. Tsubota, K. Kasamatsu, and M. Kobayashi, "Quantized vortices in superfluid helium and atomic Bose-Einstein condensates," in *Novel Superfluids* (K.-H. Bennemann and J. B. Ketterson, eds.), vol. 1, ch. 3, pp. 156–252, Oxford: Oxford University Press, Feb. 2013.

[310] V. P. Mineev, M. M. Salomaa, and O. V. Lounasmaa, "Superfluid 3He in rotation," *Nature*, vol. 324, pp. 333–340, Nov. 1986.

[311] M. Lesieur, *Turbulence in Fluids*, vol. 84 of *Fluid Mechanics and its Applications*. Dordrecht: Springer Netherlands, 4 ed., 2008.

[312] D. K. Cheng, M. W. Cromar, and R. J. Donnelly, "Influence of an Axial Heat Current on Negative-Ion Trapping in Rotating Helium II," *Physical Review Letters*, vol. 31, pp. 433–436, Aug. 1973.

[313] M. Tsubota, C. F. Barenghi, T. Araki, and A. Mitani, "Instability of vortex array and transitions to turbulence in rotating helium II," *Physical Review B*, vol. 69, p. 134515, Apr. 2004.

[314] J. Maurer and P. Tabeling, "Local investigation of superfluid turbulence," *Europhysics Letters (EPL)*, vol. 43, pp. 29–34, July 1998.

[315] S. R. Stalp, L. Skrbek, and R. J. Donnelly, "Decay of Grid Turbulence in a Finite Channel," *Physical Review Letters*, vol. 82, pp. 4831–4834, June 1999.

[316] S. R. Stalp, J. J. Niemela, W. F. Vinen, and R. J. Donnelly, "Dissipation of grid turbulence in helium II," *Physics of Fluids*, vol. 14, pp. 1377–1379, Apr. 2002.

[317] C. F. Barenghi, V. S. L'vov, and P.-E. Roche, "Experimental, numerical, and analytical velocity spectra in turbulent quantum fluid," *Proceedings of the National Academy of Sciences*, vol. 111, pp. 4683–4690, Mar. 2014.

[318] M. S. Paoletti, M. E. Fisher, K. R. Sreenivasan, and D. P. Lathrop, "Velocity Statistics Distinguish Quantum Turbulence from Classical Turbulence," *Physical Review Letters*, vol. 101, p. 154501, Oct. 2008.

[319] P. M. Walmsley, D. E. Zmeev, F. Pakpour, and A. I. Golov, "Dynamics of quantum turbulence of different spectra," *Proceedings of the National Academy of Sciences*, vol. 111, pp. 4691–4698, Mar. 2014.

[320] E. Fonda, D. P. Meichle, N. T. Ouellette, S. Hormoz, and D. P. Lathrop, "Direct observation of Kelvin waves excited by quantized vortex reconnection," *Proceedings of the National Academy of Sciences*, vol. 111, pp. 4707–4710, Mar. 2014.

[321] S. N. Burmistrov, L. B. Dubovskii, and V. L. Tsymbalenko, "Rayleigh-Taylor instability of crystallization waves at the superfluid-solid 4He interface," *Physical Review E*, vol. 79, p. 051606, May 2009.

[322] V. B. Eltsov, A. I. Golov, R. de Graaf, R. Hänninen, M. Krusius, V. S. L'vov, and R. E. Solntsev, "Quantum Turbulence in a Propagating Superfluid Vortex Front," *Physical Review Letters*, vol. 99, p. 265301, Dec. 2007.

[323] D. I. Bradley, S. N. Fisher, A. M. Guénault, R. P. Haley, S. O'Sullivan, G. R. Pickett, and V. Tsepelin, "Fluctuations and Correlations of Pure Quantum Turbulence in Superfluid 3He-B," *Physical Review Letters*, vol. 101, p. 065302, Aug. 2008.

[324] A. P. Finne, S. Boldarev, V. B. Eltsov, and M. Krusius, "Measurement of Turbulence in Superfluid 3He-B," *Journal of Low Temperature Physics*, vol. 136, pp. 249–279, Sept. 2004.

[325] V. B. Eltsov, R. de Graaf, P. J. Heikkinen, J. J. Hosio, R. Hänninen, M. Krusius, and V. S. L'vov, "Stability and Dissipation of Laminar Vortex Flow in Superfluid 3He-B," *Physical Review Letters*, vol. 105, p. 125301, Sept. 2010.

[326] A. P. Finne, V. B. Eltsov, G. Eska, R. Hänninen, J. Kopu, M. Krusius, E. V. Thuneberg, and M. Tsubota, "Vortex Multiplication in Applied Flow: A Precursor to Superfluid Turbulence," *Physical Review Letters*, vol. 96, p. 085301, Feb. 2006.

[327] G. E. Volovik, "On the Kelvin-Helmholtz instability in superfluids," *Journal of Experimental and Theoretical Physics Letters*, vol. 75, pp. 418–422, Apr. 2002.

[328] D. A. Abanin, "Surface instability of a multicomponent condensate and Andreev-Bashkin effect," *Journal of Experimental and Theoretical Physics Letters*, vol. 77, pp. 191–195, Feb. 2003.

[329] A. Mastrano and A. Melatos, "Kelvin-Helmholtz instability and circulation transfer at an isotropic-anisotropic superfluid interface in a neutron star," *Monthly Notices of the Royal Astronomical Society*, vol. 361, pp. 927–941, Aug. 2005.

[330] M. Ruderman and P. G. Sutherland, "Rotating Superfluid in Neutron Stars," *The Astrophysical Journal*, vol. 190, pp. 137–139, May 1974.

[331] C. Peralta, A. Melatos, M. Giacobello, and A. Ooi, "Global Three-dimensional Flow of a Neutron Superfluid in a Spherical Shell in a Neutron Star," *The Astrophysical Journal*, vol. 635, pp. 1224–1232, Dec. 2005.

[332] C. Peralta, A. Melatos, M. Giacobello, and A. Ooi, "Transitions between Turbulent and Laminar Superfluid Vorticity States in the Outer Core of a Neutron Star," *The Astrophysical Journal*, vol. 651, pp. 1079–1091, Nov. 2006.

[333] D. I. Jones and N. Andersson, "Freely precessing neutron stars: model and observations," *Monthly Notices of the Royal Astronomical Society*, vol. 324, pp. 811–824, July 2001.

[334] L. Lindblom and G. Mendell, "Does gravitational radiation limit the angular velocities of superfluid neutron stars," *The Astrophysical Journal*, vol. 444, pp. 804–809, May 1995.

[335] B. Link, "Instability of superfluid flow in the neutron star core," *Monthly Notices of the Royal Astronomical Society*, vol. 421, pp. 2682–2691, Apr. 2012.

[336] A. Melatos and B. Link, "Pulsar timing noise from superfluid turbulence," *Monthly Notices of the Royal Astronomical Society*, vol. 437, pp. 21–31, Nov. 2013.

[337] N. Andersson, G. L. Comer, and R. Prix, "Are Pulsar Glitches Triggered by a Superfluid Two-Stream Instability?," *Physical Review Letters*, vol. 90, p. 091101, Mar. 2003.

[338] N. Andersson, G. L. Comer, and R. Prix, "The superfluid two-stream instability," *Monthly Notices of the Royal Astronomical Society*, vol. 354, pp. 101–110, Oct. 2004.

[339] N. Andersson and G. L. Comer, "On the dynamics of superfluid neutron star cores," *Monthly Notices of the Royal Astronomical Society*, vol. 328, pp. 1129–1143, Dec. 2001.

[340] N. Andersson, K. Glampedakis, and M. Hogg, "Superfluid instability of r-modes in "differentially rotating" neutron stars," *Physical Review D*, vol. 87, p. 063007, Mar. 2013.

[341] M. Chan, N. Mulders, and J. Reppy, "Helium in Aerogel," *Physics Today*, vol. 49, pp. 30–37, Aug. 1996.

[342] W. P. Halperin and J. A. Sauls, "Helium-Three in Aerogel," *arXiv preprint*, pp. 1–10, Aug. 2004.

[343] J. V. Porto and J. M. Parpia, "Superfluid 3He in Aerogel," *Physical Review Letters*, vol. 74, pp. 4667–4670, June 1995.

[344] D. T. Sprague, T. M. Haard, J. B. Kycia, M. R. Rand, Y. Lee, P. J. Hamot, and W. P. Halperin, "Homogeneous Equal-Spin Pairing Superfluid State of 3He in Aerogel," *Physical Review Letters*, vol. 75, pp. 661–664, July 1995.

[345] R. G. Bennett, N. Zhelev, E. N. Smith, J. Pollanen, W. P. Halperin, and J. M. Parpia, "Modification of the 3He Phase Diagram by Anisotropic Disorder," *Physical Review Letters*, vol. 107, p. 235504, Nov. 2011.

[346] J. Pollanen, J. I. A. Li, C. A. Collett, W. J. Gannon, W. P. Halperin, and J. A. Sauls, "New chiral phases of superfluid 3He stabilized by anisotropic silica aerogel," *Nature Physics*, vol. 8, pp. 317–320, Feb. 2012.

[347] F. Chevy and J. Dalibard, "Bose-Einstein condensation of atomic gases," in *Novel Superfluids* (K.-H. Bennemann and J. B. Ketterson, eds.), vol. 1, ch. 7, pp. 398–428, Oxford: Oxford University Press, Feb. 2013.

[348] C. Raman, M. Köhl, R. Onofrio, D. S. Durfee, C. E. Kuklewicz, Z. Hadzibabic, and W. Ketterle, "Evidence for a Critical Velocity in a Bose-Einstein Condensed Gas," *Physical Review Letters*, vol. 83, pp. 2502–2505, Sept. 1999.

[349] D. S. Jin, J. R. Ensher, M. R. Matthews, C. E. Wieman, and E. A. Cornell, "Collective Excitations of a Bose-Einstein Condensate in a Dilute Gas," *Physical Review Letters*, vol. 77, pp. 420–423, July 1996.

[350] M. R. Andrews, D. M. Kurn, H.-J. Miesner, D. S. Durfee, C. G. Townsend, S. Inouye, and W. Ketterle, "Propagation of Sound in a Bose-Einstein Condensate," *Physical Review Letters*, vol. 79, pp. 553–556, July 1997.

[351] V. B. Shenoy and T.-L. Ho, "First and Second Sound Modes of a Bose-Einstein Condensate in a Harmonic Trap," *Physical Review Letters*, vol. 80, pp. 3895–3898, May 1998.

[352] C. J. Myatt, E. A. Burt, R. W. Ghrist, E. A. Cornell, and C. E. Wieman, "Production of Two Overlapping Bose-Einstein Condensates by Sympathetic Cooling," *Physical Review Letters*, vol. 78, pp. 586–589, Jan. 1997.

[353] T.-L. Ho and V. B. Shenoy, "Binary Mixtures of Bose Condensates of Alkali Atoms," *Physical Review Letters*, vol. 77, pp. 3276–3279, Oct. 1996.

[354] K. Kasamatsu, M. Tsubota, and M. Ueda, "Vortices in Multicomponent Bose-Einstein Condensates," *International Journal of Modern Physics B*, vol. 19, pp. 1835–1904, Apr. 2005.

[355] S. J. Woo, S. Choi, L. O. Baksmaty, and N. P. Bigelow, "Dynamics of vortex matter in rotating two-species Bose-Einstein condensates," *Physical Review A*, vol. 75, p. 031604, Mar. 2007.

[356] R. Navarro, R. Carretero-González, and P. G. Kevrekidis, "Phase separation and dynamics of two-component Bose-Einstein condensates," *Physical Review A*, vol. 80, p. 023613, Aug. 2009.

[357] S. B. Papp, J. M. Pino, and C. E. Wieman, "Tunable Miscibility in a Dual-Species Bose-Einstein Condensate," *Physical Review Letters*, vol. 101, p. 040402, July 2008.

[358] D. S. Hall, M. R. Matthews, J. R. Ensher, C. E. Wieman, and E. A. Cornell, "Dynamics of Component Separation in a Binary Mixture of Bose-Einstein Condensates," *Physical Review Letters*, vol. 81, pp. 1539–1542, Aug. 1998.

[359] P. Ao and S. T. Chui, "Binary Bose-Einstein condensate mixtures in weakly and strongly segregated phases," *Physical Review A*, vol. 58, pp. 4836–4840, Dec. 1998.

[360] M. A. Hoefer, M. J. Ablowitz, I. Coddington, E. A. Cornell, P. Engels, and V. Schweikhard, "Dispersive and classical shock waves in Bose-Einstein condensates and gas dynamics," *Physical Review A*, vol. 74, p. 023623, Aug. 2006.

[361] M.-O. Mewes, M. R. Andrews, N. J. van Druten, D. M. Kurn, D. S. Durfee, C. G. Townsend, and W. Ketterle, "Collective Excitations of a Bose-Einstein Condensate in a Magnetic Trap," *Physical Review Letters*, vol. 77, pp. 988–991, Aug. 1996.

[362] E. A. Cornell and C. E. Wieman, "Nobel Lecture: Bose-Einstein condensation in a dilute gas, the first 70 years and some recent experiments," *Reviews of Modern Physics*, vol. 74, pp. 875–893, July 2002.

[363] P. O. Fedichev, G. V. Shlyapnikov, and J. T. M. Walraven, "Damping of Low-Energy Excitations of a Trapped Bose-Einstein Condensate at Finite Temperatures," *Physical Review Letters*, vol. 80, pp. 2269–2272, Mar. 1998.

[364] V. W. Liu, "Theoretical Study of the Damping of Collective Excitations in a Bose-Einstein Condensate," *Physical Review Letters*, vol. 79, pp. 4056–4059, Nov. 1997.

[365] V. M. Kaurov, A. B. Kuklov, and A. E. Meyerovich, "Drag Effect and Topological Complexes in Strongly Interacting Two-Component Lattice Superfluids," *Physical Review Letters*, vol. 95, p. 090403, Aug. 2005.

[366] P. P. Hofer, C. Bruder, and V. M. Stojanović, "Superfluid drag of two-species Bose-Einstein condensates in optical lattices," *Physical Review A*, vol. 86, p. 033627, Sept. 2012.

[367] N. Gemelke and C. Chin, "Atomic Bose fluids in optical lattices," in *Novel Superfluids* (K.-H. Bennemann and J. B. Ketterson, eds.), vol. 2, ch. 16, pp. 159–192, Oxford: Oxford University Press, Nov. 2014.

[368] C. Chin, R. Grimm, P. Julienne, and E. Tiesinga, "Feshbach resonances in ultracold gases," *Reviews of Modern Physics*, vol. 82, pp. 1225–1286, Apr. 2010.

[369] H. Feshbach, "Unified theory of nuclear reactions," *Annals of Physics*, vol. 5, pp. 357–390, Dec. 1958.

[370] E. Tiesinga, B. J. Verhaar, and H. T. C. Stoof, "Threshold and resonance phenomena in ultracold ground-state collisions," *Physical Review A*, vol. 47, pp. 4114–4122, May 1993.

[371] S. Inouye, M. R. Andrews, J. Stenger, H.-J. Miesner, D. M. Stamper-Kurn, and W. Ketterle, "Observation of Feshbach resonances in a Bose-Einstein condensate," *Nature*, vol. 392, pp. 151–154, Mar. 1998.

[372] P. Courteille, R. S. Freeland, D. J. Heinzen, F. A. van Abeelen, and B. J. Verhaar, "Observation of a Feshbach Resonance in Cold Atom Scattering," *Physical Review Letters*, vol. 81, pp. 69–72, July 1998.

[373] J. L. Roberts, N. R. Claussen, J. P. Burke, C. H. Greene, E. A. Cornell, and C. E. Wieman, "Resonant Magnetic Field Control of Elastic Scattering in Cold 85Rb," *Physical Review Letters*, vol. 81, pp. 5109–5112, Dec. 1998.

[374] J. L. Roberts, N. R. Claussen, S. L. Cornish, E. A. Donley, E. A. Cornell, and C. E. Wieman, "Controlled Collapse of a Bose-Einstein Condensate," *Physical Review Letters*, vol. 86, pp. 4211–4214, May 2001.

[375] E. A. Donley, N. R. Claussen, S. L. Cornish, J. L. Roberts, E. A. Cornell, and C. E. Wieman, "Dynamics of collapsing and explosing Bose-Einstein condensates," *Nature*, vol. 412, pp. 295–299, July 2001.

[376] N. R. Cooper, "Rapidly rotating atomic gases," *Advances in Physics*, vol. 57, pp. 539–616, Nov. 2008.

[377] D. A. Butts and D. S. Rokhsar, "Predicted signatures of rotating Bose-Einstein condensates," *Nature*, vol. 397, pp. 327–329, Jan. 1999.

[378] J. W. Reijnders and R. A. Duine, "Pinning of Vortices in a Bose-Einstein Condensate by an Optical Lattice," *Physical Review Letters*, vol. 93, p. 060401, Aug. 2004.

[379] S. Tung, V. Schweikhard, and E. A. Cornell, "Observation of Vortex Pinning in Bose-Einstein Condensates," *Physical Review Letters*, vol. 97, p. 240402, Dec. 2006.

[380] M. P. Mink, C. M. Smith, and R. A. Duine, "Vortex-lattice pinning in two-component Bose-Einstein condensates," *Physical Review A*, vol. 79, p. 013605, Jan. 2009.

[381] P. Bak, C. Tang, and K. Wiesenfeld, "Self-organized criticality," *Physical Review A*, vol. 38, pp. 364–374, July 1988.

[382] L. Warszawski and A. Melatos, "Gravitational-wave bursts and stochastic background from superfluid vortex avalanches during pulsar glitches," *Monthly Notices of the Royal Astronomical Society*, vol. 423, pp. 2058–2074, July 2012.

[383] J. Dunningham, K. Burnett, and W. D. Phillips, "Bose-Einstein condensates and precision measurements," *Philosophical Transactions of the Royal Society A: Mathematical, Physical and Engineering Sciences*, vol. 363, pp. 2165–2175, Sept. 2005.

[384] R. Onofrio, C. Raman, J. M. Vogels, J. R. Abo-Shaeer, A. P. Chikkatur, and W. Ketterle, "Observation of Superfluid Flow in a Bose-Einstein Condensed Gas," *Physical Review Letters*, vol. 85, pp. 2228–2231, Sept. 2000.

[385] C. Ryu, M. Andersen, P. Cladé, V. Natarajan, K. Helmerson, and W. D. Phillips, "Observation of Persistent Flow of a Bose-Einstein Condensate in a Toroidal Trap," *Physical Review Letters*, vol. 99, p. 260401, Dec. 2007.

[386] P. Engels and C. Atherton, "Stationary and Nonstationary Fluid Flow of a Bose-Einstein Condensate Through a Penetrable Barrier," *Physical Review Letters*, vol. 99, p. 160405, Oct. 2007.

[387] V. Hakim, "Nonlinear Schrödinger flow past an obstacle in one dimension," *Physical Review E*, vol. 55, pp. 2835–2845, Mar. 1997.

[388] E. A. L. Henn, J. A. Seman, G. Roati, K. M. F. Magalhães, and V. S. Bagnato, "Emergence of Turbulence in an Oscillating Bose-Einstein Condensate," *Physical Review Letters*, vol. 103, p. 045301, July 2009.

[389] M. Kobayashi and M. Tsubota, "Quantum turbulence in a trapped Bose-Einstein condensate," *Physical Review A*, vol. 76, p. 045603, Oct. 2007.

[390] O. M. Maragò, S. A. Hopkins, J. Arlt, E. Hodby, G. Hechenblaikner, and C. J. Foot, "Observation of the Scissors Mode and Evidence for Superfluidity of a Trapped Bose-Einstein Condensed Gas," *Physical Review Letters*, vol. 84, pp. 2056–2059, Mar. 2000.

[391] N. G. Parker and C. S. Adams, "Emergence and Decay of Turbulence in Stirred Atomic Bose-Einstein Condensates," *Physical Review Letters*, vol. 95, p. 145301, Sept. 2005.

[392] R. Zamora-Zamora, O. Adame-Arana, and V. Romero-Rochín, "Macroscopic Excitations in Confined Bose-Einstein Condensates, Searching for Quantum Turbulence," *Journal of Low Temperature Physics*, vol. 180, pp. 109–125, July 2015.

[393] A. C. White, C. F. Barenghi, N. P. Proukakis, A. J. Youd, and D. H. Wacks, "Nonclassical Velocity Statistics in a Turbulent Atomic Bose-Einstein Condensate," *Physical Review Letters*, vol. 104, p. 075301, Feb. 2010.

[394] C. K. Law, C. M. Chan, P. T. Leung, and M.-C. Chu, "Critical velocity in a binary mixture of moving Bose condensates," *Physical Review A*, vol. 63, p. 063612, May 2001.

[395] M. Abad, A. Recati, S. Stringari, and F. Chevy, "Counter-flow instability of a quantum mixture of two superfluids," *The European Physical Journal D*, vol. 69, p. 126, May 2015.

[396] H. Takeuchi, S. Ishino, and M. Tsubota, "Binary Quantum Turbulence Arising from Countersuperflow Instability in Two-Component Bose-Einstein Condensates," *Physical Review Letters*, vol. 105, p. 205301, Nov. 2010.

[397] C. Hamner, J. J. Chang, P. Engels, and M. A. Hoefer, "Generation of Dark-Bright Soliton Trains in Superfluid-Superfluid Counterflow," *Physical Review Letters*, vol. 106, p. 065302, Feb. 2011.

[398] M. A. Hoefer, J. J. Chang, C. Hamner, and P. Engels, "Dark-dark solitons and modulational instability in miscible two-component Bose-Einstein condensates," *Physical Review A*, vol. 84, p. 041605, Oct. 2011.

[399] I. Corro, R. G. Scott, and A. M. Martin, "Dynamics of two-component Bose-Einstein condensates in rotating traps," *Physical Review A*, vol. 80, p. 033609, Sept. 2009.

[400] D. Kobyakov, A. Bezett, E. Lundh, M. Marklund, and V. Bychkov, "Turbulence in binary Bose-Einstein condensates generated by highly nonlinear Rayleigh-Taylor and Kelvin-Helmholtz instabilities," *Physical Review A*, vol. 89, p. 013631, Jan. 2014.

[401] S. Gautam and D. Angom, "Rayleigh-Taylor instability in binary condensates," *Physical Review A*, vol. 81, p. 053616, May 2010.

[402] J. Stenger, S. Inouye, D. M. Stamper-Kurn, H.-J. Miesner, A. P. Chikkatur, and W. Ketterle, "Spin domains in ground-state Bose-Einstein condensates," *Nature*, vol. 396, pp. 345–348, Nov. 1998.

[403] K. Fujimoto and M. Tsubota, "Counterflow instability and turbulence in a spin-1 spinor Bose-Einstein condensate," *Physical Review A*, vol. 85, p. 033642, Mar. 2012.

[404] B. Villaseñor, R. Zamora-Zamora, D. Bernal, and V. Romero-Rochín, "Quantum turbulence by vortex stirring in a spinor Bose-Einstein condensate," *Physical Review A*, vol. 89, p. 033611, Mar. 2014.

[405] M. O. Borgh and J. Ruostekoski, "Topological Interface Engineering and Defect Crossing in Ultracold Atomic Gases," *Physical Review Letters*, vol. 109, p. 015302, July 2012.

[406] M. O. Borgh and J. Ruostekoski, "Topological interface physics of defects and textures in spinor Bose-Einstein condensates," *Physical Review A*, vol. 87, p. 033617, Mar. 2013.

[407] L. A. Sidorenkov, M. K. Tey, R. Grimm, Y.-h. Hou, L. P. Pitaevskii, and S. Stringari, "Second sound and the superfluid fraction in a Fermi gas with resonant interactions," *Nature*, vol. 498, pp. 78–81, May 2013.

[408] M. Greiner, C. A. Regal, and D. S. Jin, "Emergence of a molecular BoseâĂŞEinstein condensate from a Fermi gas," *Nature*, vol. 426, pp. 537–540, Dec. 2003.

[409] S. Jochim, M. Bartenstein, A. Altmeyer, G. Hendl, S. Riedl, C. Chin, J. Hecker Denschlag, and R. Grimm, "Bose-Einstein Condensation of Molecules," *Science*, vol. 302, pp. 2101–2103, Dec. 2003.

[410] M. W. Zwierlein, C. A. Stan, C. H. Schunck, S. M. F. Raupach, S. Gupta, Z. Hadzibabic, and W. Ketterle, "Observation of Bose-Einstein Condensation of Molecules," *Physical Review Letters*, vol. 91, p. 250401, Dec. 2003.

[411] S. Giorgini, L. P. Pitaevskii, and S. Stringari, "Theory of ultracold atomic Fermi gases," *Reviews of Modern Physics*, vol. 80, pp. 1215–1274, Oct. 2008.

[412] M. J. H. Ku, A. T. Sommer, L. W. Cheuk, and M. W. Zwierlein, "Revealing the Superfluid Lambda Transition in the Universal Thermodynamics of a Unitary Fermi Gas," *Science*, vol. 335, pp. 563–567, Feb. 2012.

[413] M. W. Zwierlein, "Superfluidity in ultracold atomic Fermi gases," in *Novel Superfluids* (K.-H. Bennemann and J. B. Ketterson, eds.), vol. 2, ch. 18, pp. 269–422, Oxford: Oxford University Press, Nov. 2014.

[414] J. Joseph, B. Clancy, L. Luo, J. Kinast, A. Turlapov, and J. E. Thomas, "Measurement of Sound Velocity in a Fermi Gas near a Feshbach Resonance," *Physical Review Letters*, vol. 98, p. 170401, Apr. 2007.

[415] A. Gezerlis and J. Carlson, "Strongly paired fermions: Cold atoms and neutron matter," *Physical Review C*, vol. 77, p. 032801, Mar. 2008.

[416] A. Bulgac, M. M. Forbes, and R. Sharma, "Strength of the Vortex-Pinning Interaction from Real-Time Dynamics," *Physical Review Letters*, vol. 110, p. 241102, June 2013.

[417] G. Wlazlowski, A. Bulgac, M. M. Forbes, and K. J. Roche, "Life cycle of superfluid vortices and quantum turbulence in the unitary Fermi gas," *Physical Review A*, vol. 91, p. 031602, Mar. 2015.

[418] M. J. H. Ku, W. Ji, B. Mukherjee, E. Guardado-Sanchez, L. W. Cheuk, T. Yefsah, and M. W. Zwierlein, "Motion of a Solitonic Vortex in the BEC-BCS Crossover," *Physical Review Letters*, vol. 113, p. 065301, Aug. 2014.

[419] I. Ferrier-Barbut, M. Delehaye, S. Laurent, A. T. Grier, M. Pierce, B. S. Rem, F. Chevy, and C. Salomon, "A mixture of Bose and Fermi superfluids," *Science*, vol. 345, pp. 1035–1038, Aug. 2014.

[420] J. J. Kinnunen and G. M. Bruun, "Induced interactions in a superfluid Bose-Fermi mixture," *Physical Review A*, vol. 91, p. 041605, Apr. 2015.

[421] M. Delehaye, S. Laurent, I. Ferrier-Barbut, S. Jin, F. Chevy, and C. Salomon, "Critical Velocity and Dissipation of an Ultracold Bose-Fermi Counterflow," *Physical Review Letters*, vol. 115, p. 265303, Dec. 2015.

[422] Y. Castin, I. Ferrier-Barbut, and C. Salomon, "La vitesse critique de Landau d'une particule dans un superfluide de fermions," *Comptes Rendus Physique*, vol. 16, pp. 241–253, Mar. 2015.

[423] F. Steglich, J. Aarts, C. D. Bredl, W. Lieke, D. Meschede, W. Franz, and H. Schäfer, "Superconductivity in the Presence of Strong Pauli Paramagnetism: CeCu2Si2," *Physical Review Letters*, vol. 43, pp. 1892–1896, Dec. 1979.

[424] J. E. Hirsch, M. B. Maple, and F. Marsiglio, "Superconducting materials classes: Introduction and overview," *Physica C: Superconductivity and its Applications*, vol. 514, pp. 1–8, July 2015.

[425] A. B. Pippard, "An Experimental and Theoretical Study of the Relation between Magnetic Field and Current in a Superconductor," *Proceedings of the Royal Society A: Mathematical, Physical and Engineering Sciences*, vol. 216, pp. 547–568, Feb. 1953.

[426] J. Bardeen, "Theory of the Meissner Effect in Superconductors," *Physical Review*, vol. 97, pp. 1724–1725, Mar. 1955.

[427] J. Bardeen, "Two-Fluid Model of Superconductivity," *Physical Review Letters*, vol. 1, pp. 399–400, Dec. 1958.

[428] D. Linden, T. Orlando, and W. Lyons, "Modified two-fluid model for superconductor surface impedance calculation," *IEEE Transactions on Appiled Superconductivity*, vol. 4, pp. 136–142, Sept. 1994.

[429] C. A. M. dos Santos, C. J. V. Oliveira, M. S. da Luz, A. D. Bortolozo, M. J. R. Sandim, and A. J. S. Machado, "Two-fluid model for transport properties of granular superconductors," *Physical Review B*, vol. 74, p. 184526, Nov. 2006.

[430] A. J. Bray and H. Schmidt, "Collective modes in charged superconductors near Tc," *Solid State Communications*, vol. 17, pp. 1175–1178, Nov. 1975.

[431] C. J. Pethick and H. Smith, "Relaxation and collective motion in superconductors: a two-fluid description," *Annals of Physics*, vol. 119, pp. 133–169, May 1979.

[432] R. V. Carlson and A. M. Goldman, "Propagating Order-Parameter Collective Modes in Superconducting Films," *Physical Review Letters*, vol. 34, pp. 11–15, Jan. 1975.

[433] E. H. Brandt, "The flux-line lattice in superconductors," *Reports on Progress in Physics*, vol. 58, pp. 1465–1594, Nov. 1995.

[434] U. Essmann and H. Träuble, "The direct observation of individual flux lines in type II superconductors," *Physics Letters A*, vol. 24, pp. 526–527, May 1967.

[435] M. C. Marchetti and D. R. Nelson, "Theory of double-sided flux decorations," *Physical Review B*, vol. 52, pp. 7720–7726, Sept. 1995.

[436] I. V. Grigorieva, "Magnetic flux decoration of type-II superconductors," *Superconductor Science and Technology*, vol. 7, pp. 161–176, Apr. 1994.

[437] H. F. Hess, R. B. Robinson, R. C. Dynes, J. M. Valles, and J. V. Waszczak, "Scanning-Tunneling-Microscope Observation of the Abrikosov Flux Lattice and the Density of States near and inside a Fluxoid," *Physical Review Letters*, vol. 62, pp. 214–216, Jan. 1989.

[438] D. C. Peets, J. D. F. Mottershead, B. Wu, I. S. Elfimov, R. Liang, W. N. Hardy, D. A. Bonn, M. Raudsepp, N. J. C. Ingle, and A. Damascelli, "Tl2Ba2CuO6+δ brings spectroscopic probes deep into the overdoped regime of the high-Tc cuprates," *New Journal of Physics*, vol. 9, p. 28, Feb. 2007.

[439] O. B. Hyun, J. R. Clem, and D. K. Finnemore, "Motion of a single superconducting vortex," *Physical Review B*, vol. 40, pp. 175–181, July 1989.

[440] P. Leiderer, J. Boneberg, P. Brüll, V. Bujok, and S. Herminghaus, "Nucleation and growth of a flux instability in superconducting YBa2Cy3O7-x films," *Physical Review Letters*, vol. 71, pp. 2646–2649, Oct. 1993.

[441] H. Suderow, I. Guillamón, J. G. Rodrigo, and S. Vieira, "Imaging superconducting vortex cores and lattices with a scanning tunneling microscope," *Superconductor Science and Technology*, vol. 27, p. 063001, June 2014.

[442] M. Machida and H. Kaburaki, "Structure of Flux Lines in Three-Dimensional Layered Type-II Superconductor: Numerical Experiments," *Physical Review Letters*, vol. 74, pp. 1434–1437, Feb. 1995.

[443] B. Lake, K. Lefmann, N. B. Christensen, G. Aeppli, D. F. McMorrow, H. M. Ronnow, P. Vorderwisch, P. Smeibidl, N. Mangkorntong, T. Sasagawa, M. Nohara, and H. Takagi, "Three-dimensionality of field-induced magnetism in a high-temperature superconductor," *Nature Materials*, vol. 4, pp. 658–662, Sept. 2005.

[444] M. M. Doria, A. R. Antonio, and F. M. Peeters, "Effect of the boundary condition on the vortex patterns in mesoscopic three-dimensional superconductors: Disk and sphere," *Physical Review B - Condensed Matter and Materials Physics*, vol. 75, p. 064505, Feb. 2007.

[445] D. M. Broun and W. A. Huttema, "Effective magnetic penetration depth in superconducting cylinders and spheres with highly anisotropic electrodynamics," *Physical Review B*, vol. 79, p. 094527, Mar. 2009.

[446] S. Vélez, A. García-Santiago, J. M. Hernandez, and J. Tejada, "Rotating magnetic field experiments in a pure superconducting Pb sphere," *Physical Review B*, vol. 80, p. 144502, Oct. 2009.

[447] A. B. Kolton, D. Domínguez, C. J. Olson, and N. Grønbech-Jensen, "Driven vortices in three-dimensional layered superconductors: Dynamical ordering along the c axis," *Physical Review B*, vol. 62, p. R14657, Dec. 2000.

[448] O. M. Auslaender, L. Luan, E. W. J. Straver, J. E. Hoffman, N. C. Koshnick, E. Zeldov, D. A. Bonn, R. Liang, W. N. Hardy, and K. A. Moler, "Mechanics of individual isolated vortices in a cuprate superconductor," *Nature Physics*, vol. 5, pp. 35–39, Jan. 2009.

[449] M. Pleimling and U. C. Täuber, "Relaxation and glassy dynamics in disordered type-II superconductors," *Physical Review B*, vol. 84, p. 174509, Nov. 2011.

[450] A. F. Hildebrandt, "Magnetic Field of a Rotating Superconductor," *Physical Review Letters*, vol. 12, pp. 190–191, Feb. 1964.

[451] A. A. Verheijen, J. M. van Ruitenbeek, R. de Bruyn Ouboter, and L. J. de Jongh, "Measurement of the London moment in two high-temperature superconductors," *Nature*, vol. 345, pp. 418–419, May 1990.

[452] M. A. Sanzari, H. L. Cui, and F. Karwacki, "London moment for heavy-fermion superconductors," *Applied Physics Letters*, vol. 68, p. 3802, June 1996.

[453] V. K. Vlasko-Vlasov, U. Welp, G. W. Crabtree, D. Gunter, V. V. Kabanov, V. I. Nikitenko, and L. M. Paulius, "Meissner holes and turbulent structures in superconductors in unidirectional and rotating fields," *Physical Review B*, vol. 58, pp. 3446–3456, Aug. 1998.

[454] M. Avila, L. Civale, A. Silhanek, R. Ribeiro, O. Lima, and H. Lanza, "Irreversible magnetization under rotating fields and lock-in effect on a ErBa2Cu3O7-δ single crystal with columnar defects," *Physical Review B*, vol. 64, p. 144502, Sept. 2001.

[455] R. Cortés-Maldonado, J. E. Espinosa-Rosales, A. F. Carballo-Sanchez, and F. Pérez-Rodríguez, "Flux-cutting and flux-transport effects in type-II superconductor slabs in a parallel rotating magnetic field," *Low Temperature Physics*, vol. 37, pp. 947–956, Nov. 2011.

[456] C. P. Bean, "Magnetization of Hard Superconductors," *Physical Review Letters*, vol. 8, pp. 250–253, Mar. 1962.

[457] C. P. Bean, "Magnetization of High-Field Superconductors," *Reviews of Modern Physics*, vol. 36, pp. 31–39, Jan. 1964.

[458] Y. B. Kim, C. F. Hempstead, and A. R. Strnad, "Critical Persistent Currents in Hard Superconductors," *Physical Review Letters*, vol. 9, pp. 306–309, Oct. 1962.

[459] S. J. Chapman, "A Hierarchy of Models for Type-II Superconductors," *SIAM Review*, vol. 42, pp. 555–598, Jan. 2000.

[460] E. Altshuler and T. H. Johansen, "Colloquium: Experiments in vortex avalanches," *Reviews of Modern Physics*, vol. 76, pp. 471–487, Apr. 2004.

[461] N. Alfasi, S. Masis, O. Shtempeluk, V. Kochetok, and E. Buks, "Diamond Magnetometry of Meissner Currents in a Superconducting Film," *arXiv preprint*, pp. 1–5, Jan. 2016.

[462] A. M. Campbell and J. E. Evetts, "Flux vortices and transport currents in type II superconductors," *Advances in Physics*, vol. 21, pp. 199–428, Mar. 1972.

[463] D. Dew-Hughes, "Flux pinning mechanisms in type II superconductors," *Philosophical Magazine*, vol. 30, pp. 293–305, Aug. 1974.

[464] G. Blatter, M. V. Feigel'man, V. B. Geshkenbein, A. I. Larkin, and V. M. Vinokur, "Vortices in high-temperature superconductors," *Reviews of Modern Physics*, vol. 66, pp. 1125–1388, Oct. 1994.

[465] P. Martinoli, "Static and dynamic interaction of superconducting vortices with a periodic pinning potential," *Physical Review B*, vol. 17, pp. 1175–1194, Feb. 1978.

[466] V. V. Moshchalkov, L. Gielen, M. Baert, V. Metlushko, G. Neuttiens, C. Strunk, V. Bruyndoncx, X. Qiu, M. Dhalle, K. Temst, C. Potter, R. Jonckheere, L. Stockman, M. van Bael, C. van Haesendonck, and Y. Bruynseraede, "Quantum interference and confinement phenomena in mesoscopic superconducting systems," *Physica Scripta*, vol. T55, pp. 168–176, Jan. 1994.

[467] L. van Look, B. Y. Zhu, R. Jonckheere, B. R. Zhao, Z. X. Zhao, and V. V. Moshchalkov, "Anisotropic vortex pinning in superconductors with a square array of rectangular submicron holes," *Physical Review B*, vol. 66, p. 214511, Dec. 2002.

[468] M. Miura, B. Maiorov, S. A. Baily, N. Haberkorn, J. O. Willis, K. Marken, T. Izumi, Y. Shiohara, and L. Civale, "Mixed pinning landscape in nanoparticle-introduced YGdBa2Cu3Oy films grown by metal organic deposition," *Physical Review B*, vol. 83, p. 184519, May 2011.

[469] J. L. MacManus-Driscoll, S. R. Foltyn, Q. X. Jia, H. Wang, A. Serquis, L. Civale, B. Maiorov, M. E. Hawley, M. P. Maley, and D. E. Peterson, "Strongly enhanced current densities in superconducting coated conductors of YBa2Cu3O7-x+BaZrO3," *Nature Materials*, vol. 3, pp. 439–443, July 2004.

[470] O. V. Dobrovolskiy, E. Begun, M. Huth, V. A. Shklovskij, and M. I. Tsindlekht, "Vortex lattice matching effects in a washboard pinning potential induced by Co nanostripe arrays," *Physica C: Superconductivity*, vol. 471, pp. 449–452, Aug. 2011.

[471] V. Ortalan, M. Herrera, M. W. Rupich, and N. D. Browning, "Three dimensional analyses of flux pinning centers in Dy-doped YBa2Cu3O7-x coated superconductors by STEM tomography," *Physica C: Superconductivity and its Applications*, vol. 469, pp. 2052–2059, Dec. 2009.

[472] I. A. Sadovskyy, A. E. Koshelev, A. Glatz, V. Ortalan, M. W. Rupich, and M. Leroux, "Simulation of the Vortex Dynamics in a Real Pinning Landscape of YBa2Cu3O7-δ Coated Conductors," *Physical Review Applied*, vol. 5, p. 014011, Jan. 2016.

[473] E. V. Thuneberg, J. Kurkijärvi, and D. Rainer, "Elementary-flux-pinning potential in type-II superconductors," *Physical Review B*, vol. 29, pp. 3913–3923, Apr. 1984.

[474] E. V. Thuneberg, "Elementary pinning potentials in superconductors with anisotropic Fermi surface," *Cryogenics*, vol. 29, pp. 236–244, Mar. 1989.

[475] C. J. van der Beek, M. Konczykowski, A. Abal'oshev, I. Abal'osheva, P. Gierlowski, S. J. Lewandowski, M. V. Indenbom, and S. Barbanera, "Strong pinning in high-temperature superconducting films," *Physical Review B*, vol. 66, p. 024523, July 2002.

[476] T. Shapoval, V. Metlushko, M. Wolf, V. Neu, B. Holzapfel, and L. Schultz, "Enhanced pinning of superconducting vortices at circular magnetic dots in the magnetic-vortex state," *Physica C: Superconductivity*, vol. 470, pp. 867–870, Oct. 2010.

[477] S. J. Chapman, "A Mean-Field Model of Superconducting Vortices in Three Dimensions," *SIAM Journal on Applied Mathematics*, vol. 55, pp. 1259–1274, Oct. 1995.

[478] A. I. Larkin and Y. N. Ovchinnikov, "Electrodynamics of inhomogeneous type-II superconductors," *Soviet Physics JETP*, vol. 38, pp. 854–858, Apr. 1974.

[479] A. I. Larkin and Y. N. Ovchinnikov, "Pinning in type II superconductors," *Journal of Low Temperature Physics*, vol. 34, pp. 409–428, Feb. 1979.

[480] H. R. Kerchner, "The statistical summation of weak flux-line pins in type II superconductors," *Journal of Low Temperature Physics*, vol. 50, pp. 337–370, Feb. 1983.

[481] W. R. White, A. Kapitulnik, and M. R. Beasley, "Collective vortex motion in a -MoGe superconducting thin films," *Physical Review Letters*, vol. 70, pp. 670–673, Feb. 1993.

[482] U. Yaron, P. L. Gammel, D. A. Huse, R. N. Kleiman, C. S. Oglesby, E. Bucher, B. Batlogg, D. J. Bishop, K. Mortensen, K. Clausen, C. A. Bolle, and F. De La Cruz, "Neutron Diffraction Studies of Flowing and Pinned Magnetic Flux Lattices in 2H-NbSe2," *Physical Review Letters*, vol. 73, pp. 2748–2751, Nov. 1994.

[483] J. Chandra, M. Manekar, V. K. Sharma, P. Mondal, P. Tiwari, and S. B. Roy, "Pinning and elastic properties of vortex matter in highly strained Nb75Zr25: Analogy with viscous flow of disordered solids," *arXiv preprint*, pp. 1–29, Sept. 2015.

[484] G. W. Crabtree, D. O. Gunter, H. G. Kaper, A. E. Koshelev, G. K. Leaf, and V. M. Vinokur, "Numerical simulations of driven vortex systems," *Physical Review B*, vol. 61, pp. 1446–1455, Jan. 2000.

[485] Y. B. Kim, C. F. Hempstead, and A. R. Strnad, "Flux Creep in Hard Superconductors," *Physical Review*, vol. 131, pp. 2486–2495, Sept. 1963.

[486] P. W. Anderson, "Theory of Flux Creep in Hard Superconductors," *Physical Review Letters*, vol. 9, pp. 309–311, Oct. 1962.

[487] P. W. Anderson and Y. B. Kim, "Hard Superconductivity: Theory of the Motion of Abrikosov Flux Lines," *Reviews of Modern Physics*, vol. 36, pp. 39–43, Jan. 1964.

[488] A. R. Strnad, C. F. Hempstead, and Y. B. Kim, "Dissipative Mechanism in Type-II Superconductors," *Physical Review Letters*, vol. 13, pp. 794–797, Dec. 1964.

[489] W. A. Reed, E. Fawcett, and Y. B. Kim, "Observation of the Hall Effect in Superconductors," *Physical Review Letters*, vol. 14, pp. 790–792, May 1965.

[490] P. G. De Gennes and J. Matricon, "Collective Modes of Vortex Lines in Superconductors of the Second Kind," *Reviews of Modern Physics*, vol. 36, pp. 45–49, Jan. 1964.

[491] W. F. Vinen and A. C. Warren, "Flux flow resistivity in type II superconductors: I. Experimental results," *Proceedings of the Physical Society*, vol. 91, pp. 399–408, June 1967.

[492] N. B. Kopnin, "Forces acting on vortices moving in a pure type II superconductor," *Soviet Physics JETP*, vol. 44, pp. 861–867, Oct. 1976.

[493] Y. B. Kim, C. F. Hempstead, and A. R. Strnad, "Flux-Flow Resistance in Type-II Superconductors," *Physical Review*, vol. 139, pp. A1163–A1172, Aug. 1965.

[494] W. F. Vinen and A. C. Warren, "Flux flow resistivity in type II superconductors: II. Theoretical discussion," *Proceedings of the Physical Society*, vol. 91, pp. 409–421, June 1967.

[495] M. Tinkham, "Viscous Flow of Flux in Type-II Superconductors," *Physical Review Letters*, vol. 13, pp. 804–807, Dec. 1964.

[496] J. Bardeen and M. J. Stephen, "Theory of the Motion of Vortices in Superconductors," *Physical Review*, vol. 140, pp. A1197–A1207, Nov. 1965.

[497] M. M. Cyrot, "Ginzburg-Landau theory for superconductors," *Reports on Progress in Physics*, vol. 36, pp. 103–158, Feb. 1973.

[498] L. Gor'kov and N. Kopnin, "Vortex motion and resistivity of type-ll superconductors in a magnetic field," *Uspekhi Fizicheskih Nauk*, vol. 116, p. 413, July 1975.

[499] G. Blatter, V. B. Geshkenbein, and N. B. Kopnin, "From microscopic theory to Boltzmann kinetic equation: Application to vortex dynamics," *Physical Review B*, vol. 59, pp. 14663–14673, June 1999.

[500] J. R. Clem, "Two-dimensional vortices in a stack of thin superconducting films: A model for high-temperature superconducting multilayers," *Physical Review B*, vol. 43, pp. 7837–7846, Apr. 1991.

[501] J. W. Guikema, H. Bluhm, D. A. Bonn, R. Liang, W. N. Hardy, and K. A. Moler, "Two-dimensional vortex behavior in highly underdoped YBa2Cu3O6+x observed by scanning Hall probe microscopy," *Physical Review B*, vol. 77, p. 104515, Mar. 2008.

[502] M. P. A. Fisher, "Vortex-glass superconductivity: A possible new phase in bulk high-Tc oxides," *Physical Review Letters*, vol. 62, pp. 1415–1418, Mar. 1989.

[503] E. Zeldov, D. Majer, M. Konczykowski, V. B. Geshkenbein, V. M. Vinokur, and H. Shtrikman, "Thermodynamic observation of first-order vortex-lattice melting transition in Bi2Sr2CaCu2O8," *Nature*, vol. 375, pp. 373–376, June 1995.

[504] I. Guillamón, H. Suderow, A. Fernández-Pacheco, J. Sesé, R. Córdoba, J. M. De Teresa, M. R. Ibarra, and S. Vieira, "Direct observation of melting in a two-dimensional superconducting vortex lattice," *Nature Physics*, vol. 5, pp. 651–655, Sept. 2009.

[505] T. Nattermann and S. Scheidl, "Vortex-glass phases in type-II superconductors," *Advances in Physics*, vol. 49, pp. 607–704, July 2000.

[506] O. Bossen and A. Schilling, "Estimates for the thermodynamic signatures of vortex-lattice melting in conventional superconductors," *Physica C: Superconductivity*, vol. 483, pp. 201–206, Dec. 2012.

[507] E. H. Brandt, "Thermal fluctuation and melting of the vortex lattice in oxide superconductors," *Physical Review Letters*, vol. 63, pp. 1106–1109, Sept. 1989.

[508] P. Berghuis and P. H. Kes, "Two-dimensional collective pinning and vortex-lattice melting in a-Nb1-xGex films," *Physical Review B*, vol. 47, pp. 262–272, Jan. 1993.

[509] R. Lortz, F. Lin, N. Musolino, Y. Wang, A. Junod, B. Rosenstein, and N. Toyota, "Thermal fluctuations and vortex melting in the Nb3Sn superconductor from high resolution specific heat measurements," *Physical Review B*, vol. 74, p. 104502, Sept. 2006.

[510] J. R. Clem, "Spiral-Vortex Expansion Instability in Type-II Superconductors," *Physical Review Letters*, vol. 38, pp. 1425–1428, June 1977.

[511] F. Irie, T. Matsushita, S. Otabe, T. Matsuno, and K. Yamafuji, "Critical current density of superconducting NbTa tapes in a longitudinal magnetic field," *Cryogenics*, vol. 29, pp. 317–320, Mar. 1989.

[512] E. H. Brandt, "Longitudinal critical current in type II superconductors. I. Helical vortex instability in the bulk," *Journal of Low Temperature Physics*, vol. 44, pp. 33–57, July 1981.

[513] I. H. Stairs, A. G. Lyne, and S. L. Shemar, "Evidence for free precession in a pulsar," *Nature*, vol. 406, pp. 484–486, Aug. 2000.

[514] T. V. Shabanova, A. G. Lyne, and J. O. Urama, "Evidence for Free Precession in the Pulsar B1642-03," *The Astrophysical Journal*, vol. 552, pp. 321–325, May 2001.

[515] F. Haberl, R. Turolla, C. P. De Vries, S. Zane, J. Vink, M. Méndez, and F. Verbunt, "Evidence for precession of the isolated neutron star RX J0720.4-3125," *Astronomy and Astrophysics*, vol. 451, pp. L17–L21, May 2006.

[516] M. A. R. LeBlanc, S. Celebi, S. X. Wang, and V. Plechácêk, "Cross-flow of flux lines in the weak link regime of high-Tc superconductors," *Physical Review Letters*, vol. 71, pp. 3367–3370, Nov. 1993.

[517] M. A. R. LeBlanc and S. Elebi, "Flux line cutting and cross-flow in a high-Tc superconducting YBCO tube," *Superconductor Science and Technology*, vol. 16, pp. 329–338, Mar. 2003.

[518] J. R. Clem, "Flux-line-cutting losses in type-II superconductors," *Physical Review B*, vol. 26, pp. 2463–2473, Sept. 1982.

[519] M. G. Blamire and J. E. Evetts, "Critical cutting force between flux vortices in a type-II superconductor," *Physical Review B*, vol. 33, pp. 5131–5133, Apr. 1986.

[520] A. Palau, R. Dinner, J. H. Durrell, and M. G. Blamire, "Vortex Breaking and Cutting in Type II Superconductors," *Physical Review Letters*, vol. 101, p. 097002, Aug. 2008.

[521] E. Pardo, J. H. Durrell, and M. G. Blamire, "Vortex deformation and breaking in superconductors: a microscopic description," *Philosophical Magazine*, vol. 87, pp. 4359–4381, Oct. 2007.

[522] A. M. Campbell, "Flux cutting in superconductors," *Superconductor Science and Technology*, vol. 24, p. 091001, Sept. 2011.

[523] K. E. Eliassen, *Investigation of thermo-magnetic instability in superconducting NbN thin-films by automated real-time magneto-optical imaging.* Master thesis, University of Oslo, Sept. 2008.

[524] M. Wertheimer and J. le G. Gilchrist, "Flux jumps in type II superconductors," *Journal of Physics and Chemistry of Solids*, vol. 28, pp. 2509–2524, Jan. 1967.

[525] R. G. Mints and A. L. Rakhmanov, "Magnetic instabilities in hard superconductors," *Soviet Physics Uspekhi*, vol. 20, pp. 249–263, Mar. 1977.

[526] C. J. Olson, C. Reichhardt, and F. Nori, "Superconducting vortex avalanches, voltage bursts, and vortex plastic flow: Effect of the microscopic pinning landscape on the macroscopic properties," *Physical Review B*, vol. 56, pp. 6175–6194, Sept. 1997.

[527] S. Field, J. Witt, F. Nori, and X. Ling, "Superconducting Vortex Avalanches," *Physical Review Letters*, vol. 74, pp. 1206–1209, Feb. 1995.

[528] K. Wiesenfeld, C. Tang, and P. Bak, "A physicist's sandbox," *Journal of Statistical Physics*, vol. 54, pp. 1441–1458, Mar. 1989.

[529] R. A. Richardson, O. Pla, and F. Nori, "Confirmation of the modified Bean model from simulations of superconducting vortices," *Physical Review Letters*, vol. 72, pp. 1268–1271, Feb. 1994.

[530] T. H. Johansen, M. Baziljevich, D. V. Shantsev, P. E. Goa, Y. M. G. pe Rin, W. N. Kang, H. J. Kim, E. M. Choi, M.-S. Kim, and S. I. Lee, "Dendritic magnetic instability in superconducting MgB2 films," *Europhysics Letters (EPL)*, vol. 59, pp. 599–605, Aug. 2002.

[531] P. Mikheenko, J. I. Vestgaarden, S. Chaudhuri, I. J. Maasilta, Y. M. Galperin, and T. H. Johansen, "Metal frame as local protection of superconducting films from thermomagnetic avalanches," *arXiv preprint*, pp. 1–5, Jan. 2016.

[532] J. I. Vestgården, D. V. Shantsev, Y. M. Galperin, and T. H. Johansen, "Lightning in superconductors," *Scientific Reports*, vol. 2, p. 886, Nov. 2012.

[533] R. P. Huebener and R. T. Kampwirth, "Pattern of flux tubes in superconducting lead films," *Journal of Low Temperature Physics*, vol. 15, pp. 47–52, Apr. 1974.

[534] J. Ge, J. Gutierrez, J. Cuppens, and V. V. Moshchalkov, "Quantification of the flux tubes and the stability of stripe pattern in the intermediate state of a type-1 superconducting film," *Physica C: Superconductivity*, vol. 503, pp. 38–41, Aug. 2014.

[535] E. H. Brandt and M. P. Das, "Attractive Vortex Interaction and the Intermediate-Mixed State of Superconductors," *Journal of Superconductivity and Novel Magnetism*, vol. 24, pp. 57–67, Jan. 2011.

[536] E. Babaev, J. Carlström, and M. Speight, "Type-1.5 Superconducting State from an Intrinsic Proximity Effect in Two-Band Superconductors," *Physical Review Letters*, vol. 105, p. 067003, Aug. 2010.

[537] Y. Wang, T. Plackowski, and A. Junod, "Specific heat in the superconducting and normal state (2-300 K, 0-16 T), and magnetic susceptibility of the 38 K superconductor MgB2: evidence for a multicomponent gap," *Physica C: Superconductivity*, vol. 355, pp. 179–193, June 2001.

[538] V. V. Moshchalkov, M. Menghini, T. Nishio, Q. H. Chen, A. V. Silhanek, V. H. Dao, L. F. Chibotaru, N. D. Zhigadlo, and J. Karpinski, "Type-1.5 Superconductivity," *Physical Review Letters*, vol. 102, p. 117001, Mar. 2009.

[539] J. Gutierrez, B. Raes, A. V. Silhanek, L. J. Li, N. D. Zhigadlo, J. Karpinski, J. Tempere, and V. V. Moshchalkov, "Scanning Hall probe microscopy of unconventional vortex patterns in the two-gap MgB2 superconductor," *Physical Review B*, vol. 85, p. 094511, Mar. 2012.

[540] U. Essmann, "Observation of the mixed state," *Physica*, vol. 55, pp. 83–93, Oct. 1971.

[541] J. Hove, S. Mo, and A. Sudbø, "Vortex interactions and thermally induced crossover from type-I to type-II superconductivity," *Physical Review B*, vol. 66, p. 064524, Aug. 2002.

[542] J. Schelten, H. Ullmaier, and W. Schmatz, "Neutron diffraction by vortex lattlices in superconducting Nb and Nb0.73Ta0.27," *Physica Status Solidi (b)*, vol. 48, pp. 619–628, Dec. 1971.

[543] J. Auer and H. Ullmaier, "Magnetic Behavior of Type-II Superconductors with Small Ginzburg-Landau Parameters," *Physical Review B*, vol. 7, pp. 136–145, Jan. 1973.

[544] E. Di Grezia, S. Esposito, and G. Salesi, "Magnetic properties of two-phase superconductors," *Physica C: Superconductivity*, vol. 468, pp. 883–888, June 2008.

[545] L. Komendová, M. V. Milosevic, F. M. Peeters, M. V. Milosevic, and F. M. Peeters, "Soft vortex matter in a type-I/type-II superconducting bilayer," *Physical Review B*, vol. 88, p. 094515, Sept. 2013.

[546] W. E. Lawrence and S. Doniach, "Theory of layer structure superconductors," in *Proceedings of the 12th International Conference on Low Temperature Physics* (E. Kanda, ed.), (Tokyo), pp. 361–362, Academic Press of Japan, 1971.

[547] S. J. Chapman, Q. Du, and M. D. Gunzburger, "On the Lawrence-Doniach and Anisotropic Ginzburg-Landau Models for Layered Superconductors," *SIAM Journal on Applied Mathematics*, vol. 55, pp. 156–174, Feb. 1995.

[548] C. M. Aegerter, H. Keller, S. L. Lee, C. Ager, F. Y. Ogrin, R. Cubitt, E. M. Forgan, W. J. Nutall, P. G. Kealey, S. H. Lloyd, S. T. Johnson, T. M. Riseman, and M. P. Nutley, "Transition from Type-I to Type-II Superconducting Behaviour with Temperature observed by μSR and SANS," *arXiv preprint*, pp. 1–8, May 2003.

[549] P. Cadden-Zimansky and V. Chandrasekhar, "Nonlocal Correlations in Normal-Metal Superconducting Systems," *Physical Review Letters*, vol. 97, p. 237003, Dec. 2006.

[550] R. Mélin, F. S. Bergeret, and A. L. Yeyati, "Self-consistent microscopic calculations for nonlocal transport through nanoscale superconductors," *Physical Review B*, vol. 79, p. 104518, Mar. 2009.

[551] C. J. Lambert and R. Raimondi, "Phase-coherent transport in hybrid superconducting nanostructures," *Journal of Physics: Condensed Matter*, vol. 10, pp. 901–941, Feb. 1998.

[552] F. Liu, M. Mondello, and N. Goldenfeld, "Kinetics of the superconducting transition," *Physical Review Letters*, vol. 66, pp. 3071–3074, June 1991.

[553] A. B. Pippard, "Kinetics of the phase transition in superconductors," *The London, Edinburgh, and Dublin Philosophical Magazine and Journal of Science*, vol. 41, pp. 243–255, Mar. 1950.

[554] J. E. Hirsch, "Dynamics of the normal-superconductor phase transition and the puzzle of the Meissner effect," *Annals of Physics*, vol. 362, pp. 1–23, Nov. 2015.

[555] W. Meissner, F. Schmeissner, and H. Meissner, "Messungen im Übergangsgebiet zur Supraleitung. III," *Zeitschrift für Physik*, vol. 132, pp. 529–543, Oct. 1952.

[556] T. E. Faber, "Creation and Growth of Superconducting Nuclei," *Nature*, vol. 164, pp. 277–278, Aug. 1949.

[557] W. Meissner, "Vorgänge in Supraleitern beim Übergang Normalleitung-Supraleitung," *Die Naturwissenschaften*, vol. 41, pp. 437–440, Oct. 1954.

[558] H. Frahm, S. Ullah, and A. T. Dorsey, "Flux dynamics and the growth of the superconducting phase," *Physical Review Letters*, vol. 66, pp. 3067–3070, June 1991.

[559] W. W. Mullins and R. F. Sekerka, "Stability of a Planar Interface During Solidification of a Dilute Binary Alloy," *Journal of Applied Physics*, vol. 35, p. 444, Feb. 1964.

[560] A. T. Dorsey, "Dynamics of Interfaces in Superconductors," *Annals of Physics*, vol. 233, pp. 248–269, Aug. 1994.

[561] A. D. Hernández and D. Domínguez, "Surface barrier in mesoscopic type-I and type-II superconductors," *Physical Review B*, vol. 65, p. 144529, Apr. 2002.

[562] G. J. Carty, M. Machida, and D. P. Hampshire, "Numerical studies on the effect of normal-metal coatings on the magnetization characteristics of type-II superconductors," *Physical Review B*, vol. 71, p. 144507, Apr. 2005.

[563] M. Martinello, A. Romanenko, M. Checchin, A. . Grassellino, A. C. Crawford, A. Melnychuk, and D. A. Sergatskov, "Cooling Dynamics Through Transition Temperature of Niobium SRF Cavities Captured by Temperature Mapping," *arXiv preprint*, pp. 1–12, Apr. 2015.